



HAL
open science

Structural, petrological and geochronological contribution to intracontinental tectonics of the European Variscan Belt (Sudetes, Vosges Mts)

Etienne Skrzypek

► **To cite this version:**

Etienne Skrzypek. Structural, petrological and geochronological contribution to intracontinental tectonics of the European Variscan Belt (Sudetes, Vosges Mts). Earth Sciences. Université de Strasbourg, 2011. English. NNT: . tel-00773597

HAL Id: tel-00773597

<https://theses.hal.science/tel-00773597>

Submitted on 14 Jan 2013

HAL is a multi-disciplinary open access archive for the deposit and dissemination of scientific research documents, whether they are published or not. The documents may come from teaching and research institutions in France or abroad, or from public or private research centers.

L'archive ouverte pluridisciplinaire **HAL**, est destinée au dépôt et à la diffusion de documents scientifiques de niveau recherche, publiés ou non, émanant des établissements d'enseignement et de recherche français ou étrangers, des laboratoires publics ou privés.

UNIVERSITE DE STRASBOURG

THESE

présentée pour l'obtention du grade de

DOCTEUR ÈS SCIENCES NATURELLES

Spécialité Géologie

par

ETIENNE SKRZYPEK

**Contribution structurale, pétrologique et
géochronologique à la tectonique intracontinentale de
la chaîne hercynienne d'Europe (Sudètes, Vosges)**

Soutenue publiquement le 13 Octobre 2011, devant la Commission d'Examen :

M ^{me} Duchêne Stéphanie	Université Paul Sabatier, Toulouse	Rapporteur externe
M. Burg Jean-Pierre	Eidgenössische Technische Hochschule, Zürich	Rapporteur externe
M. Faure Michel	Université d'Orléans	Examineur
M. Manatschal Gianreto	Université de Strasbourg	Rapporteur interne
M. Żelaźniewicz Andrzej	Instytut Nauk Geologicznych, Wrocław	Examineur
M. Schulmann Karel	Université de Strasbourg	Directeur de thèse
M. Rossi Philippe	Bureau de Recherches Géologiques et Minières, Orléans	Directeur de thèse

SOMMAIRE

Résumé, Abstract, Zusammenfassung, Streszczenie	5
Avant propos	9
Résumé étendu	10
Introduction	39
PART ONE : CONTRIBUTION OF MID-CRUSTAL STRUCTURAL, PETROLOGICAL AND GEOCHRONOLOGICAL RECORDS TO THE UNDERSTANDING OF INTRACONTINENTAL BURIAL AND EXHUMATION PROCESSES (SUDETES)	
Introduction to part one	47
Chapter I – Geological background	49
Chapter II – Structural evolution of the orogenic middle crust	63
Chapter III – Tectono-metamorphic evolution of the orogenic middle crust	79
Chapter IV – Microstructural and petrological constraints from garnet porphyroblasts	119
Chapter V – Chronological constraints	143
Chapter VI – Burial and exhumation processes	159
Summary and conclusions to part one	171
PART TWO : STRUCTURAL, PETROLOGICAL AND GEOCHRONOLOGICAL CHARACTERISATION OF INTRACONTINENTAL TECTONIC PROCESSES IN THE OROGENIC CRUST (VOSGES MOUNTAINS)	
Introduction to part two	179
Chapter I – The significance of Late Devonian ophiolites in the Variscan orogen: a record from the Vosges Klippen Belt	181
Chapter II – The origin of zircon and the significance of U–Pb ages during high-grade metamorphism: a case study from the Variscan orogenic root	209
Chapter III – Geodynamic evolution of the Variscan Vosges Mountains	247
Summary and conclusions to part two	301
Conclusions	305
Bibliographie	315
Remerciements	355
Appendix	359
Liste des figures	399
Liste des tables	403
Liste des annexes	404
Table des matières	405

RÉSUMÉ

La tectonique intracontinentale de la chaîne hercynienne d'Europe est explorée en combinant géologie structurale, pétrologie métamorphique et géochronologie. Cette approche est appliquée à l'étude de différents niveaux de la croûte orogénique dans deux témoins hercyniens – le dôme d'Orlica-Śnieżnik (Sudètes) et les Vosges (NE France) – afin de reconstituer leur évolution paléozoïque. Au Dévonien, l'activité de zones de subduction peut localement aboutir à l'ouverture de bassins d'arrière-arc, mais génère essentiellement un épaissement crustal en domaine intracontinental. Dans les deux massifs, la croûte orogénique se forme alors par amalgamation de portions autochtones et allochtones. La collision dévono-carbonifère est ensuite responsable d'une évolution tectono-métamorphique polyphasée. Au début du Carbonifère inférieur, des transferts verticaux de matière s'opèrent grâce à un plissement d'échelle crustale et juxtaposent ainsi la croûte moyenne enfouie avec la croûte inférieure extrudée. Ce phénomène est remplacé par un aplatissement localisé conduisant à la formation d'une discontinuité intra-orogénique majeure au niveau de la croûte moyenne. Cette discontinuité va permettre un découplage total de la déformation entre croûte supérieure et croûte inférieure, et sa réactivation en régime extensif va favoriser l'exhumation de l'ensemble du système. A la fin du Carbonifère inférieur, l'exhumation est simultanément accommodée par un mécanisme d'amincissement ductile opérant en régime coaxial au cœur de l'orogène et par l'activité de systèmes de détachement fortement non-coaxiaux développés vers les bordures de la chaîne. Dans le cadre de l'orogénèse hercynienne, l'évolution des Sudètes paraît contrôlée par la fermeture du bassin saxothuringien situé au Nord. A l'inverse, le socle vosgien enregistre initialement l'influence des subductions quasi-orthogonales du bassin saxothuringien et de l'océan Paléotéthys avant de subir les effets de la fermeture du système rhénohercynien. Les processus reconnus dans ce travail suggèrent finalement que le caractère de la tectonique intracontinentale n'a que peu varié au cours du Phanérozoïque.

Mots-clés : Tectonique intracontinentale, Orogénèse hercynienne, Dôme d'Orlica-Śnieżnik, Vosges, Géologie structurale, Pétrologie métamorphique, Géochronologie

ABSTRACT

Intracontinental tectonic processes acting during Variscan orogeny are explored using a combination of structural geology, metamorphic petrology and geochronology. This approach is applied to study different levels of the orogenic crust in two Variscan massifs – the Orlica-Śnieżnik Dome (Sudetes) and the Vosges Mountains (NE France) – in order to decipher their Palaeozoic evolution. During the Devonian, the activity of subduction zones may have locally triggered back-arc opening, but more importantly generated crustal thickening within an intracontinental setting. In both massifs, the orogenic crust was consequently formed by the welding of autochthonous and allochthonous portions. During the subsequent Devonian-Carboniferous collision, the orogenic system underwent a polyphase tectono-metamorphic evolution. In the early Lower Carboniferous, vertical material transfers were achieved through crustal-scale folding and led to the juxtaposition of the buried middle crust with the extruded lower crust. It was followed by a localized flattening event which produced a major intra-orogenic boundary zone at mid-crustal level. The presence of such a zone allowed deformation decoupling between the upper and lower crust, and also favoured exhumation of the system during later extensional reactivation. In the late Lower Carboniferous, exhumation was simultaneously accommodated by a ductile thinning mechanism which operated under a coaxial regime in the core of the orogen, and by the activity of highly non-coaxial detachment systems which developed towards the margins of the orogenic belt. In the Variscan framework, the evolution of the Sudetes appears to be controlled by the closure of the Saxothuringian basin. Conversely, the Vosges basement initially recorded the influence of the quasi-orthogonal subduction zones of the Saxothuringian basin and the Palaeotethys Ocean, and later documented closure of the Rhenohercynian basin. The processes recognized in this work finally suggest that the character of intracontinental tectonics has not significantly changed throughout the entire Phanerozoic.

Keywords : intracontinental tectonics, Variscan orogeny, Orlica-Śnieżnik Dome, Vosges Mountains, structural geology, metamorphic petrology, geochronology.

ZUSAMENFASSUNG

Die intrakontinentale Tektonik des variszischen Gebirges wird dank Strukturgeologie, metamorphischer Petrologie und Geochronologie untersucht. Diese Beobachtungen sind für verschiedene Stufen der orogenischen Erdkruste in zwei variszischen Kristallinmassiven – das Orlica-Śnieżnik-Gewölbe (Sudeten) und die Vogesen (NO Frankreich) – benutzt, um die paläozoische Entwicklung beider Massiven herzustellen. Im Devon führen Subduktionszonen teilweise Randmeeröffnung, aber meistens produzieren eine Verdickung der intrakontinentalen Kruste. In beiden Kristallinmassiven wird die orogenische Kruste aus autochthonen und allochthonen Teilen gebildet. Die oberdevonische-unterkarbonische Kollision ist danach für mehrphasige Deformation und Metamorphose verantwortlich. Im früh-Unterkarbon produzieren Falten, die in der ganzen Kruste entwickelt sind, vertikale Bewegungen und legen die mittlere Kruste neben die tiefsten Teile des Orogens. Diese Phase ist von einer Abflachung der mittleren Kruste, die eine wichtige Gliederung der orogenischen Kruste gründet, verfolgt. Später wird die Deformation getrennt und wird nur in der oberen Kruste sichtbar, während die untere Kruste sich schon als ein passiver Sockel verhält. Die folgende Exhumierung entspricht einem Dehnungsmechanismus, das auch dank der intra-orogenischen Gliederung ermöglicht ist. Am Ende des Unterkarbons ist die Exhumierung gleichzeitig durch einen coaxialen duktilen Verdünnungsmechanismus und duktile Abschiebungen ausgeführt. Im Rahmen des variszischen Gebirgsbaues scheint wahrscheinlich die Entwicklung der Sudeten durch den Verschluss des Saxothuringischen Beckens, der im Norden liegt, kontrolliert zu sein. Im Gegenteil dazu entsprechen die Vogesen erst dem Einfluss des Saxothuringischen Beckens und des Paleothetys Ozeans, die quasi-orthogonale Subduktionszonen herstellen. Danach wird der Sockel der Vogesen wegen des Verschlusses des Rhenohercynischen Beckens deformiert. Die Mechanismen, die in dieser Arbeit aufgewiesen sind, schlagen jedoch vor, dass die Eigenschaften der intrakontinentalen tektonischen Prozesse sich im Laufe des Phanerozoikums nur schwach verändert haben.

Stichwörter : intrakontinentale Tektonik, variszische Gebirge, Orlica-Śnieżnik-Gewölbe, Vogesen, Strukturgeologie, metamorphische Petrologie, Geochronologie

STRESZCZENIE

Procesy tektoniki intrakontynentalnej zachodzące podczas orogenezy hercyńskiej są analizowane na podstawie danych z dziedziny geologii strukturalnej, petrologii metamorficznej i geochronologii. Ta metoda jest stosowana do badania różnych poziomów skorupy ziemskiej w dwóch masywach orogenu hercyńskiego – w kopule Orlicy-Śnieżnika w Sudetach (Czechy-Polska) i w Wogezach (Francja) – aby zrekonstruować ich historię paleozoiczną. W dewonie, aktywność stref subdukcji powoduje lokalnie wytworzenie się basenów załukowych, ale przede wszystkim powoduje zgrubienie skorupy ziemskiej na obszarze intrakontynentalnym. W obu masywach, skorupa ziemska jest formowana poprzez amalgamację kawałków allochtonicznych i autochtonicznych. Następnie, kolizja dewońsko-karbońska prowadzi do polifazowej ewolucji tektono-metamorficznej. Na początku wczesnego karbonu, na skutek fałdowania o dużej amplitudzie mają miejsce pionowe ruchy w skorupie ziemskiej, które powodują umieszczenie obok siebie środkowej i dolnej warstwy skorupy. W następstwie tego zjawiska dokonuje się lokalne spłaszczenie w skorupie środkowej, które powoduje wytworzenie się ważnej nieciągłości w orogenie. Obecność tej nieciągłości sprawia, że tylko górna warstwa skorupy ziemskiej jest deformowana podczas następnego fałdowania, ale nie dolna skorupa. Późniejsze mechanizmy ekstensji też opierają się na tej nieciągłości. Pod koniec wczesnego karbonu, ekshumacja całego systemu następuje z powodu procesu spłaszczenia i deformacji współosiowej w sercu orogenu, a także procesu osuwania dolnej skorupy na krawędzi orogenu. W ramach orogenezy hercyńskiej, ewolucja Sudetów wydaje się być opanowana przez zamknięcie basenu Saksoturyngii na północy. Podstawa Wogezów, przeciwnie, podlega wpływowi dwóch subdukcji: basenu Saksoturyngii na zachodzie i Oceanu Paleotetydy na południu, zanim podda się skutkom zamknięcia basenu renohercyńskiego. Mechanizmy opisane w tej pracy, ukazują, że charakter procesów tektoniki intrakontynentalnej tylko nieznacznie zmienił się podczas fanerozoiku.

Słowa kluczowe : tektonika intrakontynentalna, orogeneza hercyńska, kopula Orlicy-Śnieżnika, Wogesy, geologia strukturalna, petrologia metamorficzna, geochronologia.

AVANT PROPOS

Le travail de thèse dont les résultats sont présentés dans ce manuscrit m'a été proposé par P. ROSSI et P. LEDRU du Bureau de Recherches Géologiques et Minières à Orléans (BRGM), et par K. SCHULMANN de l'Université Louis Pasteur de Strasbourg. Le travail de recherche a pu être mené à bien grâce à un soutien financier du BRGM et de la Région Alsace. Le coût des missions de terrain et des diverses analyses a été couvert par le Programme de la carte géologique de France ainsi que par le projet de l'Agence Nationale pour la Recherche 'LFO in orogens'. Ces personnes et organismes sont vivement remerciés pour leur concours.

La rédaction de ce manuscrit de thèse a suivi une structure linéaire, essayant ainsi d'éviter les répétitions inévitablement liées à la simple juxtaposition de communications scientifiques. On pourra tout de même y trouver tout ou partie des publications scientifiques dérivées du travail de thèse, dont la liste est donnée à la suite des références bibliographiques. Cependant, des données n'ayant pas fait l'objet de publications scientifiques sont également présentées, satisfaisant ainsi à la vocation que j'attribue à un manuscrit de thèse.

L'ouvrage est divisé en deux parties : la première est consacrée aux travaux menés dans le dôme d'Orlica-Śnieżnik (Sudètes), la seconde aux recherches entreprises dans le massif vosgien. Les résultats obtenus dans les Sudètes sont le fruit d'une étroite collaboration avec F. CHOPIN, dont la thèse consacrée à la géologie de cette région a été soutenue en Septembre 2010 à Strasbourg. Certaines conclusions sur la partie NE du massif ont également bénéficié de travaux préliminaires de J. LEHMANN. Enfin, plusieurs axes de recherche font suite à des travaux initiés par M. ROMANOVÁ. Les autres personnes ayant participé aux travaux sur le dôme d'Orlica-Śnieżnik sont : P. ŠTÍPSKÁ, O. LEXA et J. HALODA. Les recherches entreprises dans le massif vosgien reflètent principalement une collaboration avec A-S. TABAUD, dont la thèse sur les roches ignées des Vosges doit s'achever au printemps 2012. Plusieurs autres données ont été acquises grâce au concours de J-B. EDEL, Z. KRATINOVÁ, A. COCHERIE et C. GUERROT. Au lecteur je demande donc l'indulgence de me pardonner si, d'aventure, j'ai pu implicitement faire référence à des observations issues de ces nombreux échanges. Hormis cela, je garde à l'esprit que « la science, mon garçon, est faite d'erreurs, mais d'erreurs qu'il est bon de commettre, car elles mènent peu à peu à la vérité. »¹

¹Otto Lindenbrock dans Jules Verne, *Voyage au centre de la Terre*.

RÉSUMÉ ÉTENDU

L'importance des mouvements horizontaux dans la genèse des chaînes de montagne a été reconnue depuis le début du XX^{ème} siècle. Ces forces horizontales ont par la suite été intégrées au concept de tectonique des plaques qui a permis d'expliquer les grands traits de la formation des systèmes orogéniques. Cependant, certains enregistrements structuraux ou métamorphiques dans les orogènes intracontinentaux ne sont pas directement corrélables avec la dynamique des blocs lithosphériques, suggérant un découplage entre tectonique des plaques et tectonique intracontinentale. En conséquence, il est nécessaire de caractériser les mécanismes opérant au sein des orogènes de collision et de détecter leur possible lien avec les processus opérant aux limites de plaques. Le présent travail de thèse se propose de répondre à ces interrogations en se concentrant sur deux massifs appartenant à la chaîne hercynienne d'Europe : le dôme d'Orlica-Śnieżnik dans les Sudètes (Pologne-République tchèque) et le massif des Vosges (NE France). Ces deux témoins ont l'avantage de contenir des portions ayant appartenu à la croûte supérieure, moyenne et inférieure, permettant ainsi de reconstituer des sections relativement complètes de la croûte orogénique paléozoïque. En combinant les données structurales, pétrologiques et géochronologiques pour les différents étages crustaux, il sera donc possible de discuter les mécanismes ayant présidé à la formation de ces deux systèmes orogéniques et leur relation avec la tectonique des plaques.

Première partie : Contribution de l'enregistrement structural, pétrologique et géochronologique de la croûte moyenne à la compréhension des processus d'enfouissement et d'exhumation (Sudètes)

La première partie du manuscrit de thèse est consacrée à l'étude des processus d'enfouissement et d'exhumation au sein de la croûte orogénique des Sudètes. Dans la mesure où la plupart des études se sont préalablement concentrées sur l'exhumation de la croûte orogénique inférieure, il est proposé ici d'utiliser l'enregistrement structural, pétrologique et géochronologique de la croûte moyenne afin de préciser l'évolution de l'orogène. Ceci est particulièrement pertinent dans le dôme d'Orlica-Śnieżnik (Sudètes), car cette zone d'étude présente fréquemment des roches de haut degré métamorphique juxtaposées à des roches de degré métamorphique nettement moindre. L'accent est donc mis sur la comparaison entre les évolutions Pression–Température–Déformation–temps ($P-T-D-t$) obtenues dans les deux portions différentes de la croûte orogénique.

Chapitre I : Contexte géologique

Le premier chapitre propose une revue des grandes lignes de la géologie des Sudètes. Même si un lien direct avec les zones lithotectoniques hercyniennes reconnues vers l'ouest reste difficile, les Sudètes sont principalement considérées comme le prolongement de la zone saxothuringienne. Du NO au SE, différents ensembles peuvent être reconnus : les unités de la zone lusatienne, le bloc d'Izera-Karkonosze, le bassin intra-sudétique, le bloc de Góry Sowie, le dôme d'Orlica-Śnieżnik (OSD) et enfin la zone moravo-silésienne.

La zone lusatienne est composée au NO d'un socle granitique neoprotérozoïque à cambro-ordovicien et de sédiments néoprotérozoïques, alors que l'unité de Görlitz au SE préserve des sédiments du Paléozoïque inférieur. Latéralement, l'unité de Kaczawa renferme des sédiments ordoviciens à siluriens avec intercalations de laves basiques de type MORB. Certaines parties de cette unité témoignent également d'un métamorphisme de faciès schiste bleu. Les portions de la zone lusatienne représenteraient donc une marge passive d'affinité saxothuringienne mise en place au Paléozoïque inférieur. Celle-ci aurait ensuite été impliquée dans une subduction vers le SE au Dévonien supérieur.

Le bloc d'Izera-Karkonosze contient des granitoïdes et sédiments cambro-ordoviciens envahis par un large pluton carbonifère. En périphérie, des sédiments et une association de roches basiques à ultrabasiques métamorphisées dans le faciès schiste bleu sont également trouvés. Les différentes lithologies indiquent ainsi la présence d'un bassin océanique au

Paléozoïque inférieur et l'activité d'une zone de subduction au Dévonien supérieur. Cet enregistrement similaire à celui de la zone lusatienne suggère une continuité latérale entre les deux ensembles pourtant séparés par la faille intra-sudétique.

Au SE du bloc d'Izera-Karkonosze se dessine le bassin intra-sudétique. Il s'agit d'une structure elliptique renfermant par endroit près de 6500 m de sédiments flyschoides tardi-dévonien à carbonifères. Ce bassin représenterait un ensemble de dépressions ayant accueilli les produits abondants de l'érosion des massifs cristallins voisins.

A l'est du bassin intra-sudétique, le bloc de Góry Sowie correspond à des roches de moyen à haut degré métamorphique entourées par une ceinture discontinue de témoins ophiolitiques faiblement métamorphisés. Il faut souligner que l'évolution tectono-métamorphique polyphasée des métasédiments et orthogneiss de Góry Sowie est datée du Dévonien inférieur : elle est ainsi nettement antérieure aux événements reconnus dans les autres ensembles des Sudètes. A ce titre, le bloc de Góry Sowie pourrait être considéré comme un fragment continental allochtone amalgamé entre les zones saxothuringienne et moravo-silésienne.

Vers le SE, le dôme d'Orlica-Śnieżnik comprend une zone centrale (OSD) à roches de moyen à haut degré métamorphique entourée par les unités plus faiblement métamorphiques de Nové Město, Staré Město et Zabřeh. A l'ouest et au sud de l'OSD, les unités de Nové Město et Zabřeh sont composées de métasédiments et métavolcanites de facies schiste vert à amphibolite dont l'enregistrement structural est fortement discordant avec celui du centre de l'OSD. En raison de leur âge probablement néoprotérozoïque, ces deux unités sont corrélées avec la zone teplá-barrandienne à l'ouest. A l'est de l'OSD, l'unité de Staré Město comprend des roches felsiques et mafiques polydéformées et polymétamorphisées qui témoignent de la présence d'un rift intracontinental cambro-ordovicien, puis d'un épisode de collision dévono-carbonifère. Toutes ces unités périphériques sont intrudées par un étroit sill de granodiorite mis en place au Carbonifère inférieur.

A l'extrémité SE des Sudètes, la zone moravo-silésienne correspond à un socle néoprotérozoïque variablement métamorphisé (Brunovistulien) alternant avec des sédiments dévoniens à carbonifères (Culm). L'enregistrement tectono-métamorphique de la zone moravo-silésienne suggère un épisode de rifting dévonian suivi d'une collision générale au Carbonifère.

Le dôme d'Orlica-Śnieżnik, communément rattaché à la zone moldanubienne (ou lugienne) comporte deux lithologies majeures. Les roches les plus abondantes correspondent à des orthogneiss œillés ou lités de type Śnieżnik, ou bien à des orthogneiss mylonitiques/migmatitiques de type Gierałtów. Ces deux variétés d'orthogneiss seraient issues d'un même

protolithe granitique mis en place au Cambro-Ordovicien. Ils alternent avec une épaisse série métasédimentaire à caractère varié : la formation de Stronie-Młynowiec. Celle-ci est essentiellement composée de micaschistes et paragneiss avec diverses intercalations de marbre, schiste graphitique, quartzite et métavolcanite acide ou basique, tous dérivés de protolithes très probablement cambro-ordoviciens. De rares témoins de haut degré métamorphique sont présents au sein des orthogneiss. Ils affleurent en une étroite bande de granulite felsique et basique, ainsi que sous forme de lentilles d'éclogite. La structure générale de l'OSD montre une alternance entre synformes de métasédiments et antiformes gneissiques renfermant en leur cœur les roches de haut degré. Cette zonation structurale se reflète également en termes de métamorphisme : les métasédiments montrent un métamorphisme maximal dans le faciès amphibolite, les orthogneiss dans le faciès amphibolite à eclogite, et les roches de haut degré atteignent les conditions du faciès éclogite ou granulite de haute pression. Ces résultats permettent donc de considérer la formation de Stronie-Młynowiec comme la croûte moyenne, tandis que les orthogneiss et les témoins de (ultra) haute pression représenteraient la croûte moyenne à inférieure. Les nombreuses données géochronologiques suggèrent que l'évolution tectono-métamorphique polyphasée de l'OSD est d'âge Dévonien supérieur-Carbonifère inférieur, mais l'existence d'événements éo-hercyniens n'est pas exclue.

En résumé, les unités formant les Sudètes représentent une section relativement complète d'un système orogénique de collision. Au NO, les unités lusatiennes et le bloc d'Izera-Karkonosze correspondent à une marge passive cadomienne à cambro-ordovicienne bordée par les reliques ophiolitiques d'un bassin océanique cambro-ordovicien. Cet ensemble préserve les indices d'une subduction dévonienne vers le SE, sous le bassin intra-sudétique et les unités périphériques du dôme d'Orlica-Śnieżnik. Vers le SE, le dôme d'Orlica-Śnieżnik correspond à la racine de l'orogène, tandis que les unités trouvées plus à l'est représentent les reliques d'un rift cambro-ordovicien et d'un bloc continental cadomien accrétés à l'OSD au cours de la collision carbonifère.

Chapitre II : Evolution structurale de la croûte orogénique moyenne

Le second chapitre se concentre sur l'enregistrement structural de la croûte moyenne métasédimentaire, même si un lien est gardé avec les lithologies voisines. A travers l'OSD, trois phases de déformation majeures ont été identifiées (D1, D2, D3). Le caractère hétérogène de la déformation permet de reconnaître une succession de trois foliations métamorphiques associées : une foliation S1 initialement subhorizontale, une foliation S2 subverticale et une foliation S3 subhorizontale. En fonction de la structuration dominante, différents domaines ont pu également être distingués.

Dans le domaine Nord, les reliques de S1 sont rares et la foliation subverticale S2, dont l'azimut est NE-SO, n'est visible que localement. C'est donc la foliation S3 faiblement inclinée vers le N ou NO qui domine dans cette partie de l'OSD. La linéation majeure correspond à l'intersection entre S2 et S3, et est orientée NE-SO. Il faut noter que ces marqueurs tectoniques sont observés aussi bien dans les métasédiments que dans les orthogneiss et granulites adjacents, suggérant une continuité structurale dans tout le domaine Nord.

Dans le domaine central, la succession des structures diffère entre la formation monotone de Młynowiec et celle de Stronie. Dans les paragneiss de Młynowiec situés au SE, il est possible d'observer des reliques du litage sédimentaire métamorphisé et verticalisé. Celui-ci est principalement affecté par la déformation D1 et se retrouve horizontalisé. Très rarement, une schistosité de plan axial subverticale et orientée N-S témoigne de la déformation D2. A l'inverse, dans la formation de Stronie, la structure dominante est la foliation S3 légèrement inclinée vers le NE, alors que des reliques N-S et subverticales de S2 sont rares.

Dans le domaine Sud, la foliation subhorizontale S1, bien que variablement plissée, est fréquemment visible. C'est cependant la foliation subverticale S2 qui est dominante dans cette partie du dôme. Elle a un azimut N-S parallèle à la linéation d'intersection entre S1 et S2 et n'est que localement affectée par une schistosité de plan axial subhorizontale liée à D3. L'enregistrement structural dans les roches adjacentes est relativement similaire : les orthogneiss œillés sont moins déformés et montrent plus fréquemment la foliation S1 subhorizontale, mais la bande d'orthogneiss mylonitiques/migmatitiques entourant les reliques éclogitiques préserve clairement la foliation N-S et subverticale S2. A travers le domaine Sud, les différentes portions de la croûte orogénique ont donc enregistré une succession de déformations identique.

Chapitre III : Evolution tectono-métamorphique de la croûte orogénique moyenne

Le but du troisième chapitre est de présenter, dans diverses parties de la croûte moyenne métasédimentaire, les relations entre la cristallisation des minéraux métamorphiques et les différentes phases de déformation. Les observations microstructurales sont couplées à des analyses chimiques des minéraux afin de déterminer les conditions Pression-Température ($P-T$) atteintes par les métasédiments. Celles-ci sont estimées de manière qualitative ou plus précisément en modélisant les assemblages minéraux à l'équilibre à l'aide du programme Thermocalc et d'une base de données thermodynamiques. Suivant cette approche, différentes synformes de métasédiments ont été étudiées afin de comprendre l'influence des roches adjacentes sur leur évolution $P-T-D$. Les échantillons collectés sont majoritairement des

micaschistes à muscovite, biotite et quartz. Ils contiennent des proportions variables de grenat, staurotide et plagioclase, montrent parfois disthène, sillimanite, andalousite, cordiérite, chloritoïde ou chlorite et ont pour minéraux accessoires tourmaline, ilménite, apatite, zircon et monazite.

Dans le domaine Nord, les métasédiments situés à proximité de la bande de granulite de haute pression ont été examinés. Ils indiquent une croissance de grenat suivant S1, puis de staurotide, grenat et disthène suivant S2. Par la suite, sillimanite et biotite orientées parallèlement à S3 remplacent le grenat, alors que l'apparition d'andalousite, cordiérite et chlorite est probablement postérieure à la déformation D3. Combinées à une forte zonation chimique du grenat, ces observations sont utilisées pour définir un chemin $P-T-D$ initialement prograde pendant D1 et D2 et atteignant des conditions maximales de 6–7 kbar/630 °C. L'évolution associée à D3 et post-D3 a un caractère rétrograde et s'achève à des conditions $P-T$ de 2–3 kbar/530–630 °C.

Au NO du domaine Nord, une seconde synforme de métasédiments se trouve plus éloignée de la bande granulitique, mais est intrudée par le granitoïde de Javorník. Dans les micaschistes, une paragenèse à grenat–staurotide est développée parallèlement à S1, mais une croissance de grenat et sillimanite est également associée à la foliation S2. De l'andalousite est aussi observée selon S2, alors que de la cordiérite semble se développer le long de la schistosité S3 naissante. La cartographie chimique des grenats révèle deux domaines chimiquement différents : le cœur du grenat préserve une zonation avec légère diminution de Ca vers la bordure, tandis que les surcroissances périphériques irrégulières sont très pauvres en Ca et dérivent probablement de la disparition du staurotide. Ces deux épisodes distincts permettent de définir un chemin $P-T-D$ prograde durant D1 et D2, et atteignant ~6 kbar/650 °C. Cependant, la présence d'andalousite indique que D2 a également un caractère rétrograde qui se poursuit pendant et après D3 vers des conditions inférieures à 2 kbar et 500 °C.

La synforme de métasédiments située dans le domaine Sud est enserrée entre une première antiforme contenant des éclogites à l'ouest et une seconde composée d'orthogneiss migmatitiques à l'est. Lorsque la foliation S1 y est préservée, il est possible d'observer l'assemblage grenat–staurotide parallèle au litage métamorphique. Une seconde génération de grenat et staurotide selon S2 est également visible dans les échantillons remaniés par D2. La chlorite parallèle à S2 et en équilibre avec le grenat est également abondamment trouvée dans certains échantillons. Ces relations microstructurales indiquent que les déformations D1 et D2 ont un caractère initialement prograde vers des conditions maximales de ~7 kbar/630 °C. Cependant, D2 est également associée à une rétrogression vers le champ de stabilité de la chlorite, c'est-à-dire vers des températures inférieures à ~540 °C.

A travers le domaine central qui est quasi exclusivement composé de métasédiments, le degré de métamorphisme augmente progressivement du NO vers le SE. Celui-ci n'a été déterminé que de manière qualitative. Au NO, la foliation S2 est caractérisée par une paragenèse à grenat–chloritoïde indiquant une évolution prograde. A l'inverse, la présence de chlorite suivant S3 suggère un métamorphisme rétrograde pendant et après la déformation D3. Vers le centre de la série métasédimentaire, la présence de grenat et staurotide parallèlement à S2 indique également un métamorphisme prograde, mais atteignant des conditions légèrement supérieures à celles de la partie NO. La croissance de sillimanite selon S3 témoigne de conditions certes rétrogrades, mais à température encore relativement élevée ($T > 500$ °C). A l'extrémité SE de la formation de Stronie, grenat, staurotide et disthène sont associés à la foliation S2 et suggèrent une évolution prograde vers des conditions encore supérieures à celles proposées dans les parties plus à l'ouest. La présence de sillimanite puis chlorite parallèlement à S3 indique quant à elle un métamorphisme rétrograde pendant et après D3.

Dans la formation de Młynowiec, les paragneiss à quartz, plagioclase et biotite indiquent qu'une foliation métamorphique s'est superposée au litage sédimentaire. Elle est caractérisée par la présence de grenat, staurotide et disthène qui définit une évolution prograde avant la déformation D1. Les conditions maximales seraient ainsi équivalentes à celles observées dans la partie SE du domaine central. A l'inverse, la croissance de sillimanite puis d'andalousite selon S1 témoigne de conditions rétrogrades lors de D1.

La synthèse des évolutions $P-T-D$ pour les différentes parties de la formation de Stronie-Młynowiec permet de mettre en lumière les variations spatiales du métamorphisme dans la croûte moyenne. La phase de déformation D1 est associée à un métamorphisme prograde dans l'ensemble de la formation métasédimentaire. Les conditions atteintes à la fin de D1 varient faiblement entre l'isograde à grenat ou à staurotide. Au cours de la déformation D2, la majeure partie de la croûte moyenne subit un nouveau métamorphisme prograde aboutissant à des conditions maximales contrastées. En effet, le degré de métamorphisme augmente progressivement vers l'est, c'est-à-dire vers la large antiforme d'orthogneiss partiellement fondu. Les métasédiments atteignent l'isograde à disthène ou sillimanite à proximité des orthogneiss et granulites, tandis que des parties plus éloignées montrent un métamorphisme moindre. Certaines portions de la croûte moyenne indiquent même une évolution prograde puis rétrograde lors de la déformation D2. Finalement, la déformation D3 se produit sous des conditions rétrogrades dans toute la formation de Stronie-Młynowiec, avec cependant des variations de régime thermique. Les isogrades métamorphiques s'organisent de manière concentrique autour de l'antiforme contenant des granulites et la présence de sillimanite à

proximité de cette antiforme indique que la température est restée relativement élevée lors de D3. A l'inverse, la croissance de chlorite dans les parties plus distantes témoigne de températures inférieures à ~500 °C lors de cette dernière phase de déformation.

Chapitre IV : Contraintes microstructurales et pétrologiques dérivées des porphyroblastes de grenat

Le quatrième chapitre apporte de nouvelles données microstructurales et pétrologiques sur la croûte moyenne en se basant sur l'étude des porphyroblastes de grenat. Ceux-ci ont été prélevés dans la synforme métasédimentaire située à proximité de la bande de granulite. Les échantillons de micaschiste ont été collectés pour différents stades du gradient de déformation D3, depuis des zones préservant la foliation S2 intacte jusqu'à des parties totalement remaniées par D3. Les différents domaines structuraux échantillonnés correspondent ainsi à diverses étapes de la transposition de la foliation S2 en une nouvelle foliation S3 et peuvent être caractérisés à l'échelle macroscopique et microscopique.

Dans les domaines structuraux, quatre types de porphyroblastes de grenat ont été définis sur la base de leur morphologie et de l'allure de leurs traces d'inclusions. Le type I possède des traces orthogonales pouvant correspondre aux foliations S1 et S2, tandis que le type II préserve des traces rectilignes susceptibles de représenter S2. Les grenats de type III ont des traces légèrement incurvées corrélées avec la foliation S2 plissée et les grenats IV montrent des traces sigmoïdes pouvant correspondre à S2 et S2 plissée.

Afin de quantifier ces structures internes, une nouvelle technique d'analyse microstructurale a été mise en place. Elle repose sur la mesure de l'orientation cristallographique préférentielle des inclusions d'ilménite à l'aide d'un microscope électronique à balayage équipé d'un dispositif d'analyse des électrons rétrodiffusés. Cette approche révèle que les ilménites incluses dans les grenats définissent de structures planaires ou linéaires en fonction de la section examinée. Par comparaison avec les observations macroscopiques, il est démontré que les porphyroblastes peuvent préserver les foliations S1 et S2 alors que celles-ci sont entièrement effacées dans la matrice. De plus, une linéation verticale correspondant à l'axe de microplis affectant la foliation interne S2 est mise en évidence, alors qu'elle n'est jamais observée au niveau macroscopique. Les foliations internes sont également utilisées pour définir des axes d'intersection de foliations (FIA) qui peuvent renseigner sur la direction générale de compression. Ainsi, des FIA orientées N-S et NE-SO indiquent-elles qu'un premier épisode de compression E-O a été suivie par un second orienté NO-SE. Ceci est compatible avec les structures observées à plus grande échelle dans l'ensemble de l'OSD.

La chimie de porphyroblastes de grenat a également été explorée afin de définir les conditions $P-T$ associées avec les différentes structures internes. La zonation en manganèse est compatible avec une évolution prograde lors des déformations D1 et D2, et est utilisée pour définir des conditions maximales de 6.5–7.5 kbar/640–670 °C à la fin de D2. En revanche, la déformation D3 est associée à une résorption partielle des grenats préexistants. Il faut noter que des chemins $P-T$ similaires sont révélés par plusieurs types de porphyroblastes appartenant à des échantillons ayant une chimie contrastée. Cela renforce la pertinence de la modélisation qui tient compte non seulement de la composition des minéraux, mais aussi de la composition de la roche totale.

L'enregistrement microstructural des porphyroblastes est discuté en termes de rotation ou non des grenats lors des phases successives de déformation. La forte compatibilité entre les structures internes et les mesures macroscopiques suggère que les porphyroblastes n'ont été que peu perturbés par les compressions orthogonales D1, D2 et D3. Une légère variation de pendage des foliations internes S2 pourrait refléter un plissement isopaque et une légère rotation au début de la déformation D3. Cependant, la majorité des résultats reste en faveur d'une absence de rotation des grenats expliquée par un régime de déformation D3 principalement coaxial. Ceci se traduit par une amplification passive des plis déjà initiés et aboutit à la formation de plis similaires au sein desquels les marqueurs tels que les grenats restent relativement immobiles.

Les données pétrologiques sont comparées à celles déjà détaillées pour la même synforme métasédimentaire. Elles concordent avec un enfouissement progressif de la croûte moyenne au cours des déformations D1 et D2, et avec une exhumation lors de D3. Il est finalement suggéré que ce type d'étude combiné peut conduire à la reconstitution précise de chemins $P-T-D$.

Chapitre V : Contraintes géochronologiques

Le cinquième chapitre cherche à fournir des âges absolus pour les différentes phases de déformation observées au sein de la croûte moyenne de l'OSD. A cet effet, des datations U–Th–Pb à la microsonde électronique sur monazites ont été effectuées pour trois échantillons appartenant à trois synformes de métasédiments distinctes.

Le premier échantillon, collecté à proximité de la bande de granulite, a pour foliation dominante S3. Il contient des monazites incluses à la bordure du grenat et dans la matrice. Ces dernières sont en équilibre avec l'apatite, mais en déséquilibre avec la sillimanite rétrograde. La population de monazites analysée est homogène et est caractérisée par une teneur faible en Yttrium (Y). L'âge associé qui a été calculé à partir d'une isochrone dans un diagramme $Pb=f(Th^*)$ est de 340 ± 15 Ma. Les différents arguments chimiques et texturaux sont utilisés

pour proposer une croissance de monazite sur un chemin $P-T$ prograde, aux dépens de l'allanite et proche de l'isograde métamorphique à disthène. Suivant cette interprétation, le résultat d'environ 340 Ma correspondrait à l'âge des conditions métamorphiques maximales, c'est-à-dire à la fin de la phase de déformation D2.

Le second échantillon provient de la synforme intrudée par le granitoïde de Javorník au NO du domaine Nord. Il préserve S2 comme foliation majeure et certaines monazites y sont trouvées sous la forme d'inclusions dans des porphyroblastes de grenat ayant grandi selon la foliation antérieure S1. Des monazites sont également trouvées dans la matrice. Toutes les monazites analysées appartiennent à une unique population relativement riche en Y et associée à un âge de 365 ± 21 Ma. A partir de cartographies chimiques des grenats préservant des inclusions de monazite, mais aussi en fonction de la teneur élevée des monazites en Y, la croissance de monazite dans cet échantillon est corrélée avec des épisodes de résorption-croissance du grenat au niveau de l'isograde métamorphique à staurotide, lors d'une évolution $P-T$ prograde. Dans la mesure où, dans cette synforme, la croissance de staurotide est associée à la foliation S1, il est suggéré que la déformation D1 s'est produite à environ 365 Ma.

Le troisième échantillon a été collecté dans le domaine Sud, dans la synforme métasédimentaire jouxtant les orthogneiss à reliques éclogitiques. Cet échantillon a pour structure dominante la foliation S2 et préserve des monazites uniquement dans la matrice. Ces dernières forment des chapelets (staphylo-monazites) principalement autour des porphyroblastes de grenat partiellement résorbés. Leur chimie montre des teneurs en Y intermédiaires par rapport aux deux échantillons précédemment étudiés. L'isochrone calculée pour cette population fournit un âge de 332 ± 40 Ma qui, malgré sa large incertitude, est préféré à l'âge moyen en raison de la possible présence de plomb initial dans les monazites. Les relations texturales indiquent que les monazites dérivent très probablement de la résorption du grenat. Ceci est confirmé par des teneurs moyennes en Y qui ne suggèrent qu'une résorption partielle des porphyroblastes. Puisque cette réaction métamorphique rétrograde se produit suivant la foliation S2, l'âge d'environ 330 Ma est considéré comme celui d'une phase tardive et rétrograde de la déformation D2.

Chapitre VI : Processus d'enfouissement et d'exhumation

Le sixième et dernier chapitre consacré au Sudètes propose une discussion des processus opérant au sein de la croûte orogénique. A cet effet, il s'attache à comparer les données structurales, pétrologiques et géochronologiques obtenues pour la croûte moyenne avec celles des lithologies adjacentes. En guise d'introduction, les chemins $P-T$ associés à divers mécanismes d'enfouissement et d'exhumation sont présentés pour appuyer la discussion, puis trois coupes distinctes sont étudiées.

Dans un premier temps, les évolutions $P-T-D-t$ de la bande granulitique et de la synforme métasédimentaire adjacente sont résumées. Puis, l'enregistrement des métasédiments situés au NO du domaine Nord est mis en relation avec l'intrusion du granitoïde de Javorník. Enfin, l'histoire $P-T-D-t$ de l'antiforme gneissique contenant des éclogites est comparée à celle des métasédiments étudiés dans la synforme voisine du domaine Sud. L'ensemble des données permet ainsi de proposer une signification géodynamique aux épisodes tectono-métamorphiques successifs.

La foliation subhorizontale S1 est caractérisée par un métamorphisme prograde dans l'ensemble de la croûte orogénique à environ 360 Ma. Cependant, ce métamorphisme atteint des conditions maximales variables en fonction des différents étages crustaux. En effet, les conditions $P-T$ dans la croûte moyenne n'excèdent pas celles du faciès amphibolite, tandis que celle proposées pour la croûte orogénique inférieure se trouvent dans le faciès éclogite ou granulite de haute pression. Il est proposé que ces variations reflètent la dynamique de particules au sein d'un prisme d'accrétion. En conséquence, la phase de déformation D1 est interprétée comme un flux subhorizontal de matériel crustal au sein d'un prisme orogénique. A plus grande échelle, ceci est considéré comme le résultat de la subduction continentale d'une marge passive d'affinité saxothuringienne sous une plaque supérieure corrélée avec la zone teplá-barrandienne.

La foliation subverticale S2, probablement formée à environ 340 Ma, est le témoin d'évolutions métamorphiques contrastées. Alors que la majeure partie de la croûte moyenne métasédimentaire continue à être enfouie dans cette structure, la croûte orogénique inférieure est quant à elle exhumée. Ces chemins $P-T$ opposés indiquent des échanges verticaux de matière qui sont très probablement le résultat d'un plissement affectant l'ensemble de la croûte orogénique. Cette hypothèse est renforcée par les données pétrologiques de la croûte moyenne qui indiquent une diminution du degré de métamorphisme au loin des antiformes gneissiques, c'est-à-dire une diminution de l'amplitude du plissement vers l'ouest de l'OSD. C'est à la faveur de ces mouvements verticaux mais opposés que la croûte inférieure granulitique ou éclogitique est juxtaposée à la croûte moyenne. Bien qu'une composante gravitaire (diapirisme) puisse être à l'origine de l'ascension du matériel felsique profond, l'indentation latérale du micro-continent brunovistulien situé à l'est est considérée comme le facteur majeur contrôlant le développement des échanges verticaux au sein du prisme orogénique.

La foliation subhorizontale S3 est associée, dans l'ensemble de l'OSD, à un métamorphisme rétrograde indiquant une exhumation de la croûte orogénique vers 330 Ma. Cette phase d'exhumation se déroule majoritairement à basse température, mais la distribution des isogrades métamorphiques dans la croûte moyenne indique la présence d'un domaine plus

chaud à l'est de l'OSD, autour de l'antiforme contenant des roches granulitiques. La persistance de l'anomalie thermique est expliquée par une advection de chaleur par les granulites qui ont été exhumées vers la croûte moyenne lors de la déformation D2. En outre, l'absence de rotation des porphyroblastes de grenat suggère qu'un régime principalement coaxial a prévalu lors de la déformation D3. En conséquence, l'exhumation est interprétée comme le résultat d'un amincissement ductile de la croûte moyenne sous une croûte supérieure plus rigide et froide. Ce mécanisme d'exhumation opère essentiellement en cisaillement pur et amène les métasédiments et roches de haut degré vers la surface pendant qu'une importante érosion dénude la partie supérieure de la croûte orogénique.

Les conclusions pour cette première partie concernent l'analyse microstructurale des porphyroblastes, la pétrogenèse des monazites, la géologie régionale et les processus tectoniques. La nouvelle technique utilisant l'orientation préférentielle des inclusions d'ilménite dans les grenats fournit une mesure directe des structures internes planaires et linéaires qui sont effacées dans la matrice. De tels résultats permettent ainsi de discuter le régime de déformation pendant et après la croissance des minéraux porphyroblastiques. L'étude texturale, chimique et géochronologique des monazites permet de reconnaître trois différents modes de formation. Les monazites peuvent se former lors d'une évolution $P-T$ prograde, aux conditions métamorphiques maximales ou encore sur un chemin rétrograde. Elles ont donc le potentiel de dater des phases bien distinctes de l'évolution orogénique. En termes de géologie régionale, la cartographie des assemblages métamorphiques dans la formation de Stronie-Młynowiec permet de mettre en évidence l'influence des différentes antiformes gneissiques, et notamment de l'antiforme de Gierałtów sur l'enfouissement et le réchauffement de la croûte moyenne. D'après les datations effectuées sur les monazites, ce métamorphisme s'est limité à la période hercynienne et aucun âge pré-Dévonien n'est ici reconnu. La reconstitution géodynamique de l'OSD est enfin résumée en trois épisodes. Elle débute par un flux subhorizontal de matériel à la faveur d'une subduction continentale, probablement sous une croûte partiellement amincie. Elle se poursuit par une indentation latérale produisant des échanges verticaux de matière et de chaleur lors d'un plissement à grande échelle de la croûte orogénique. Le dernier événement correspond finalement à une exhumation de l'ensemble du système accommodée par un amincissement ductile de la croûte moyenne et une forte érosion de la croûte supérieure.

Deuxième partie : Caractérisation structurale, pétrologique et géochronologique des processus tectoniques intracontinentaux dans la croûte orogénique (Vosges)

La deuxième partie du manuscrit de thèse traite des processus tectoniques qui ont pu être identifiés dans le socle hercynien des Vosges (NE France). Alors que beaucoup d'études n'utilisent que rarement des techniques combinées et ne se concentrent que sur un niveau crustal donné, il est ici proposé d'employer une combinaison des observations structurales, pétrologiques ou géochronologiques pour les différents étages de la croûte orogénique. Cette approche peut être mise en œuvre dans les Vosges, car ce massif préserve des témoins allant de la croûte supérieure jusqu'au manteau. Ainsi, il est possible de caractériser l'évolution temporelle et spatiale de la déformation et du métamorphisme durant le cycle orogénique hercynien. Cela pourra concerner les épisodes extensifs précoces, la phase paroxysmale de collision ou encore les événements tardi-orogéniques.

Chapitre I : La signification des ophiolites tardi-dévonniennes dans la chaîne hercynienne : l'exemple de la « Ligne des Klippes » (Vosges)

Le premier chapitre explore la signification régionale des témoins ophiolitiques trouvés dans les Vosges du Sud au niveau de la « Ligne des Klippes ». Cette étude tente également d'intégrer les résultats à plus grande échelle dans l'évolution de la chaîne hercynienne d'Europe. En introduction, il est rappelé que les ophiolites des Vosges du Sud peuvent être classées parmi les témoins de domaines océaniques tardi-dévonniens, tout comme les roches de la Brévenne (Massif Central), de Vrbno-Drahany (Moravie) et possiblement de Beja-Acebuches (SO Ibérie). Cependant, la signification de ces domaines reste énigmatique dans la mesure où leur ouverture coïncide avec une fermeture globale du système hercynien. Il est donc envisagé, à partir de l'exemple des Vosges, de proposer une origine à l'expansion de ces domaines océaniques syn-convergence.

Les roches *pro parte* ophiolitiques affleurent de manière discontinue le long d'un segment appelé « Ligne de Klippes ». Celui-ci représente la limite entre une série sédimentaire viséenne allochtone au nord (Markstein) et une série volcano-sédimentaire viséenne autochtone au sud (Oderen). Ces deux séries d'âge similaire pourraient respectivement correspondre à la partie distale et proximale d'un bassin turbiditique de type flysch recevant les produits de l'érosion de la chaîne de montagne adjacente. L'ensemble est également parcouru de nombreuses intrusions granitiques datées à environ 340 Ma.

Les différentes Klippen (1–2 km²) préservent des lithologies contrastées qui présentent néanmoins une répartition constante. A la base, des roches ultrabasiques sont fréquentes et correspondent à des harzburgites serpentinisées ou à des ophicalcites dont il s'agit de la

première mention dans le massif vosgien. Elles sont associées à des dolérites ou gabbros à texture fréquemment cumulative. Ces lithologies sont recouvertes par de la grauwacke conglomératique pouvant comporter des blocs plurimétriques, mais montrant généralement des galets centimétriques de serpentinite, gabbro, orthogneiss ou amphibolite. L'ensemble est scellé par une couche de sédiments pélitiques versicolores et très siliceux, épaisse de quelques mètres. Des filons de microgranite sont aussi fréquemment observés à la périphérie des Klippen.

Dans les séries sédimentaires environnantes, la cartographie des plans de stratification S0 révèle une nette discontinuité structurale au sud de la « Ligne des Klippen ». Alors que la stratification est affectée par des plis plurikilométriques d'axe NO-SE au centre de la série allochtone, elle devient brutalement N-S et faiblement inclinée dans la série autochtone. Ceci coïncide avec un contraste lithologique : les assises orientées NO-SE sont uniquement sédimentaires, tandis que les sédiments ayant une S0 d'azimut N-S alternent avec des passées volcaniques. Ces observations conduisent à replacer la limite entre la série allochtone et autochtone au sud de la « Ligne des Klippen ». Cette hypothèse est appuyée par de nouvelles données gravimétriques révélant la présence d'un corps de relativement faible densité sous la « Ligne des Klippen » et au niveau de la discontinuité structurale. Cette anomalie est expliquée par un prolongement en profondeur des unités granitiques adjacentes (granite des Crêtes).

Des travaux pétrologiques et géochimiques ont également été menés sur les lithologies gabbroïques trouvées dans les différentes Klippen. Elles indiquent que les gabbros sont composés de plagioclase de type labrador et de clinopyroxène de type diopside. D'autre part, les profils en éléments traces sont relativement constants et montrent un faible appauvrissement en terres rares légères, une légère anomalie positive en Eu et un enrichissement significatif en Ba, U, Th et Sr. Ces caractéristiques sont compatibles avec celles des lithologies de type N-MORB.

L'âge des différentes lithologies trouvées dans la « Ligne des Klippen » a été contraint grâce à diverses méthodes. Dans un échantillon de gneiss, la datation U-Pb sur zircons par ICP-MS laser fournit une série d'âges paléoproterozoïques à archéens hérités et un âge néoproterozoïque de 575 ± 29 Ma interprété comme l'âge de cristallisation du protolithe granitique. Pour un échantillon de gabbro, une isochrone tracée grâce aux analyses Sm-Nd de la roche totale et des minéraux indique un âge de 372 ± 18 Ma. Cette estimation, interprétée comme l'âge de mise en place du gabbro, est en accord avec l'âge Faménien des sédiments versicolores trouvés dans les Klippen et confirme l'âge Dévonien supérieur initialement proposé pour les témoins ophiolitiques des Vosges du Sud.

La signification lithologique, tectonique, géochimique et chronologique des différentes données présentées est ensuite discutée. De fortes similarités entre la succession des lithologies décrite dans les Klippen et la disposition typique des séries ophiolitiques téthysiennes conduit à considérer la « Ligne des Klippes » comme un fragment distal d'une zone de transition océan-continent. Les larges blocs gneissiques seraient ainsi reliés à des blocs allochtones continentaux isolés pendant le rifting. Par ailleurs, la déformation des assises sédimentaires reflète un comportement de type « fold and thrust belt ». Celui-ci s'exprime par un plissement d'axe général NO–SE, par le chevauchement vers le sud de l'unité allochtone sur l'unité autochtone et par la formation probable de structures en duplex. D'après l'âge de 340 Ma obtenu sur un filon de microgranite syn-tectonique, cette phase de compression NE–SO est datée du Viséen moyen. Les données géochimiques des gabbros concordent avec les compositions de roches médio-océaniques trouvées au niveau de dorsales lentes, mais l'enrichissement en éléments continentaux (Ba, U, Th, Sr) suggère une possible contamination par des fluides libérés au toit d'une zone de subduction. Une origine en tant que bassin d'arrière-arc n'est donc pas exclue pour le domaine océanique des Vosges du Sud. Enfin, les datations isotopiques précisent qu'un socle néoprotérozoïque a été affecté par un épisode de rifting au Dévonien supérieur.

Les interprétations sont intégrées dans une reconstruction de l'évolution géodynamique des Vosges du Sud. Au Dévonien supérieur, un amincissement de la croûte continentale néoprotérozoïque génère une marge passive associée à une zone de transition océan-continent. Le bassin océanique ainsi formé accueille ensuite d'abondants dépôts flyschoïdes du Tournaisien au Viséen inférieur. Au Viséen moyen, les séries sédimentaires sont déformées en réponse à l'inversion du bassin. Ceci conduit notamment à la formation d'un duplex de taille kilométrique au sein duquel les anciennes parties profondes du bassin, c'est-à-dire les lithologies de la « Ligne des Klippes », sont exhumées. Cette phase de déformation est également contemporaine d'intrusions granitiques à l'intérieur ou à la périphérie des assises sédimentaires.

L'origine du bassin tardi-dévonien reconnu dans les Vosges du Sud est discutée à plus grande échelle à l'aide des travaux antérieurs sur la chaîne hercynienne d'Europe. Une ouverture océanique liée à la subduction du système rhénohercynien situé au nord des Vosges est exclue pour des raisons chronologiques. En effet, les indices d'une subduction du bassin rhénohercynien sont enregistrés à 335–330 Ma dans les Vosges du Nord. À l'inverse, la subduction de domaines océaniques ouverts au Paléozoïque inférieur est plus à même de générer une expansion d'arrière-arc au Dévonien supérieur. L'influence de la subduction du domaine saxothuringien au NO est envisagée, mais celle de la subduction de l'Océan

Paléotéthys situé au sud des Vosges est préférée. Dans ce cas, le terme Paléotéthys se réfère au domaine océanique, peut-être peu étendu, séparant le macro-continent Gondwana de l'ensemble des blocs péri-armoricains. Cette interprétation est basée sur la géométrie du bassin qui s'accorde plutôt avec une direction d'extension puis de convergence N-S. Ce scénario est également compatible avec l'évolution proposée dans la Forêt-Noire du Sud (zone de Badenweiler-Lenzkirch) où la subduction, vers le nord, d'un océan situé au sud a été suggérée. Par analogie, il est donc avancé que le bassin des Vosges du Sud correspond à un bassin d'arrière-arc lié à la subduction, vers le nord, de l'Océan Paléotéthys se trouvant plus au sud du socle vosgien. Les témoins ophiolitiques contemporains trouvés dans les séries de la Brévenne (Massif Central) pourraient ainsi représenter un équivalent latéral de ce domaine d'arrière-arc. Finalement, la majorité des bassins océaniques tardi-dévonien trouvés dans la chaîne hercynienne d'Europe sont interprétés comme des bassins d'arrière-arc marginaux se formant à l'avant de domaines océaniques Paléozoïque inférieur en cours de fermeture.

Chapitre II : Origine des zircons et signification des âges U-Pb dans les roches de haut degré métamorphique : étude de cas de la racine orogénique hercynienne (Vosges)

Le deuxième chapitre cherche à démontrer l'importance des études géochronologiques et pétrologiques combinées à travers l'exemple de la racine orogénique des Vosges. En effet, un défi majeur dans l'étude des roches de haut degré métamorphique consiste à estimer avec précision l'âge de début, de fin et donc la durée de leur évolution métamorphique. Ceci est d'une importance primordiale dans la discussion des processus tectoniques, notamment d'exhumation, qui sont généralement déduits des données obtenues sur les roches profondes. Dans cette optique, la méthode de datation U-Pb sur zircons a été couplée à une étude attentive de la pétrogenèse des zircons métamorphiques.

L'introduction est orientée vers un rappel des processus de croissance du zircon dans les roches de haut degré métamorphique. Les mécanismes majoritairement invoqués sont la résorption de phases riches en Zr, la recristallisation à l'état solide ou encore la cristallisation à partir d'un liquide anatectique. En fonction des relations texturales et chimiques entre zircon et minéraux adjacents, ces mécanismes peuvent être reliés à une évolution métamorphique prograde, rétrograde ou bien aux conditions métamorphiques maximales. Les travaux antérieurs soulignent donc que les zircons métamorphiques et les âges U-Pb associés peuvent refléter une large gamme d'événements tectono-métamorphiques. A partir de l'exemple de trois unités métamorphiques des Vosges centrales, il est alors proposé de discuter la formation de zircon et la signification des âges U-Pb associés dans l'évolution géodynamique de la racine orogénique hercynienne.

L'étude pétrologique et géochronologique se concentre sur les unités métamorphiques des Vosges centrales qui affleurent au niveau de Sainte-Marie-aux-Mines. On y distingue généralement trois unités: l'unité monotone formée de paragneiss à biotite–sillimanite, l'unité variée composée de paragneiss à grenat, d'amphibolites et de marbres, et l'unité granulitique constituée essentiellement de granulite felsique. Toutes trois comportent fréquemment des intercalations de péridotite serpentinisée et leur évolution métamorphique est caractérisée par un épisode initial de MP-HP/MT fortement oblitéré par une phase de BP/HT. Aussi bien l'âge de dépôt des séries métasédimentaires monotone et variée que l'âge de mise en place du protolithe magmatique (?) de l'unité granulitique reste inconnu. A l'inverse, le métamorphisme d'âge hercynien a été estimé entre 340 et 330 Ma par de nombreuses méthodes géochronologiques. Il est contemporain de l'intrusion de granitoïdes magnésio-potassiques au sein de la racine orogénique à 340–335 Ma.

Les datations sur zircons ont été réalisées à l'aide d'un spectromètre de masse à plasma couplé par induction, équipé d'un multi-collecteur et doté d'un dispositif d'ablation laser. Les analyses isotopiques ont été effectuées sur des zircons montés en sections polies et ayant fait l'objet d'un examen en lumière transmise et réfléchi ainsi qu'en cathodoluminescence. Trois échantillons ont été explorés et environ 60 analyses ont été obtenues pour chaque unité métamorphique. Les âges isotopiques ont ensuite été comparés à la structure interne et aux teneurs en U et Th des zircons.

Dans l'unité monotone, les zircons ont uniquement livré des âges précambriens à cambro-ordoviciens et aucun âge hercynien n'a été trouvé. Les résultats comprennent quelques âges hérités archéens et paléoprotérozoïques (3400, 2700, 2400, 2000 Ma), mais surtout des âges cadomiens s'étalant entre 700 et 500 Ma. Ces deux populations ne peuvent être distinguées ni sur la base des concentrations en U–Th, ni sur la base des structures internes observées en cathodoluminescence.

Dans l'unité variée, les résultats obtenus correspondent à de rares héritages paléoprotérozoïques (2600, 2100, 1900 Ma), un large spectre cambro-ordovicien allant de 600 à 450 Ma et une majorité d'âges métamorphiques hercyniens à 340–335 Ma. Les zircons paléoprotérozoïques préservent des teneurs en U–Th relativement faibles, tandis que les zircons cambro-ordoviciens ou hercyniens montrent une plus large variation. Parmi la population hercynienne, deux sous-groupes sont distingués. Le premier sous-groupe correspond à des zircons ayant une structure interne «floue» et des concentrations en U–Th faibles, similaires à celles des zircons cambro-ordoviciens. Les zircons du deuxième sous-groupe sont plus riches en U–Th et apparaissent uniformément sombres en cathodoluminescence.

Dans l'unité granulitique, seules deux analyses discordantes indiquent un possible héritage à 2000 Ma, alors que toutes les autres sont d'âge Paléozoïque. Les résultats paléozoïques correspondent en fait à une série continue d'analyses concordantes s'étalant entre deux maxima à 550 à 320 Ma. Cependant, seuls les âges de 510–500 Ma et 345 Ma qui sont calculés avec suffisamment d'analyses ponctuelles sont considérés comme représentatifs. Dans les échantillons de granulite felsique, il existe un lien systématique entre l'âge des zircons et leur structure interne. Les âges cambriens proviennent des cœurs de zircons préservant une zonation oscillatoire, les âges d'environ 345 Ma sont obtenus sur des grains ou surcroissances uniformément sombres et les âges intermédiaires sont associés à une zonation oscillatoire «floue». Ce contraste est également visible en termes de composition : les zircons cambriens et intermédiaires sont pauvres en U, tandis que les zircons datés à 345 Ma montrent un enrichissement en U.

Dans la mesure où l'unité monotone n'a livré aucun âge hercynien, une étude pétrologique n'a été menée que dans les unités variée et granulitique. Dans les paragneiss de la série variée, la succession des paragenèses comprend : un stade initial à biotite–rutile–grenat (8% grossulaire), un second stade à disthène–K-feldspath–grenat (5% grossulaire) et un ultime stade à biotite–sillimanite–K-feldspath–grenat (2% grossulaire). Les deux premières paragenèses sont essentiellement observées dans les porphyroblastes de grenat ou K-feldspath, alors que la dernière est visible dans la matrice. Dans les échantillons de granulite felsique, un premier assemblage à grenat–disthène–K-feldspath–rutile est suivi par un second à grenat–sillimanite–K-feldspath, puis le grenat est remplacé par de la biotite et chlorite. Les grenats arrondis et riches en inclusions lobées de K-feldspath ne sont jamais zonés chimiquement en raison d'un important rééquilibrage par diffusion.

La modélisation thermodynamique des assemblages minéraux à l'équilibre est tout d'abord appliquée pour contraindre les conditions P – T enregistrées par les deux unités. Comme les échantillons ont subi une fusion partielle non négligeable, une approche inverse est ici utilisée. Dans un premier temps, les conditions P – T sont déterminées pour le stade d'équilibrage de la bordure du grenat avec la dernière phase fluide présente dans le système. Ensuite, une proportion de liquide granitique est réintégrée à la composition de la roche afin de tenter d'accéder aux conditions précédant l'anatexis. Pour l'unité variée, cela permet de reconstituer une évolution P – T démarrante à 9–10.5 kbar/600–650 °C et atteignant des conditions maximales de 12–14 kbar/840–880 °C. Celles-ci sont suivies d'une décompression isotherme vers 8–10 kbar/820–860 °C, puis d'une diminution de pression et température vers des conditions inférieures à ~5 kbar/750 °C. Dans le cas de l'unité granulitique, un protolithe,

possiblement de type granitique, a suivi un métamorphisme prograde de 6–10 kbar/600–700 °C à 10–13 kbar/ 810–830 °C, suivi d'une décompression isotherme vers 6.5–8.5 kbar/800–820 °C, puis d'une diminution de pression et température vers des conditions inférieures à ~4.5 kbar/700 °C.

Grâce à de récents modèles thermodynamiques tenant compte de la répartition du zirconium, des pseudosections ont ensuite été utilisées pour explorer le comportement des zircons le long des chemins $P-T$ proposés pour les unités variée et granulitique. De manière générale, une augmentation de pression et température vers les conditions du faciès granulite de haute pression provoque une dissolution progressive des zircons préexistants dans le liquide anatectique. Une phase de décompression isotherme est également associée à une légère dissolution de zircon en raison de la forte dépendance en température des isoplèthes du zircon. D'après les modélisations, de nouveaux zircons ne peuvent se former que sur un chemin $P-T$ associé à une diminution de température et une cristallisation du liquide anatectique. Pour chaque unité, les fractions volumiques de zircons hérités et néoformés sont confrontées aux prédictions des pseudosections et les températures maximales sont déduites du pourcentage de zircon résorbé au cours du chemin prograde. Dans l'unité variée le taux de résorption est en accord avec des conditions maximales de 850–900°C, tandis que dans l'unité granulitique la dissolution importante des zircons du protolithe suggère des températures plus élevées de l'ordre de ~950 °C. Enfin, la croissance de nouveaux zircons prédite par les pseudosections indique que les zircons métamorphiques se seraient plutôt formés à la fin du stade de BP/HT, et non aux conditions métamorphiques maximales.

La discussion résume tout d'abord l'évolution métamorphique de l'ensemble de la racine orogénique. L'unité monotone a probablement atteint les conditions du faciès amphibolite supérieur, alors que les unités variée et granulitique montrent toutes deux un équilibre dans le faciès granulite de haute pression. A ce titre, l'unité monotone peut être considérée comme une portion de la croûte moyenne et les deux autres unités comme la croûte inférieure de l'orogène.

Les trajectoires $P-T$ sont ensuite combinées aux datations U–Pb et à la chimie et structure interne des zircons pour discuter l'origine des zircons hercyniens. L'unité monotone, vierge de tout âge hercynien, n'a probablement pas atteint des conditions de fusion partielle suffisantes pour générer une croissance significative de nouveaux zircons. A l'inverse, les zircons hercyniens de l'unité variée sont reliés à deux mécanismes de formation : les zircons à structure «floue» sont considérés comme des cristaux cambro-ordoviciens affectés par une recristallisation transgressive et les zircons uniformément sombres sont interprétés comme des produits de la cristallisation du liquide anatectique. Ces deux populations marqueraient

alors la fin du métamorphisme de haute température. Dans les granulites felsiques, les zircons datés à ~500 Ma et ayant une zonation oscillatoire indiquent probablement l'âge du protolithe granitique. Les zircons à structure «floue» et d'âge intermédiaire reflèteraient alors une homogénéisation partielle de la zonation oscillatoire des zircons du protolithe au cours d'un épisode de haute température. Enfin, la population dominante de zircons uniformément sombres dériverait de la cristallisation du liquide anatectique à la fin du métamorphisme de BP/HT.

Des conséquences sur l'évolution tectonique du segment vosgien sont finalement proposées. Les nouvelles datations sur zircons fournissent pour la première fois une approximation de l'âge des protolithes. L'unité monotone apparaît plus ancienne et s'est probablement déposée au Cambro-Ordovicien, alors que l'unité variée témoigne d'une sédimentation à l'Ordovicien supérieur. D'autre part, les zircons d'environ 500 Ma trouvés dans la granulite felsique indiquent un épisode magmatique contemporain de la sédimentation de l'unité monotone. Les unités variée et granulitique subissent ensuite un enfouissement vers les conditions du faciès granulite de haute pression. Ceci reflète vraisemblablement un épisode de subduction continentale lors de la convergence hercynienne. L'âge de ce métamorphisme de haute pression n'est pas déterminé, mais les travaux sur la diffusion dans le zircon indiquent qu'il pourrait se situer vers 360–350 Ma. L'ensemble de la croûte orogénique subit ensuite un épisode de haute température qui s'achève à faible profondeur vers 340 Ma. Cet âge récurrent de 340 Ma, très proche des âges de refroidissement $^{40}\text{Ar}/^{39}\text{Ar}$, n'indique donc pas une exhumation rapide de la croûte profonde, mais date plutôt la fin de la juxtaposition entre croûte orogénique moyenne et inférieure.

Chapitre III : Evolution géodynamique des Vosges hercyniennes

Le troisième et dernier chapitre présente une synthèse des données disponibles sur les Vosges et une discussion de l'évolution orogénique de ce segment hercynien. En introduction, les différentes zones lithotectoniques de la chaîne hercynienne d'Europe sont décrites. Au nord, la zone rhénohercynienne préserve les témoins d'une ouverture océanique au Dévonien inférieur, puis d'une inversion du bassin sédimentaire au Dévon-Carbonifère. Elle est en contact vers le sud avec le seuil cristallin médio-germanique qui représente une juxtaposition d'unités lithotectoniques contrastées. Plus au sud, la zone saxothuringienne indique qu'une expansion océanique au Paléozoïque inférieur a été suivie d'une subduction vers le SE au Dévonien supérieur, puis d'une phase de collision et inversion du bassin au Carbonifère inférieur. En effet, plusieurs observations montrent que la zone saxothuringienne est aujourd'hui chevauchée par le domaine moldanubien situé au sud. Ce dernier est principalement formé de roches métamorphiques intrudées par de larges complexes plutoniques et est considéré comme la

racine profonde de l'orogène. Enfin, la zone teplá-barrandienne est constituée des fragments discontinus de socle néoproterozoïque recouverts par des sédiments néoproterozoïques à paléozoïques et est localisée entre les zones saxothuringienne et moldanubienne. En suivant ce schéma, les Vosges ont communément été divisées en une partie saxothuringienne au nord et une partie moldanubienne au sud, et une subdivision identique a été adoptée pour la Forêt-Noire voisine.

La synthèse des données débute par une présentation de la lithostratigraphie des Vosges. Les différentes lithologies y sont détaillées chronologiquement pour trois zones majeures définies dans ce travail : les Vosges du Nord, les Vosges centrales et les Vosges du Sud. Les Vosges du Nord sont formées de séries (volcano)-sédimentaires peu ou pas métamorphisées intrudées par un complexe magmatique. Dans la succession nord (Série de la Bruche), la sédimentation débute au Dévonien moyen par des dépôts conglomératiques et carbonatés accompagnés d'un volcanisme bimodal. Elle se prolonge par des dépôts côtiers puis turbiditiques jusqu'au Viséen inférieur. Suite à une lacune au Viséen moyen, elle reprend par des dépôts continentaux au Viséen supérieur puis au Permien. Dans la succession sud (Séries de Villé et Steige), des schistes cambriens à siluriens sont trouvés jusqu'à la zone E-O déformée de Lalaye-Lubine. Les deux successions sédimentaires sont séparées par un complexe magmatique (Complexe du Champ du Feu) renfermant des roches plutoniques intermédiaires à acides, mais aussi des volcanites, toutes mises en place entre 335 et 330 Ma.

Les Vosges centrales sont composées d'un socle métamorphique et magmatique parcouru par la faille NE-SO de Sainte-Marie-aux-Mines. Au nord, les unités métamorphiques (Séries monotone et variée de Sainte-Marie-aux-Mines) comprennent des séries métasédimentaires issues d'une sédimentation grésopélimitique de l'Ordovicien au Silurien, ainsi qu'une série granulitique probablement dérivée de granitoïdes cambriens. Ces lithologies sont intrudées par un premier cortège de granitoïdes magnésio-potassiques (Mg-K) qui sont datés à 340–335 Ma et sont trouvés du nord au sud des Vosges centrales. Un second ensemble de granites anatectiques, daté à 330–325 Ma, se met en place au sein des unités métamorphiques (Granites du Bilstein-Brézouard-Thannenkirch), mais occupe essentiellement la partie sud (Granite fondamental). Localement, des reliques de roches métamorphiques sont trouvées au sein du granite anatectique sous la forme de lentilles plurikilométriques de migmatite ou d'orthogneiss. Les roches ultrabasiques sont fréquentes dans les Vosges centrales et affleurent aussi bien dans les unités métamorphiques au nord qu'au milieu des zones migmatitiques plus au sud. Ce sont des péridotites serpentinisées à reliques de grenat ou spinelle.

Les Vosges du Sud sont majoritairement occupées par d'épaisses séries (volcano)-sédimentaires recoupées par des granitoides Mg-K. Au sud, la série autochtone (Série d'Oderen) montre des dépôts carbonatés du Dévonien supérieur surmontés par des sédiments grésopélitiques du Viséen inférieur qui deviennent progressivement continentaux au Viséen supérieur (Série de Thann) puis au Permien. Tous ces dépôts sont accompagnés d'un volcanisme bimodal et sous-marin au Viséen inférieur, devenant andésitique à rhyolitique et aérien au Viséen supérieur. Au nord, la série sédimentaire allochtone (Série du Markstein) est caractérisée par des dépôts turbiditiques distaux datés du Viséen inférieur. A la base de cette unité, des affleurements discontinus de péridotite, gabbro, gneiss, pélite et conglomérat (Ligne des Klippes) correspondent aux parties les plus profondes du bassin océanique ouvert au Dévonien supérieur. La série allochtone est entourée de granitoïdes, principalement de type Mg-K, mis en place vers 340 Ma, alors qu'un complexe magmatique Mg-K plus large intrude la série autochtone au sud. Ce dernier (Complexe des Ballons) comprend des intrusions périphériques basiques à intermédiaires datées à 345 Ma et une large zone granitique centrale mise en place à 340 Ma.

Les différents gradients métamorphiques observables dans les Vosges sont ensuite détaillés. En raison de la mise en place de larges domaines granitiques, un métamorphisme de contact est fréquemment trouvé à travers l'ensemble du socle vosgien. Il est développé dans les sédiments et schistes situés respectivement au nord et au sud du complexe magmatique des Vosges du Nord, ainsi qu'à la périphérie de la série sédimentaire allochtone des Vosges du Sud. Une évolution de type barrowienne allant de bas à moyen degré métamorphique est également identifiée dans les Vosges du Nord. Du nord au sud, les schistes y montrent une augmentation du métamorphisme depuis l'anchizone jusqu'à la limite inférieure du faciès amphibolite indiquée par la présence de micaschiste à grenat. Les unités métamorphiques des Vosges centrales montrent quant à elles une évolution $P-T$ comprenant un stade initial de MP-HP/HT suivi d'un épisode de BP/HT. Dans un premier temps, l'unité monotone a subi des conditions maximales dans le faciès amphibolite supérieur (6–9 kbar/600–700 °C), tandis que les unités variée et granulitique ont atteint le faciès granulite de haute pression (12–15 kbar/700–850 °C). En revanche, les trois unités ont ensuite été affectées par un événement de haute température (800–900°C) à relativement basse pression (6–8 kbar). Par ailleurs, les péridotites témoignent de conditions initiales de ultra haute pression (~49 kbar/1000 °C) avant leur exhumation puis incorporation dans les séries variée et granulitique.

Les données géochronologiques disponibles pour les différentes lithologies des Vosges sont ensuite présentées. La distribution statistique des âges radiométriques obtenus sur les

roches magmatiques montre clairement un rajeunissement du magmatisme du sud vers le nord. Elle souligne également les trois épisodes majeurs à environ 340, 335 et 330 Ma. Les plutons les plus anciens sont trouvés dans le complexe des Vosges du Sud mis en place à 345–340 Ma. Dans les Vosges centrales, ces manifestations sont suivies d'un magmatisme Mg-K à 340–335 Ma, puis de la mise en place de granite anatectique à 330–325 Ma. De plus, un magmatisme de type d'arc est enregistré à 335–330 Ma au niveau des Vosges du Nord. Par ailleurs, les âges métamorphiques reportés pour les Vosges centrales se limitent exclusivement au Carbonifère inférieur. Les datations par la méthode U–Pb fournissent généralement des âges de 345–340 Ma, tandis que les données $^{40}\text{Ar}/^{39}\text{Ar}$ montrent des âges de refroidissement légèrement plus jeunes entre 340 et 325 Ma.

Une description détaillée de l'enregistrement structural à travers le socle vosgien fait suite aux données métamorphiques et géochronologiques. Elle est basée sur l'observation des structures dans les lithologies sédimentaires ou métamorphiques, ainsi que sur les données d'anisotropie de susceptibilité magnétique (ASM) dans les roches magmatiques. Dans les Vosges du Nord, les sédiments de la succession nord montrent un plissement plurikilométrique d'axe N–S du litage sédimentaire. Ils sont ensuite affectés par un plissement kilométrique d'axe NE–SO associé à une schistosité de fracture NE–SO subverticale. Le complexe magmatique est séparé en deux compartiments distincts : la partie granitique au nord préserve des foliations et linéations magnétiques orientées NO–SE, tandis que la partie granodioritique au sud montre des structures NE–SO à E–O. Les schistes de la succession sud sont structurés parallèlement à la partie sud du complexe magmatique. Ils montrent les reliques d'une foliation métamorphique initialement horizontale qui est variablement affectée par une nouvelle schistosité E–O subverticale. Cette structure est elle-même parallèle à la faille majeure de Lalaye-Lubine qui marque la limite avec les Vosges centrales.

Dans les unités métamorphiques des Vosges centrales, une succession de trois structures majeures a pu être déterminée. La foliation la plus ancienne est dominante de part et d'autre du granitoïde Mg-K et correspond à des plans subverticaux orientés N–S à NE–SO. Ceux-ci sont progressivement aplatis vers l'est où ils deviennent transposés en une nouvelle foliation métamorphique subhorizontale. Ces deux structures planaires orthogonales sont développées dans toutes les unités métamorphiques. En revanche, la phase de déformation postérieure affecte quasi uniquement l'unité monotone située à l'est. Elle produit un plissement plurimétrique de la foliation horizontale selon un axe E–O, mais ne génère pas de nouvelle foliation métamorphique. Le résultat de cette déformation se limite alors à des plans E–O fortement inclinés vers le N ou S.

Les leucogranites intrusifs dans les séries métamorphiques préservent systématiquement une combinaison de structures orthogonales. Chaque granite montre une zone nord peu anisotrope et à structures magnétiques N–S juxtaposée à une zone sud plus étroite, fortement anisotrope et à structuration E–O. Des reliques d’une foliation E–O subverticale sont également trouvées dans les orthogneiss et migmatites isolés au milieu du granite anatectique. L’imposant granite anatectique des Vosges centrales témoigne d’une mise en place en régime extensif et préserve les caractères d’une déformation à basse comme à haute température. À l’ouest de la faille de Sainte-Marie-aux-Mines, il montre une gneissosité subhorizontale associée à une linéation d’étirement et des zones de cisaillement inclinées vers le SO, tandis qu’à l’est seules les données d’ASM peuvent y révéler une linéation magnétique uniformément orientée N–S et plongeant vers le S ou SE. Bien qu’intrusifs dans différentes portions de la croûte orogénique, les granitoïdes Mg-K conservent toujours le même enregistrement comprenant deux directions orthogonales. Celui-ci reflète la transposition variable d’une foliation magnétique initialement NE–SO et subverticale en une nouvelle foliation subhorizontale associée à une linéation NO–SE.

Dans les Vosges du Sud, les sédiments de la série autochtone sont initialement affectés par un faible plissement plurikilométrique d’axe N–S. La stratification sédimentaire est ensuite déformée par des plis d’axe NO–SE qui représentent la structure dominante de la série autochtone. Ce plissement est également développé au centre de la série allochtone, alors que la périphérie montre une stratification N–S probablement antérieure. Localement, les plis NO–SE sont associés à une schistosité de plan axial naissante. Les filons de microgranite trouvés dans la série allochtone sont le plus souvent parallèles à la stratification verticalisée, mais peuvent aussi être sécants. Enfin, les plans de stratification verticaux sont réactivés plus tardivement par des mouvements décrochants. Dans le complexe magmatique Mg-K situé au sud, deux orientations majeures sont distinguées. À l’est du complexe, les structures magnétiques sont N–S, mais deviennent progressivement E–O dans la partie ouest qui pourrait correspondre à un niveau moins profond du complexe plutonique.

La discussion des données est finalement orientée vers une caractérisation des processus tectoniques, mais essaye également de replacer les Vosges dans l’évolution de la chaîne hercynienne au cours du Paléozoïque. Les rares informations disponibles pour le début du Paléozoïque indiquent une évolution péri-gondwanienne typique. La phase orogénique cadomienne fait place à des processus extensifs cambro-ordoviciens associés à un important magmatisme acide et au dépôt d’épaisses séries sédimentaires. Ceci est révélé par la datation des zircons dans les différentes unités métamorphiques des Vosges centrales. Par comparaison avec les massifs voisins, les protolithes sédimentaires des unités monotone et variée sont

alors interprétés comme le remplissage, de l'Ordovicien au Silurien, du bassin océanique saxothuringien. Le dépôt contemporain de séries marines au sud de la Forêt-Noire est également discuté pour proposer l'existence d'un domaine océanique méridional corrélé avec l'Océan Paléotéthys. En revanche, l'enregistrement sédimentaire des Vosges du Nord suggère qu'un socle cambro-ordovicien est resté émergé jusqu'au Dévonien moyen, période à laquelle un bassin s'approfondissant vers le nord a été ouvert. La chronologie des événements a donc conduit à considérer les Vosges du Nord comme une partie de la marge passive sud du bassin rhénohercynien.

L'accent est ensuite mis sur la période tardi-dévonienne qui marque le début de phénomènes convergents dans l'ensemble de la chaîne. Dans l'évolution du socle vosgien, l'activité de plusieurs zones de subduction est envisagée. La génération d'un métamorphisme de haut degré dans les lithologies sédimentaires (unité variée) et magmatiques (unité granulitique) est interprété comme le résultat d'une subduction continentale vers 360–350 Ma. D'après l'orientation initialement NE–SO des structures dans les unités métamorphiques, la zone de subduction est corrélée avec la subduction, vers le SE, de la marge passive saxothuringienne, comme proposé au NO du massif de Bohême. Dans le même temps, un bassin océanique de type arrière-arc est ouvert dans les Vosges du Sud. La polarité des dépôts et les structures résultant de son inversion suggèrent une ouverture N–S. Ceci serait compatible avec la fermeture, vers le nord, d'un domaine océanique situé au sud des Vosges et reconnu dans la Forêt-Noire du Sud. En résumé, le Dévonien supérieur verrait la fermeture progressive du bassin saxothuringien vers le SE et celle de l'Océan Paléotéthys vers le nord. À l'inverse, les dépôts présents dans les Vosges du Nord indiquent un environnement relativement calme, toujours rattaché à la présence du bassin rhénohercynien vers le nord.

Dans les Vosges, la convergence Dévono-Carbonifère culmine en une phase de collision au Carbonifère inférieur. La tectonique polyphasée associée à cette collision peut être séparée en quatre phases majeures. La première phase (D1) correspond à une compression E–O visible dans les lithologies appartenant à la croûte orogénique supérieure, moyenne et inférieure. Dans les unités métamorphiques, elle est caractérisée par une exhumation des roches de haut degré métamorphique et par un probable enfouissement contemporain de la croûte moyenne. Ceci est interprété comme une extrusion de matériel profond lors d'un échange vertical de matière au sein de la croûte. À cette période, un couplage complet existait donc entre les différents niveaux crustaux. La déformation D1 est suivie d'une compression verticale (D2) affectant principalement les unités monotone et variée préalablement juxtaposées, c'est-à-dire la croûte moyenne. La compression est gouvernée par une accumulation continue de matériel felsique à la base de l'orogène qui aboutit à un aplatissement progressif des

structures initialement subverticales. De cette manière, une discontinuité majeure se forme au sein de la croûte orogénique. Cette discontinuité va permettre un découplage important entre croûte supérieure et inférieure lors de la phase de déformation suivante (D3). En effet, une compression N-S n'est ensuite enregistrée que dans les lithologies appartenant à la croûte supérieure à moyenne. La phase D3 prend alors le caractère d'une tectonique de couverture dans laquelle la croûte profonde est passivement charriée vers le sud sous les unités supracrustales déformées. A plus grande échelle, la migration de la déformation D3 vers le nord est corrélée avec l'indentation du macro-continent Gondwana venant du sud. La dernière phase de déformation (D4) est caractérisée par un régime extensif à la fin du Carbonifère inférieur. Elle est associée à l'activité de systèmes de détachement opérant à basse et haute température, et montrant un transport vers le SO, le SE et possiblement vers le nord. La structuration générale héritée de la phase D4 indiquerait qu'un dôme métamorphique a progressivement été décoiffé de sa couverture lors d'un effondrement de l'orogène. Ce processus a probablement été contrôlé par une instabilité gravitaire, mais un affaiblissement thermique, généré par un apport de chaleur par désintégration radioactive dans les granitoïdes Mg-K, a également pu faciliter l'extension. L'orientation des détachements pourrait aussi être gouvernée par la subduction vers le sud du bassin rhénohercynien dont les témoins sont reconnus dans les Vosges du Nord.

Les conclusions à la deuxième partie englobent la pétrogenèse des zircons, la géologie régionale du massif vosgien et la caractérisation des processus tectoniques intracontinentaux. Les arguments géochronologiques, chimiques, texturaux et pétrologiques, suggèrent que les zircons à structure interne «floue» n'ont pas de signification géologique directe, mais témoignent d'une réhomogénéisation du système isotopique U-Pb lors d'un métamorphisme de haut degré. Ils sont ainsi de bons indicateurs de conditions $P-T$ élevées. Par ailleurs, la majorité des zircons étudiés semble dériver de la cristallisation d'un liquide anatectique. A ce titre, ils n'enregistrent pas l'âge du métamorphisme de haute pression, mais plutôt la fin du métamorphisme de haute température dans la croûte moyenne. Enfin, l'absence d'âges hercyniens dans l'unité des gneiss monotones indique que les conditions du faciès amphibolite supérieur ne sont pas suffisantes pour générer une croissance significative de zircon. Plusieurs événements nouveaux ont été proposés pour l'évolution hercynienne des Vosges. Parmi les plus significatifs, on retiendra : (1) le dépôt, de l'Ordovicien au Silurien, des protolithes des unités monotone et variée sur une marge passive d'affinité saxothuringienne ; (2) l'activité de deux zones de subduction au Dévonien : la subduction du bassin saxothuringien dirigée vers le SE et la subduction de l'Océan Paléotéthys dirigée vers le N ; (3) la formation d'un bassin

d'arrière-arc dans les Vosges du Sud au Dévonien supérieur ; (4) une collision polyphasée accompagnée de l'intrusion à 340–335 Ma de granitoïdes Mg-K depuis la croûte inférieure jusqu'à la croûte supérieure ; (5) un effondrement de l'orogène assisté par une thermicité élevée à la fin du Carbonifère inférieur. Dans un tel scénario, la suture entre saxothuringien et moldanubien est placée au nord du socle vosgien et la faille de Lalaye-Lubine est considérée comme une possible zone de détachement. Plusieurs processus tectoniques ont finalement été utilisés pour expliquer l'épisode de collision. Les structures subverticales et rétrogrades dans la croûte orogénique inférieure indiquent une extrusion de matériel profond et un possible échange vertical avec la croûte moyenne sus-jacente. L'accumulation de matériel à la base de l'orogène est ensuite utilisée pour expliquer un aplatissement dans la croûte moyenne et la genèse d'une discontinuité intra-orogénique majeure. Celle-ci permet un futur découplage de la déformation, aussi bien en compression qu'en extension. En effet, sa réactivation tardive en régime extensif permet de détacher les parties supérieures de la croûte orogénique et aboutit à un effondrement gravitaire de l'orogène.

Les conclusions générales du travail de thèse rappellent l'importance des données microstructurales et géochronologiques dans la détermination des évolutions $P-T-D-t$. En analysant l'orientation préférentielle des inclusions d'ilménite dans les porphyroblastes, il est possible d'accéder à des structures antérieures effacées dans la matrice. De plus, les monazites peuvent être utilisées pour dater des épisodes métamorphiques progrades, rétrogrades ou associés aux conditions $P-T$ maximales. Enfin, les zircons étudiés dans les roches de haut degré métamorphique sont plutôt susceptibles de dater la fin du métamorphisme de haute température. Dans les deux massifs étudiés (dôme d'Orlica-Śnieżnik, Vosges), des processus tectoniques similaires ont été identifiés. Ils résultent tous d'un flux de matériel dans un prisme orogénique lors d'un épisode de subduction continentale. Cela génère une croûte orogénique à partir de fragments crustaux autochtones et allochtones. Les contraintes latérales produisent ensuite un échange vertical de matière et de chaleur entre la croûte inférieure ascendante et la croûte moyenne descendante. Puis, la progression de la subduction continentale aboutit à un amincissement ductile de la croûte moyenne et à la formation d'une discontinuité intra-orogénique majeure. Initialement développée en régime coaxial, celle-ci évolue finalement vers des systèmes de détachement qui facilitent l'effondrement de l'orogène à la fin de la collision. En guise d'ouverture, il est rappelé que plusieurs caractéristiques et processus identifiés dans ce travail sont similaires à ceux observés dans d'autres systèmes orogéniques plus anciens ou plus récents. Le caractère « hercynotype » de l'orogène n'est donc pas retenu, et une invariabilité de la tectonique intracontinentale au cours du Phanérozoïque est préférée.

INTRODUCTION



INTRODUCTION

Les mouvements horizontaux à la surface de la Terre (Wegener, 1912 ; Argand, 1916), plus tard intégrés au concept de tectonique des plaques (p.ex. Hess, 1962; McKenzie & Parker, 1967; Le Pichon, 1968), ont largement contribué à expliquer la formation des chaînes de montagne (Dewey & Bird, 1970). A l'origine des phénomènes de subduction et collision, ils ont également été invoqués comme un moteur des processus tectoniques ayant lieu à une distance relativement importante des limites de plaques, c'est-à-dire dans les systèmes orogéniques intracontinentaux. Ainsi, le magmatisme, le métamorphisme et la réactivation du socle ont-ils été reliés à la convergence des plaques lithosphériques lors de phases de collision continent/continent (Dewey & Burke, 1973). Cependant, les mécanismes opérant au sein des orogènes intracontinentaux ne sont pas toujours directement corrélables avec la dynamique des blocs lithosphériques. En effet, certains marqueurs tectoniques observés dans les orogènes sont souvent incompatibles avec les directions de convergence aux limites des plaques (voir p.ex. l'esquisse structurale des Sudètes par H. Teisseyre, 1968, ou les directions d'extension tardi-hercynienne par Burg *et al.*, 1994). De même, les échelles de temps des processus orogéniques sont parfois nettement différentes des vitesses classiques de convergence (p.ex. Gebauer *et al.*, 1997). Sans remettre en cause le rôle des forces horizontales, ces discordances indiquent tout de même un découplage partiel entre la dynamique des plaques et la tectonique intracontinentale.

Le caractère polyphasé de la tectonique intracontinentale reflète la contribution de plusieurs autres mécanismes à l'évolution globale d'une chaîne de montagne. Ceux-ci s'expriment généralement à toutes les échelles et peuvent être caractérisés grâce à différents types d'observations. Les données structurales montrent que, de manière récurrente, la croûte orogénique préserve une succession de structures verticales et horizontales considérées comme les témoins de phases compressives et extensives syn-convergence (p.ex. Bell & Johnson, 1989). De plus, la pétrologie métamorphique révèle que certaines parties de la croûte continentale enregistrent des évolutions progrades variablement oblitérées par des épisodes rétrogrades, témoignant ainsi de phases d'enfouissement puis d'exhumation au sein de l'orogène (p.ex. Thompson & England, 1984). Enfin, les différentes techniques géochronologiques renseignent sur l'état thermique de la croûte et mettent particulièrement en évidence la persistance de domaines de haute température au cours de l'orogénèse (p.ex. Schlunegger & Willett, 1999).

Ces différentes approches ont été utilisées afin de contraindre les processus d'enfouissement ou d'exhumation dans la croûte orogénique. Ainsi, l'approximation de la

dynamique orogénique à un flux de matière dans un prisme (Platt, 1986) a fourni une base importante pour expliquer la superposition des structures ou encore certaines évolutions métamorphiques couplées (Miyashiro, 1961). Par ailleurs, les structures verticales montrant un métamorphisme rétrograde ont été connectées à des mécanismes d'extrusion verticale ou de plissement d'échelle crustale (Chamberlain, 1986 ; Thompson *et al.*, 1997). A l'inverse, les assemblages métamorphiques rétrogrades observés dans des structures subhorizontales ont été interprétés en termes d'amincissement ductile (Ring & Brandon, 1999), ou de flux de matériel à la base de l'orogène (Vanderhaeghe *et al.*, 1999). L'importance des forces gravitaires dans l'exhumation de la croûte orogénique profonde est quant à elle mise en évidence par la genèse de diapirs migmatitiques ou de dômes gneissiques, dont l'enregistrement structural et thermo-chronologique est caractéristique (Eskola, 1949; Calvert *et al.*, 1999).

Tous ces travaux antérieurs soulignent ainsi l'importance d'intégrer différentes sources de données pour contraindre au mieux les processus orogéniques. De manière importante, cette approche ne doit pas uniquement s'appliquer aux lithologies de haut degré métamorphique, mais bien à la totalité de la croûte continentale. A ce titre, les témoins paléozoïques de la chaîne hercynienne d'Europe représentent des objets privilégiés dans la mesure où ils permettent aujourd'hui l'accès aussi bien aux parties profondes qu'aux zones les plus superficielles de l'orogène. Guidé par ces convictions, le présent travail de thèse se propose donc d'explorer l'enregistrement structural, pétrologique et géochronologique de deux témoins hercyniens d'Europe : le dôme d'Orlica-Śnieżnik (Sudètes) et le massif des Vosges (NE France).

Dans les Sudètes, la particularité du dôme d'Orlica-Śnieżnik est de montrer une juxtaposition de lithologies de haut degré métamorphique avec des roches de la croûte supérieure à moyenne. En conséquence, l'évolution pression-température-déformation-temps ($P-T-D-t$) de différents segments de la croûte moyenne métasédimentaire (formation de Stronie-Młynowiec) est comparée à celle de la croûte inférieure granulitique ou éclogitique afin de préciser les mécanismes présidant à leur juxtaposition. A l'inverse, le socle paléozoïque des Vosges représente une succession de lithologies originellement situés dans la croûte inférieure, moyenne ou supérieure de l'orogène. Les épisodes de déformation et métamorphisme à travers cette section crustale complète sont donc évalués dans le but de caractériser l'évolution tectonique et la place du segment vosgien dans l'orogénèse hercynienne. Ces études conjointes sont utilisées pour discuter la tectonique intracontinentale dans la chaîne hercynienne d'Europe.

INTRODUCTION

Horizontal movements across the Earth's surface (Wegener, 1912; Argand, 1916), which were later integrated into the concept of plate tectonics (e.g. Hess, 1962; McKenzie & Parker, 1967; Le Pichon, 1968), have been largely used to explain the formation of mountain belts (Dewey & Bird, 1970). Because they are regarded as the cause of subduction and collision, they have additionally been invoked as a motor of tectonic processes occurring relatively far from plate boundaries, i.e. within intracontinental orogenic systems. In this view, magmatism, metamorphism and basement reactivation occurring during continent/continent collision events have been connected to the convergence of lithospheric plates (Dewey & Burke, 1973). However, the mechanisms operating within intracontinental orogens can not always be directly linked with the dynamics of lithospheric blocks. Indeed, some tectonic markers in orogenic systems are often incompatible with the directions of the advancing plates (see for instance the structural scheme of the Sudetes by H. Teisseyre, 1968, or directions of late-orogenic extension in the Variscan Belt by Burg *et al.*, 1994). Similarly, the time scales of orogenic processes sometimes differ from the typical plate convergence rates (e.g. Gebauer *et al.*, 1997). Although the role of horizontal forces is not questioned, these discrepancies therefore point to a partial decoupling between the dynamics of lithospheric plates and intracontinental tectonics.

The polyphase character of intracontinental tectonics actually reflects the contribution of additional mechanisms to the global evolution. The consequences of these mechanisms are visible at all scales and can generally be constrained using different types of observations. Structural data show that the orogenic crust rather consistently preserves a succession of vertical and horizontal fabrics which are seen as the witnesses of syn-convergent compressional and extensional events (e.g. Bell & Johnson, 1989). In addition, metamorphic petrology reveals that parts of the continental crust record prograde evolutions variably overprinted by retrograde events, thereby pointing to burial and exhumation phases during orogeny (e.g. Thompson & England, 1984). Finally, the different geochronological tools mostly document the thermal state of the crust, and especially unravel the persistence of high-temperature domains within the crust (Schlunegger & Willett, 1999).

These different features have been used in order to constrain burial and exhumation processes in the orogenic crust. Indeed, the critical wedge theory applied to orogenic systems (Platt, 1986) has provided a reliable explanation for the origin of fabric superpositions or paired metamorphic belts (Miyashiro, 1961). Besides, vertical fabrics showing retrograde metamorphism have been connected either to vertical extrusion or crustal-scale folding

mechanisms (Chamberlain, 1986; Thompson *et al.*, 1997). Conversely, retrograde metamorphic assemblages which are developed in flat-lying fabrics have been interpreted as a result of ductile thinning (Ring & Brandon, 1999) or lower crustal flow (Vanderhaeghe *et al.*, 1999). The role of gravitational forces on exhumation mechanisms is also evidenced by the occurrence of diapirically rising gneiss domes which are commonly characterised by a fairly diagnostic structural and thermochronological record (Eskola, 1949; Calvert *et al.*, 1999).

Previous studies have underlined the importance of integrating all possible sources of data when dealing with orogenic processes. Importantly, this approach should not only focus on high-grade lithologies, but alternatively take into account the entire continental crust. In this view, the Palaeozoic massifs of the Variscan Belt of Europe represent key areas since they allow to access to the deepest as well as the shallowest parts of the orogen. Accordingly, the present thesis tries to explore the structural, petrological and geochronological records in two Variscan regions: the Orlica-Śnieżnik Dome (Sudetes) and the Vosges Mountains (NE France).

In the Sudetes, the main feature of the Orlica-Śnieżnik Dome is a juxtaposition of high-grade rocks with upper- to mid-crustal lithologies. Consequently, the pressure-temperature-deformation-time (P–T–D–t) evolution of different parts of the metasedimentary middle crust (Stronie-Młynowiec formation) is compared to that of lower crustal eclogite or granulite in order to understand the mechanisms which are responsible for the juxtaposition of such contrasted crustal portions. By contrast, the Palaeozoic basement of the Vosges Mountains corresponds to lithologies originally located in the lower, middle and upper orogenic crust. The succession of deformation and metamorphic events is therefore investigated across this complete crustal section with the aim of characterising the tectonic evolution of the Vosges and its place during Variscan orogeny. Both studies are finally compared to discuss the processes of intracontinental tectonics in the Variscan Belt of Europe.

PART ONE

CONTRIBUTION OF MID-CRUSTAL STRUCTURAL, PETROLOGICAL
AND GEOCHRONOLOGICAL RECORDS TO THE UNDERSTANDING OF
INTRACONTINENTAL BURIAL AND EXHUMATION PROCESSES (SUDETES)

PREMIÈRE PARTIE

CONTRIBUTION DE L'ENREGISTREMENT STRUCTURAL,
PÉTROLOGIQUE ET GÉOCHRONOLOGIQUE DE LA CROÛTE MOYENNE
À LA COMPRÉHENSION DES PROCESSUS D'ENFOUISSEMENT ET
D'EXHUMATION (SUDÈTES)

INTRODUCTION TO PART ONE

Combined petrological and geochronological studies which constrain P – T – t paths have contributed significantly to the understanding of thermal processes related to the exhumation of deep-seated rocks in orogens (e.g. Duchêne *et al.*, 1997; Rubatto & Hermann, 2001; Carswell *et al.*, 2003). However, these studies are commonly not coupled with structural and microstructural investigations of the metamorphic fabrics, precluding fuller understanding of the tectonic mechanisms of exhumation. Notwithstanding, several studies linking structural and metamorphic records have proposed that shallow-dipping fabrics which are commonly associated with retrograde metamorphic assemblages and telescoped cooling ages can be interpreted as a result of exhumation driven by extension or gravitational spreading of the overthickened crust (e.g. Dewey *et al.*, 1993; Vanderhaeghe *et al.*, 1999). By contrast, other petrological and structural studies have showed that the retrograde P – T evolution in orogenic lower crustal rocks may be connected with subvertical fabrics suggesting vertical extrusion flow to be a major exhumation mechanism (e.g. Štípská *et al.*, 2004).

Nevertheless, both concepts are deduced from studies of deep-seated rocks representing the orogenic lower crust, but the link between structural and metamorphic records in the nearby mid- to supra-crustal rocks is rarely concurrently explored (e.g. Racek *et al.*, 2006). Once lower- and mid-crustal rocks with convergent P – T paths reach lower-grade conditions, they commonly show the same deformation pattern (e.g. Štípská *et al.*, 2006) indicating that they shared the same tectonic evolution during the last part of the exhumation process. Because the exhumed lower crustal rocks lack sensitive records of the late P – T evolution, it may therefore be possible to use the retrograde fabrics and associated metamorphic records in mid-crustal rocks to infer the exhumation evolution of the whole crust. Moreover, in mid-crustal units the tectono-metamorphic record related to the thickening process is commonly better preserved because the exhumation structures are heterogeneous and less intense. Consequently, the petrological and structural evolution of mid-crustal rocks is also likely to provide information about the burial process which has been obliterated in the orogenic lower crust.

An area where these burial and exhumation processes can be deciphered occurs in the internal part of the Bohemian Massif (Fig. 1). There, recent determinations of the P – T – D paths in deep-seated rocks led to the development of an exhumation model involving vertical extrusion of the lower crust and subsequent subhorizontal deformation at a mid-crustal level (Štípská *et al.*, 2004; Franěk *et al.*, 2006; Tajčmanová *et al.*, 2006). Because the exhumed high-grade rocks are commonly surrounded by belts of mid-crustal metasediments, it is therefore possible to challenge the tectonic evolution in the light of the P – T – D data

for these neighbouring lithologies. This approach was already adopted in the SE Bohemian Massif where the tectono-metamorphic evolution of the middle crust was explained in terms of crustal-scale folding (Ráček *et al.*, 2006), which is a process already proposed by e.g. Chamberlain (1986).

The present part of the thesis investigates the structural, petrological and geochronological records in metasedimentary belts of the Orlica-Šnieżnik Dome (Sudetes). The structural succession in metasediments is associated with crystallization-deformation relationships among the major metamorphic minerals, and especially garnet porphyroblasts, in order to assess the prograde and retrograde character of each metamorphic fabric. Mineral equilibria modelling is further used to decipher the P - T - D evolution of the different parts of the metasedimentary middle crust. In addition, the timing of tectono-metamorphic processes is unraveled by electron microprobe (EMP) monazite dating correlated with monazite petrogenesis. All the data are combined into P - T - D - t paths which are compared to those documented in the juxtaposed high-grade rocks. The coupled evolutions are finally discussed in terms of intracontinental burial and exhumation processes in the orogenic crust.

CHAPTER I

GEOLOGICAL BACKGROUND

The Orlica-Śnieżnik Dome (OSD) represents a witness of the Variscan orogen in Central Europe. The Variscan orogenic cycle that spans the entire Palaeozoic is defined by the drifting of continental blocks away from the northern Gondwana margin, and the subsequent amalgamation of terranes located between the already assembled Laurentia and Baltica (Laurussia) macrocontinents to the North and Gondwana to the South (e.g. Matte, 1986; Ziegler, 1986). The associated subduction/collision events (e.g. Franke, 2000) resulted in the formation of a *ca.* 8000 km-long orogenic belt that is now exposed from the Appalachians to the Ural Mountains. Lithostratigraphic correlations led Suess (1926) and Kossmat (1927) to define several zones across Europe (the Rhenohercynian, Saxothuringian, Moldanubian and Moravo-Silesian zones) and especially in the Bohemian Massif, which represents a relatively large exposure of Variscan rocks (Fig. 1). Nevertheless, the Sudetes represent an “extremely complex mosaic region” (Żelaźniewicz, 1995) which challenges the continuity of these zones in the NE Bohemian Massif. There, NW–SE striking fault zones isolate the Sudetic mosaic (Fig. 1) and prevent from drawing direct correlations with the neighbouring Saxothuringian and Moldanubian zones.

1) Sudetes

The Sudetes are represented by a NW–SE striking mountain belt that extends from East Germany to Silesia along the border between Czech Republic and Poland. Suess (1926) introduced the term *Lugicum* (or *Lugian*) for the domain covering the West and Central Sudetes. This *Lugian* domain is bounded by NW–SE striking fault zones: the NE Odra fault zone and the SW Elbe fault zone, and is in contact with the Moravo-Silesian zone towards the SE (Fig. 1). The centre of the massif is also affected by two major NW–SE striking faults: the Intra-Sudetic fault and the Sudetic Marginal fault (Fig. 2). A detailed description of the Sudetes is given in Dallmeyer *et al.* (1995) or Mazur *et al.* (2006), and this section presents only an overview of the main lithological, structural or metamorphic features reported for the different zones or blocks composing the Sudetic mosaic (Fig. 2), namely from NW to SE: (1) the western units including the Lusatian zone, the Görlitz Belt and the Kaczawa unit, (2) the Iżera-Karkonosze Block, (3) the Intra-Sudetic Basin, (4) the Góry Sowie Block, (5) the Orlica-Śnieżnik Dome and (6) the Moravo-Silesian zone.

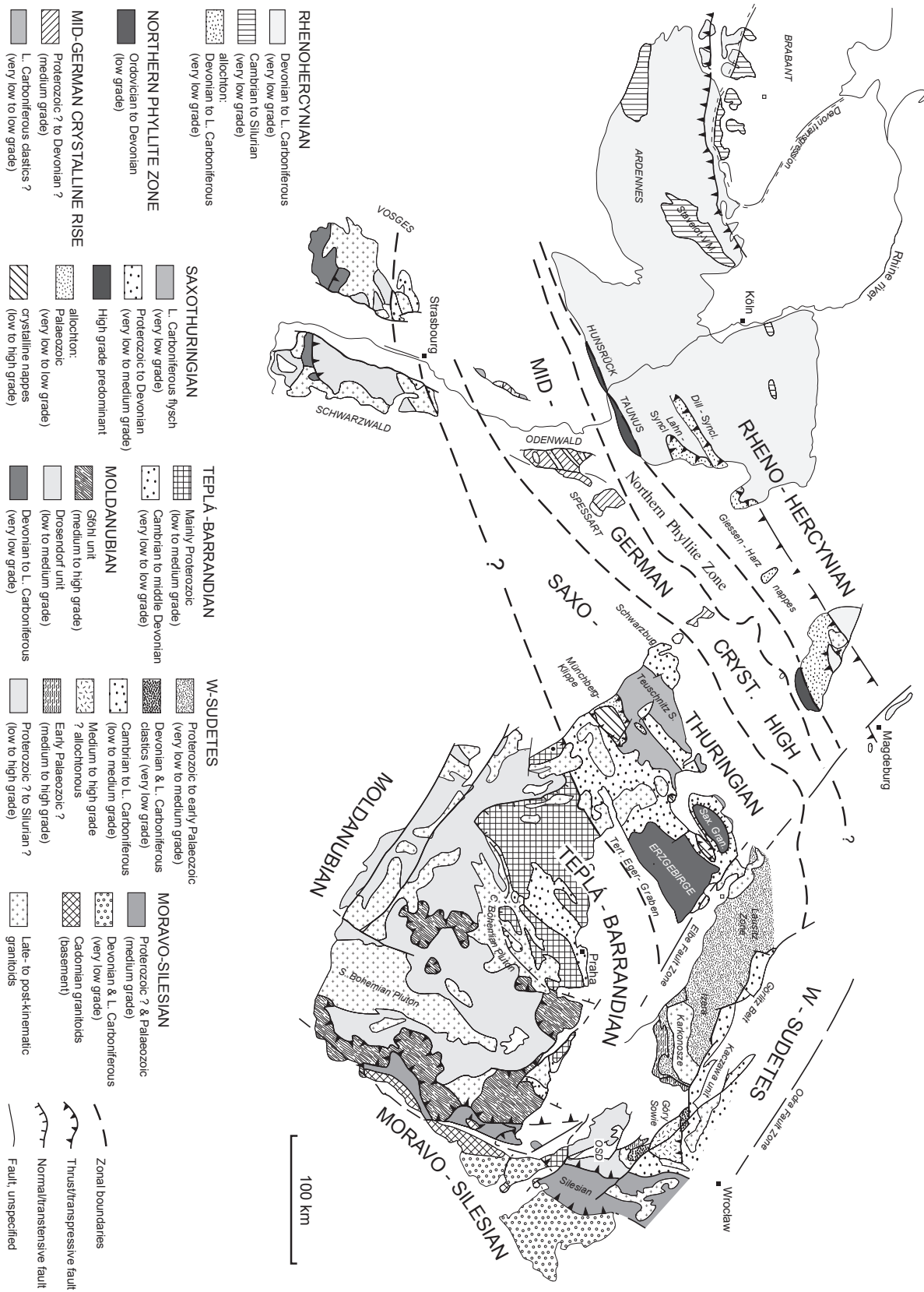


Figure 1. Map of the Variscan Belt in Central Europe (after Franke *et al.*, 2000).

Western units (Lusatian zone, Görlitz Belt, Kaczawa unit)

The northwestern part of the Sudetes (Fig. 2) is occupied by the Lusatian zone which comprises Late Proterozoic turbiditic sediments intruded by Late Proterozoic to Early Cambrian granitoids (Tikhomirova, 2002; Żelaźniewicz *et al.*, 2004). To the SE, the adjacent Görlitz Belt preserves Cambrian carbonates, sandstones and volcanics overlain by rare Ordovician siliciclastic deposits and Silurian to Devonian monotonous quartzites, pelites and greywackes. This succession is followed by Early Carboniferous flyschoid sedimentation (Urbanek *et al.*, 1995). The easterly Kaczawa unit is composed of Ordovician limestones and Silurian to Devonian deep marine sediments. In addition bimodal volcanism and pillow lavas of E-MORB to N-MORB affinity alternate with Cambrian (?) to Silurian sediments (Furnes *et al.*, 1994). The upper part of the Palaeozoic succession is represented by Late Devonian to Early Carboniferous clastics and olistostromes. In several parts of the Kaczawa unit, relicts of blueschist-facies metamorphism have been found despite a later greenschist-facies overprint (Kryza *et al.*, 1990).

In the Lusatian zone, only Proterozoic deformation is documented, whereas in the Görlitz Belt, NE–SW shortening probably occurred during Variscan times (Żelaźniewicz *et al.*, 1995). In the Kaczawa unit, the structure is characterised by thrust sheets and mélangé bodies. Seston *et al.* (2000) proposed a polyphase tectonic evolution involving thrusting towards the W to NW during the Devonian, SE-directed extensional reactivation of the previous thrust surfaces in the mid-Carboniferous, and later N–S shortening.

The geodynamic evolution of this part of the Sudetes starts with Late Proterozoic sedimentation and plutonism in the Lusatian zone. In the Kaczawa unit, continental rifting initiated at *ca.* 500–485 Ma (Kryza *et al.*, 2007) progressively reached a true oceanic stage in the Silurian (Furnes *et al.*, 1994; Kryza & Zalasiewicz, 2008). This oceanic domain is tentatively linked with ophiolitic remnants found in the Izera-Karkonosze Block to the South (Seston *et al.*, 2000). During subsequent convergence, rocks from the Kaczawa unit were involved in the formation of an accretionary prism (Baranowski *et al.*, 1990) and underwent Late Devonian subduction (Collins *et al.*, 2000). This subduction event is commonly paralleled to the SE-directed subduction of the Saxothuringian basin which is documented in the Izera-Karkonosze Block located to the South.

Izera-Karkonosze Block

The Izera-Karkonosze Block (Fig. 2) is mostly occupied by the large Karkonosze granitic body which was emplaced at 329 ± 17 Ma (Rb–Sr dating; Duthou *et al.*, 1991). It is surrounded by metasediments and the Izera gneiss which both show Cambro-Ordovician protolith ages

(Borkowska *et al.*, 1980; Kröner *et al.*, 2001) and Variscan tectono-metamorphic overprint. To the South, low- to medium-grade Devonian-Carboniferous metasediments (Jěstěd unit) are tectonically overlain by a metamorphic unit (South Karkonosze unit) containing glaucophane-bearing metavolcanic rocks and high-pressure metapelite (Smulikowski, 1995; Záčková *et al.*, 2010), and by a meta-igneous complex (Leszczyńiec unit) of N-MORB affinity representing a *ca.* 500 Ma-old remnant of oceanic crust (Oliver *et al.*, 1993; Kryza & Mazur, 1995).

The structural pattern in the Izera-Karkonosze Block is characterised by NW–SE to N–S trending stretching lineations related to NW-directed ductile thrusting that occurred in the Late Devonian to Early Viséan (Mazur & Aleksandrowski, 2001). This stage was most likely preceded by a high-pressure/low-temperature event, the end of which was estimated at *ca.* 360 Ma by $^{40}\text{Ar}/^{39}\text{Ar}$ dating on phengite from the mafic blueschist (Maluski & Patočka, 1997). In addition, later SE-directed extension during the Carboniferous is documented by E–W trending lineations (Mazur & Aleksandrowski, 2001).

In summary, rocks from the Izera-Karkonosze Block indicate a SE-directed subduction and basin closure during the Late Devonian, followed by a thrust imbrication involving Cambro-Ordovician seafloor of probable Saxothuringian affinity, blueschist-facies rocks and para-autochthonous low- to medium-grade metasediments and gneiss. This evolution led Mazur & Aleksandrowski (2001) to propose that the southern part of the Izera-Karkonosze Block corresponds to a Variscan suture between the Saxothuringian zone and a hypothetical Teplá-Barrandian zone which is now hidden beneath the Intra-Sudetic Basin towards the SE.

Intra-Sudetic Basin

The Intra-Sudetic Basin is a NW–SE depression that occupies a large part of the Central Sudetes. Together with the associated Świebodzice and Bardo basins, it is surrounded by the Izera-Karkonosze Block to the W, the Kaczawa unit to the N, and the Góry Sowie Block and Orlica-Śnieżnik Dome to the E and SE (Fig. 2). The Świebodzice basin preserves nearly 4000 m of Upper Devonian to Tournaisian coarse, land-derived detritus mostly composed of polymictic conglomerates and showing a N-directed sediment supply (Porębski, 1990). The Bardo Basin is formed by ~300 m of Ordovician to Tournaisian pelagic deposits and ~800 m of Late Devonian to Early Carboniferous carbonates and flysch (Hajdukiewicz, 1990). In the Intra-Sudetic Basin, the oldest sediments are represented by Lower Carboniferous, partly marine and partly terrestrial deposits that can be up to 6500 m thick (Dziedzic & Teisseyre, 1990). In this basin, gneissic material represents a significant amount of the detrital sediments (Teisseyre, 1968; 1971), and paleocurrent analysis points to northern, southern and southeastern provenance, the latter being considered as the most important (Teisseyre, 1975).

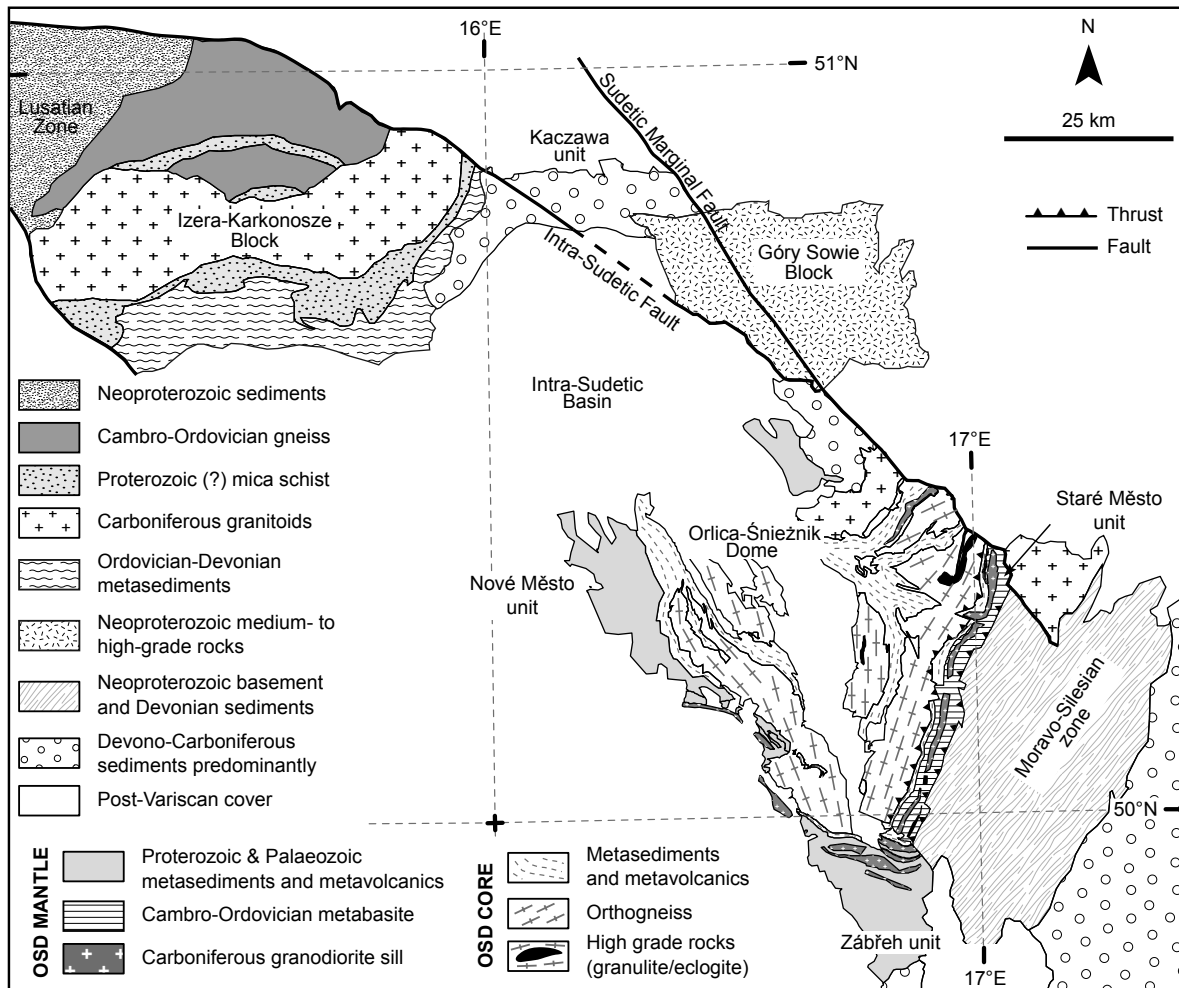


Figure 2. Geological map of the Sudetes (after Aleksandrowski *et al.*, 1997).

Sedimentological studies indicate that the Late Devonian to Early Carboniferous basins probably correspond to intramontane depressions filled by abundant detritus derived from the surrounding metamorphic basement (Dziedzic & Teisseyre, 1990). The northern source region is considered to be the Kaczawa unit, whereas the southeastern provenance is commonly associated with the erosion of the Góry Sowie Block (Teisseyre, 1975).

Góry Sowie Block

The Góry Sowie Block corresponds to a fault bounded metamorphic unit within the Central Sudetes (Fig. 2). It is surrounded by discontinuous ophiolitic remnants forming the so-called Circum Góry Sowie ophiolite (Kryza, 1995). These ultramafic bodies (Ślęza, Braszowice and Nowa Ruda) represent relicts of Silurian oceanic crust (Oliver *et al.*, 1993; Dubińska *et al.*, 2004), probably thermally imprinted around 350 Ma (Pin *et al.*, 1988). The basement of the Góry Sowie Block is composed of paragneiss derived from Neoproterozoic greywacke, pelite and psammite, migmatitic orthogneiss with precursor ages of 488–473 Ma (Kröner & Hegner,

1998), and several slices of amphibolite, granulite and serpentized peridotite (Želažniewicz, 1987).

Polyphase deformation in the Góry Sowie Block was detailed by Želažniewicz (1990). He recognised an early recumbent folding associated with the incorporation of granulite and peridotite slices into the paragneiss, subsequent upright folding related to N–S to NE–SW shortening, strike-slip along the block margin and final vertical shortening. The first deformation is associated with an upper amphibolite-facies metamorphic event reaching kyanite grade, whereas the subsequent deformation phase coincides with a strong overprinting at lower pressure but higher temperature conditions. This second event is responsible for the widespread occurrence of sillimanite, K-feldspar, cordierite or andalusite, and for intense migmatization in the paragneiss (Želažniewicz, 1987). By contrast, high-grade granulitic rocks preserve peak conditions of 15–20 kbar and 900 °C and later equilibration at 4–10 and 600–900 °C (Kryza *et al.*, 1996; O’Brien *et al.*, 1997). The age of peak metamorphism in high-grade lithologies is estimated at 400–395 Ma (O’Brien *et al.*, 1997) and the subsequent high temperature event is constrained by U–Pb and Rb–Sr dating at *ca.* 380 Ma (Bröcker *et al.*, 1998; Timmermann *et al.*, 2000).

The puzzling superposition of the high-grade Góry Sowie Block over the surrounding, weakly deformed and metamorphosed ophiolitic remnants led to contrasted geodynamic interpretations (e.g. Kröner & Hegner, 1998). However, the important feature is that metamorphism in the Góry Sowie Block occurred significantly earlier than in the other units of the Sudetes. Indeed, high-grade metamorphic rocks probably indicate Early Devonian continental subduction followed by exhumation and final imbrication with ophiolitic rocks during the Late Devonian (Mazur *et al.*, 2006). In this view, the Góry Sowie Block represents an allochthonous and isolated continental domain which was amalgamated between the Saxothuringian and the Moravo-Silesian zones.

Western and southern OSD mantle (Nové Město and Zabřeh units)

The low- to medium-grade Nové Město, Staré Město and Zabřeh units which surround the medium- to high-grade Orlica-Šniežnik Dome core are classically referred to as the OSD mantle zone (Fig. 2). On the western flank of the OSD core, the Nové Město unit is composed of phyllite, greenstone and amphibolite of probable Neoproterozoic age (Chaloupský *et al.*, 1995). The metamorphic grade increases from greenschist to amphibolite facies from the W to the E of the unit (Opletal *et al.*, 1980), and a zone of amphibolite with MORB-type affinity occurs along the contact with the OSD core (Floyd *et al.*, 1996). This N–S striking boundary is intruded by late-tectonic Carboniferous granitoids. The Zabřeh unit which is located on

the southern edge of the OSD core is formed by metasediments and metavolcanics intruded by granodiorite sills in the northern part. The whole unit is affected by amphibolite-facies metamorphism.

Fajst (1976) already recognised a structural unconformity between the N–S structures in the OSD mantle and the NW–SE to E–W structures in the surrounding Nové Město and Zabřeh units, respectively. In the Nové Město unit, Mazur *et al.* (2005) documented early E-directed thrusting on moderately W-dipping foliation planes, followed by E–W shortening with increasing intensity of folding towards the OSD core. The resulting N–S striking anisotropy was reactivated by dextral shearing and was probably associated with normal movement leading to the present-day juxtaposition of the OSD core with the Nové Město unit. In the Zabřeh unit, Verner *et al.* (2009) recognised a first E–W subvertical structure subsequently flattened into a S-dipping foliation which preserves a stretching lineation plunging to the SE.

The boundary between the Nové Město unit and the OSD core corresponds to a high metamorphic gradient, shows a Carboniferous downthrow of the Nové Město unit, and is intruded by late-tectonic granitoids. Accordingly, Mazur *et al.* (2005) interpreted this zone as a typical Teplá-Barrandian/Moldanubian boundary. In a same way, the Zabřeh unit hosts a significant amount of granodioritic intrusions and records SE-directed normal displacement (Chopin *et al.*, 2011a). These similarities suggest that the western and southern parts of the OSD mantle were most likely deformed during the rise of the OSD core (Fajst, 1976) and could therefore represent the detached upper part of the OSD (Chopin *et al.*, 2011a).

Eastern OSD mantle (Staré Město unit)

The eastern flank of the OSD core is occupied by the Staré Město unit (Fig. 2). It corresponds to a 4–5 km-wide belt of metagabbro, granodiorite, migmatitic metasediments, leptyno-amphibolite and peridotite slices bounded by thrust faults. Numerous ages around 500 Ma indicate that all magmatic precursors were formed during the Cambro-Ordovician (Kröner *et al.*, 2000b).

Štípská (1999) distinguished between a Cambro-Ordovician and a Variscan deformation event in the Staré Město unit. Whereas Cambro-Ordovician magmatic textures are preserved in the leptyno-amphibolite complex, Variscan deformation produced foliations steeply dipping towards the NW which were intruded by magmatic sills at 339 ± 1.1 Ma (Parry *et al.*, 1997) and later dextrally sheared. Similarly, the metamorphic evolution consists of two distinct Cambro-Ordovician and Variscan events that show identical HT/MP conditions (Štípská, 1999) but contrasted microstructural records (Baratoux *et al.*, 2005). These microstructures were used

by Lexa *et al.* (2005) to propose that the HT events had different durations.

According to Štípská *et al.* (2001), the Staré Město unit indicates a first episode of Cambro-Ordovician rifting and associated HT metamorphism in the attenuated lower crust. Subsequent Variscan convergence was characterised by a high thermal regime and a weak thickening of the Staré Město unit. This is interpreted as the result of underthrusting of the neighbouring OSD core and Moravo-Silesian zone below the relatively cold and rigid Staré Město unit.

Moravo-Silesian zone

Following Misař & Urban (1995), the Moravo-Silesian zone includes the Brunovistulian (or Brunia) basement (Dudek, 1980) as well as the Moravicum and Silesicum allochthonous nappes defined by Suess (1912). In the East Sudetes, this zone is represented by a succession of NE–SW trending domains corresponding either to metamorphosed Brunia-derived fragments to the W, or to the Brunovistulian basement to the E (Kalvoda *et al.*, 2008). From W to E are distinguished: the Velké Vrbno Dome preserving eclogitic rocks inserted into orthogneiss and metasedimentary rocks (Štípská *et al.*, 2006), the Keprník and Desná Domes exposing Neoproterozoic basement and a Devonian sedimentary cover, and the Culm Basin filled with Tournaisian to Namurian turbidites. Across the Desná, Keprník and Velké Vrbno Domes, Souček (1978) observed inverted metamorphism with increasing grade from E to W, i.e. towards the structurally higher Velké Vrbno Dome. The structural evolution of the Moravo-Silesian zone was investigated by Schulmann & Gayer (2000) and chiefly involves Variscan thrusting associated with significant strike-slip movements. In some parts, W-dipping foliations were strongly overprinted by extensional structures.

To sum up, the geodynamic evolution of the Moravo-Silesian zone was interpreted in terms of Devonian rifting generating crustal-scale boudins, Carboniferous oblique underthrusting of the assembled domes producing an inverted metamorphic sequence, and late extensional unroofing (Schulmann & Gayer, 2000).

2) Orlica-Śnieżnik Dome

The Orlica-Śnieżnik Dome is located in the Central Sudetes at the boundary between Czech Republic and Poland. This 70 km-long and 20 to 50 km-large basement exposure is divided by the N–S Cretaceous Nysa graben into a western Orlica massif and an eastern Śnieżnik massif (Fig. 3). The OSD is bordered by the Neoproterozoic low- to medium-grade mantle zone represented by the Nové Město unit to the W, the Zabřeh unit to the S and the Staré Město unit to the E. Towards the NW, the OSD is covered by Carboniferous deposits of the

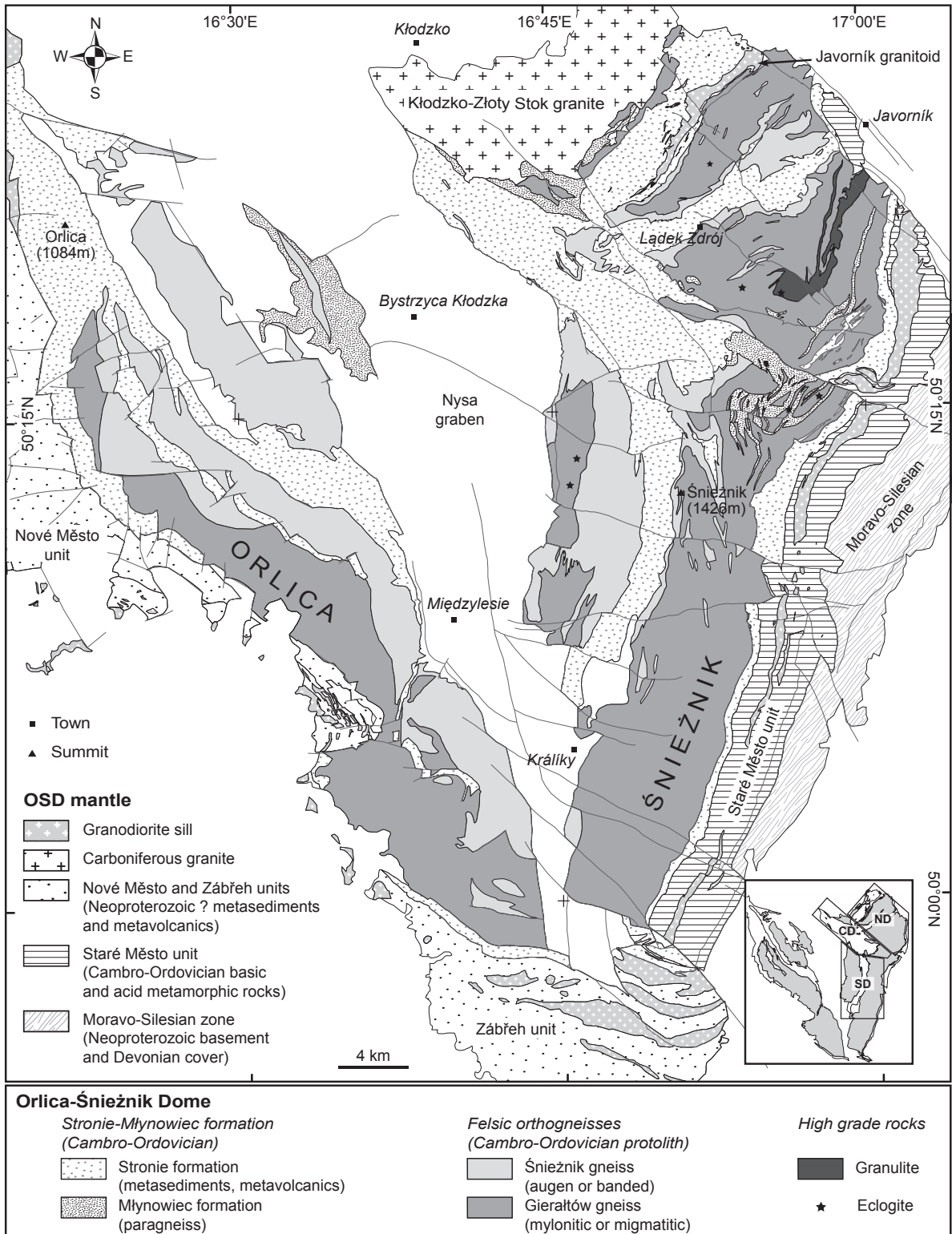


Figure 3. Geological map of the Orlica-Śnieżnik Dome and the surrounding units (after Don *et al.*, 2003; Żelaźniewicz *et al.*, 2006). Bottom right hand inset shows the three structural domains detailed in Part 1-Chapter II (ND=northern domain; CD=central domain; SD=southern domain).

Intra-Sudetic Basin, whereas its NE termination is obliterated by the Carboniferous Złoty Stok pluton. The first detailed description of the OSD, mostly focusing on its eastern part (formerly called “Glatzer Schneegebirge”), was given by Fischer (1935). A later summary by Don *et al.* (1990) described the OSD as predominantly composed of orthogneiss, metasedimentary-metavolcanic rocks and scarce occurrences of high-grade rocks.

Lithology

Since Fischer (1935), the felsic orthogneissic rocks which occupy the largest part of the OSD (Fig. 3) have been subdivided into two types. The first type corresponds to the augen to banded Śnieżnik orthogneiss (“Schneeberg Orthogneis”), whereas the second type corresponds to the fine-grained mylonitic or migmatitic Gierałtów orthogneiss (“Gersdorfer gneis”). Both orthogneisses have a granitic composition and mostly show quartz, K-feldspar, plagioclase and biotite with minor occurrences of garnet or phengitic muscovite (Chopin *et al.*, 2011b). The link between the Śnieżnik and the Gierałtów gneisses is still debated. Major and trace element chemistry as well as Sr and Nd isotopes are used by Lange *et al.* (2005b) to suggest that the Śnieżnik and Gierałtów orthogneisses represent textural variations due to Variscan metamorphism of a similar granitic precursor. On the contrary, gneissic enclaves in the Śnieżnik gneiss (Grześkowiak & Żelaźniewicz, 2002) as well as geochronological investigations (Żelaźniewicz *et al.*, 2006) are used to propose that the metamorphism of the older Gierałtów gneiss occurred during the emplacement of the protolith of the Śnieżnik orthogneiss.

The metasedimentary-metavolcanic rocks belong to the Stronie-Młynowiec Group (Don *et al.*, 1990). Originally, Fischer (1935) distinguished between the monotonous Młynowiec (“Mühlbach Serie”) and the varied Stronie (“Seitendorfer Gruppe”) formations, and Don & Dowidar (1988) later observed that they are separated by a layer of basal quartzite. The Młynowiec formation is chiefly composed of paragneiss with only rare intercalations of mica schist and amphibolite. Apart from abundant albite and biotite, Ansilewski (1966) observed staurolite, garnet and sillimanite in the paragneiss. The spatially larger Stronie formation – the main purpose of this work – is characterised by abundant mica schist, some paragneiss and numerous m- to km-scale intercalations of basic and acid metavolcanite (amphibolite and leptite), quartzite, graphitic schist, and calcitic to dolomitic marble. The mica schists contain quartz, albite, micas and garnet with local occurrences of staurolite, sillimanite, kyanite or chloritoid (Butkiewicz, 1968; Smulikowski, 1979). Based on trace element patterns, Floyd *et al.* (1996) concluded that the amphibolites have a basaltic composition approaching a MORB-type chemistry, whereas Wojciechowska *et al.* (2001) proposed that the leptite bodies (the

“Haniak” gneiss of Kozłowska-Koch, 1973) represent metamorphosed rhyolites or tuffs. The mineralogy of calc-silicate rocks has been investigated by Jastrzębski (2005) who observed phlogopite, tremolite or diopside in addition to calcite and dolomite.

High-grade rocks occur as relatively narrow bodies of felsic or mafic granulite and eclogite in the core of the gneissic massifs (Fig. 3). Granulitic rocks have been traditionally associated with the Gieraltów gneiss (e.g. Fischer, 1935) and form a NE–SW belt in the NE part of the OSD. The dominant felsic granulite variety is composed of quartz, K-feldspar, plagioclase and garnet with few kyanite and rutile while the mafic granulite mostly comprises omphacitic clinopyroxene, garnet and plagioclase (Kozłowski, 1965). Eclogite is present as discontinuous lenses within the orthogneisses. The location and petrography of eclogitic relicts has been described in detail by Smulikowski (1967) or Bakun-Czubarow (1968). They observed a primary assemblage of garnet and omphacite with some hornblende, phengite, kyanite or zoisite.

Structure

A polyphase structural evolution has been recurrently proposed for the OSD (e.g. Kasza, 1964). In the Orlica Dome, Żelaźniewicz (1978) recognised a first foliation which is probably subhorizontal and corresponds to the axial plane cleavage of E-vergent recumbent folds with N–S trending hinges. However, the dominant structural pattern of the OSD is marked by N–S to NE–SW trending upright folds affecting the metasediments and the underlying gneisses (e.g. Don, 1964). This folding produces km-scale gneissic antiforms and metasedimentary synforms which were already partly recognised by Bederke (1944) in the centre of the OSD (Fig. 4). Don (1964; 1982) extended this view to the whole massif and proposed the existence of four major gneissic anticlines separated by three large synclines occupied by rocks of the Stronie-Młynowiec formation. According to Dumicz (1979), the E–W shortening event was followed by transposition of the subvertical structures into shallow-dipping foliation planes. This resulted in an upward movement of the upper crust while the lower crust was subjected to horizontal flow (Dumicz, 1979). Later top-to-the-N thrusting along the shallow-dipping foliation or weak horizontal shortening has additionally been documented by Jastrzębski (2008) in metasedimentary rocks.

Although there is a general consensus on the structural evolution, the timing of deformation remains strongly debated. J. Don (in Don *et al.*, 1990) favoured a deformation cycle occurring during the Early Palaeozoic, whereas M. Dumicz considered that the whole history took place during Devono-Carboniferous times. Recent finding of an Ordovician syenite dyke cross-cutting gneissified rocks is used by Żelaźniewicz *et al.* (2006) to attest

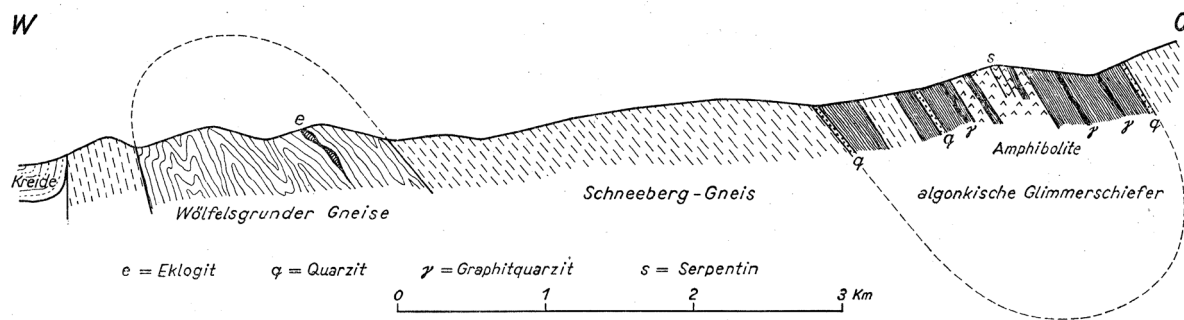


Figure 4. Bederke's (1944) section across the central part of the OSD. This section illustrates the long recognised - and yet relatively undisputed - general structure of the OSD involving an antiform of Śnieżnik (=Schneeberg) and Gieraltów (=Wölfelsgrunder) orthogneiss and a synform of Stronie metasedimentary rocks (=algonkische Glimmerschiefer). The section roughly goes from the eastern margin of the Nysa Graben up to the Śnieżnik Mt.

for pre-Variscan deformation. Nevertheless, the growing amount of “younger” Devonian-Carboniferous metamorphic ages (see *Metamorphic ages* section) suggests a dominant Variscan deformation history. During that period, the OSD most likely underwent tangential compression followed by orogenic collapse (Dumicz, 1979).

Metamorphism

The metamorphic conditions in both orthogneiss types have been poorly investigated. Żelaźniewicz & Bakun-Czubarow (2002) proposed conditions of 10–11 kbar and 650–700 °C for the Gieraltów gneiss surrounding the eclogite, and Żelaźniewicz *et al.* (2006) found a higher temperature of 722–752 °C at 7 kbar in the Orlica region. By contrast, Bröcker & Klemd (1996) suggested that some orthogneissic rocks shared the ultrahigh-pressure (UHP) metamorphic evolution of the eclogite. Based on a garnet-titanite-zoisite assemblage, they deduced conditions of 700–880 °C at pressures over 27 kbar. The subsequent retrograde stage was constrained at 7–9 kbar and 600–620 °C, which roughly corresponds to the initial estimates of Kowzłowska-Koch (1973).

Several lithologies of the Stronie-Młynowiec formation have been used to constrain the *P–T* evolution of this crustal level. The results show that the Stronie-Młynowiec formation underwent peak metamorphism in the amphibolite facies with increasing metamorphic grade from the West to the East of the OSD (Jastrzębski, 2008). A paragneiss of the Młynowiec formation yielded 570–610 °C and 6–9 kbar while paragneiss, mica schist or marble samples of the Stronie formation preserve *P–T* conditions between 500–650 °C and 6.5–9 kbar (Józefiak, 1999; Romanová & Štípská, 2001; Jastrzębski, 2002; 2005; Murtezi, 2006). In mica schist from the Orlica Dome, Mazur *et al.* (2005) obtained similar *P–T* estimates, whereas in amphibolite intercalations from the Śnieżnik area Nowak & Żelaźniewicz (2002) favoured higher temperatures of 625–645 °C at 8 kbar. In addition, Jastrzębski (2008) connected

the metamorphic evolution to the superposition of structures. In the centre of the OSD, he proposed that peak conditions of 9–10 kbar and ~510 °C were attained in the subvertical foliation and that progression towards ~620 °C and 7–8 kbar occurred in the subsequent subhorizontal foliation.

Eclogitic rocks are thought to derive from a sedimentary (Smulikowski, 1967) or MORB (Bakun-Czubarow, 1998) protolith. The presence of pseudomorphs after coesite led Bakun-Czubarow (1991; 1992) to propose UHP conditions of ~28 kbar at 700–800 °C. These *P–T* estimates are similar to those obtained by Bröcker & Klemd (1996) who additionally recognised a retrogression stage at 4–11 kbar and 600–650 °C. A polyphase exhumation from 15–20 kbar and 680–750 °C to 6–12 kbar and 640–700 °C was also proposed by Żelaźniewicz & Bakun-Czubarow (2002). Peak *P–T* conditions in granulite approach those of eclogite (Klemd & Brocker, 1999) but show lower pressure and higher temperature. Peak pressure is estimated to lie at 19–25 kbar for temperatures of 850–900 °C (Steltenpohl *et al.*, 1993; Kryza *et al.*, 1996). Importantly, Štípská *et al.* (2004) linked peak conditions of ~18 kbar and ~900 °C with an early subhorizontal fabric while retrogression towards ~10 kbar and ~700 °C was mostly achieved in the subsequent subvertical foliation.

Protolith ages

Protolith ages for the granitic precursors of both orthogneiss types range between 530 and 490 Ma (Oliver *et al.*, 1993; Turniak *et al.*, 2000; Kröner *et al.*, 2001; Mazur *et al.*, 2010). This supports the view of Lange *et al.* (2005b) who believe that the Śnieżnik and Gierałtów orthogneisses are derived from the same Cambro-Ordovician protolith. Alternatively, Grześkowiak & Żelaźniewicz (2005) interpret similar SHRIMP zircon ages in the Gierałtów orthogneiss as a result of migmatization during the intrusion of the Śnieżnik protolith at 515–480 Ma. Nevertheless, in the absence of older ages, it is presently difficult to support that the Gierałtów protolith was formed before the Cambro-Ordovician.

The Stronie-Młynowiec formation was long thought to be the oldest lithology in the OSD (Fischer, 1935; Vangerow, 1943). Micropaleontological investigations in marble intercalations further supported the view of a Neoproterozoic to Lower Cambrian deposition age (Gunia, 1984a; 1984b; 1990). However, recent U–Pb dating of detrital zircon indicate a continuous sedimentation of the distal Młynowiec formation and the more proximal Stronie formation during the Middle Cambrian to Lower Ordovician (Jastrzębski, 2008; Jastrzębski *et al.*, 2010). These estimates are in agreement with U–Pb zircon ages of *ca.* 500 Ma obtained in metarhyolite intercalations of the Stronie formation (Murtezi & Fanning, 2005). It is therefore tempting to link this Cambro-Ordovician acid volcanism with the contemporaneous

intrusion(s) of the gneissic protolith(s).

Protolith ages for the high-grade rocks are only poorly constrained. Indeed, dating of granulite and eclogite systematically results in a broad spectrum of ages stretching between 600 and 400 Ma (e.g. Bröcker *et al.*, 2010). Although significant Pb loss can be the major cause of this age spread, Bröcker *et al.* (2010) proposed that protolith were chiefly formed at 550–500 Ma. In this view, eclogite and granulite protoliths would be nearly coeval with the generation of granitic rocks during the Cambro-Ordovician.

Metamorphic ages

As emphasised by Bröcker *et al.* (2009), metamorphic ages in the OSD fall into two groups: a pre-350 Ma and a 340–330 Ma group. The identification of several Devonian ages has continued the debate about pre-Variscan events, especially concerning the two orthogneiss varieties. According to Żelaźniewicz *et al.* (2006), even Cambro-Ordovician ages in the Gierałtów gneiss reflect migmatization and not emplacement. In orthogneiss, U–Th–Pb monazite data led Gordon *et al.* (2005) to propose a metamorphic event at 375 Ma in Orlica, while Lange *et al.* (2005b) attributed Devonian ages only to a disturbance of the Rb–Sr system. Surprisingly, the pre-350 Ma ages have never been reported in the Stronie-Młynowiec formation. On the contrary, Anczkiewicz *et al.* (2007) interpreted a 387 ± 5 Ma Lu–Hf garnet–whole-rock age from a felsic granulite as a record of garnet growth on a prograde UHP path.

The thermal event which occurred at 340–330 Ma is far the best documented feature in the OSD. In orthogneiss, U–Pb zircon ages of 342 ± 6 Ma are thought to reflect the peak of HT metamorphism (Turniak *et al.*, 2000). It is supported by U–Pb zircon dating of granitic leucosomes yielding 345–330 Ma (Bröcker *et al.*, 2009). In the Stronie-Młynowiec formation, peak metamorphism is constrained by 340–330 Ma-old zircon rims from a metarhyolite sample (Murtezi & Fanning, 2005), and by a Sm–Nd garnet–whole-rock age of 346.5 ± 4.4 Ma from a Stronie mica schist (Jastrzębski, 2008). In both the eclogite and granulite, ages clustering at 350–330 Ma are interpreted as reflecting the timing of peak UHP metamorphism (Brueckner *et al.*, 1991; Štípská *et al.*, 2004; Lange *et al.*, 2005a; Bröcker *et al.*, 2009). However, this opinion is not shared by Anczkiewicz *et al.* (2007) or Kusiak *et al.* (2008) who believe that Lu–Hf or U–Th–Pb ages of 347–340 Ma reflect a late thermal event during retrogression of the granulite.

The overall exhumation of the OSD is thought to have shortly followed the Early Carboniferous thermal event. Indeed, the vanishing stage of Variscan metamorphism is documented by numerous Rb–Sr (Lange *et al.*, 2002; 2005b) or $^{40}\text{Ar}/^{39}\text{Ar}$ cooling ages on amphibole and micas which cluster between 340 and 310 Ma in both the orthogneisses and the metasediments (Steltenpohl *et al.*, 1993; Maluski *et al.*, 1995; Schneider *et al.*, 2006).

CHAPTER II

STRUCTURAL EVOLUTION OF THE OROGENIC MIDDLE CRUST

The structural succession presented in this chapter is derived from observations of fabric superpositions in all lithologies of the OSD. The observations for separate outcrops were correlated according to the deformation style and the orientation of structures, and were combined to produce maps showing the dominant structural trend of each fabric. The structural pattern of the OSD has been recently detailed by Chopin (2010), and the present work will mostly focus on the structural evolution of the metasedimentary Stronie-Młynowiec formation in order to further link the macroscopic fabrics with the growth of metamorphic minerals.

1) Northern domain

Based on the dominant structural pattern, three main domains were distinguished in the eastern OSD (Chopin, 2010). The northern domain encompasses the N and NE parts of the OSD and is formed by the Góry Złote/Rychlebské Hory mountain range (Fig. 3). This region exhibits NE–SW trending gneissic anticlines and metasedimentary synclines, namely from NW to SE: the Skrzyńka-Złoty Stok anticline, the Orłowiec-Bílá Voda syncline, the Radochów anticline, the Łądek Zdrój-Javorník syncline, and the Gierałtów anticline hosting a narrow zone of felsic and mafic granulite in its core. The anticlines are mostly composed of banded to mylonitic orthogneiss, but migmatitic orthogneiss is also present on both sides of the granulite belt to the SE (Fig. 5). Abundant metarhyolite and quartzite intercalations are observed in the NW Orłowiec-Bílá Voda valley, whereas amphibolite and marble intercalations dominate in the SE Łądek Zdrój-Javorník valley (Fig. 6).

D1 structures

The first foliation rarely occurs in the Orłowiec-Bílá Voda valley which is located in the NW part of the northern domain (Fig. 5). It is preserved in quartz-rich lithologies as a weak, shallow-dipping schistosity without distinct metamorphic differentiation (Fig. 7a). In orthogneiss, it is commonly refolded by rootless isoclinal folds (Fig. 7b). The regional orientation of S1 is difficult to determine, but few outcrops (Fig. 7a) suggest that it was predominantly subhorizontal. The shallow-dipping S1 foliation was also observed by Štípská *et al.* (2004), although only rarely, in granulite located to the SE (Fig. 5).

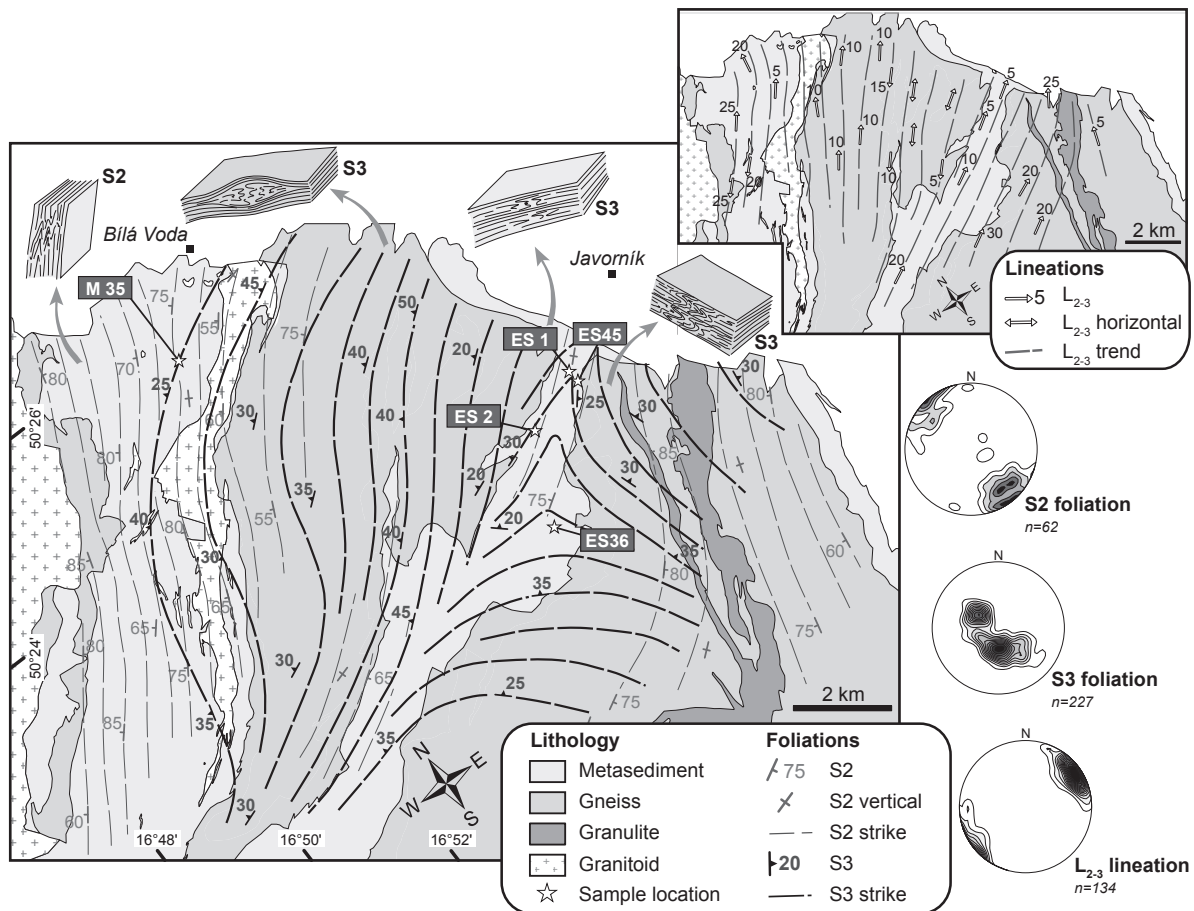


Figure 5. Structural map of the northern domain. Schematic blocks illustrate the dominant structural patterns across the area and stereonets show the orientation of the D2 and D3 structures (Schmidt's net, lower hemisphere projection). The location of samples used for petrology (Part 1-Chapter III.3) and EBSD analysis (Part 1-Chapter IV) is indicated.

D2 structures

The subhorizontal S1 foliation is variably transposed into a NE–SW subvertical S2 fabric which is dominant in the Orłowiec–Bílá Voda valley (Fig. 7c). There, the S1 foliation is deformed by close to isoclinal upright F2 folds and a subvertical S2 cleavage develops parallel to the F2 axial plane (Fig. 7b). In the SE Łądek Zdrój–Javorník valley, S1 is entirely transposed into a continuous S2 foliation which is best preserved in the northeastern termination of the belt. The S2 foliation is defined by compositional banding in marble, amphibolite and quartzitic schist (Figs 8a, b & 9a), and by a regularly-spaced alternation of quartz-rich and mica-rich layers in mica schist (Fig. 9c). In the surrounding orthogneiss, recrystallised quartz and K-feldspar augen and ribbons alternating with biotite- and muscovite-rich layers define the S2 foliation.

In metasedimentary rocks, the F2 folds exhibit an axial planar cleavage S2 steeply dipping to the NW or SE (Figs 5 & 6) and fold hinges plunging shallowly to moderately to the NE or SW. In the orthogneiss and the granulite belt, the dominant NE–SW striking S2 fabric dips steeply to the NW or SE (Fig. 6).

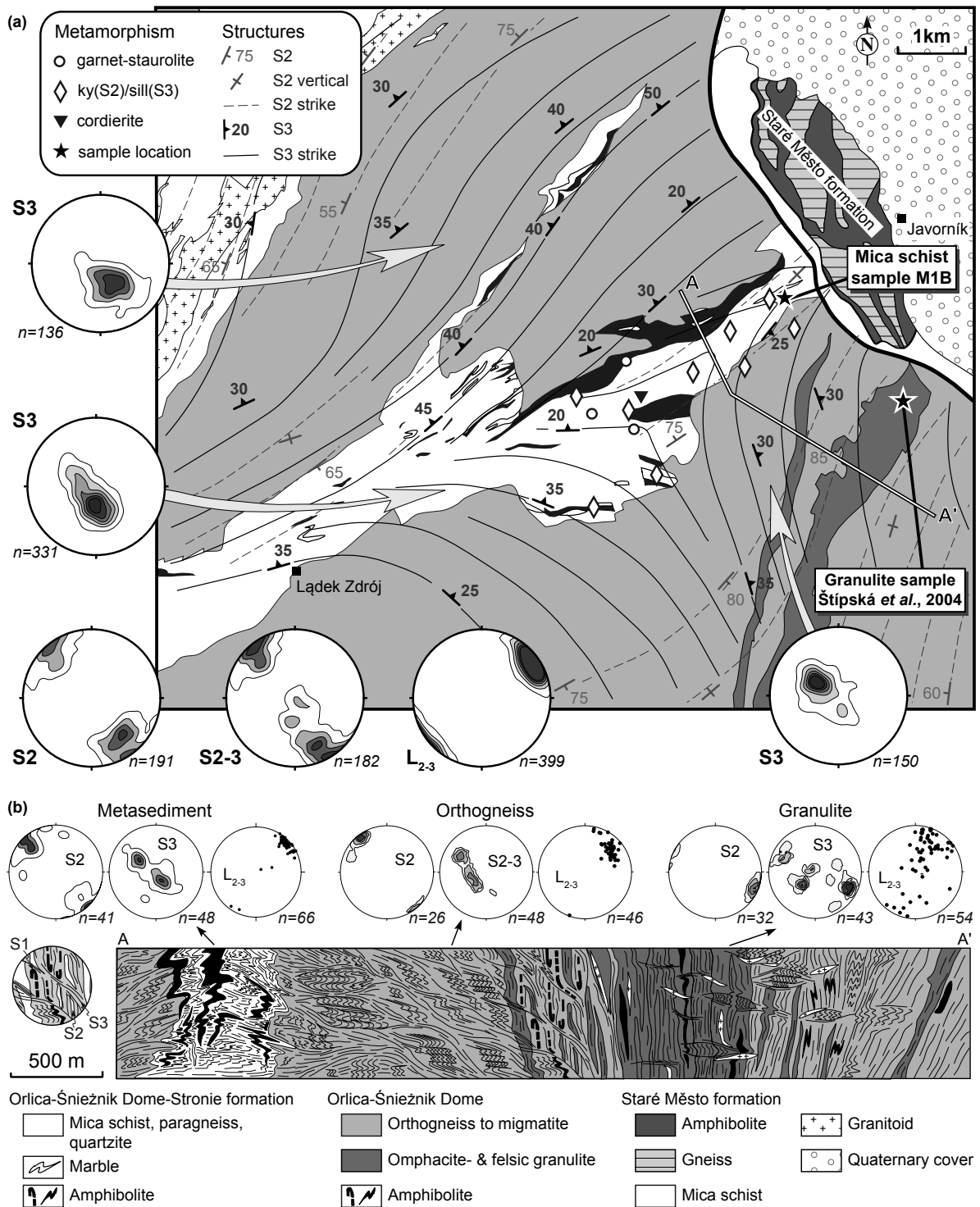


Figure 6. Detail of the structural record in the Lądek Zdrój-Javorník valley, northern domain. (a) Geological and structural map with occurrences of metamorphic minerals. The location of the sample M1B used for petrology (Part 1-Chapter III.2), and the position of the structural profile are indicated. Stereonets show the orientation of S2, S3 and L₂₋₃ structures (Schmidt's net, lower hemisphere projection). (b) Interpretative geological cross-section showing the early subvertical structure S2 and the style of the superimposed D3 deformation in metasedimentary rocks, surrounding orthogneiss and granulite. Stereonets show D2 and D3 structures along the profile. Vertical axis is not to scale. The eastern part of the section is modified after Štípská *et al.* (2004).



Figure 7. Field photographs illustrating the succession of structures in the northern domain. NW Orłowiec-Bilá Voda valley: (a) Subhorizontal S1 foliation in quartzitic schist (M35), (b) S1 foliation affected by isoclinal F2 folds and S2 cleavage in orthogneiss (FC295), and (c) subvertical S2 foliation in orthogneiss (FC521). SE Lądek Zdrój-Javorník valley: (d) Open F3 fold in amphibolite (ES2), (e) close F3 folds and S3 axial plane cleavage in mica schist (ES80), (f) subhorizontal S3 foliation in orthogneiss (FC594), and (g) L_{2-3} intersection lineation in mica schist (ES81).

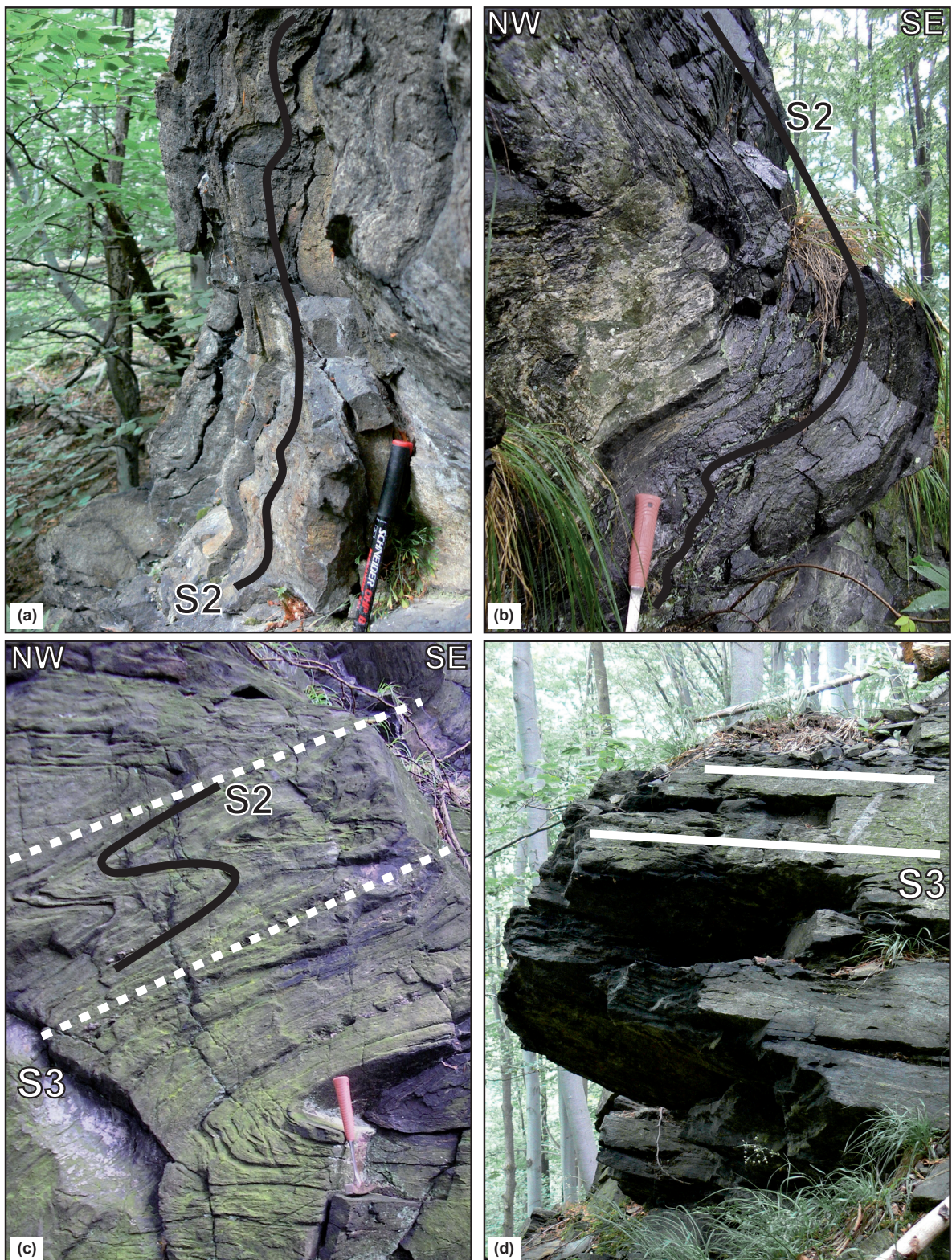


Figure 8. Field photographs illustrating typical structural relationships in the Łądek Zdrój-Javorník valley, northern domain. (a) Steeply dipping S2 foliation in interlayered marble and amphibolite. (b) Steeply dipping foliation folded by open F3 folds in amphibolite. (c) Isoclinal F3 folds in amphibolite. (d) Subhorizontal S3 foliation in mica schist.

D3 structures

The D3 deformation heterogeneously affects the subvertical S2 fabric and produces the subhorizontal S3 foliation. The S3 fabric is dominantly developed in the Łądek Zdrój-Javorník valley and only weakly in the Orłowiec-Bílá Voda valley (Fig. 6). To the NW, the S2 is deformed by open recumbent folds associated with minor development of the subhorizontal S3 axial plane cleavage. Towards the SE, the intensity of the D3 increases and in the Łądek Zdrój-Javorník valley, the subvertical S2 fabric is deformed by m- to mm-scale open to isoclinal F3 folds (Figs 7d, e & 8c) with subhorizontal axial planes and subhorizontal NE–SW trending hinges (Fig. 6a). In places rich in marble and amphibolite, the F3 folds are commonly open to close, whereas in areas where mica schist dominates, the folds tend to be close to isoclinal (Fig. 9a, c). The hinge zones of the folds are commonly crenulated on the centimetre to millimetre scale (Fig. 9c), and in the mica schist, the S3 cleavage defined by mm-spaced alternation of mica-rich and quartz-rich layers develops parallel to the axial plane.

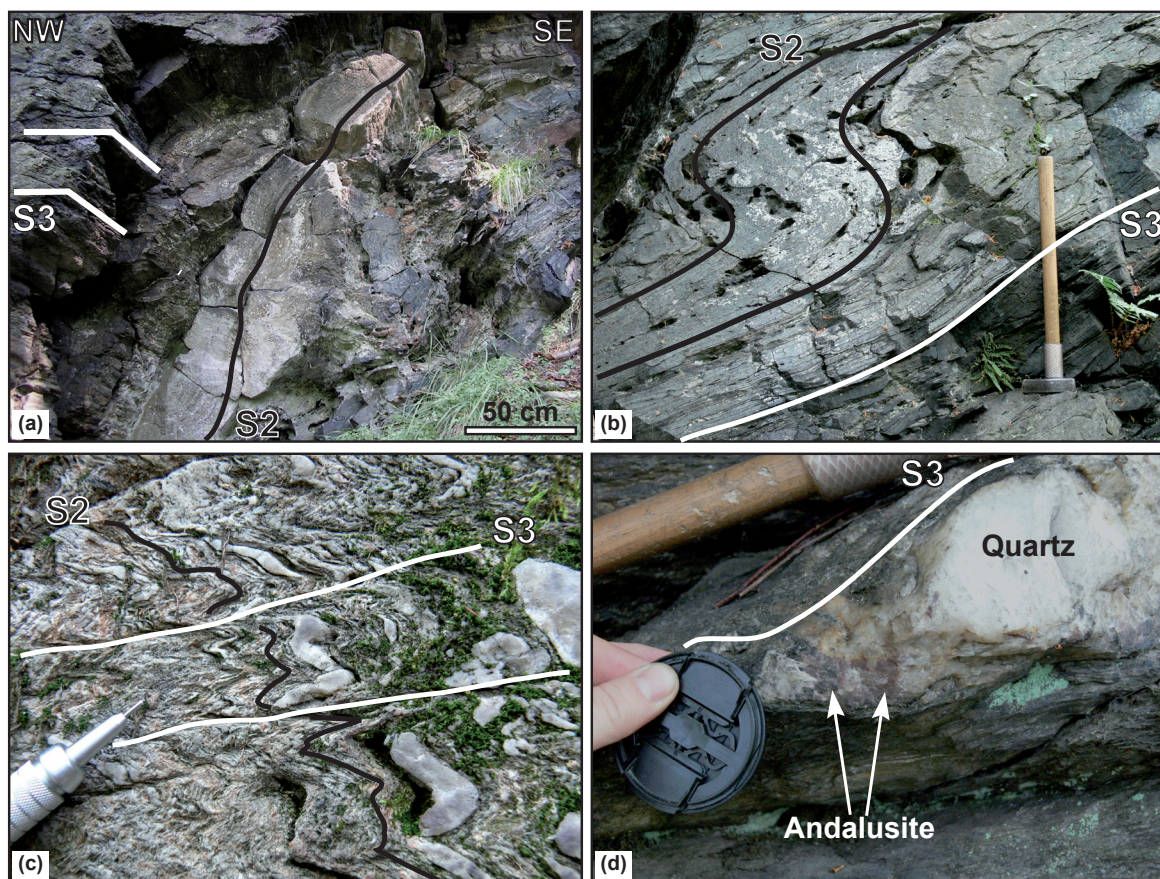


Figure 9. Field photographs illustrating structural details in the Łądek Zdrój-Javorník valley, northern domain. (a) Rheological contrast between marble with a steeply dipping S2 foliation and surrounding mica schist transposed into the S3 fabric. (b) Asymmetrical F3 fold in amphibolite with attenuated subhorizontal limbs. (c) Detail of subhorizontal crenulation cleavage S3 in quartzitic mica schist. (d) Andalusite in quartz exudation parallel to the shallow-dipping S3 fabric in mica schist.

The shape of F3 folds varies from symmetrical to highly asymmetrical with weakly deformed subvertical short limbs and stretched subhorizontal long limbs nearly parallel to the axial plane (Fig. 9b). In the central and western parts of the belt, the F3 folding commonly leads to complete transposition of the S2 foliation into the shallow-dipping S3 cleavage (Fig. 8c).

The shallow-dipping S3 foliation is the dominant structure in orthogneiss located on both sides of the metasedimentary belt (Fig. 7f). Close to isoclinal m-scale folds with shallow dipping axial planes are locally preserved, and hinge zones show isoclinal microfolds of quartz-, K-feldspar- and biotite-rich bands. These hinge zones are in many places the only witness of the earlier steeply dipping S2 foliation. The D3 deformation is weaker in the granulite and mostly produces open F3 folds and localised shallow-dipping shear-zones (Štípská *et al.*, 2004).

The S3 foliation is subhorizontal (Figs 5 & 6) and dips shallowly to the NW in the Orłowiec-Bílá Voda valley. In the Łądek Zdrój-Javorník valley, the S3 is moderately dipping towards the NW in the northern part, towards the N to NE in the centre and towards the SE near the granulite belt (Fig 6a, b). The F3 folds always show shallow-dipping axial planes and subhorizontal NE–SW trending hinges parallel to the $L_{2,3}$ intersection lineation (Fig. 7g).

2) Central domain

The central domain represents a NW–SE trending zone located in the eastern OSD, and corresponds to the Krowiarki mountain range (Fig. 3). This area is almost entirely composed of metasedimentary rocks belonging to the Śnieżnik syncline (Don, 1964), and can be divided into the larger Stronie formation to the NW and the less exposed Młynowiec formation to the SE (Fig. 3). The monotonous Młynowiec formation is chiefly composed of paragneiss, whereas the Stronie formation exhibits abundant mica schist and frequent intercalations of marble, amphibolite, quartzite and graphitic schist. The two formations are separated by a basal quartzite layer (Don & Dowidar, 1988), and show contrasted structural records. They will therefore be described separately.

S0 sedimentary bedding

Relicts of the S0 sedimentary bedding are only visible in the SE **Młynowiec** formation (Fig. 10). Although metamorphosed, the S0 corresponds to cm-spaced alternations of white quartz-rich layers and darker pelitic material (Fig. 11a). Because of the subsequent D1 overprint, the orientation of S0 is rarely preserved, but several observations reveal that this structure strikes N–S and is subvertical (Fig. 10). This suggests that a tectonic event of unknown age occurred before the D1 deformation.

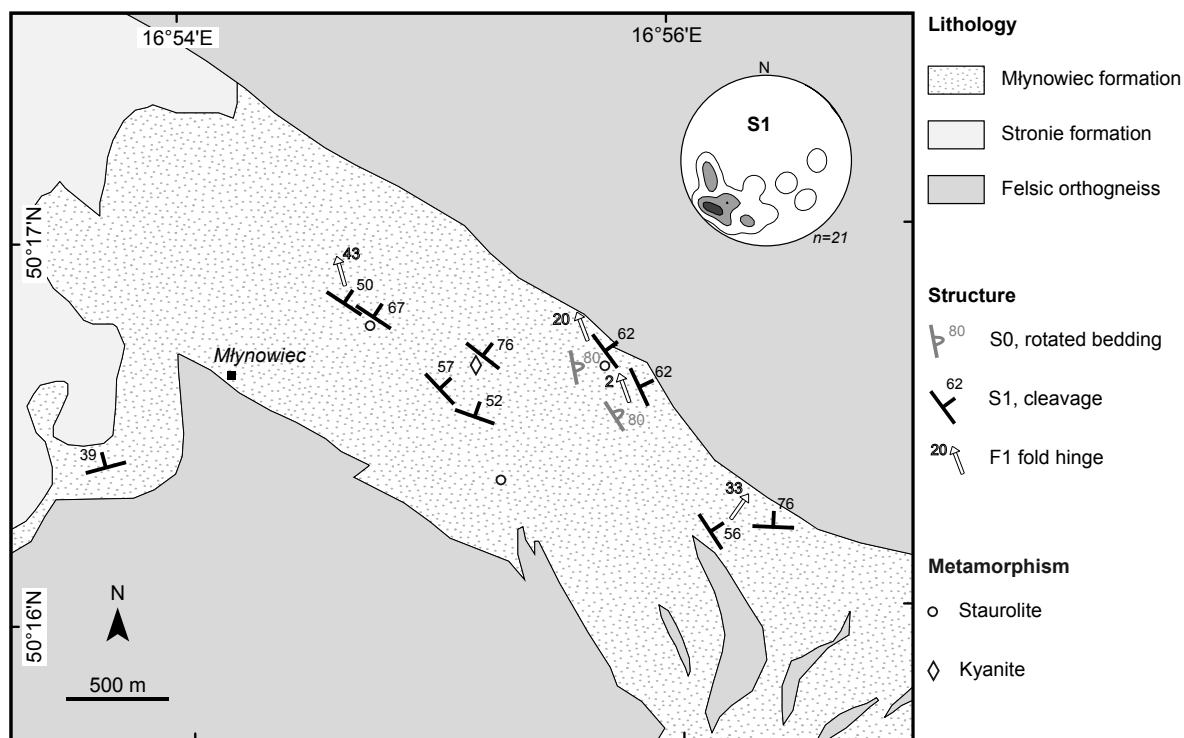


Figure 10. Structural map of the Mlynowiec formation, central domain. Stereonet shows the orientation of the S1 foliation (Schmidt's net, lower hemisphere projection). The occurrences of key metamorphic minerals are indicated.

D1 structures

In the **Mlynowiec** formation, the S0 bedding is deformed by close m-scale F1 folds with NW–SE trending hinges (Fig. 11b), or is completely transposed into a new S1 foliation which is dominant in this area (Fig. 11c). In zones of partial D1 reworking, a moderately dipping cleavage develops and can be observed in F1 fold hinges as well as in subvertical limbs (Fig. 11a, b). Because the original S0 bedding preserves a marked differentiation, the pervasive S1 cleavage shows significant refraction in quartz-rich layers (Fig. 11a). However, in most cases the D1 overprint produces a continuous S1 foliation which is still strongly differentiated and consists of quartz-rich layers alternating with biotite-rich layers locally preserving macroscopically visible staurolite and tourmaline.

The axial planes of F1 folds and the continuous S1 foliation strike NW–SE and are moderately to steeply dipping towards the NE (Fig. 10). These structures are concordant with the consistently NE-dipping metamorphic foliation observed in the neighbouring orthogneiss body (Chopin, 2010). F1 fold hinges mostly trend NW–SE and variably plunge to the NW (Fig. 10).

In the **Stronie** formation, the S1 metamorphic foliation is only rarely observed. Few outcrops in the NW part of the belt show a cm-spaced differentiation between quartz-rich and mica-rich layers, or alternating graphite-rich and mica-rich schists (Fig. 12a, c). Because of the subsequent D2 overprint, the orientation of the S1 foliation can not be reconstructed.

D2 structures

The D2 deformation only locally affects the rocks of the **Mlynowiec** formation. In paragneiss, a cm- to mm-scale F2 crenulation develops and is associated with a weak axial plane cleavage S2 (Fig. 11d). The rare S2 cleavage planes strike N–S and are almost subvertical.

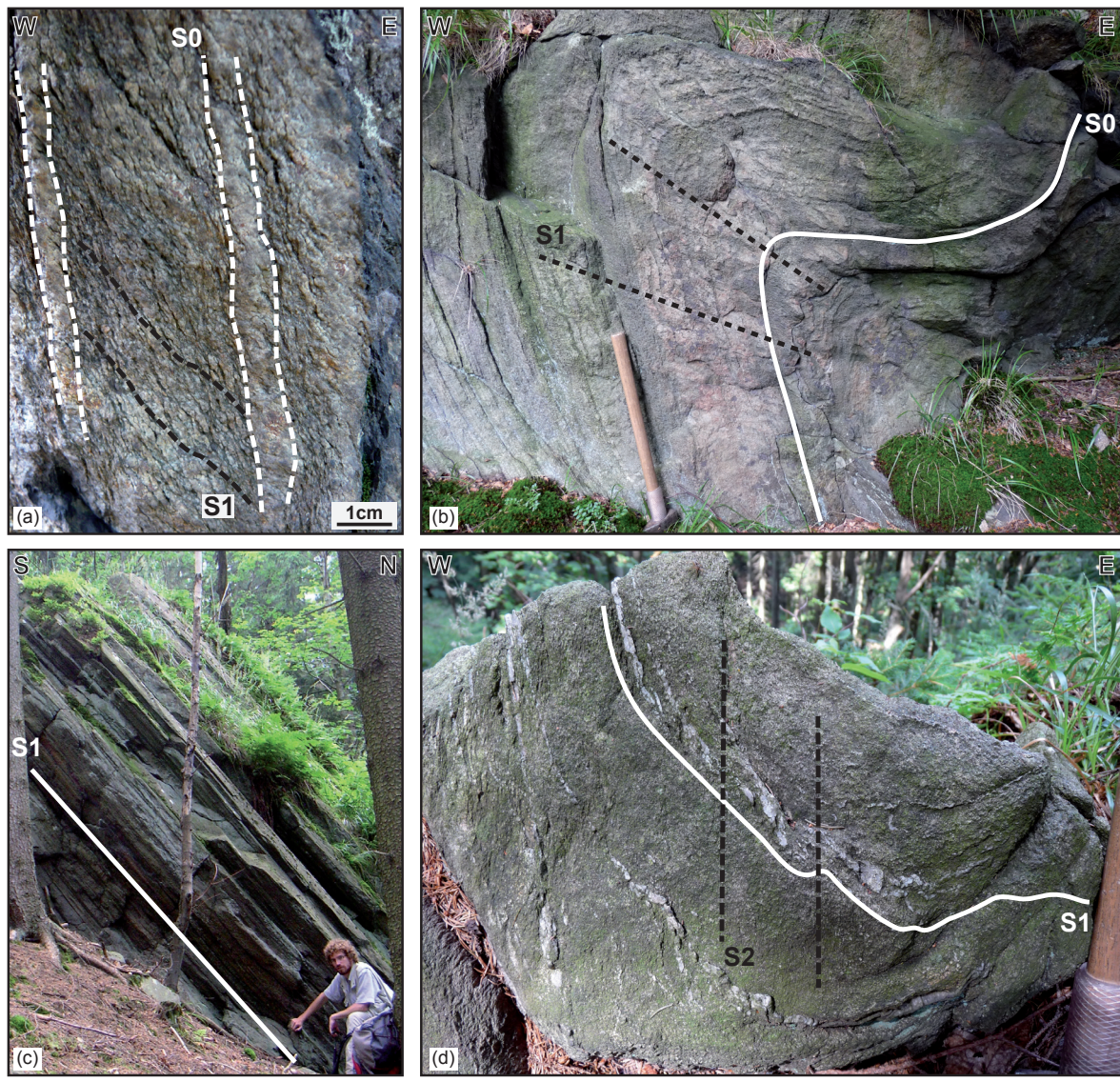


Figure 11. Field photographs illustrating the succession of structures in the Mlynowiec formation, central domain. (a) Subvertical S0 sedimentary bedding affected by a moderately dipping S1 cleavage refracted in quartz-rich layers (ES123). (b) F1 fold reworking the S0 sedimentary bedding, and fan-shaped distribution of S1 axial plane cleavage in the hinge zone (ES124). (c) N-dipping S1 foliation in paragneiss (ES129, F. Chopin for scale). (d) Weakly developed subvertical S2 cleavage in paragneiss (ES129).

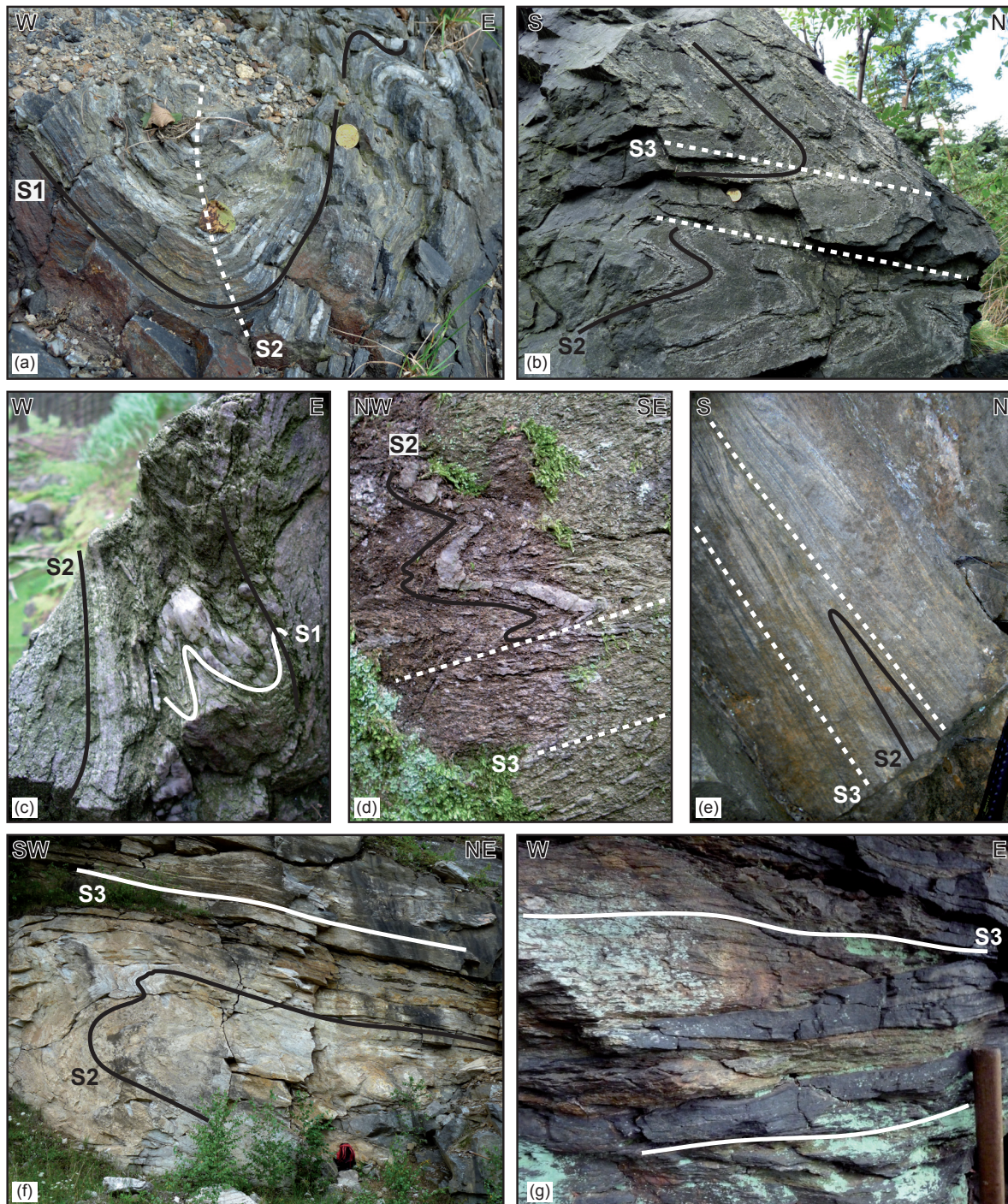


Figure 12. Field photographs illustrating the succession of structures in the Stronie formation, central domain. (a) Upright F2 fold reworking the S1 foliation in graphitic schist (ES154). (b) Subvertical S2 foliation deformed by recumbent F3 folds in graphitic schist (EV143). (c) Isoclinal F2 folds (EV66) and (d) tight F3 folds in quartz-rich mica schist (EV110). (e) Isoclinal rootless F3 fold surrounded by the dominant S3 foliation in mica schist (FC223). (f) Plurimetric-scale recumbent F3 fold affecting marble and mica schist alternations in the Mt. Krzyżnik quarry (EV152). (g) Subhorizontal differentiated S3 foliation in mica schist (ES151).

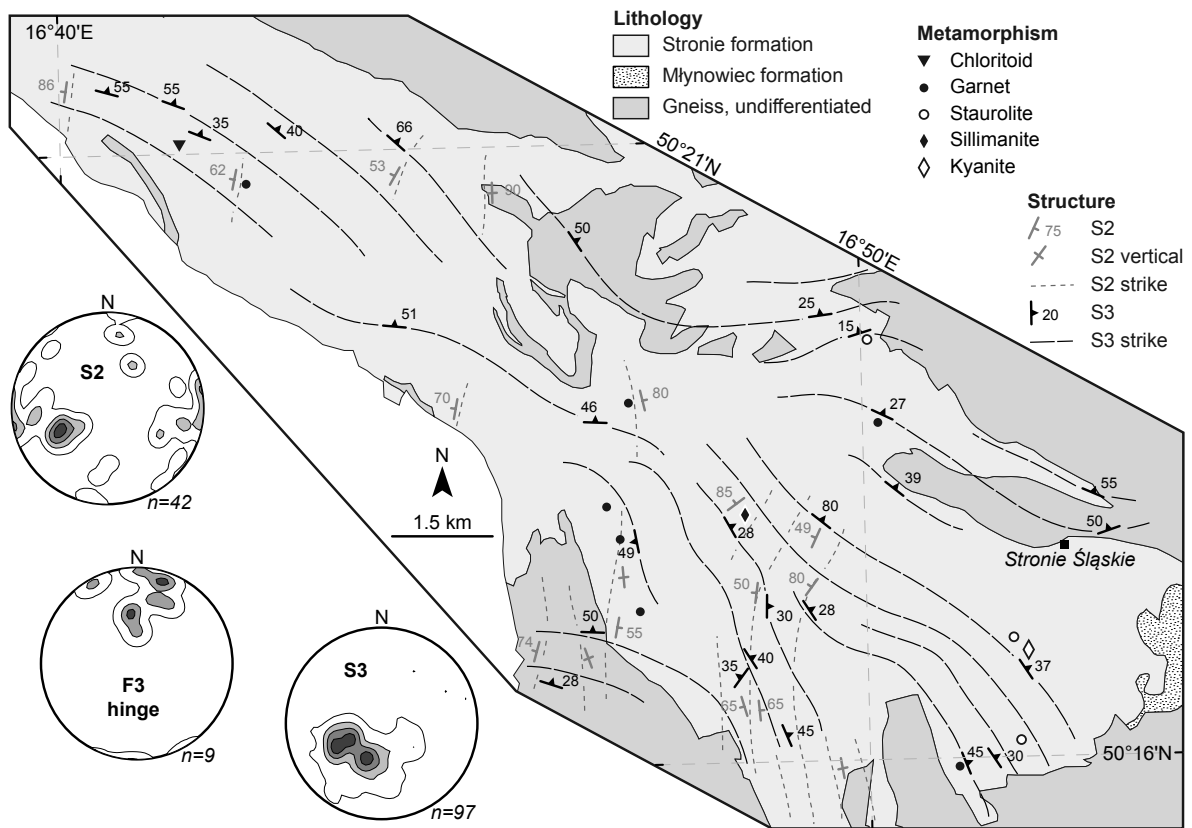


Figure 13. Structural map of the central domain. Stereonets show the orientation of the D2 and D3 structures (Schmidt's net, lower hemisphere projection). The occurrences of key metamorphic minerals are indicated (kyanite occurrence in the SE part is after Jastrzębski, 2008).

In rocks of the **Stronie** formation, the S1 foliation is deformed by tight to isoclinal F2 folds with a steeply dipping axial plane cleavage and N–S trending hinges (Fig. 12a, c), but is more commonly entirely transposed into the subvertical S2 foliation. The S2 foliation is mostly preserved in the SE part of the Stronie belt where it is probably in continuity with the S2 foliation observed in the southern domain (Fig. 13). It consists of a continuous metamorphic foliation with alternating quartz-rich and mica-rich layers in mica schist (Fig. 12c, d), but it is also highlighted by thin (< 1 cm) quartz-rich layers in graphitic schist (Fig. 12b). Like in the Młynowiec formation, the orientation of S2 corresponds to N–S striking planes steeply dipping to the E or W (Fig. 13).

D3 structures

The subsequent D3 deformation generates the subhorizontal S3 foliation which is only observed in the **Stronie** formation and is the dominant structure across the central domain (Fig. 13). In places, the earlier S2 foliation is reworked by isoclinal and recumbent F3 folds with shallow-dipping axial planes. The F3 folding ranges from a mm-scale crenulation in

quartz-rich mica schist (Fig. 12d, e) to a m- to km-scale folding of interbedded marble, graphitic schist and mica schist (Fig. 12b, e, f). In zones where the D3 deformation is more intense, a new subhorizontal S3 foliation develops. It is marked by alternating quartz-rich and mica-rich layers and may correspond, in few cases, to a strongly differentiated layering (Fig. 12g). The preservation of such a differentiation in the S3 foliation can be explained by the km-scale wavelength of the F3 folds in the SE part of the metasedimentary belt.

Across the entire central domain, the S3 foliation consistently dips at moderate angle towards the NE (Fig. 13). Similarly, the axial planes of F3 folds are subhorizontal and mostly dip to the NE, while fold hinges trend N–S and are subhorizontal (Fig. 13).

3) Southern domain

The southern domain actually represents the SE part of the OSD (Fig. 3) and coincides with the Králický-Śnieżnik Massif and the Góry Bialskie mountain range. It is composed of the N–S trending Sienna metasedimentary syncline flanked by the western Międzygórze and the eastern Śnieżnik gneissic anticlines. On the one hand, the western gneiss body preserves a narrow (1–2 km) core of mylonitic to migmatitic gneiss hosting discontinuous exposures of eclogite along a N–S trending belt, but is dominantly composed of weakly deformed Śnieżnik augen gneiss. On the other hand, the eastern gneissic anticline is chiefly occupied by migmatitic Gieraltów orthogneiss, while the Śnieżnik orthogneiss only represents a small (~1 km) peripheral rim (Figs 3 & 14). Metasedimentary rocks with abundant marble and quartzite intercalations occur in between the gneissic rocks, and the base of the Stronie formation is probably represented by a relatively thin layer of quartzite which is found on both sides of the metasedimentary belt.

D1 structures

The earliest structure observed in the area is a shallow-dipping S1 foliation which is best preserved in orthogneiss. In augen gneiss, it corresponds to a weak to moderate gneissosity surrounding large K-feldspar phenocrysts (Fig. 15a). In places, a more intense D1 deformation results in a mylonitization of the granitic protolith and produces a S1 foliation defined by alternating quartz–K-feldspar and biotite layers (Chopin, 2010). In the Stronie metasedimentary belt, the S1 foliation is commonly folded, and the crenulated S1 layering can only be observed in the basal quartzite layer which marks the boundary between metasediments and orthogneiss (Fig. 16a). In most cases, the S1 is highlighted by m-scale quartzite or marble intercalations in mica schist, or at a smaller scale by garnet- and garnet–staurolite-bearing layers alternating with quartz-rich layers (Fig. 16b, c).

The primary orientation of the subhorizontal S1 foliation is mostly preserved in the western orthogneiss. There, the S1 strikes N–S and shallowly dips to the E or W (Fig. 14). In addition, N-verging folds with E–W trending hinges, K-feldspar σ -clasts showing top to the N sense of shear and N–S stretching L1 lineations in orthogneiss are used by Štípská *et al.* (2011) to propose that a north-directed shearing occurred during a late stage of the D1 deformation. In metasediments, the orientation of the S1 foliation cannot be constrained

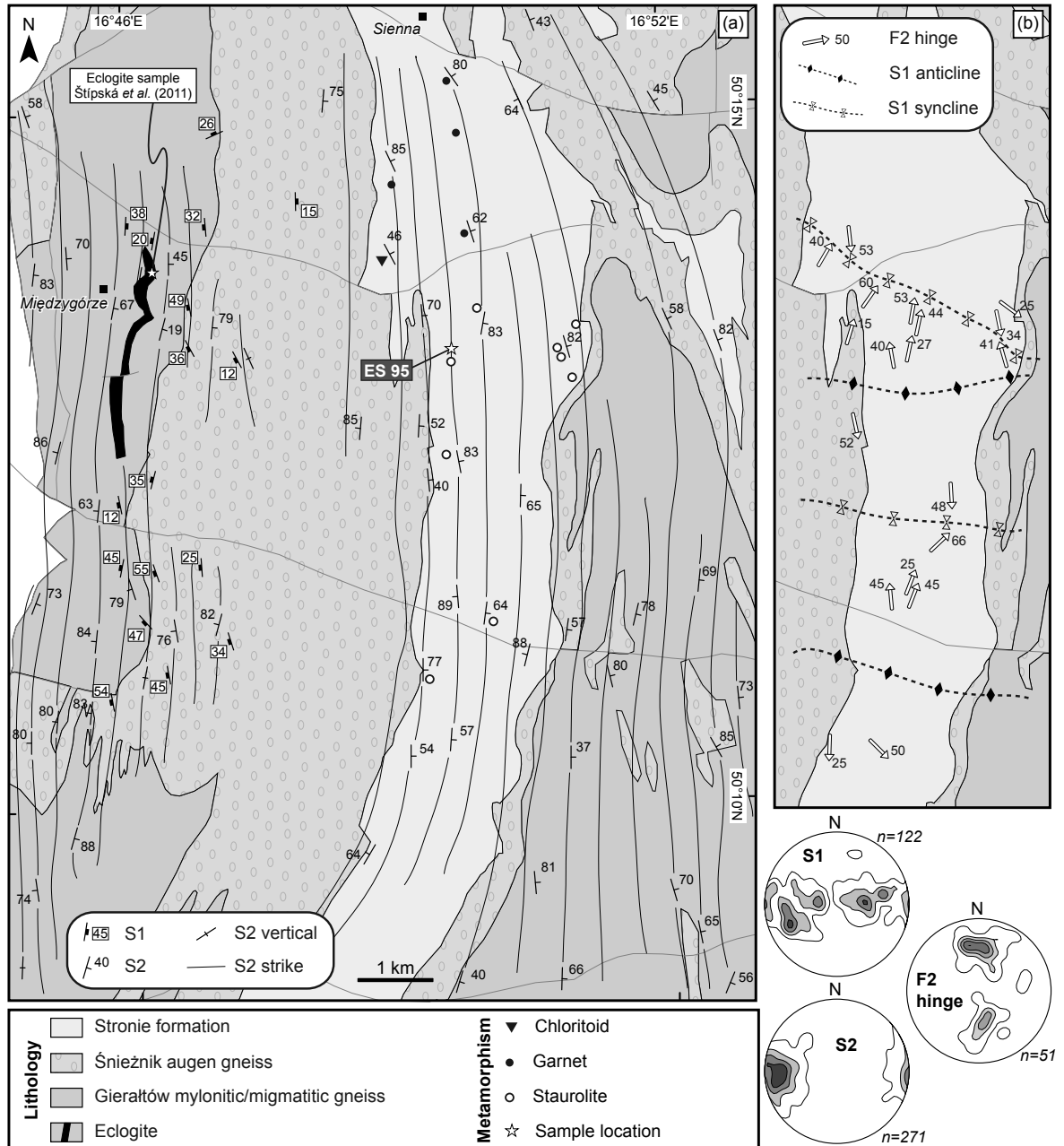


Figure 14. Structural maps of the southern domain. (a) Structural map showing the orientation of the S1 and S2 foliations. (b) Map of F2 fold hinge orientations and inferred antiformal and synformal pattern of the earlier S1 foliation. Stereonets show the orientation of the D1 and D2 structures (Schmidt's net, lower hemisphere projection). The location of the mica schist sample ES95 used for petrology (Part 1-Chapter III.4) as well as the eclogite sample investigated by Štípská *et al.* (2011) is indicated.

precisely because of the strong intensity of the subsequent D2 reworking. However, the F2 fold axes are variably plunging either to the N or S (Fig. 14b), thereby suggesting that before the D2 deformation, the S1 foliation was probably affected by E–W trending F1 folds with variably N- or S-dipping limbs. This earlier D1 deformation event is compatible with observations in the neighbouring orthogneiss.

D2 structures

The D2 deformation transposes the S1 foliation into a N–S subvertical S2 fabric which is pervasively developed in metasedimentary rocks as well as in eclogite and orthogneiss located close to the eclogite belt (Fig. 14). Only the augen gneiss located between these two zones is weakly affected by the D2 reworking. In rare eclogite outcrops, the S2 foliation is defined by a mm-spaced alternation of garnet- and omphacite-rich layers (Fig. 15c), whereas in both orthogneiss and metasediments the S2 foliation ranges from a weakly-developed axial

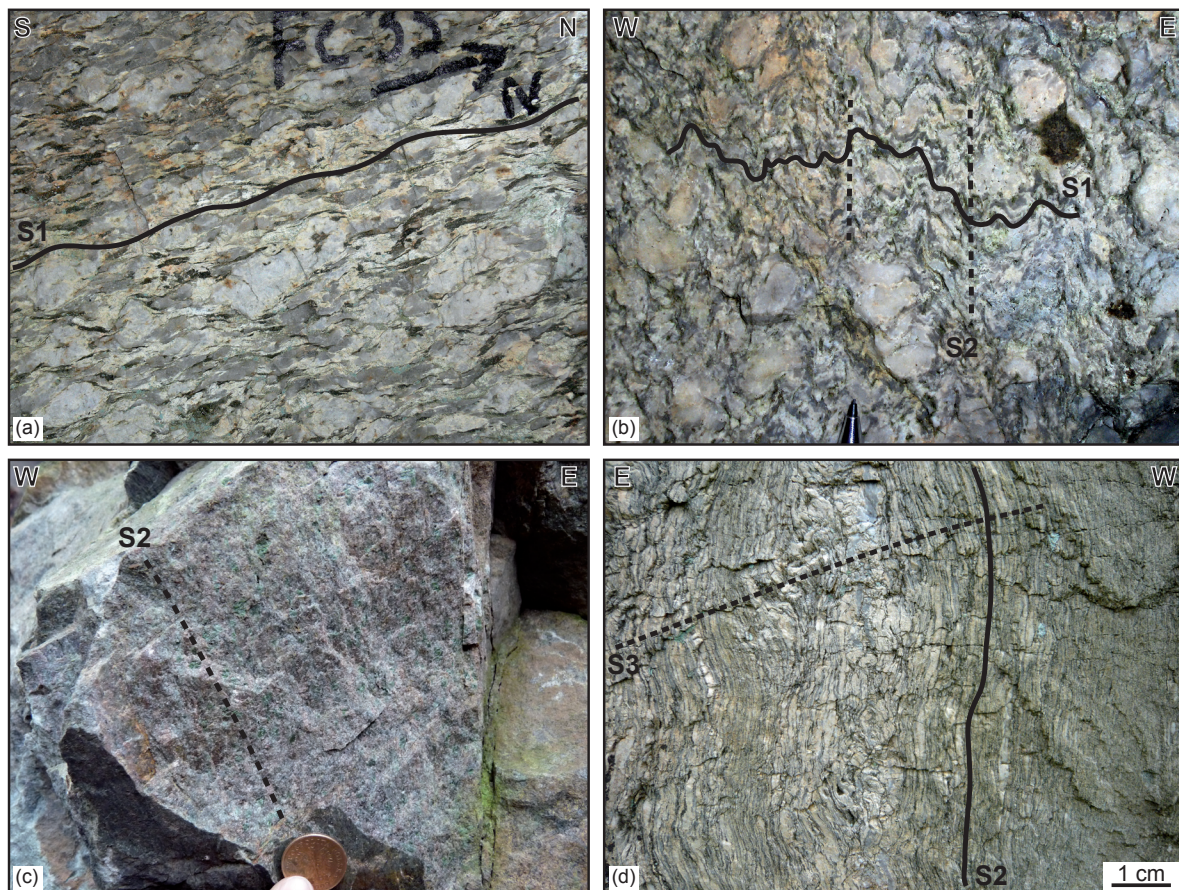


Figure 15. Field photographs illustrating the succession of structures in orthogneiss and eclogite of the southern domain. (a) Subhorizontal S1 foliation in Snieżnik augen gneiss. K-feldspar phenocrysts indicate top to the N sense of shear (FC35). (b) Weakly developed subvertical S2 cleavage in Snieżnik augen gneiss (FC137). (c) Steeply dipping S2 foliation marked by alternating garnet- and omphacite-rich layers in eclogite (NW-Nowa Wieś). (d) Subvertical S2 foliation affected by moderate F3 folding in banded Snieżnik orthogneiss (FC339).

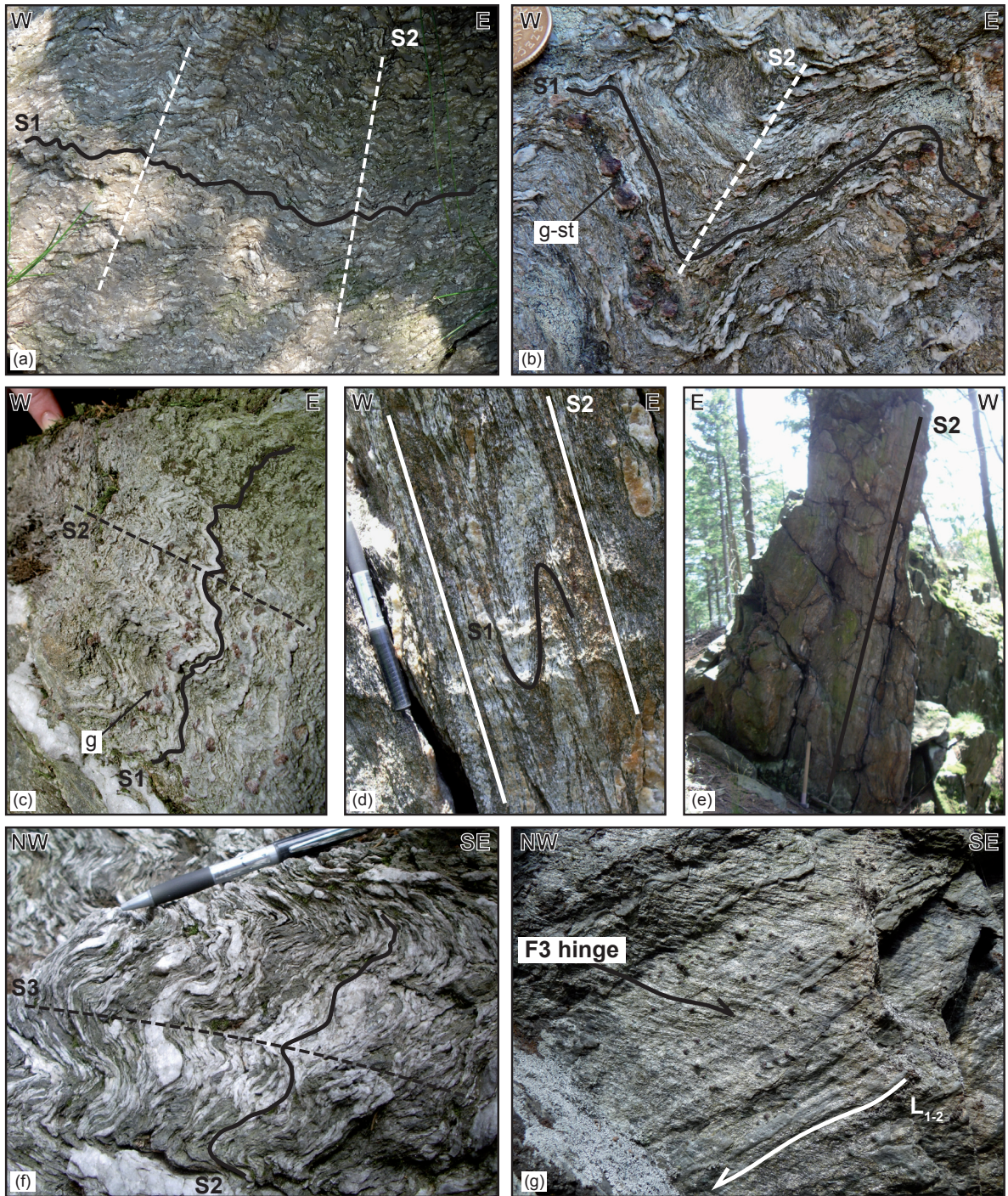


Figure 16. Field photographs illustrating the succession of structures in Stronie metasediments of the southern domain. (a) S1 foliation affected by moderate F2 folding in a basal quartzite layer (ES92). (b) Garnet-staurolite-bearing (ES 98) and (c) garnet-bearing (ES95) metamorphic foliation S1 affected by tight cm- to mm-scale F2 folds with steeply dipping S2 axial plane cleavage in mica schist. (d) Isoclinal rootless fold and well-developed S2 cleavage in mica schist (MS-Mariańskie Skały). (e) Subvertical S2 foliation in mica schist (ES 94). (f) Tight recumbent F3 folds in quartz-rich mica schist (ES89). (g) $L_{1,2}$ intersection lineation, and mullion structures parallel to F3 fold hinge visible on a S2 surface in mica schist (ES96).

plane cleavage of F2 folds to a continuous subvertical foliation (Figs 15 & 16). In weakly deformed augen gneiss, the S1 layering shows mm- to cm-scale crenulation, the wavelength of which is probably controlled by the size of relictual K-feldspar phenocrysts (Fig. 15b), and in completely transposed orthogneiss the S2 is defined by thin (< 1 mm) biotite layers and quartz–K-feldspar layers of variable thickness (Fig. 15d). The metasediments exhibit open to isoclinal and locally rootless F2 folds (Fig. 16a-d) with a N–S striking axial plane cleavage, but more commonly preserve the continuous S2 foliation (Fig. 16e), which is defined by alternating quartz-rich and mica-rich layers in mica schist.

Across the whole southern domain, the S2 foliation consistently strikes N–S and is generally steeply dipping. Around the eclogite belt, S2 dips to the E or W, whereas in the metasedimentary belt S2 dips mostly towards the E (Fig. 14). As mentioned above, F2 folds with steep E-dipping axial planes in metasediments show N–S trending fold hinges that are variably (25–65°) plunging to the N or to the S. The different groups of N- and S-dipping hinges define antiformal and synformal structures which are thought to represent the folded pattern of the former S1 fabric (Fig. 14b). This pre-D2 folding of S1 additionally explains the variable plunge of the $L_{1,2}$ intersection lineation which is commonly observed on the steep S2 surfaces (Fig. 16g).

D3 structures

The subsequent D3 deformation is only poorly observed in the southern domain. Open m-scale recumbent F3 folds with subhorizontal axial planes and N–S trending hinges are locally developed in orthogneiss (Fig. 15e). Rare open F3 folds also affect the subvertical foliation in the eclogite and subhorizontal fractures are commonly filled by dark green amphibolite-facies minerals. In the Stronie metasedimentary belt, rare open to close F3 folds with subhorizontal axial planes and N–S trending subhorizontal hinges occur (Fig. 16f), but no development of a new schistosity is observed. In zones of weak D3 deformation, mm-scale mullion structures develop as a consequence of viscosity contrasts in mica schist. This gives rise to N–S trending linear elements that are parallel to F3 fold hinges, but clearly oblique to the older $L_{1,2}$ intersection lineation (Fig. 16g).

CHAPTER III

TECTONO-METAMORPHIC EVOLUTION OF THE OROGENIC MIDDLE CRUST

Structural observations show that the OSD is built of alternating gneissic antiforms and metasedimentary synforms. However, the spatial distribution of metasedimentary rocks is appealing: narrow belts are nearly juxtaposed with high-grade rocks while others are intruded by elongated plutonic bodies (Fig. 3). It is therefore crucial to assess the $P-T-D$ evolution of the different parts of the Stronie-Młynowiec formation in order to understand the interplay between metasediments and the neighbouring high-grade or magmatic rocks. This approach will shed more light on the tectono-metamorphic behaviour of the middle crust within an intracontinental orogenic system. In this chapter, crystallisation-deformation relationships in metasediments are explored in order to link deformation events with metamorphic assemblages. Mineral equilibria modelling is further used to constrain the $P-T$ conditions of each metamorphic fabric.

1) Methodology

Petrography

In order to determine the metamorphic conditions associated with the different macroscopic foliations, paragneiss and mica schist samples of both the Stronie and Młynowiec formations have been investigated. In thin section, the different metamorphic minerals are described as well as their orientation with respect to the surrounding microscopic fabric. It is assumed that the orientation of pre-tectonic minerals is preserved in the hinge zone of microfolds during subsequent stages of deformation, whereas minerals located in the limbs may rotate and can acquire a different orientation. This assumption is similar to what was proposed by e.g. Bell & Rubenach (1983) for crenulation cleavage development and will be further supported by a quantitative microstructural study of garnet porphyroblasts (see Part I-Chapter IV). Accordingly, samples were collected from zones with well-preserved earlier fabrics as well as from hinge zones generated by subsequent folding events. In this part, mineral abbreviations are defined as follows: and=andalusite; ap=apatite; bi=biotite; chl=chlorite; cd=cordierite; czo=clinozoisite; ep=epidote; g=garnet with end members alm=almandine [Fe/(Fe+Mg+Ca+Mn)], grs=grossular [Ca/(Fe+Mg+Ca+Mn)], prp=pyrope [Mg/(Fe+Mg+Ca+Mn)] and sps=spessartine [Mn/(Fe+Mg+Ca+Mn)]; ilm=ilmenite;

ksp=K-feldspar; ky=kyanite; mnz=monazite; mu=muscovite; pa=paragonite; pl=plagioclase with end members ab=albite [Na/(Na+Ca+K)], an=anorthite [Ca/(Na+Ca+K)], or=orthoclase [K/(Na+Ca+K)]; qtz=quartz; ru=rutile; sill=sillimanite; st=staurolite; trm=tourmaline.

Chemistry

Chemical analyses of the different metamorphic minerals have been performed on different apparatus. Spot analyses or chemical profiles were carried out in:

- Centre de Géochimie de la Surface (Université de Strasbourg) on a TESCAN VEGA XMU electron microscope equipped with an energy-dispersive spectrometer (EDS) and with operating conditions of 15 kV and 15 nA,
- Institut für Mineralogie und Kristallchemie (Universität Stuttgart) on a Cameca SX 100 equipped with four wavelength-dispersive spectrometers (WDS) and with operating conditions of 15 kV and 15 nA.
- Bureau des Recherches Géologiques et Minières (Orléans) on a Cameca SX 50 equipped with five wavelength-dispersive spectrometers (WDS) and with operating conditions of 15 kV and 12 nA.

Compositional X-ray maps of garnet porphyroblasts are of variable resolution and were obtained using a step size of 7–10 μm and a counting time of 40 ms/pixel with a 100 nA beam current (Universität Stuttgart).

Whole-rock geochemical analyses were performed in:

- Czech Geological Survey (Prague) using standard wet chemical method for major elements,
- ACME Laboratories (Vancouver) using inductively coupled plasma (ICP) emission spectrometry for major elements and ICP-mass spectrometry for trace elements.

Whole-rock analyses and major element compositions used for mineral equilibria modelling presented in Part 1-Chapters III & IV are listed in Tabs 1 & 2.

Mineral equilibria modelling

Several assumptions have been made for mineral equilibria modelling and need to be clarified. Considering that chemical zoning in metamorphic minerals reflects changes in pressure, temperature and composition of the matrix (Pattison & Bégin, 1994), garnet zoning has been used to help constraining the P – T conditions during polyphase metamorphism. Because all

Table 1. Major and minor element geochemical analyses for selected mica schist samples of the OSD.

Sample	M1B Javorník, ND	M35i Bílá Voda, ND	ES95D Międzygórze, SD	ES122A Młynowiec, CD	ES2C Javorník, ND	ES36L Javorník, ND
Major elements (wt.%)						
SiO ₂	61.44	62.04	65.87	57.32	69.22	63.76
Al ₂ O ₃	19.76	18.60	17.05	21.76	15.11	17.49
Fe ₂ O ₃	0.99	6.23*	7.03*	6.71*	4.94*	6.92*
FeO	4.82	-	-	-	-	-
MgO	1.73	2.23	2.09	3.19	1.93	2.48
CaO	0.89	0.90	0.64	1.11	1.08	1.33
Na ₂ O	1.00	2.53	1.01	3.24	1.27	1.74
K ₂ O	3.96	3.78	3.69	3.41	3.77	3.61
TiO ₂	0.99	0.62	0.84	0.92	0.70	0.85
P ₂ O ₅	0.08	0.12	0.34	0.13	0.14	0.15
MnO	0.37	0.22	0.08	0.10	0.16	0.09
Cr ₂ O ₃	-	0.01	0.01	0.02	0.01	0.02
LOI	3.25	2.10	1.20	1.80	1.50	1.30
CO ₂	0.13	-	-	-	-	-
Sum	99.41	99.37	99.85	99.71	99.83	99.74
Trace elements (ppm)						
Ni	-	35.7	43.0	25.0	33.0	60.0
Sc	-	14.8	15.0	21.0	12.0	16.0
Ba	-	616.7	571.0	690.0	506.0	531.0
Be	-	-	5.0	5.0	2.0	3.0
Co	-	12.5	17.7	6.6	10.3	16.2
Cs	-	12.5	7.2	15.9	14.6	10.3
Ga	-	-	21.3	25.2	18.9	21.9
Hf	-	4.9	4.0	8.3	7.3	4.9
Nb	-	14.6	20.6	18.3	15.1	17.7
Rb	-	175.9	174.8	201.0	150.1	168.9
Sn	-	4.7	3.0	21.0	3.0	4.0
Sr	-	239.0	63.2	142.1	83.3	139.4
Ta	-	1.4	1.6	1.4	1.1	1.2
Th	-	17.2	16.0	16.8	13.2	12.6
U	-	3.4	2.8	4.8	2.4	2.4
V	-	87.6	90.0	143.0	72.0	101.0
W	-	1.4	1.6	2.7	1.7	0.5
Zr	-	169.3	128.4	268.7	245.6	192.5
Y	-	38.5	32.5	32.2	30.9	28.3
La	-	52.6	53.5	48.7	37.7	38.8
Ce	-	95.7	118.7	106.1	78.3	78.3
Pr	-	11.3	12.9	11.2	8.9	8.9
Nd	-	41.2	50.0	40.3	33.2	31.8
Sm	-	8.0	8.7	7.0	6.1	5.8
Eu	-	1.5	1.7	1.6	1.2	1.2
Gd	-	6.8	7.5	5.8	6.0	5.3
Tb	-	1.0	1.1	1.0	0.9	0.8
Dy	-	6.4	6.1	6.0	5.1	4.6
Ho	-	1.4	1.2	1.3	1.1	1.0
Er	-	3.5	3.2	3.7	3.1	2.9
Tm	-	0.6	0.5	0.6	0.5	0.5
Yb	-	3.5	2.9	3.9	3.2	2.9
Lu	-	0.6	0.4	0.6	0.5	0.5
Mo	-	-	<i>d.l.</i>	0.4	0.2	0.2
Cu	-	26.5	59.0	22.1	8.3	23.0
Pb	-	46.6	3.0	13.3	6.3	5.4
Zn	-	93.2	16.0	30.0	70.0	82.0
Ni	-	-	33.2	19.3	22.8	36.0
As	-	-	<i>d.l.</i>	17.4	0.6	0.6
Cd	-	-	<i>d.l.</i>	<i>d.l.</i>	<i>d.l.</i>	<i>d.l.</i>
Sb	-	0.1	<i>d.l.</i>	<i>d.l.</i>	<i>d.l.</i>	<i>d.l.</i>
Bi	-	-	0.1	0.4	0.2	<i>d.l.</i>
Ag	-	-	<i>d.l.</i>	0.5	<i>d.l.</i>	<i>d.l.</i>
Au	-	-	<i>d.l.</i>	<i>d.l.</i>	2.7	1.9
Hg	-	-	<i>d.l.</i>	<i>d.l.</i>	<i>d.l.</i>	<i>d.l.</i>
Tl	-	-	0.5	1.1	0.3	0.5
Se	-	-	<i>d.l.</i>	<i>d.l.</i>	<i>d.l.</i>	<i>d.l.</i>

* total Fe expressed as Fe₂O₃ ; LOI = loss on ignition ; '-' = not analysed ; *d.l.* = below detection limit

ND, CD, SD = northern, central and southern domain

analysed garnet porphyroblasts show strong compositional zoning, it is therefore assumed that intracrystalline diffusion only played a minor role during the metamorphic evolution.

Chemical profiles in garnet porphyroblasts also suggest that element fractionation during garnet growth was important. This would require modelling using modified compositions corrected for incremental fractionation. However, several works have showed that this approach has only little influence on P – T estimates for pelitic rocks with less than 5% of garnet modal proportions (Tinkham *et al.*, 2001; Zuluaga *et al.*, 2005). Preliminary tests with PERPLEX and THERMOCALC programs confirmed these observations and showed only small changes in pseudosection topology. Moreover, although garnet is abundant in the analysed mica schists, the modal proportion is commonly not higher than 5%. The effect of element fractionation has therefore been neglected in this work.

The choice of the system of components used for mineral equilibria modelling was influenced by several factors. At first, the MnNCKFMASH (MnO-Na₂O-CaO-K₂O-FeO-MgO-Al₂O₃-SiO₂-H₂O) system was favoured because of the lack of reliable estimate of ferric iron proportions. Indeed, mica schist samples, although relatively fresh, commonly show hematite stripes parallel to the schistosity due to late alteration, leading to overestimated Fe₂O₃ values. Modelled isopleths obtained using this system were generally compatible with measured concentrations, but modelled $m(\text{garnet}) = \text{Mn}/(\text{Fe} + \text{Mg} + \text{Mn} + \text{Ca})$ values for garnet core were significantly higher than the measured spessartine content. This discrepancy was attributed to excessive Mn incorporation in garnet. Indeed, in the calculations using this system, garnet and chlorite are the only phases with Mn-bearing models that are present at low P – T conditions. However, several studies have demonstrated that MnO can also be trapped in other minerals (Spear & Cheney, 1989), especially in ilmenite (Caddick & Thompson, 2008) which is generally abundant in the matrix of pelitic samples. Therefore, calculations taking into account TiO₂ would be likely to decrease $m(\text{garnet})$ values at low P – T conditions. Accordingly, subsequent P – T pseudosections were constructed in the MnNCKFMASHTO system. In these calculations, the amount of O was set to small values (0.01–0.03) in order to test its influence on the stability of ilmenite and rutile.

Because mica schist samples are rich in muscovite and quartz, these minerals as well as H₂O were treated as excess phases. In most cases, the composition was also corrected for apatite ($\text{CaO}_{\text{corrected}} = \text{CaO} - 3 * \text{P}_2\text{O}_5$), which is commonly observed in the analysed samples. Pseudosections were calculated with THERMOCALC program (Powell *et al.*, 1998) and the database 5.5 (November 2003 update; Holland & Powell, 1998). In the MnNCKFMASH system (sample M1B adjacent to the granulite belt), activity–composition relationships are after: Holland *et al.* (1998) for chlorite, Powell & Holland (1999) for biotite, Coggon &

Table 2. Major oxide compositions (in moles adjusted to 100%) of samples used for mineral equilibria modelling. The amount of ferric iron (expressed as O in 2FeO.O) was arbitrarily chosen.

Sample	M1B Javorník, ND	M35i Bílá Voda, ND	ES95D Międzygórze, SD	ES2C Javorník, ND	ES36L Javorník, ND
Major oxides (moles adjusted to 100%)					
SiO ₂	72.75	71.40	74.76	79.09	72.13
Al ₂ O ₃	13.79	12.61	11.40	9.27	11.66
FeO	4.77	4.85	5.40	3.23	5.30
MgO	3.05	3.83	3.54	2.97	4.18
CaO	1.13	0.94	0.29	0.93	1.40
Na ₂ O	1.15	2.82	1.11	1.24	1.91
K ₂ O	2.99	2.78	2.67	2.57	2.60
TiO ₂	-	0.53	0.72	0.55	0.72
MnO	0.37	0.21	0.08	0.13	0.09
O	-	0.02	0.03	0.02	0.01

ND, CD, SD = northern, central and southern domain

Holland (2002) for white mica, Holland & Powell (2003) for feldspars, White *et al.* (2007) for silicate melt, Mahar *et al.* (1997) and Holland & Powell (1998) for cordierite and staurolite, and White *et al.* (2005) for garnet. In the MnNCKFMASHTO system, activity–composition relationships are similar except for biotite and ilmenite which are after White *et al.* (2005). Compositional isopleths used in the MnNCKFMASH system are defined as follows: $x(g)=Fe/(Fe+Mg)$; $z(g)=Ca/(Fe+Mg+Ca+Mn)$; $m(g)=(Fe+Mg+Ca+Mn)$; $x(st, bi)=Fe/(Fe+Mg)$. In the MnNCKFMASHTO system, isopleths are similar except $x(g)=Fe/(Fe+Mg+Ca+Mn)$.

2) Tectono-metamorphic evolution near the granulite belt (northern domain)

The metamorphic evolution has been investigated in metasedimentary rocks located close to the granulite belt (NE OSD). This area corresponds to a NE–SW belt of rocks of the Stronie formation which extends from Łądek Zdrój (Poland) to Javorník (Czech Republic), and was defined by Don (1964) as the Łądek syncline. The petrography is illustrated in Figs 17 & 18 and the interpretation of mineral growth with respect to the deformation phases is summarized in Fig. 19.

Petrography

Samples collected within the well-preserved S2 fabric in the eastern termination of the Stronie belt display coarse-grained quartz-rich ribbons that alternate with muscovite-rich layers containing a variable amount of biotite oriented parallel to the S2 foliation (Fig. 17a–c). Garnet porphyroblasts (2–4 mm) are commonly elongated parallel to the S2 fabric and contain straight

inclusion trails of quartz and ilmenite that are continuous with the external S2 foliation (Fig. 17a). Plagioclase forms large elongated porphyroblasts (1–4 mm) that commonly include oriented ilmenite, quartz, white mica and rare chlorite parallel to the external S2 fabric (Fig. 17b). Plagioclase also occurs as small grains in the matrix. Kyanite (up to 1 mm) is present only locally and is elongated parallel to the S2 foliation (Fig. 17c). Staurolite was not found in samples with the well-preserved subvertical S2 fabric but is included in garnet that contains S2 inclusion trails perpendicular to the surrounding S3 foliation (Figs 17d & 20d). Other common accessory phases in the matrix are apatite or tourmaline, and rare rutile is included in garnet.

Samples which were collected in the hinge zones of the F3 folds exhibit a variable intensity of the S3 cleavage development and a variable degree of preservation of the S2 structures. With increasing intensity of the F3 folding, three stages are distinguished based on the microstructural pattern of the matrix. First, the matrix composed of the quartz-rich and mica-rich S2 layers is microfolded (Fig. 17a–c). Then, a spaced S3 cleavage develops and is marked by the orientation of biotite and muscovite with some preserved isoclinal and rootless folds of quartz-rich ribbons (Fig. 17e). In the last stage, the original matrix is completely deformed (Fig. 18); quartz- and mica-rich layers are subhorizontal and rarely contain rootless folds of quartz aggregates.

Porphyroblasts and inclusion trails in porphyroblasts of the hinge zone show variable orientation. In some cases the inclusion trails of several neighbouring porphyroblasts are straight and oriented almost perpendicular with respect to the external foliation (Fig. 17f). They are therefore interpreted as porphyroblasts that grew during or after the formation of the S2 fabric and that did not rotate during the F3 folding. In some samples, neighbouring porphyroblasts show straight inclusion trails that are oriented at high angle with respect to each other and at variable angle to the S3 cleavage. In these samples, the different orientation of the inclusion trails is probably caused by rotation of the grains within the limbs of the F3 microfolds (Fig. 17e). The exact orientation of the S2 fabric cannot be inferred from such porphyroblasts, but their growth can still be assigned to the S2 fabric.

Garnet (up to 6 mm) includes numerous ilmenite and quartz grains, and rare chlorite, staurolite and rutile. Ilmenite and quartz generally form straight inclusion trails that are oriented at high angle to the external S3 foliation (Fig. 18a). Some garnet porphyroblasts show straight inclusion trails in the core and curved inclusion trails at the outermost rim passing continuously into the S3 fabric (Fig. 18b). The microstructural relationships suggest that the major garnet growth occurred during the development of the S2 fabric, but in some samples a small amount of garnet crystallised during the development of the S3 fabric. In

addition, garnet porphyroblasts with inclusion trails oriented at high angle to the S2 fabric in the inner core suggest the presence of an earlier foliation S1. In few cases, this included S1 foliation shows a crenulated pattern (Fig. 20d).

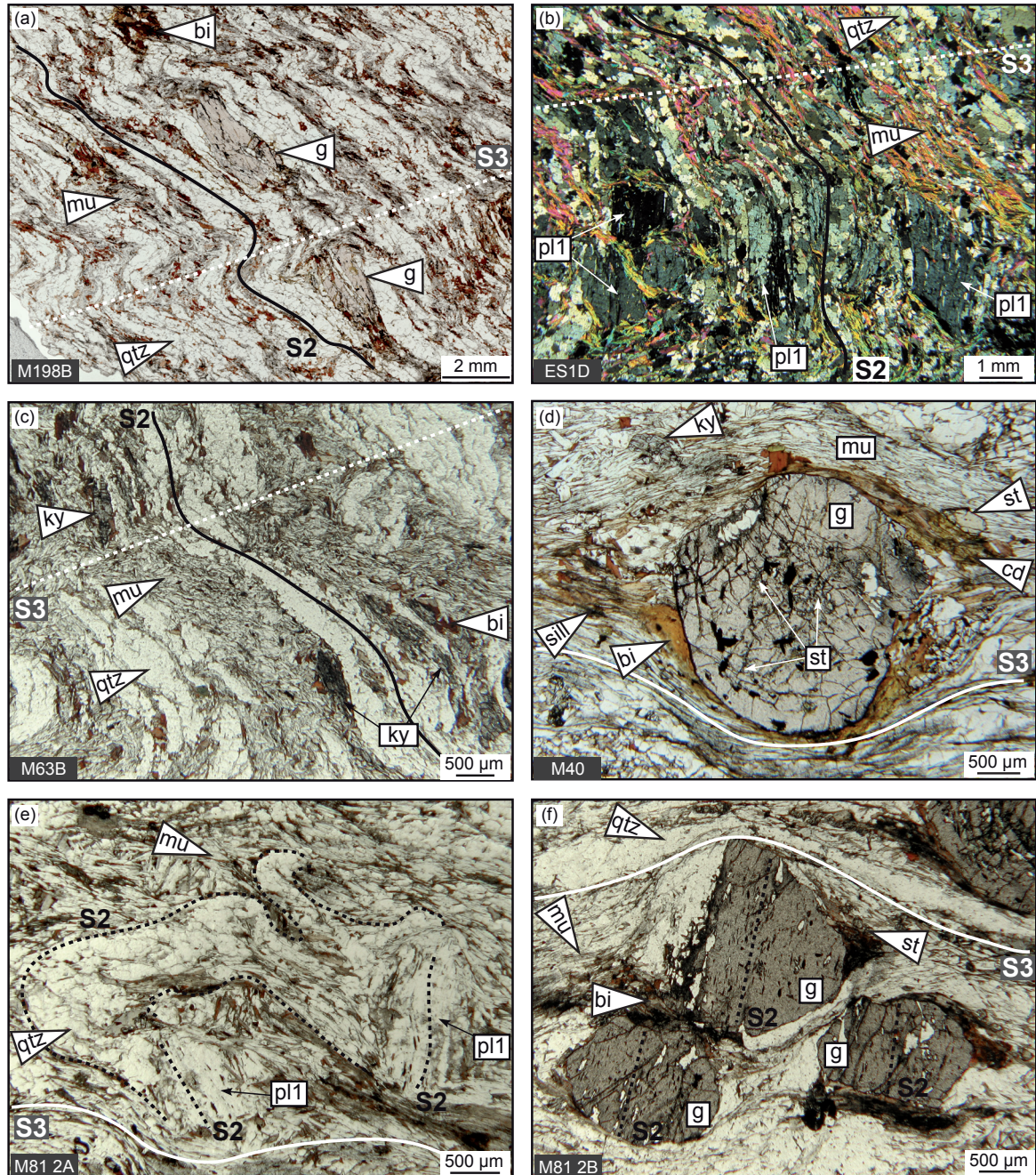


Figure 17. Photomicrographs illustrating relationships between porphyroblasts and the S2 fabric in metasediments near the granulite belt. (a) Elongated garnet and (b) plagioclase porphyroblasts with inclusion trails parallel to the S2 metamorphic layering. (c) Kyanite crystals parallel to the S2 fabric. (d) Staurolite included in garnet with ilmenite inclusion trails perpendicular to the external S3 fabric. (e) Elongated plagioclase with inclusion trails oblique or perpendicular to the S3 fabric in the hinge zone of an F3 microfold. (f) Garnet porphyroblasts with consistent inclusion trails perpendicular to the external S3 fabric. Full lines indicate the dominant foliation, whereas dashed lines denote the inferred internal foliation in porphyroblasts or the orientation of the superimposed cleavage. Plane-polarised light except for (b).

Plagioclase forms porphyroblasts (2 mm) and small grains (0.3 mm) within the matrix. Porphyroblasts contain numerous ilmenite, white mica, some quartz and rare chlorite. Ilmenite needles usually form straight inclusion trails that are oriented at high angle to the external S3 foliation, but that can be curved at porphyroblast rims and continuous with the S3 foliation (Fig. 18c). Small recrystallised plagioclase occurs within micaceous layers of the S3 cleavage, and in samples which show almost complete transposition of the S3 foliation the majority of plagioclase is present as small recrystallised grains in the matrix. The major porphyroblast growth is therefore assigned to the S2 fabric with a small amount assigned to the beginning of the S3 fabric development. The small recrystallised grains are associated with the S3 cleavage.

Staurolite (1–2 mm) is occasionally included in garnet (Figs 17d & 20d) and commonly occurs in the matrix. In samples exhibiting relicts of the S2 quartz-rich layers, staurolite is

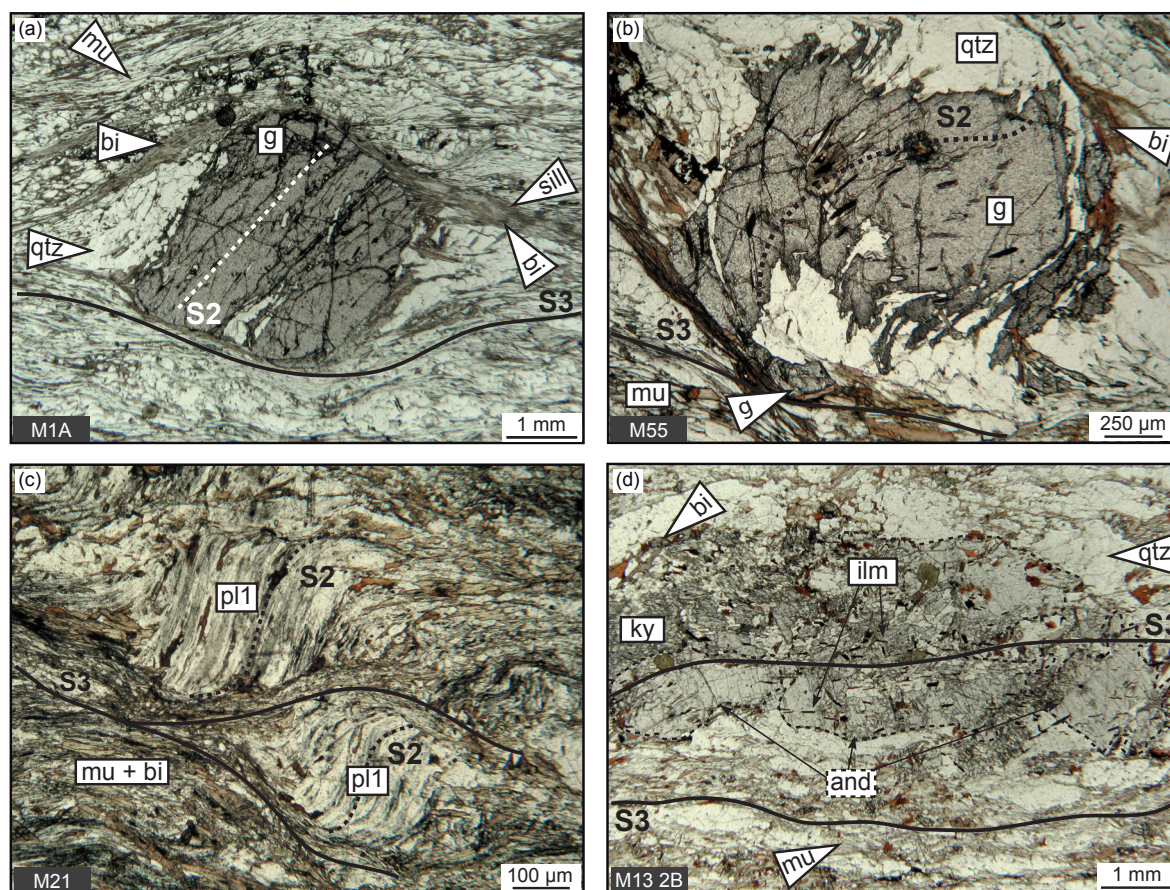


Figure 18. Photomicrographs illustrating the relationships between the metamorphic minerals and the S3 fabric in metasediments near the granulite belt. (a) Garnet with inclusion trails oblique to the external S3 foliation and sillimanite–biotite intergrowths in the pressure shadows parallel to S3. (b) Garnet with inclusion trails at high angle to the external S3 foliation in the core and parallel to the S3 fabric at the outermost rim. (c) Plagioclase porphyroblasts with core inclusion trails at high angle to the external S3 fabric and rim inclusion trails passing continuously into the anastomosing S3 foliation. (d) Large and randomly oriented andalusite crystals including ilmenite which passes continuously into the external S3 fabric. Full lines indicate the dominant foliation, whereas dashed lines denote the inferred foliation in porphyroblasts or relicts of older fabrics. Plane-polarised light.

oriented parallel to the S2 fabric. Its orientation in the matrix of strongly deformed samples is random or parallel to the S3 fabric. Staurolite inclusions in garnet and matrix staurolite oriented parallel to the S2 fabric indicate a growth during the D2 deformation. The orientation parallel to the S3 fabric in strongly overprinted samples is ascribed to reorientation during the D3 event.

Kyanite (0.5–1 mm) is common in the matrix and was not found in garnet. It is oriented parallel to the S2 quartz-rich layers in microfolded samples, but the elongated grains are generally rotated within the limbs of the F3 microfolds. In samples exhibiting a strong D3 deformation without relicts of folded quartz-rich domains, kyanite orientation is random or mostly parallel to the S3 cleavage (Fig. 17d). Kyanite growth is assigned to the S2 fabric only; its orientation parallel to the S3 fabric in some samples is explained by reorientation during F3 microfolding.

Mica in weakly folded samples mostly occurs parallel to the S2 quartz-rich layers, and is slightly rotated with the limbs of the F3 microfolds. A small amount of biotite and white mica occurs in the spaced S3 cleavage. In strongly overprinted samples, the micas are oriented parallel to the S3 fabric and biotite prevails over muscovite. In some samples with a strong S3 fabric, biotite-rich pressure shadows commonly associated with sillimanite are developed around garnet (Fig. 18a) and occasional ribbons of biotite and sillimanite are parallel to the S3 foliation. It is assumed that the majority of micas grew during the D2 event, but a significant amount of biotite also grew in the spaced S3 cleavage. In strongly overprinted samples it is impossible to distinguish between the different generations of micas, but it is likely that they chemically equilibrated during the D3 event. The biotite associated with sillimanite is assigned to the S3 fabric.

Sillimanite occurs only in samples which show strong D3 deformation. It is associated with biotite in the pressure shadows around garnet and with biotite-rich layers oriented parallel to the S3 foliation. It was never found microfolded. Its growth is therefore connected to the D3 deformation.

Andalusite is found only in samples with strong D3 deformation. It occurs in quartz–andalusite segregations parallel to the S3 fabric (Fig. 9d), in some pressure shadows of garnet and as large, randomly oriented porphyroblasts in the matrix. Andalusite commonly includes ilmenite oriented parallel to the S3 fabric and continuously passing into the matrix (Fig. 18d). Andalusite in the pressure shadows indicates that its growth probably started during the D3 deformation, but the majority of porphyroblasts is interpreted as late overgrowths on the already developed S3 foliation.

Structure Mineral	S 1 (subhorizontal)	S 1-2	S 2 (subvertical)	S 2-3	S 3 (subhorizontal)	Post-S 3
Muscovite	-----	-----	-----	-----	-----	-----
Chlorite	-----	-----	-----	-----	-----	-----
Biotite		-----	-----	-----	-----	-----
Plagioclase 1	-----	-----	-----	-----	-----	-----
Plagioclase 2			-----	-----	-----	-----
Garnet	-----	-----	-----	-----	-----	-----
Staurolite			-----	-----	-----	-----
Kyanite			-----	-----	-----	-----
Sillimanite			-----	-----	-----	-----
Andalusite					-----	-----
Cordierite					-----	-----

Figure 19. Summary of crystallisation-deformation relationships observed in metasediments near the granulite belt. Quartz and ilmenite are always present.

Cordierite was found in one sample as elongated stripes (1.5 mm) or small highly pinitized grains in the S3 matrix and around garnet porphyroblasts (Fig. 17d). Its growth is interpreted as post-tectonic with respect to the D3 deformation.

Chlorite occurs in the cores of some garnet and plagioclase porphyroblasts and rare chlorite is randomly oriented around garnet porphyroblasts. Chlorite included in garnet and plagioclase is assigned to the S2 fabric while the matrix chlorite replacing garnet is considered to be a late, post-D3 feature.

Chemistry

Sample M1B shows alternating quartz- and mica-rich bands corresponding to the S3 fabric (Fig. 20a, c). It is composed of garnet, staurolite, kyanite, sillimanite, biotite, muscovite, plagioclase and quartz with accessory ilmenite. Because samples from the area of study commonly preserve the same mineralogy (Fig. 6), sample M1B is considered as representative of this part of the Stronie formation. Mineral analyses for sample M1B are listed in Tab. 3. Garnet (< 5%) and plagioclase (2–3%) form porphyroblasts (1–4 mm) which generally display inclusion trails oblique to the external S3 foliation. Plagioclase porphyroblasts (p11) have outermost rims recrystallised into fine-grained aggregates (p12), and tiny plagioclase grains (p12) occur within the S3 matrix. Relicts of staurolite and kyanite appear as small grains (0.5 mm) randomly distributed within the matrix or lying next to garnet porphyroblasts. Staurolite is additionally included in garnet with inclusions trails oblique to S3 (Fig. 20d). Intergrowths of biotite and sillimanite commonly appear in the garnet pressure shadows or as thin layers in the S3 matrix. Garnet shows strong zoning from core ($\text{alm}_{0.60} \text{prp}_{0.04} \text{grs}_{0.16} \text{sps}_{0.20}$; $X_{Fe}=0.94$) to rim ($\text{alm}_{0.78} \text{prp}_{0.12} \text{grs}_{0.06} \text{sps}_{0.04}$; $X_{Fe}=0.85$) (Figs 20b & 21a). Staurolite is not zoned and its

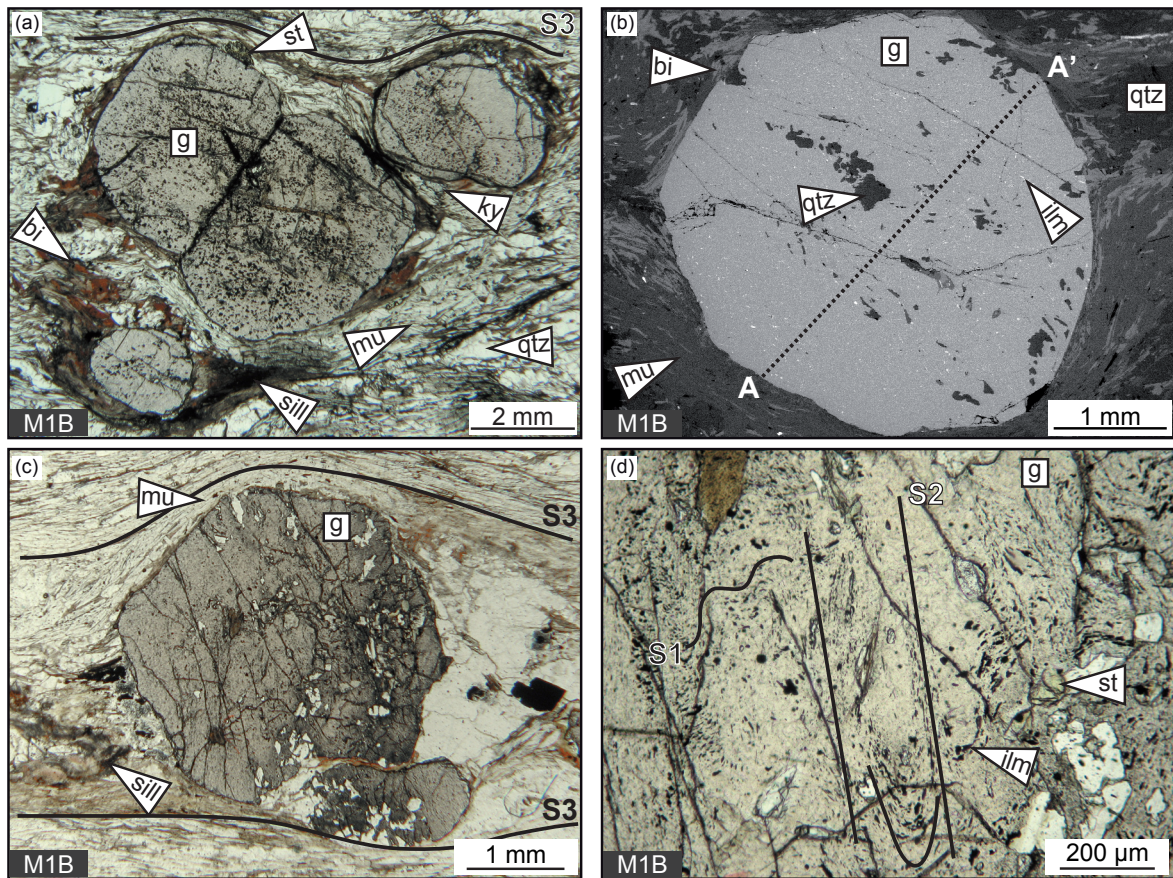


Figure 20. Photomicrographs and backscatter electron (BSE) image of sample M1B selected for mineral chemistry and mineral equilibria modelling. (a) Garnet, staurolite, kyanite and sillimanite in the muscovite–biotite matrix. (b) Location of the garnet profile presented in Fig. 21a (BSE). (c) Sillimanite in the D3 pressure shadow of a garnet hosting staurolite and crenulated ilmenite inclusions trails. (d) Detail of the garnet core shows crenulated S1 inclusion trails and S2 cleavage which is perpendicular to the external S3 fabric. Plane-polarised light for all photomicrographs.

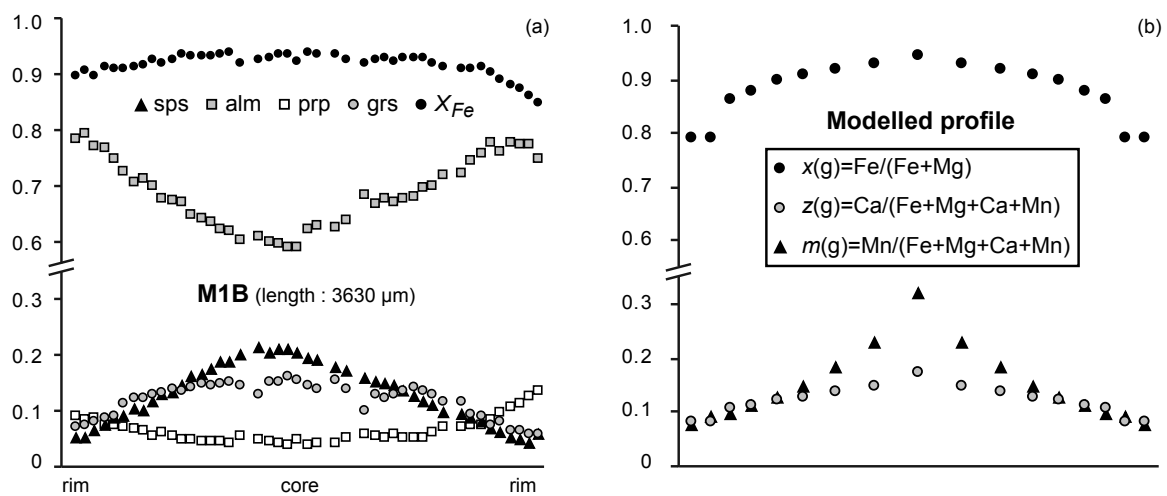


Figure 21. (a) Garnet profile from sample M1B. The location of the profile is shown in Fig. 20b. (b) Modelled garnet profile for the P – T path represented by the white arrow (stage 1 to 2) in Fig. 22.

Table 3. Representative chemical analyses for minerals of sample M1B.

Sample Mineral Position	M1B									
	g core	g rim	st core	st rim	bi matrix	mu matrix	pl 1 core	pl1 rim	pl 2 matrix	
Wt. %										
SiO ₂	37.24	37.21	27.16	26.63	36.12	46.15	67.20	64.87	64.89	
TiO ₂	0.16	0.29	0.85	0.93	2.35	0.76	0.00	0.05	0.00	
Al ₂ O ₃	21.09	21.43	54.38	53.98	20.49	37.21	20.80	21.73	22.32	
FeO	28.23	35.23	11.57	12.07	19.61	0.94	0.25	0.19	0.16	
MnO	7.85	1.98	0.56	0.56	0.00	0.05	0.00	0.05	0.00	
MgO	1.06	2.66	1.35	1.36	8.70	0.65	0.16	0.11	0.10	
CaO	5.17	2.34	0.14	0.06	0.00	0.00	0.63	1.64	2.22	
Na ₂ O	0.11	0.00	0.00	0.00	0.36	1.14	11.24	10.51	10.48	
K ₂ O	0.09	0.10	0.07	0.08	9.07	9.30	0.18	0.10	0.09	
ZnO	<i>n.a.</i>	<i>n.a.</i>	2.23	2.01	<i>n.a.</i>	<i>n.a.</i>	<i>n.a.</i>	<i>n.a.</i>	<i>n.a.</i>	
Total	101.00	101.24	98.31	97.68	96.70	96.20	100.46	99.25	100.26	
Cations										
Si	2.98	2.96	7.69	7.59	2.79	3.03	2.93	2.87	2.84	
Ti	0.01	0.02	0.18	0.20	0.14	0.04	0.00	0.00	0.00	
Al	1.99	2.01	18.15	18.14	1.86	2.88	1.07	1.13	1.15	
Fe ³⁺	0.05	0.03	0.00	0.00	0.00	0.00	0.01	0.01	0.01	
Fe ²⁺	1.84	2.31	2.74	2.88	1.27	0.05	0.00	0.00	0.00	
Mn	0.53	0.13	0.13	0.14	0.00	0.00	0.00	0.00	0.00	
Mg	0.13	0.32	0.57	0.58	1.00	0.06	0.01	0.01	0.01	
Ca	0.44	0.20	0.04	0.02	0.00	0.00	0.03	0.08	0.10	
Na	0.02	0.00	0.00	0.00	0.05	0.15	0.95	0.90	0.89	
K	0.01	0.01	0.03	0.03	0.89	0.78	0.01	0.01	0.01	
Zn	-	-	0.47	0.42	-	-	-	-	-	
Total	8	8	30	30	8	7	5	5	5	
X_{Fe}	0.94	0.88	0.83	0.83	0.56		an	0.03	0.08	0.10
alm	0.62	0.78					ab	0.96	0.91	0.89
prp	0.04	0.10					or	0.01	0.01	0.01
grs	0.16	0.07								
sps	0.18	0.05								

Structural formulae calculated on the basis of 12 oxygens for garnet, 23 for staurolite, 22 for biotite and muscovite and 8 for plagioclase
n.a. = not analysed

X_{Fe} varies between 0.81 and 0.85. Plagioclase is always albite, but porphyroblast cores show lower anorthite content ($an_{0.03}$) compared to the rims or to small grains in the matrix ($an_{0.07-0.10}$). Typical X_{Fe} values for biotite are 0.55–0.57 and titanium clusters around 0.15 a.p.f.u.

Mineral equilibria modelling

The pseudosection was calculated up to the P – T conditions where melt appears (640–680 °C). The major features of the pseudosection (Fig. 22a) include garnet stability over the range of calculated P – T conditions, staurolite stability from 550 °C (at 3.1 kbar) to 630 °C (at 6.2 kbar), chlorite stability up to 575–615 °C, and biotite stability above 500–550 °C. Kyanite is stable above ~610 °C (between 6 and 8.6 kbar), sillimanite from 580 °C (at 4 kbar) to 660 °C

(at 6 kbar), andalusite between 520 and 630 °C at 2.4–4 kbar and cordierite between 500 and 650 °C with an upper pressure limit at 3 to 3.5 kbar.

Sequential growth observed in the thin section involves oriented ilmenite, chlorite and white mica in plagioclase porphyroblasts, and garnet porphyroblasts with straight inclusion trails of ilmenite. It is complemented by the presence of randomly oriented staurolite and kyanite in the S3 matrix, and sillimanite in garnet S3 pressure shadows as well as parallel to the S3 matrix foliation. This suggests a medium pressure prograde path starting in the univariant *g-pl-chl* field, continuing across the quadrivariant *bi-g-pl-st* field to the *bi-g-pl-ky* field followed by a pressure drop into the *bi-g-pl-sill* field.

The beginning of the *P-T* path is deduced from garnet core chemistry where grossular and X_{Fe} values ($X_{Fe}=0.94$; $grs=0.16$) fit approximately the isopleths, but modelled $m(g)=0.32$ is higher than the measured spessartine ($sps=0.21$) content (Fig. 21b). This discrepancy is attributed to excessive Mn incorporation in garnet and it is proposed that the *P-T* evolution is likely to start at 3.5–5 kbar and 490–520 °C (Fig. 22a–c, stage 1). Inclusions in garnet porphyroblasts together with staurolite and kyanite occurrences in the matrix indicate further

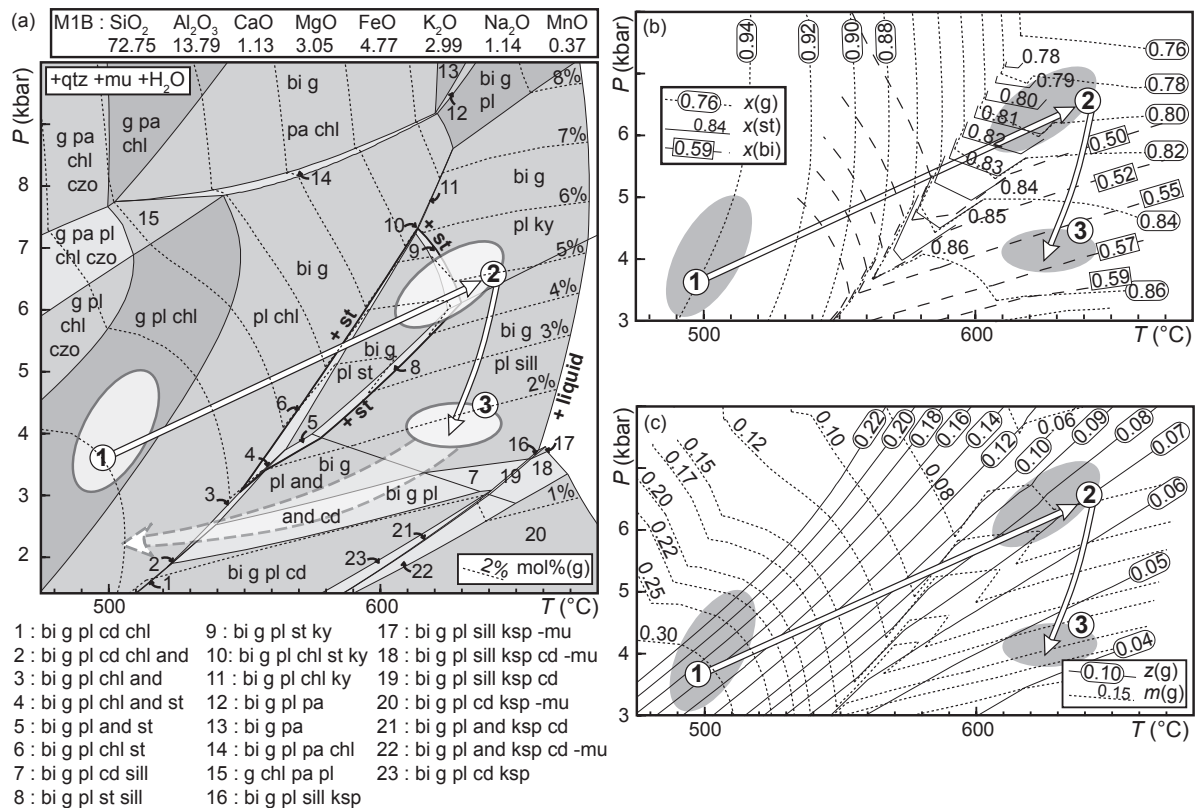


Figure 22. (a) *P-T* pseudosection in the MnNCKFMASH system for sample M1B (in moles adjusted to 100%), contoured for garnet modal proportion. Full and dashed white arrows indicate the *P-T* path derived by comparing the modelled assemblages and isopleths with the observed assemblages and mineral compositions. Ellipses denote the probable *P-T* range for the different stages of the *P-T* path. (b, c) Simplified part of the pseudosection with modelled isopleths of garnet, staurolite and biotite.

prograde P – T evolution. This is confirmed by staurolite chemistry ($X_{\text{Fe}}=0.81$ – 0.85) compatible with the calculated isopleths (Fig. 22b) and by the observed grossular and spessartine contents at the garnet rim ($\text{grs}=0.06$; $\text{sps}=0.04$) which lie close to the calculated isopleths of $z(\text{g})$ and $m(\text{g})$ in the kyanite field. This indicates P – T conditions of about 6–7 kbar and ~ 630 °C for the peak of metamorphism (Fig. 22a–c, stage 2), supported by the modelled garnet zoning closely reproducing the measured garnet profile (Fig. 21). In the absence of migmatization, the maximum temperature is bounded by the liquid-in line at 670 °C (Fig. 21a).

The interpretation of the sillimanite and biotite growing at the expense of garnet in the pressure shadows is compatible with pressure decrease and decrease in the modal proportions of garnet. This retrograde reaction is likely to modify the garnet rim chemistry. If Fe–Mg exchanges are considered to be dominant during this process, this could result in the observed difference between garnet rim X_{Fe} and the calculated $x(\text{g})$ isopleths at pressure peak (Figs 21b & 22b), while grossular and spessartine contents remain relatively unchanged. Therefore, the modelled values of $x(\text{bi})=0.55$ – 0.57 and $x(\text{g})=0.85$ similar to X_{Fe} of biotite and garnet rim suggest that garnet–biotite re-equilibration occurred in the sillimanite stability field. This points to retrogression towards ~ 4 kbar and ~ 630 °C (Fig. 22b, stage 3).

Additional petrographic information from other samples is also correlated with the pseudosection to roughly estimate the P – T evolution during further decompression. Because andalusite is widespread in samples with a penetrative S3 foliation and is not stable in the pseudosection above 4 kbar, it is only possible to draw a cooling curve which lies below this upper pressure limit (Fig. 22a). Cordierite is present in one sample only; it is associated with andalusite, biotite, garnet, plagioclase, muscovite and quartz, which allows to speculate that pressure decrease in the area of study, at least locally, continued to ~ 2 – 3 kbar at temperatures above 530–630 °C where this assemblage occurs in the pseudosection. The widespread presence of chlorite indicates further cooling below 530 °C.

3) Tectono-metamorphic evolution near the Javorník granitoid (northern domain)

In the northeastern part of the OSD, metasedimentary rocks of the Stronie formation are intruded by the Javorník granitoid which is thought to be emplaced during D3 deformation (Gotowała, 2003). Mica schist samples from the valley located between Orłowiec (Poland) and Bílá Voda (Czech Republic) have therefore been investigated in order to understand the influence of this magmatism on the metamorphic evolution of the metasedimentary unit. This area corresponds to the Orłowiec syncline as defined by Don (1964). The relationships between the different metamorphic minerals and the microstructures are illustrated in Figs 23 & 24, and summarized in Fig. 25.

Petrography

Across this metasedimentary belt, the dominant lithology corresponds to muscovite–biotite schist with a varying amount of quartz and minor garnet. All the observed mica schist samples exhibit the continuous S2 foliation which is marked by alternating quartz-rich and mica-rich layers. Relicts of the S1 metamorphic layering are rarely preserved in isoclinal F2 microfolds. In thin section, the crystallisation-deformation relationships can be deduced from the orientation of minerals with respect to the microfolded S1 foliation and the pervasive S2 fabric, and from the shape of the inclusion trails in porphyroblasts.

Garnet porphyroblasts (1–2 mm) are commonly observed in the mica-rich samples and exhibit variable morphologies. Most crystals are subhedral or elongated and host oriented inclusions of ilmenite, quartz, tourmaline and rare white mica. Staurolite inclusions are also frequently found in the core as well as at the rim of garnet porphyroblasts (Fig. 23a–c). In zones weakly affected by the D2 deformation, garnet inclusion trails lie parallel to the preserved S1 foliation (Fig. 23a), but garnet porphyroblasts are more commonly found oblique or perpendicular to the continuous S2 fabric (Fig. 23b, c). In some sections, several neighbouring garnet crystals show quartz pressure shadows and inclusion trail patterns that are consistently oriented perpendicular to the surrounding S2 foliation. In addition, a small curvature of the inclusion trails is observed at the rim of some elongated garnet crystals (Fig. 23a). Besides, a second type of garnet porphyroblast is represented by small (1 mm) and nicely rounded crystals that may be locally abundant (Fig. 24c). These porphyroblasts are almost inclusion-free and preserve a compositional zoning which is visible under the microscope: the light grey garnet core passes to a darker inner rim which is surrounded by a tiny bright outer rim (Fig. 24c). Importantly, the bright outer rims slightly overgrow the pre-existing S2 foliation and the S2 layering is almost not deflected around the rounded garnet porphyroblasts.

The textural arguments suggest that the dominant garnet type overgrew the subhorizontal S1 foliation, but also indicate limited growth during D2 deformation. By contrast, the small rounded porphyroblasts point to garnet growth after the development of the S2 fabric.

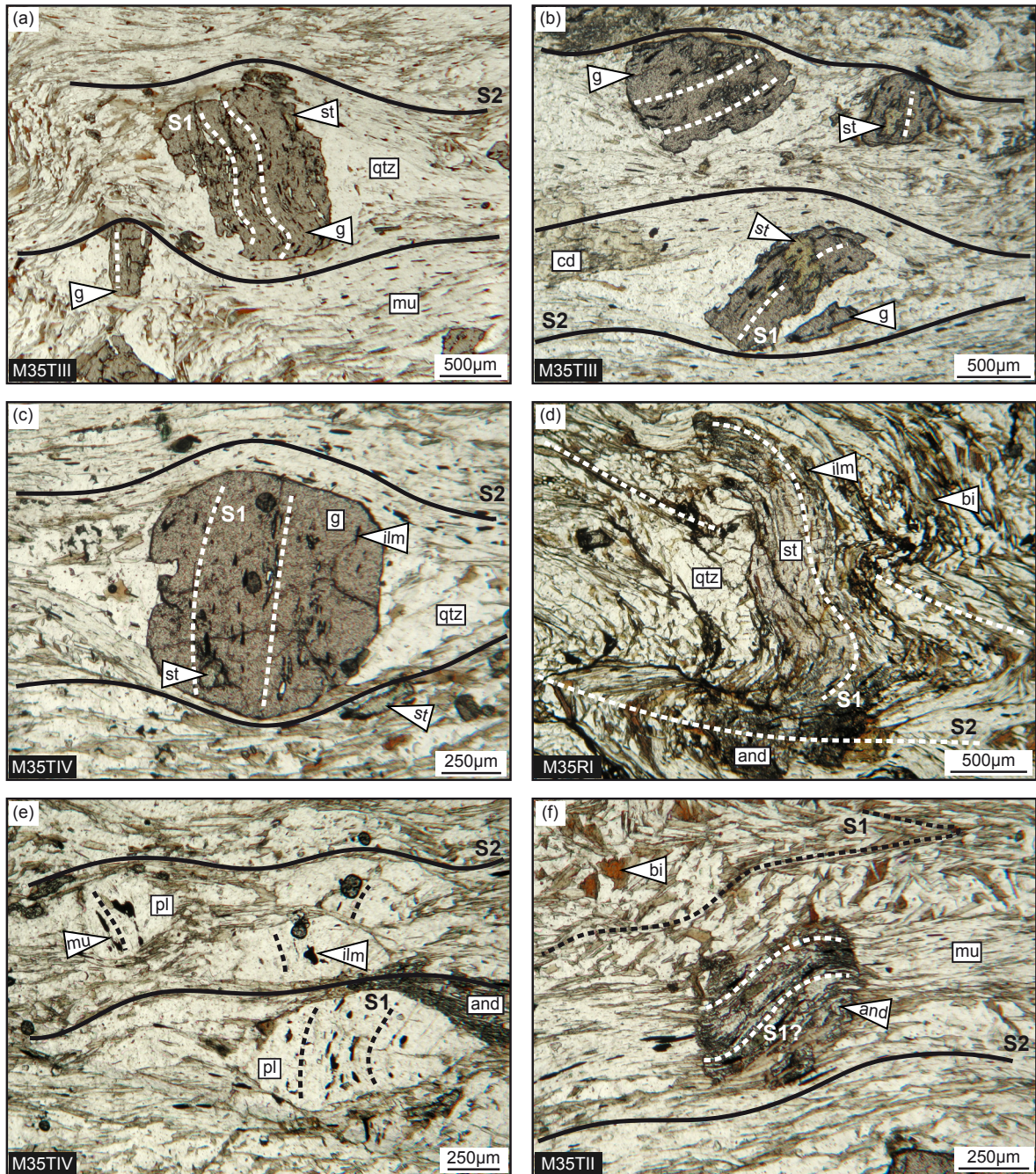


Figure 23. Photomicrographs illustrating the metamorphic minerals associated with the S1 fabric near the Javorník granitoid. (a) Garnet porphyroblast with inclusion trails parallel to S1 in the core and curved towards S2 at the rim. Staurolite is included at garnet rim. (b, c) Garnet porphyroblasts hosting staurolite and ilmenite inclusion trails oblique or perpendicular to the external S2 foliation. (d) Staurolite porphyroblast with inclusion trails parallel to S1 in the core and parallel to S2 at the rim. Andalusite is growing after staurolite along the S2 cleavage. (e) Lens-shaped plagioclase porphyroblasts with inclusion trails nearly perpendicular to the external S2 fabric. (f) Andalusite porphyroblast with sigmoidal inclusion trails continuous with S2 at the rims. Plane-polarised light.

Staurolite occurs as elongated porphyroblasts (1–2 mm), small crystals (0.2–0.5 mm) inside and around garnet porphyroblasts, or minute anhedral crystals (~0.2 mm) within the mica-rich matrix (Fig. 23c, d). Staurolite porphyroblasts frequently contain inclusions of quartz and ilmenite which define a curved pattern. The inclusion trails are mostly perpendicular to the surrounding S2 cleavage in the core but become parallel to S2 towards the rim (Fig. 23d). Smaller relicts of staurolite are additionally found within stripes of andalusite that are commonly developed around garnet (Fig. 24f). The shape of staurolite porphyroblasts together with staurolite inclusions in garnet suggest that both minerals were in equilibrium during or after the development of the S1 foliation. However, andalusite growth after staurolite points staurolite breakdown in the S2 fabric.

Plagioclase corresponds to lens-shaped porphyroblasts (0.5–1 mm) either entirely surrounded by micaceous layers or occurring together with quartz in coarse-grained layers. They commonly host tiny (<0.1 mm) inclusions of ilmenite and white mica which are consistently oriented at high angle to the external S2 foliation (Fig. 23e). Backscatter electron images additionally reveal that plagioclase cores are surrounded by a recrystallised rim preferentially developed in the pressure shadows produced by the D2 deformation (Fig. 24e).

Sillimanite has been observed around garnet crystals in one sample only. There, thin layers of fibrous sillimanite interlayered with biotite (<50 µm) are wrapped around garnet and lie parallel to the S2 foliation (Fig. 24a). Importantly, the sillimanite does not replace garnet in garnet pressure shadows, but is in equilibrium with garnet rim. This strongly suggests that sillimanite growth is associated with the development of the S2 fabric.

Andalusite forms tiny crystals (0.5–1 mm) in the matrix or elongated aggregates (1–2 mm) around garnet or plagioclase porphyroblasts. Few andalusite porphyroblasts have a sigmoidal shape and contain curved inclusion trails of ilmenite that are oblique to S2 in the core and continuous with the S2 fabric at the rims (Fig. 23f). More commonly, andalusite appears as fine-grained aggregates parallel to the S2 foliation (Fig. 24b). Electron microscope images show that these aggregates are composed of andalusite, quartz and biotite, and surround partially resorbed relicts of staurolite (Fig. 24f). The textural relationships indicate that andalusite developed in equilibrium with the garnet rims at the expense of staurolite. In this case, the demise of staurolite can be ascribed to a typical terminal reaction with garnet, biotite and Al_2SiO_5 as product phases (Fig. 25b), andalusite being the most abundant Al_2SiO_5 polymorph in the investigated samples. This reaction most likely took place during the formation of the S2 foliation, but the curved inclusions trails in some andalusite crystals do not exclude a possible earlier growth over the S1 foliation.

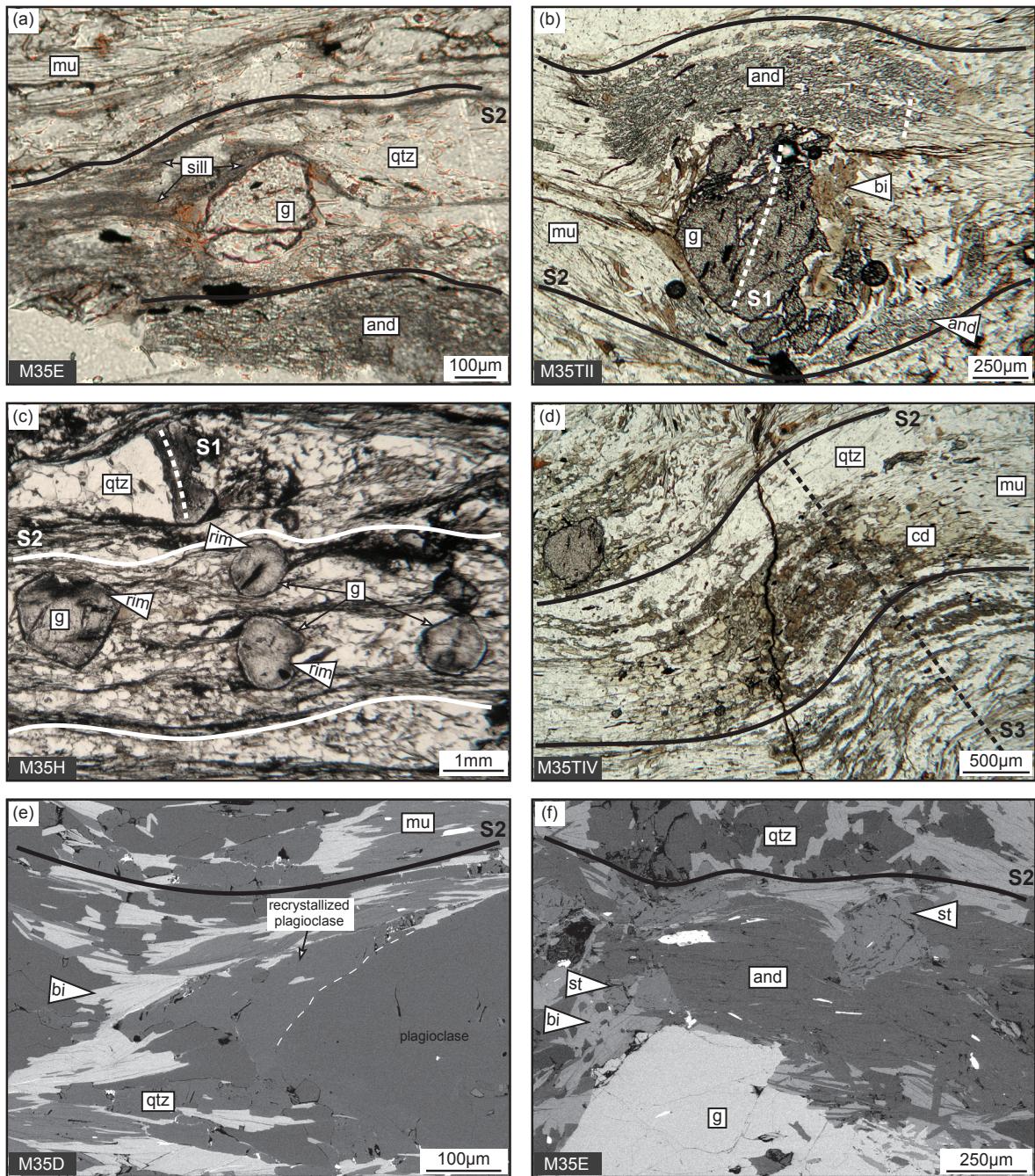


Figure 24. Photomicrographs and BSE images illustrating the metamorphic minerals associated with the S2 or S3 fabrics near the Javorník granitoid. (a) Fibrous sillimanite growing parallel to S2 in equilibrium with garnet and biotite. (b) Fine-grained andalusite aggregate developed parallel to S2 around garnet porphyroblast. (c) Rounded garnet crystals slightly overgrowing the S2 foliation. A compositional zoning in garnet is reflected by the variation from a light grey core to a darker inner rim and a bright outer rim. (d) Pinitized cordierite stripes mostly parallel to S2 but preferentially developed along the incipient S3 cleavage. (e) BSE image showing recrystallised plagioclase in the D2 pressure shadow of a primary plagioclase porphyroblast. (f) Detailed view of andalusite aggregate parallel to S2. The BSE image shows relictual staurolite surrounded by andalusite, biotite and quartz developed at garnet rim. Plane-polarised light for all photomicrographs.

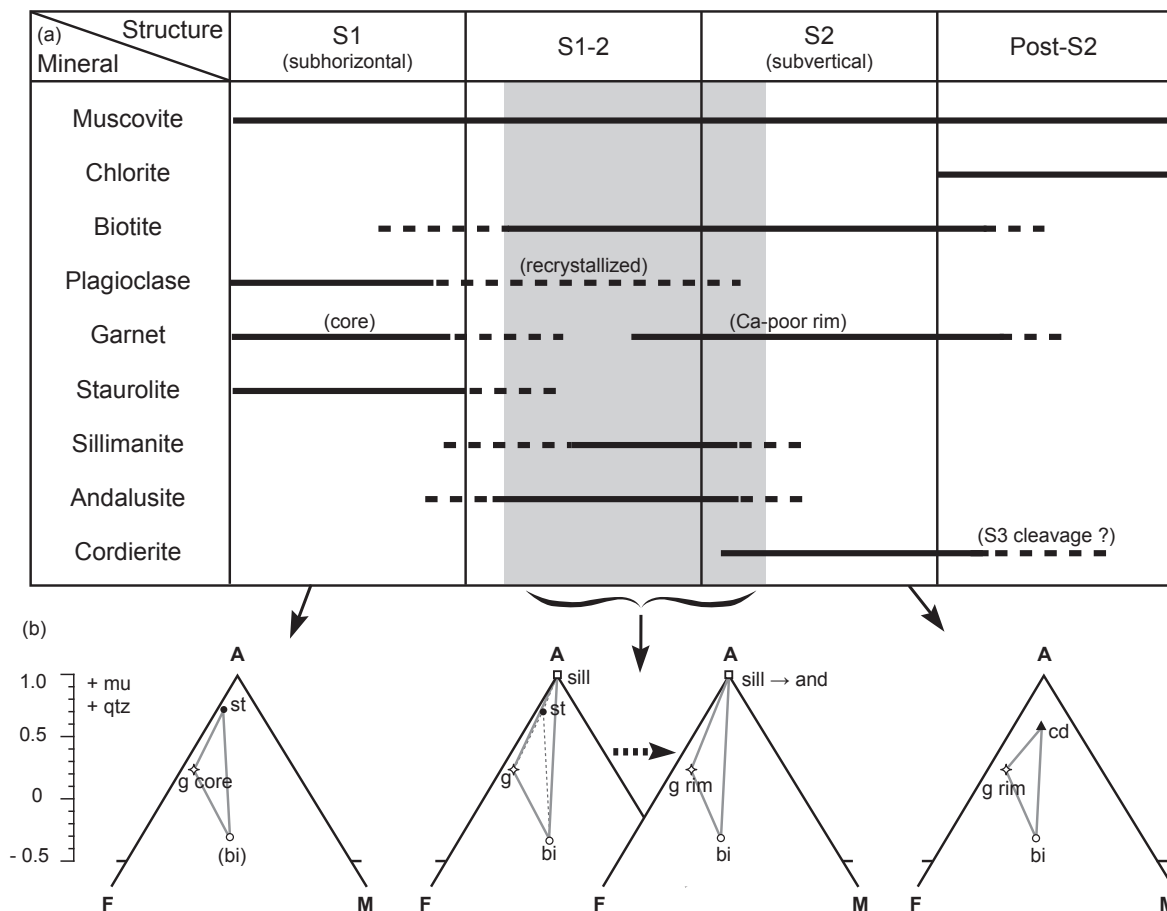


Figure 25. Summary of crystallisation-deformation relationships observed in metasediments near the Javorník granitoid. (a) Table showing the stability of the different minerals with respect to the macroscopic fabrics. Quartz and ilmenite are always present. (b) AFM diagrams illustrating the main metamorphic reactions.

Micas form continuous layers where muscovite is commonly more abundant than biotite. In places where the S1 foliation is preserved, it is defined by the microfolded and discontinuous alignment of muscovite, whereas the dominant S2 foliation is defined by thick (1–2.5 mm) muscovite and biotite layers (Fig. 23a-c). Muscovite is additionally included in garnet and plagioclase porphyroblasts where it defines trails perpendicular to the external S2 foliation (Fig. 23e). Biotite is rarely parallel to the S1 layering and more commonly develops in the axial plane cleavage of F2 microfolds or parallel to the S2 foliation together with sillimanite or andalusite (Fig. 24a, b).

Cordierite lies within mica-rich layers and corresponds to elongated stripes (up to 2 mm long) or randomly oriented flakes (Fig. 24d). It shows a yellowish colour due to widespread pinitization and commonly overgrows the S2 foliation. Few cordierite stripes are also developed along the axial plane cleavage of later F3 microfolds (Fig. 24d). This suggests that cordierite growth has occurred after the D2 deformation, and possibly during the development of the weak S3 cleavage.

Chlorite is rarely observed around garnet porphyroblasts and corresponds to a late retrograde phase with respect to the metamorphic evolution.

Chemistry

Four samples collected at the locality M35 have been analysed in order to examine the composition of the main metamorphic minerals. Although the samples preserve contrasted microstructures and varying amounts of quartz, micas, plagioclase, garnet or staurolite, the composition of the different metamorphic minerals shows only minor variations (Tabs 4 & 5).

The sample M35D exhibits numerous rounded garnet and plagioclase porphyroblasts surrounded by the continuous S2 foliation (Fig. 24e). In addition, staurolite and andalusite are observed around garnet, and cordierite stripes lie parallel to S2. The sample M35E corresponds to the hinge of an F2 fold and exhibits rootless isoclinal microfolds of quartz-rich layers surrounded by mica-rich domains where garnet (1–4 mm) and plagioclase porphyroblasts are common. Importantly, this sample preserves fibrous sillimanite and andalusite that are developed around garnet and parallel to the S2 cleavage (Fig. 24a, f). It additionally

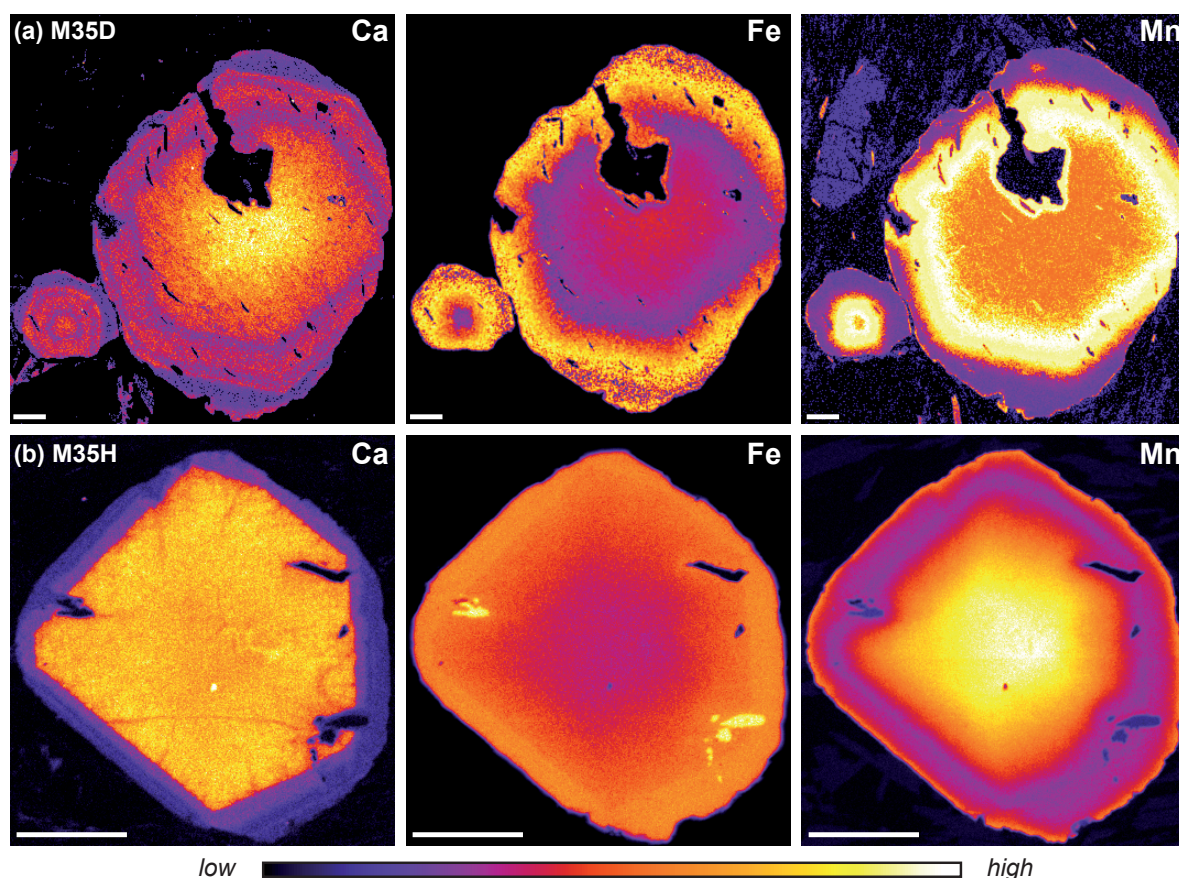


Figure 26. Compositional X-ray maps of Ca, Fe and Mn distribution in garnet porphyroblasts from sample (a) M35D and (b) M35H. Mg maps indicate only weak zoning and are not shown. Scale bar is always 100 μm .

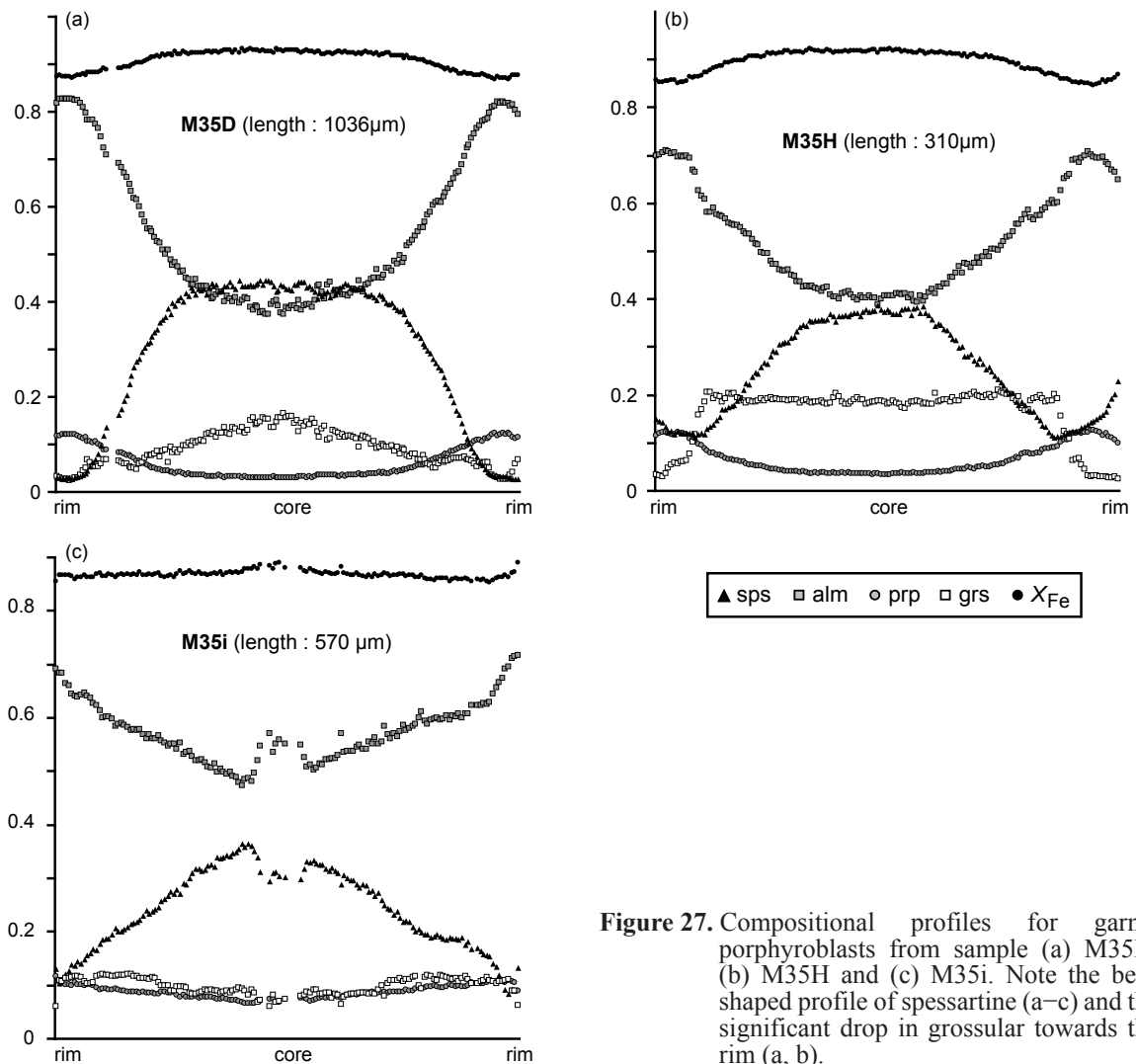


Figure 27. Compositional profiles for garnet porphyroblasts from sample (a) M35D, (b) M35H and (c) M35i. Note the bell-shaped profile of spessartine (a–c) and the significant drop in grossular towards the rim (a, b).

contains staurolite in the matrix and in garnet, minor cordierite and accessory tourmaline. The sample M35H preserves the continuous S2 foliation defined by alternating coarse-grained quartz layers and thin bands of micas that are rich in biotite. Small (0.5 mm) and nicely rounded garnet porphyroblasts are abundant and show a clear compositional zoning marked by variations in the refractive index across a single grain (Fig. 24c). Minor staurolite is also observed in quartz-rich layers. The sample M35i corresponds to the hinge zone of an F2 fold and shows microfolded quartz-rich and mica-rich layers. It contains garnet and plagioclase porphyroblasts, small (200 μm) staurolite either included in garnet or present in the matrix, and pinitized cordierite.

In all analysed samples, X-ray compositional mapping of garnet porphyroblasts reveals a strong zoning in Ca and Mn and a slightly weaker zoning in Fe (Fig. 26). From core ($\text{alm}_{0.40} \text{prp}_{0.03-0.07} \text{grs}_{0.16-0.18} \text{sps}_{0.36-0.44}$; $X_{\text{Fe}}=0.88-0.93$) to rim ($\text{alm}_{0.70-0.82} \text{prp}_{0.10-0.14} \text{grs}_{0.03} \text{sps}_{0.03-0.12}$; $X_{\text{Fe}}=0.85-0.87$), the associated profiles commonly show a strong decrease in

Table 4. Representative chemical analyses for minerals of sample M35i.

Sample Mineral Position	M35i							
	g core	g rim	st inclusion	st matrix	bi matrix	cd matrix pin.	cd matrix pin.	pl matrix
Wt. %								
SiO ₂	35.96	36.27	27.66	26.96	34.45	45.95	46.60	67.50
TiO ₂	0.32	0.15	0.46	0.48	1.63	0.00	0.03	0.00
Al ₂ O ₃	20.60	20.66	53.85	54.36	19.65	31.32	32.30	19.47
FeO	26.06	31.79	12.23	12.08	19.35	4.79	6.71	0.06
MnO	13.30	5.14	0.37	0.37	0.14	0.03	0.04	0.01
MgO	1.71	2.60	1.79	1.29	8.91	1.96	2.32	0.00
CaO	2.43	3.65	0.01	0.03	0.01	0.68	0.82	0.19
Na ₂ O	0.00	0.00	0.00	0.00	0.22	0.09	0.11	11.92
K ₂ O	0.00	0.00	0.00	0.02	9.14	5.30	3.51	0.11
ZnO	<i>n.a.</i>	<i>n.a.</i>	1.43	1.40	0.03	0.01	0.07	<i>n.a.</i>
Total	100.38	100.26	97.81	97.01	93.53	90.13	92.50	99.26
Cations								
Si	2.92	2.92	3.92	3.86	2.74	-	-	2.96
Ti	0.02	0.01	0.05	0.05	0.10	-	-	0.00
Al	1.97	1.96	9.00	9.17	1.84	-	-	2.96
Fe ³⁺	0.16	0.19	0.00	0.00	0.00	-	-	0.00
Fe ²⁺	1.60	1.95	1.45	1.45	1.29	-	-	2.96
Mn	0.91	0.35	0.04	0.05	0.01	-	-	0.00
Mg	0.21	0.31	0.38	0.28	1.06	-	-	0.00
Ca	0.21	0.31	0.00	0.00	0.00	-	-	0.01
Na	0.00	0.00	0.00	0.00	0.03	-	-	1.01
K	0.00	0.00	0.00	0.00	0.93	-	-	0.01
Zn	-	-	0.15	0.15	0.00	-	-	-
Total	8	8	15	15	8	-	-	5
X_{Fe}	0.89	0.86	0.79	0.84	0.55			an 0.01
alm	0.55	0.66						ab 0.99
prp	0.07	0.11						or 0.00
grs	0.07	0.11						
sps	0.31	0.12						

Structural formulae calculated on the basis of 12 oxygens for garnet, 23 for staurolite and 8 for plagioclase.

Analyses of pinitized cordierite are not recalculated ; *n.a.* = not analysed ; pin. = pinitized

spessartine, a weaker decrease in X_{Fe} , a marked increase in almandine and a small increase in pyrope (Fig. 27). In garnet porphyroblasts with inclusion trails perpendicular to the S2 foliation the grossular content is nearly constant, whereas in rounded porphyroblasts it shows a nearly flat profile in the core followed by a significant drop at the rim. In the case of these small rounded garnets, the bright outer rim therefore corresponds to a Ca-poor overgrowth (Fig. 27a,b). Chemical analyses additionally reveal that staurolite porphyroblasts are not zoned and exhibit a constant X_{Fe} (0.82–0.86) while staurolite inclusions in garnet commonly show lower X_{Fe} values (0.76–0.79). Plagioclase is generally albite with negligible anorthite contents ($an_{0.01}$), but large primary plagioclase with oligoclase composition ($an_{0.12-0.26}$) is also found. Primary albite is recrystallised into oligoclase ($an_{0.12-0.15}$) in pressure shadows related

Table 5. Representative chemical analyses for minerals of samples M35D, M35E and M35H.

Sample Mineral Position	M35D				M35E				M35H	
	g core	g rim	pl rim	pl rec. rim	pl core	bi matrix	st matrix	st inclusion	g core	g rim
Wt. %										
SiO ₂	35.29	36.40	67.84	64.46	60.76	34.65	27.20	26.28	36.64	36.37
TiO ₂	0.22	0.08	0.00	0.01	0.01	1.65	0.50	0.46	0.16	0.06
Al ₂ O ₃	20.02	21.12	19.47	21.64	23.87	19.33	54.48	54.65	21.10	21.07
FeO	22.52	38.13	0.02	0.00	0.03	19.63	12.54	12.42	27.51	32.73
MnO	17.20	1.19	0.01	0.00	0.00	0.20	0.46	0.74	6.66	6.21
MgO	0.92	2.96	0.00	0.00	0.01	9.41	1.53	2.20	1.94	3.06
CaO	3.42	0.86	0.12	2.94	5.44	0.00	0.00	0.03	6.08	1.11
Na ₂ O	0.00	0.00	11.68	10.13	8.88	0.21	0.00	0.00	0.00	0.03
K ₂ O	0.00	0.00	0.16	0.15	0.17	8.69	0.00	0.00	0.01	0.02
ZnO	<i>n.a.</i>	<i>n.a.</i>	<i>n.a.</i>	<i>n.a.</i>	<i>n.a.</i>	<i>n.a.</i>	1.38	1.51	<i>n.a.</i>	<i>n.a.</i>
Total	99.59	100.74	97.63	95.36	99.16	93.76	98.09	98.29	100.10	100.66
Cations										
Si	2.90	2.92	2.98	2.85	2.71	2.75	3.85	3.70	2.94	2.92
Ti	0.01	0.00	0.00	0.00	0.00	0.10	0.05	0.05	0.01	0.00
Al	1.94	2.00	1.01	1.13	1.25	1.81	9.09	9.08	2.00	1.99
Fe ³⁺	0.24	0.14	0.00	0.00	0.00	0.00	0.00	0.00	0.11	0.17
Fe ²⁺	1.30	2.42	0.00	0.00	0.00	1.30	1.48	1.46	1.74	2.02
Mn	1.20	0.08	0.00	0.00	0.00	0.01	0.05	0.09	0.45	0.42
Mg	0.11	0.35	0.00	0.00	0.00	1.11	0.32	0.46	0.23	0.37
Ca	0.30	0.07	0.01	0.14	0.26	0.00	0.00	0.00	0.52	0.10
Na	0.00	0.00	0.99	0.87	0.77	0.03	0.00	0.00	0.00	0.01
K	0.00	0.00	0.01	0.01	0.01	0.88	0.00	0.00	0.00	0.00
Zn	-	-	-	-	-	-	0.14	0.16	-	-
Total	8	8	5	5	5	8	15	15	8	8
X_{Fe}	0.92	0.87	an	0.01	0.14	0.25	0.54	0.82	0.59	0.69
alm	0.45	0.83	ab	0.99	0.85	0.74			0.59	0.70
prp	0.04	0.12	or	0.01	0.01	0.01			0.08	0.13
grs	0.10	0.02							0.18	0.02
sps	0.41	0.03							0.15	0.15

Structural formulae calculated on the basis of 12 oxygens for garnet, 22 for biotite, 23 for staurolite and 8 for plagioclase.

n.a. = not analysed ; rec. rim = recrystallised rim

to the D2 deformation (Fig. 24e). Biotite has a rather constant X_{Fe} (0.52–0.60) and Ti content (Ti=0.05–0.15 a.p.f.u.), and pinitized cordierite commonly shows a significant amount of K₂O (2–5 wt.%).

Mineral equilibria modelling

The pseudosection was calculated using the whole-rock composition of the mica schist sample M35i up to partial melting occurring at ~650 °C (Fig. 28). The pseudosection topology shows biotite stability in the whole range of the calculated P – T conditions, garnet stability above ~480 °C, staurolite stability field stretching from 560 °C and 3.5 kbar to 640 °C and 7 kbar, and ilmenite stability up to 7.5–8.5 kbar. Kyanite has a narrow stability field above ~630 °C

and ~6 kbar, whereas sillimanite is stable above 580 to 630 °C at pressures between 4 and 6 kbar, and andalusite between ~550 and 650 °C at pressures ranging from 2.5 to 4 kbar. The cordierite stability field occurs between 520 and 650 °C with an upper pressure limit at 2.5–3 kbar.

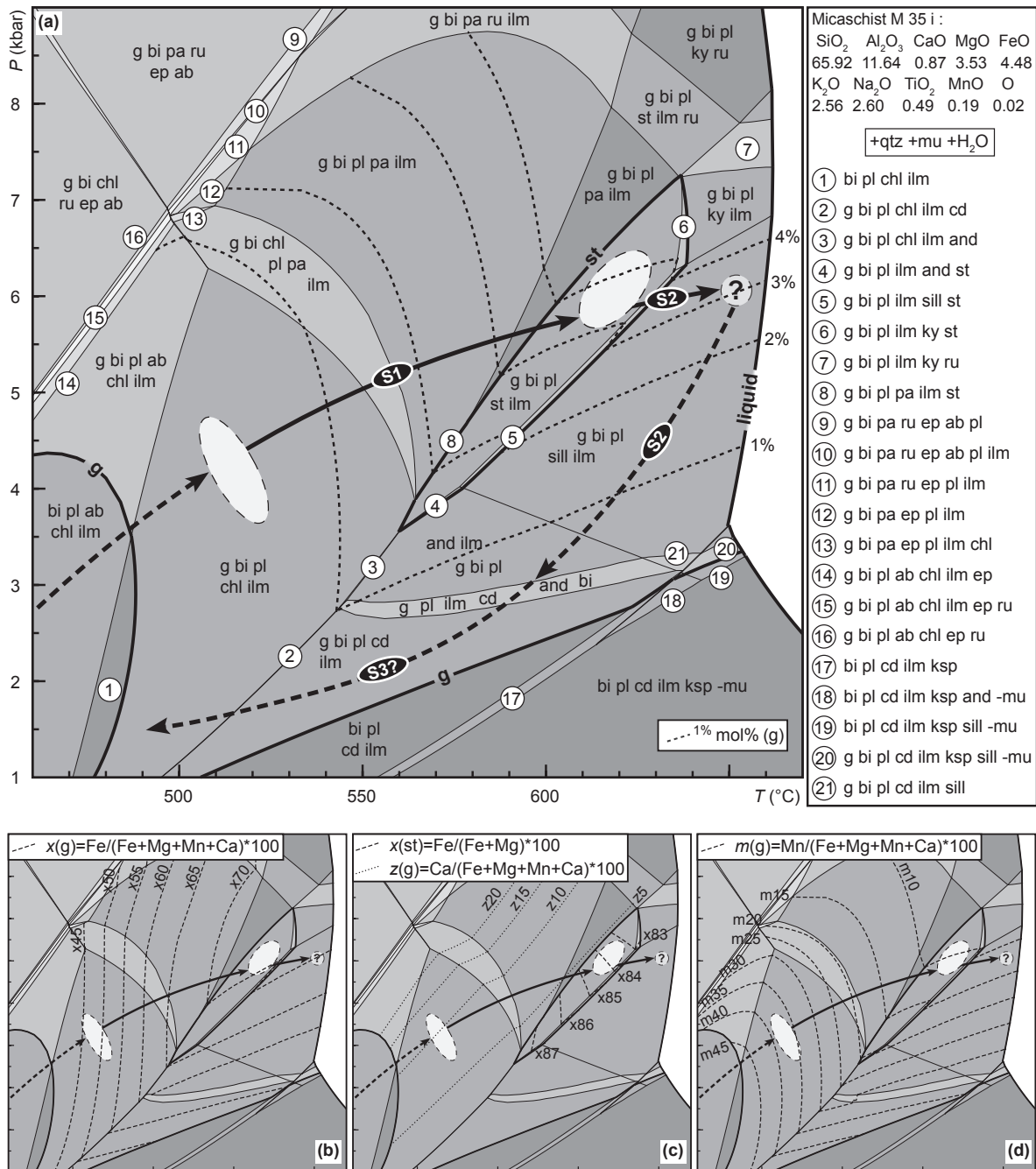


Figure 28. (a) *P-T* pseudosection in the MnNCKFMASHTO system for sample M35i (in moles adjusted to 100%), contoured for garnet modal proportion. Full and dashed black lines indicate the *P-T* path derived by comparing the modelled assemblages and isopleths with the observed assemblages and mineral compositions. Ellipses denote the probable *P-T* range for the different stages of the *P-T* path. (b-d) Modelled isopleths for garnet and staurolite. The stability of garnet, staurolite and granitic melt is highlighted.

The samples collected at the locality M35 show garnet porphyroblasts with inclusions of ilmenite, staurolite and white mica oriented perpendicular to the S2 foliation (Fig. 23). Similarly, plagioclase porphyroblasts host ilmenite and white mica inclusions at high angle to S2. These observations point to a crossing of both the garnet and staurolite isograds during or after the formation of the earlier S1 fabric. Staurolite is subsequently replaced by sillimanite/andalusite and biotite oriented parallel to the S2 fabric, and this terminal reaction is associated with a new garnet growth episode (Fig. 24). These relationships therefore indicate that the Al_2SiO_5 isograd was crossed during the development of the S2 foliation. Finally, cordierite growth occurs after D2 or during the weak D3 deformation.

In the pseudosection, crystallisation-deformation relationships suggest an evolution from the g–bi–chl–pl–ilm–mu–qtz to the g–bi–st–pl–ilm–mu–qtz field in the S1 foliation (Fig. 28a). The beginning of this P – T path can be further constrained at ~4 kbar and ~520 °C where the modelled $x(\text{g})$, $z(\text{g})$ and $m(\text{g})$ isopleths lie close to the core composition ($\text{alm}_{0.37-0.40} \text{grs}_{0.16-0.18} \text{sps}_{0.38-0.44}$) of garnet from sample M35i (Figs 27 & 28b-d). However, the garnet isopleths do not intersect on the garnet-in line. By contrast, the chemistry of garnet porphyroblasts from samples M35D and M35H ($\text{alm}_{0.48} \text{grs}_{0.09} \text{sps}_{0.36}$) indicates P – T estimates closer to the garnet-in line (Fig. 27a, b), suggesting that the onset of garnet growth is better preserved in these samples. The discrepancy observed for sample M35i is therefore ascribed to the use of a section which does not pass exactly through the core of the grain. The end of the P – T path related to the S1 foliation lies in the staurolite stability field where the X_{Fe} of staurolite ($X_{\text{Fe}}=0.83-0.84$) and the garnet rim composition ($\text{alm}_{0.70} \text{grs}_{0.06} \text{sps}_{0.10}$) are compatible with staurolite and garnet isopleths intersecting at ~5.5 kbar and ~620 °C (Fig. 28b-d).

The growth of Ca-poor garnet and sillimanite after staurolite in the S2 foliation requires a subsequent increase in both pressure and temperature towards the g–bi–sill–pl–ilm–mu–qtz field (Fig. 28a). However, the Ca-poor garnet rims are not observed in sample M35i, but are common in sample M35H. The above-discussed results show that the composition of garnet from sample M35H can reliably be used in the calculated pseudosection. Therefore, a nearly isobaric heating path towards ~6 kbar and ~650 °C can be derived from the modelled isopleths corresponding to the outermost rim composition ($\text{alm}_{0.70} \text{grs}_{0.03} \text{sps}_{0.12}$) of garnet from sample M35H (Figs 27b & 28b-d). Microscopic observations indicate that the S2 foliation also developed in the stability field of andalusite. Nevertheless, the measured garnet composition points to significantly higher pressure conditions. Consequently, andalusite is considered as a pseudomorph after sillimanite which grew during a later stage of D2 deformation. This suggests that the S2 foliation was also associated with decompression below 3.5–4 kbar while the temperature, although poorly constrained, remained relatively high at 550–630 °C (Fig.

28a). The subsequent growth of cordierite parallel to the S2 foliation or to the S3 cleavage points to $P-T$ conditions below 3 kbar and still above 500 °C, whereas retrograde chlorite accounts for post-D3 cooling below 500 °C (Fig. 28a).

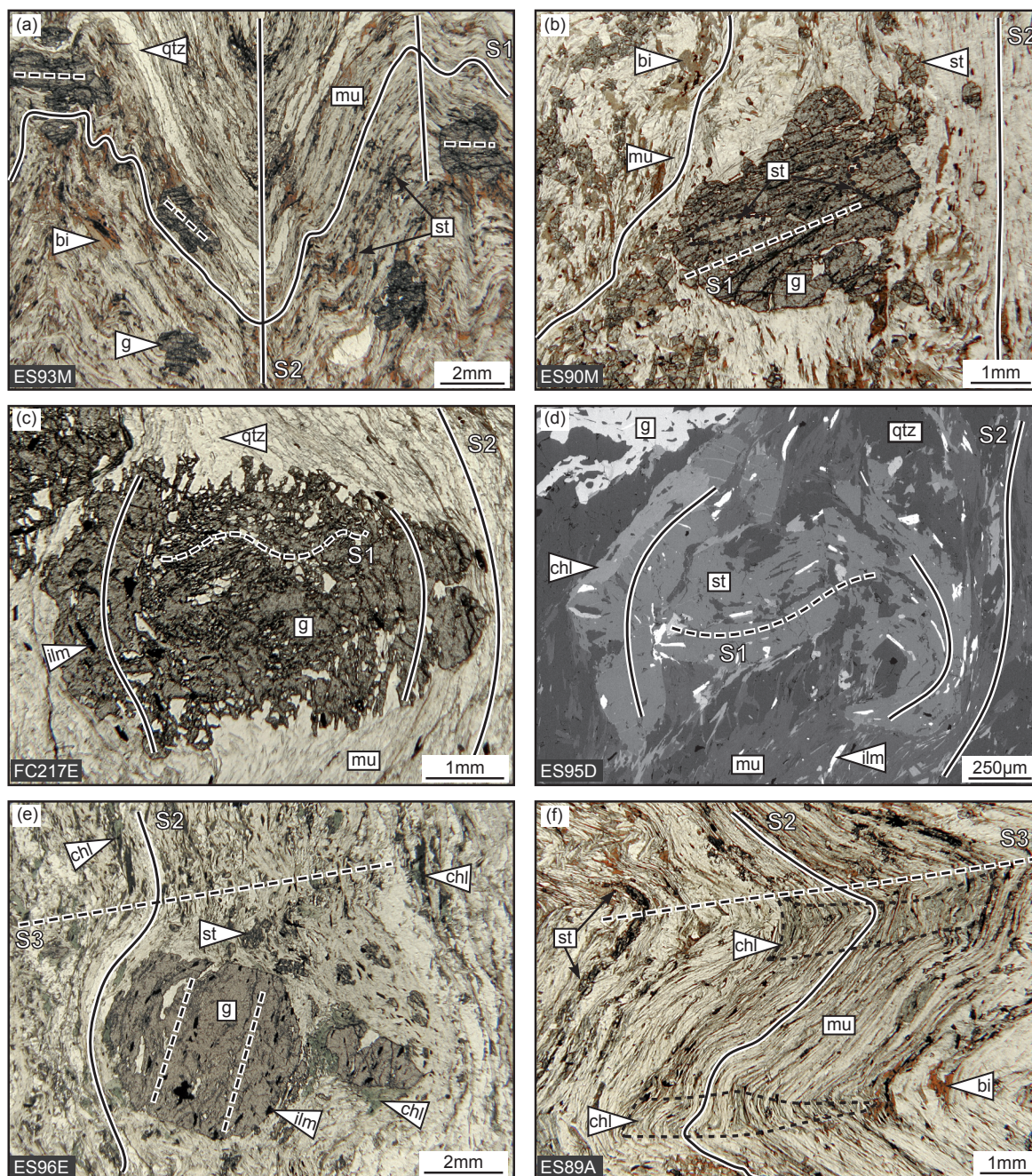


Figure 29. Photomicrographs and BSE image illustrating crystallisation-deformation relationships in metasediments near the eclogite belt. (a) S1 foliation containing muscovite, quartz, biotite, garnet, and staurolite affected by F2 microfolds. (b) Garnet with staurolite inclusions (highlighted by dashed lines) and straight inclusion trails oriented oblique to the surrounding S2 foliation. (c) Garnet with quartz inclusion trails marking the crenulated S1 foliation in the core and ilmenite inclusions continuous with the external S2 foliation at the rim. (d) Staurolite with quartz and ilmenite oriented at high angle to the external S2 foliation in the core and nearly parallel to S2 at the rim. (e) Chlorite growing parallel to the S2 foliation around staurolite and garnet. (f) Domains rich in chlorite (highlighted by dashed lines) located in the axial plane cleavage of F3 microfolds. Plane-polarised light for all photomicrographs.

4) Tectono-metamorphic evolution near the eclogite belt (southern domain)

In the southern domain, the metamorphic record in metasediments adjacent to the N–S trending eclogite belt has been investigated. The metasedimentary rocks are located to the East of the Międzygórze gneiss dome (central OSD), in a relatively narrow (2 km) belt that stretches from Králíky (Czech Republic) to Sienna (Poland). This area was referred to as the Sienna syncline by Don (1982). The main crystallisation-deformation relationships are illustrated in Fig. 29 and summarized in Fig. 30.

Petrography

The S1 metamorphic layering is preserved rarely as a microfolded alternation of quartz- and muscovite-rich bands (Fig. 29a). Discontinuous layers rich in garnet and staurolite following the S1 foliation are commonly observed (Fig. 29a). Garnet (1–2 mm) and staurolite (up to 1 mm) show inclusion trails of quartz and ilmenite parallel to the S1 foliation. In places, large staurolite grains are included at the outer rim of garnet porphyroblasts which show S1 inclusion trails oblique to the S2 cleavage (Fig. 29b). Biotite parallel to the S1 foliation is scarce.

The S2 fabric ranges from a weak spaced cleavage to a continuous metamorphic foliation (Fig. 29b). Biotite (0.5 mm) shows preferential orientation parallel to the S2 axial plane cleavage and is more abundant than in the S1 fabric. Garnet with straight to weakly crenulated inclusion trails corresponding to the S1 fabric is overgrown by garnet with ilmenite inclusions continuous with the external S2 foliation (Fig. 29c, e). Staurolite porphyroblasts with S1 inclusion trails are locally overgrown by rims with ilmenite inclusions parallel to

Structure Mineral	S 1 (subhorizontal)	S 1-2	S 2 (subvertical)	Post-S 2
Muscovite				
Chlorite			---	(S3 cleavage)
Biotite	—		-----	
Plagioclase		---		
Garnet				
Staurolite			-----	
Chloritoid (in garnet)	---			

Figure 30. Summary of crystallisation-deformation relationships observed in metasediments near the eclogite belt. Quartz and ilmenite are always present.

the matrix S2 foliation (Fig. 29d). Some samples exhibit widespread chlorite parallel to the S2 fabric, and chlorite aggregates show a sharp contact with garnet rims, but clearly replace staurolite (Fig. 29d, e). Chlorite additionally occurs parallel to the axial plane of the F3 microfolds (areas highlighted in Fig. 29f).

Chemistry

Sample ES95DI was collected in the hinge of a F2 fold in order to study the relationship between crystallisation and deformation, and to assign $P-T$ conditions to the individual deformation phases. The sample contains garnet, staurolite, biotite, muscovite, quartz, few plagioclase and accessory ilmenite, tourmaline, chlorite and apatite. The matrix displays microfolded quartz- and muscovite-rich S1 bands, and an S2 cleavage which is marked mostly by oriented biotite. Garnet porphyroblasts (2–4 mm) host inclusions of quartz, ilmenite, tourmaline, rare muscovite and plagioclase which are commonly oriented at high angle to the surrounding S2 cleavage (similarly as in Fig. 29a). Small staurolite crystals are also partly enclosed at garnet rims. The inclusion trails are slightly curved towards the garnet rims and are continuous with the external S2 foliation. It is interpreted as dominant garnet growth during or after the formation of the shallow-dipping S1 foliation and limited growth in the S2 fabric. Staurolite (up to 1 mm) is abundant in the matrix and includes quartz, ilmenite and tourmaline which are oriented at high angle to the external S2 fabric in the core and parallel to S2 at the rim (Fig.

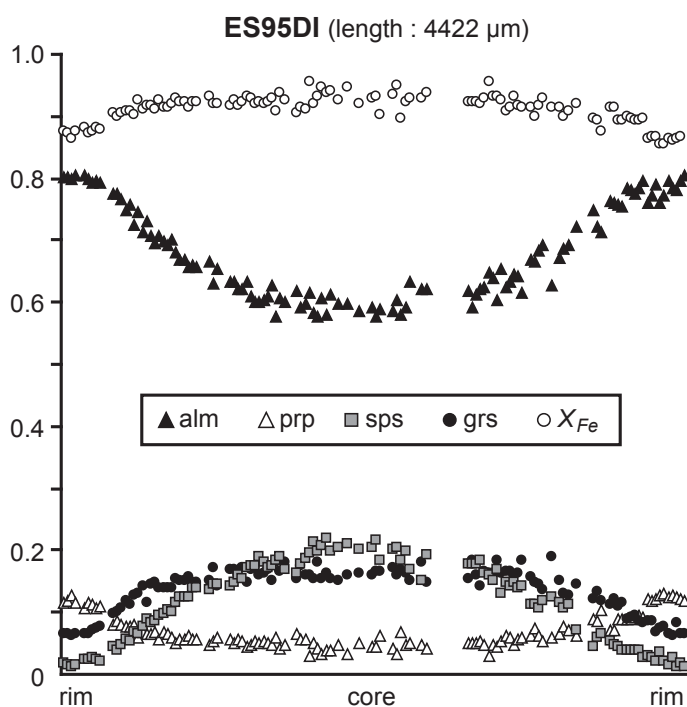


Figure 31. Garnet profile for sample ES95D.

Table 6. Representative chemical analyses for minerals of sample ES95D.

Sample Mineral Position	ES95DI							
	g core	g rim	st core	st rim	bi matrix	chl matrix	mu matrix	pl matrix
Wt. %								
SiO ₂	36.40	37.00	27.97	27.55	36.50	23.24	44.83	64.04
TiO ₂	0.15	0.55	0.56	0.73	1.73	0.27	0.26	0.00
Al ₂ O ₃	21.08	22.40	54.30	54.58	20.06	22.60	37.68	23.08
FeO	26.61	33.73	12.19	12.64	19.03	28.76	0.91	0.11
MnO	8.11	1.07	0.21	0.25	0.00	0.10	0.00	0.00
MgO	0.83	2.65	1.48	1.27	9.56	11.59	0.51	0.08
CaO	5.74	2.31	0.10	0.08	0.07	0.14	0.00	3.29
Na ₂ O	0.00	0.08	0.33	0.26	0.40	0.00	2.45	8.89
K ₂ O	0.00	0.16	0.00	0.00	8.61	0.03	7.33	0.00
ZnO	<i>n.a.</i>	<i>n.a.</i>	0.57	0.37	<i>n.a.</i>	<i>n.a.</i>	<i>n.a.</i>	<i>n.a.</i>
Total	98.92	99.93	97.71	97.72	95.97	86.73	93.97	99.49
Cations								
Si	2.98	2.97	7.91	7.74	2.82	5.07	2.99	2.85
Ti	0.01	0.03	0.12	0.15	0.10	0.04	0.01	0.00
Al	2.03	2.12	18.09	18.03	1.83	5.81	2.96	1.21
Fe ³⁺	0.00	0.00	0.00	0.00	0.00	0.00	0.00	0.00
Fe ²⁺	1.82	2.26	2.88	3.12	1.23	5.25	0.05	0.00
Mn	0.56	0.07	0.05	0.08	0.00	0.02	0.00	0.00
Mg	0.10	0.32	0.62	0.58	1.10	3.77	0.05	0.01
Ca	0.50	0.20	0.03	0.02	0.01	0.03	0.00	0.16
Na	0.00	0.01	0.18	0.15	0.06	0.00	0.32	0.77
K	0.00	0.02	0.00	0.00	0.85	0.01	0.62	0.00
Zn	-	-	0.12	0.14	-	-	-	-
Total	8	8	30	30	8	20	7	5
X_{Fe}	0.95	0.88	0.82	0.84	0.53	0.58		
alm	0.61	0.79						an 0.83
prp	0.03	0.11						ab 0.17
grs	0.17	0.07						or 0.00
sps	0.19	0.03						

Structural formulae calculated on the basis of 12 oxygens for garnet, 23 for staurolite, 22 for biotite and muscovite, 28 for chlorite and 8 for plagioclase ; *n.a.* = not analysed

29d). This is interpreted as syn- or post-D1 staurolite growth followed by continuous growth during the development of the subvertical S2 cleavage.

Garnet shows zoning with decreasing spessartine, grossular and X_{Fe} , and increasing pyrope and almandine from core (alm_{0.60} prp_{0.04} grs_{0.17} sps_{0.19}; X_{Fe} =0.94) to rim (alm_{0.75} prp_{0.15} grs_{0.08} sps_{0.02}; X_{Fe} =0.83) (Fig. 31d & Tab. 6). Staurolite is not regularly zoned and its X_{Fe} varies between 0.82 and 0.86 with Zn=0.07–0.14 a.p.f.u. and Ti=0.10–0.15 a.p.f.u. (Tab. 6). Rare plagioclase has a low anorthite content (an_{0.15–0.19}), biotite has X_{Fe} =0.53–0.55 and Ti=0.07–0.10 a.p.f.u., and chlorite found around garnet and staurolite shows X_{Fe} =0.56–0.60.

Mineral equilibria modelling

The stability of quartz, muscovite, garnet, staurolite, biotite and ilmenite has been documented in both the S1 and S2 foliations. The modelled compositional isopleths of garnet with values similar to garnet core ($alm_{0.60} grs_{0.17} sps_{0.19}$) intersect at the garnet-in line and constrain the onset of garnet growth to ~ 5 kbar and 530°C (Fig. 32b–d). The observed garnet zoning

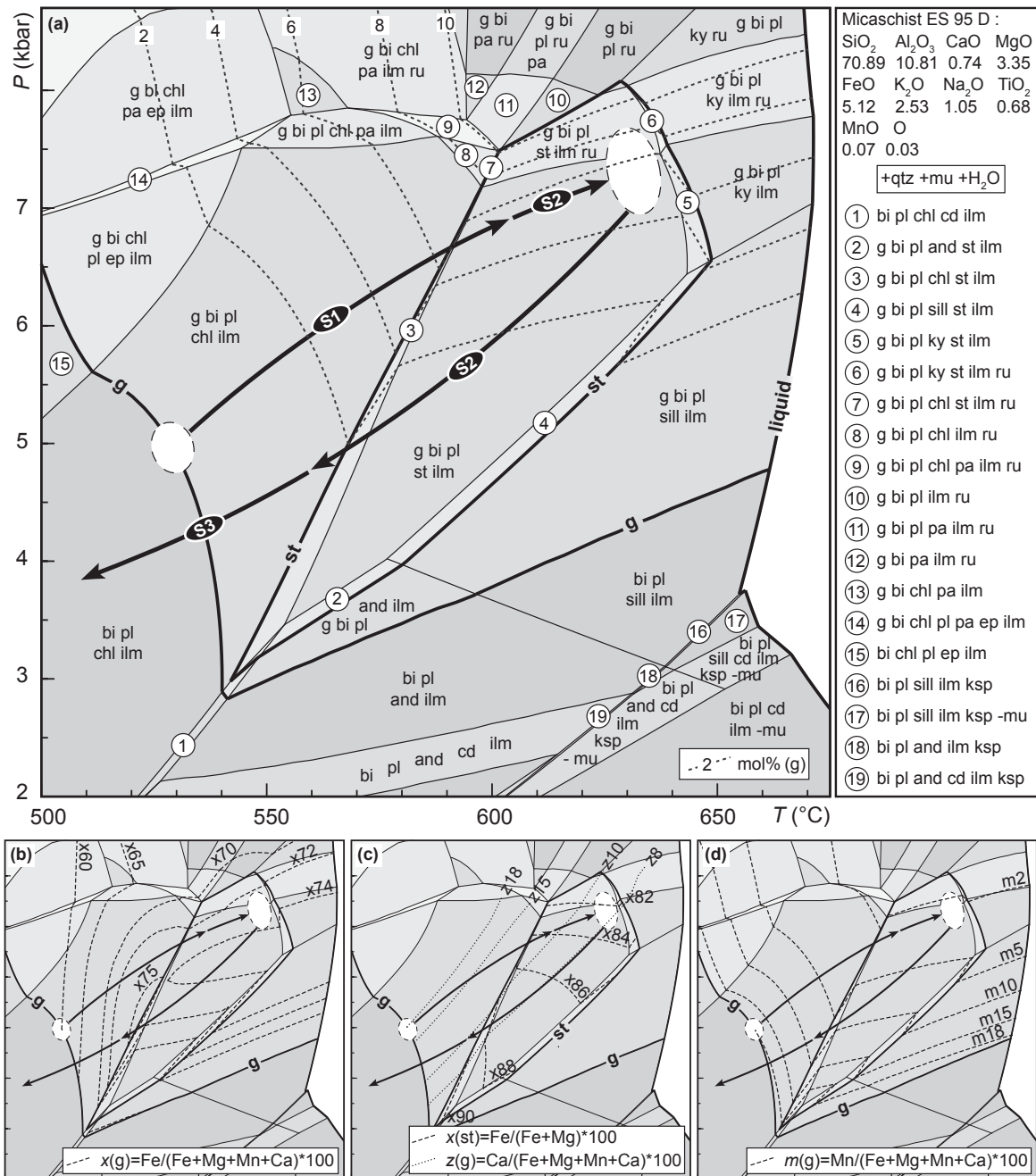


Figure 32. (a) P – T pseudosection in the MnNCKFMASHTO system for sample ES95D (in moles adjusted to 100%), contoured for garnet modal proportion. (b–d) Modelled isopleths for garnet and staurolite. The stability of garnet, staurolite and granitic melt is highlighted. White ellipses show areas corresponding to garnet core and rim compositions. Black arrows indicate the P – T path derived by comparing the modelled assemblages and isopleths with the observed assemblages and mineral compositions.

indicates a prograde evolution crossing the staurolite-in line, which is in agreement with the occurrence of staurolite inclusions in garnet. This P – T path reaches the g–bi–pl–st–ilm field (Fig. 32a) at ~ 7 kbar and 630 °C where $x(\text{g})$, $z(\text{g})$, $m(\text{g})$ and $x(\text{st})$ values (Fig. 32b–d) are close to staurolite ($X_{\text{Fe}}=0.82$) and garnet rim compositions ($\text{alm}_{0.75}\text{grs}_{0.08}\text{sps}_{0.02}$). Garnet and staurolite rims (Fig. 29c, d) are associated with the S2 fabric suggesting that the transposition of the shallow-dipping S1 fabric into the subvertical S2 foliation started near the peak P – T conditions (Fig. 32). Chlorite replacing staurolite in the S2 foliation can be correlated with a retrograde path crossing the chlorite-in line and possibly connected with garnet rim ($\text{alm}_{0.75}$) re-equilibration below ~ 570 °C at the end of the D2 deformation (Fig. 32b). Further evolution during the D3 deformation is revealed by chlorite occurrence in the F3 fold hinges which indicates temperatures lower than ~ 540 °C for the end of the retrograde path in the bi–pl–chl–ilm field (Fig. 32a).

5) Tectono-metamorphic evolution across the central domain

The central domain corresponds to a wide NW–SE trending belt of metasedimentary rocks which is located relatively far from the granulite and eclogite belts (Fig. 3). This area may therefore be considered as a part of the orogenic middle crust that was only weakly or even not influenced by the exhumation of the lower crustal lithologies. Accordingly, mica schist samples have been examined in order to understand the P – T – D evolution of this peculiar part of the Stronie formation.

Petrography

A detailed mineralogical study on marble and metapelite of the central domain has revealed that metamorphism increases towards the East (Jastrzębski, 2005; 2008). Similarly, the investigated samples preserve Barrovian metamorphic minerals that document increasing grade from NW to SE. The crystallisation–deformation relationships can therefore be described for separate parts of the central domain (Figs 33 & 34).

The Stronie formation is only poorly exposed in the *northwest part* of the central domain. In thin section, mica schist samples generally exhibit the subhorizontal S3 foliation and relicts of the earlier S2 layering are rare. In places where it is preserved, the S2 metamorphic foliation consists of microfolded alternations of muscovite–biotite layers and quartz microlithons where a bulging recrystallisation process is clearly observed. Plagioclase porphyroblasts with inclusions of ilmenite, muscovite and biotite, and rare rounded garnet crystals are found parallel to the unaffected S2 foliation. Locally, garnet porphyroblasts in equilibrium with widespread chlorite show inclusions of ilmenite, quartz and chloritoid

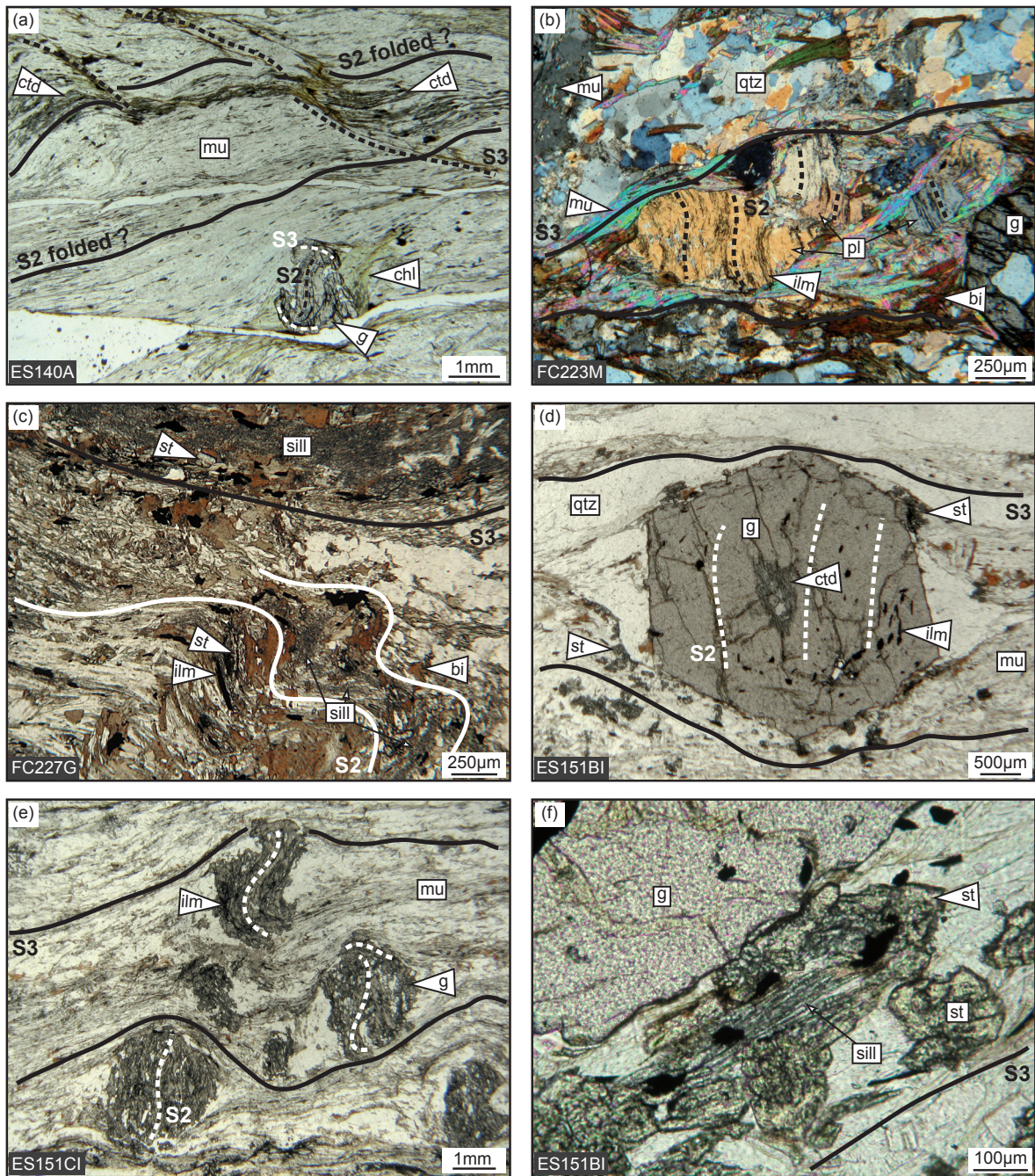


Figure 33. Photomicrographs illustrating crystallisation-deformation relationships in metasediments of the central domain. Northwest part: (a) Garnet porphyroblast with inclusion trails perpendicular to the S3 cleavage in the core and parallel to S3 at the rim. Chloritoid needles are parallel to the folded S2 layering and chlorite is in equilibrium with garnet; (b) plagioclase porphyroblasts with inclusions of ilmenite and white mica oriented perpendicular to the surrounding S3 fabric. Central part: (c) Microfolded S2 foliation containing staurolite, biotite and minor sillimanite. Fibrous sillimanite is also widespread along the S3 foliation. Southeast part: (d) Garnet porphyroblast with inclusions of chloritoid and ilmenite oriented perpendicular to the surrounding S3 foliation; (e) garnet porphyroblasts with consistently oriented inclusion trail patterns. Quartz and ilmenite inclusions are perpendicular to S3 in the core and become gradually parallel to S3 at the rim; (f) prismatic sillimanite growing after staurolite next to garnet. Plane-polarised light, except for (b) with mica plate inserted.

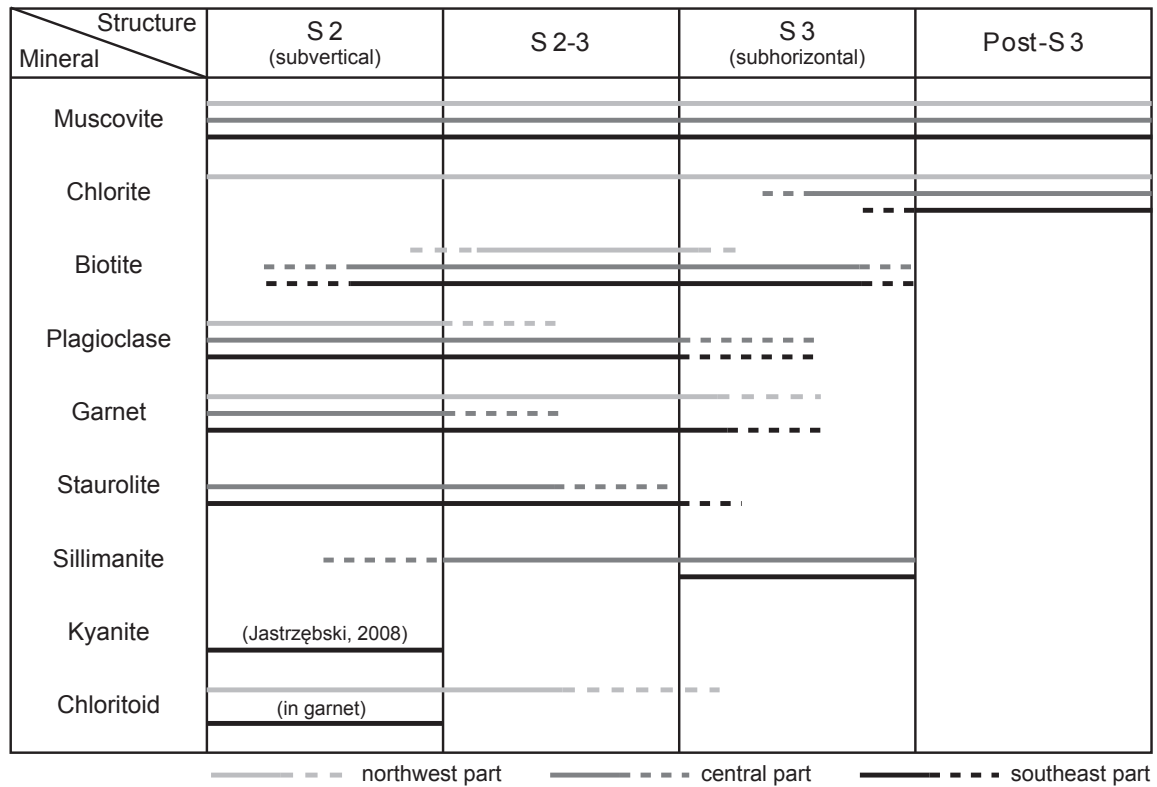


Figure 34. Summary of crystallisation-deformation relationships observed in metasediments of the central domain. Quartz and ilmenite are always present. Kyanite occurrence in the southeast part is after Jastrzębski (2008).

oriented at high angle to the surrounding S3 fabric. Chloritoid is additionally found parallel to the folded S2 foliation (Fig. 33a). The dominant S3 metamorphic foliation is characterised by continuous layers of mica surrounding quartz lenses or plagioclase and garnet porphyroblasts. Porphyroblast inclusion trails are commonly perpendicular to S3 in the core, but can be nearly parallel to S3 at the rims (Fig. 33a, b). Biotite is frequently observed in equilibrium with garnet rims and may also be partly chloritized in the matrix. In samples collected in the northernmost part of the area, biotite is absent and chlorite is abundant in garnet pressure shadows (Fig. 33a, b).

In the *central part* of the metasedimentary belt, the S3 foliation is dominant but the weakly crenulated S2 is also frequently observed. The S2 metamorphic layering is marked by quartz-rich bands and mica-rich bands containing muscovite, sericite and minor biotite. Plagioclase is elongated parallel to S2 and rare garnet porphyroblasts show ilmenite inclusions trails continuous with S2. Towards the South, one sample preserves staurolite crystals parallel to the S2 layering and fibrous sillimanite that could also be associated with S2 (Fig. 33c). The S3 foliation is defined by alternating quartz-rich and mica-rich layers that are commonly wrapped around plagioclase porphyroblasts showing inclusion trails perpendicular, oblique or parallel to S3. In places where F3 microfolds are preserved, biotite is preferentially growing

parallel to the S3 axial plane cleavage. Similarly, sillimanite is chiefly developed parallel to the S3 cleavage or the continuous S3 foliation (Fig. 33c). Chlorite is additionally observed parallel to the S3 fabric and locally replaces biotite.

Relicts of the S2 metamorphic foliation are hardly observed in the *southeast part* of the central domain. The associated mineral parageneses are therefore mostly deduced from oriented inclusions in porphyroblasts. Garnet porphyroblasts commonly host numerous inclusions of ilmenite and quartz oriented perpendicular to the surrounding S3 foliation. Chloritoid and white mica are additionally found in the core of such porphyroblasts (Fig. 33d). In places where the S2 foliation is affected by isoclinal microfolds, small (~250 µm) staurolite crystals are arranged parallel to this earlier layering. Abundant staurolite is also found in contact with garnet. These observations suggest that the S2 foliation is associated with staurolite-grade metamorphism. Following data reported by Jastrzębski (2008), this part of the central domain may have also reached the kyanite grade during D2 deformation (Fig. 34). The dominant S3 foliation corresponds to a continuous layering of quartz and mica which is slightly deflected around the pre-existing garnet porphyroblasts. The porphyroblasts show a core with inclusion trails perpendicular to S3 overgrown by a smaller rim where ilmenite inclusions are parallel to S3 (Fig. 33e). A similar feature is also observed in plagioclase porphyroblasts where inclusion trails are curved towards the rims. Conversely, staurolite is no longer stable in the S3 fabric as indicated by its incipient replacement by prismatic sillimanite (Fig. 33f). Locally, the fine-grained texture of quartz and plagioclase together with the presence of small euhedral garnet in the matrix could indicate limited partial melting. The retrograde chlorite observed in the matrix and around garnet is probably linked with a post-D3 event.

Qualitative P–T–D evolutions

Qualitative *P–T–D* evolutions can be inferred from crystallisation-deformation relationships described for the different parts of the central domain. They reliably highlight the *P–T* variations between the successive macroscopic fabrics. In the *northwest part* of the central domain, chloritoid parallel to the S2 layering and garnet inclusion trails perpendicular to the S3 cleavage point to a crossing of both the chloritoid and garnet isograds during D2 deformation. It is most likely the result of increasing temperature and pressure, but widespread chlorite indicates that the temperature probably did not exceed ~500 °C (Fig. 35). A subsequent increase in pressure and temperature is also needed to account for garnet growth along the S3 fabric (Fig. 35). In some samples, the later growth of retrograde chlorite after garnet and biotite is related to decreasing *P–T* conditions, either during D3 deformation or distinctly after.

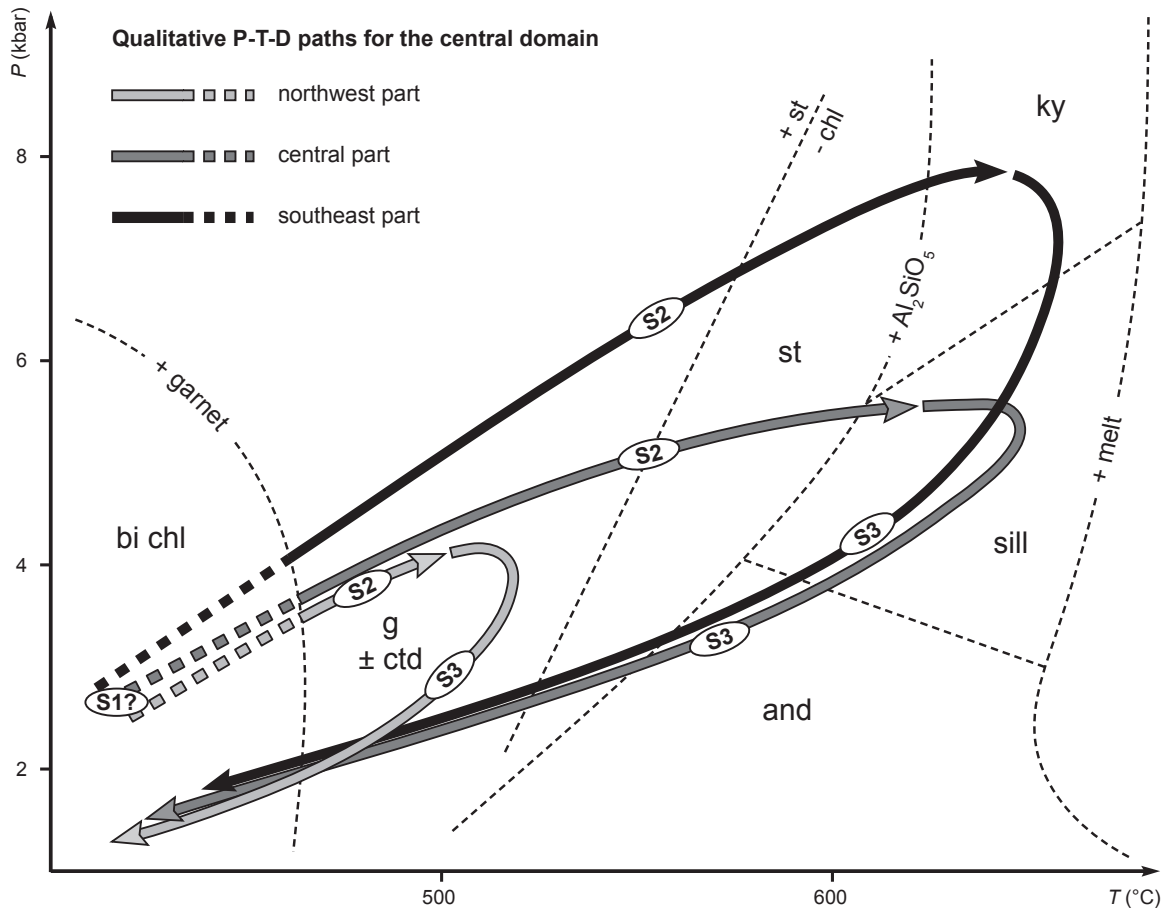


Figure 35. Qualitative P - T - D evolutions for the different parts of the central domain. Curves and stability fields are drawn after a compilation of the pseudosections for metapelitic samples presented in this chapter. The P - T scale is only indicative.

In the *central part* of the metasedimentary belt, microscopic observations show that the assemblage bi-pl-g-st-mu-qtz is associated with the S2 foliation. This is indicative of a P - T increase towards the staurolite stability field at temperatures possibly higher than ~ 500 °C (Fig. 35). Minor sillimanite parallel to the preserved S2 fabric could even indicate that the end of this P - T path reached the sillimanite isograd with an upper pressure limit of ~ 6 kbar. By contrast, widespread sillimanite along S3 clearly points to a subsequent temperature increase during D3 deformation (Fig. 35). Because retrograde chlorite is developed parallel to S3, it is proposed that the D3 deformation was also associated with decreasing P - T conditions towards the chlorite stability field.

In the *southeast part* of the central domain, chloritoid inclusions in garnet as well as the orientation of garnet and staurolite porphyroblasts perpendicular to S3 indicate an evolution from a g-ctd to a g-st assemblage in the S2 foliation. According to Jastrzębski (2008), kyanite growth is also ascribed to the S2 fabric. This points to a significant P - T increase towards the kyanite stability field at pressures and temperatures most likely above ~ 6 kbar and ~ 600 °C

(Fig. 35). Sillimanite growth after staurolite is indicative of a subsequent pressure decrease to 4–6 kbar at temperatures still above 550–600 °C during the development of the S3 foliation (Fig. 35). The occurrence of retrograde chlorite in the matrix is probably related to a post-D3 growth at lower P – T conditions.

6) Tectono-metamorphic evolution of the Młynowiec formation (central domain)

Located in the easternmost part of the central domain, the Młynowiec formation shows a structural record markedly different from the one observed in the neighbouring lithologies. Indeed, field observations indicate that the primary bedding, although metamorphosed, is preserved across this area. The characterisation of mineral assemblages present in the Młynowiec formation can therefore give insights on the early metamorphic evolution of the metasedimentary middle crust.

Petrography

The Młynowiec formation is chiefly composed of biotite–plagioclase paragneiss which displays a clear alternation of plagioclase-rich and mica-rich layers on the macroscopic scale. Although this distinction is still visible under the microscope, the texture observed in thin section is more granoblastic and shows quartz–plagioclase aggregates surrounded by thin discontinuous micaceous bands (Fig. 36a). The mica-rich bands locally contain abundant biotite and are parallel to the orientation of the S1 cleavage. In all samples, rounded plagioclase porphyroblasts have a poikilitic texture and host numerous inclusions of muscovite, biotite, quartz or rare relicts of garnet and kyanite (Fig. 36b, d). The mica inclusions are commonly oriented oblique or perpendicular to the S1 fabric (Fig. 36a). Similarly, elongated staurolite porphyroblasts with quartz and ilmenite inclusions perpendicular to S1 are found (Fig. 36c). Kyanite is also observed in the matrix where it is parallel to S1. However, the presence of kyanite inclusions in staurolite and plagioclase oriented perpendicular to S1 suggests that kyanite was most likely developed before the formation of the S1 fabric (Fig. 36d, e). This is corroborated by the occurrence of sillimanite stripes and andalusite porphyroblasts parallel to the incipient S1 cleavage (Fig. 36c, f). In general, garnet is rare and only relicts can be observed within the plagioclase-rich matrix. By contrast, tourmaline is frequent in biotite-rich layers.

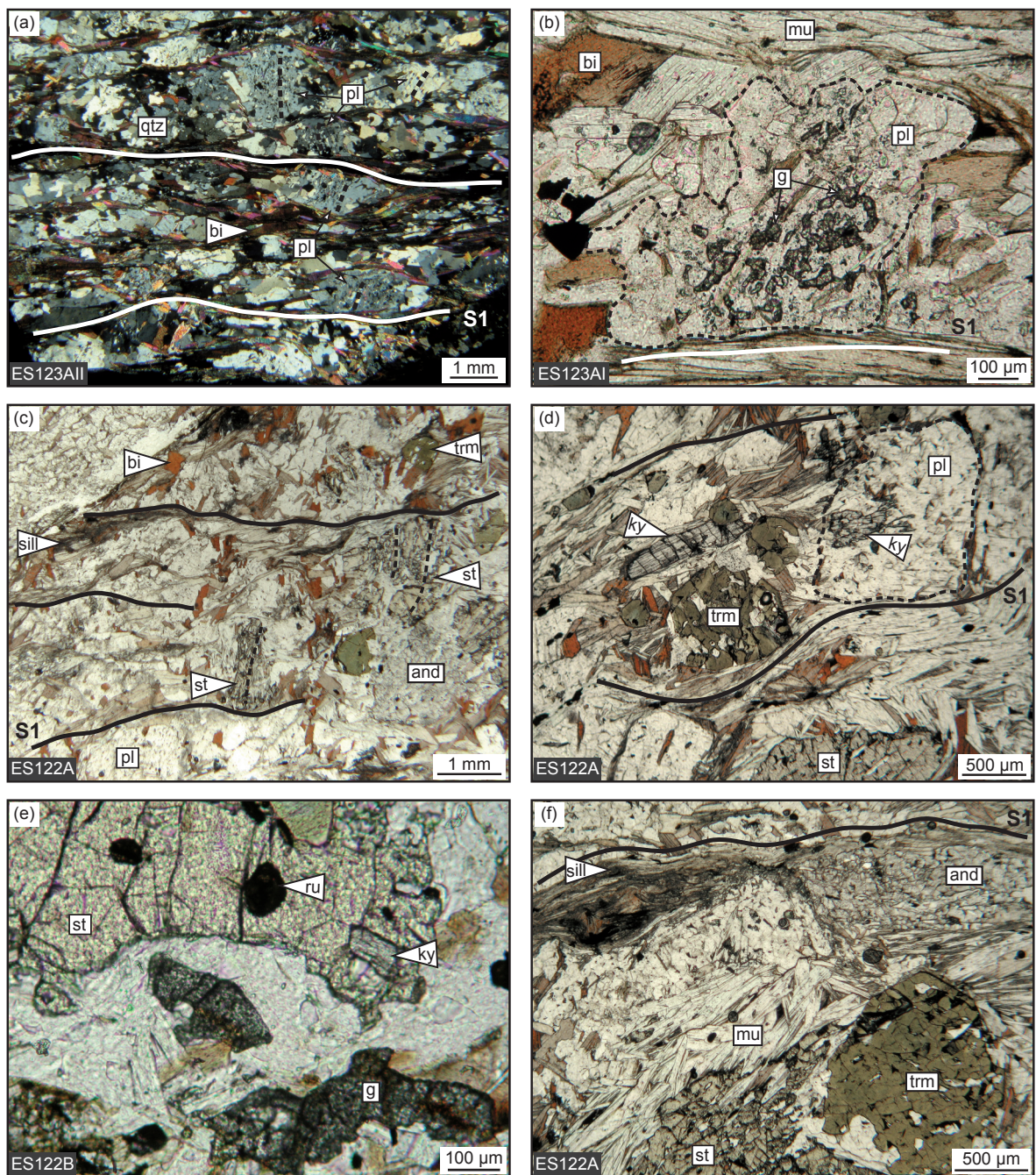


Figure 36. Photomicrographs illustrating crystallisation-deformation relationships in paragneiss samples of the Młynowiec formation. (a) Plagioclase porphyroblasts with inclusions of quartz, ilmenite and mica oriented perpendicular to the surrounding S1 cleavage. (b) Biotite and garnet relicts included in plagioclase. (c) Staurolite porphyroblasts with quartz inclusion trails perpendicular to S1. Sillimanite is developed parallel to the S1 cleavage. (d) Kyanite in the matrix and included in plagioclase. (e) Kyanite and rutile inclusions in staurolite porphyroblast. (f) Fibrous sillimanite and andalusite porphyroblast parallel to the S1 cleavage. Plane-polarised light, except for (a).

Qualitative P–T–D evolution

In the Młynowiec formation, microstructural observations indicate that several Barrovian metamorphic minerals grew before the development of the S1 cleavage. Indeed, staurolite and plagioclase porphyroblasts oriented perpendicular to S1 host inclusions of muscovite, biotite, garnet or kyanite, suggesting that a metamorphic foliation developed parallel to the S0 sedimentary bedding. This metamorphic event is associated with a *P–T* increase which most likely reached conditions above ~6 kbar and ~600 °C and which is comparable to the S2 evolution observed in the southeast part of the central domain (Fig. 35). The subsequent growth of sillimanite has also been documented in the southeast central domain, but andalusite porphyroblasts parallel to the S1 cleavage in the Młynowiec formation indicate that the temperature was probably higher during decompression below ~4 kbar.

7) Summary of *P–T–D* relationships

The *P–T–D* relationships detailed in this chapter have also been used to produce a map of metamorphic isograds across the entire Stronie-Młynowiec metasedimentary formation (Fig. 37). This was complemented by an estimation of the degree of anatexis in the neighbouring orthogneiss bodies (Chopin, 2010). All these data are now combined in order to reveal the dominant metamorphic regime of each macroscopic fabric.

D1 parageneses

Because of the successive tectonic overprints, relicts of the D1 structures are scarce across the OSD (Figs 10 & 14). Consequently, the access to the metamorphic records associated with this deformation event is restricted to few samples from the northern and southern domains. In the SE part of the northern domain, prograde garnet growth up to 5 kbar/550 °C in the S1 fabric is documented, whereas in the NW part the microfolded garnet- and staurolite-rich S1 layering indicates that the metamorphic conditions reached the g–st stability field in the same foliation (Fig. 37a). In the southern domain, microstructural evidences point to the occurrence of a g–st assemblage in the S1 fabric (Fig. 29a, b) and indicate a prograde evolution up to ~6 kbar/580 °C during D1 deformation in metasediments near the eclogite belt.

D2 parageneses

Metamorphic minerals associated with the S2 foliation are better observed because this fabric is commonly well-preserved across the OSD. In the northern domain, a prolonged prograde metamorphism towards the kyanite field in the SE part (Fig. 17c) and towards the sillimanite stability field in the NW part (Fig. 24a) is observed. In the SE metasedimentary belt located

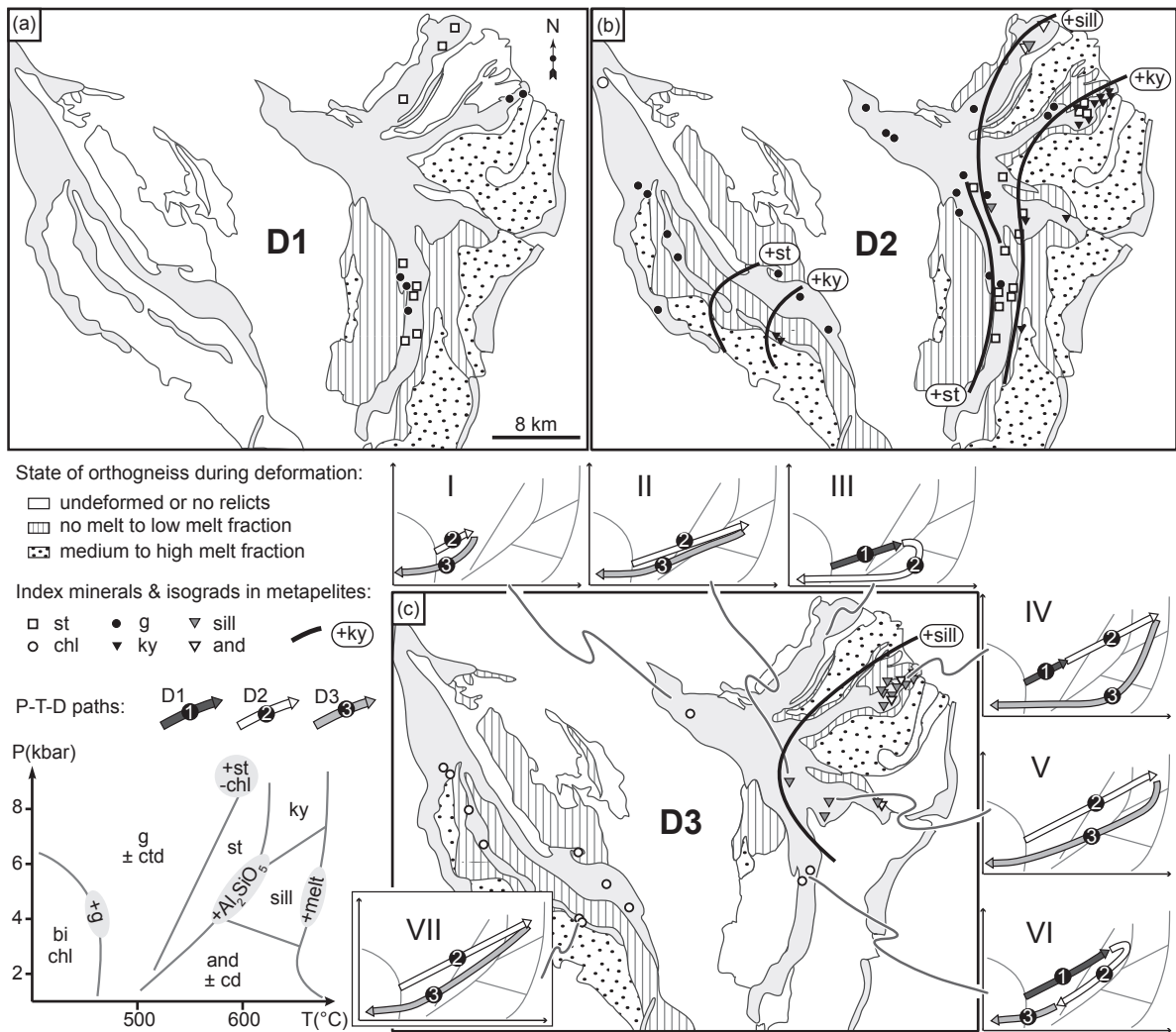


Figure 37. (a–c) Maps showing the occurrences of metamorphic minerals and the associated isograds in metasediments. The state of orthogneissic rocks during the D1, D2 and D3 deformation events is also reported (Chopin, 2010). Insets I to VII show qualitative P – T – D paths deduced from crystallisation–deformation relationships in metapelites. Mineral stability fields are schematically drawn using pseudosections presented in this chapter. Metamorphic isograds in the western Orlica domain are partly drawn after Opletal *et al.* (1980).

near the granulite, a g – st – ky paragenesis developed parallel to the S2 fabric is associated with peak conditions of ~ 7 kbar/630 °C and is related to the end of the D2 deformation (Fig. 22). Peak P – T conditions for the NW belt where staurolite decomposes into the assemblage g – $sill$ – bi lie below ~ 6 kbar at similar temperatures (Fig. 28). However, the syn-D2 growth of andalusite in the NW valley reflects a subsequent pressure decrease during the development of S2, i.e. during the intrusion of the Javorník granitoid.

In the central domain, metamorphic minerals parallel to the folded relicts of S2 indicate prograde metamorphism towards variable peak assemblages (Fig. 37b). From NW to SE, a g – ctd paragenesis is followed by a g – st ± $sill$ one (Fig. 33) and finally by a g – st – ky assemblage. The latter assemblage was observed by Jastrzębski (2008) who proposed peak conditions of

9–10 kbar/510 °C achieved in the vertical fabric. This view is supported by the occurrence of kyanite parallel to the vertical foliation in a paragneiss of the Młynowiec formation to the E (Fig. 37b).

In the southern domain, a second generation of both garnet and staurolite (Fig. 29c, d) parallel to S2 indicates prograde metamorphism up to ~ 7.5 kbar/630 °C in the subvertical fabric. However, chlorite blastesis parallel to the S2 foliation suggests that retrograde metamorphism down to 5 kbar (Fig. 37b) also occurred during this deformation event.

Although it has not been detailed in this chapter, the tectono-metamorphic evolution of metasedimentary rocks located in the Orlica region was also investigated (Fig. 3). There, garnet with chloritoid inclusions is in equilibrium with staurolite and elongated kyanite in the matrix. Both garnet inclusion trails and mineral elongation are parallel to the S2 fabric and therefore point to a prograde evolution from the g–ctd to the g–st–ky stability field during D2 in this area (Fig. 37b).

D3 parageneses

The heterogeneous D3 overprint produced wide areas where the growth of metamorphic minerals can be linked with the S3 foliation. In the SE part of the northern domain, garnet is resorbed and kyanite is successively replaced by sillimanite and andalusite oriented parallel to the S3 foliation (Fig. 18a). This retrograde evolution is constrained at 2–3 kbar/560–620 °C.

In the NW and central parts of the central domain, metamorphism associated with the D3 deformation is deduced from chlorite growth after garnet (Fig. 37b), while in the southeast part sillimanite replacing staurolite is observed (Fig. 33f). The whole central domain therefore shows retrograde conditions during D3. In the SE part, Jastrzębski (2008) proposed that it corresponds to decreasing P – T conditions from 7–8 kbar/620 °C to ~ 4 kbar/500 °C in the shallow-dipping fabric.

In the southern domain, chlorite develops parallel to the axial plane of F3 microfolds and is not in equilibrium with garnet. The resulting P – T path during D3 is therefore a prolonged retrograde evolution (Fig. 37b) towards temperatures lower than 550 °C.

In the western Orlica domain, chlorite is abundant in garnet pressure shadows related to the D3 deformation and indicates that the metamorphic peak was followed by a decrease in both pressure and temperature during the formation of the S3 foliation (Fig. 37b).

CHAPTER IV

MICROSTRUCTURAL AND PETROLOGICAL CONSTRAINTS FROM GARNET PORPHYROBLASTS

1) Review of concepts and techniques

Porphyroblasts commonly host rows of oriented inclusions that have been extensively used to infer crystallisation-deformation relationships (e.g. Zwart, 1962) and decipher orogenic processes (e.g. Bell & Johnson, 1989). Microstructural studies of matrix foliation (S_c) and porphyroblast inclusion trails (S_i) have improved understanding of the deformational regimes during porphyroblast growth (Olesen, 1978; Vernon, 1978; Vernon *et al.*, 1993; Johnson & Vernon, 1995; Bell *et al.*, 1998). However, the accumulated data have continued the debate about rotation and non-rotation of porphyroblasts during growth (Bell *et al.*, 1992; Passchier *et al.*, 1992; Fay *et al.*, 2008; Bons *et al.*, 2009). Today, both rotational (Prior, 1987; Chan & Crespi, 1999; Ikeda *et al.*, 2002) and non-rotational (Fyson, 1980; Johnson, 1990; Aerden, 1995) behaviours have been documented in nature. The observed geometries of inclusion trails have been explained, for instance, by flexural flow folding (Visser & Mancktelow, 1992), coaxial deformation associated with passive folding (Ramsay, 1962; Stallard & Hickey, 2001; Timms, 2003), or deformation partitioning of bulk non-coaxial deformation into pure and simple shear components (Bell, 1981; Lister & Williams, 1983).

The different porphyroblast records have been investigated using a wide range of techniques. In order to retrieve orientation data from inclusion trails, serial thin sectioning (Bell *et al.*, 1995), serial polishing of samples (Jung *et al.*, 1999), statistical fitting of inclusion traces (Aerden, 2003) or more recently, computed X-ray tomography (Huddleston-Holmes & Ketcham, 2005; Robyr *et al.*, 2007) have been used. P - T conditions of porphyroblast growth have been assessed via thermobarometry (e.g. St Onge, 1987) or pseudosection modelling of chemical zoning (Kim & Bell, 2005), while absolute time constraints were generally based on electron microprobe U-Th-Pb dating of monazite inclusions (Bell & Welch, 2002).

2) Sampled structural domains

Ten mica schist samples containing abundant macroscopically visible garnet have been collected at four localities in the metasedimentary belt adjacent to the granulite belt (Fig. 5). In all samples, the S_3 foliation and $L_{2,3}$ intersection lineation were measured to allow precise reorientation in the laboratory. In order to quantify inclusion trail microstructures in sections

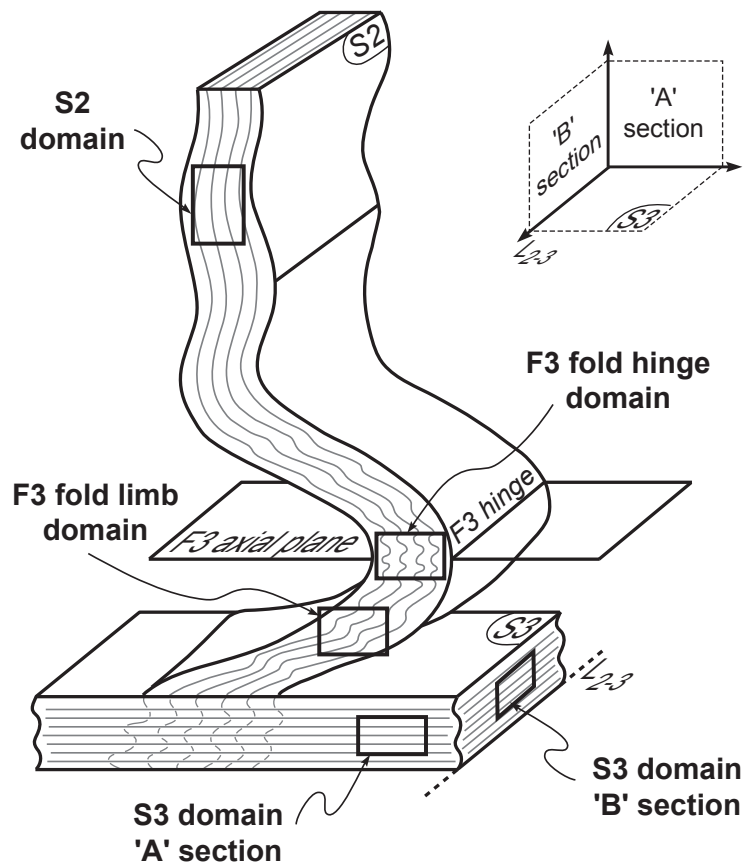


Figure 38. Idealised schematic view of the different structural domains related to the progressive transposition of the S2 into the S3 foliation. Arbitrary reference frame used for thin sections (upper right hand corner) is based on the D3 structures.

parallel and perpendicular to F3 fold axis (L_{2-3}), two types of thin sections have been cut (Fig. 38): sections perpendicular to both the S3 and the L_{2-3} ('A' sections), and sections perpendicular to the S3 and parallel to the L_{2-3} ('B' sections). In the different structural domains where S2 is progressively overprinted by a weak to intense S3 cleavage (Fig. 38), thin sections have been prepared parallel to the S3 foliation or the axial plane of F3 microfolds.

Four sampling domains were distinguished according to the intensity of the D3 overprinting and the position of samples with respect to the F3 folds (Figs 38 & 39). These domains are regarded as different stages of crenulation cleavage development as defined by Bell & Rubenach (1983).

Domain of preserved S2 foliation – stages 1 to 2 of crenulation cleavage development

Meter-scale domains preserve the steeply dipping S2 foliation, which was only gently folded during D3 deformation. The axial plane cleavage of F3 folds is discontinuous and produces an L_{2-3} intersection lineation, which is well visible on the S2 surfaces. In thin section, the dominant metamorphic layering corresponds to the subvertical S2 fabric and appears as a mm-

spaced alternation of quartz-rich and mica-rich domains (Fig. 39a). This layering is weakly crenulated, reorientation of micas is limited, and there is no evidence for a new metamorphic differentiation.

Domain of F3 fold hinge – stages 2 to 4 of crenulation cleavage development

Despite a strong D3 deformation in mica schist, it is possible to observe m-scale, close to isoclinal F3 folds (Fig. 7e). They exhibit narrow hinge zones with a smaller-scale crenulation of quartz-rich and mica-rich layers of the S2 foliation. Thin sections display varying degrees of crenulation cleavage development (Fig. 39b, c). In weakly deformed hinges, open to tight symmetrical F3 microfolds are defined by the continuous S2 layering, but the thickness of quartz-rich domains is highly variable (Fig. 39b). In places where the D3 deformation is

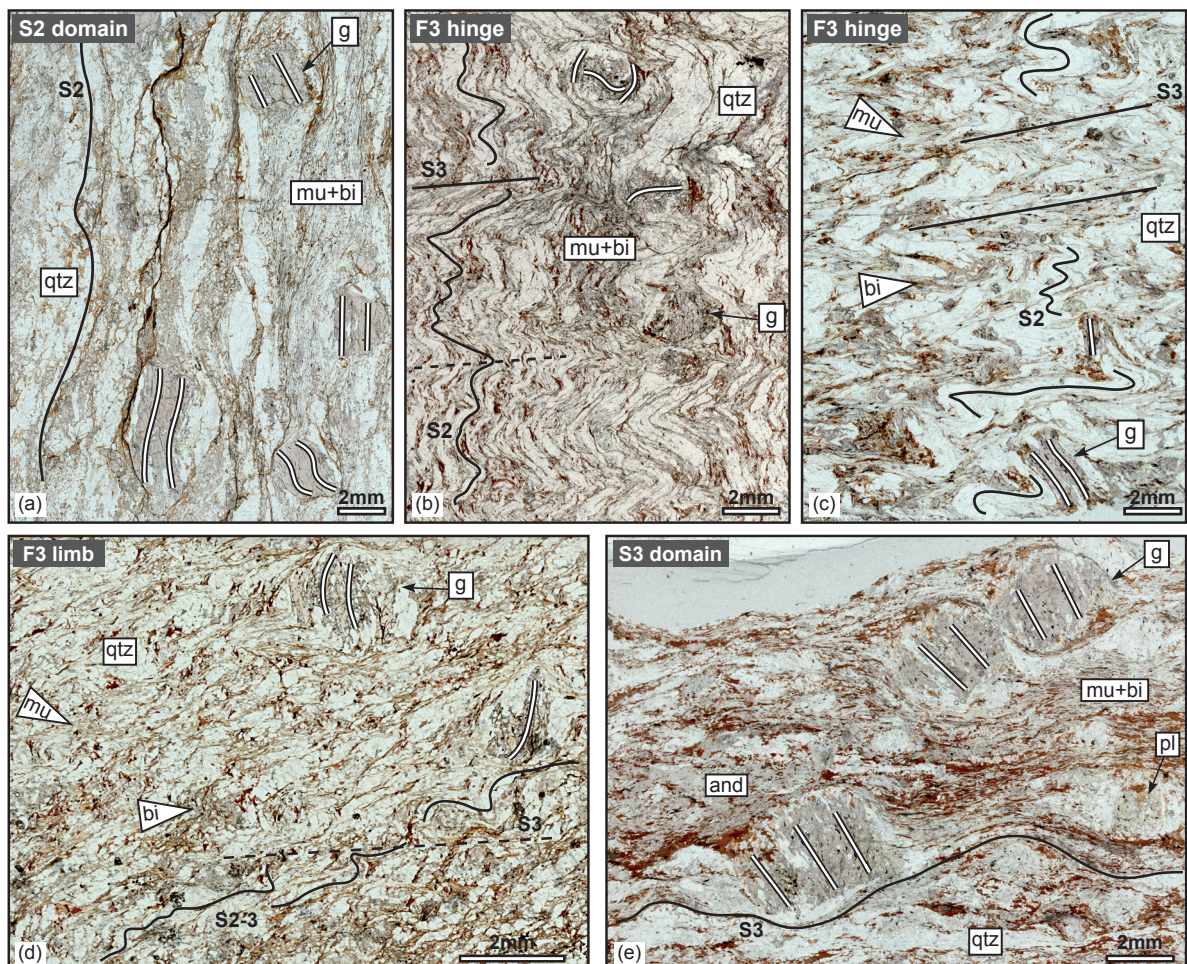


Figure 39. Photomicrographs illustrating the microstructural pattern of the matrix in the different structural domains. (a) Continuous S2 layering in the domain of preserved S2 foliation (sample M76B). (b, c) Variable microfolding of the S2 foliation and incipient S3 cleavage in the F3 fold hinge domain (samples ES2CII and ES20C). (d) ‘S’-shaped S2 layering in the F3 fold limb domain (sample ES2i). (e) Continuous S3 foliation wrapped around garnet and plagioclase porphyroblasts in the S3 domain (sample ES36L). Vertical ‘A’ sections, upper edge of photomicrographs is horizontal. Plane-polarised light. For mineral abbreviations, see Part 1-Chapter III.1.

more intense, micro-crenulations become tight to isoclinal and the S2 quartz-mica layering is completely disrupted. The resulting microstructural pattern shows rootless folds of thick quartz lithons separated by thin mica-rich S3 cleavage planes (Fig. 39c).

Domain of F3 fold limb – stage 4 of crenulation cleavage development

The limbs of F3 folds show asymmetrical folding of the originally subvertical S2 fabric. This produces ‘S’ or ‘Z’ shaped microfolds that are crosscut by mica-rich bands parallel to S3 (Fig. 39d). Micas are variably reoriented parallel to the S3 cleavage. They form an irregular network that wraps around rare garnet or plagioclase porphyroblasts, and quartz grains aggregated in isolated lenses.

Domain of continuous S3 foliation – stages 5 to 6 of crenulation cleavage development

The shallow-dipping S3 foliation corresponds to a new continuous metamorphic schistosity. It consists of thin quartz-rich layers alternating with thicker mica-rich layers (in both ‘A’ and ‘B’ sections). A variable amount of garnet and plagioclase is also present (Fig. 39e). The S3 alternation can be locally deflected around garnet and plagioclase porphyroblasts.

2) Garnet types

Across the sequence of structural domains defined above, four types of garnet porphyroblasts are distinguished according to their morphology and shape of the inclusion trails (Fig. 40). Although different cuts may reveal contrasted shapes, the representative features described for each garnet type rely on the observation of numerous orthogonal thin sections. In all garnet porphyroblasts, inclusion trails are dominated by rounded to elongated quartz grains and ilmenite needles. Preliminary assumptions about the significance of inclusion trails are based on garnet shapes and S_1 – S_c relationships.

Type I garnet

Type I garnet occurs only in the F3 fold hinge domain. It usually shows an irregular shape with lobate boundaries and small skeletal apophyses (Fig. 40a) that can even be absent. Rare euhedral crystals also occur. Porphyroblasts (2–4 mm) mostly include quartz and are partly mantled by large quartz grains. This garnet type is characterised by a staircase shape of the inclusion trails (Fig. 40a, b). A relatively large core (1–2 mm) with subhorizontal inclusion trails is surrounded by a narrow rim (0.1–0.2 mm) where the inclusion trails become progressively subvertical and continuous with the external crenulated S2 foliation. In thin section, Type I garnet porphyroblasts commonly show nearly parallel inclusion trails. The

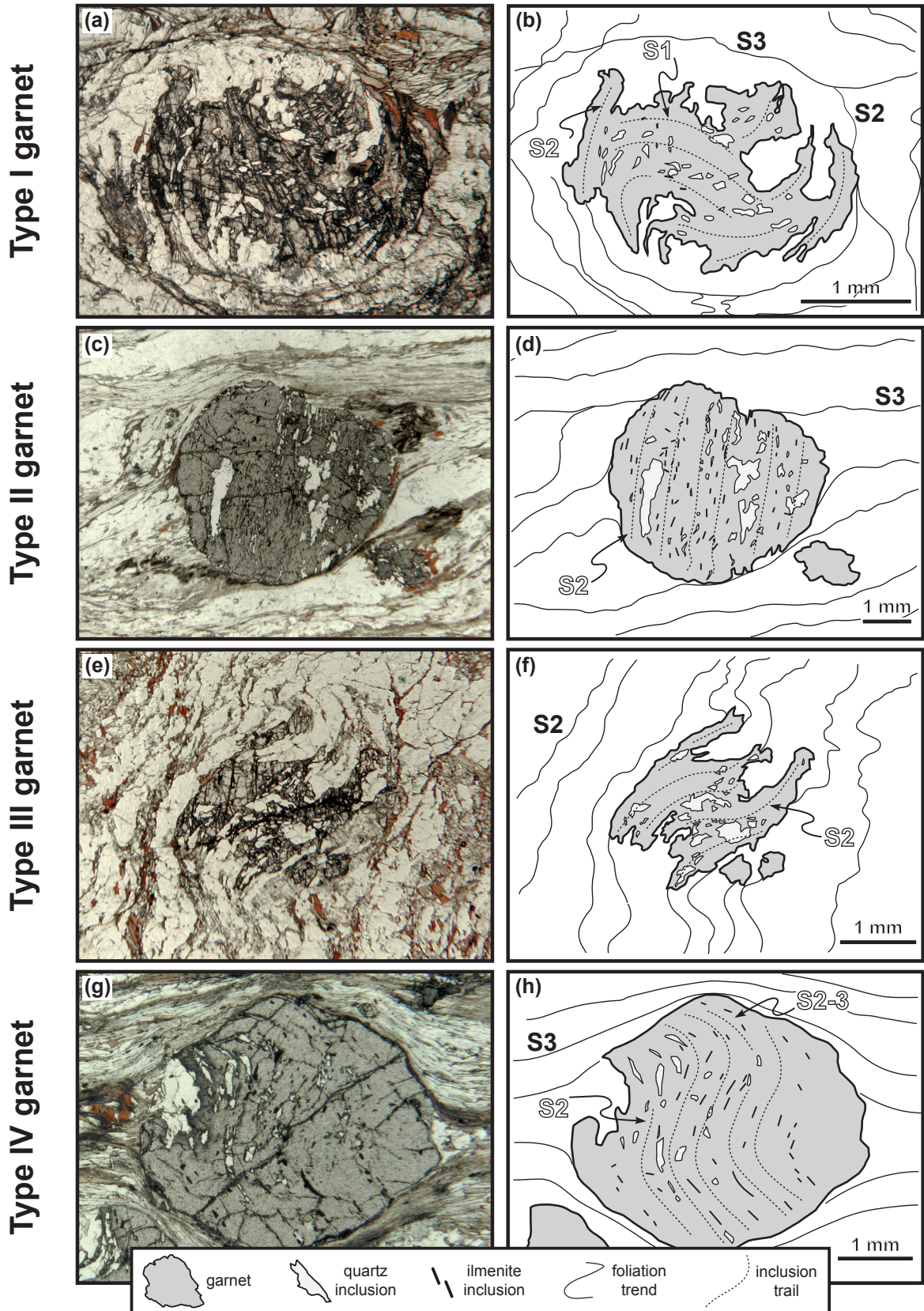


Figure 40. Photomicrographs and associated line drawings exemplifying the different garnet types. (a, b) Type I garnet with staircase inclusion trails (sample ES2CII). (c, d) Type II garnet with straight inclusion trails (sample M1B). (e, f) Type III garnet with smoothly folded inclusion trails (sample ES2CII). (g, h) Type IV garnet with curved inclusion trails (sample M1A). Vertical sections, upper edge of photomicrographs is horizontal. Plane-polarised light.

succession of inclusion trail patterns suggests that the garnet rims record the S2 foliation, while the core pattern could represent the S1 foliation (Fig. 40b).

Type II garnet

Type II garnet is found in the domains of preserved S2 foliation, in F3 fold limb domains, and in samples showing the continuous S3 foliation. Porphyroblasts (up to 5 mm) are subhedral, commonly rounded, and contain abundant ilmenite inclusions (Fig. 40c). The inclusions mostly define straight patterns that are either nearly continuous with the subvertical foliation in the S2 domain, or truncated and almost perpendicular to the external subhorizontal S3 foliation in domains overprinted by D3 (Fig. 40c, d). A striking feature of this garnet type is the nearly consistent orientation of inclusion trails in porphyroblasts present in the same thin section, especially in the S3 domain (Fig. 39e). S_i – S_e relationships suggest that the growth of Type II garnet could have occurred during or after the development of the S2 foliation (Fig. 40d).

Type III garnet

Type III garnet is only observed in F3 fold hinge domain. Porphyroblasts are commonly elongated (2–4 mm), exhibit a curved shape, and occur as single anhedral crystals or small skeletal grains partly enclosing larger quartz (Fig. 40e). The skeletal growth results in the formation of larger garnet crystals in mica-rich layers, and only small apophyses along quartz grain boundaries in quartz-rich layers (Fig. 40e, f). Inclusion trails, although diffuse, display a smoothly curved pattern that coincides with the garnet shape and the gently folded outer S2 foliation (Fig. 40f). The continuity between S_i and S_e suggests that Type III garnet possibly records the S2 fabric weakly folded by the D3 deformation.

Type IV garnet

Type IV garnet is observed in all structural domains except in F3 fold limbs. Porphyroblasts are rounded to slightly elongated (1–3 mm) and commonly exhibit rims with asymmetrical inclusion trails (Fig. 40g). Abundant ilmenite inclusions define sigmoidal trails that are subvertical in garnet core, but gradually curve into a subhorizontal position at the rims (Fig. 40g, h). In the S2 domain, the core inclusion trails are parallel to the external S2 fabric, whereas inclusions at the rim seem to be parallel to an ill-defined S3 cleavage. In the S3 domain, the rim trails are continuous with the matrix S3 foliation. These observations indicate that Type IV garnet could have entrapped both the S2 foliation and, to a lesser extent, the S3 foliation (Fig. 40h).

3) Measurement technique

When viewed in ‘A’ and ‘B’ sections, matrix and included ilmenite needles commonly define discontinuous trails (Figs 39 & 40). Nevertheless, scanning electron microscope (SEM) images of ilmenite trapped in porphyroblasts reveal that the apparent needles are sections of tabular crystals (Fig. 41). Therefore, it is inferred that the shape-preferred orientation (SPO) of matrix or included ilmenite platelets corresponds to a foliation plane. Accessing ilmenite lattice-preferred orientation (LPO) via electron backscatter diffraction (EBSD) analysis is likely to test the following assumptions. Does the LPO of matrix ilmenite trails correspond to the macroscopic foliation and, if so, could the LPO of included ilmenite trails be related to earlier structures?

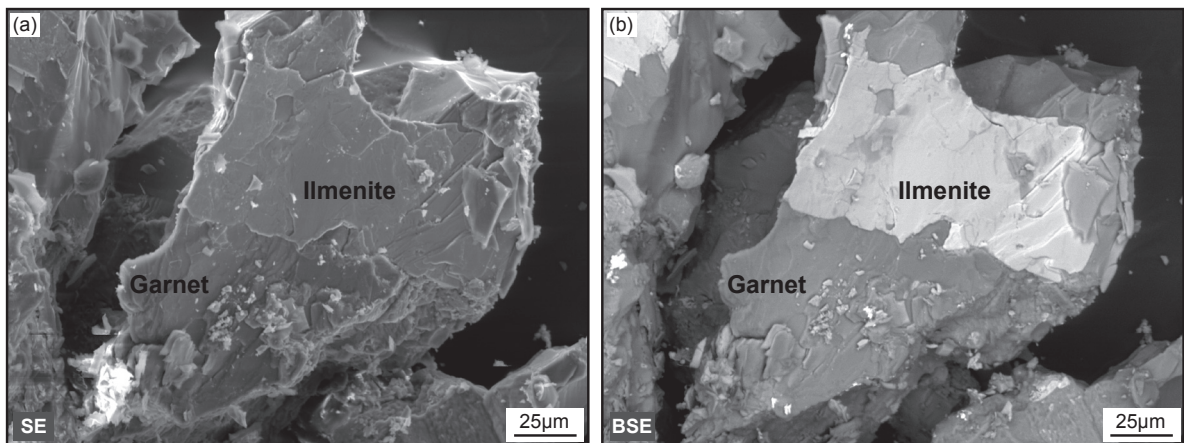


Figure 41. Scanning electron microscope (SEM) images illustrating the typical tabular shape of ilmenite inclusions in garnet porphyroblasts. (a) Secondary electron and (b) backscatter electron images showing a tabular ilmenite crystal stuck to the garnet surface (crushed garnet, sample ES45).

Data processing

The EBSD results were processed with PFch5 software (Mainprice, 2005) to provide a[100] and c[001] axis patterns of ilmenite (Fig. 42; for analytical details, see Appendix). However, because of hexagonal pseudosymmetry in ilmenite, [a] axis patterns show data repetition. It is therefore more convenient to focus on ilmenite [c] axis patterns; the ilmenite [c] axis is usually the direction parallel to the short dimension in tabular ilmenite (Moseley, 1981), i.e. the pole to ilmenite platelets. Eigenvalues (E1, E2, E3) and eigenvectors (λ_1 , λ_2 , λ_3) of the [c] axis distribution were determined (Scheidegger, 1965), and two end-members are recognised. In the first end-member, [c] axis data show a cluster-type distribution, implying that tabular ilmenite crystals define a plane which is perpendicular to the direction of the smallest eigenvector λ_3 (Fig. 42b). In the second end-member, [c] axis data show a girdle-type

distribution, implying that tabular ilmenite crystals define a zone axis, i.e. a linear structure which is parallel to the direction of the smallest eigenvector λ_3 (Fig. 42d). Provided that the [c] axis distribution is well-constrained, principal direction data can be transformed into geographic coordinates, and compared to the orientation of S3 and L_{2-3} .

Matrix ilmenite data

This procedure was applied to matrix ilmenite trails defining the S3 foliation (sample ES36L from S3 domain). Both [a] and [c] axis patterns are tightly constrained and define a plane which is subparallel to the orientation of S3 measured in the field (Fig. 42a). The slight misfit is attributable to a minor deflection of matrix S3 around garnet porphyroblasts. This result demonstrates that the LPO of matrix ilmenite crystals corresponds to the macroscopic foliation.

Included ilmenite data

Because the LPO data of matrix ilmenite reveal a planar structure, the same approach was used for ilmenite inclusions in porphyroblasts. Representative end-members of [c] axis distribution are now presented.

Garnet porphyroblasts with straight to smoothly curved inclusion trails (Type II or III) show a cluster-type distribution of [c] axis patterns in 'A' sections. Moreover, the [a] axis patterns show a continuous girdle distribution instead of three isolated clusters (Fig. 42b). This confirms that the tabular objects define a plane which can be rotated back to geographic coordinates.

Porphyroblasts which contain curved inclusion trails (Type I or IV) follow the same example, but preserve distinct trails that can be separated according to BSE images. In this case, the [c] axis pattern defines an incomplete girdle formed by two broad maxima that reflect the presence of two planar fabrics (Fig. 42c). Separating core and rim data allows the incomplete girdle to be split into two [c] axis clusters associated with two different [a] axis girdles (Fig. 42c). These records are then used to reconstruct two different internal foliations.

In 'B' sections, garnet porphyroblasts generally display relatively straight inclusion trails (Type II). However, instead of a single cluster, ilmenite [c] axis patterns exhibit a girdle-type distribution (Fig. 42d). This suggests that ilmenite crystals define a linear internal structure (L_i).

These observations demonstrate that the LPO of included ilmenite trails not only corresponds to planar structures, but could also define linear elements, depending on the analysed section. In addition, the quantification of internal foliations allows the definition of

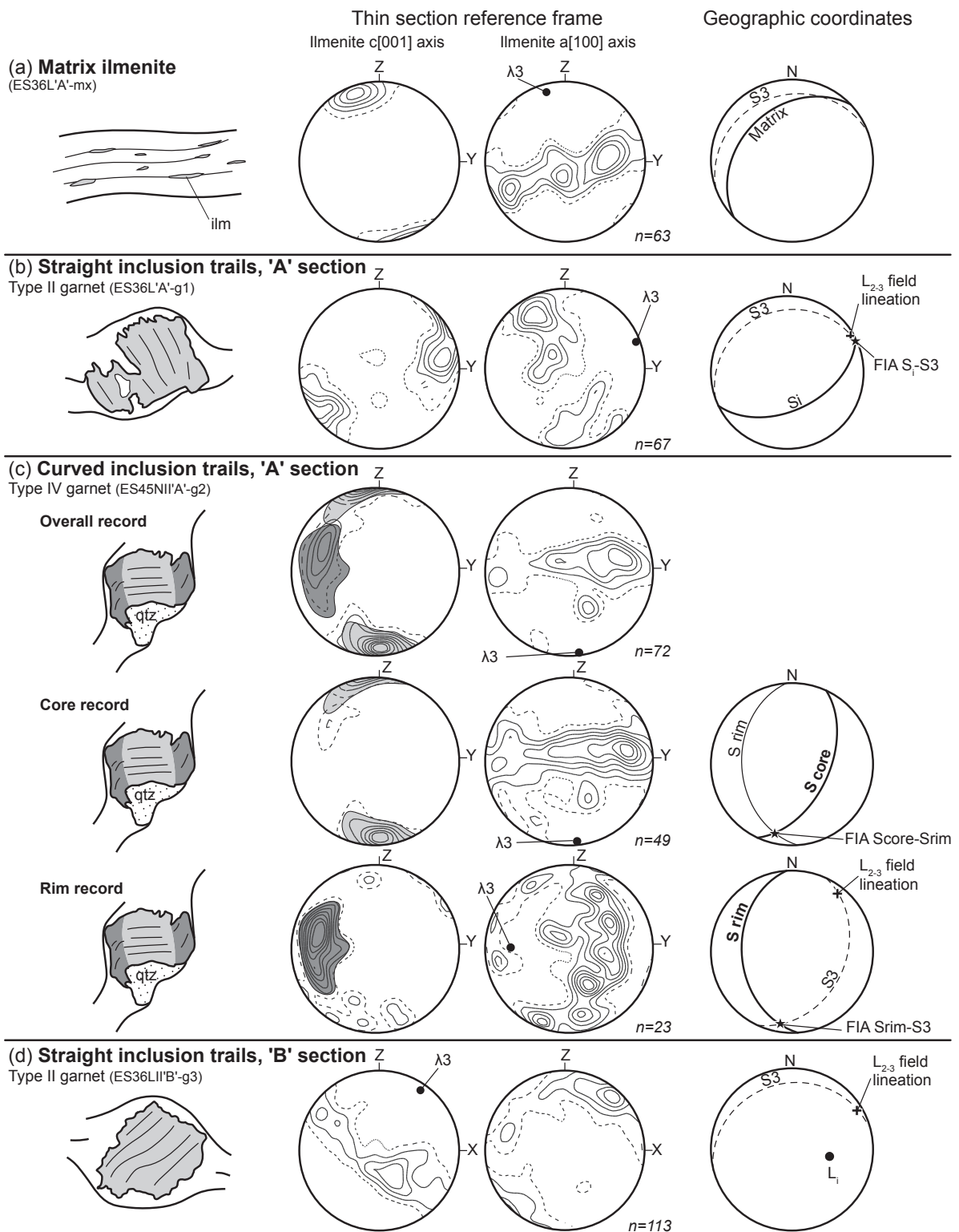


Figure 42. Data processing and representative microstructural results obtained using EBSD analysis of (a) matrix ilmenite and (b–d) included ilmenite. (a) Matrix ilmenite data defining the S₃ foliation. (b) Single foliation recorded in Type II garnet with straight inclusion trails, 'A' section. (c) Distinct foliations preserved in Type IV garnet with curved inclusion trails, 'A' section. (d) Lineation recorded in Type II garnet with straight inclusion trails, 'B' section. Stereonets are contoured at multiples of the uniform distribution.

two types of foliation intersection axis (FIA): FIA resulting from the intersection between two internal foliations (*sensu* Bell *et al.*, 1995), and FIA corresponding to the intersection between an internal foliation and the matrix foliation (Fig. 42c).

4) Microstructural analysis of porphyroblast inclusion trails

Internal foliations

It has been demonstrated that the LPO of ilmenite inclusions defines planar structures that represent foliations (Fig. 42). Thus, quantitative measurements can be correlated with the orientation of macroscopic field fabrics (Figs 43, 44, 45 & Tab. 7).

Type I garnet porphyroblasts document a polyphase history. Rare subhorizontal planes are preserved in the cores, and rims generally show NE–SW planes moderately to steeply ($54\text{--}88^\circ$) dipping to the NW (Fig. 43a). The core record could correspond to the poorly-preserved S1 foliation, whereas the rim record is mostly similar to the subvertical S2 fabric (Fig. 43a). This shows that garnet porphyroblasts from different hinge zones consistently preserved the succession of S1 and S2 fabrics (Fig. 45).

In all the structural domains where they are observed, Type II garnet porphyroblasts reveal NE–SW striking planes compatible with the S2 foliation (Figs 43a–c & 44a). Nevertheless, a progressive decrease of the dip angle with increasing intensity of the D3 deformation is observed. In the domain of preserved S2 foliation, NE–SW planes are subvertical, whereas they are moderately dipping ($56\text{--}69^\circ$) to the SE in the F3 limb domain and gently dipping ($40\text{--}49^\circ$) to the SE in the S3 domain (Fig. 45).

Smoothly-curved inclusion trails in Type III garnet porphyroblasts define steeply to moderately dipping NE–SW striking foliations (Fig. 43b). This suggests that, although Type III porphyroblasts were interpreted to have grown early during D3 deformation, they consistently preserve planar fabrics that are subparallel to the S2 foliation (Fig. 45).

In Type IV garnet porphyroblasts, core inclusions preserve nearly subvertical planes striking either N–S (S2 domain) or NE–SW (F3 hinge domain). These records are attributed to the S2 foliation. However, rim records show N–S planes moderately dipping to the E or W that are different from the matrix S3 foliation (Fig. 43a, b). These trails, previously considered as S3, could correspond to S2 that rotated halfway towards S3 at the onset of D3 deformation (Fig. 45). This rotated S2 foliation will be termed S2r.

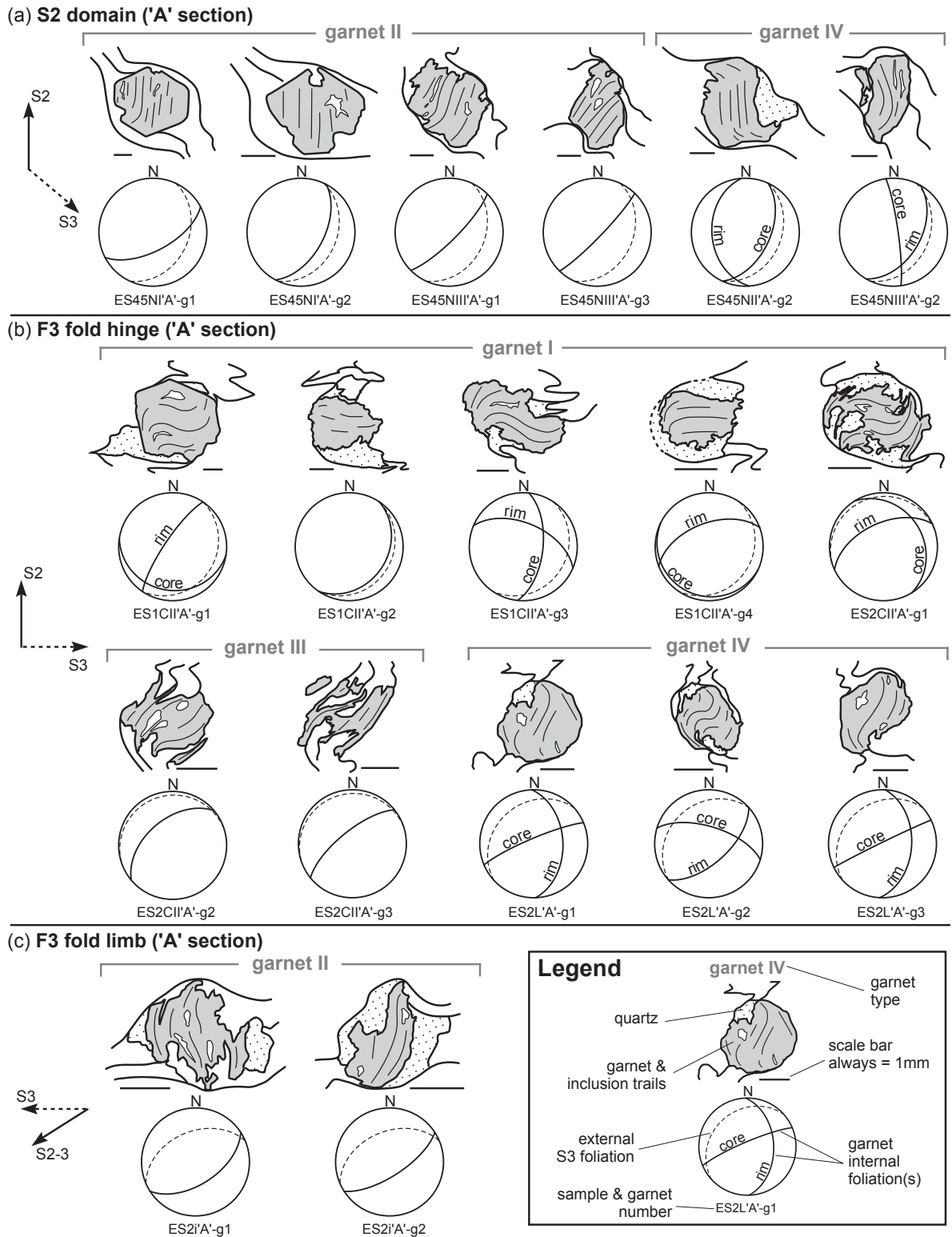


Figure 43. Schematic sketches of S_2 – S_3 relationships in garnet porphyroblasts and associated microstructural results. Porphyroblasts ('A' section) are from (a) S₂ domain, (b) F3 fold hinge domain, and (c) F3 fold limb domain. Orientation of the external foliation is indicated.

Internal lineation

The study of Type II garnet porphyroblasts suggests that the LPO ilmenite pattern depends on the analysed section. Indeed, while LPO data reveal the planar S2 foliation in 'A' sections, they define lines moderately plunging to the SE in 'B' sections (Fig. 44b). This lineation is coplanar with the orientation of S2 obtained in 'A' sections (Fig. 45, L2 lineation).

If it is assumed that the S2 foliation is predominantly entrapped in Type II garnet, it follows that: 'A' sections should display thin traces of S2, whereas 'B' sections, which are by definition subparallel to S2, should exhibit a higher proportion of tabular ilmenite sections. This is evidenced by the dependence of ilmenite aspect ratios on the [c] axis plunge (Fig. 46). In addition, if the internal foliation is considered to be weakly folded, as shown by

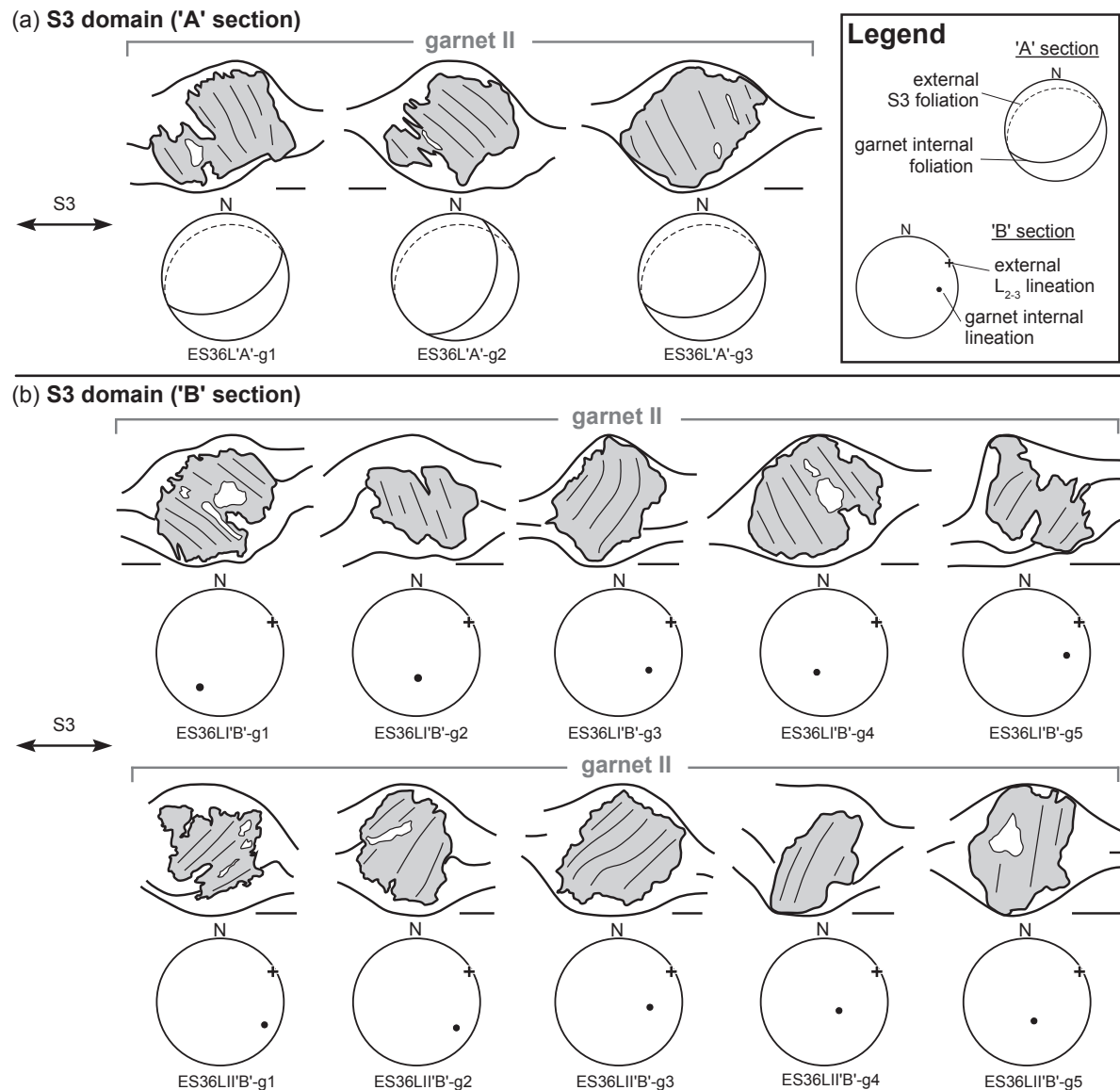


Figure 44. Schematic sketches of S_1 – S_3 relationships in garnet porphyroblasts from S3 domain and associated microstructural results. Porphyroblasts are from (a) 'A' section, and (b) 'B' section. Orientation of the external foliation is indicated. For further details on the legend, see Fig. 43.

studies using computed X-ray tomography (e.g. Huddlestone-Holmes & Ketcham, 2005), the ilmenite LPO in 'B' sections could well define a line corresponding to the axis of the microfolded foliation (Fig. 47a).

In this view, the internal lination recorded in Type II porphyroblasts is interpreted as the hinge of microfolds affecting the S2 fabric (Fig. 47a) and not as a proper FIA. The former interpretation is favoured because no evidence for an intersection between two distinct planes is observed. This lination will be termed L2.

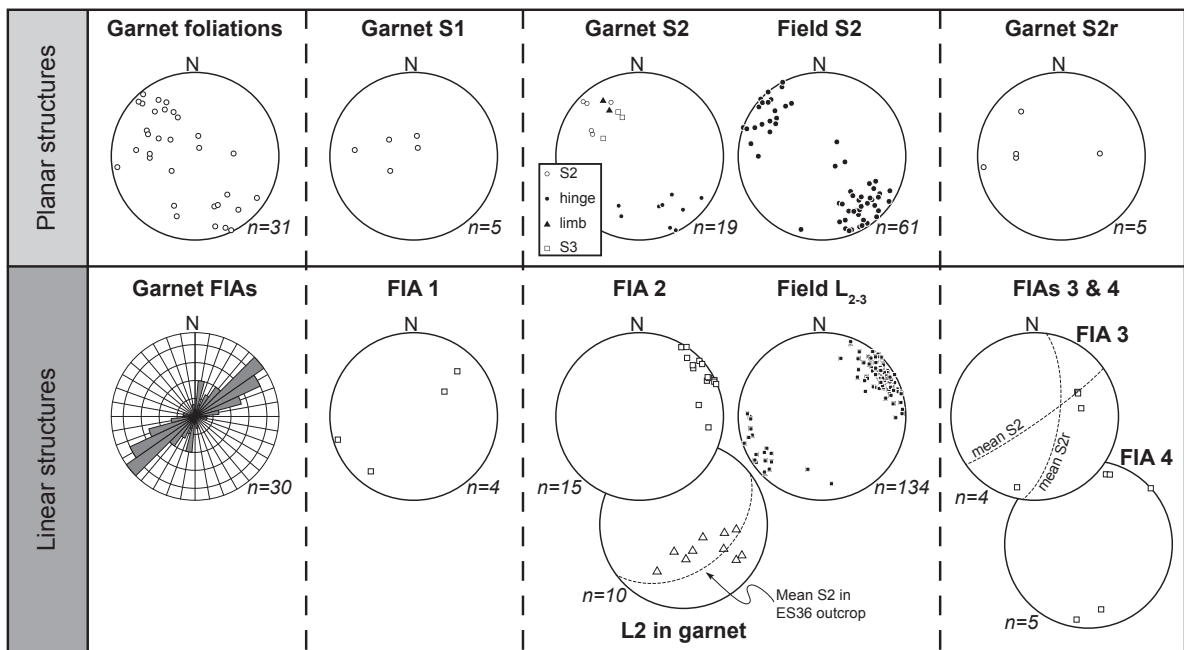


Figure 45. Summary of planar and linear structures measured in garnet porphyroblasts and comparison with field data.

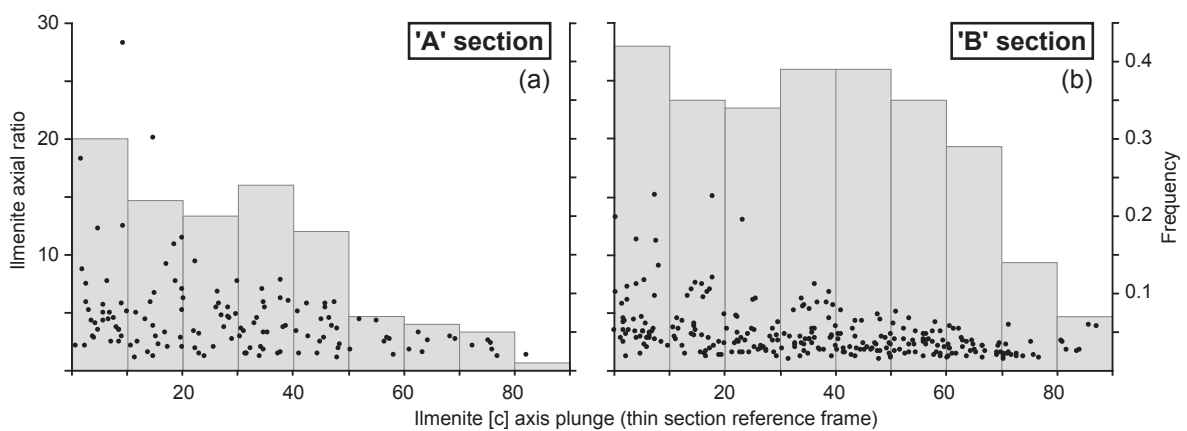


Figure 46. Plot of ilmenite axial ratio as a function of [c] axis plunge and histogram of [c] axis plunge values for inclusions viewed in 'A' and 'B' sections. [c] axis plunge is given in thin section coordinates, i.e. vertical [c] axis is normal to the thin section. (a) Results for five porphyroblasts viewed in 'A' section. Note that [c] axis plunge rarely exceeds 50°. (b) Results for five porphyroblasts viewed in 'B' section. Note the dependence of axial ratio on [c] axis plunge.

Foliation intersection axis

FIA commonly results from the intersection between superposed subvertical and subhorizontal foliations. Bell *et al.* (1995) underlined that the orientation of the FIA is controlled by the azimuth of the vertical foliation and does not depend on the direction of shearing in the subhorizontal foliation. In addition, Bell & Johnson (1989) have previously proposed that the FIA lies perpendicular to the direction of bulk compression during orogenesis. Therefore, the origin, relative timing and orientation of the FIA sets have been constrained in order to further test their use as tectonic indicators. Using the quantification of included foliations and the orientation of matrix S3, four different FIA sets were defined (Fig. 47b).

FIA 1 is rare and is only revealed by Type I porphyroblasts. It is defined by the intersection between the internal S1 and S2 foliations (Fig. 47b), and corresponds to a shallowly plunging NE–SW trending lineation (Fig. 45). Because FIA 1 results from the superposition of the subvertical S2 on the subhorizontal S1, it is interpreted as an indicator of a NW–SE directed D2 shortening event.

FIA 2 is reconstructed from garnet porphyroblasts which preserve S2 and which are truncated by the matrix S3 foliation. It is therefore defined by the intersection between S2 and S3 foliations (Fig. 47b). FIA 2 corresponds to a consistent set of subhorizontal, NE–SW trending lines (Fig. 45) that is similar to the macroscopic $L_{2,3}$ intersection lineation. This illustrates that, although internal S2 records may show variable dip, their NE–SW strike is consistently preserved in garnet porphyroblasts.

Nevertheless, a stage of S2 reorientation (S2r) is evidenced by rims of Type IV garnet porphyroblasts. This allows the definition of FIA 3 and FIA 4. FIA 3 corresponds to the intersection between the S2 and S2r internal records in Type IV porphyroblasts (Fig. 47b), and results in rare lines moderately plunging to the NE (Fig. 45). This FIA set can be considered as the axis of microfolds deforming S2 into S2r.

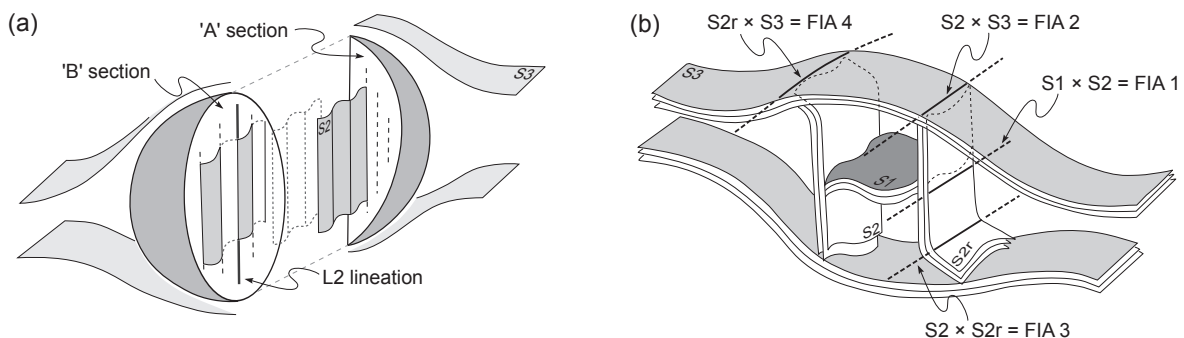


Figure 47. Idealised sketches illustrating garnet internal records. (a) L2 lineation in garnet. (b) FIA sets defined by the intersections of internal and/or external foliations.

Table 7. Orientation data of internal structures measured using single grain inclusion trail analysis.

Sample & garnet	Part	Garnet type	Analysed inclusions	Internal structure				FIA		
				Type	Measurement		Inter- pretation	Measurement		Inter- pretation
					Azimuth	Dip		Azimuth	Dip	
S2 DOMAIN										
ES45NI'A'-g1	-	II	35	planar	152	62	S2	79	29	FIA2
ES45NI'A'-g2	-	II	12	planar	118	55	S2	31	4	FIA2
ES45NII'A'-g2	rim	IV	23	planar	266	38	S2r	189	10	FIA4
ES45NII'A'-g2	core	IV	49	planar	115	52	S2	194	14	FIA3
ES45NIII'A'-g1	-	II	40	planar	135	78	S2	48	15	FIA2
ES45NIII'A'-g2	rim	IV	11	planar	120	48	S3	-	-	-
ES45NIII'A'-g2	core	IV	17	planar	82	83	S2r	169	22	FIA4
ES45NIII'A'-g3	-	II	18	planar	134	83	S2	46	13	FIA2
F3 HINGE										
ES01CI'A'-g1	rim	I	7	planar	304	78	S2	34	0	FIA2
ES01CI'A'-g1	core	I	10	planar	189	20	S1	218	18	FIA1
ES01CII'A'-g2	-	I	27	planar	124	29	S1	-	-	-
ES01CII'A'-g3	rim	I	11	planar	23	54	S2	99	18	FIA2
ES01CII'A'-g3	core	I	9	planar	96	60	S1	51	51	FIA1
ES01CII'A'-g4	rim	I	6	planar	339	54	S2	62	10	FIA2
ES01CII'A'-g4	core	I	12	planar	206	9	S1	253	6	FIA1
ES2CII'A'-g1	rim	I	8	planar	335	54	S2	64	1	FIA2
ES2CII'A'-g1	core	I	15	planar	58	27	S1	44	26	FIA1
ES2CII'A'-g2	-	III	9	planar	320	50	S2	47	3	FIA2
ES2CII'A'-g3	-	III	12	planar	321	71	S2	50	3	FIA2
ES2L'A'-g1	rim	IV	14	planar	88	45	S2r	14	15	FIA4
ES2L'A'-g1	core	IV	30	planar	337	82	S2	60	41	FIA3
ES2L'A'-g2	rim	IV	15	planar	138	61	S2r	48	0	FIA4
ES2L'A'-g2	core	IV	34	planar	17	64	S2	80	43	FIA3
ES2L'A'-g3	rim	IV	13	planar	93	45	S2r	17	14	FIA4
ES2L'A'-g3	core	IV	9	planar	334	88	S2	62	41	FIA3
F3 LIMB										
ES2i-g1	-	II	24	planar	147	56	S2	61	6	FIA2
ES2i-g2	-	II	20	planar	147	69	S2	60	7	FIA2
S3 DOMAIN 'A' section										
ES36L'A'-g1	-	II	67	planar	154	49	S2	65	2	FIA2
ES36L'A'-g2	-	II	40	planar	116	40	S2	39	11	FIA2
ES36L'A'-g3	-	II	65	planar	156	42	S2	67	1	FIA2
S3 DOMAIN 'B' section										
ES36LI'B'-g1	-	II	44	linear	210	37	L2	-	-	-
ES36LI'B'-g2	-	II	39	linear	176	57	L2	-	-	-
ES36LI'B'-g3	-	II	65	linear	120	44	L2	-	-	-
ES36LI'B'-g4	-	II	73	linear	200	63	L2	-	-	-
ES36LI'B'-g5	-	II	26	linear	94	37	L2	-	-	-
ES36LII'B'-g1	-	II	42	linear	117	23	L2	-	-	-
ES36LII'B'-g2	-	II	77	linear	123	26	L2	-	-	-
ES36LII'B'-g3	-	II	117	linear	100	49	L2	-	-	-
ES36LII'B'-g4	-	II	31	linear	121	68	L2	-	-	-
ES36LII'B'-g5	-	II	35	linear	160	64	L2	-	-	-

More importantly, FIA 4 is defined by the intersection between the internal S2r and the matrix S3 foliations in Type IV garnet porphyroblasts (Fig. 47b). This yields few subhorizontal NNE–SSW trending lines (Fig. 45). Because FIA 4 represents the overprinting of the N–S striking S2r foliation by the subhorizontal S3 fabric, it is interpreted as an indicator of E–W directed shortening at the onset of D3 deformation.

5) Garnet chemistry and modelling

Garnet chemistry

The analysed samples correspond to different stages of D3 deformation and were selected because they preserve a variable mineralogy and distinct garnet types.

Sample ES2C, F3 fold hinge domain, Type I and III garnet porphyroblasts

Sample ES2C was collected in the hinge of a F3 fold. This is a quartz-rich metapelite with thick quartz lithons separated by thin muscovite–biotite layers (Fig. 39b). The crenulated S2 layering contains garnet, plagioclase and a small amount of chlorite. Plagioclase porphyroblasts (2.5 mm) commonly host inclusions of white mica, biotite and ilmenite oriented parallel to the S2 layering, whereas chlorite is replacing garnet.

Type I and III porphyroblasts have inclusion trails defined by elongated quartz and ilmenite needles. Type I garnet exhibits a succession of subhorizontal and subvertical inclusion trails in the core and at the rim, respectively. It shows significant zoning in Mn and Mg whereas Fe and Ca remain relatively constant (Fig. 48a). Zoning of Type I garnet (Fig. 48b, Tab. 8) shows a core which varies from $\text{alm}_{0.66} \text{prp}_{0.06} \text{grs}_{0.16} \text{sps}_{0.12}$ ($X_{\text{Fe}}=0.92$) to $\text{alm}_{0.70} \text{prp}_{0.08} \text{grs}_{0.14} \text{sps}_{0.08}$ ($X_{\text{Fe}}=0.90$), followed by a decrease in X_{Fe} and spessartine towards the rim ($\text{alm}_{0.72} \text{prp}_{0.10} \text{grs}_{0.14} \text{sps}_{0.04}$; $X_{\text{Fe}}=0.88$). Type III garnet shows smoothly curved inclusion trails continuously passing to the crenulated S2 foliation. Compositional mapping (Fig. 48a) reveals a weak zoning with respect to Mn and Mg, and core ($\text{alm}_{0.73} \text{prp}_{0.07} \text{grs}_{0.13} \text{sps}_{0.07}$; $X_{\text{Fe}}=0.91$) and rim ($\text{alm}_{0.71} \text{prp}_{0.09} \text{grs}_{0.14} \text{sps}_{0.06}$; $X_{\text{Fe}}=0.88$) analyses differ only slightly (Fig. 48b, Tab. 8). The composition of Type III garnet is comparable to the rim of Type I garnet, but compositions similar to the core of the Type I garnet are never observed.

Sample ES36L, S3 domain, Type II garnet porphyroblasts

Sample ES36L was collected in a zone showing the continuous S3 foliation. It is a muscovite–biotite schist where thick micaceous bands wrap around quartz lenses, plagioclase and garnet porphyroblasts (Fig. 39e). Relicts of staurolite are observed in the matrix and Al_2SiO_5 polymorphs are common. Kyanite is found in the matrix as small (0.5 mm) randomly oriented

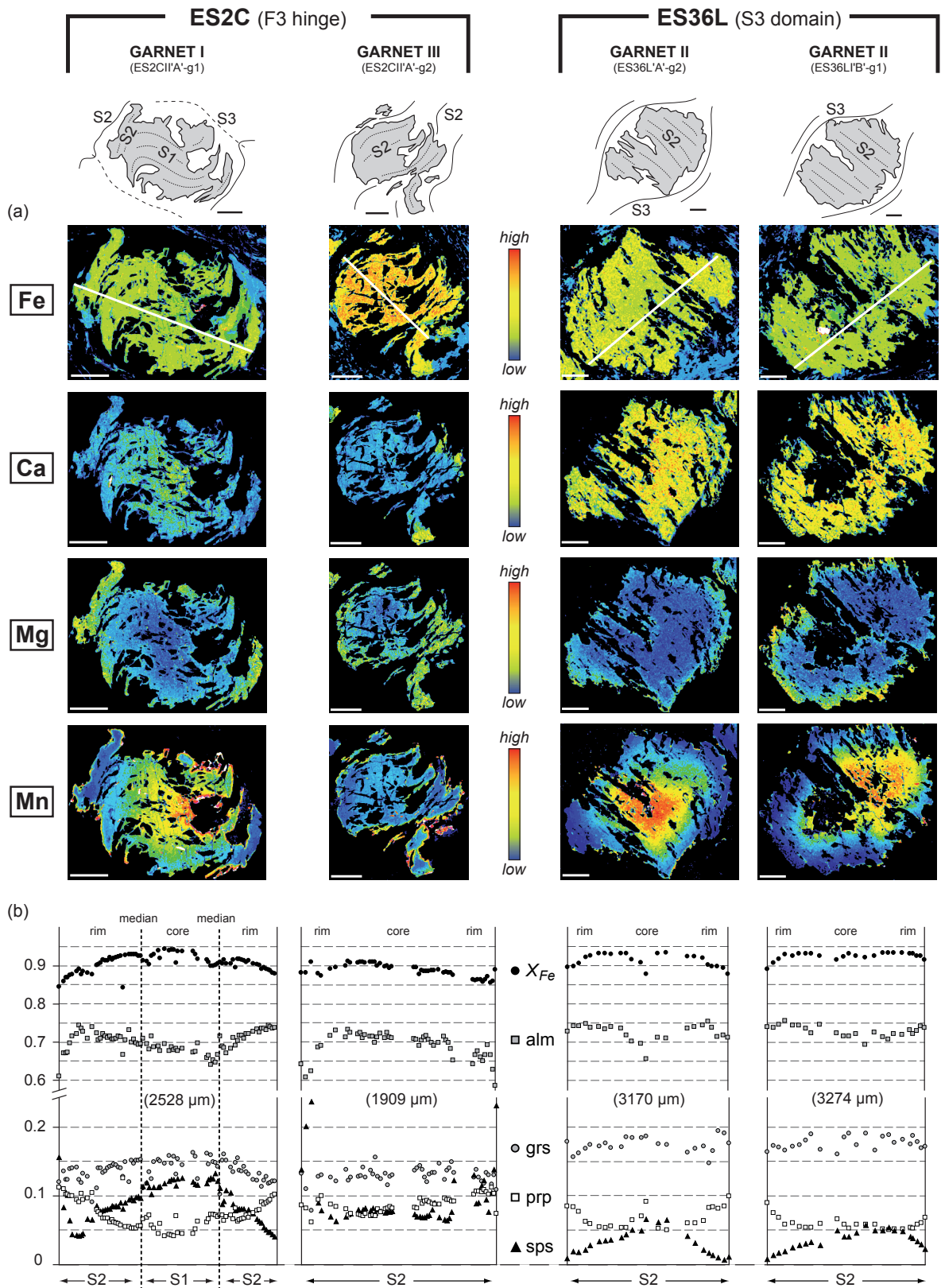


Figure 48. Qualitative and quantitative garnet chemistry for samples ES2C (F3 fold hinge domain) and ES36L (S3 domain). (a) Compositional X-ray maps of Fe, Ca, Mg and Mn distribution in Type I, II and III garnet porphyroblasts. (b) Chemical profiles across Type I, II and III garnet porphyroblasts. The location of the profiles is indicated on Fe X-ray maps. Scale bar is always 1 mm.

Table 8. Representative chemical analyses of garnet porphyroblasts.

Structural domain Garnet type & sample Position	F3 HINGE					S3 DOMAIN			
	Garnet I			Garnet III		Garnet II		Garnet II	
	ES2CII'A'-g1			ES2CII'A'-g2		ES36L'A'-g2		ES36LI'B'-g1	
	core	median	rim	core	rim	core	rim	core	rim
Wt. %									
SiO ₂	36.68	36.71	37.28	36.22	36.18	36.22	36.87	35.66	36.73
TiO ₂	0.17	0.13	0.12	0.13	0.15	0.16	0.19	0.15	0.11
Al ₂ O ₃	20.64	21.08	21.33	20.84	20.96	21.00	21.28	20.57	21.15
FeO	30.72	32.69	33.42	33.60	33.14	34.42	34.64	33.21	34.50
MnO	5.11	3.40	1.95	3.17	2.75	1.86	0.60	2.08	0.33
MgO	1.51	1.88	2.51	1.76	2.28	1.30	2.08	1.23	2.21
CaO	5.56	4.82	4.88	4.38	4.64	6.27	5.69	6.21	5.64
Na ₂ O	0.00	0.00	0.00	0.00	0.00	0.00	0.00	0.00	0.00
K ₂ O	0.00	0.00	0.00	0.00	0.00	0.00	0.00	0.00	0.00
Total	100.39	100.70	101.47	100.08	100.10	101.21	101.36	99.11	100.66
Cations									
Si	2.95	2.94	2.95	2.93	2.91	2.89	2.93	2.91	2.93
Ti	0.01	0.01	0.01	0.01	0.01	0.01	0.01	0.01	0.01
Al	1.96	1.99	1.99	1.99	1.99	1.98	1.99	1.98	1.99
Fe ³⁺	0.11	0.11	0.09	0.14	0.17	0.21	0.13	0.18	0.13
Fe ²⁺	1.95	2.08	2.12	2.13	2.06	2.09	2.17	2.08	2.17
Mn	0.35	0.23	0.13	0.22	0.19	0.13	0.04	0.14	0.02
Mg	0.18	0.22	0.30	0.21	0.27	0.15	0.25	0.15	0.26
Ca	0.48	0.41	0.41	0.38	0.40	0.54	0.48	0.54	0.48
Na	0.00	0.00	0.00	0.00	0.00	0.00	0.00	0.00	0.00
K	0.00	0.00	0.00	0.00	0.00	0.00	0.00	0.00	0.00
Total	8	8	8	8	8	8	8	8	8
X_{Fe}	0.92	0.90	0.88	0.91	0.88	0.93	0.90	0.93	0.89
alm	0.66	0.70	0.72	0.73	0.71	0.72	0.74	0.71	0.74
prp	0.06	0.08	0.10	0.07	0.09	0.05	0.08	0.05	0.09
grs	0.16	0.14	0.14	0.13	0.14	0.19	0.17	0.19	0.16
sps	0.12	0.08	0.04	0.07	0.06	0.04	0.01	0.05	0.01

Structural formulae calculated on the basis of 12 oxygens

prisms and fibrous sillimanite occurs rarely. The most abundant polymorph is represented by andalusite porphyroblasts which host numerous ilmenite inclusions and lie parallel to S3 (2–4 mm).

Type II garnet porphyroblasts preserve numerous ilmenite needles that define straight trails oriented nearly perpendicular (60–90°) to the external S3 foliation. They are strongly zoned (Fig. 48a) showing decreasing spessartine and increasing pyrope (Fig. 48b, Tab. 8) from core (alm_{0.72}prp_{0.05}grs_{0.18}sps_{0.05}; X_{Fe} =0.93) to rim (alm_{0.74}prp_{0.09}grs_{0.16}sps_{0.01}; X_{Fe} =0.89).

Garnet growth modelling

Pseudosections have been calculated for samples ES2C and ES36L in the MnNCKFMASHTO system (for whole-rock compositions and activity–composition relationships, see Part I-Chapter III.1 and Tabs 1 & 2).

Sample ES2C

The pseudosection for sample ES2C is bounded by the liquid-in line at 660–670 °C; the stability of garnet and ilmenite is highlighted by thick lines (Fig. 49a). Garnet is stable above 470–500 °C except for the low pressure region between 520 and 650 °C and ilmenite is stable in almost all the investigated P – T range except for the region in the upper pressure range.

Inclusions of muscovite, biotite and ilmenite in plagioclase and garnet porphyroblasts suggest an evolution starting in the bi–g–pl–chl field (Fig. 49a). The onset of garnet growth is estimated at 4–4.5 kbar and 490–510 °C where the modelled isopleths ($x(g)=0.92$; $z(g)=0.16$) are compatible with observed X_{Fe} and grossular values in the core of Type I garnet (Fig. 49b). The core zoning of Type I garnet represents an evolution towards 5–5.5 kbar and 530–550 °C where the measured values of $X_{Fe}=0.90$ and $grs=0.14$ lie close to $x(g)$ and $z(g)$ isopleths. The rim of Type I garnet ($X_{Fe}=0.88$ and $grs=0.14$) is comparable to $x(g)$ and $z(g)$ values at 6–6.5 kbar and 570–590 °C, and indicates the end of the P – T path in the bi–g–pl field (Fig. 49a, b), which is in agreement with the absence of chlorite in the matrix. The evolution from ~5 kbar and ~535 °C to ~6 kbar and ~575 °C is further supported by the composition of Type III garnet which is interpreted to grow contemporaneously with garnet I rims because X_{Fe} and grossular values are similar (Fig. 49b, Tab. 8).

Sample ES36L

The pseudosection for sample ES36L (Fig. 49c) is bounded by the liquid-in line at 660–670 °C; garnet and ilmenite stability (highlighted by thick lines) is reduced compared to the pseudosection for sample ES2C.

The presence of mica inclusions in garnet and plagioclase porphyroblasts together with matrix staurolite suggests a prograde evolution from the bi–g–pl–chl field to the bi–g–pl–st field (Fig. 49c). Crystallisation relationships among the Al_2SiO_5 polymorphs indicate earliest growth of kyanite, followed by sillimanite, and later growth of large andalusite. It points to the end of the prograde path in the bi–g–pl–ky–ilm–ru field (Fig. 49c). Core composition of Type II garnet ($X_{Fe}=0.93$ and $grs=0.18$ – 0.19) matches the modelled $x(g)$ and $z(g)$ isopleths at 5.5–6 kbar and 520–540 °C, close to the garnet-in line (Fig. 49c, d). Values of $X_{Fe}=0.89$ and $grs=0.16$ at the rim indicate increase in pressure and temperature to 6.5–7.5 kbar and 560–580 °C (Fig. 49d). Further progression towards the kyanite stability field to 6.5–7.5 kbar and

640–670 °C is nearly isobaric and occurs parallel to garnet modal isopleths (Fig. 49d). This is compatible with very limited garnet growth at the end of the prograde P – T path and with the general absence of kyanite inclusions in garnet.

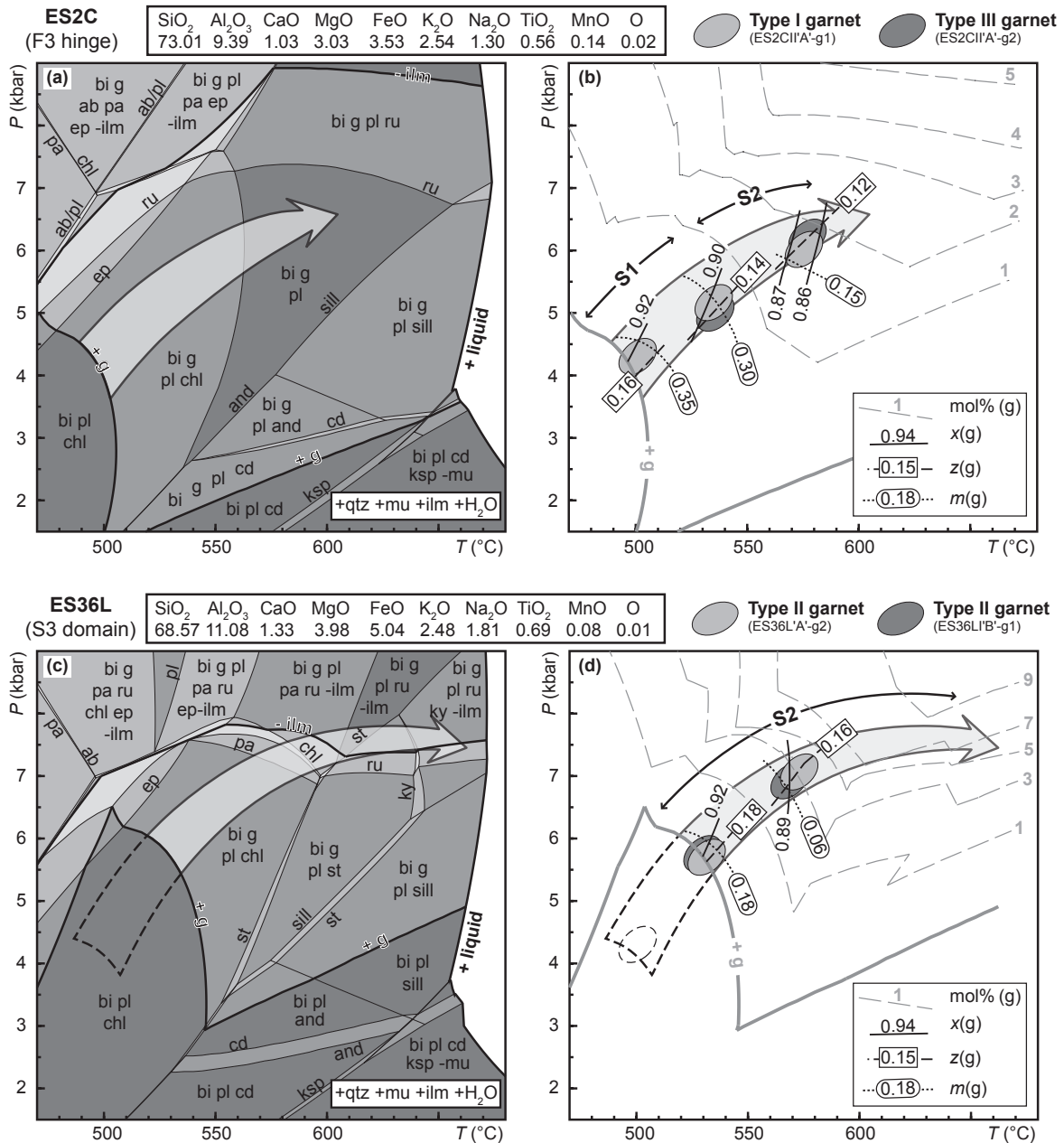


Figure 49. P – T pseudosections and modelled compositional isopleths of garnet for representative samples. (a, b) Metamorphic evolution of sample ES2C (F3 fold hinge domain) derived from Type I and III garnet porphyroblasts. (c, d) Metamorphic evolution of sample ES36L (S3 domain) derived from Type II garnet porphyroblasts. The $x(g)$ compositional isopleth is defined as $x(g)=Fe/(Fe+Mg)$.

6) Microstructural evolution: garnet rotation and non-rotation

Detailed inspection of quantitative microstructural results shows a variation of internal S2 records through the different structural domains (Fig. 45). The S2 foliation shows minor fluctuation in the hinges of F3 folds, whereas the dip of S2 notably decreases from F3 fold hinges to S3 domains (Figs 43 & 44). This could result from (1) garnet growth over an already folded S2 foliation, (2) reorientation of porphyroblasts due to vorticity in the matrix, or (3) non-coaxial deformation during D3.

The small variation observed in the hinge of F3 folds, where D3 is supposed to be mostly coaxial, could be explained by static overgrowth. It can equally be produced by matrix vorticity, because D3 produces a crenulation with a wavelength nearly similar to the grain size of garnet porphyroblasts. However, both hypotheses suppose non-systematic reorientation of garnet records. This contradicts the apparent decrease in S2 dip with increasing intensity of the D3 deformation (Fig. 45, garnet S2 records). Williams & Jiang (1999) demonstrated that porphyroblast rotation increasing with the fold limb dip can occur during pure shear folding associated with layer-parallel shearing. Because such shearing was not observed, it is believed that the microstructural S2 records indicate an episode of non-coaxial deformation involving limited, but systemic garnet rotation with respect to the position of samples in F3 folds. This could be achieved during a D3 buckling stage.

Nevertheless, in the case of dominant non-coaxial deformation, porphyroblasts from different structural domains may show a spread of inclusion trail data (e.g. Johnson *et al.*, 2006). This was not observed in garnet porphyroblasts analysed in this work. By contrast, the EBSD data show that garnet consistently records the succession of subhorizontal and subvertical fabrics (Fig. 45). Some EBSD results even show that crystals with contrasted shapes preserve the same internal records (see for example ES2L'A'-g1 and -g2 in Fig. 43a). This appears to be in contradiction with the theoretical motion of rigid particles in a simple shear dominated viscous flow that depends, among other factors, on the shape of the particles (e.g. Jeffery, 1922; Ježek *et al.*, 1996; Ceriani *et al.*, 2003).

All these microstructural arguments suggest that no significant rotation occurred during the polyphase tectonic history. Natural (e.g. Aerden, 2004) and numerical (e.g. Jiang, 2001) examples have been used to argue that limited rotation due to deformation partitioning (Bell, 1981; Lister & Williams, 1983) can occur in non-coaxial deformation. However, macroscopic shear indicators were not observed and porphyroblasts do not show systematic development of asymmetrical tails. A pure shear folding mechanism (Ramsay, 1962), which was already

invoked by Ilg & Karlstrom (2000) to explain the presence together of rotated and non-rotated porphyroblasts, is therefore favoured. In this view, the foliation passively rotates around static porphyroblasts and is subsequently overgrown (Fig. 50). Consequently, the preservation of primary orientations in garnet porphyroblasts is interpreted as a result of dominant coaxial deformation.

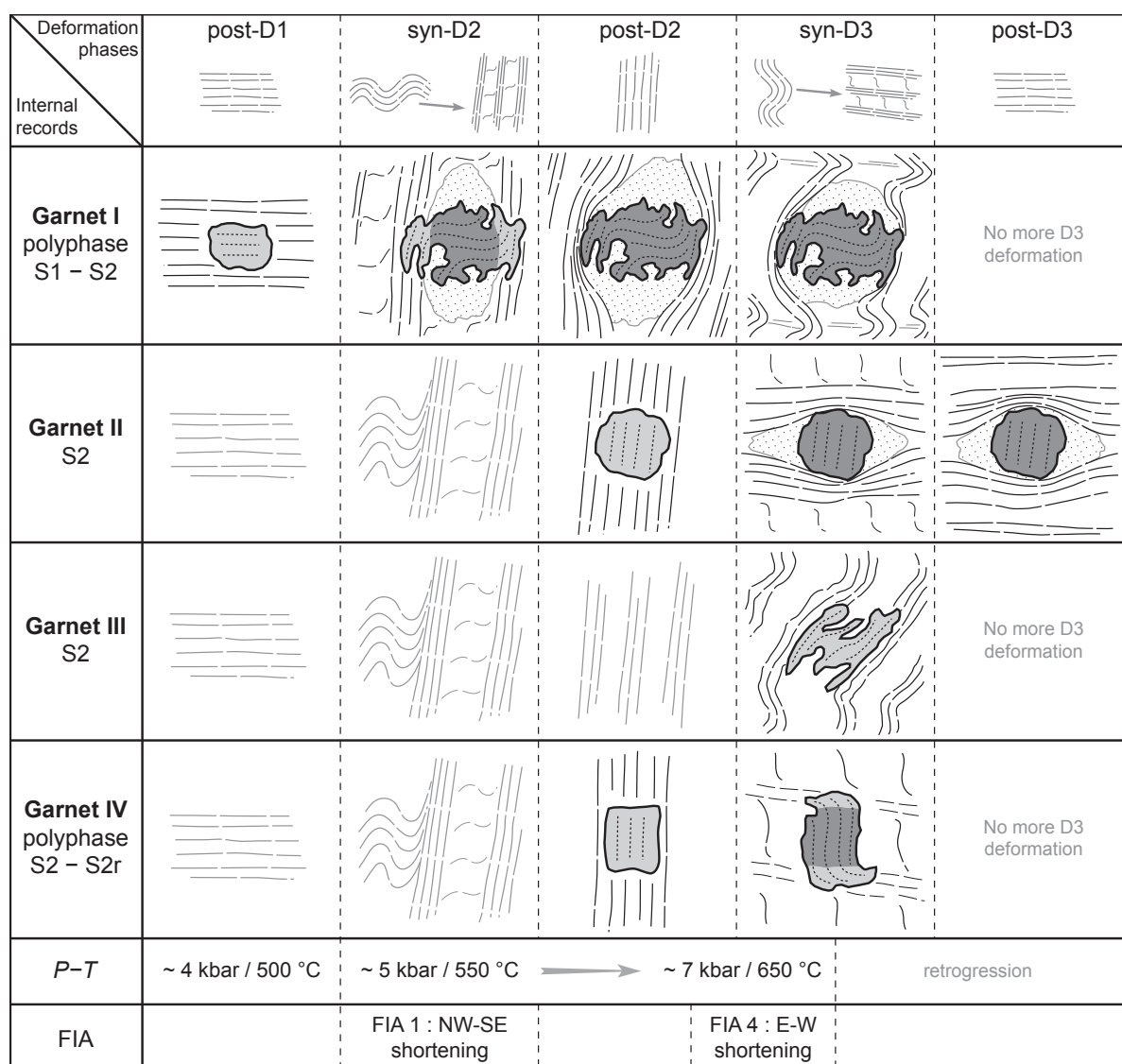


Figure 50. Summary of crystallisation-deformation relationships, metamorphic records and microstructural data associated with the different types of garnet porphyroblasts. Light grey=newer garnet, dark grey=older garnet.

7) Metamorphic evolution: polyphase garnet growth and resorption

The core of Type I garnet preserves the subhorizontal S1 foliation (Fig. 45) and is associated with a prograde evolution from 4–4.5 kbar and 490–510 °C to 5–6 kbar and 520–550 °C (Fig. 49a, b). This first garnet growth episode therefore documents prograde metamorphism during or after the development of the subhorizontal S1 foliation (Fig. 50).

Ilmenite inclusion trails at the rims of Type I garnet and in Type II and III porphyroblasts are interpreted as relicts of the S2 foliation (Fig. 45). The composition of Type I garnet rims and Type III garnet points to a second garnet growth episode from 5–6 kbar and 520–550 °C to 6.5–7.5 kbar and 560–590 °C (Fig. 49b). Despite a different pseudosection topology resulting from lower manganese content in the rock (Fig. 49), the sample containing Type II garnet indicates P – T conditions consistent with this second garnet growth episode (Fig. 49d). Staurolite and kyanite, which have been ascribed to the S2 fabric (Part 1-Chapter III.2), document the end of the P – T path at 6.5–7.5 kbar and 640–670 °C (Fig. 49c, d). All these observations point to a prograde evolution occurring during development of the subvertical S2 foliation (Fig. 50).

Limited garnet growth at the onset of D3 is documented by S2r records (Fig. 45). However, garnet is commonly replaced by sillimanite and biotite in the pressure shadows associated with the D3 deformation (Part 1-Chapter III.2). In addition, the crystallisation of andalusite parallel to the S3 foliation (Fig. 39e) indicates further pressure decrease during D3. This textural evidence indicates garnet resorption associated with retrograde P – T conditions during the development of the subhorizontal S3 foliation (Fig. 50).

CHAPTER V

CHRONOLOGICAL CONSTRAINTS

Crystallisation-deformation relationships show that metamorphism is heterogeneous across the orogenic middle crust. Indeed, the different parts of the metasedimentary Stronie-Młynowiec formation underwent contrasted metamorphic evolutions and peak P - T conditions (Part 1-Chapter III). In order to assess the timing of such diverse P - T - D paths, one needs to examine the age record of a mineral that could be sensitive to these metamorphic changes. Monazite [(Ce, La, Th)PO₄] is a ubiquitous accessory mineral in pelitic rocks (Overstreet, 1967) and its growth has been documented in diagenetic to anatectic conditions (e.g. Kingsbury *et al.*, 1993; Rubatto, 2001; Evans *et al.*, 2002; Cocherie *et al.*, 2005; Rasmussen *et al.*, 2007). Moreover, monazite represents a potential mineral for U-Th-Pb electron microprobe (EMP) dating because: (1) it incorporates significant amounts of U and Th that decay into Pb, (2) its initial Pb content is generally low (e.g. Parrish, 1990), and (3) diffusive Pb loss in monazite is estimated to be negligible (e.g. Montel *et al.*, 2000; Cherniak *et al.*, 2004; McFarlane *et al.*, 2006). Accordingly, metapelite samples have been collected near the granulite belt, the Javorník granitoid and the eclogite belt in order to investigate the geochronological record in the metasedimentary middle crust. The goal of the present chapter is to correlate monazite growth with the observed metamorphic reactions and thus to constrain the age of the different tectono-metamorphic events.

1) Analytical procedure and data processing

Electron microprobe analyses

The monazites were analysed at BRGM Orléans under a CAMECA SX 50 electron microprobe equipped with five wavelength-dispersive spectrometers. The analyses were directly performed on standard thin sections (30 μm thickness) using an accelerating voltage of 20 kV and a beam current of 200 nA. The results include a correction of the spectral interference of Y on PbM α and of ThM β 1 on UM α . Additional details on the analytical conditions are listed in Tab. 9.

Age calculation

The microprobe data were processed using the “EPMA dating” program (Pommier, 2002) and plotted using Isoplot/Ex(3.1) (Ludwig, 2004). Only the analyses with a sum between 97–103 wt.% and a Pb concentration above the detection limit of 150 ppm were selected (analyses are presented in Appendix). A single chemical age is obtained for each analysis using U,

Table 9. Analytical conditions and standards used for electron microprobe monazite analysis.

Element	X-ray line	Crystal	Standard	Counting time (s)	
				peak	background
Si	<i>Kα</i>	TAP	Andradite	20	20
P	<i>Kα</i>	TAP	Apatite	20	20
Ca	<i>Kα</i>	PET (1)	Apatite	20	20
Y	<i>Lα</i>	TAP	Synthetic phosphate (XPO ₄)	20	20
La	<i>Lα</i>	PET (1)	Synthetic phosphate (XPO ₄)	20	20
Ce	<i>Lα</i>	PET (1)	Synthetic phosphate (XPO ₄)	20	20
Pr	<i>Lβ</i>	LIF	Synthetic phosphate (XPO ₄)	20	20
Nd	<i>Lβ</i>	LIF	Synthetic phosphate (XPO ₄)	20	20
Sm	<i>Lα</i>	LIF	Synthetic phosphate (XPO ₄)	20	20
Gd	<i>Lβ</i>	LIF	Synthetic phosphate (XPO ₄)	20	20
Pb	<i>Mα</i>	PET(2)	Galena PbS	120	120
Th	<i>Mα</i>	PET(3)	Thorite ThO ₂	20	20
U	<i>Mα</i>	PET(3)	Uraninite UO ₂	100	100

Th and Pb concentrations and the equation described in Montel *et al.* (1996). A weighted average age can further be calculated with these pooled ages. Nevertheless, in this work the calculation of the U–Th–Pb age follows the method proposed by Suzuki & Adachi (1991). For each analysis, a concentration of Th* corresponding to the sum of Th and U is calculated and plotted against the Pb concentration. Assuming that all monazite grains contain a similar amount of initial Pb, the slope of the straight line which is defined by the data can be used to calculate an isochron age. This approach has been favoured in order to observe the possible presence of initial Pb (Pb₀) which should be indicated by the intercept of the isochron.

2) Monazite record near the granulite belt (northern domain)

Sample description and monazite petrography

Sample M81-2A is a muscovite–biotite schist containing garnet, plagioclase, staurolite, kyanite, sillimanite and accessory ilmenite, tourmaline and apatite. This sample exhibits the subhorizontal S3 foliation marked by thick (~1 mm) mica layers surrounding rootless folds of quartz aggregates. Garnet and plagioclase porphyroblasts are oriented oblique or perpendicular to S3, staurolite and kyanite relicts are found in the matrix or around garnet, and fibrous sillimanite develops preferentially around garnet.

Monazite is small (20–50 μm, rarely 100 μm) and commonly rounded or anhedral. It is abundant in the mica-rich matrix and only rarely observed in porphyroblasts (Fig. 51). In the matrix, monazite is found as isolated crystals in muscovite–biotite layers and may occur

next to apatite or resorbed staurolite (Fig. 51a). Matrix monazite is also in contact with fibrous sillimanite and shows a clear disequilibrium texture marked by irregular grain boundaries (Fig. 51b). In addition, monazite grains seldom occur at the outermost rim of plagioclase or garnet porphyroblasts (Fig. 51c, d). Although inclusions are mostly located close to small cracks, some crystals suggest that monazite was probably developed before or during the very last stage of garnet growth (Fig. 51d).

Monazite chemistry

In the sample collected near the granulite belt, monazite grains are all characterised by a low Y_2O_3 concentration which does not exceed 1 wt.% (Fig. 52a). Besides, they show a homogenous LREE composition together with low HREE ($Gd_2O_3=0-1$ wt.%), low CaO (<1 wt.%) and negligible SiO_2 contents (Tab. 10). The UO_2 concentration shows a broad distribution between 0–1 wt.%, whereas ThO_2 and PbO cluster around 2–4 wt.% and 500 ppm

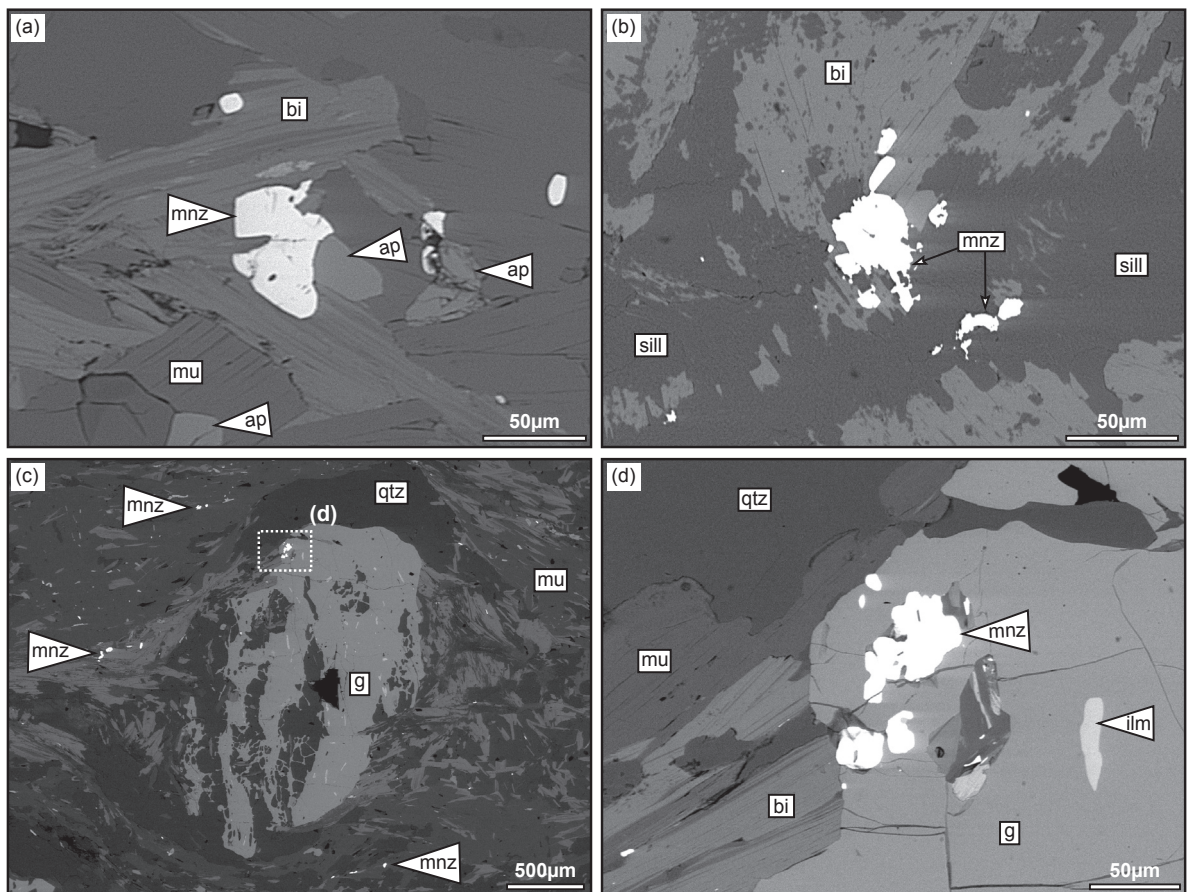


Figure 51. BSE images illustrating the position and textural relationships of monazite grains in the sample collected near the granulite belt (M81-2A). (a) Anhedral monazite grain in contact with apatite in the mica-rich matrix. (b) Matrix monazite surrounded by fibrous sillimanite and biotite. Note the irregular grain boundaries of monazite suggesting disequilibrium. (c) Monazite grains in muscovite and biotite layers as well as at the outermost rim of garnet. (d) Enlarged view of (c) showing a monazite aggregate inside garnet. The monazite grains lie next to small cracks but few crystals seem to be entirely enclosed in garnet.

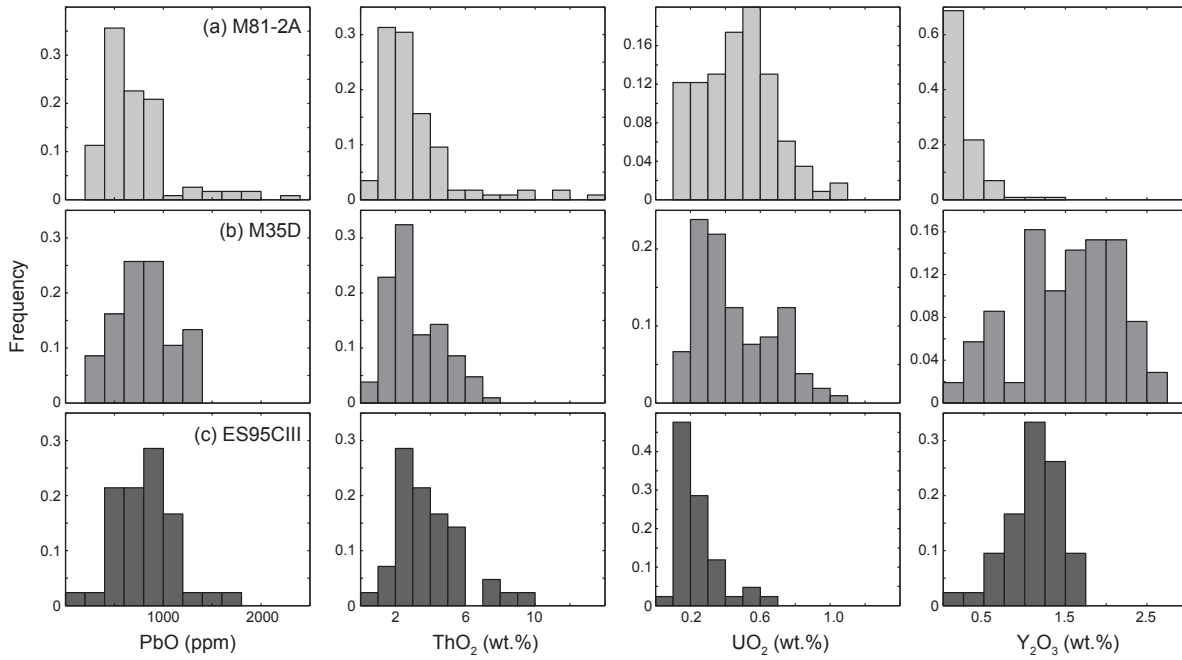


Figure 52. Frequency histograms of PbO (in ppm), ThO₂, UO₂ and Y₂O₃ (in wt.%) concentrations in monazite grains of the investigated samples. (a) Sample M81-2A located near the granulite belt. (b) Sample M35D located near the Javorník granitoid. (c) Sample ES95CIII located near the eclogite belt.

respectively (Fig. 52a). No distinction between included and matrix monazite can be made on the basis of the different oxides. The presence of only one monazite population is further illustrated by the Y₂O₃ content which remains uniformly low for a narrow range of ThO₂ concentrations as well as for a broader UO₂ distribution (Fig. 53a, b). The Th+U vs. Ca diagram clearly shows that Th and U are balanced by Ca and indicates that the brabantite exchange [2REE³⁺ ↔ (Th, U)⁴⁺ + Ca²⁺] is dominant in the analysed monazites (Fig. 53c). The monazite grains commonly show a weak zoning pattern. They exhibit a large and homogeneous Th-rich core which abruptly passes to a Th-poor rim while U varies only slightly. Importantly, the Y distribution is homogeneously low, but small patches of higher concentration are visible in some monazite cores (Fig. 54a, b).

Age results

In sample M81-2A, 124 spot analyses were performed and only 9 were rejected because they showed low oxide sums. Following monazite chemistry, the remaining 115 analyses were treated considering a single low-Y monazite population (Fig. 53). This is confirmed by the statistical distribution of individual ages which shows a single maximum at *ca.* 360 Ma, and by a weighted average age calculated at 364±8 Ma (Fig. 55a). However, the Th* vs. Pb diagram indicates an age of 340±15 Ma (MSWD=0.94) defined by an isochron which does not pass through the origin (Fig. 55a). The associated intercept of 54±30 ppm is therefore

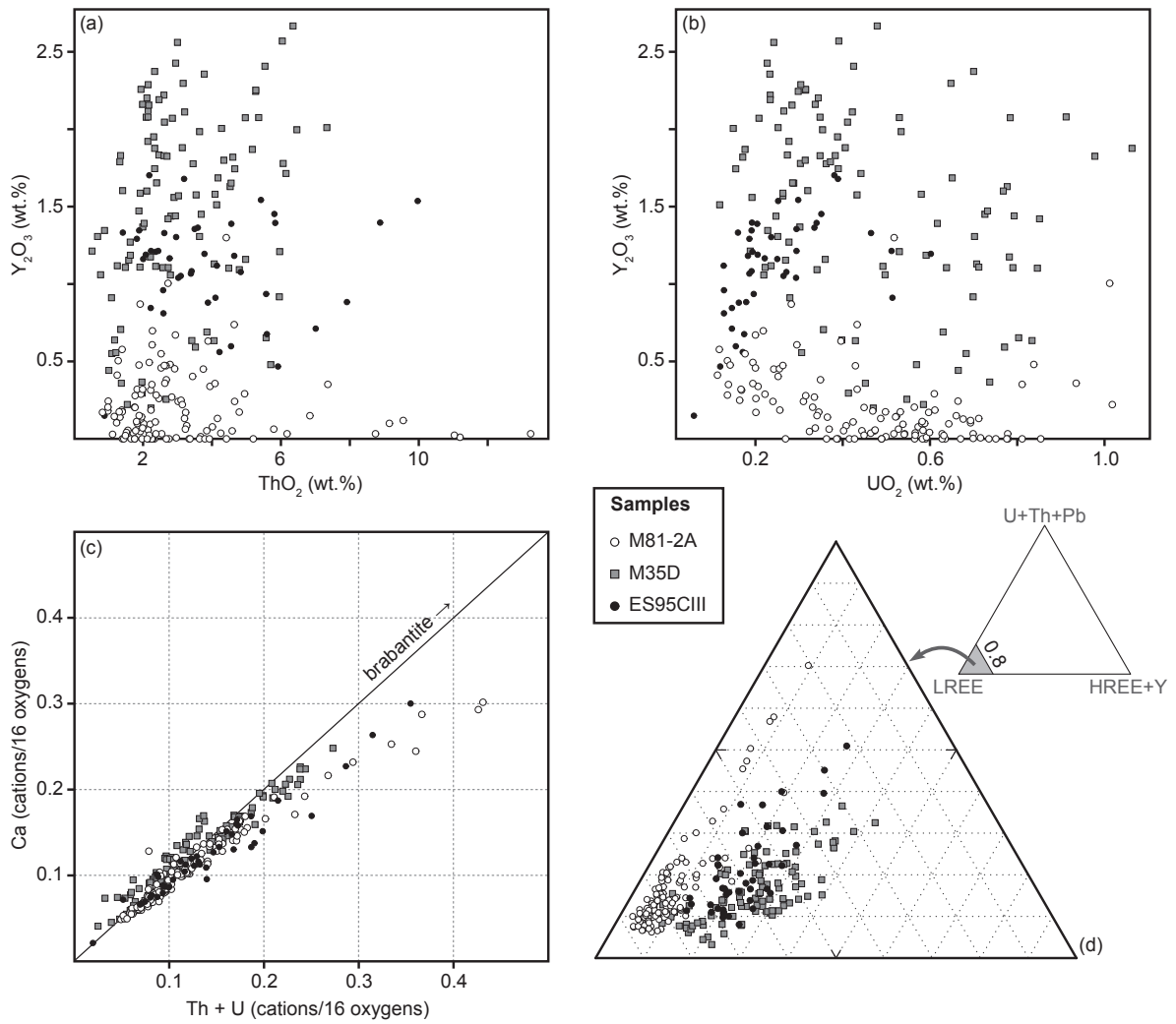


Figure 53. Monazite chemistry for the different metapelite samples. (a, b) ThO_2 and UO_2 vs. Y_2O_3 diagrams showing the presence of a single monazite population in each sample. (c) Th+U vs. Ca diagram highlighting the dominant brabantite exchange in the analysed monazites. (d) Ternary diagram illustrating the chemical contrast between monazites from the different samples.

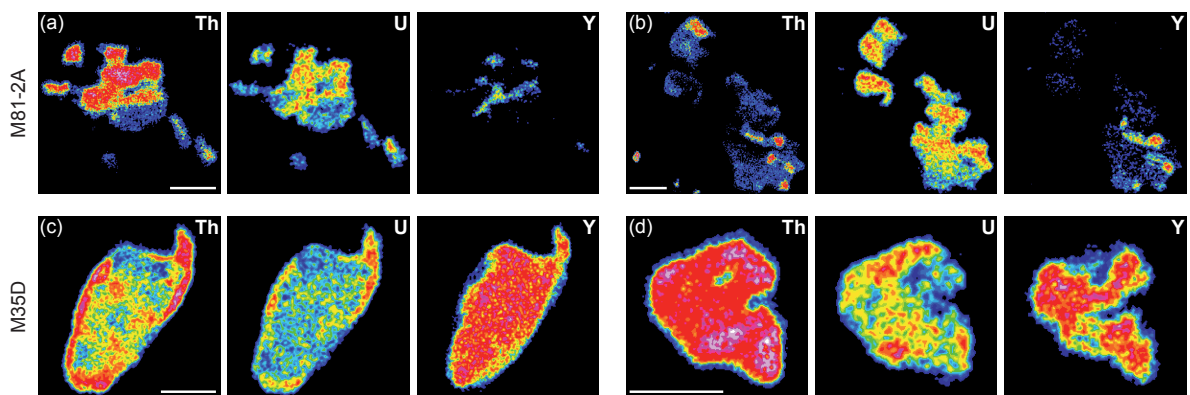
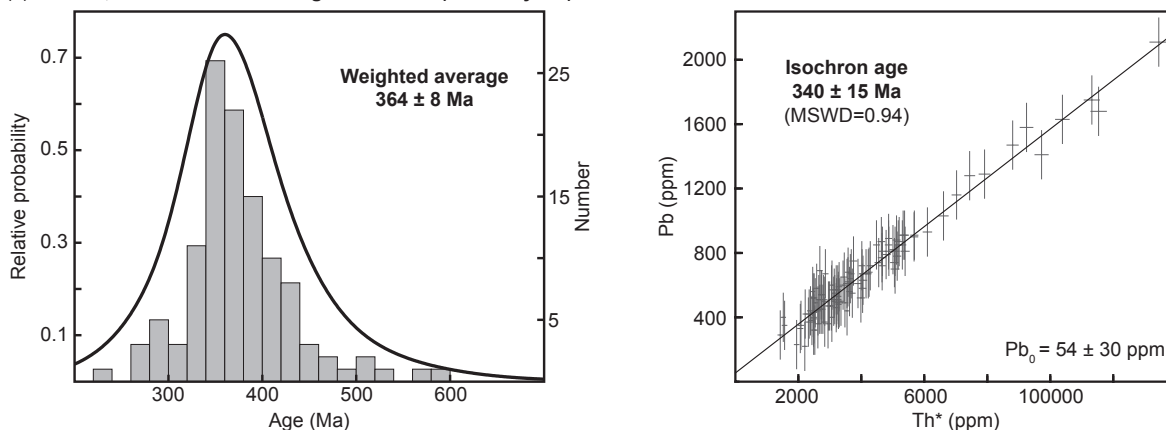


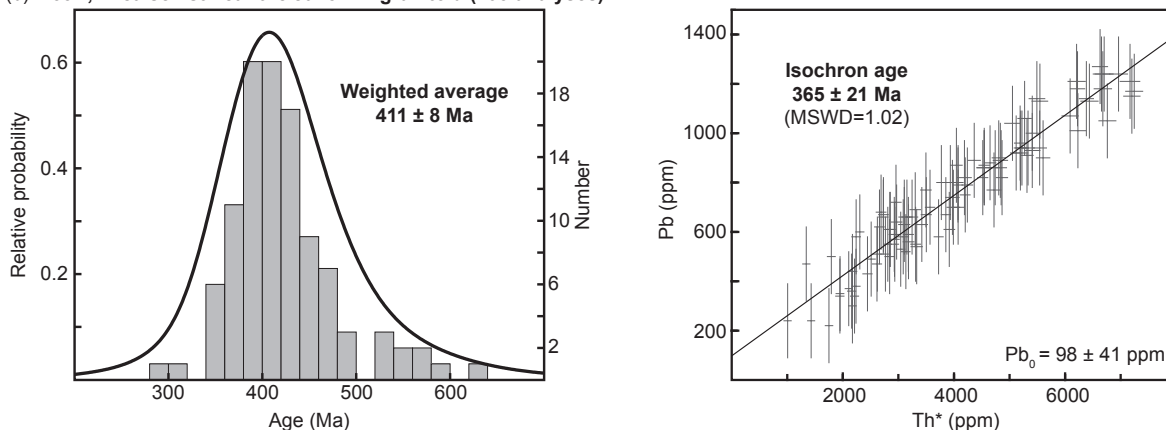
Figure 54. Compositional X-ray maps of Th, U and Y distribution in monazite grains from (a, b) sample M81-2A and (c, d) sample M35D. Warm colours indicate higher concentrations. Scale bar is always 20 μm .

thought to reflect the presence of initial Pb in the analysed monazites. This would explain the systematically older individual U–Th–Pb ages and the higher average age of 364 ± 8 Ma. Consequently, although the 340 ± 15 Ma estimate has a larger uncertainty, it will be considered as a representative age for monazite grains in this sample.

(a) M81-2A, mica schist near the granulite belt (115 analyses)



(b) M35D, mica schist near the Javornik granitoid (105 analyses)



(c) ES95CIII, mica schist near the eclogite belt (41 analyses)

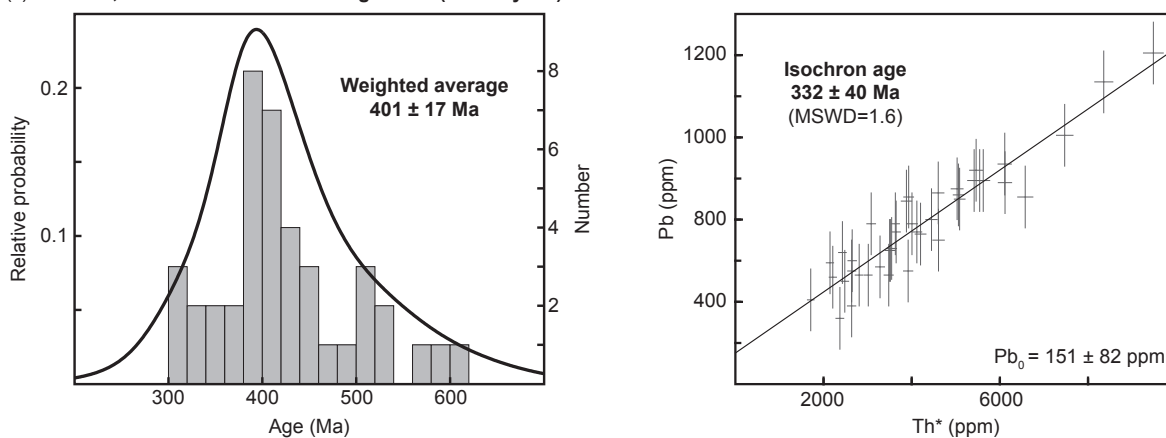


Figure 55. U–Th–Pb monazite age results for the investigated samples. On the left hand side, histograms show the distribution of the individual chemical ages and the associated probability density curve. The weighted average age is indicated. On the right hand side, Th* vs. Pb diagrams show the calculated isochron ages. The Pb_0 intercept is also indicated. (a) Sample M81-2A, (b) sample M35D and (c) sample ES95CIII.

3) Monazite record near the Javorník granitoid (northern domain)

Sample description and monazite petrography

Sample M35D is a muscovite–biotite schist containing garnet, plagioclase, staurolite, andalusite and cordierite together with accessory ilmenite and tourmaline. Alternating mica-rich and quartz-rich layers define the subvertical S2 foliation, but the microfolded S1 is frequently visible. Garnet and plagioclase porphyroblasts are oriented at high angle to S2, andalusite is developed parallel to S2 around garnet, staurolite relicts are isolated in the matrix and cordierite stripes lie parallel to S2.

Monazite is generally small (10–70 μm) and has a rounded to slightly elongated shape. It mostly occurs in the matrix and less frequently inside garnet porphyroblasts (Fig. 56). Matrix monazite is associated with muscovite or biotite and shows regular grain boundaries (Fig. 56a, b). By contrast, monazite included in garnet corresponds to aggregates of minute (10–20 μm) anhedral grains. This texture suggests that monazite could represent a pseudomorph after a former unknown mineral (Fig. 56e). Importantly, garnet X-ray maps further reveal that the monazite inclusions are present in the first garnet type which is characterised by Ca zoning, and not in the homogeneous Ca-poor overgrowths (Fig. 56c–e, see also Part 1-Chapter III.3).

Monazite chemistry

The distinctive feature of monazites from the sample collected near the Javorník granitoid is a relatively high Y content (Fig. 52b). The Y_2O_3 concentration is generally higher than 1 wt.% and is associated with varying Ce_2O_3 (28–33 wt.%) and relatively high HREE ($\text{Gd}_2\text{O}_3=1\text{--}2$ wt.%) values, while CaO (<1.4 wt.%) and SiO_2 remain low (Tab. 10). The monazite composition in UO_2 , ThO_2 and PbO is homogeneous and only UO_2 shows a slight variation (Fig. 52b). The Y_2O_3 content is neither correlated with the uniform ThO_2 distribution nor with the broader range of UO_2 values (Fig. 53a, b), reflecting the occurrence of a single monazite population in the sample. This is also suggested by the similarity between the analyses of included and matrix monazites. Like for sample M81-2A, Ca is strongly correlated with Th+U and indicates a dominant brabantite exchange in monazite (Fig. 53c). Compositional X-ray mapping reveals that the monazite grains have a rather uniform Th, U and Y distribution. Only a very small rim zone shows higher U, and lower Th and Y concentrations (Fig. 54c, d).

Age results

148 spot analyses were performed on sample M35D and 43 of them were rejected. The discarded analyses are characterised by a low oxide sum and are chiefly associated with

monazite inclusions in garnet which were most likely too thin to yield reliable data. Monazite chemistry shows that there is no distinction between the remaining 115 analyses and suggests the presence of a unique high-Y monazite population. Similarly, the individual ages for both included and matrix monazite grains define a distribution with a single maximum and yield an average estimate of 411 ± 8 Ma (Fig. 55b). By contrast, an isochron age of 365 ± 21 Ma (MSWD=1.02) is calculated using the Th* vs. Pb approach. This isochron does not pass through the origin and the intercept of 98 ± 41 ppm indicates the presence of initial Pb in the investigated monazites (Fig. 55b). This significant amount of Pb_0 is responsible for the older apparent U–Th–Pb ages which can be considered as overestimated values. Therefore, the 365 ± 21 Ma estimate is preferred despite its higher uncertainty.

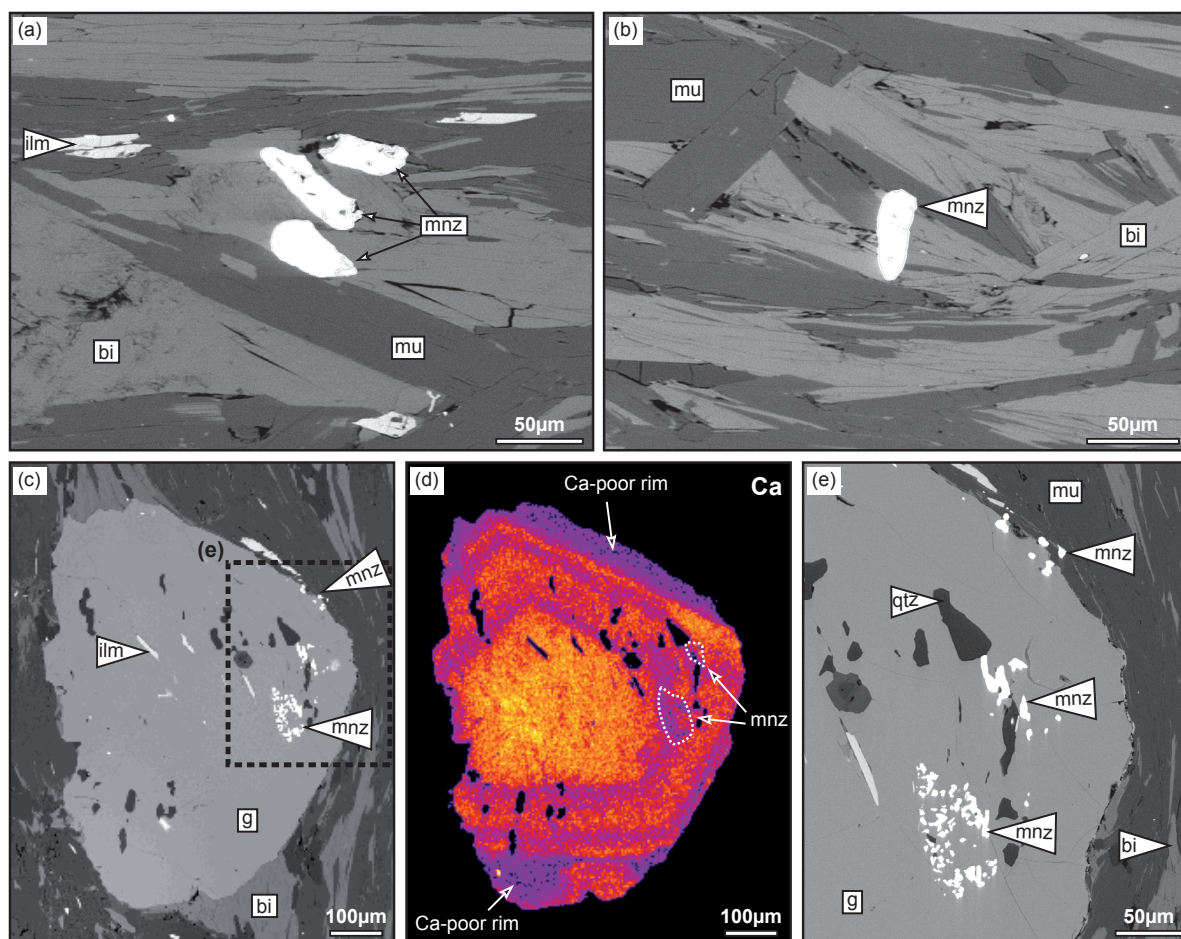


Figure 56. BSE images and X-ray map illustrating the position and textural relationships of monazite grains in the sample collected near the Javorník granitoid (M35D). (a) Slightly elongated monazite grains in matrix biotite. (b) Monazite grain in a muscovite–biotite layer. (c) Monazite aggregates inside and around a garnet porphyroblast. (d) Compositional X-ray map of Ca distribution in garnet from (c), illustrating that monazite aggregates are included in the core with Ca zoning, and not in the homogeneous Ca-poor overgrowths. (e) Enlarged view of (c) showing the texture of included monazite aggregates.

Table 10. Representative monazite analyses for the investigated samples.

Sample Analysis	M81-2A			M35D			ES95CIII		
	8	13	87	46	59	99	88	108	109
Wt. %									
SiO ₂	0.21	1.37	0.83	0.22	0.36	0.16	0.79	1.27	0.35
P ₂ O ₅	29.93	30.17	27.80	28.93	29.60	29.68	29.43	31.09	30.89
CaO	0.66	0.51	1.69	0.95	1.14	0.59	0.78	0.49	0.90
ThO ₂	2.54	2.46	11.03	4.17	5.27	2.09	4.55	2.58	4.56
UO ₂	0.78	0.20	0.57	0.65	0.32	0.35	0.16	0.13	0.20
Y ₂ O ₃	0.03	0.26	0.02	1.69	2.25	2.08	0.60	0.96	1.39
La ₂ O ₃	15.46	16.51	13.57	16.55	13.74	14.42	12.28	16.69	13.83
Ce ₂ O ₃	31.05	31.27	26.41	29.73	28.30	31.54	29.42	29.43	28.33
Pr ₂ O ₃	3.66	3.49	3.25	3.17	3.26	3.49	4.02	3.24	3.60
Nd ₂ O ₃	13.12	11.57	11.12	10.39	11.25	12.13	14.48	11.77	13.02
Sm ₂ O ₃	2.17	1.39	1.99	1.72	2.33	1.98	2.19	1.74	2.31
Gd ₂ O ₃	0.90	0.43	1.07	1.17	1.76	1.22	1.16	1.03	1.45
PbO	0.09	0.06	0.19	0.10	0.12	0.05	0.09	0.04	0.10
Total	100.59	99.69	99.56	99.45	99.70	99.77	99.94	100.47	100.93
Cations									
Si	0.03	0.21	0.13	0.04	0.06	0.02	0.12	0.19	0.05
P	3.97	3.93	3.80	3.90	3.93	3.95	3.91	3.98	4.01
Ca	0.11	0.08	0.29	0.16	0.19	0.10	0.13	0.08	0.15
Th	0.09	0.09	0.41	0.15	0.19	0.07	0.16	0.09	0.16
U	0.03	0.01	0.02	0.02	0.01	0.01	0.01	0.00	0.01
Y	0.00	0.02	0.00	0.14	0.19	0.17	0.05	0.08	0.11
La	0.89	0.94	0.81	0.97	0.79	0.84	0.71	0.93	0.78
Ce	1.78	1.76	1.56	1.73	1.63	1.81	1.69	1.63	1.59
Pr	0.21	0.20	0.19	0.18	0.19	0.20	0.23	0.18	0.20
Nd	0.73	0.64	0.64	0.59	0.63	0.68	0.81	0.64	0.71
Sm	0.12	0.07	0.11	0.09	0.13	0.11	0.12	0.09	0.12
Gd	0.05	0.02	0.06	0.06	0.09	0.06	0.06	0.05	0.07
Pb	0.00	0.00	0.01	0.00	0.00	0.00	0.00	0.00	0.00
Total	8.01	7.97	8.04	8.05	8.03	8.03	8.01	7.94	7.97
<i>Xhuttonite</i>	0.008	0.051	0.034	0.009	0.014	0.006	0.031	0.046	0.013
<i>Xcheralite</i>	0.992	0.949	0.966	0.991	0.986	0.994	0.969	0.954	0.987
<i>Xmonazite</i>	0.942	0.953	0.823	0.917	0.902	0.954	0.924	0.954	0.919
<i>Xbrabantite</i>	0.058	0.047	0.177	0.083	0.098	0.046	0.076	0.046	0.081

Structural formulae calculated on the basis of 16 oxygens, normalized to 32 charges

Xhuttonite (Si); *Xcheralite* (P); *Xmonazite* (REE+Y); *Xbrabantite* (Ca+U+Th+Pb)

4) Monazite record near the eclogite belt (southern domain)

Sample description and monazite petrography

Sample ES95CIII is a muscovite–biotite schist containing abundant garnet, few plagioclase, chlorite, tourmaline and accessory ilmenite and apatite. The sample exhibits the microfolded S1 foliation with mica-rich bands dominantly reoriented parallel to the incipient S2 cleavage. Numerous garnet porphyroblasts preserve quartz and ilmenite trails parallel to S1 in the core and slightly curved at the rim. Garnet additionally hosts plagioclase inclusions and is variably replaced by chlorite.

In this sample, monazite almost always forms aggregates of tiny (5–50 μm) anhedral grains that are only found in the matrix (Fig. 57). These monazite grains will be further called staphylo-monazites after the classical Greek term σταφυλή (“grapes” or “bunch of grapes”). The texture of staphylo-monazites strongly suggests that they grew at the expense of a primary phase which can no longer be determined (Fig. 57a, b). Importantly, staphylo-monazites are commonly found in contact with garnet rim or parallel to the S2 cleavage close to garnet porphyroblasts (Fig. 57c, d). These textural relationships points to a clear link between garnet and monazite petrogenesis.

Monazite chemistry

In the mica schist sample collected near the eclogite belt, monazites are characterised by low U and intermediate Y contents (Fig. 52a). The UO_2 concentration is commonly lower than 0.4 wt.% while the Y_2O_3 content lies between 0.5–1.5 wt.% (Tab. 10). The monazite grains additionally show a narrow range of Ce_2O_3 (25–30 wt.%), ThO_2 (2–6 wt.%) and

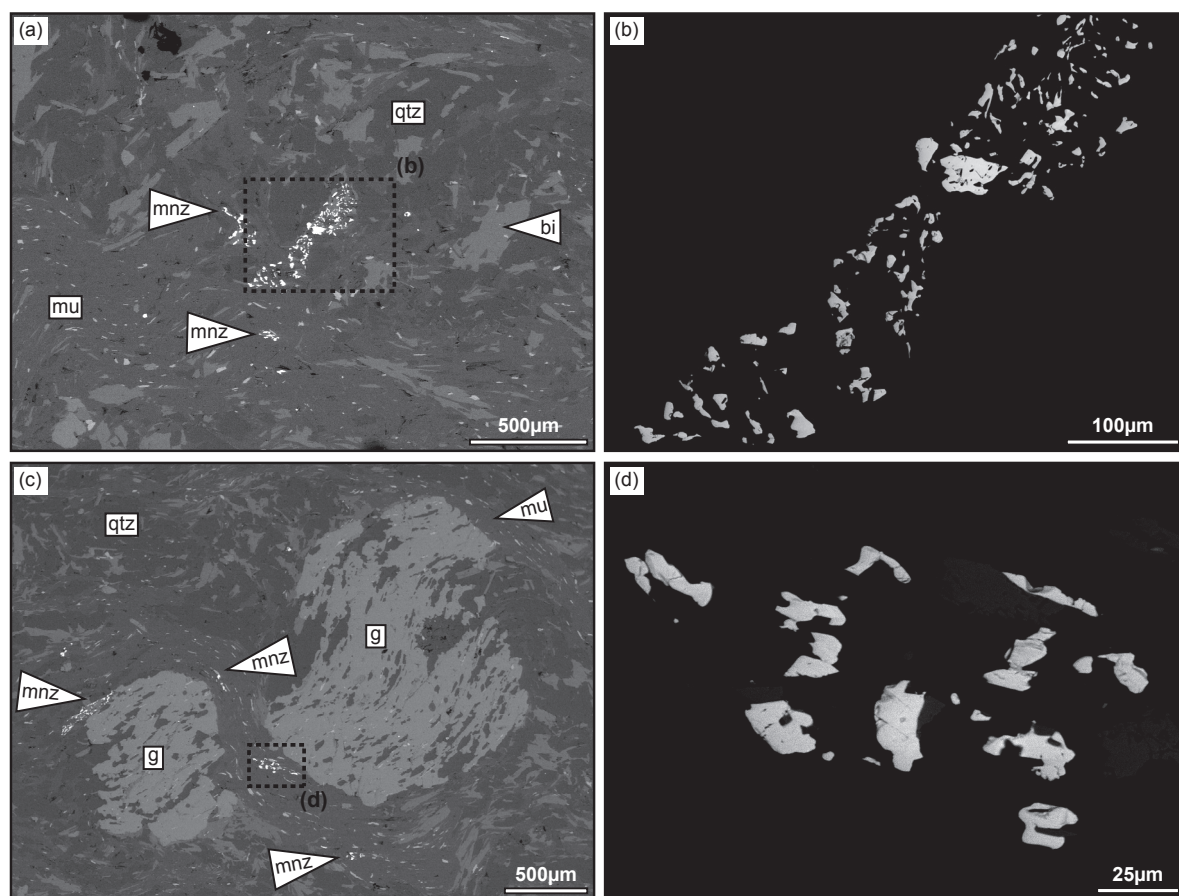


Figure 57. BSE images illustrating the position and textural relationships of monazite grains in the sample collected near the eclogite belt (ES95CIII). (a) Elongated staphylo-monazites in the matrix. (b) Enlarged view of (a) suggesting a possible origin of the staphylo-monazites as pseudomorphs. (c) Widespread staphylo-monazites parallel to the S2 layering and close to garnet porphyroblasts. (d) Detailed view of (c) showing staphylo-monazites from a muscovite-rich layer.

PbO (500–1000 ppm) concentrations, an intermediate HREE content ($\text{Gd}_2\text{O}_3=1\text{--}1.5$ wt.%), and low CaO (<1.5 wt.%). Some analyses yield significant SiO_2 values (up to 6–7 wt.%) suggesting that the huttonite substitution [$\text{REE}^{3+} + \text{P}^{5-} \leftrightarrow (\text{Th}, \text{U})^{4+} + \text{Si}^{4+}$] could play a role, although a correlation between Ca and Th+U points to a major brabantite exchange (Fig. 53c). A single monazite population is inferred from the absence of correlation between Y_2O_3 , UO_2 and ThO_2 (Fig. 53a, b).

Age results

In sample ES95CIII, 116 analyses were performed on matrix monazite grains. Because the investigated staphylo-monazites are commonly small (~20 μm), 75 analyses yielded low oxide sums or high SiO_2 contents and were not taken into account for age calculations. The remaining 41 analyses were considered as a single, low-U and intermediate-Y population on the basis of chemical data. These analyses define a clear maximum at *ca.* 400 Ma and give a weighted average age of 401 ± 17 Ma (Fig. 55c). However, the isochron age of 332 ± 40 Ma (MSWD=1.6) is markedly younger. This discrepancy is again explained by the presence of initial Pb in monazite as indicated by the high intercept of 151 ± 82 ppm (Fig. 55c). This significant amount of Pb_0 most likely leads to overestimated individual ages and the less precise estimate of 332 ± 40 Ma is therefore favoured for this sample.

4) Interpretations

Despite the probable presence of initial Pb, monazites from different parts of the metasedimentary middle crust clearly preserve distinct age records (Fig. 55). Importantly, the age difference is associated with a marked chemical contrast, especially in Y (Fig. 53). Because whole-rock analyses of metasedimentary rocks show only minor variations in U, Th, Y or REE contents (Tab. 1), it is believed that this contrast reflects different processes of monazite growth. Monazite petrogenesis should therefore be chiefly discussed in terms of REE and Y behaviour during *P–T* evolution. This approach would unravel the significance of U–Th–Pb ages in the tectono-metamorphic evolution of the orogenic middle crust.

Age significance near the granulite belt

Near the granulite belt, monazite is observed at the outermost rim of garnet and plagioclase porphyroblasts and around staurolite or apatite. It also shows disequilibrium with fibrous sillimanite in the matrix (Fig. 51). These textural relationships suggest that monazite growth occurred during the very last stage of garnet growth and before the development of the S3 foliation characterised by retrograde sillimanite. Chemical data additionally indicate that

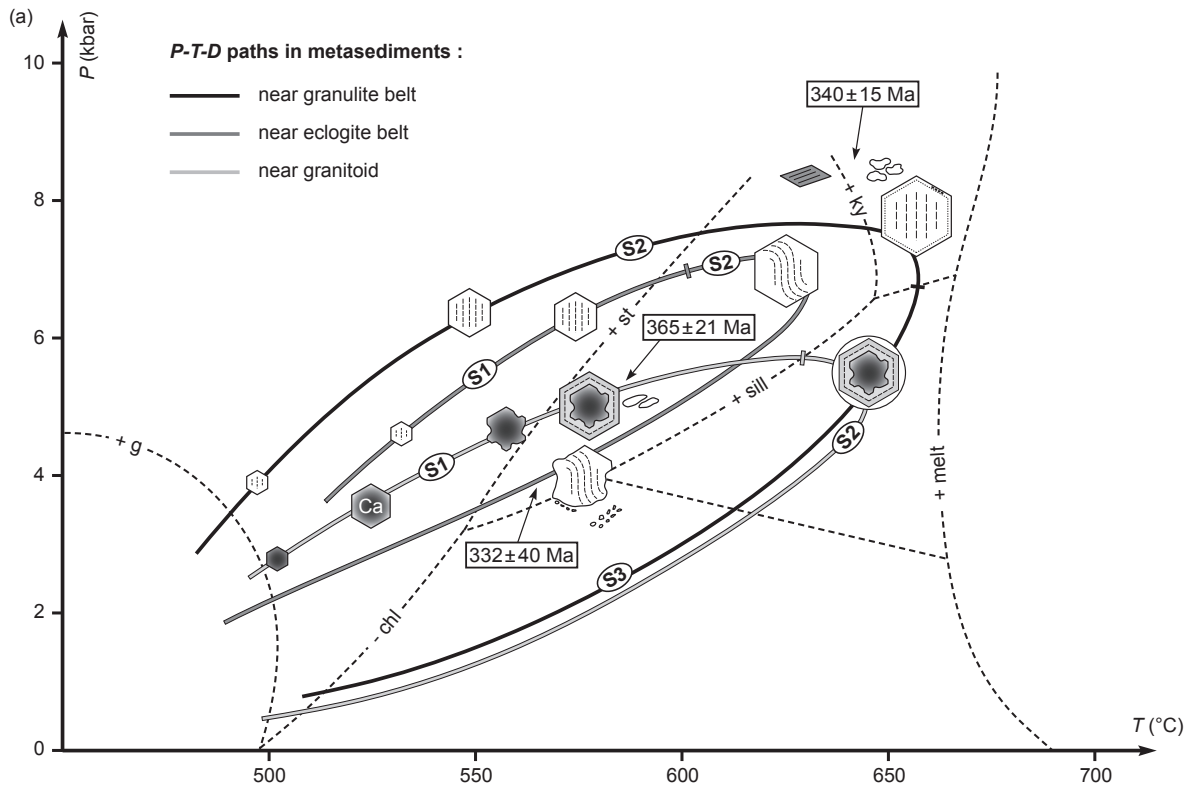
a single monazite population is present in the investigated sample (Fig. 53). This low-Y population is associated with an isochron age of 340 ± 15 Ma (Fig. 55a).

The growth of the low-Y monazite population has to be explained by the breakdown of LREE-rich and Y-poor phase(s). Common REE-bearing minerals in metamorphic rocks are xenotime [(Y,HREE)PO₄], allanite [(Ca,REE)(Al₂,Fe³⁺)Si₃O₁₁O(OH)], apatite [(Ca,REE)₅(PO₄)₃(F,OH,Cl)], garnet or zircon, and among them mostly apatite and allanite can have a relatively low Y content. Retrograde monazite growth after apatite has been documented by Finger & Krenn (2007) in exhumed high-pressure rocks. However, the investigated sample shows that monazite grew before retrograde conditions and that apatite is not replaced by monazite (Fig. 51). By contrast, the analysed monazites are more similar in composition to the prograde monazites reported by Finger & Krenn (2007) who interpreted this population as having grown in equilibrium with apatite and garnet. In the investigated sample, the apparent equilibrium between monazite and apatite therefore suggests that the dominant source of REE could be allanite instead of apatite.

Monazite replacing allanite has been observed in several samples of the metasedimentary belt. Nevertheless, the allanite to monazite transition can occur at various *P–T* conditions and is strongly dependent on the CaO whole-rock content (Spear, 2010). Yang & Pattison (2006) proposed monazite growth after allanite before the staurolite isograd while Wing *et al.* (2003) recognised allanite breakdown and monazite growth at the Al₂SiO₅ isograd. The former reaction implies monazite growth in a relatively Y-rich environment, whereas the latter should occur in a Y-poor environment since garnet usually fractionates Y in the course of prograde metamorphism (e.g. Bea & Montero, 1999). In this view, the growth of the low-Y monazite population is better correlated with allanite breakdown at the kyanite isograd. Mineral equilibria modelling additionally shows that garnet growth slows down close to the kyanite isograd (Fig. 49). This could further explain the scarcity of monazite inclusions in garnet and their sole occurrence at the outermost rims which were probably formed during the very end of the prograde *P–T* evolution (Fig. 51c, d). Consequently, it can be considered that monazite grew at the kyanite isograd, i.e. close to peak *P–T* conditions associated with the S2 metamorphic fabric (Fig. 58).

Age significance near the Javorník granitoid

In the sample collected near the granitoid, monazites are found inside garnet as well as in the matrix. Notwithstanding, chemical and age data suggest that they correspond to the same high-Y population defining an isochron age of 365 ± 21 Ma (Fig. 55b). The occurrence of monazite inclusions in the core of a zoned garnet indicates that monazite was developed



(b) Garnet-monzonite relationships

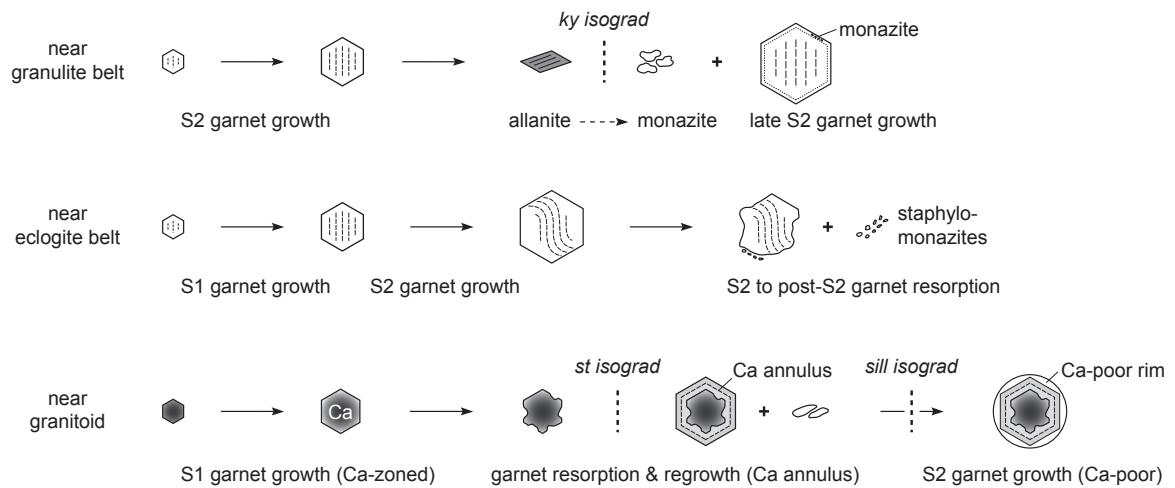


Figure 58. Summary of monazite growth mechanisms during tectono-metamorphic evolution of the middle crust. (a) *P-T-D* paths for the different parts of the metasedimentary formation and associated garnet and monazite growth episodes. Monazite isochron ages are indicated. (b) Schematic sketches showing garnet and monazite petrogenesis through the different *P-T-D* evolutions in metasediments.

before the staurolite breakdown and the associated growth of sillimanite, biotite and Ca-poor garnet (Part 1-Chapter III.3). Textural observations also suggest that some monazite grains may represent pseudomorphs (Fig. 56c–e).

Both prograde and retrograde metamorphic reactions can account for the growth of this high-Y monazite population. Based on textural relationships, the hypothesis of a retrograde growth can be ruled out. Indeed, garnet resorption is hardly documented in the investigated samples but most likely occurs after D2. Because monazite inclusions additionally point to a pre-D2 growth, the retrograde origin appears unlikely. By contrast, different prograde metamorphic reactions can produce monazite. This could be achieved via (1) allanite breakdown, (2) xenotime breakdown or (3) episodic garnet resorption.

Yang & Pattison (2006) have proposed that monazite can form after allanite before the staurolite isograd. This mechanism also implies monazite growth in equilibrium with garnet. However, the Y and HREE uptake capacity of garnet is significantly greater than that of monazite (Pyle *et al.*, 2001) and allanite contains relatively low amounts of Y and HREE (e.g. Krenn & Finger, 2007). Therefore, such a reaction would probably not produce monazite with significant Y and HREE concentrations such as those reported for this sample.

Conversely, a common source for Y and HREE at low to medium metamorphic grade is xenotime [(Y,HREE)PO₄]. Several criteria have been proposed by Spear & Pyle (2002) in order to recognise monazite derived from xenotime breakdown. Importantly, this reaction occurs together with continuous garnet growth and is thought to produce clear Th or Y zoning patterns in monazite (e.g. Pyle *et al.*, 2001). This is in contradiction with the analysed grains which show a homogeneous composition (Fig. 54c, d). In addition, relicts of xenotime have never been observed in other mica schist samples and only the monazite aggregates in garnet could correspond to a pseudomorph after xenotime. Consequently, xenotime breakdown is not considered as a major monazite-forming reaction in this sample.

Besides, numerous works have proposed that monazite can originate from garnet resorption at the staurolite isograd (Smith & Barreiro, 1990; Kingsbury *et al.*, 1993; Pyle & Spear, 1999; Kohn & Malloy, 2004). This mechanism is explained by an initial Y and HREE release due the garnet-consuming reaction garnet + chlorite + muscovite = staurolite + biotite + quartz + water, followed by garnet regrowth and monazite development. The resulting garnet zoning shows a sharp Y annulus (Pyle & Spear, 1999) while high-Y monazite remains relatively homogeneous (Kohn & Malloy, 2004). These features are in agreement with chemical data from the investigated monazites suggesting garnet resorption as a dominant source for monazite growth. Nevertheless, mass balance calculations indicate that limited garnet resorption can not explain widespread monazite development (Yang & Pattison, 2006).

Based on the occurrence of successive Ca-rich annuli in the analysed garnet porphyroblasts (Figs 26a & 56d), it can be further postulated that several episodes of garnet resorption–regrowth have occurred close to the staurolite isograd. Alternatively, it is possible to consider that garnet resorption was not the only active mechanism, but that xenotime breakdown could have contributed to the availability of Y and HREE. Despite these uncertainties, all arguments indicate that monazite growth occurred between the garnet and sillimanite isograds, and can therefore be associated with the development of the S1 metamorphic fabric (Fig. 58).

Age significance near the eclogite belt

Near the eclogite belt, monazite is only found in the matrix of pelitic samples. In the investigated mica schist, it mostly occurs close to garnet porphyroblasts and lies parallel to the S2 foliation. Some staphylo-monazites are also isolated in the matrix and form aggregates oriented oblique to S2. They could correspond to pseudomorphs after a metamorphic phase associated with the S1 foliation (Fig. 57). The EMP analyses additionally indicate that the monazites which are found in different textural positions belong to the same intermediate-Y population and define an isochron age of 332 ± 40 Ma (Fig. 55c).

The genesis of this monazite population also needs to be addressed in terms of Y mobility. As stated above, Y-rich environments are usually related to prograde xenotime breakdown before or during garnet growth, or alternatively to retrograde garnet breakdown. In the case of this sample, the textural position of staphylo-monazites and the systematic absence of monazite inclusions in garnet suggest a retrograde origin. Several studies have invoked garnet resorption during retrograde metamorphism as a major source for Y (Foster *et al.*, 2000; 2002; Yang & Pattison, 2006; Hinchey *et al.*, 2007). Depending on the amount of released Y, this can lead to the growth of monazite rims, monazite single crystals or even xenotime (Pyle & Spear, 1999). Following the qualitative scheme proposed by Gibson *et al.* (2004), Y release chiefly depends on the degree of garnet resorption. Consumption of the garnet rim would typically yield monazite with an intermediate Y content, whereas breakdown of the core would produce Y-richer monazite. Considering that garnet porphyroblasts are only slightly retrogressed, Y release was probably limited in the investigated sample. It is in agreement with the intermediate Y content in the analysed monazite population (Fig. 52c). In this view, staphylo-monazites would represent pseudomorphs after former garnet crystals. Monazite petrogenesis is therefore better explained by garnet breakdown during retrograde metamorphism. According to petrological data (Part 1-Chapter III.4), this retrograde event is thought to occur at the end of the D2 deformation. Consequently, monazite growth can be confidently ascribed to a late low-pressure stage of the S2 fabric development (Fig. 58).

CHAPTER VI

BURIAL AND EXHUMATION PROCESSES

1) Burial–exhumation mechanisms and associated P – T paths

Although several mechanisms can account for burial and/or exhumation of mid- and lower-crustal rocks, they produce distinct P – T paths. An overview of the observed and modelled P – T evolutions is likely to provide a basis for further discussing the different tectonic scenarios (Fig. 59).

Isothermal decompression is a typical metamorphic evolution in *orogenic lower crustal* lithologies (e.g. Brown & Dallmeyer, 1996), but various processes can produce steep *retrograde* P – T paths (Fig. 59a). This could be either the result of diapiric rise (Teyssier & Whitney, 2002; Gerya *et al.*, 2004), vertical extrusion (e.g. Thompson *et al.*, 1997) or crustal-scale folding (Schulmann *et al.*, 2005; Tajčmanová *et al.*, 2006), where limited thermal exchange due to rapid exhumation is a key parameter and cooling is only reported for late parts of the P – T evolution. By contrast, a temperature increase followed by cooling during decompression is observed for erosional unroofing models (England & Thompson, 1984; Thompson *et al.*, 1997).

These mechanisms related to the exhumation of the lower crust have contrasted thermal consequences for *prograde* P – T paths of the associated *mid-crustal* rocks (Fig. 59b). As an example, rocks from a syncline rimming a diapiric dome may follow a P – T path associated with exceptionally strong heating (Warren & Ellis, 1996), whereas models involving pure shear crustal thickening (Ruppel & Hodges, 1994) or crustal-scale folding reveal only a moderate temperature increase during burial (Chamberlain, 1986; Kim & Bell, 2005).

Subsequent exhumation of the *juxtaposed orogenic lower and mid-crustal rocks* from mid-crustal to shallower crustal levels can also occur along distinct *retrograde* P – T paths (Fig. 59c). During this phase, the time that elapses before rocks reach a colder level, i.e. the duration of thermal relaxation at depth, plays a major role on the shape of the P – T loop (England & Thompson, 1984, their Fig. 2). The result is a more or less pronounced temperature increase after peak pressure or even a decrease in both pressure and temperature. This timing is critical for ductile extrusion models where mid-crustal rocks surrounding the hot channel are exhumed more slowly than the low-viscosity deep crustal rocks (e.g. Jamieson *et al.*, 2002).

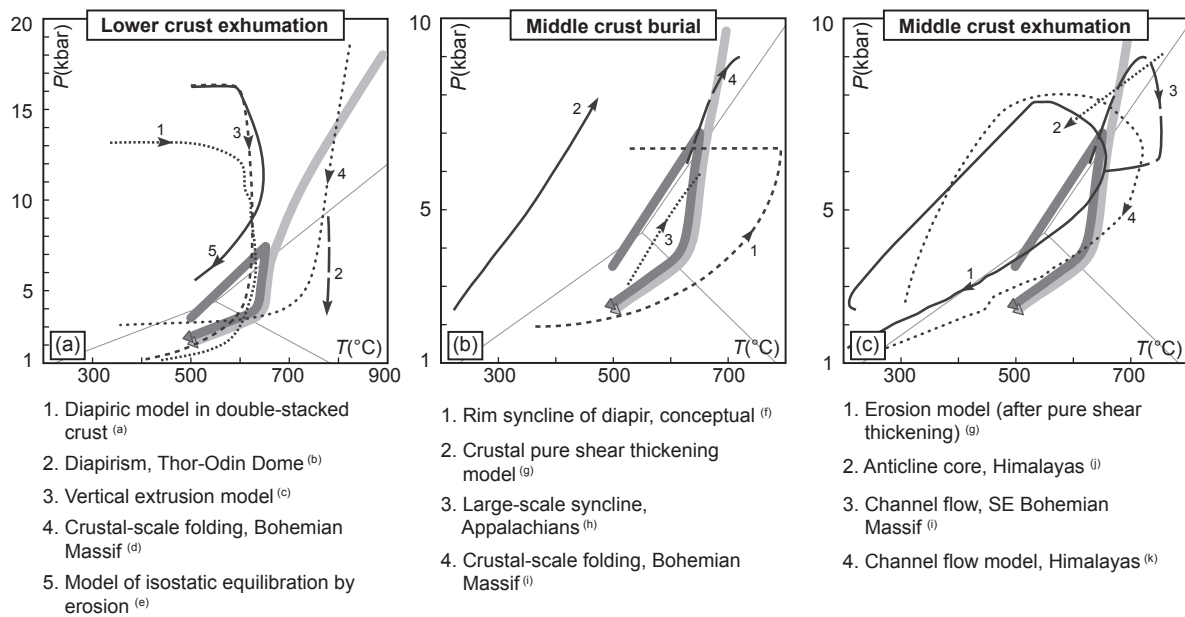


Figure 59. Comparison between P – T paths for metasedimentary rocks (dark grey) and granulites (light grey) investigated by Štípská *et al.* (2004), and published P – T paths for different mechanisms of (a) exhumation of the orogenic lower crust, (b) burial of associated mid-crustal rocks, and (c) exhumation of rocks located at mid-crustal level. Modelled or observed P – T paths are after: (a) Gerya *et al.* (2004), (b) Norlander *et al.* (2002), (c, e) Thompson *et al.* (1997), (d) Tajčmanová *et al.* (2006), (f) Warren & Ellis (1996), (g) Ruppel & Hodges (1994), (h) Chamberlain (1986), (i) Racek *et al.* (2006), (j) Burg *et al.* (1997), and (k) Jamieson *et al.* (2004). Al_2SiO_5 phase diagram is shown for orientation.

2) P – T – D – t relationships between metasediments and neighbouring rocks

P – T – D – t relationships between metasediments and the granulite belt

The P – T – D path for metasediments located near the granulite belt (Figs 22 & 49) shows that rocks from the middle crust probably underwent early burial to 12 km under greenschist-facies conditions during the formation of an early shallow-dipping S1 fabric. Further burial from 12 km (~3.5 kbar) to 25 km (6–7 kbar) occurred during the development of the regionally well-preserved subvertical S2 fabric together with an increase in temperature from ~500 °C to 630–660 °C (Fig. 22). According to EMP monazite dating, the age of the metamorphic peak should lie close to 340 ± 15 Ma (Fig. 58). This is in good agreement with the Sm–Nd garnet–WR isochron age of *ca.* 345 Ma obtained on a kyanite-bearing metapelite of the central domain where garnet growth was ascribed to the S2 fabric (Jastrzębski, 2008). A subsequent exhumation stage within the late shallow-dipping S3 foliation is responsible for a minimum of 10 km of vertical displacement towards a depth of ~12 km at still elevated temperatures of ~580 °C (Fig. 22).

An identical succession of fabrics in pelites, as well as in orthogneiss and granulite (Štípská *et al.*, 2004), indicates a complete structural continuity across the investigated area (Fig. 6). Therefore, the tectono-metamorphic history of the metasedimentary rocks can be compared to that of granulite. In granulite, an early probably subhorizontal S1 fabric is folded into the subvertical S2 foliation which develops at a pressure peak of ~18 kbar and ~850 °C, and is followed by heterogeneous shallow-dipping D3 deformation at 6–10 kbar and ~700 °C. The prograde character of the early shallow-dipping fabric is not demonstrated, but it is likely that peak metamorphic assemblages in granulite developed before the onset of the D2 deformation (Štípská *et al.*, 2004). The timing of the metamorphic peak is constrained by a SHRIMP U–Pb zircon age of *ca.* 342 Ma. The time span of granulite exhumation was further estimated by the Pb–Pb zircon age of a syntectonic granodiorite sill emplaced parallel to the S3 fabric in adjacent rocks at *ca.* 339 Ma (Parry *et al.*, 1997; Štípská *et al.*, 2001; Lexa *et al.*, 2005). The shallow-dipping S3 fabric affected the hinge zone of the orthogneiss–granulite anticline, but because of the lack of pressure and temperature sensitive equilibria, the amount of vertical movement associated with this fabric was not assessed in the high-grade rocks. Nevertheless, Štípská *et al.* (2004) showed that the shallow-dipping fabric is probably associated with exhumation of the granulite belt from 10 kbar to 6 kbar, i.e. towards a depth of ~20 km.

Accordingly, the originally mid-crustal metasedimentary rocks and the lower crustal granulites were juxtaposed at a depth of 25–35 km during the formation of the subvertical S2 fabric (Fig. 22). The peak metamorphic conditions in the metasedimentary rocks and the retrograde amphibolite-facies conditions in the granulites were roughly achieved at the same time of 345–340 Ma. This implies that the burial and exhumation events were fast, occurring in *ca.* 5 Ma, and that the metasedimentary rocks and the granulites reached the same crustal level as a result of synchronous, but opposite vertical movements. The subsequent evolution during the D3 deformation involved exhumation of both lithologies towards a depth of ~12 km.

P–T–D–t relationships between metasediments and the Javorník granitoid

In the NW part of the northern domain, petrological investigations show that metasediments located near the Javorník granitoid underwent burial during or after the development of the subhorizontal S1 fabric (Fig. 28). During this event, mid-crustal rocks reached a depth of ~16 km at temperature conditions of ~600 °C. Monazite petrogenesis additionally suggests that an EMP age of 365±21 Ma can be associated with this early burial episode (Fig. 58). The subsequent development of the subvertical S2 foliation is associated with a prolonged

pressure and mostly temperature increase towards conditions not exceeding ~6 kbar and 650 °C (Fig. 28). It indicates that the rocks of the metasedimentary belt have been brought to a maximum depth of ~20 km during D2 deformation. Peak P – T conditions could further be correlated with the age of 340–330 Ma obtained on few metamorphic zircon overgrowths in neighbouring metarhyolite intercalations (Murtezi, unpublished results). Finally, the late- to post-D2 evolution involves exhumation to a depth lower than 10 km at temperatures probably above 550 °C (Fig. 28).

The Javorník granitoid partly shared the structural evolution which is documented in the neighbouring metasedimentary and gneissic lithologies (Fig. 5). In places, cm-scale granitic veins commonly exhibit a pervasive solid-state deformation fabric which lies parallel to the subvertical S2 foliation. In addition, anisotropy of magnetic susceptibility data reveal that the granitoid preserves a subvertical NE–SW striking magnetic foliation which is similar to the orientation of S2 (Hroudá, unpublished data). However, several aplitic veins and patches of isotropic granite also show intrusive contacts with the surrounding metasediments and clearly crosscut the S2 fabric. These combined observations therefore suggest that granitoid emplacement occurred during a late- to post-D2 stage. The intrusion of the Javorník granitoid body is constrained by several geochronological methods. A Pb–Pb zircon age of *ca.* 353 Ma (Kröner, unpublished data) is thought to reflect magmatic emplacement while several $^{40}\text{Ar}/^{39}\text{Ar}$ ages on amphibole and micas indicate subsequent cooling around 351–345 Ma (Białek & Werner, 2004).

Combined structural and age data indicate that the Javorník granitoid intruded the metasedimentary belt at *ca.* 350 Ma during a late stage of the D2 deformation. Importantly, this could corroborate the EMP monazite age of 365 ± 21 Ma which is thought to reflect metamorphism in the earlier S1 foliation. Nevertheless, the influence of the granitoid on the inferred P – T path in metasediments remains unclear. The granitoid could be responsible for the marked temperature increase towards ~650 °C indicated by sillimanite growth parallel to S2 (Fig. 28). However, the small time lag between crystallisation and cooling ages in the granitoid is not in agreement with the P – T increase which is documented by the early S2 g–bi–sill paragenesis. It alternatively suggests rapid cooling and probable emplacement during exhumation (Białek & Werner, 2004). In this view, the thermal anomaly related to the granitoid would be better explained by the widespread occurrence of andalusite (Fig. 24b, f). This points to a shallower intrusion level of ~10 km and is more compatible with the retrograde character of the late S2 and \pm cd assemblage (Fig. 28). Such an episode of magma ascent during D2 is also in line with medium to high partial melting along the S2 fabric in neighbouring orthogneiss (Fig. 37c). To summarize, P – T – D – t relationships between

metasediments and the Javorník granitoid point to a relatively rapid burial and exhumation history that lasted from *ca.* 365 to 345 Ma. The metasedimentary rocks were initially buried to ~20 km during subhorizontal and later subvertical flow. They were subsequently intruded by a large sill-like granitic body during exhumation towards a depth of ~10 km. Importantly, they were only weakly affected by the later D3 deformation which developed while they were already in the upper orogenic crust.

P–T–D–t relationships between metasediments and the eclogite belt

The *P–T–D* evolution of metasedimentary rocks located near the eclogite belt (southern domain) indicates that the early subhorizontal S1 foliation is associated with initial burial to a depth of ~12 km (Fig. 32). Renewed garnet and staurolite growth parallel to the subvertical S2 fabric subsequently points to a *P–T* increase towards peak conditions not exceeding ~7 kbar and ~630 °C (Fig. 32). Burial of this part of the middle crust therefore culminates at ~16 km depth and may be also linked with the *ca.* 345 Ma age ascribed to peak metamorphism in the central domain (Jastrzębski, 2008). Nevertheless, mineral parageneses observed in the S2 foliation also suggest exhumation of metasediments towards a crustal depth lower than ~10 km at temperatures below 550 °C (Fig. 32). Monazite growth along the retrograde *P–T* path is additionally used to propose an indicative age of 332±40 Ma for this exhumation event (Fig. 58). Later exhumation and cooling below 500 °C is ascribed to the weakly developed shallow-dipping S3 cleavage.

The similar successions of fabrics in eclogite and metasedimentary rocks (Fig. 14) suggest that the different parts of the orogenic crust experienced the same deformation history. Nevertheless, the *P–T–D* record in eclogite lenses is partly different (Štípská *et al.*, 2011). There, prograde and peak metamorphic assemblages observed in the S1 fabric point to a *P–T* increase towards 19–22 kbar and 700–750 °C. The age of peak metamorphic conditions probably lies at 350–345 Ma as suggested by concordant results obtained with different dating techniques (Sm–Nd WR–mineral isochron by Brueckner *et al.*, 1991; Rb–Sr WR–mineral isochron by Bröcker *et al.*, 2009; U–Pb zircon by Bröcker *et al.*, 2010). It is presently not clear, whether the widespread amphibolite-facies paragenesis already developed in the S1 foliation or in the subsequent S2 fabric, but metamorphic conditions at the end of D2 deformation can be confidently estimated at ~9 kbar and 700 °C. It is proposed that metamorphism associated with the subvertical S2 foliation involved nearly isothermal decompression followed by *P–T* decrease below 4–5 kbar and 550 °C. Accordingly, the later D3 overprint occurred while the eclogites were already at a shallow crustal level. ⁴⁰Ar/³⁹Ar cooling ages obtained in surrounding orthogneiss indicate that greenschist-facies conditions were attained at *ca.* 340 Ma (Schneider

et al., 2006), i.e. only shortly after peak metamorphism.

P–T–D–t relationships indicate contemporaneous burial of both the metasedimentary rocks and the eclogite in the subhorizontal S1 fabric. At *ca.* 350 Ma, the eclogite together with mylonitic orthogneiss which shows similar peak *P–T* conditions (Chopin *et al.*, 2011b) formed the orogenic lower crust, whereas the metasedimentary rocks were buried to the middle crust at a depth of ~20 km (Fig. 32). The eclogite were subsequently exhumed from 50–60 km to ~30 km depth either in a flat-lying S1 or subvertical S2 fabric. Although this major exhumation event remains obscure, amphibolite-facies assemblages clearly testify for further exhumation of the eclogite from ~30 to ~25 km during D2 deformation (Štípská *et al.*, 2011). Oppositely, the metasediments initially underwent burial to ~22 km in the subvertical S2 fabric (Fig. 32), suggesting vertical material transfer between the upward-moving lower crust and the downward-moving middle crust. During a later stage of D2 deformation, the nearly juxtaposed crustal levels were exhumed together towards ~10 km depth and probably reached the upper crust at 340–330 Ma (Fig. 58). A last exhumation increment was possibly accommodated by the subhorizontal S3 cleavage which developed at greenschist-facies conditions (Fig. 32).

3) Tectonic significance of the *P–T–D–t* evolutions

Detrital zircon ages indicate that the sediments of the Stronie-Młynowiec formation were deposited during the Middle Cambrian–Lower Ordovician (Jastrzębski *et al.*, 2010). Contemporaneous magmatism is reflected by the emplacement of the granitic precursor of the Śnieżnik and Gieraltów gneisses in the underlying basement (Turniak *et al.*, 2000; Kröner *et al.*, 2001), and by volcanism in the sedimentary basins (Murtezi & Fanning, 2005). Accordingly, the lithologies of the Orlica-Śnieżnik Dome represent a Cambro-Ordovician sequence involving granitic basement covered by psammitic to pelitic sedimentary successions. During the Devonian–Carboniferous, this sequence underwent a polyphase evolution which is characterised by three major tectono-metamorphic events. Their significance will now be discussed in terms of burial and exhumation processes in the orogenic crust.

Tectonic significance of *P–T–D–t* evolutions in the subhorizontal S1 fabric

In the Orlica-Śnieżnik Dome, all lithologies document prograde metamorphism during D1 deformation. The metasedimentary rocks reached the garnet or staurolite isograd (Fig. 37), whereas mylonitic orthogneiss and high-grade lithologies show eclogite or HP granulite-facies conditions associated with the development of the S1 foliation (Štípská *et al.*, 2004; Chopin *et al.*, 2011b; Štípská *et al.*, 2011). Importantly, macroscopic observations as well as

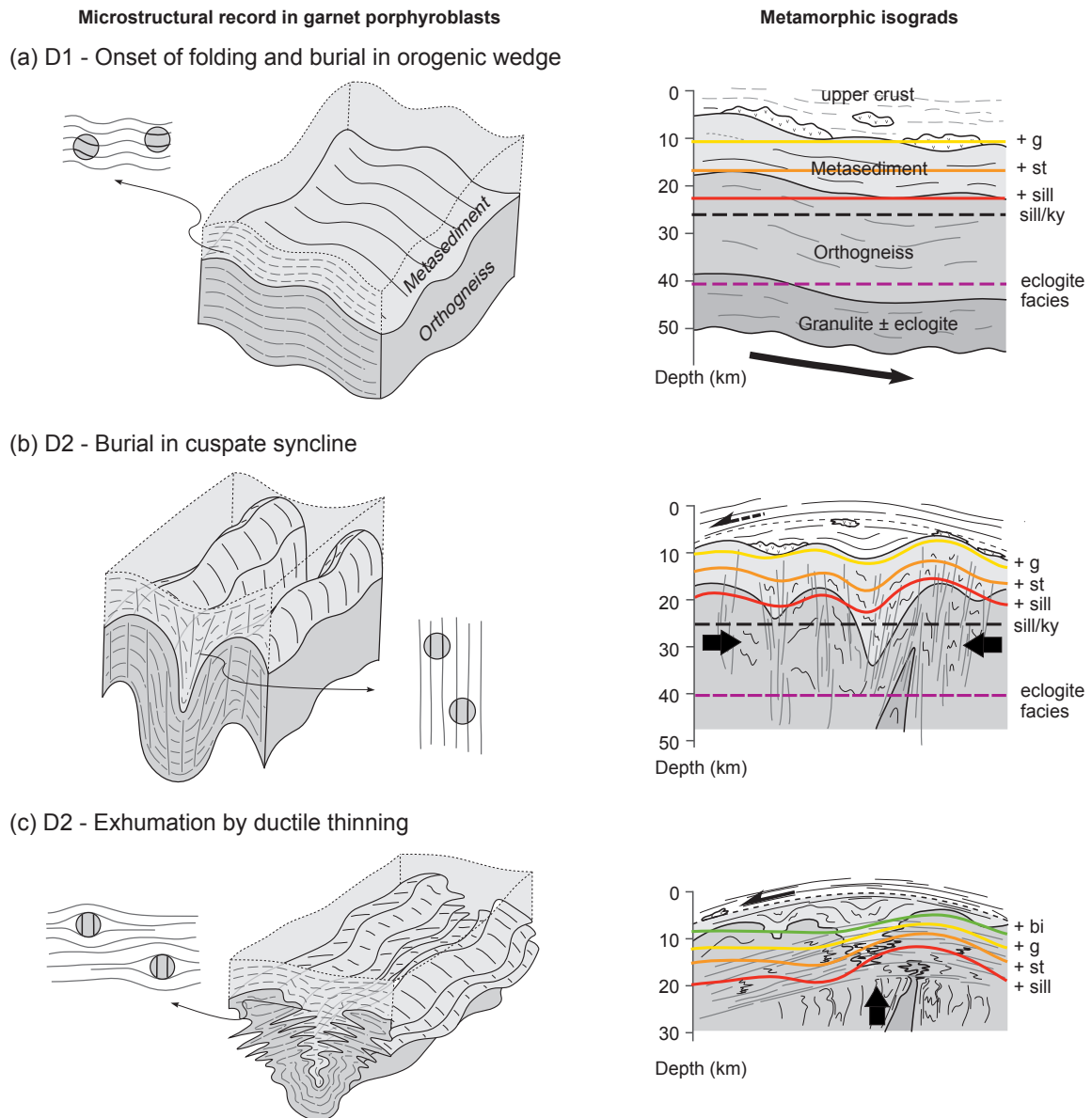


Figure 60. Schematic blocks and sections summarizing the tectono-metamorphic evolution of the orogenic crust in the Orlica-Śnieżnik Dome. Block diagrams highlight the behaviour of garnet porphyroblasts while sections show the distribution of metamorphic isograds during polyphase deformation. (a) D1 deformation, (b) D2 deformation and (c) D3 deformation.

microstructural records in garnet porphyroblasts indicate that burial towards different crustal depths occurred in a flat-lying, probably slightly folded foliation (Figs 60a & 61). Contrasted $P-T$ trajectories during subhorizontal flow of rocks originally located at different levels of a pile is typical for the dynamics of an accretionary wedge system (e.g. Allemand & Lardeaux, 1997; Batt & Braun, 1997). Consequently, the tectono-metamorphic record in the S1 fabric is thought to represent horizontal influx of material in an orogenic wedge from *ca.* 365 to 350 Ma (Figs 58 & 60a). In addition, blueschist occurrence in the NW Izera-Karkonosze Block reveals that this event was preceded by oceanic subduction at *ca.* 360 (Maluski & Patočka, 1997). Therefore, HP granulite-facies metamorphism observed in high-grade lithologies of

the OSD can be seen as the result of a subsequent continental subduction episode. In this view, the Stronie sediments and the granitic basement would represent a lower plate material which was subducted towards the SE (Chopin *et al.*, 2011a). However, maximum pressure estimates of ~6 kbar reached by metasediments during D1 indicate that the upper plate probably did not have a standard thickness of ~35 km. Accordingly, continental subduction is thought to occur below an attenuated continental margin which was most likely thinned during the Devonian, since widespread rifting is commonly reported in the neighbouring Moravo-Silesian zone at this period (e.g. Schulmann & Gayer, 2000).

Tectonic significance of P–T–D–t evolutions in the subvertical S2 fabric

The D2 deformation is characterised by widespread exhumation of lower crustal lithologies in the core of large gneissic anticlines. It is coeval with burial of the metasedimentary middle crust towards contrasted peak conditions (Fig. 37). Indeed, metapelites located next to high-grade bodies show prograde metamorphism reaching kyanite grade at *ca.* 340 Ma (Fig. 58), while metasediments occurring farther preserve lower grade assemblages. The metamorphic isograds associated with D2 define a concentric pattern showing decreasing *P–T* conditions away from the granulitic anticline (Fig. 37b). This strong correlation between the position of metasediments with respect to the granulite and the intensity of metamorphism indicates that it is essential to examine the *P–T* record in metasediments in order to understand the processes responsible for granulite exhumation.

If the granulites are considered as a diapirically rising dome for which isothermal decompression paths are classically documented (Norlander *et al.*, 2002; Duchêne *et al.*, 2006), the neighbouring rocks from the rim syncline should record an anticlockwise *P–T* evolution (Fig. 59b) as proposed by Warren & Ellis (1996). However, the cooling of the granulite during exhumation together with the clockwise prograde path, high initial temperature and low density of the middle crust all seem to invalidate the diapiric hypothesis. By contrast, folding mechanisms involving burial in synforms are likely to produce prograde *P–T* paths similar to the one presented in Fig. 22 (e.g. Chamberlain, 1986; Fig. 59b). If the folding model of Sleep (1979) is invoked, buckling of the lithological boundaries involves conservation of mass but does not allow shortening to occur parallel to the fold axial plane surface. This also implies that the heating rate within synforms should be similar to the cooling rate within antiforms. However, given the discrepancy between heating of the Stronie metasediments and cooling of the granulites (Fig. 59), a different folding mechanism should be envisaged.

Field observations suggest that the fold pattern resembles an alternation of orthogneiss antiforms with a large wavelength and pinched synforms of metasedimentary rocks with

a shorter wavelength (Dumicz, 1979; Don, 1982). Such geometry has also been observed in the southern domain where eclogites and metasediments are pinched on both sides of a weakly deformed orthogneiss body. Therefore, a mechanism of passive amplification of an initially cusped–lobate interface producing large-scale folds is preferred in order to explain the vertical exchange between the middle and the lower crust in the subvertical S2 fabric (Fig. 61). In addition, consistently oriented internal records in garnet porphyroblasts suggest that the pervasive S2 fabric probably results from pure shear dominated deformation (Fig. 60b).

According to this view, the prograde P – T path in metasediments could be explained by burial in a narrow syncline (Chamberlain, 1986; Fig. 59b), while the retrograde path in granulites is compatible with a vertical extrusion model (e.g. Thompson *et al.*, 1997; Fig. 59a) additionally involving erosion in order to account for further cooling. Significant erosion during this period is potentially reflected by an abundant Lower Carboniferous sediment input showing southeast provenance in the Intra-Sudetic Basin (Teisseyre, 1968; 1971; 1975). Alternatively, cooling of the exhumed granulites could have been achieved during thermal exchange with the metasediments once both lithologies were juxtaposed at mid-crustal level.

In the metasedimentary belt located next to the Javorník granite, the P – T – D data are also in agreement with the model of crustal-scale folding. Indeed, peak pressure conditions are lower than in metasediments located near the granulite belt and reflect the decreasing amplitude of large-scale folding away from the granulitic anticline, as emphasised by the metamorphic isograd pattern (Fig. 37). In addition, granitic intrusions during D2 are compatible with widespread migmatization parallel to the S2 fabric in gneissic anticlines, and especially in orthogneiss around the granulite belt. This felsic magma could be even considered as melt which was partially lost by the lower crustal granulitic lithologies. Accordingly, the metasedimentary belt intruded by the Javorník granite is interpreted as a shallower level of the orogenic middle crust (Fig. 60b). A similar view can be adopted for the northwest and central parts of the central domain which show only weak P – T increase during D2. By contrast, the exhumation of the eclogite belt during crustal-scale folding remains unclear. Indeed, crystallisation–deformation relationships do not rule out exhumation in the early flat-lying S1 fabric. This could have been achieved by back-thrusting along a predisposed subduction plane (Chemenda *et al.*, 1995) and would not leave a structural trace in the exhumed eclogite (Klápová *et al.*, 1998). Nevertheless, a part of the D2 evolution shows eclogite exhumation during contemporaneous burial of the neighbouring metasediments. Consequently, it is believed that large-scale folding affected the entire orogenic crust, though with a varying degree of intensity.

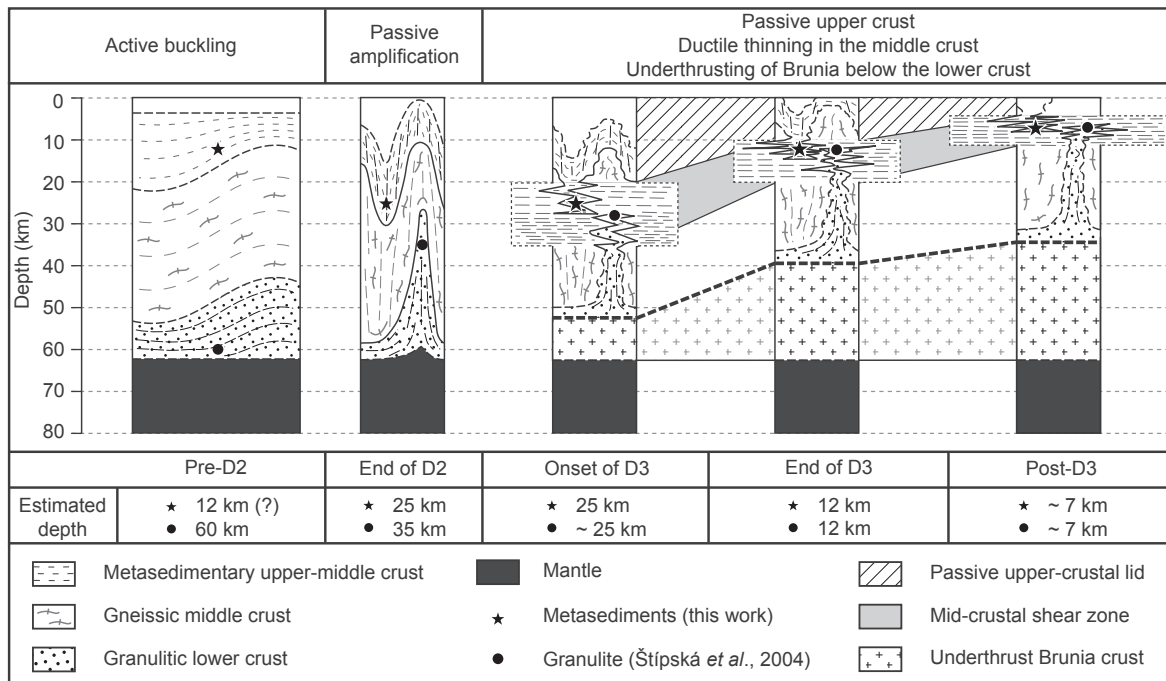


Figure 61. Schematic evolution of the orogenic crust from thickening to exhumation. Inferred position of the Stronie formation metasedimentary rocks (black star) and neighbouring granulites (black circle) are indicated.

Tectonic significance of P–T–D–t evolutions in the shallow-dipping S3 fabric

In the Stronie-Młynowiec formation, the S3 foliation always develops under retrograde conditions, but is associated with a variable thermal regime. Around the granulite belt, sillimanite and andalusite occurrences suggest the persistence of high temperature conditions compared to the rest of the OSD where D3 develops in the chlorite stability field (Fig. 37c). Because the S3 is mostly present in the northern domain, the significance of this fabric will be discussed in the light of P–T–D relationships between the granulite belt and the neighbouring metasedimentary belt.

In the SE part of the Bohemian Massif, mid- and lower-crustal rocks record juxtaposition at a similar crustal level by opposite vertical movements, followed by subhorizontal deformation (Racek *et al.*, 2006). In this region the middle crust was further heated from 650 °C to ~750 °C after peak pressure (Fig. 59c), indicating that thermal relaxation or additional heat supply has to occur. These observations have been explained in terms of horizontal influx of hot granulitic and migmatitic rocks into colder mid-crustal lithologies that were subsequently mixed in a crustal channel (Racek *et al.*, 2006; Schulmann *et al.*, 2008; Štípská *et al.*, 2008). This process is described as a heterogeneous channel flow, where a mass of hot lower crustal rocks transports remnants of mid-crustal synclines over the continental basement. Evolution in a hot horizontal channel is also documented in the Himalayas by

Jessup *et al.* (2006) and associated P – T paths involving post-peak heating (Fig. 59c) have been modelled by e.g. Jamieson *et al.* (2004).

However, petrological data presented in this work do not fit the channel flow model. Indeed, metapelites and granulites indicate a decrease in both pressure and temperature as long as the shallow-dipping fabric evolves (Figs 22 & 59c). Although producing compatible retrograde P – T paths, the model of exhumation in the core of a large antiform associated with erosion (Burg *et al.*, 1997) can probably be ruled out because no shallow-dipping fabrics are created during this process. By contrast, the early retrograde P – T path of granulites suggests that strong erosion already acted during the subvertical fabric development. This mechanism is likely to persist during later exhumation and may therefore enhance cooling of the crust (Fig. 59c), as demonstrated by the erosional models of Ruppel & Hodges (1994). The temperature decrease could also be explained by the relatively small amount of hot granulitic material that has been brought in contact with the middle crust.

However, there is further need for an exhumation mechanism that would be responsible for the widespread flattening which is observed in the whole area (Fig. 6). The mechanism of ductile thinning (Ring & Brandon, 1999; Ring *et al.*, 1999) may be responsible for the unroofing of the high-grade core of continental orogens either by homogeneous vertical shortening process (Vanderhaeghe & Teyssier, 2001), or by the activity of localised extensional detachments (Platt, 1993). In summary, the ductile thinning brings rocks closer to the surface by vertical shortening of the overlying crustal column at a given crustal level (Fig. 61), in conjunction with continuous cooling which accelerates as the rocks approach the surface (Feehan & Brandon, 1999). According to structural, microstructural (Fig. 60c) and petrological observations, ductile thinning together with erosion can therefore account for the retrograde P – T – D path of both the granulites and the metapelites.

The driving force for the formation of the horizontal foliation and the ductile thinning process is suggested to be the underthrusting of the Orlica-Śnieżnik root by the eastern Staré Město unit and the Brunovistulian continent during the Carboniferous (Fig. 61). Alternatively, isostatic re-equilibration of a thickened root could also lead to horizontal flow generally localised underneath the rigid lid (Dewey *et al.*, 1993; Koyi *et al.*, 1999; Milnes & Koyi, 2000). Nevertheless, in the investigated area the restoration of a standard crustal thickness of 35 km (Fig. 61) was probably achieved during late Carboniferous extensional stretching and thinning of the whole thickened crust due to the activity of a major detachment zone (the Ramzová detachment) located close to the Orlica-Śnieżnik Dome and the imbricated Brunovistulian boundary (Schulmann & Gayer, 2000).

4) Diagnostic paired P – T – D paths?

A wide range of mechanisms can usually be related to any observed P – T path. However, because the resolution of petrology is generally not sufficient, a strong link between deformation structures and metamorphism can help distinguishing between different tectonic processes. In the present case two major mechanisms, i.e. diapirism and large-scale folding, can account for vertical transfers between shallow and deep crustal rocks, and for the subsequent flattening of the exhumed lithologies (Burg *et al.*, 2004). However, important features of the diapiric model such as the lack of subhorizontal fabrics in the buried rocks and the high thermal regime (Warren & Ellis, 1996) are incompatible with both the observed structural and metamorphic records in the investigated metasediments and neighbouring granulites (Štípská *et al.*, 2004). By contrast, the converging P – T paths of mid- and lower-crustal rocks associated with vertical flow are compatible with vertical exchanges of material through crustal-scale folding (Racek *et al.*, 2006), whereas the subsequent joint decompression and cooling experienced by both lithologies in a shallow-dipping foliation suggest that exhumation was achieved by dominant ductile thinning (Ring & Brandon, 1999) and erosional unroofing. It is finally proposed that the identification of paired P – T – D paths with similar features to those presented in this work could be further used to favour the proposed burial and exhumation processes, not only in the Variscan belt of Europe, but also in other continental wedges worldwide.

SUMMARY AND CONCLUSIONS TO PART ONE

Summary

Structural analysis in metasedimentary rocks of the Orlica-Śnieżnik Dome (Sudetes) reveals a superposition of three heterogeneously developed fabrics: the subhorizontal S1, the subvertical S2 and the subhorizontal S3 foliations. Crystallisation-deformation relationships in mica schists and paragneisses show that the S1 fabric is always associated with a $P-T$ increase towards the garnet or staurolite isograd. The subsequent S2 metamorphic foliation is connected with mostly prograde metamorphism towards contrasted $P-T$ conditions, but may also be linked with retrogression. Metamorphism in the S2 fabric can reach the staurolite, sillimanite or kyanite isograd with peak $P-T$ conditions never exceeding ~ 9 kbar and ~ 650 °C. Conversely, the subhorizontal S3 fabric has always a retrograde character, though with different thermal regimes. Retrograde metamorphism in the S3 foliation can occur at relatively high temperature in the sillimanite or andalusite stability field, or alternatively at low-grade conditions in the chlorite stability field. A similar tectono-metamorphic history is confidently recorded in garnet porphyroblasts. EBSD analysis of ilmenite inclusion trails reveals that an identical succession of subhorizontal and subvertical foliations is preserved in garnet while it has been partly obliterated in the surrounding matrix. In addition, compositional zoning points to prograde garnet growth during the D1 and D2 deformations, whereas garnet is subsequently resorbed in the retrograde S3 foliation. Finally, EMP monazite dating is used to constrain the age of each metamorphic fabric. Prograde metamorphism in the S1 foliation is estimated at 365 ± 21 Ma based on the growth of high-Y monazites, probably at the staurolite isograd. The timing of peak metamorphism in the S2 fabric is approximated by an age of 340 ± 15 Ma given by a low-Y monazite population which is thought to reflect allanite breakdown at the kyanite isograd. Garnet breakdown at a late stage of D2 or during D3 deformation is ultimately indicated by intermediate-Y monazites yielding 332 ± 40 Ma.

Porphyroblast microstructures

The present work introduces a new and precise technique for determining internal records preserved in porphyroblasts. It is based on EBSD analysis of ilmenite inclusion trails in single garnet crystals. Compared to previous methods, this approach therefore allows to

perform *in situ* measurements of both the planar and linear structures included in individual porphyroblasts. The results obtained with this technique are essential in the way that they provide information on:

- the **orientation of earlier structures** which have been partly or even entirely obliterated at all scales,
- the **deformational regime** during and after porphyroblast growth.

As a perspective, it is proposed that this method should be tested on other strongly anisotropic and oblate inclusions like micas, and in other porphyroblastic minerals such as staurolite, andalusite or plagioclase.

Monazite petrogenesis

EMP monazite analyses reveal a strong correlation between age results and monazite chemistry. Together with textural relationships, it is used to propose that monazite petrogenesis is linked with different steps of the P – T evolution, and that monazite ages can consequently reflect:

- **prograde metamorphism** across the staurolite isograd,
- **peak metamorphic conditions** at the kyanite isograd,
- **retrograde metamorphism** during garnet resorption.

Further work could involve isotopic dating of monazite and analysis of Y distribution in garnet in order to better constrain the timing of metamorphic reactions, and thus the age of the different metamorphic fabrics.

Regional geology

The following new features are revealed by the study of the Stronie-Młynowiec metasedimentary formation:

- Mineral assemblages show that the degree of metamorphism increases towards the east of the OSD. More precisely, the **metamorphic isograds define a concentric pattern around the granulitic Gieraltów anticline.**
- EMP monazite ages of *ca.* 365, 340 and 335 Ma all point to **Variscan tectono-metamorphic events** in the orogenic middle crust. Although older ages may be recorded in the neighbouring Orlica Dome, no evidence for pre-Devonian metamorphism is recognised in this work.

Intracontinental tectonic processes

The sensitivity of the middle crust to orogenic processes is clearly illustrated by the contrasted $P-T-D-t$ evolutions recorded in different parts of the metasedimentary unit. If these $P-T-D-t$ paths are additionally combined with those reported in high-grade lithologies, they provide decisive constraints on burial and exhumation mechanisms. In the case of the Orlica-Śnieżnik Dome structural, petrological and geochronological data obtained for the metasedimentary middle crust favour the following evolution:

- **Subhorizontal influx of material in an orogenic wedge** during continental subduction, probably below an attenuated crust (D1).
- **Vertical material transfer** leading to the juxtaposition of the orogenic middle and lower crust during **crustal-scale folding** (D2). Crustal-scale folding shows decreasing amplitude away from an eastern rigid buttress and is locally accompanied by subvertical granitic intrusions in the middle crust.
- **Exhumation** of the whole crust by a **dominant ductile thinning process** which generates a localised flattening zone at mid-crustal depth (D3). Erosion may also contribute to cooling and exhumation of the crustal column.

PART TWO

STRUCTURAL, PETROLOGICAL AND GEOCHRONOLOGICAL
CHARACTERISATION OF INTRACONTINENTAL TECTONIC PROCESSES IN
THE OROGENIC CRUST (VOSGES MOUNTAINS)

DEUXIÈME PARTIE

CARACTÉRISATION STRUCTURALE, PÉTROLOGIQUE ET
GÉOCHRONOLOGIQUE DES PROCESSUS TECTONIQUES
INTRACONTINENTAUX DANS LA CROÛTE OROGÉNIQUE (VOSGES)

INTRODUCTION TO PART TWO

Orogenic belts are commonly formed by thickening of the crust close to convergent plate margins (e.g. Dewey & Bird, 1970). However, crustal growth probably does not result from simple thickening of a homogeneous continental portion. Alternatively, several studies have emphasised the role of subcretion or relamination processes in the genesis of orogenic crust (Currie *et al.*, 2007; Johnston & Canil, 2007; Hacker *et al.*, 2011). Following these views, the orogenic crust better corresponds to a complex imbrication of continental and oceanic fragments with contrasted origins and affinities (e.g. Oncken, 1997; Walsh & Hacker, 2004). The formation of such a heterogeneous crustal assemblage can be investigated by several methods. A detailed structural study of the relative timing and superposition of fabrics can reveal the changes in the global architecture of the orogenic system through time (e.g. Milnes *et al.*, 1997; Lehmann *et al.*, 2010). In addition, the preservation of compositional zoning in metamorphic minerals (e.g. Spear & Selverstone, 1983) and the strong resistance of zircon to high-grade metamorphic processes (e.g. Watson, 1996; Möller *et al.*, 2002) are key features that may be used to access to the early stages of the orogenic evolution, and to unveil the origin of the welded crustal portions.

The quest for the early orogenic history has classically focused on deep-seated rocks in mountain belts (e.g. Schulmann *et al.*, 2005). Nevertheless, polyphase tectonic and metamorphic overprints are known to affect the entire crust during subduction and collision, though with varying intensity. Therefore, the systematic study of lithologies located at different crustal levels is essential to the understanding of the dynamics of the orogenic system. Indeed, because ophiolites and rift-related structures are commonly well preserved in the upper crust (e.g. Beltrando *et al.*, 2010), they can be used to explore the role of structural inheritance on the collisional evolution (e.g. Oncken *et al.*, 1999; Mohn *et al.*, 2011). Conversely, assessing the P - T - D - t evolution of mid- and lower-crustal lithologies is key for understanding burial and exhumation mechanisms operating in the deeper part of the crust (e.g. Racek *et al.*, 2006). Consequently, combining structural, petrological and geochronological records for the upper, middle and lower crust is likely to highlight the thermo-mechanical response of the composite orogenic crust to plate convergence. In other words, this would help to characterise intracontinental tectonic processes acting during orogeny.

The Palaeozoic basement of the Vosges Mountains (NE France) represents an ideal place to study intracontinental tectonic processes for two main reasons. Like in other remnants of the Variscan orogen in Europe, the Vosges exhibit high-grade lithologies and therefore allow direct access to the root zone of an orogenic system. More importantly, all the different

levels of the orogenic crust are exposed in the present-day Vosges basement. Consequently, it is possible to investigate deformation and metamorphism from the base up to the uppermost part of the crust. In the Southern Vosges sedimentary units, partly ophiolitic remnants can be used to unravel the early orogenic history and its influence on future collision. In the Central Vosges root, medium- to high-grade metamorphic rocks additionally allow to explore zircon record during the metamorphic processes which affected the deep part of the orogenic crust. Finally, a detailed structural study of the entire Vosges basement is presented in order to discuss the main features of extensional and compressional tectonic processes which operated during orogeny. Because intracontinental tectonics is also addressed in terms of far-field forces, the geodynamic evolution of the Vosges is further integrated in the Variscan framework.

CHAPTER I

THE SIGNIFICANCE OF LATE DEVONIAN OPHIOLITES IN THE VARISCAN OROGEN: A RECORD FROM THE VOSGES KLIPPEN BELT

1) Introduction

Two major episodes of oceanic crust generation are clearly documented in the Variscan Belt of Europe (Behr *et al.*, 1984; Matte, 1986; Ziegler, 1986; Pin, 1990). The first Cambro-Ordovician event is associated with the formation of the large Rheic oceanic realm and rifting of continental blocks away from the northern Gondwana margin (Crowley *et al.*, 2000; Tait *et al.*, 2000; Matte, 2001; von Raumer & Stampfli, 2008). The second event corresponds to a well-documented Early Devonian oceanic stage (Holder & Leveridge, 1986; Franke, 2000), while some Late Devonian ophiolites may reflect back-arc spreading (Pin & Paquette, 1997).

The episodes of Palaeozoic rifting led to the formation of basins with contrasted sedimentary and deformational records. The basins which opened during the Cambro-Ordovician preserve Ordovician to Devonian autochthonous sediments that are indicative of long-lived oceanic domains. They are also characterised by Devonian to Visean flysch deposits (e.g. Saxothuringian stratigraphy; Falk *et al.*, 1995). Subsequent inversion of these relatively old sequences was associated with the growth of a thick oceanic wedge and resulted in large thrust imbrications of sedimentary units, ophiolites and backthrust high-pressure rocks (Franke, 1984). By contrast, Devonian basin sequences are related to short-lived oceanic domains. They comprise Early to Middle Devonian undisturbed marine sediments followed by a Middle Devonian to Carboniferous input of flysch sediments (e.g. Rhenohercynian stratigraphy; Franke, 1995; Leveridge & Hartley, 2006). Inversion of the Devonian basins produced a fold and thrust belt geometry (Oncken *et al.*, 1999) with imbrications of non- to weakly-metamorphosed sediments and obduction of ophiolites (Shail & Leveridge, 2009) with some high-pressure remnants (Massonne & Schreyer, 1983; Ganssloser *et al.*, 1996). In a similar way, Late Devonian successions are related to very short-lived back-arc domains because they exhibit Late Devonian sediments shortly followed by Early Carboniferous flyschoid sedimentation (Hartley & Otava, 2001). Inversion of these probably small basins is characterised by the exhumation of the deepest parts of the basin between younger sediments (e.g. the Horní Benešov-Šternberk Belt in Moravia; Dvořák, 1995).

Thus, the life span of an oceanic basin seems to be a key parameter controlling its future inversion. It is all the more important for Late Devonian remnants because this period

corresponds to a general closure of the Variscan subduction systems and a widespread exhumation of HP rocks (e.g. Matte, 1998; Stampfli & Borel, 2002; Ballèvre *et al.*, 2009). It is therefore critical to assess the timing and tectonic evolution of the Late Devonian oceanic domains in order to better understand their origin and significance during Variscan orogeny.

The opportunity to address such problems is given by the ophiolitic remnants exposed in the Southern Vosges Klippen Belt (“Ligne des Klippes”, Jung, 1928). There, the closure of a Devonian oceanic basin was documented by Krecher & Behrmann (2007), but information on the preceding opening stage is lacking. This chapter therefore proposes a re-evaluation of ophiolitic rocks from the Klippen Belt. Detailed mapping of the Klippen Belt together with structural and geophysical data from the adjacent units are used to decipher the tectonic history of the Southern Vosges. In addition, geochemical investigations on gabbroic rocks and geochronological data from oceanic and basement lithologies mixed in the Klippen Belt are combined to constrain the origin, geodynamic setting and timing of the basin. A tectonic evolution is proposed and implications for the dynamics of the Variscan Belt are discussed.

2) Geological background

Devonian ophiolites in the Variscan belt of Europe

Two groups of Devonian ophiolitic remnants can be distinguished in the Variscan Belt of Europe (Fig. 62). The first group comprises oceanic rocks of the Lizard Complex which document Early to Middle Devonian extension in SW England (Floyd *et al.*, 1993; Clark *et al.*, 1998; Cook *et al.*, 2002), and the Giessen and Harz MOR-type metabasalts overlain by Middle Devonian sediments in NW Germany (Floyd, 1995; Franke, 1995). These ophiolites are interpreted as relicts of the Early Devonian Rhenohercynian oceanic basin which was subsequently inverted in the Middle to Late Devonian (Franke, 2000). The second group is represented by the Brévenne Séries in the French Massif Central which preserve Late Devonian subduction-related magmatic rocks (Pin & Paquette, 1997; Leloix *et al.*, 1999), or by Devonian deep marine sediments and arc to back-arc magmatic rocks of the Vrbno and Drahany facies in Moravia (Patočka & Valenta, 1996; Hladil *et al.*, 1999; Janoušek *et al.*, 2006). The Beja–Acebuches Ophiolite Complex indicating opening of a basin at 400–370 Ma in SW Iberia (Ribeiro *et al.*, 2010) could also be associated with the group of Late Devonian ophiolites, though this interpretation is still debated (Azor *et al.*, 2008; Pin *et al.*, 2008). This group of ophiolites is generally related to the existence of small back-arc domains during Devonian times.

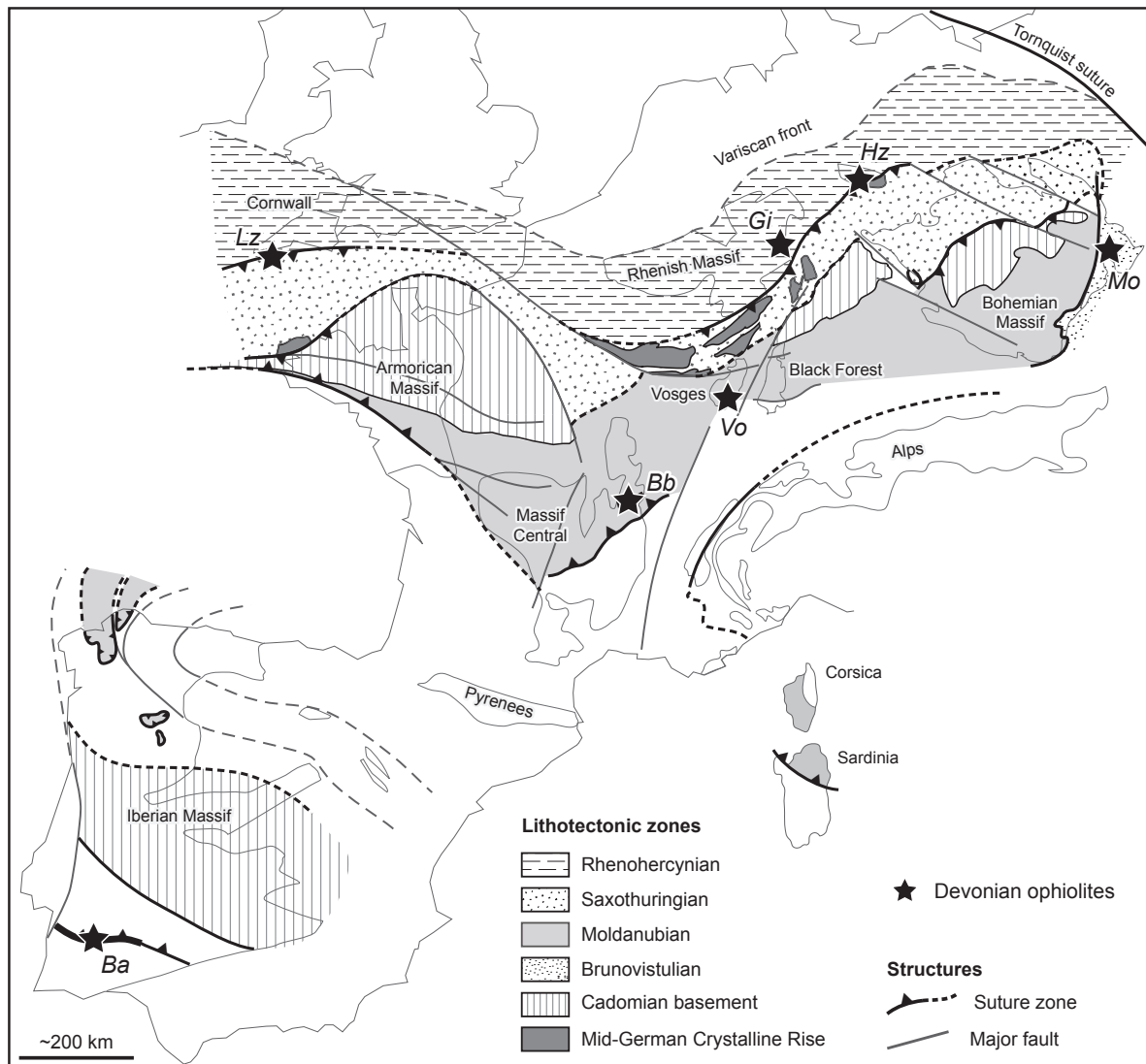


Figure 62. Devonian ophiolites in the Variscan Belt of Europe. Ba=Beja-Acebuches Ophiolite Complex, Lz=Lizard Complex, Bb=Brévenne-Beaujolais, Vo=Vosges Klippen Belt, Gi=Giessen and Hz=Harz Nappes, Mo=Vrbno-Drahany facies and Horní Benešov-Šternberk Belt in Moravia. Variscan framework is modified after Edel & Schulmann (2009), Ballèvre *et al.* (2009) and Pitra *et al.* (2010).

Southern Vosges Mountains

In the Southern Vosges, ophiolitic rocks (*sensu* Coleman, 1977) are found in the so-called Klippen Belt, which represents a discontinuous exposure of exotic rocks between two sedimentary basins (Fig. 63). Based on structural observations, Jung (1928) originally distinguished between a northern allochthonous unit (Markstein unit) and a southern group of autochthonous units (Oderen and Thann units). The allochthonous sedimentary unit is composed of interbedded pelite and greywacke (Fig. 64) and represents an Early Carboniferous (Corsin & Mattauer, 1957; Corsin & Ruhland, 1959) siliciclastic turbidite basin preserving distinct facies of sandy submarine fans (Gagny, 1962; Krecher *et al.*, 2007). To the South, the autochthonous units chiefly correspond to Lower to Upper Visean volcano-sedimentary rocks. The base

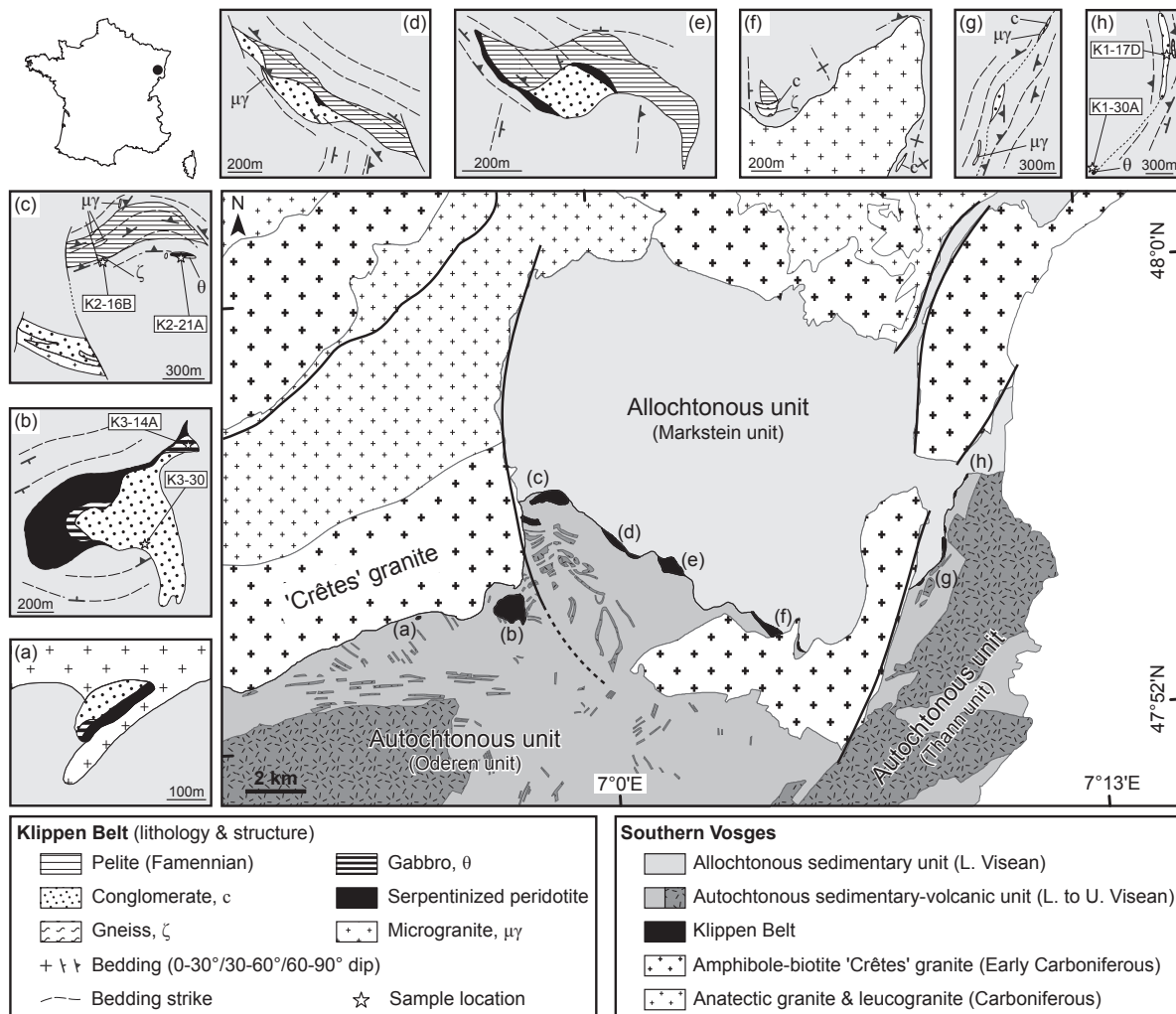


Figure 63. Lithological map of the Southern Vosges and detailed maps of the different klippen. Klippen names: (a) Drumont, (b) Thalhorn, (c) Kruth-Sauwas, (d) Treh, (e) Markstein, (f) Arutsch-Rennenbachfels, (g) Lautenbach, (h) Murbach-Rimbach.

of the Oderen unit (Fig. 64) is characterised by a relatively thin succession of Frasnian (?) carbonates conformably overlain by Famennian sediments (Asselberghs, 1926) and Early Carboniferous pelite and greywacke, whereas the thick Lower to Middle Visean deposits involve interbedded pelite and greywacke turbidites accompanied by mostly submarine basaltic (“spilitic”) volcanism (Vogt, 1981; Schneider, 1990; Hammel, 1996; Montenari *et al.*, 2002). The Upper Visean continental deposits of the Thann unit (Fig. 64) are represented by coarse-grained greywacke and conglomerate alternating with volcanic rocks that range from trachyte and andesite to rhyodacite and rhyolite (Coulon *et al.*, 1978). The sedimentary basins are surrounded by amphibole–biotite-bearing granite (“Crêtes” granite) and voluminous anatectic granite (Fig. 63) emplaced at *ca.* 340 Ma and *ca.* 326 Ma, respectively (Schaltegger *et al.*, 1996; Schaltegger *et al.*, 1999).

The deformation in the sedimentary units mostly involves folding of the primary bedding. In the allochthonous unit, Ruhland (1958) recognised N–S trending folds at the border of the massif, and dominant NW–SE trending folds in the centre. The NW–SE folding event is believed to be broadly coeval with granitic intrusions at *ca.* 340 Ma (Petrini & Burg, 1998). On the contrary, Krecher & Behrmann (2007) interpreted the structural record in the Southern Vosges basins as a result of southward thrusting followed by dextral transpression.

3) The Vosges Klippen Belt

Enigmatic occurrences of serpentinite and gabbro within sediments of the Southern Vosges have long been recognised (Delesse, 1847; Delbos & Kœchlin-Schlumberger, 1866). The first detailed description of the associated gneiss, conglomerates and pelites was proposed by Linck (1892). Later, von Seidlitz (1914) suggested a tectonic origin for these rocks, and Jung (1928) interpreted them as thrust-derived slices of deep parts of the allochthonous sedimentary basin. The latter author introduced the term Klippen Belt by analogy with the Pieniny Klippen Belt found in the Western Carpathians. The tectonic origin was contested

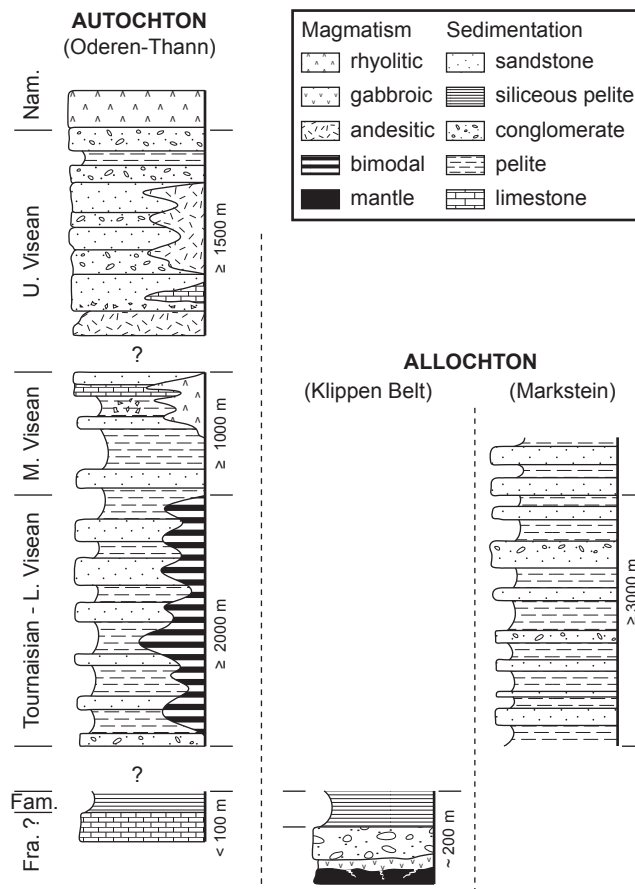


Figure 64. Lithostratigraphic columns of the Southern Vosges allochthonous and autochthonous units.

by Fluck (1987) who proposed that the contrasted lithologies represent olistoliths lying in a greywacke matrix. However, Wickert & Eisbacher (1988) observed shear criteria indicative of dextral strike-slip and thrusting. Based on a review of all klippen, Schneider *et al.* (1990) more recently distinguished between a tectonically-derived Klippen Belt to the West (LK1), and an alignment of resedimented conglomeratic lenses to the East (LK2) (Fig. 63).

The mineralogy of basic and ultrabasic rocks of the Klippen Belt was detailed by Weigand (1875) and Linck (1892). They observed that the serpentinite was originally harzburgitic in composition and may be linked with the presence of gabbroic rocks. Based on recalculated highly positive ϵNd values (+7.1 to +8.8), Pin & Carme (1988) proposed that the gabbroic rocks were probably derived from partial melting of a strongly depleted mantle source. Because the chemistry of both serpentinite and gabbro indicates a tholeiitic affinity, Kam (1983) suggested that these rocks may represent a fragment of an ophiolitic complex.

The age of the ophiolitic rocks has remained poorly investigated. Pin & Carme (1988) tried to constrain the age of the gabbroic material, but a Sm–Nd mineral isochron yielded a *ca.* 300 Ma age interpreted as late isotopic re-homogenisation. The only time constraints concerning the Klippen Belt were therefore derived from the paleontological records in pelites. Doubinger & Ruhland (1963) first used chitinozoans to propose an Early to Middle Devonian age, but conodonts found by Mass & Stoppel (1982) indicate that sedimentation more likely occurred during the Famennian. In addition, conventional U–Pb dating of detrital zircon in the pelites points to the existence of a magmatic or metamorphic event at *ca.* 386 Ma (Schaltegger *et al.*, 1996), i.e. close to the Givetian–Frasnian boundary.

Lithology

The klippen are dominantly composed of siliceous pelite and coarse-grained to conglomeratic greywacke with local occurrences of peridotite, gabbro and gneiss (Fig. 64). Detailed mapping (Fig. 63a–h, Tab. 11) reveals that a consistent succession is preserved, and involves ultrabasic to basic rocks and basement lithologies overlain by conglomeratic greywacke and fine-grained sediments. This superposition is only observed in the western klippen (Fig. 63a–f), i.e. in the LK1 after Schneider *et al.* (1990).

Ultrabasic rocks are represented by massive outcrops of serpentinitized peridotite. Some rocks have also been recognised for the first time as ophicalcite (Fig. 65a). Serpentinitized peridotite shows a typical ochre alteration and preserves abundant macroscopic serpentine and calcite veins. The intense serpentinitization leaves only few relicts of brownish spinel and orthopyroxene which suggest that the rock was originally of harzburgitic composition. Ophicalcite is observed either as the product of *in situ* fracturing of peridotite, or as pebbles

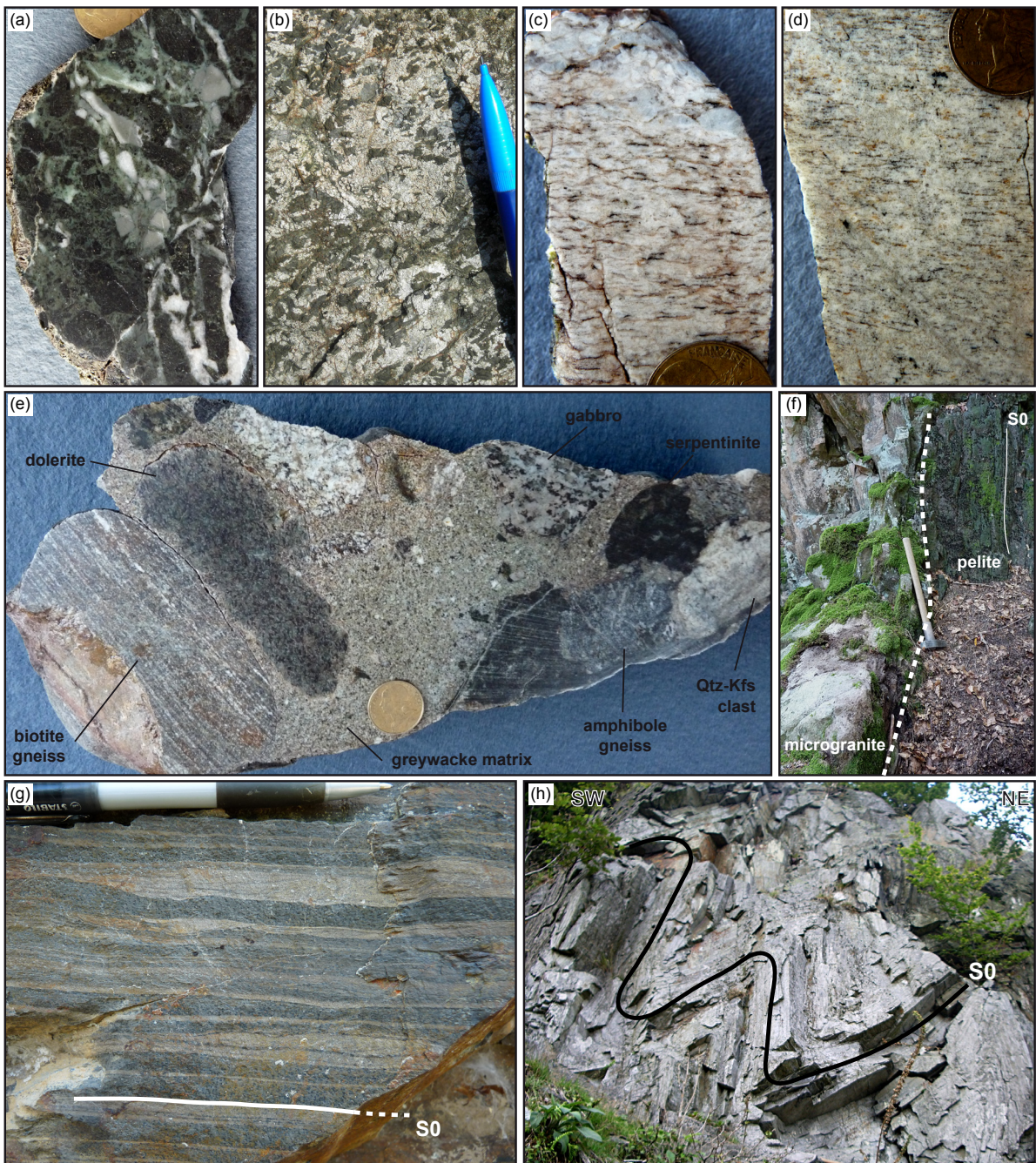


Figure 65. Photographs illustrating the lithologies of the Vosges Klippen Belt and structures in the surrounding sediments. (a) Ophicalcite, Treh klippe. (b) Gabbro showing a cumulative texture, (c) deformed metagranite, (d) mylonitic gneiss (“leptynite”) displaying a granulitic texture, and (e) polymictic conglomerate with contrasted types and shapes of pebbles, Thalhorn klippe. (f) Microgranite intrusion parallel to the subvertical bedding in the allochthonous unit. (g) Typical sedimentary bedding defined by alternating sandy and pelitic layers. Black spots in pelitic layers are due to contact metamorphism generated by the surrounding granite. (h) Upright folds affecting the bedding in the core of the allochthonous unit.

within the conglomeratic greywacke (respectively OC1 and OC2 after Lemoine *et al.*, 1987). It corresponds to clasts of serpentinized spinel-peridotite cemented by fine-grained calcite veins where detrital spinel is abundant.

Basic rocks occur as massive gabbro and dolerite, or as gabbroic and doleritic pebbles in the conglomerate. These rocks display a continuous evolution from a rare fine-grained doleritic texture to a widespread cumulative texture (Fig. 65b). Gabbro is composed of sericitized plagioclase, ortho- and clinopyroxene variably replaced by greenish amphibole, minor quartz and opaque minerals.

Basement rocks are found as isolated blocks or as pebbles in the conglomeratic greywacke. They are represented by weakly-deformed gneiss, mylonitic orthogneiss, garnet amphibolite or amphibole gneiss. The weakly-deformed gneiss (Fig. 65c) displays features indicative of cataclastic deformation and shows coarse-grained quartz–K-feldspar–plagioclase lenses surrounded by muscovite, few biotite, and small (0.25–0.5 mm) garnet. The mylonitic orthogneiss (so-called “leptynite”) exhibits a fine-grained, almost granulitic texture with large (1–7 mm) K-feldspar porphyroclasts and a small amount of biotite (Fig. 65d). Amphibolite is composed of green to brown hornblende, plagioclase, some garnet porphyroblasts (0.75–7 mm) and minor biotite and titanite.

The conglomerate covers large zones of the different klippen (Fig. 63). The matrix is a coarse-grained greywacke with quartz and plagioclase clasts surrounded by anastomosing bands of fine-grained quartz, chlorite, biotite and clay minerals. Occasionally, detrital pyroxene, amphibole or spinel are observed. The conglomerate is composed of cm-scale pebbles to m-scale blocks of all the above-described lithologies. Gneiss pebbles are commonly rounded, whereas gabbro or dolerite pebbles have a toothed shape, and ultrabasic rocks form only small angular clasts (Fig. 65e). The conglomeratic greywacke is locally strongly deformed showing significant grain size reduction, and in places it is difficult to distinguish between deformed massive blocks of gneiss or gabbro and the deformed greywacke and pebbles.

Fine-grained siliceous sediments generally overlie the conglomeratic greywacke and the exotic blocks. Whereas the upper yellowish siltstone may belong to the base of the overlying allochthonous unit, the lower red and green pelites (the so-called “Treh shales”) are a common feature of the Klippen Belt. They are finely-laminated siltstones that display a clear sedimentary bedding defined by alternating quartz-rich and clay-rich layers.

Microgranite does not strictly belong to the lithological succession, but is an important feature of the Klippen Belt. Several m-thick intrusive bodies of pinkish microgranite (Fig.

Table 11. Summary of lithologies from the different klippen.

	K1		K2		K3	K4	K5	K6		K7	K8
	Murb. S	Laut. S	Kruth	Sauwas	Thalhorn	Treh	Mark.	Arutsch	Renn.	Drumont	W.-A.
Sediments											
yellow siltstone	X			X	?	X	X	X			
red & green pelite				X		X	X				
conglomerate	X		X		X		X	X	X	X	X
- siltstone/pelite											X
- quartz	X				X						
- gneiss	X		X		X		X		X		X
- mylonitic gneiss	X										
- amphibolite					X		X				
- gabbro	X		X		X			X	X	X	
- serpentinite					X		X			X	
fine conglomerate, breccia		X									
Basement rocks											
gneiss				X	X	X	X	X			(3)
mylonitic gneiss					X						
amphibolite	X										(1)
Basic & ultrabasic rocks											
gabbro	X		X	X	X	(3)		X			X
dolerite	X				X						
serpentinized peridotite					X	X	X		(2)	X	
ophicalcite						X	X				
intrusive microgranite		X	X	X	X	X		X	X		

X: own observations ; numbers refer to lithologies reported by (1) Delbos & Kœchlin-Schlumberger, 1866; (2) De Billy; (3) Jung, 1928
 Abbreviations: Murb.S. = Murbach Sud; Laut.S. = Lautenbach Sud; Mark. = Markstein; Renn. = Rennenbachfels; W.-A. = Willer-Altrain

65f) are almost always found in the different klippen, and are commonly localised at their periphery (Fig. 63). In thin section, the microgranite exhibits abundant biotite phenocrysts (1–2.5 mm) which are partly chloritized, large (0.5–2 mm) actinolitic amphibole needles and rare anhedral quartz lying in a microcrystalline matrix.

Structural setting

The primary bedding (S0) is the dominant structure that can extensively be mapped in sediments around the Klippen Belt (Fig. 66a). It is also rarely observed in the fine-grained pelite in some klippen (Fig. 63). The sedimentary bedding is commonly defined by cm-spaced alternations of fine-grained sandy and pelitic material (Fig. 65g), by graded-bedding in coarse-grained greywacke, or by m-scale successions of greywacke and pelite beds. Structural mapping reveals two contrasted domains (Fig. 66a). A NW–SE striking bedding is dominant both in the core of the allochthonous unit (S0_{core}) and in the Klippen Belt, whereas a N–S striking, mostly subhorizontal bedding is observed at the border of the allochthonous unit and in the autochthonous unit (S0_{border}).

In the core of the allochthonous unit, the $S0_{\text{core}}$ bedding strikes NW–SE and variably dips either to the NE or SW. In few places, the sedimentary bedding is deformed by upright asymmetrical folds with subhorizontal hinges and subvertical axial planes (Fig. 65h). In a limited area to the South of the Klippen Belt, $S0_{\text{core}}$ strikes NW–SE but consistently dips towards the NE. This orientation is similar to that observed in pelitic sediments of the Klippen Belt (Fig. 63). The northern and western boundaries of the allochthonous unit preserve a N–S striking $S0_{\text{border}}$ bedding, moderately to steeply dipping to the E or W. Towards the East of the allochthonous unit and to the South of the Klippen Belt, the $S0_{\text{border}}$ strikes N–S, but is mostly subhorizontal. In this domain, a vertical section reveals that the contact between the autochthonous unit and the underlying “Crêtes” granite is nearly horizontal (Fig. 66c). Intrusions of amphibole–biotite-bearing microgranite are common in the allochthonous unit as well as around the Klippen Belt. The orientation of the m-scale intrusions is closely linked with the orientation of the folded bedding; they are dominantly parallel to the subvertical NW–SE striking $S0_{\text{core}}$ bedding planes (Fig. 65f) and only rarely crosscut the moderately dipping bedding.

The contrasted orientations of the primary bedding define a clear structural discontinuity to the South of the western Klippen Belt (Fig. 66a). It coincides with a limit between sedimentary rocks to the North and sediments with volcanic intercalations to the South. Both arguments are therefore used to redefine the boundary between the allochthonous and autochthonous units along this structural and lithological discontinuity (Fig. 66). The consistent orientation of $S0_{\text{core}}$ to the North of the boundary further suggests that the deformation was shared between the Klippen Belt and the surrounding allochthonous unit. It also implies that the Klippen Belt forms an integral, probably basal part of the allochthonous unit.

Geophysical constraints

A Bouguer anomaly map (Fig. 66b) was produced in order to evaluate the structural importance of the Klippen Belt lineament within the Southern Vosges. Gravity measurements were performed at 238 stations with an upgraded Lacoste-Romberg gravimeter (sensitivity: $2\mu\text{Gal}$). The map was calculated using a density of $2.67\text{ g}\cdot\text{cm}^{-3}$ for the Bouguer corrections. Terrain correction was calculated using a digital elevation model with a grid spacing of 75 m, to a maximum radius of 22 km. The station density is about 1.2 station/ km^2 . The dataset was converted into the International Gravity Standardization Net 1971 system (IGSN71).

The core of the allochthonous unit corresponds to a zone of relatively high density (Fig. 66b). It is potentially related to a thick pile of sediments. By contrast, the border of the allochthonous unit is related to zones of lower density that nearly coincide with the surface exposures of the surrounding granitic rocks (Fig. 66b). Similarly, the Klippen Belt is located on a low-density zone which can be correlated with a NW–SE trending branch of the “Crêtes” granite. It means that a granitic ridge occurs below the Klippen Belt and that the major boundary between the granite and the allochthonous sedimentary unit is slightly shifted towards the NE with respect to the surface boundary (Fig. 66c). It is also consistent with field observations showing that the roof of the “Crêtes” granite is subhorizontal. A similar observation can be made for the NNE–SSW branch of the granite body. The associated gravity anomaly being shifted towards the West, it is proposed that the “Crêtes” granite extends further West beneath the allochthonous unit (Fig. 66b).

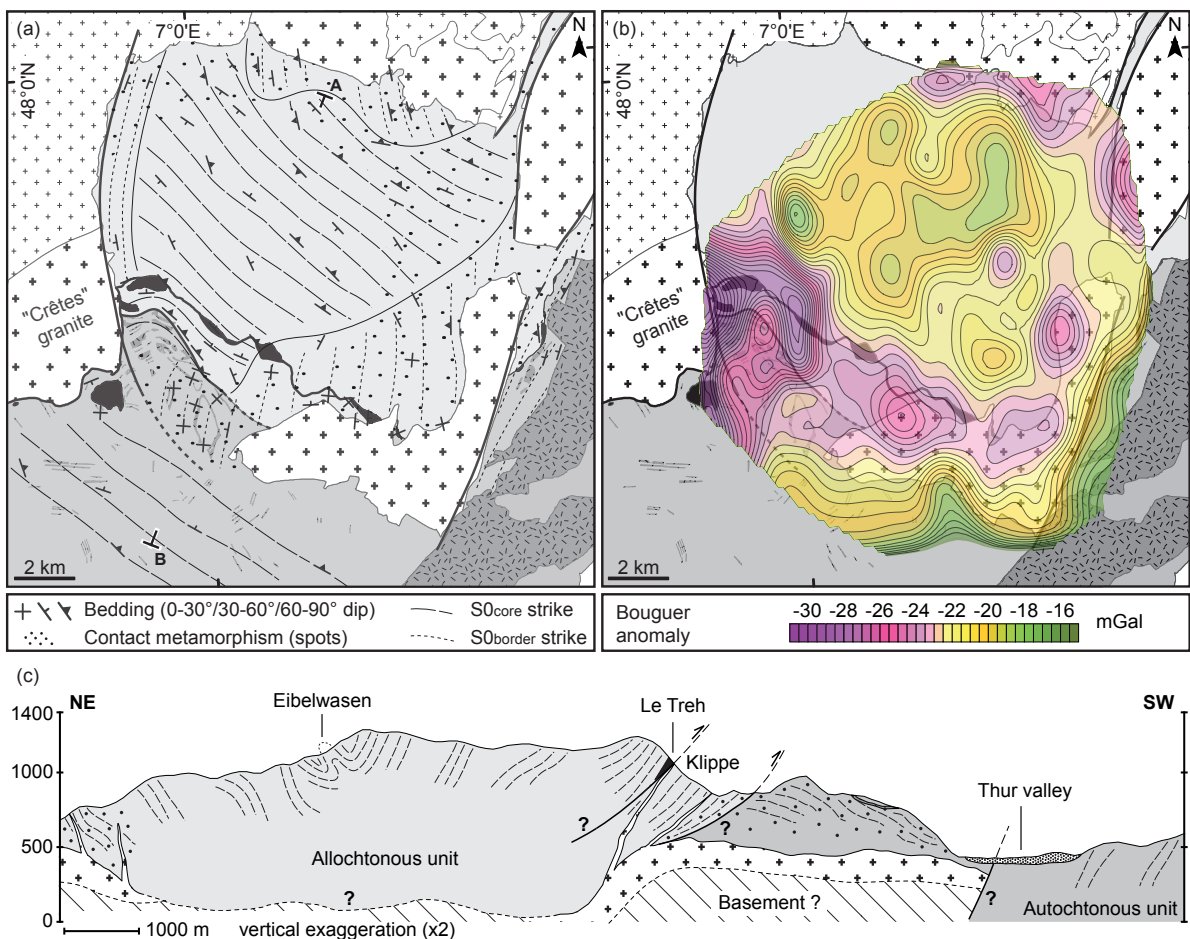


Figure 66. (a) Structural and (b) Bouguer anomaly maps of the Southern Vosges. (c) Interpretative cross-section through the Klippen Belt. The shape of the granite at depth is drawn after gravity data. (Bouguer anomaly grid acquired by J-B. Edel).

4) Petrology and geochemistry of gabbroic rocks

Analytical techniques

Detailed mapping of the various klippen was undertaken in order to carefully collect samples for geochemical analyses. Out of twenty four gabbro and dolerite samples, only two turned out to show fresh pyroxene in thin section (K1-30A and K2-21A). Accordingly, mineral compositions for these two gabbro samples were determined using a CAMECA SX 50 electron microprobe at BRGM Orléans, with accelerating voltage of 15 kV and beam current of 12 nA. Whole-rock compositions for six relatively fresh gabbro samples were determined at the University of Strasbourg. Fusion technique with lithium tetraborate was used and the molten bead was then digested in a weak nitric acid solution. Major elements were analysed by inductively coupled plasma atomic emission spectrometry (ICP-AES), while trace elements were determined by ICP mass spectrometry (ICP-MS). Mineral analyses are reported in Fig. 67 and Tab. 12, and whole-rock data are shown in Fig. 68 and Tab. 13.

Mineral chemistry

Gabbro consists of approximately equal proportions of relatively fresh clinopyroxene and sericitized plagioclase. It shows an equigranular to inequigranular texture, with large (1–2 mm) plagioclase grains and medium to large (0.5–1.5 mm) clinopyroxene crystals that host some rounded plagioclase inclusions.

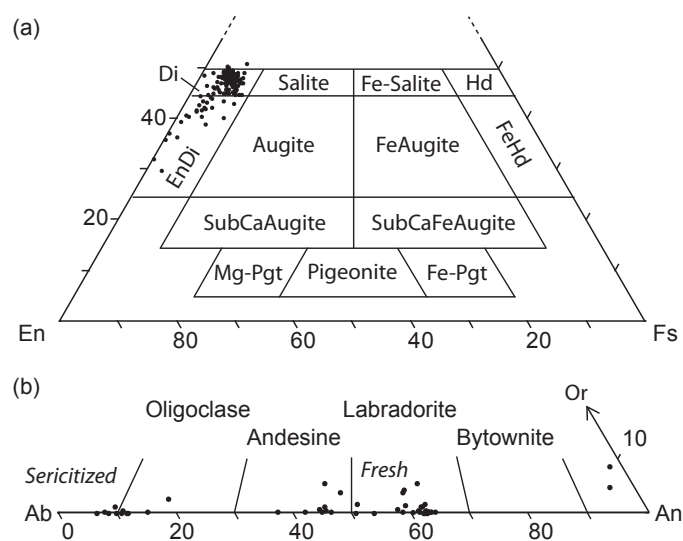


Figure 67. Mineral chemistry for (a) pyroxene and (b) plagioclase from gabbro samples. In the present chapter, mineral abbreviations follow IUGS recommendations after Kretz (1983).

Table 12. Representative mineral analyses of gabbro from the Vosges Klippen Belt.

Mineral	Plagioclase			Clinopyroxene	
	<i>fresh</i>	<i>fresh</i>	<i>sericitized</i>		
Sample	K2-21A	K2-21A	K2-21A	K1-30A	K2-21A
Wt.%					
SiO ₂	52.85	56.99	64.59	50.79	50.70
TiO ₂	0.02	0.01	0.01	0.87	0.76
Al ₂ O ₃	29.99	27.39	22.39	3.45	3.87
Cr ₂ O ₃	0.00	0.06	0.00	0.01	0.10
FeO ^T	0.17	0.18	0.01	6.59	6.79
MnO	0.00	0.06	0.00	0.35	0.24
MgO	0.02	0.09	0.00	14.53	14.90
CaO	13.40	9.32	3.15	24.02	23.45
Na ₂ O	4.41	6.30	9.93	0.35	0.37
K ₂ O	0.02	0.23	0.08	0.02	0.00
Total	100.90	100.60	100.20	101.00	101.20
Cations					
Si	2.37	2.54	2.84	1.88	1.87
Ti	0.00	0.00	0.00	0.02	0.02
Al ^{IV}	1.59	1.44	1.16	0.15	0.17
Cr	0.00	0.00	0.00	0.00	0.00
Fe ²⁺	0.01	0.01	0.00	0.20	0.21
Mn	0.00	0.00	0.00	0.01	0.01
Mg	0.00	0.01	0.00	0.80	0.82
Ca	0.65	0.45	0.15	0.95	0.92
Na	0.38	0.54	0.85	0.03	0.03
K	0.00	0.01	0.01	0.00	0.00
Σcations	5	5	5	4	4
Mg#				0.80	0.80
An	62.6	44.4	14.8		

Cations calculated of the basis of 8 oxygens for plagioclase and 6 for pyroxene

FeO^T=Total Fe expressed as FeO; Mg# = moles of cations Mg/(Mg+Fe^T);

An = anorthite content of plagioclase (mol.%).

Clinopyroxene composition corresponds to diopside (Fig. 67a, Tab. 12) with a high Mg# (0.76–0.82) and does not preserve core to rim chemical zoning. Minor element composition of clinopyroxene shows moderate Al₂O₃ (2.4–4.9 wt.%; Al^{IV}=0.10–0.30), moderate to low TiO₂ (0.39–1.05 wt.%), and low Cr₂O₃ (≤0.22 wt.%) and Na₂O (0.20–0.49 wt.%). Both matrix plagioclase and plagioclase inclusions have a homogenous composition (Fig. 67b, Tab. 12) ranging from labradorite (An₆₄) to andesine (An₃₇). Similarly to pyroxene, plagioclase crystals do not exhibit chemical zoning.

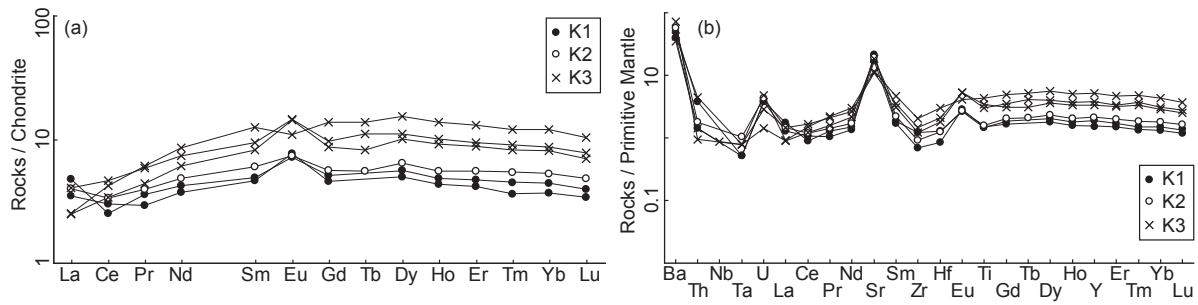


Figure 68. Chondrite- and primitive mantle-normalised trace element compositions of gabbro. Normalisation after Boynton (1984) and Sun & McDonough (1989), respectively.

Whole-rock geochemistry

Major element composition of gabbro shows weak variations of SiO_2 content (48–54 wt.%) and Mg# (0.69–0.76). The Rare Earth Element (REE) patterns (Fig. 68a) normalised to chondrite (Boynton, 1984) are generally characterised by Light-REE depletion ($\text{La}_N/\text{Sm}_N=0.20\text{--}0.71$), Eu positive anomalies ($\text{Eu}/\text{Eu}^*=1.27\text{--}1.69$), and nearly flat Heavy-REE trends ($\text{Dy}_N/\text{Yb}_N=1.28\text{--}1.35$). Only one sample (K3-14A) differs in having high concentrations of CaO, MnO, TiO_2 and ΣREE , and low concentrations of Al_2O_3 , Na_2O and Ba (Fig. 68 & Tab. 13). This sample is also characterised by a weak negative Eu anomaly ($\text{Eu}/\text{Eu}^*=0.82$). In primitive mantle-normalised diagrams (Sun & McDonough, 1989), some samples show Th and Nb anomalies. They exhibit pronounced positive Ba and Sr anomalies, enrichment in Th, U and Eu, and depletion in Zr and Hf relative to primitive mantle (Fig. 68b).

5) Geochronology

U–Pb zircon dating

Approximately 10 kg of gneiss were crushed and sieved, and the 100–315 μm fraction was processed using a Frantz magnetic separator and heavy liquids. Zircons were finally hand picked under a binocular microscope. U–Pb zircon analyses were carried out at BRGM Orléans using a LASER ablation system coupled with a Neptune multicollector ICP-MS (TermoFisherScientific). A new CETAC 213 nm UV laser was used allowing the U/Pb fractionation to be significantly reduced. The MC-ICP-MS was equipped with a multi-ion counting system (MIC) operating in static mode; all masses of interest were recorded simultaneously (^{202}Hg , ^{204}Pb , ^{206}Pb , ^{207}Pb , ^{208}Pb on ion-counters, and ^{232}Th , ^{238}U on Faraday cup collectors). Isotope ratios were normalised using the zircon standard 91500 from Ontario (1065 \pm 1 Ma; Wiedenbeck *et al.*, 1995). Detailed analytical conditions are described in Cocherie & Robert (2008) and Cocherie *et al.* (2009).

Table 13. Major and trace element compositions of gabbro from the Vosges Klippen Belt.

Sample	K1-17D	K1-30A	K2-21A	K3-14A	K3-30A	K3-30B
Major oxides (wt.%)						
SiO ₂	52.00	52.20	48.40	50.80	52.60	53.90
TiO ₂	0.29	0.30	0.31	0.86	0.60	0.68
Al ₂ O ₃	17.63	20.17	16.58	10.93	13.79	15.42
Fe ₂ O ₃ ^T	5.76	5.25	7.01	8.10	7.73	7.30
MnO	0.13	0.12	0.12	0.18	0.15	0.16
MgO	8.98	6.71	10.80	11.00	9.93	8.10
CaO	9.92	7.67	7.67	13.44	9.32	8.88
Na ₂ O	2.94	2.98	3.24	1.50	2.85	3.17
K ₂ O	0.99	1.98	0.96	1.07	0.90	1.46
P ₂ O ₅	0.10	<i>d.l.</i>	<i>d.l.</i>	<i>d.l.</i>	<i>d.l.</i>	<i>d.l.</i>
LOI	2.15	1.99	3.03	1.29	1.41	1.53
Total	100.90	99.36	98.12	99.17	99.27	100.59
Mg#	0.76	0.72	0.75	0.73	0.72	0.69
Trace elements (ppm)						
Ba	327	260	371	226	272	464
Rb	52	100	47	68	57	89
Cs	18	29	8	56	6	39
Sr	447	355	402	238	227	382
Pb	5	7	9	7	6	9
Th	0.32	0.12	0.15	0.12	0.37	0.08
U	0.08	0.08	0.09	0.1	0.06	0.03
Zr	13	8	10	22	16	13
Nb	<i>d.l.</i>	<i>d.l.</i>	<i>d.l.</i>	<i>d.l.</i>	0.08	<i>d.l.</i>
Y	8	8	10	22	16	14
Co	33	25	38	37	35	30
V	143	109	156	360	214	241
Ni	74	71	125	81	55	44
Cr	250	430	440	1880	560	530
Zn	60	120	70	90	60	60
Ta	0.02	0.02	0.04	0.03	0.03	0.03
Hf	0.38	0.25	0.37	0.89	0.62	0.53
<i>REEs</i>						
La	0.82	1.12	0.94	0.59	0.95	0.58
Ce	1.82	1.52	2.01	2.53	2.80	2.06
Pr	0.26	0.32	0.35	0.54	0.52	0.39
Nd	1.70	1.90	2.18	3.85	3.33	2.75
Sm	0.72	0.68	0.88	1.85	1.38	1.21
Eu	0.40	0.43	0.41	0.61	0.81	0.80
Gd	1.00	0.90	1.10	2.70	1.90	1.70
Tb	<i>d.l.</i>	<i>d.l.</i>	0.20	0.50	0.40	0.30
Dy	1.37	1.21	1.56	3.74	2.67	2.44
Ho	0.27	0.24	0.31	0.76	0.56	0.51
Er	0.75	0.66	0.88	2.07	1.50	1.40
Tm	0.09	0.07	0.11	0.29	0.22	0.20
Yb	0.69	0.60	0.82	1.96	1.40	1.31
Lu	0.07	0.06	0.09	0.25	0.19	0.17
La _N /Sm _N	0.71	1.03	0.67	0.20	0.43	0.30
Dy _N /Yb _N	1.33	1.35	1.27	1.28	1.28	1.25
Eu/Eu*	1.43	1.67	1.27	0.83	1.52	1.69
εNd		+ 12.6	+ 11.3			

FeO^T = Total Fe expressed as Fe₂O₃; LOI = loss on ignition; *d.l.* = below detection limit;

Mg# = molar Mg / (Mg+Fe^T); Eu/Eu* = Eu_N / (Sm_N x Gd_N)^{0.5}

Sample K2-16B is a gneiss which was collected at the klippe (Fig. 63c) cropping out near the locality Runsche [47°56'12.351"N; 6°58'37.17"E]. It belongs to a several m-scale block entirely surrounded by siliceous pelite and is therefore considered as representative for the continental basement found in the Klippen Belt. In thin section, coarse-grained quartz–K-feldspar–plagioclase–muscovite lenses are surrounded by brownish biotite-rich layers (Fig. 69a). Large secondary chlorite is common and small garnet is also present. Accessory minerals include tourmaline and zircon, the latter being mostly found within the biotite-rich layers (Fig. 69a inset).

Zircon crystals extracted from this sample are clear, mostly anhedral and poorly elongated (200–250 μm in size). Prismatic faces are only rarely observed and cracks are visible in some grains. Cathodoluminescence images reveal common patchy or oscillatory zoning and some rim overgrowths (Fig. 69b). U–Pb geochronological results are listed in Tab. 14 and plotted in Fig. 70 using Ispolot/Ex 3.1 program (Ludwig, 2004). Sixteen analyses were performed on nine zircon grains. Only one grain yielded a relatively young concordant age of

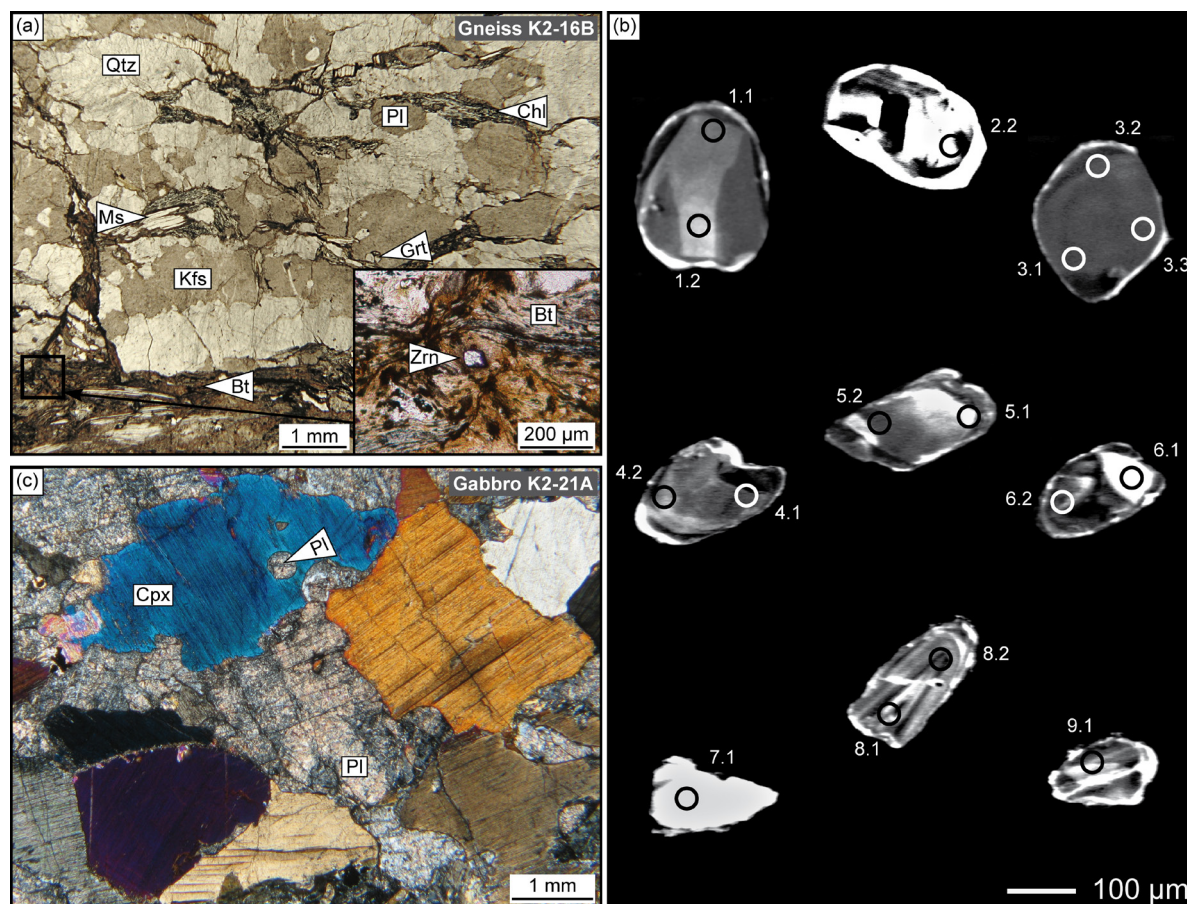


Figure 69. Representative images of rock samples and zircon crystals used for geochronology. (a) Photomicrograph of gneiss sample K2-16B, and typical position of zircon within the matrix (inset). (b) Cathodoluminescence images of analysed zircon crystals. Spot locations refer to analyses listed in Tab. 14. (c) Photomicrograph of gabbro sample K2-21A showing possible plagioclase inclusions in clinopyroxene.

Table 14. LA-MC-ICP-MS U–Pb zircon data for gneiss sample K2-16B.

Grain. point	U (ppm)	Th (ppm)	Th/U	²⁰⁶ Pb* (ppm)	²⁰⁶ Pb/ ²⁰⁴ Pb	f _{206%} [2]	Radiogenic ratios					r	Age (Ma)				Conc. % [3]			
							²⁰⁶ Pb/ ²³⁸ U ± [1]	²⁰⁷ Pb/ ²³⁵ U ± [1]	²⁰⁷ Pb/ ²⁰⁶ Pb ±	²⁰⁶ Pb/ ²³⁸ U ± [1]	²⁰⁷ Pb/ ²³⁵ U ± [1]		²⁰⁷ Pb/ ²⁰⁶ Pb ± [1]							
<i>Gneiss K2-16B</i>																				
1.1	213	17	0.08	104	17665	0.070	0.5652	0.0046	19.745	0.199	0.2534	0.0015	0.811	2888	19	3079	10	3206	9	90
1.2	104	9	0.09	47	7681	0.160	0.5288	0.0038	17.557	0.195	0.2408	0.0020	0.653	2736	16	2966	11	3125	13	88
2.2	70	19	0.27	5	-	-	0.0887	0.0006	0.724	0.007	0.0592	0.0004	0.737	548	4	553	4	575	14	95
3.1	574	8	0.01	172	12091	0.116	0.3458	0.0039	6.176	0.090	0.1296	0.0012	0.772	1914	19	2001	13	2092	16	92
3.2	446	5	0.01	145	76246	0.018	0.3768	0.0029	7.471	0.066	0.1438	0.0006	0.882	2061	14	2170	8	2273	7	91
3.3	208	3	0.01	70	-	-	0.3908	0.0045	8.745	0.112	0.1623	0.0009	0.907	2127	21	2312	12	2480	9	86
4.1	324	29	0.09	120	59769	0.024	0.4278	0.0031	9.639	0.081	0.1634	0.0007	0.856	2296	14	2401	8	2491	7	92
4.2	212	24	0.11	77	10528	0.134	0.4244	0.0042	9.823	0.123	0.1679	0.0013	0.790	2280	19	2418	11	2536	13	90
5.1	81	20	0.25	27	-	-	0.3868	0.0034	6.872	0.069	0.1289	0.0006	0.874	2108	16	2095	9	2082	9	101
5.2	227	74	0.33	72	-	-	0.3669	0.0032	6.569	0.063	0.1299	0.0005	0.899	2015	15	2055	8	2096	7	96
6.1	102	6	0.06	37	-	-	0.4252	0.0040	9.797	0.117	0.1671	0.0012	0.797	2284	18	2416	11	2529	12	90
6.2	560	17	0.03	99	23577	0.060	0.2035	0.0084	4.250	0.183	0.1515	0.0019	0.959	1194	45	1684	35	2363	21	51
7.1	35	5	0.14	13	7356	0.191	0.4481	0.0065	9.637	0.180	0.1560	0.0018	0.775	2387	29	2401	17	2412	20	99
8.1	243	28	0.11	104	-	-	0.4940	0.0042	11.811	0.112	0.1734	0.0008	0.888	2588	18	2590	9	2591	7	100
8.2	242	15	0.06	88	23891	0.059	0.4207	0.0049	8.684	0.117	0.1497	0.0010	0.871	2263	22	2305	12	2343	11	97
9.1	198	28	0.14	81	20592	0.067	0.4732	0.0047	10.826	0.127	0.1659	0.0010	0.851	2498	21	2508	11	2517	10	99

[1] Uncertainties given at 1σ level

[2] f_{206%} denotes the percentage of ²⁰⁶Pb that is initial Pb, using ²⁰⁴Pb correction (Stacey & Kramers, 1975)

[3] Concordancy %, 100% denotes a concordant analysis

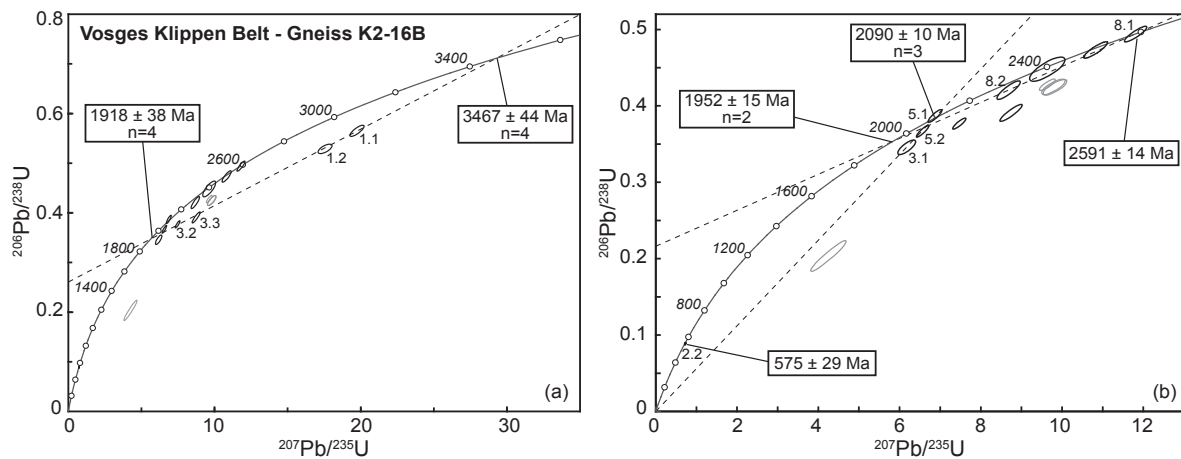


Figure 70. (a, b) U–Pb Concordia diagrams with age results for gneiss sample K2-16B of the Vosges Klippen Belt. Black ellipses denote concordant analyses or data used for Discordia calculations. Labels of analyses used for Discordia calculations are indicated. Error ellipses are plotted at 2σ level.

575±29 Ma (Fig. 70b). Besides, several inherited ages are documented by older concordant analyses or Discordias. The oldest ²⁰⁷Pb*/²⁰⁶Pb* age is given by the 1.1 spot analysis at 3206±19 Ma. More importantly, analyses from grains 1 and 3 (3.2 and 3.3) define a clear trend which does not pass through the origin. The upper intercept at 3467±44 Ma (MSWD=1.4) is interpreted as the crystallisation age of grains 1 and 3 while the lower intercept could document partial opening of the U–Pb system at 1918±38 Ma considering that the third spot analysis of grain 3 (3.1) reflects a recent slight Pb* loss (Fig. 70a). Grain 8 is younger, but also of Archaean age, the 8.1 spot analysis being perfectly concordant at 2591±15 Ma (Tab. 14). In addition, both analyses of the same grain (8.2 and 8.1) define a lower intercept at

1952±15 Ma which could be related to the above-mentioned event at 1918±38 Ma (Fig. 70a, b). Therefore, a significant event was recorded at about 1945 Ma. A second Palaeoproterozoic event is also precisely defined at 2090±10 Ma by an upper intercept (MSWD=0.74) of a Discordia anchored at the origin and derived from the sub-concordant 5.1, 5.2 and 3.1 spot analyses (Fig. 70b). The other analysed zircon grains could be of Archaean origin but are too discordant to give reliable ages.

Sm–Nd dating

Approximately 10 kg of gabbro were crushed and sieved, and the 100–160 µm fraction was processed using a Frantz magnetic separator after removal of the magnetic fraction. Plagioclase and pyroxene concentrates were further purified by hand picking under a binocular microscope. Approximately 100 mg of plagioclase and pyroxene concentrates were dissolved. REE extraction and separation between Sm and Nd was performed using ion exchange columns following the method of Richard *et al.* (1976). Whole-rock concentrations of Sm and Nd were measured by ICP-MS at ACME Laboratories (Vancouver), and mineral concentrations were measured on a Finnigan MAT 261 mass spectrometer at BRGM (Orléans). The Nd isotopic ratios were all obtained from a Finnigan MAT 262 mass spectrometer at BRGM (Orléans). The decay constant used for Sm is $\lambda^{147}\text{Sm}=6.54 \cdot 10^{-12} \text{ y}^{-1}$.

Sample K2-21A is a gabbro which was collected at the klippe (Fig. 63c) cropping out near the locality Runsche [47°56'11.41"N; 6°59'5.64"E]. In thin section, large zones of sericitized plagioclase alternate with clinopyroxene that tend to form aggregates and few chlorite veins occur. Rounded inclusions of plagioclase in pyroxene are observed (Fig. 69c),

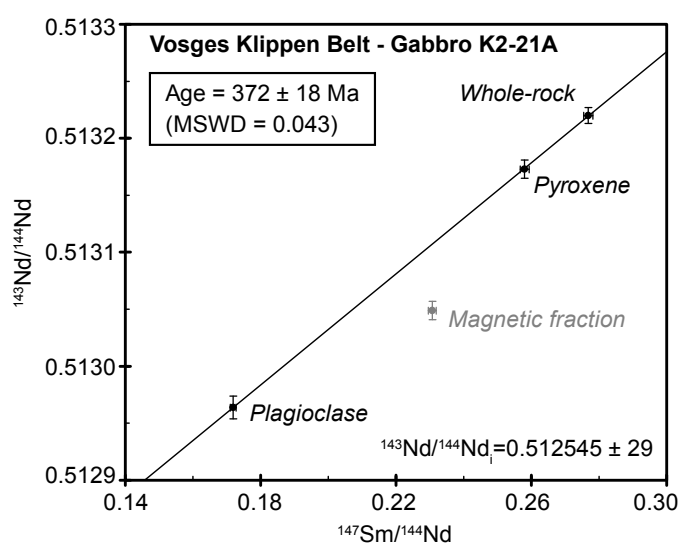


Figure 71. Sm–Nd isochron for gabbro sample K2-21A of the Vosges Klippen Belt.

Table 15. Sm and Nd concentrations, and isotopic ratios of gabbro sample K2-21A.

Material	Sm (ppm)	Nd (ppm)	$^{147}\text{Sm}/^{144}\text{Nd}$	$^{143}\text{Nd}/^{144}\text{Nd}$	2 σ
<i>K2-21A</i>					
Whole rock	0.99	2.16	0.27680	0.513220	0.000007
Plagioclase	0.17	0.59	0.17189	0.512964	0.000010
Pyroxene	1.17	2.75	0.25799	0.513173	0.000008
(Magnetic fraction)	0.89	2.34	0.23069	0.513049	0.000008

but small pyroxenes are also found within plagioclase crystals. The sample was selected for age dating because it does not show significant replacement of pyroxene by greenish amphibole.

The Nd isotope data are presented in Tab. 15 and Fig. 71. The Sm–Nd WR–mineral isochron yields an age of 372 ± 18 Ma (MSWD=0.043) which is interpreted as the igneous crystallisation of the gabbro. The $^{143}\text{Nd}/^{144}\text{Nd}$ initial ratio of 0.51254 ± 29 together with the initial $\epsilon\text{Nd}=+11.3$ suggest that the Klippen Belt gabbro was derived from a depleted mantle source. It should be noted that the whole-rock chemical analysis does not plot between plagioclase and pyroxene, probably as a result of an underestimated clinopyroxene ratio (Fig. 71). It is attributed to the presence of plagioclase inclusions in clinopyroxene (Fig. 69c).

6) Significance of the Southern Vosges Klippen Belt

Lithological significance

Detailed mapping and petrographic observations provide constraints on the origin of the lithologies from the Klippen Belt. The occurrence of serpentized spinel-harzburgite and of both types of ophicalcite (OC1 and OC2, Fig. 65a) points to an environment involving an altered and exhumed lithospheric mantle subsequently eroded and deposited in coarse-grained sediments. The mantle rocks are associated with a significant amount of gabbro. In addition, the observed basement lithologies (Fig. 65c, d) suggest that material from the continental crust was mixed with mafic rocks. Pebbles of oceanic and continental rocks are also found in a polymictic conglomerate (Fig. 65e), and all these lithologies are overlain by fine-grained siliceous deposits.

This lithological succession involving exhumed mantle, gabbroic intrusions and sedimentary breccias sealed by deep marine sediments is typical for Ligurian Tethys ophiolites (Lemoine *et al.*, 1987). More generally, it could be considered to represent a slow-spreading environment known as an ocean-continent transition (OCT) zone. In such a setting, the exhumed mantle is commonly brecciated and deposited in neighbouring depressions as a result

of mass flows on the slopes of submarine cliffs (Tricart & Lemoine, 1983). An OCT may also be characterised by the presence of allochthonous blocks of the continental upper crust over the exhumed mantle (Froitzheim & Manatschal, 1996), which could explain the occurrence of large gneissic blocks in the Klippen Belt. In this view, the polymictic conglomerate could be the result of submarine erosion of the juxtaposed continental and oceanic lithologies. Additionally, some authors have demonstrated that fossil OCT-type successions can be preserved inside orogenic belts, such as in the Western Alps (e.g. Manatschal & Müntener, 2009; Beltrando *et al.*, 2010). These arguments suggest that the Southern Vosges Klippen Belt may correspond to a dismembered fragment of the distal part of an OCT.

Tectonic significance

The tectonic significance of the Klippen Belt can be discussed using the distinction between the western (LK1) and the eastern (LK2) Klippen Belt already introduced by Schneider *et al.* (1990). To the South of the western Klippen Belt, a significant discontinuity has been evidenced. It marks the boundary between: (1) the klippen and the surrounding allochthonous sediments which show a folded NW–SE striking bedding, and (2) sedimentary and volcanic rocks of the autochthonous unit which preserve a subhorizontal N–S striking bedding (Fig. 66a). More precisely, NW–SE trending upright folds affect the core of the allochthonous unit, whereas the Klippen Belt and the southern allochthonous sediments show consistently NE-dipping bedding planes (Fig. 66c). Several authors (Wickert & Eisbacher, 1988; Schneider *et al.*, 1990; Krecher & Behrmann, 2007) have additionally observed shear criteria indicating thrusting along these NE-dipping planes. It is therefore proposed that the discontinuity represents a thrust surface which allowed to emplace the allochthonous unit onto the autochthonous unit (Fig. 66c).

Deformation involving folding and thrusting can be observed in the allochthonous unit. In the Rhenohercynian fold and thrust belt, Oncken *et al.* (Oncken *et al.*, 1999) demonstrated that contrasted deformation styles may depend, among other parameters, on the basement topography of the former sedimentary basin. In the present case, gravity data suggest the presence of a NW–SE low-density ridge below the Klippen Belt (Fig. 66b). It is in line with the idea that deformation could have been controlled by the pre-existing structures. Structural and geophysical arguments therefore support a tectonic origin for the western Klippen Belt (LK1) that may represent a large-scale duplex structure (Fig. 66c). In this view, the exotic rocks do not correspond to actual klippen, but to the discontinuous basal level of a thrust within the allochthonous unit. Only the Thalhorn body (Fig. 63b) which is entirely surrounded by sediments of the autochthonous unit would represent a true klippe. By contrast, the eastern Klippen Belt lacks a clear lithological succession and chiefly corresponds to small lenses of

conglomerate with rare exotic material. In addition, the structural pattern is similar in the eastern Klippen Belt and in the surrounding allochthonous and autochthonous units suggesting that no structural discontinuity occurs (Fig. 63g, h). This part of the Klippen Belt (LK2) therefore better corresponds to blocks which were resedimented during the Middle to Upper Viséan (Schneider, 1990).

Chronological constraints on the NE–SW shortening event have been proposed. The associated folding is thought to be nearly contemporaneous with contact metamorphism generated by the surrounding “Crêtes” granite (Petrini & Burg, 1998) at 340 ± 1 Ma (Schaltegger *et al.*, 1996). It is confirmed by the common emplacement of associated microgranite intrusions parallel to the subvertical NW–SE striking bedding (Fig. 65f). In the western Klippen Belt, the intrusions have been dated at 339.5 ± 2.5 Ma (Schaltegger *et al.*, 1996), further supporting the idea that the dominant deformation of the allochthonous unit occurred during the Middle Viséan, i.e. at *ca.* 340 Ma. Because the western Klippen Belt is oriented parallel to the surrounding NW–SE striking sedimentary bedding (Figs 63 & 66a), it is therefore proposed that the exhumation of the base of the allochthonous unit is related to a Middle Viséan NE–SW shortening event.

Geochemical significance

Geochemical data from gabbroic rocks are used to discuss the possible geodynamic settings associated with the Vosges Klippen Belt. Major and trace element compositions of gabbro suggest that the rocks are of cumulative rather than residual origin. In addition, chondrite-normalised REE diagrams show LREE depletion followed by flat HREE profiles at 10 times chondrite values (Fig. 68a), and Nd isotope geochemistry reveals highly positive $\epsilon_{Nd} = +11.3$ (Tab. 13). These observations are similar to those of typical N-MORB (Sun & McDonough, 1989; Arevalo & McDonough, 2010). Minor element composition of clinopyroxene and anorthite content in plagioclase (Fig. 67b) are similar to those of gabbro from the Atlantic Ridge (ODP leg 153; Cannat *et al.*, 1997) or from the SW Indian Ridge (ODP leg 176; Niu *et al.*, 2002). Whole-rock and isotope geochemistry is also comparable with results reported for the Early Devonian Lizard ophiolite (Davies, 1984; Floyd, 1984) which was interpreted as generated in a slow-spreading ridge environment (Roberts *et al.*, 1993; Cook *et al.*, 2002).

However, the primitive mantle-normalised trace element patterns show enrichment in Ba, Sr, Th, U and Eu (Fig. 68b). This has to be explained by contamination of the mantle source by typical continental elements (e.g. Plank & Langmuir, 1998), probably derived from fluids expelled from a subduction zone. Such contamination would not necessarily require significant Nb and Ta anomalies. Indeed, in western Pacific back-arc marginal basins, the

geochemical influence of the subduction zone decreases with increasing distance from the subduction through, i.e. with increasing maturity of the basin. The resulting primitive mantle-normalised trace element patterns show decreasing LREE enrichment and vanishing of the negative Nb and Ta anomalies (Auzende *et al.*, 1990). Such basins are also characterised by isotopic compositions (ϵNd and initial $^{143}\text{Nd}/^{144}\text{Nd}$ ratio) which are in the same range as those of N-MORB. According to these observations, it is proposed that gabbro from the Vosges Klippen Belt may have been emplaced in a mature spreading back-arc basin located relatively far from the subduction through.

Age significance

The Sm–Nd isochron on gabbro yields an age of 372 ± 18 Ma (Fig. 71), interpreted as its igneous crystallisation. Although more than 60 Ma can separate the opening of a basin from the age of the first sediments in an OCT (Wilson *et al.*, 2001), the Sm–Nd age is in good agreement with the Famennian (374.5 ± 2.6 to 359.2 ± 2.5 ; Gradstein *et al.*, 2004) record of the oldest sediments found in the Southern Vosges (Maass & Stoppel, 1982). It also lies close to the $^{40}\text{Ar}/^{39}\text{Ar}$ biotite cooling age of 382 ± 20 Ma obtained on a gneiss pebble from the autochthonous unit (Boutin *et al.*, 1995) which could indicate exhumation of the continental crust during rifting. In summary, the rifting event evidenced by OCT-type rocks of the Klippen Belt can be considered to have occurred during the Late Devonian.

Numerous large blocks of continental basement are found in the Klippen Belt. One sample has been studied in order to precise the origin of the basement and in order to evidence a possible eo-Variscan metamorphic overprint. U–Pb zircon geochronology indicates a range of Neoproterozoic to Archaean ages (Fig. 70). Because the coarse-grained texture of the gneiss sample suggests that it represents a weakly-deformed metagranite, the *ca.* 575 Ma age is interpreted as the igneous crystallisation of the protolith. It corresponds to a well-documented episode of continental crust production across the Variscan Belt of Europe (Zeh *et al.*, 2001). In addition, inherited ages indicate thermal events at *ca.* 1950 Ma, 2100 Ma and 3500 Ma (Fig. 70). Some of these ages lie close to inheritance already reported at *ca.* 600 Ma, 1900 Ma and 2000 Ma in metamorphic rocks of the Central Vosges (Schaltegger *et al.*, 1999), and at *ca.* 655 Ma and 2120 Ma in magmatic rocks of the Southern Vosges (Schaltegger *et al.*, 1996). The similar Precambrian ages therefore suggest that the central and Southern Vosges probably belonged to the same continental block which was subsequently rifted during the Late Devonian. Consequently, the basement rocks juxtaposed with the oceanic material can either correspond to a shoulder of the nearby continental rifted margin, or to allochthonous blocks that are commonly reported in OCT environments.

Geodynamic evolution of the Southern Vosges

Combined lithological, geochemical and geochronological data for the Vosges Klippen Belt indicate the opening of a basin during the Late Devonian (Fig. 72a). Significant thinning of a Neoproterozoic basement resulted in the formation of a rifted margin associated with an ocean-continent transition zone towards the South. Exhumed mantle and basic magmatism point to a slow-spreading environment with probable characteristics of a back-arc setting located relatively far from the subduction zone. The southern conjugate margin of the basin could be represented by Middle to Late Devonian sediments found farther to the South. There, the presence of trilobite, crinoid and ammonoid fauna (Chevillard, 1866; Asselberghs, 1926) in Famennian deposits indicates a platform environment, suggesting that this part of the margin was probably much less attenuated than the northern one (Fig. 72a).

The basin was subsequently filled by thick siliciclastic turbiditic series until the Lower Visean (Fig. 72b). This episode of flysch-type sedimentation is already associated with closure of the system, as indicated by common sedimentary instabilities (Schneider,

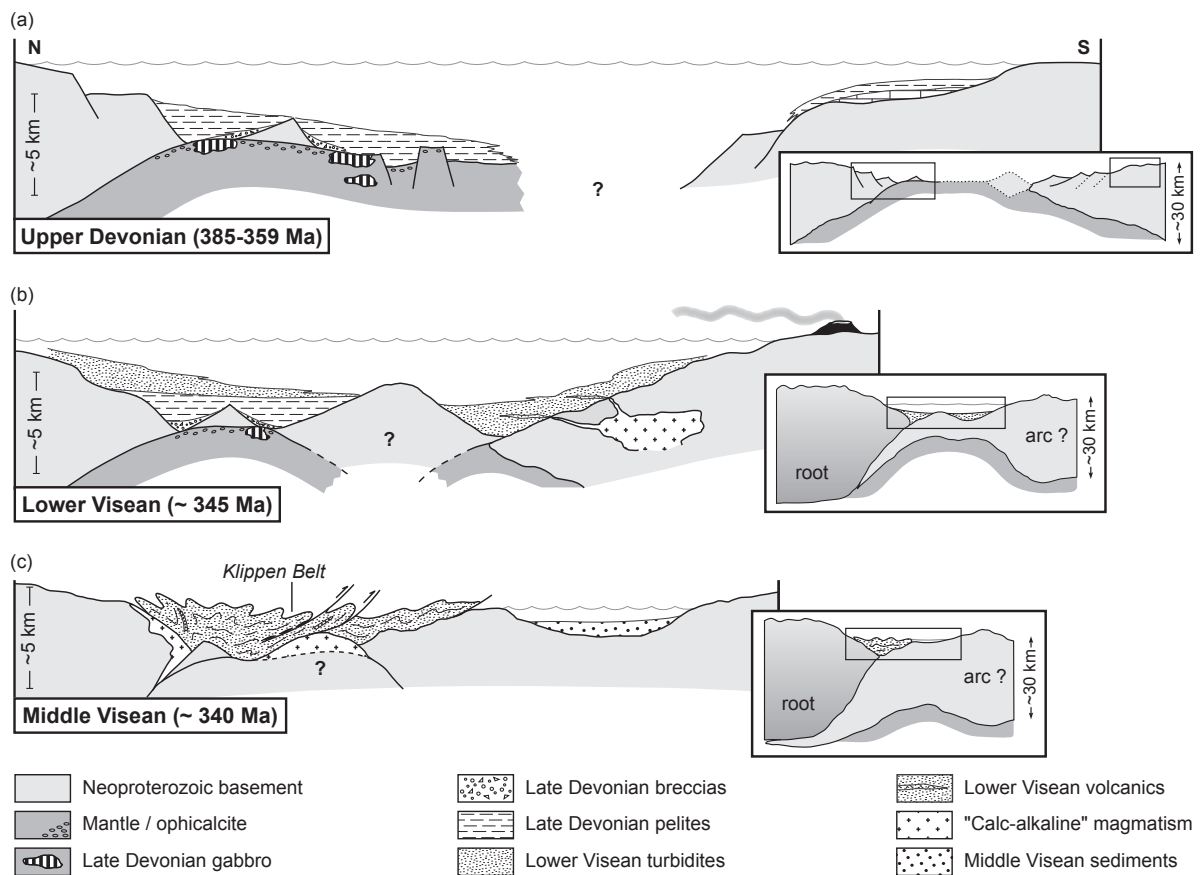


Figure 72. A possible geodynamic scenario for the Southern Vosges. (a) Late Devonian rifting and basin formation. (b) Lower Visean sedimentary (northern basin) and volcano-sedimentary (southern basin) deposits. (c) Middle Visean basin inversion, exhumation of the Klippen Belt and magmatism. Insets show the general framework from intracontinental rifting to final collision with the northern root zone.

1990). Therefore, the northern part of the basin corresponded at that time to an important topographic high developed above an already existing thickened orogenic root (Schulmann *et al.*, 2002). In the southern part of the basin flysch sediments are interlayered with abundant volcanic rocks, whereas the northern part of the basin clearly lacks volcanic material. Both areas can be considered as the proximal and distal parts of the same basin which shows increasing volcanic activity towards the South. It is supported by the occurrence of a plutonic complex (the “Ballons” granitoids) to the South of the autochthonous unit. Conversely, the absence of volcanic rocks in the northern part has been explained by the possible existence of a topographic high between the two basins (Schneider, 1990). It could be represented by a continental block isolated during rifting (Fig. 72b), a feature called “upper-crustal megaboudin” by Davis & Hardy (1981). Considering that the gravity anomaly map reveals the presence of a prominent block beneath the Klippen Belt, the proposed geodynamic reconstruction favours the occurrence of a basement high which was subsequently accreted to the inverted rifted margin (Fig. 72).

The deformation pattern in the Southern Vosges indicates folding and thrusting of the allochthonous unit over the autochthonous one. Structural observations indicate that folding of the sedimentary basins occurred during the Middle Viséan (Fig. 72c) and was nearly contemporaneous with the intrusion of granitic magmas in large portions of the basement (Petrini & Burg, 1998). During the dominantly NE–SW horizontal compression event, slices from deep parts of the basin were exhumed and formed the Vosges Klippen Belt. The coincidence of a gravity low with the thrust-related Klippen Belt may indicate the presence of a rigid basement obstacle at shallow depth (Fig. 72c). It is therefore proposed that the whole sedimentary basin was thrust over the rigid basement promontory, thereby producing strong deformation in the hinterland and an important deformation gradient towards the sole thrust. Because numerous microgranite sills are emplaced parallel to the folded bedding in sediments, this thrusting could have also been lubricated by syntectonic magmas (e.g. Hollister, 1993).

6) Significance in the Variscan Belt of Europe

Origin of the Southern Vosges basin

The basin evidenced in the Southern Vosges could be related to several Variscan events. It could represent: (1) a late ramification of the Rhenohercynian basin or a back-arc basin related to the Rhenohercynian subduction, (2) a back-arc basin connected with the northern Saxothuringian subduction, or (3) a back-arc basin linked with the southern Palaeotethys subduction.

The suggested evolution involving inversion of Devonian–Early Carboniferous basin sequences and thrusting of allochthonous sedimentary units over autochthonous units bears similarities to a Rhenohercynian evolution (e.g. Holder & Leveridge, 1986). There, Early Devonian ophiolites and sedimentary basins are inverted and covered by Middle Devonian to Early Carboniferous flysch sediments (Fig. 73). However, the geochemistry of gabbroic rocks indicates the influence of a subduction zone and probably rules out the origin of the Vosges basin as a late extension of the Rhenohercynian basin. Alternatively, because closure in the

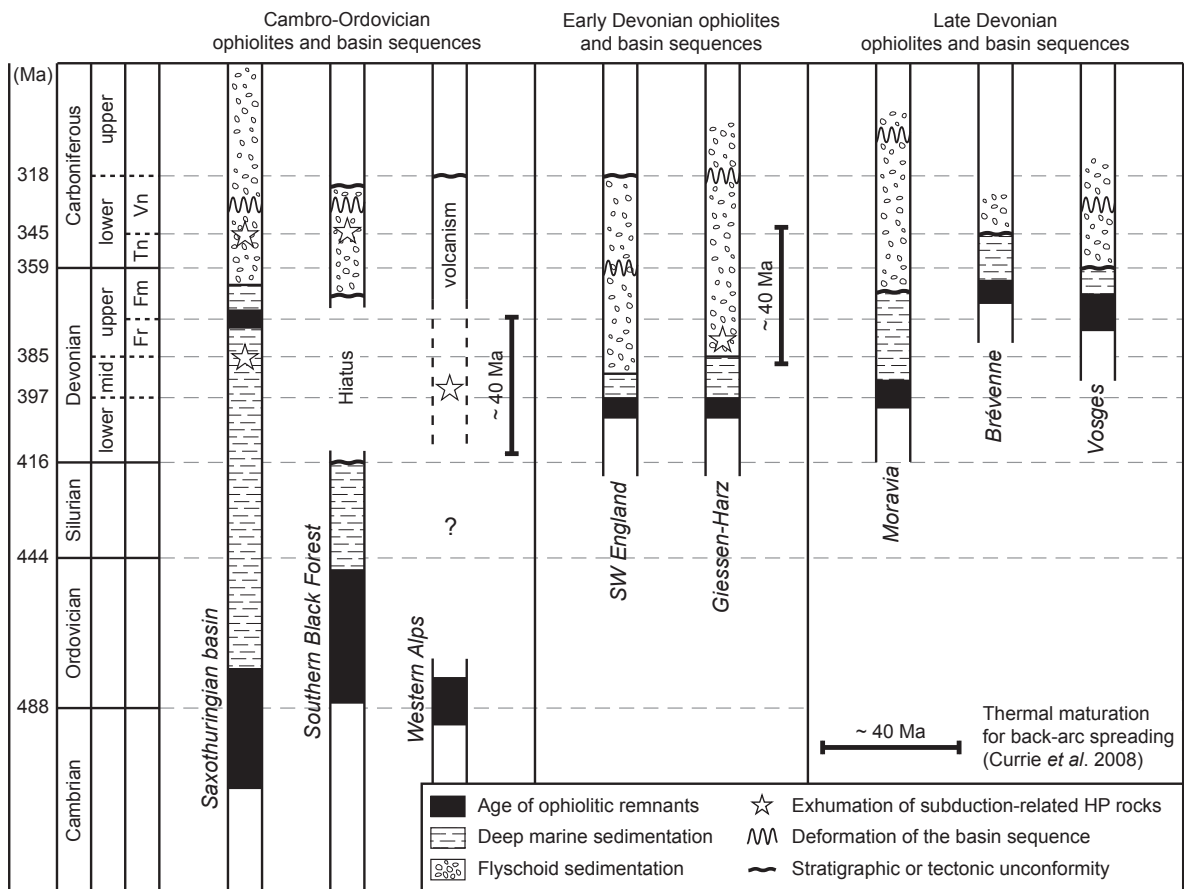


Figure 73. Chronological relationships between the different types of Palaeozoic basin sequences. For references, see text.

Rhenohercynian system starts in the Middle Devonian (Franke, 1995), the Late Devonian Vosges basin could then be viewed as the associated back-arc system. Nevertheless, Currie *et al.* (2008) showed that a minimum of ~40 My is required to bring the 1200 °C isotherm to a depth of 60 km in a back-arc basin environment. A subduction of the Rhenohercynian basin is therefore more likely to trigger extension during the Carboniferous (Fig. 73). In addition, calc-alkaline magmatism at *ca.* 335 Ma in the Northern Vosges (Altherr *et al.*, 2000) most likely reflects the magmatic arc related to this event. The age of arc magmatism coincides with a major extension associated with partial melting and emplacement of sheeted intrusions in the southern high-grade core zone of the Vosges (Rey *et al.*, 1992; Kratinová *et al.*, 2007; Schulmann *et al.*, 2009a). It is therefore the central part of the Vosges Mountains that probably recorded the extensional and high temperature event associated with the southward subduction of the Rhenohercynian basin.

The timing of the northern Saxothuringian and the southern Palaeotethyan systems is markedly different from that of the Rhenohercynian one (Fig. 73). Both zones comprise Cambro-Ordovician ophiolitic remnants (e.g. Paquette *et al.*, 1989; Bowes & Aftalion, 1991; Kalt *et al.*, 1994) covered by Ordovician to Silurian-Devonian sediments (Franke, 1984; Hann & Sawatzki, 1998), but also HP rocks exhumed during the Devonian (e.g. Timmermann *et al.*, 2004; Guillot & Ménot, 2009). These records indicate that Cambro-Ordovician basins started to be inverted in the Devonian (Fig. 73). Using the previously mentioned results of Currie *et al.* (2008), these evolutions could be concordant with the generation of back-arc basins during the Late Devonian (Fig. 73). Therefore, the Southern Vosges basin probably represents a back-arc environment associated with the subduction of an Early Palaeozoic oceanic realm. It could be either the South-directed subduction of the Saxothuringian basin recognised to the North of the Vosges (Edel & Schulman, 2009), or the North-directed subduction of the Palaeotethys Ocean proposed in the French Massif Central and in the Western Alps (Lardeaux *et al.*, 2001; Guillot & Ménot, 2009).

A tentative link

The present results can be compared to existing data for Variscan massifs located to the South of the Vosges Mountains. In the Western Alps as well as in the French Massif Central (Monts du Lyonnais), Siluro-Devonian closure of an oceanic domain and HP metamorphism is documented (Paquette *et al.*, 1989; Lardeaux *et al.*, 2001). In addition, prolonged arc magmatism from Silurian up to Carboniferous is proposed in the southern Black Forest (Loeschke *et al.*, 1998; Hegner *et al.*, 2001; Hann *et al.*, 2003), and Late Devonian back-arc spreading is inferred from for the Brévenne Séries in the NE French Massif Central (Pin &

Paquette, 1997; Leloix *et al.*, 1999). Spatial, geochemical and geochronological constraints indicate that the Southern Vosges fit in this geodynamic evolution, the only difference with the Brévenne Séries lying in the geochemical signature of basic rocks. Because the Brévenne Séries preserves a stronger geochemical influence of the subduction zone than the Southern Vosges (Pin & Paquette, 1997), the former can be considered as an incipient basin, whereas the latter may represent a mature, probably slightly older and larger basin. Consequently, the Southern Vosges lithologies most likely correspond to a back-arc basin located within a continental block of Teplá-Barrandian–Moldanubian affinity, and resulting from the North-directed subduction of the Palaeotethys Ocean (e.g. Finger & Steyrer, 1990).

More generally, it is proposed that Late Devonian back-arc basins which opened across Teplá-Barrandian–Moldanubian-type domains are linked with subduction of the Palaeotethys Ocean during general closure of the Variscan system. However, the back-arc basins recognised in Moravia (e.g. Patočka & Valenta, 1996) and South Iberia (e.g. Ribeiro *et al.*, 2010), which bears similarities to the Rhenohercynian zone, may have a different origin. Notwithstanding, the Late Devonian oceanic domains can be seen as small back-arc marginal basins which developed at the front of a large closing ocean. Such back-arc basins have also been proposed at the northern periphery of the Neotethys (e.g. Stampfli & Borel, 2002). From that perspective, the Variscan system does not seem to have been much different from the more recent Neotethyan evolution.

CHAPTER II

THE ORIGIN OF ZIRCON AND THE SIGNIFICANCE OF U–Pb AGES DURING HIGH-GRADE METAMORPHISM: A CASE STUDY FROM THE VARISCAN OROGENIC ROOT (VOSGES MOUNTAINS, NE FRANCE)

During orogenesis, the continental crust may experience high-grade metamorphism, the initiation, end and hence the duration of which remain unclear. Particularly appealing is, however, that such a process is associated with a recurrent, almost unique, time span of 340–335 Ma in different high-grade metamorphic rocks of the Variscan belt of Europe (e.g. Vosges, Schaltegger *et al.*, 1999; SE Bohemia, Kröner *et al.*, 2000a; Black Forest, Kober *et al.*, 2004; Sudetes, Lange *et al.*, 2005). Because this estimate has been taken as the age of peak pressure conditions, the small difference with $^{40}\text{Ar}/^{39}\text{Ar}$ cooling ages of 340–330 Ma led to the interpretation that exhumation rates were relatively fast (e.g. Schulmann *et al.*, 2002). It may, however, not be the case if the 340–335 Ma age actually represents a later stage of the tectonic evolution. Such an example therefore illustrates the general importance of constraining the timing of high-grade metamorphism, which is all the more essential, since it may give additional information on its driving process as well as on possible exhumation mechanisms.

The key when trying to assess the timing of eclogite- or granulite-facies metamorphism involves a strong link between the widely used U–Pb zircon dating method and zircon petrogenesis. It is why much attention was paid to the possible growth mechanisms of zircon in high-grade rocks, and efforts have been made to propose associated diagnostic features. Some works focused on the origin of zircon through metamorphic reactions involving the *breakdown of relatively Zr-rich phases*. Provided that the other product phase(s) of such reactions do not incorporate Zr, it is proposed that zircon can form after the breakdown of garnet (Degeling *et al.*, 2001; Bingen *et al.*, 2004), biotite (Vavra *et al.*, 1996), hornblende (Fraser *et al.*, 1997), ilmenite (Bingen *et al.*, 2001), or zirconolite (Pan, 1997). Further considering that new zircon nucleates relatively close to the reaction site (Degeling *et al.*, 2001), the observation of zircon rims around source minerals (Pan, 1997; Bingen *et al.*, 2001) could serve as a good indicator for this type of zircon growth. *Solid-state recrystallisation of existing zircon* has also been invoked as an important zircon-forming mechanism, especially in rocks which experienced high temperature (HT) metamorphism. It is generally associated with the fading (Pidgeon, 1992) to the complete disappearance of the original oscillatory zoning (Hoskin & Black, 2000), probably along curved reaction fronts (Schaltegger *et al.*,

1999), and may result in element migration (Pidgeon, 1992) or averaging of the U and Th concentrations (Black *et al.*, 1986). In addition, *zircon growth in the presence of anatectic melt* has been proposed by studies using the distribution of rare earth elements (REE) in zircon (Schaltegger *et al.*, 1999; Rubatto, 2002; Hermann & Rubatto, 2003; Whitehouse & Platt, 2003) or thermodynamic modelling (Roberts & Finger, 1997). This phenomenon requires preliminary dissolution of Zr-bearing phases, the most obvious being zircon, and subsequent recrystallisation governed by Zr saturation in the melt phase (Watson & Harrison, 1983). Such a process is probably best exemplified by the prominent zircon overgrowths with relatively uniform cathodoluminescence (CL) patterns reported by e.g. Vavra *et al.* (1999).

Considering the wide range of zircon growth mechanisms which are proposed, it is not surprising to see that the zircon ages have been related to different stages of metamorphism. In few examples, the presence in zircon of relict minerals suggesting dehydration melting has been used to demonstrate that zircon dates *prograde metamorphism* reaching the conditions of partial melting (Hermann & Rubatto, 2003). In other cases, U–Th and REE chemistry revealed that zircon growth was contemporaneous with a reaction producing a high-pressure (HP) assemblage (Bingen *et al.*, 2001), or even with the crystallisation of eclogite-facies minerals (Rubatto, 2002; Bingen *et al.*, 2004; Bröcker *et al.*, 2010). The associated U–Pb ages have therefore been interpreted as reliable estimates for *peak pressure* conditions. Conversely, ages obtained on zircon domains produced by solid-state recrystallisation of protolith zircon (Hoskin & Black, 2000), or on zircon overgrowths due to contact metamorphism (Möller *et al.*, 2002) are more generally correlated with the age of *peak temperature* metamorphism in granulitic rocks. When the origin of zircon can clearly be associated with a reaction involving mostly pressure decrease, such as the kyanite/sillimanite transition (Whitehouse & Platt, 2003) or the sillimanite to cordierite reaction (Degeling *et al.*, 2001), it is obvious that zircon ages should reflect *decompression*. Finally, following the idea that in partially molten rocks, zircon crystallises from melt along a retrograde path (Roberts & Finger, 1997), the associated ages should therefore correspond to *cooling* during waning high-grade metamorphism.

In the present study, the relationships between U–Pb zircon ages and high-grade metamorphism are explored in the Variscan orogenic root which is exposed in the Vosges Mountains (NE France). Three lithological units are investigated: the “monotonous gneiss”, the “varied gneiss” and the “felsic granulite” units. For each unit, the morphology, U–Th chemistry and internal structure of zircon populations are examined, and U–Pb dating is performed using a LASER ablation device connected with a multicollector inductively coupled plasma mass spectrometer (LA-MC-ICP-MS). Because the “monotonous gneiss” unit does not show Variscan ages, only the “varied gneiss” and “felsic granulite” are subject to

further petrological investigations. Due to possible melt loss associated with partial melting, a thermodynamic modelling approach involving melt re-integration (Štípská *et al.*, 2008) is used in order to assess the P – T evolution of these two units. In addition, the consequences of these P – T evolutions on zircon behaviour are investigated using the activity–composition models recently established by Kelsey & Powell (2011). All observations and analyses are used to discuss the metamorphic evolution of the orogenic root, the possible mechanisms of zircon growth during Variscan orogeny, and the geological meaning of the coupled geochronological and petrological records.

1) Geological background

In the Variscan Belt of Europe, exposures of the high-grade orogenic root can be nearly continuously followed from W to E. They occur in the Armorican Massif, the French Massif Central, in the Vosges and Black Forest Mountains as well as in several parts of the Bohemian Massif (Fig. 74a). The Vosges Mountains (NE France) exhibit only a relatively small zone of high-grade lithologies surrounded by more voluminous granites and Devonian–Carboniferous (volcano)-sedimentary basins to the North and to the South (Fig. 74b). The medium- and high-grade metamorphic rocks chiefly crop out in the Sainte-Marie-aux-Mines valley (Central Vosges Mountains) and are intruded by different Carboniferous granites (Fig. 74c).

The lithology of the Central Vosges metamorphic rocks was initially detailed by Groth (1877), and later von Eller (1961) distinguished between three major units (Fig. 74c) that he correlated with rocks of the Moldanubian zone (e.g. Zoubek, 1946):

(a) the “monotonous” gneiss unit, mostly found in the eastern part, is composed of biotite–sillimanite, partly migmatitic, paragneiss,

(b) the “varied” gneiss unit corresponds to a NE–SW trending belt of thick basal amphibolite overlain by garnet–biotite gneiss with scarce intercalations of quartz-rich gneiss (“leptynite”) and crystalline limestone (Fluck, 1980),

(c) the granulite unit, narrowly exposed in the SW part of the area and composed of felsic granulite with local occurrences of mafic granulite.

In addition, numerous slices of spinel- or garnet-bearing peridotite can be found across the whole Central Vosges, but they mostly occur in the felsic granulite unit. The gneissic and granulitic units are also frequently intruded by biotite–amphibole-rich melasyenite, commonly known as durbachite in the Variscan Belt of Europe.

The metamorphic evolution of the Central Vosges has generally been described in terms of an older MP–HP/HT metamorphism strongly obliterated by a dominant LP–MP/HT metamorphic event (Rey *et al.*, 1989; Latouche *et al.*, 1992). In the monotonous unit,

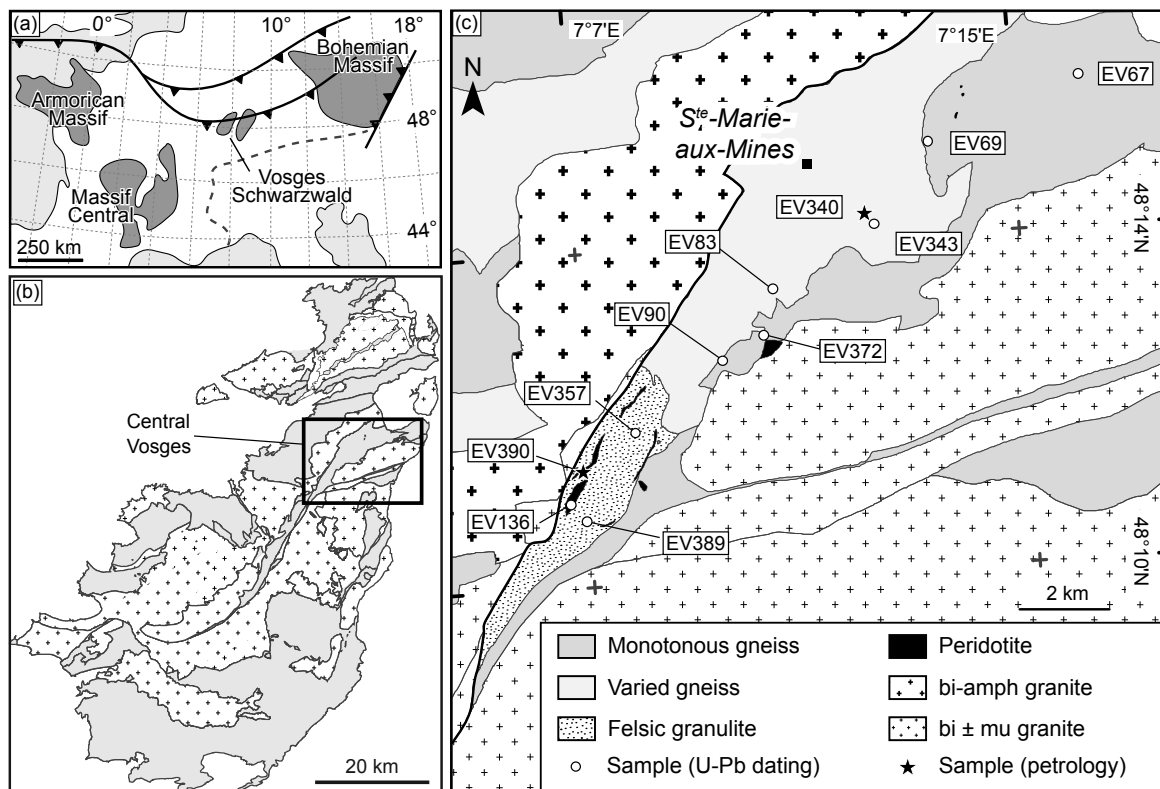


Figure 74. Geology of the Vosges orogenic root and position in the Variscan framework. (a) Location of the Vosges in the Variscan Belt of Europe. (b) Simplified map of the Vosges Mountains. (c) Geology of the Central Vosges Mountains and location of samples used for geochronology and petrology.

staurolite and kyanite relicts are used by Rey *et al.* (1992) to propose prograde metamorphism from ~ 7 kbar/620 °C to peak conditions not exceeding ~ 9 kbar/700 °C, whereas widespread sillimanite and cordierite indicate a retrograde overprint at ~ 4 kbar/680 °C. The peak P – T estimates of 7–9 kbar/750–800 °C (Fluck, 1980; Rey *et al.*, 1989) obtained in the varied gneiss unit are followed by retrograde conditions below 5 kbar and 650 °C which are nearly similar to those in the monotonous unit (Rey *et al.*, 1989; Latouche *et al.*, 1992). Regarding the felsic granulite, peak P – T conditions were thought to lie below 11 kbar at 800 °C (Pin & Vielzeuf, 1988), but Gayk & Kleinschrodt (2000) showed that granulitic rocks in contact with peridotites may have reached 12–15 kbar and 700–800 °C before being exhumed to 3 kbar at temperatures lower than 400 °C. Garnet peridotite slices are believed to record equilibration at P – T conditions higher than 49 kbar and 950 °C, and subsequent isothermal decompression towards 10 kbar/700–1000 °C when emplaced in the granulitic lower crust (Altherr & Kalt, 1996).

Protolith ages for the three major units are only poorly known. By analogy with the Bohemian Massif, the monotonous and varied gneisses have been interpreted as derived from sediments deposited during the Precambrian (e.g. von Eller, 1961). It could be corroborated

by the youngest inheritance of *ca.* 600 Ma obtained on zircon cores from the varied gneiss unit (Schaltegger *et al.*, 1999). For the granulite unit, a Rb–Sr WR isochron on felsic and mafic granulites yielded 595 ± 16 Ma which is considered as the age of the volcanic precursors (Bonhomme & Fluck, 1981). This result lies close to the age of inherited magmatic zircon cores which yield *ca.* 620 Ma (Schaltegger *et al.*, 1999). Besides, several metamorphic ages point to a major Lower Carboniferous event. U–Pb SHRIMP analyses on zircon from the felsic granulite, the varied gneiss and a leucosome from the varied gneiss unit all yield consistent ages between 335 and 325 Ma. Similarly, conventional U–Pb dating of zircon and monazite indicate a dominant event at *ca.* 335 Ma (Schaltegger *et al.*, 1999), which is coeval with the emplacement of durbachitic magmas at 332 ± 3 Ma (Schulmann *et al.*, 2002). Subsequent cooling of the whole metamorphic unit is documented by $^{40}\text{Ar}/^{39}\text{Ar}$ ages on amphibole and biotite which cluster around 340–330 Ma (Boutin *et al.*, 1995).

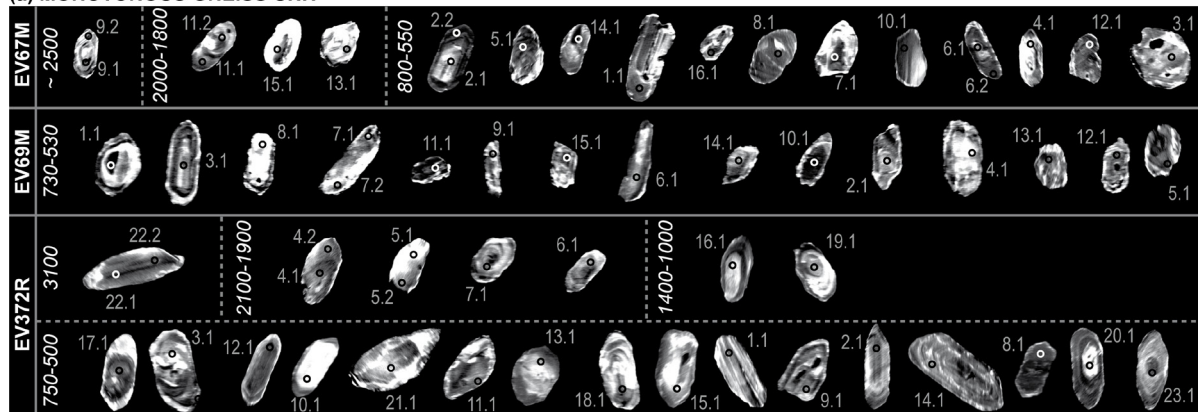
2) Geochronology

In each main lithological unit, three representative samples were collected (Fig. 74c). They were crushed and sieved, and the fraction smaller than 500 μm was processed using a Frantz magnetic separator and heavy liquids. Zircon grains were finally hand picked under a binocular microscope and mounted in araldite. For each sample, more than ~ 100 zircon grains were generally mounted in order to observe representative morphologies and internal structures. When different zircon populations were identified, the relative proportions were roughly estimated and expressed as the percentage of the total zircon volume.

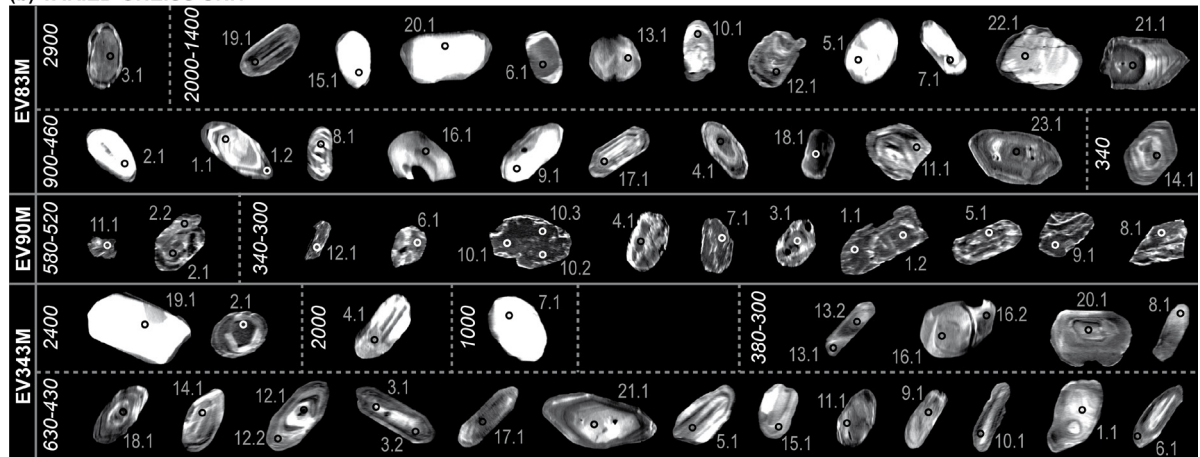
U–Pb zircon analyses were carried out at BRGM Orléans using a LASER ablation system coupled with a Neptune multicollector (MC) ICP-MS (TermoFisherScientific). A new CETAC 213 nm UV laser was used allowing the U/Pb fractionation to be significantly reduced. The MC-ICP-MS was equipped with a multi-ion counting system operating in static mode; all masses of interest were recorded simultaneously (^{202}Hg , ^{204}Pb , ^{206}Pb , ^{207}Pb , ^{208}Pb on ion-counters, and ^{232}Th , ^{238}U on Faraday cup collectors). Isotope ratios were normalised using the zircon standard 91500 from Ontario (1065 ± 1 Ma; Wiedenbeck *et al.*, 1995). Details on analytical conditions are given in Cocherie & Robert (2008) and Cocherie *et al.* (2009).

Analyses were performed on clear zircon sections and were controlled by transmitted and reflected light microphotographs as well as by backscatter electron and cathodoluminescence images (Fig. 75). The results are plotted in Figs 76, 77 & 78 using Isoplot/Ex(3.1) program (Ludwig, 2004) with error calculations at 2σ level. Zircon chemistry is additionally presented in Fig. 79. Considering that the precision and accuracy on $^{206}\text{Pb}/^{204}\text{Pb}$ determination is satisfactory for zircon grains older than *ca.* 600 Ma, the associated analyses are discussed

(a) MONOTONOUS GNEISS UNIT



(b) VARIED GNEISS UNIT



(c) FELSIC GRANULITE UNIT

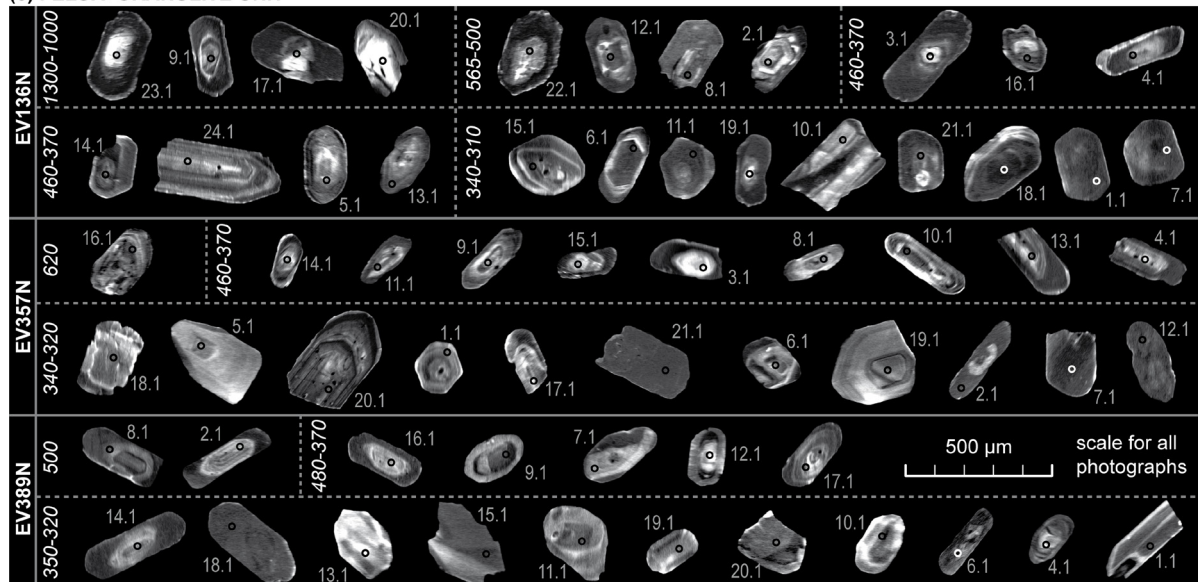


Figure 75. Cathodoluminescence images of analysed zircon grains for (a) the monotonous gneiss unit, (b) the varied gneiss unit, and (c) the felsic granulite unit. Zircon grains are sorted according to decreasing $^{206}\text{Pb}/^{238}\text{U}$ age (in Ma). Spot locations and labels are indicated.

using a conventional Concordia diagram (Wetherill, 1956). By contrast, younger analyses are concurrently examined in a conventional Concordia plot as well as in a $^{238}\text{U}/^{206}\text{Pb}$ – $^{207}\text{Pb}/^{206}\text{Pb}$ inverse Concordia diagram (Tera & Wasserburg, 1972). This dual approach was adopted because the conventional representation can easily reveal possible radiogenic Pb (Pb*) loss or Discordia trends, whereas the inverse diagram does not require initial-Pb correction and gives relatively precise average ages. In the present case, Variscan ages calculated using both methods are strongly compatible within errors, but the inverse Concordia approach systematically involves more spot analyses. Therefore, the results obtained using this latter method have been favoured in this work.

Monotonous gneiss unit

Sample description

Three biotite–sillimanite–plagioclase paragneiss samples (EV67M, EV69M & EV372R) containing a varying amount of garnet have been collected across the monotonous gneiss unit (Fig. 74c). In thin section, they display a matrix formed by thick (up to 5 mm) coarse-grained quartz–plagioclase–K-feldspar layers alternating with biotite-rich layers (1–2 mm) where muscovite is only rarely present. They also show stripes of fibrous sillimanite and yellowish pinitized cordierite parallel to the dominant foliation. In samples containing garnet (EV69M & EV372R), sillimanite pseudomorphs after garnet are observed. Additional minerals involve chlorite or chloritized biotite, ilmenite, secondary hematite, apatite, zircon and monazite. Zircon is relatively abundant and is mostly found within biotite-rich layers in the matrix.

Zircon morphology and internal structures

Zircon crystals extracted from the monotonous gneiss samples are clear and relatively large (100–300 μm). They are represented by anhedral rounded grains or weakly elongated prismatic grains with rounded tips, and frequently show small cracks. CL images reveal that the majority of rounded and prismatic zircon preserves oscillatory zoning (~90% of the total volume) with variable thickness of the bands (Fig. 75a, EV67M-9), while only few grains show homogeneous CL emission patterns (Fig. 75a, EV372R-8). From these observations, no clear distinction between different zircon populations can be made.

U–Pb age results

Sample EV67M (Frarupt, $7^{\circ}16'14''\text{E}$; $48^{\circ}15'48''\text{N}$). Twenty analyses were carried out on sixteen grains. Most of the analyses cluster at *ca.* 600 Ma, and nine spots defining a mixing line with the initial Pb ratio yield a lower intercept age of 590 ± 6 Ma (MSWD=2.9) while the other spots correspond to weak a Pb* loss (Fig. 76b). In addition, two spots from the grain 9

could define a Discordia line which passes through the dominant age group at 590 ± 6 Ma and shows an upper intercept age of 2773 ± 16 Ma. A Proterozoic age of 2003 ± 15 Ma can also be derived from the upper intercept of a Discordia involving three subconcordant analyses from grains 11 and 15 which probably underwent a recent Pb* loss (Fig. 76a). The dominant age group of *ca.* 600 Ma could be related to slightly elongated zircon grains, whereas the rare older ages are generally associated with rounded grains (Fig. 75a).

Sample EV69M (Goutte St-Blaise, $7^{\circ}13'28''\text{E}$; $48^{\circ}15'6''\text{N}$). Sixteen analyses were performed on fifteen grains. All analyses are concordant to subconcordant, span a narrow range of ages between 730–530 Ma, and mostly fall into two age groups (Fig. 76c, d). For the first group, both a concordant age of 634 ± 5 Ma on four spots (MSWD=1.6), and a lower intercept age of 637 ± 13 Ma using five analyses (MSWD=3.4) in an inverse Concordia diagram are similar within errors (Fig. 76c, d). Concerning the second age group, the use of both methods for four analyses also yields a similar age of 567 ± 4 Ma (MSWDs=0.16–1.16). Rare older concordant analyses could additionally indicate inheritance at *ca.* 730 Ma. (Fig. 76c, d).

Sample EV372R (Hohltann, $7^{\circ}10'19''\text{E}$; $48^{\circ}12'54''\text{N}$). Twenty six analyses carried out on twenty three grains point to several concordant ages around 650–500 Ma as well as various inheritance (Fig. 76e, f). The youngest age of 537 ± 10 Ma (MSWD=2.7) is represented by four analyses lying on a mixing line with initial Pb in an inverse Concordia diagram (Fig. 76f). Besides, an inherited age of 2041 ± 24 Ma (MSWD=1.3) is given by the upper intercept of a Discordia passing through three subconcordant analyses from grains 5 and 7, and a discordant analysis from grain 19. The lower intercept of this Discordia yields 569 ± 69 Ma, which is similar within errors to the above-mentioned age of 537 ± 10 Ma (Fig. 76e). Palaeoproterozoic and Archaean inherited ages are also documented by the upper intercepts of Discordia lines defined at 2385 ± 21 (MSWD=0.34) by three analyses (4.1, 4.2, 16.1), and at 3403 ± 200 (MSWD=7.5) by two analyses (22.1, 22.2), respectively (Fig. 76e). The lower intercepts of the Discordia lines probably reflect a more recent Pb* loss. Like for sample EV67M, younger ages were mostly obtained on prismatic grains, whereas some of the older analyses are associated with relatively small and rounded grains (Fig. 75a).

Zircon chemistry

According to U–Pb dating, zircon grains from the monotonous gneiss unit preserve two age groups: (1) various Proterozoic to Archaean inheritance, and (2) Neoproterozoic–Cambrian ages (Fig. 76). These two populations are relatively indistinguishable in terms of U and Th concentrations and show similar Th/U ratios (Fig. 79a). The Neoproterozoic–Cambrian zircon grains exhibit a slightly broader variation in U concentration, though this could only be an artefact of the relatively small number of analyses.

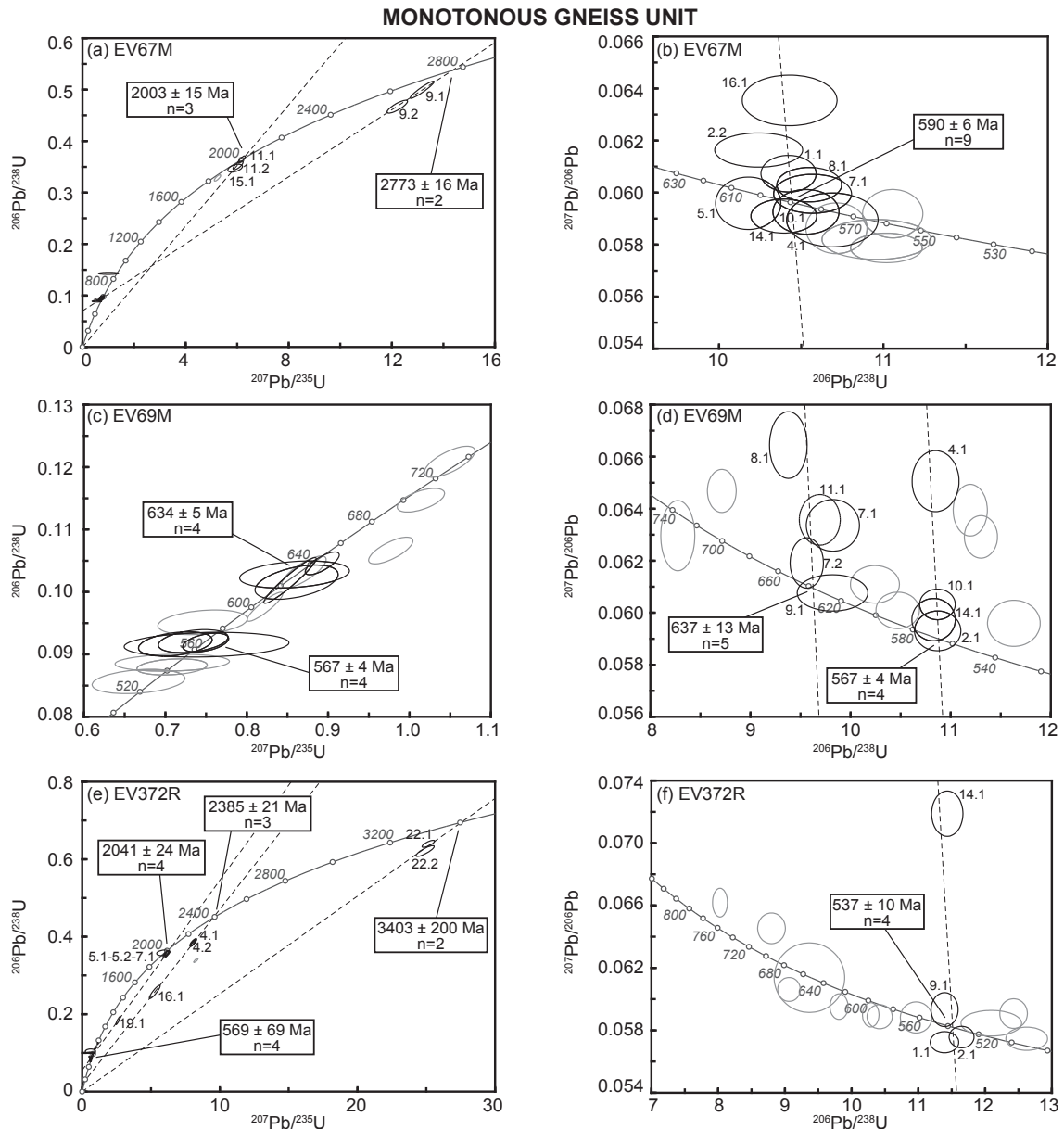


Figure 76. Concordia diagrams reporting U–Pb zircon data for the monotonous gneiss unit. (a) Sample EV67M, (b) sample EV69M, (c) sample EV372R. Black ellipses denote analyses used for age calculations, and labels correspond to zircon spot analyses from Fig. 75a. Analytical results are presented in Appendix.

Varied gneiss unit

Sample description

Three biotite–garnet gneiss samples (EV83M, EV90M, EV343M) showing textural variations were collected across the varied gneiss unit (Fig. 74c). Sample EV83M is clearly migmatitic and preserves an alternation of thick (2–3 cm) leucosomes and biotite–garnet-bearing restitic layers. Sample EV90M was collected at the contact with the monotonous gneiss unit and corresponds to a light-coloured, quartz-rich and fine-grained gneiss containing few garnet. Sample EV343M shows numerous rounded K-feldspar blasts lying in a foliated biotite–garnet-

bearing matrix. In thin section, all gneiss samples show a marked differentiation between quartz–K-feldspar-rich and biotite-rich layers, and commonly host a significant amount of garnet porphyroblasts (1–5 mm). Additional minerals are chlorite, ilmenite, secondary hematite and zircon. Relatively large (100–300 μm) zircon grains are generally located in the matrix, especially in biotite-rich layers, but smaller ($< 100 \mu\text{m}$) crystals can be observed inside or next to garnet porphyroblasts.

Zircon morphology and internal structures

Zircon grains separated from the varied gneiss samples are large (200–400 μm) and commonly clear. They are equally represented by anhedral rounded crystals, and by variably elongated prismatic grains with some well-developed pyramidal tips. In addition to this morphological contrast, CL images provide criteria to distinguish between several zircon populations. Oscillatory zoning with an important variation of band thickness is the dominant internal structure (50–60%) and is found in rounded or elongated prismatic grains (Fig. 75b, EV343M-21). In addition, a significant amount of zircon (30–40%) corresponds to anhedral or short prismatic grains with a faded oscillatory zoning or a completely blurred CL pattern (Fig. 75b, EV343M-16). Some rounded zircon crystals (5–10%) show homogeneous bright CL patterns with tiny darker overgrowths (Fig. 75b, EV83M-20) and others (5–10%) preserve uniform CL-dark patterns (Fig. 75b, EV90M-7). Occurrences of xenocrystic cores or convoluted zoning are rather rare (Fig. 75b, EV343M-1).

U–Pb age results

Sample EV83M (St-Pierre sur l'Hôte, $7^{\circ}10'32''\text{E}$; $48^{\circ}13'26''\text{N}$). Out of twenty four analyses performed on twenty three zircon grains, only one yielded a Variscan age of 343 ± 7 Ma which is purely indicative in the case of this sample. Neoproterozoic and Ordovician ages are defined by the lower intercepts of mixing lines in an inverse Concordia diagram. It is the case for the 459 ± 4 Ma (MSWD=0.24) and the 553 ± 7 Ma (MSWD=0.45) ages both calculated using three spot analyses (Fig. 77b). The older spot analyses chiefly spread along two Discordia lines which indicate Palaeoproterozoic ages (Fig. 77a). One concordant and four discordant spots define a Discordia with an upper intercept at 1895 ± 18 Ma (MSWD=1.3) and a lower intercept at 319 ± 48 Ma, further supporting the existence of a Variscan event. Four discordant analyses also give an upper intercept age of 2134 ± 37 Ma (MSWD=1.02). In addition, two zircon grains (3.1, 19.1) point to older inheritance at *ca.* 2500 and 3400 Ma. The older ages seem to be linked with larger rounded grains with either oscillatory zoning or uniform bright CL patterns, while younger ages are mostly obtained on smaller prismatic grains showing oscillatory zoning or rare blurred patterns (Fig. 75b).

Sample EV90M (Rauenthal, 7°9'33"E ; 48°12'37"N). Sixteen analyses on twelve zircon grains from this sample mostly yielded Variscan ages around 340–300 Ma. Because several subconcordant analyses are observed at *ca.* 320 Ma in both the conventional and inverse Concordia diagrams, a lower intercept age of 323±2 Ma (MSWD=1.03) can be calculated using eight analyses of this population (Fig. 77d). In a similar way, three analyses define a lower intercept age of 339±4 Ma (MSWD=0.73) which could confirm the concordant age of 335±7 Ma (MSWD=5.2) calculated with the additional 4.1 analysis. Finally, an

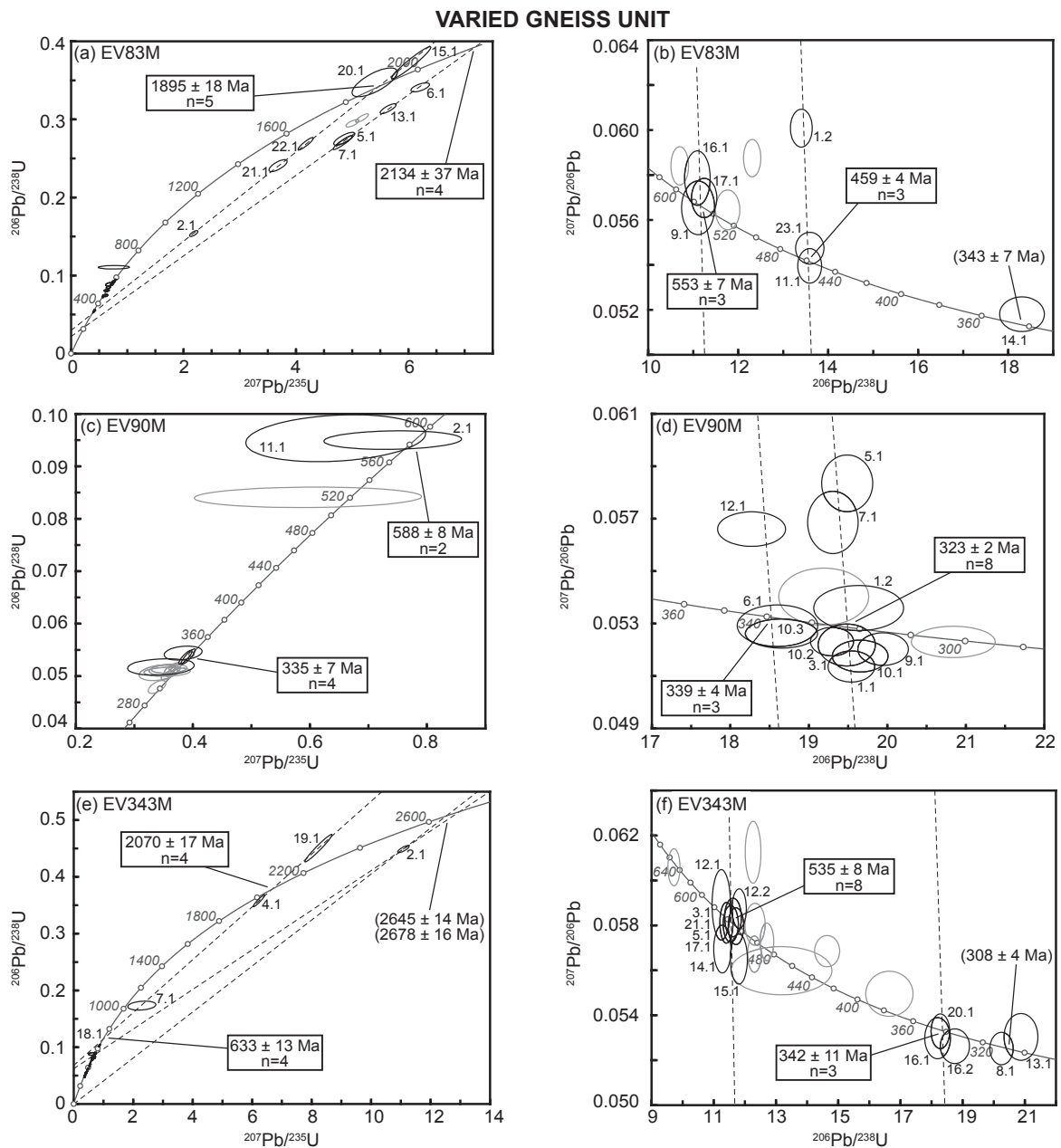


Figure 77. Concordia diagrams reporting U–Pb zircon data for the varied gneiss unit. (a) Sample EV83M, (b) sample EV90M, (c) sample EV343M. Black ellipses denote analyses used for age calculations, and labels correspond to zircon spot analyses from Fig. 75b. Ages in parentheses are indicative. Analytical results are presented in Appendix.

older concordant age of 588 ± 2 Ma, though based on two analyses (2.1, 11.1), indicates a Neoproterozoic event (Fig. 77c). In the case of this sample, Variscan ages are linked with rounded or prismatic zircon grains mostly showing dark CL patterns (Fig. 75b).

Sample EV343M (Bourgonde, Fischthal, $7^{\circ}12'24''\text{E}$; $48^{\circ}14'9''\text{N}$). Twenty five analyses have been carried out on twenty one zircon grains. Most of the analyses cluster at *ca.* 540 Ma and eight spots give a lower intercept age of 535 ± 8 Ma (MSWD=4.5) in an inverse Concordia diagram (Fig. 77f). The same approach is used to constrain the Variscan ages indicated by the grains 8, 13, 16 and 20. A lower intercept age of 342 ± 11 Ma is defined by three analyses (MSWD=2.6), while two other spots may indicate an age of *ca.* 300 Ma (Fig. 77f). Inheritance is documented by four analyses which define a Discordia with an upper intercept at 2070 ± 17 Ma (MSWD=0.29) and a lower intercept that coincides with the concordant 18.1 analysis at 633 ± 13 Ma (Fig. 77e). In addition, the 2.1 spot suggests a possible Archaean inheritance at *ca.* 2650 Ma. For this sample, the oldest ages are obtained on rounded zircon grains with a mostly bright CL pattern and Neoproterozoic ages are linked with prismatic crystals showing oscillatory zoning. By contrast younger Variscan ages are clearly associated with rounded to prismatic grains with blurred zoning (Fig. 75b).

Zircon chemistry

The U–Pb results for the varied gneiss unit can be separated into three main age groups: (1) Early Proterozoic inheritance, (2) Neoproterozoic–Ordovician ages, and (3) Variscan ages younger than 380 Ma (Fig. 77). The inherited zircon grains are characterised by low U and Th concentrations, whereas the Neoproterozoic–Ordovician and Variscan grains show a larger variation (Fig. 79b). Importantly, two subgroups can be distinguished within the Variscan age population. The first subgroup is represented by zircon grains with blurred CL patterns which preserve relatively low U (< 1000 ppm) and Th (< 150 ppm) concentrations similar to those observed in Neoproterozoic–Ordovician zircon. On the other hand, the second subgroup is composed of few zircon grains showing significantly higher U and Th concentrations and associated with a uniform CL-dark pattern (Fig. 79b).

Felsic granulite unit

Sample description

Three felsic granulite samples (EV136N, EV357N, EV389N) were collected across the southern part of the study area (Fig. 74c). They all correspond to pink or white quartz–K-feldspar rocks showing a fine mylonitic texture and hosting tiny (< 1 mm) garnet. In thin

section elongated quartz stripes alternate with large (500 μm) perthitic K-feldspar and fine-grained plagioclase-rich layers. Garnet is always present and hosts rounded inclusions of perthite or rutile. It is variably replaced by biotite or chlorite. In sample EV357N, kyanite is frequently observed in the matrix or in textural equilibrium with garnet and rutile, but sillimanite overgrowths around kyanite crystals are common. Accessory minerals are rutile, apatite and zircon. Ubiquitous zircon may be up to 500 μm in length and is found in matrix biotite, in quartz–plagioclase layers, along cracks in garnet, or as inclusions in garnet core and rim.

Zircon morphology

Zircon separated from the three samples are elongated (100–500 μm) and frequently show small cracks. Most display a short prismatic shape with nicely rounded tips and only few show rounded or subspherical shapes. CL images reveal three main patterns (Fig. 75c). The first pattern corresponds to a sharply defined oscillatory zoning which is preserved in only few (< 5%) euhedral and partly resorbed (~ 50 μm) zircon cores (Fig. 75c, EV136N-2&12). The second type of CL pattern is represented by a frequent (20–30%) blurred oscillatory zoning which is found in single crystals or in resorbed anhedral cores surrounded by homogeneous dark CL zones (Fig. 75c, EV389N-13&14). Finally, the overwhelming majority of zircon grains (70–80%) is characterised by a uniform dark CL pattern which is visible in entire crystals as well as in rims overgrowing blurred cores (Fig. 75c, EV389N-14&18).

U–Pb age results

Sample EV136N (La Roche, Col des Bagenelles, 7°6'40"E; 48°11'0"N). Twenty four analyses were performed on twenty four zircon grains. A glance at the younger results shows that two ages groups at *ca.* 500 and 340 Ma are separated by a nearly continuous array of concordant ages between the two end members (Fig. 78b). An age of 509 ± 7 Ma (MSWD=1.6) is calculated using two spots, while seven analyses from the dominant age group yield 342 ± 4 Ma (MSWD=2.1) in an inverse Concordia diagram, both groups showing only slight mixing with initial Pb (Fig. 78b). Three older discordant analyses could define a Discordia with an upper intercept age of 1793 ± 30 Ma and a lower intercept lying at the previously calculated age of 342 ± 4 Ma (Fig. 78a). The 23.1 analysis finally suggests a Palaeoproterozoic inheritance at *ca.* 2000 Ma. It should be noted that the 550–500 Ma ages are obtained on small zircon grains with clear oscillatory zoning (Fig. 75c). By contrast, progressively younger ages are derived from grain cores showing blurred zoning and from homogeneous CL-dark overgrowths or single grains.

Sample EV357N (Le Haïcot West, 7°7'54"E; 48°11'49"N). Almost all of the twenty one analyses carried out on twenty one grains yielded Palaeozoic ages. The Palaeozoic ages scatter between *ca.* 450 and 320 Ma with several intermediate ages in between (Fig. 78d). Three analyses roughly define the oldest age of 449 ± 23 Ma which is only indicative. Two lower intercept ages of 373 ± 4 Ma (MSWD=0.51) and 343 ± 2 Ma (MSWD=1.1) can be respectively calculated using three and six analyses showing a small contribution of initial Pb (Fig. 78d). These results are similar to concordant ages of 372 ± 4 Ma and 340 ± 3 Ma (with the

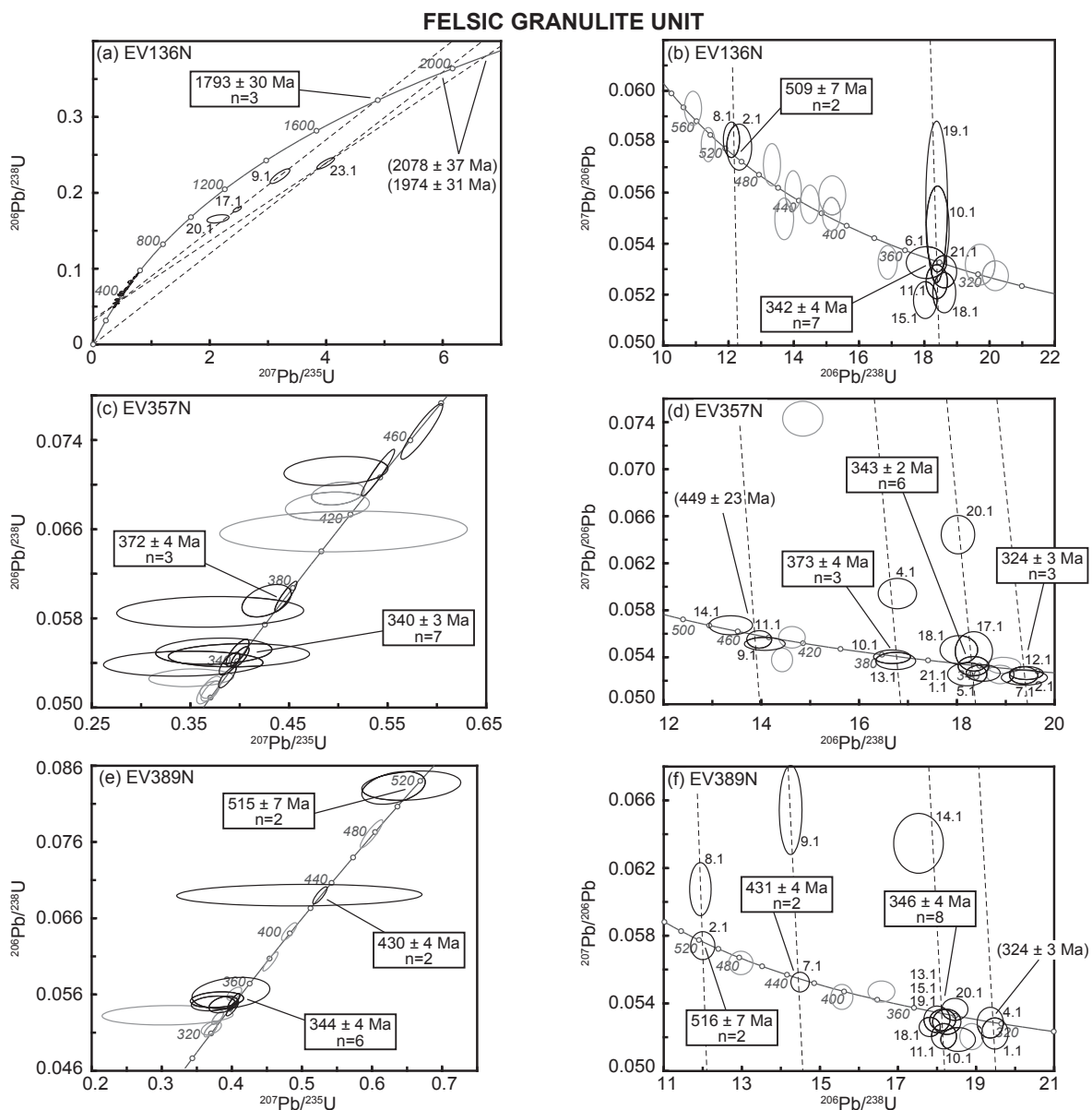


Figure 78. Concordia diagrams reporting U–Pb zircon data for the felsic granulite unit. (a) Sample EV136N, (b) sample EV357N, (c) sample EV389N. Black ellipses denote analyses used for age calculations, and labels correspond to zircon spot analyses from Fig. 75c. Ages in parentheses are indicative. Analytical results are presented in Appendix.

additional 6.1 spot) calculated in a conventional Concordia diagram (Fig. 78c). In addition, three concordant analyses document a younger age of 324 ± 3 Ma (MSWD=0.1). CL images reveal that ages older than *ca.* 340 Ma are linked with blurred cores from short prismatic zircon grains (Fig. 75c). Conversely, younger ages are mostly associated with larger crystals showing blurred or CL-dark patterns.

Sample EV389N (Les Belles Fourrières, $7^{\circ}6'56''\text{E}$; $48^{\circ}10'47''\text{N}$). Eighteen analyses performed on eighteen grains only gave Palaeozoic ages. A nearly continuous array of concordant analyses spreads between *ca.* 520 and 320 Ma. The oldest age of 516 ± 7 Ma is calculated using two analyses which define a mixing line with initial Pb in an inverse Concordia diagram (Fig. 78c). Similarly, two and eight spots define lower intercept ages of 431 ± 4 Ma (MSWD=0.2) and 346 ± 4 Ma (MSWD=3.3), respectively. The two youngest

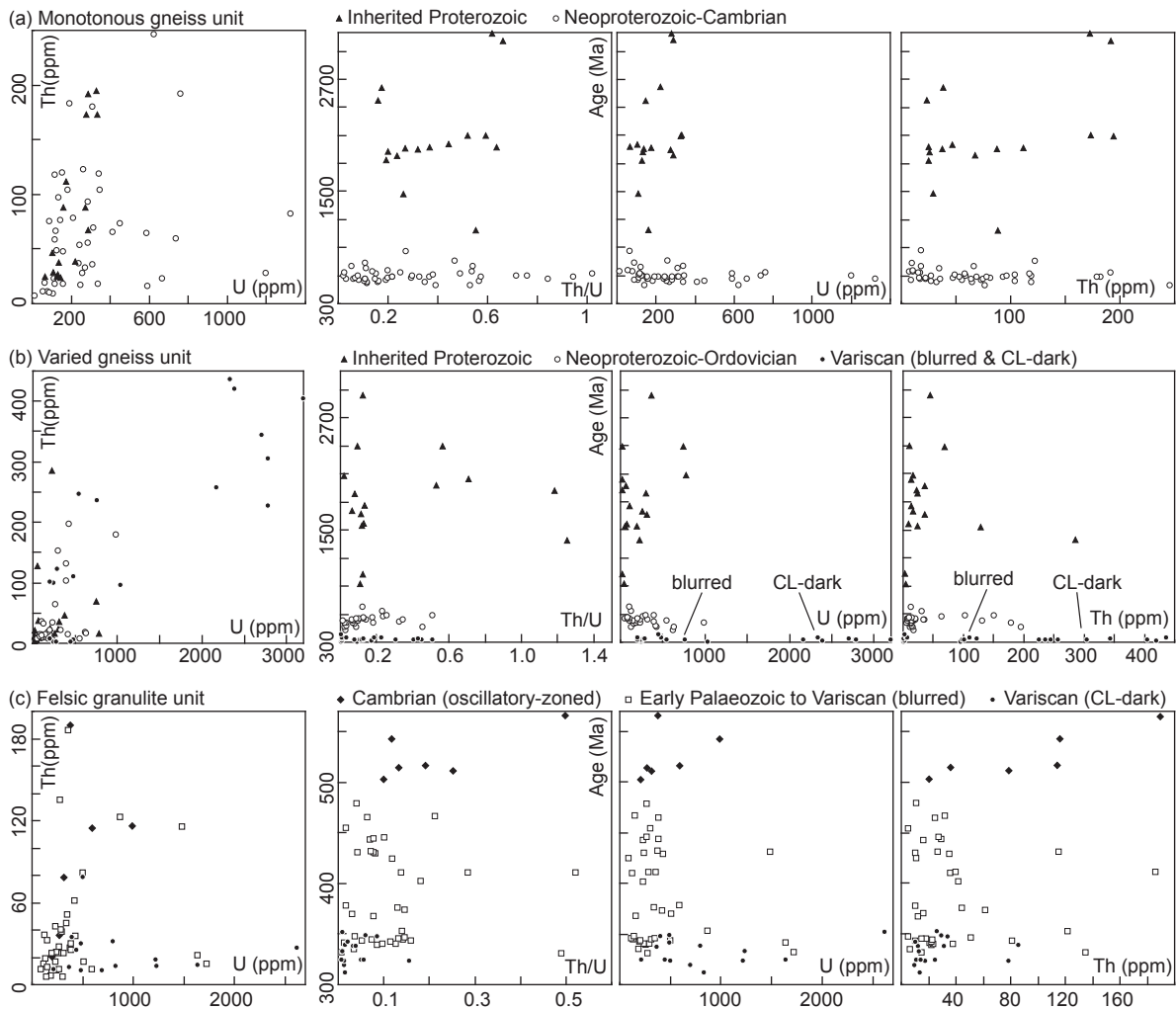


Figure 79. U and Th zircon chemistry for the distinctive age populations in each lithological unit. The apparent $^{206}\text{Pb}/^{238}\text{U}$ age (in Ma) is plotted versus Th/U, U and Th. (a) Monotonous gneiss unit, 1 data point out of range. (b) Varied gneiss unit, 1 data point out of range. (c) Felsic granulite unit, inherited Proterozoic ages are omitted. Age errors (2σ) are not shown; they are as big as the symbol size in (a–b), and twice the symbol size in (c).

concordant analyses may also indicate an age of 324 ± 3 Ma. The ages determined at 516, 431 and 346 Ma are all similar within error to those calculated in a conventional Concordia diagram (Fig. 78e), i.e. at 515 ± 7 Ma, 430 ± 4 Ma and 344 ± 4 Ma, respectively (without spots 10.1 & 18.1). It is possible to observe clear relationships between zircon ages and CL patterns. The oldest ages are related to zircon cores with oscillatory zoning, whereas the younger ages correspond either to blurred cores, blurred single crystals or CL-dark domains (Fig. 75c).

Zircon chemistry

In the felsic granulite clear relationships between U–Pb ages and zircon internal structures suggest that three populations can be defined: (1) Cambrian ages derived from rare oscillatory-zoned zircon, (2) Early Palaeozoic–Variscan ages obtained on single grains or cores with blurred patterns, and (3) younger Variscan ages related to CL-dark crystals or overgrowths (Figs 75c & 78). A clear trend of decreasing Th/U ratio is observed from Cambrian to Variscan ages, the latter showing low and rather constant Th/U ratios (Fig. 79c). This evolution reflects a decrease in Th at relatively constant U concentrations from Cambrian to Early Palaeozoic–Variscan zircon grains. By contrast, younger Variscan analyses are characterised by lower Th but significantly higher U concentrations than older zircon analyses (Fig. 79c).

3) Petrography and mineral chemistry

Varied gneiss unit

The varied unit is dominantly composed of biotite–garnet-bearing gneissic rocks that show important textural variations due to the nature of their protoliths and to heterogeneous partial melting. They could appear as quartz-rich paragneiss with only minor garnet, as m-scale quartz–K-feldspar pristine leucosomes alternating with biotite-rich restitic layers, or more commonly as ophthalmic gneiss with K-feldspar blasts. In thin section, K-feldspar, quartz and garnet are surrounded by abundant biotite, some prismatic sillimanite and pinitized cordierite (Fig. 80a). Garnet hosts lobate quartz inclusions, tiny rutile needles in the core and rare kyanite. Kyanite is also included in K-feldspar (Fig. 80c), the latter mineral being rarely replaced by muscovite.

Sample EV340B is an ophthalmic gneiss with a relatively rich mineralogy and is representative of the varied gneiss unit. Large (1–2 mm) perthitic K-feldspar and garnet porphyroblasts (1–3 mm) are surrounded by a matrix made up of quartz, biotite, muscovite, plagioclase, sillimanite, cordierite with accessory chlorite, ilmenite and zircon. Garnet cores preserve minute ($< 50\mu\text{m}$) zircon, rutile and biotite inclusions surrounded by a narrow zone of rounded quartz and kyanite inclusions, and by sillimanite inclusions at the rim (Fig. 80a-

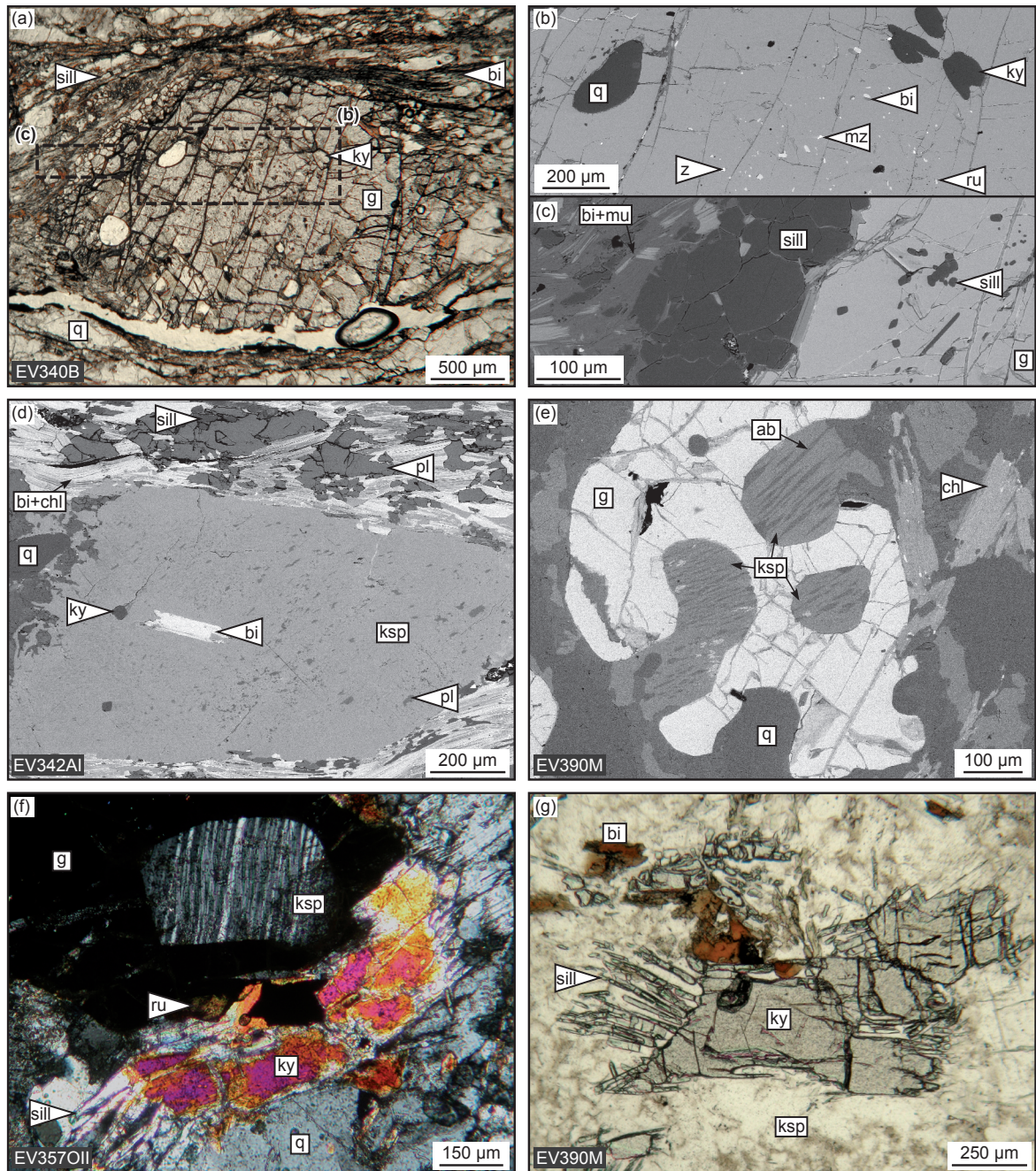


Figure 80. Photomicrographs and backscatter electron (BSE) images illustrating the representative assemblages or textures for the varied gneiss (a–d) and the felsic granulite (e–g) units. (a) Polyphase garnet with an inclusion-rich core followed by a zone of kyanite inclusions and a rim hosting sillimanite. It is surrounded by matrix sillimanite and biotite, plane-polarised light. (b) Detail of the inclusion-rich garnet core preserving mostly rutile, zircon and rare biotite, BSE. (c) Detail of the garnet rim which hosts sillimanite inclusions and is in textural equilibrium with matrix sillimanite, BSE. (d) Kyanite and biotite inclusions in a perthitic K-feldspar. The matrix shows plagioclase and prismatic sillimanite surrounded by partly chloritized biotite, BSE. (e) Typical garnet texture in the felsic granulite. Garnet partly or entirely encloses lobate perthitic K-feldspar with albite exsolutions and is surrounded by secondary chlorite, BSE. (f) Textural equilibrium between garnet with a perthitic K-feldspar inclusion, kyanite and rutile. Kyanite is partially replaced by sillimanite, crossed polars. (g) Typical replacement of kyanite by needle-shaped sillimanite, plane-polarised light. For mineral abbreviations, see Appendix.

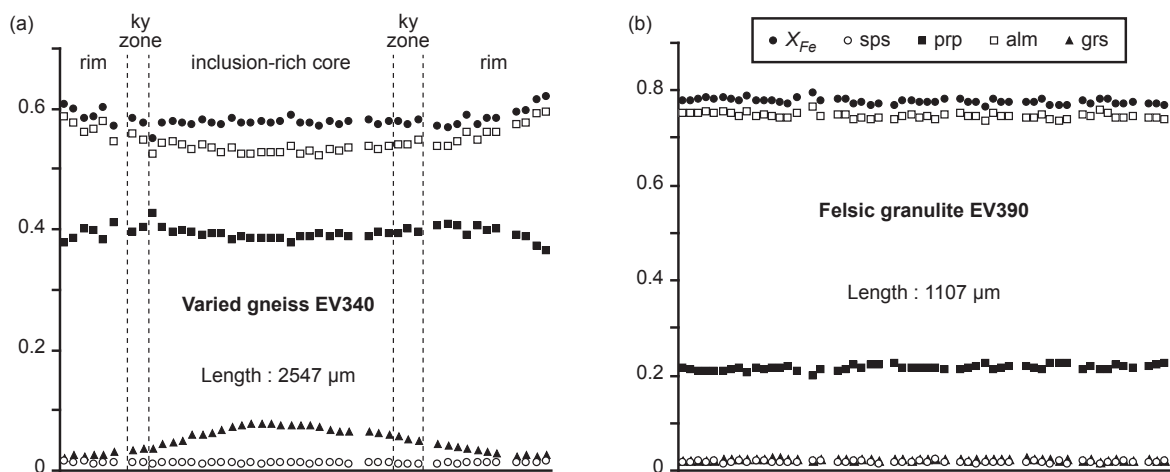


Figure 81. Chemical profiles of garnet from (a) varied gneiss sample EV340B and (b) felsic granulite sample EV390M.

c). The textural relationships in garnet suggest that the g–bi–ru paragenesis was followed by a g–ksp–pl–ky and a later g–bi–sill assemblage. In addition, matrix minerals indicate later growth of cordierite and muscovite together with ilmenite.

Garnet shows a weak Fe–Mg zoning and a more pronounced Ca variation (Fig. 81a, Tab. 16). The grossular proportion is the highest in garnet core ($\text{alm}_{53} \text{prp}_{38} \text{grs}_{08} \text{sps}_{01}$; $X_{Fe}=0.58$); it decreases in the zone of kyanite inclusions ($\text{alm}_{54} \text{prp}_{40} \text{grs}_{05} \text{sps}_{01}$; $X_{Fe}=0.57$), and reaches a negligible value at the rim ($\text{alm}_{58} \text{prp}_{39} \text{grs}_{02} \text{sps}_{01}$; $X_{Fe}=0.60$). K-feldspar is orthoclase with higher Na in the core ($\text{or}_{82} \text{ab}_{17} \text{an}_{01}$) than at the rim ($\text{or}_{91} \text{ab}_{09}$). Plagioclase is represented by albite inclusions ($\text{or}_{01} \text{ab}_{96} \text{an}_{03}$) or oligoclase exsolutions ($\text{or}_{01} \text{ab}_{73} \text{an}_{26}$) in K-feldspar, and by unzoned oligoclase ($\text{or}_{01} \text{ab}_{75} \text{an}_{24}$) in the matrix (Tab. 16). Biotite analyses show a homogeneous Ti content ($\text{Ti}=0.28\text{--}0.3$ a.p.f.u.), but rare biotite included in garnet ($X_{Fe}=0.24$) has a lower X_{Fe} than the matrix biotite ($X_{Fe}=0.3$). Kyanite inclusions and matrix sillimanite have similar compositions while sillimanite included at garnet rim has up to 1.4 wt.% of Fe_2O_3 (Tab. 16).

Felsic granulite unit

The felsic granulite exhibits a consistent mineralogy and mylonitic texture through the whole area. Perthitic K-feldspar is dominant and alternates with fine-grained plagioclase and platy quartz. Small (0.5 mm) rounded garnet shows lobate boundaries with quartz and K-feldspar embayments (Fig. 80d), and is surrounded by biotite or chlorite. Quartz, K-feldspar and rutile are also commonly included in garnet (Fig. 80d, e). Al_2SiO_5 polymorphs are rare; kyanite forms elongated prisms, whereas sillimanite is represented by small needles growing around kyanite (Fig. 80e, f) or isolated prisms.

Table 16. Representative chemical analyses for varied gneiss sample EV340B.

Sample Mineral Position	EV 340 B											
	g core	g ky zone	g rim	bi in g	bi mx	ky in g	sill in g	sill mx	ksp core	ksp rim	pl in ksp	pl exsol
Wt. %												
SiO ₂	39.78	39.11	39.46	38.27	37.62	37.76	37.40	37.05	63.14	63.69	67.67	60.77
TiO ₂	0.02	0.03	0.02	5.29	5.03	0.02	0.02	0.02	0.00	0.00	0.00	0.01
Al ₂ O ₃	22.07	21.54	22.07	16.76	17.37	62.60	62.00	61.63	19.33	18.61	19.83	23.43
FeO	27.50	27.76	29.75	9.44	11.86	0.43	1.16	0.49	0.02	0.03	0.02	0.00
MnO	0.56	0.45	0.66	0.05	0.02	0.00	0.07	0.00	0.00	0.04	0.00	0.02
MgO	10.27	10.50	10.19	17.61	15.85	0.02	0.02	0.01	0.00	0.01	0.00	0.00
CaO	2.84	1.85	0.91	0.04	0.02	0.00	0.03	0.01	0.22	0.07	0.70	5.27
Na ₂ O	0.02	0.01	0.01	0.50	0.24	0.00	0.00	0.00	1.87	0.94	11.17	8.56
K ₂ O	0.00	0.00	0.03	9.04	9.26	0.00	0.00	0.01	13.64	15.22	0.14	0.22
Total	103.07	101.24	103.09	97.03	97.32	100.91	100.75	99.30	98.23	98.62	99.54	98.28
Cations												
Si	2.96	2.96	2.95	2.82	2.79	1.01	1.01	1.01	2.94	2.98	2.98	2.74
Ti	0.00	0.00	0.00	0.29	0.28	0.00	0.00	0.00	0.00	0.00	0.00	0.00
Al	1.93	1.92	1.94	1.45	1.52	1.98	1.96	1.98	1.06	1.03	1.03	1.24
Fe ³⁺	0.16	0.16	0.17	0.00	0.00	0.00	0.02	0.00	0.00	0.00	0.00	0.00
Fe ²⁺	1.55	1.59	1.69	0.58	0.74	0.01	0.00	0.01	0.00	0.00	0.00	0.00
Mn	0.04	0.03	0.04	0.00	0.00	0.00	0.00	0.00	0.00	0.00	0.00	0.00
Mg	1.14	1.18	1.13	1.93	1.75	0.00	0.00	0.00	0.00	0.00	0.00	0.00
Ca	0.23	0.15	0.07	0.00	0.00	0.00	0.00	0.00	0.01	0.00	0.03	0.25
Na	0.00	0.00	0.00	0.07	0.03	0.00	0.00	0.00	0.17	0.09	0.95	0.75
K	0.00	0.00	0.00	0.85	0.88	0.00	0.00	0.00	0.81	0.91	0.01	0.01
Total	8	8	8	8	8	3	3	3	5	5	5	5
X_{Fe}	0.58	0.57	0.60	0.23	0.30				an	0.01	0.00	0.03
alm	0.53	0.54	0.58						ab	0.17	0.09	0.96
prp	0.38	0.40	0.39						or	0.82	0.91	0.01
grs	0.08	0.05	0.02									0.01
sps	0.01	0.01	0.01									

Structural formulae calculated on the basis of 12 oxygens for garnet, 5 for Al₂SiO₅ polymorphs, 11 for biotite, and 8 for feldspars
 mx = matrix ; ky zone = garnet inner rim with kyanite inclusions ; exsol = exsolution in perthitic K-feldspar

Sample EV390M is a typical felsic granulite representative of the whole unit, but with additional aluminosilicate minerals. Platy quartz, perthitic K-feldspar and plagioclase are abundant, and rounded garnet with numerous cracks is common. Garnet hosts rounded quartz or K-feldspar inclusions and is variably replaced by biotite or chlorite (Fig. 80d). Kyanite appears as elongated prisms which lie perpendicular to the granulitic foliation and are overgrown by prismatic sillimanite (Fig. 80f). Rutile is relatively frequent in the matrix as well as in garnet. The textural relationships suggest that an early g–ksp–pl–ky–ru paragenesis was followed by a g–ksp–pl–sill–ru assemblage, and that garnet was later replaced by biotite and chlorite.

Chemical profiles across garnet porphyroblasts reveal a nearly constant composition (Fig. 81b, Tab. 17) from core (alm₇₄prp₂₂grs₀₂sps₀₂; X_{Fe} =0.77) to rim (alm₇₅prp₂₁grs₀₂sps₀₂; X_{Fe} =0.78). Spot analyses in garnet surrounded by biotite and chlorite show higher X_{Fe} values

($X_{Fe}=0.83-0.88$) probably due to late exchange with the surrounding minerals. K-feldspar corresponds to orthoclase with varying Na content (or₆₆₋₉₂ab₀₇₋₃₂an₀₁). Plagioclase in the matrix and in plagioclase–chlorite intergrowths around garnet is oligoclase (or₀₁₋₀₂ab₈₁₋₈₄an₁₅₋₁₈), and plagioclase exsolutions in perthite are mostly oligoclase and rarely albite (or₀₁₋₀₃ab₈₁₋₉₃an₀₆₋₁₆). Biotite has Ti=0.17–0.23 a.p.f.u. and shows different X_{Fe} values (Tab. 17) depending on whether it is located next to garnet ($X_{Fe}=0.56$), or in the matrix ($X_{Fe}=0.53$). Similarly, chlorite growing close to garnet has a higher X_{Fe} ($X_{Fe}=0.6$) than matrix chlorite ($X_{Fe}=0.3$).

Table 17. Representative chemical analyses for felsic granulite sample EV390M.

Sample Mineral Position	EV 390 M									
	g core	g rim	bi next to g	bi mx	chl next to g	chl mx	ksp mx	pl exsol	pl mx	
Wt. %										
SiO ₂	38.23	37.81	36.21	36.00	27.15	27.57	65.87	65.53	64.38	
TiO ₂	0.05	0.00	3.06	4.00	0.21	0.27	0.01	0.02	0.00	
Al ₂ O ₃	21.59	21.47	19.02	17.90	21.29	22.03	18.95	22.30	22.53	
FeO	34.77	35.02	19.87	19.01	28.54	25.12	0.24	0.09	0.00	
MnO	0.88	0.83	0.10	0.00	0.06	0.14	0.00	0.09	0.00	
MgO	5.66	5.31	8.88	9.37	10.69	12.36	0.04	0.00	0.01	
CaO	0.76	0.74	0.00	0.00	0.00	0.09	0.11	3.28	3.72	
Na ₂ O	0.00	0.02	0.16	0.18	0.00	0.00	2.37	9.34	9.35	
K ₂ O	0.01	0.00	9.55	9.59	0.66	0.15	13.35	0.50	0.31	
Total	101.96	101.19	96.85	96.20	88.68	87.81	100.94	101.15	100.38	
Cations										
Si	2.98	2.97	2.80	2.81	5.83	5.89	2.99	2.87	2.84	
Ti	0.00	0.00	0.18	0.23	0.03	0.04	0.00	0.00	0.00	
Al	1.98	1.99	1.74	1.64	5.39	5.55	1.01	1.15	1.17	
Fe ³⁺	0.06	0.07	0.00	0.00	0.00	0.00	0.00	0.00	0.00	
Fe ²⁺	2.20	2.23	1.29	1.24	5.12	4.49	0.01	0.00	0.00	
Mn	0.06	0.06	0.01	0.00	0.01	0.03	0.00	0.00	0.00	
Mg	0.66	0.62	1.02	1.09	3.42	3.94	0.00	0.00	0.00	
Ca	0.06	0.06	0.00	0.00	0.00	0.02	0.01	0.15	0.18	
Na	0.00	0.00	0.02	0.03	0.00	0.00	0.21	0.79	0.80	
K	0.00	0.00	0.94	0.95	0.18	0.04	0.77	0.03	0.02	
Total	8	8	8	8	20	20	5	5	5	
X_{Fe}	0.77	0.78	0.56	0.53	0.60	0.53	an	0.01	0.16	0.18
alm	0.74	0.75					ab	0.21	0.81	0.80
prp	0.22	0.21					or	0.78	0.03	0.02
grs	0.02	0.02								
sps	0.02	0.02								

Structural formulae calculated on the basis of 12 oxygens for garnet, 11 for biotite, 28 for chlorite and 8 for feldspars
mx = matrix ; exsol = exsolution in perthitic K-feldspar

4) Mineral equilibria modelling

Calculation method

The P – T pseudosections were calculated using Thermocalc 3.33 (Powell *et al.*, 1998) and the thermodynamic database 5.5 from Holland & Powell (1998). The activity–composition relationships are as follows: garnet, biotite and silicate melt from White *et al.* (2007), cordierite from Holland & Powell (1998), white mica from Coggon & Holland (2002), feldspars from Holland & Powell (2003), and ilmenite from White *et al.* (2000). For pseudosections with additional ZrO_2 , the new zircon, melt, rutile and garnet models, and the modified biotite and ilmenite models are after Kelsey & Powell (2011). In all pseudosections, quartz is the only phase which is considered to be in excess.

Assessing the P – T evolution in the NCKFMASHTO system

Considering significant partial melting and possible melt loss, pseudosection calculations in the Na_2O – CaO – K_2O – FeO – MgO – Al_2O_3 – SiO_2 – H_2O – TiO_2 – O_2 (NCKFMASHTO) system follow a procedure detailed in Hasalová *et al.* (2008), Štípská *et al.* (2008) and Lexa *et al.* (2011). The first modelling step is based on the assumption that the garnet rim equilibrated with the last fluid phase present in the rock (e.g. Guiraud *et al.*, 2001). The retrograde evolution is therefore discussed in a pseudosection where the H_2O content is adjusted so that the modelled garnet isopleths at the dry solidus lie close to the observed garnet rim composition.

The adjusted H_2O content in the pseudosections with the dry solidus is 1.5 and 0.23 mol% for the varied gneiss and the felsic granulite, respectively. However, both the metasedimentary protolith of the varied gneiss and the probable granitic protolith of the felsic granulite (e.g. Janoušek *et al.*, 2004) may have initially contained a higher amount of H_2O , suggesting that some aqueous fluid was lost together with melt. The second step of the present approach therefore involves melt re-integration in the system. Following Sawyer (1994), melt segregation in high-grade rocks is chiefly due to deviatoric stress which leads to melt accumulation in low-pressure sites. It is then not excluded that melt segregation could have occurred close to peak pressure conditions. Consequently silicate melt has been re-integrated at peak P – T conditions in order to discuss the possible prograde evolutions in the pseudosections calculated with modified compositions.

Varied gneiss - Pseudosection with dry solidus

The pseudosection for the varied gneiss sample EV340B was calculated with the whole-rock composition given in Tab. 18, with H_2O adjusted to 1.5 mol%, and O set to 0.05 mol% in

order to allow the ilmenite–rutile transition to be present in the investigated P – T range (Fig. 82a). In the pseudosection, garnet and K-feldspar are stable in the whole P – T range, the dry solidus line lies at ~ 850 °C, and biotite is stable until ~ 880 °C. Cordierite is stable below 5–6 kbar at 600–800 °C and below ~ 7 kbar at higher temperature. Rutile is stable above ~ 7 kbar, whereas ilmenite disappears above ~ 13 kbar between 600 and 850 °C and above ~ 15 kbar at temperatures higher than 900 °C.

In sample EV340B, the succession of kyanite and sillimanite inclusions in garnet suggests that crossing of the ky–sill transition was coeval with garnet growth, but sillimanite and biotite are also included at the garnet rim (Fig. 80a–c). In addition, garnet zoning (Fig. 81a) shows a Ca decrease and an X_{Fe} increase from the zone of kyanite inclusions (grs_{05-04} ; $X_{Fe}=0.57-58$) towards the rim hosting sillimanite (grs_{02} ; $X_{Fe}=0.61-62$). The observations are compatible with a pressure decrease from the bi–g–pl–ksp–ky–liq–ru±ilm to the bi–g–pl–ksp–sill–liq–ru–ilm field, and a later P – T decrease towards the cordierite stability field (Fig. 82a). Moreover, garnet zoning is in agreement with a nearly isothermal decompression path starting at 12–14 kbar and 840–880 °C where $z(g)$ and $x(g)$ lie close to the measured garnet composition in the zone of kyanite inclusions (Fig. 82d, e), and ending with garnet rim equilibration at the melt-out line at 8–10 kbar and 820–860 °C. However, the shape of garnet modal isopleths suggests that the decompression was probably accompanied by a slight heating which would allow garnet crystallisation, while the amount of melt remained below 7–8 mol% (Fig. 82b, c). Cordierite and ilmenite occurrences in the matrix point to subsequent P – T conditions below ~ 5 kbar and ~ 750 °C without partial melting (Fig. 82a).

Varied gneiss - Pseudosection with re-integrated melt

As suggested above, the metasedimentary protolith of the varied gneiss was probably richer in H_2O . In addition, studies have proposed that garnet from partially molten high-grade rocks may correspond to a possible subsolidus garnet with weakly preserved Ca zoning (Spear *et al.*, 1999), plus a major part of garnet formed via incongruent dehydration melting reactions (e.g. Kriegsman, 2001). Granitic melt was therefore re-integrated in order to model the onset of garnet growth at subsolidus conditions: close to the H_2O -saturated solidus, without stable K-feldspar, and with only minor kyanite ($\sim 2\%$). A pseudosection with 19% of melt re-integrated at 13 kbar and 860 °C best fulfilled these conditions (Fig. 82f). It involves rutile stability in the whole P – T range, garnet stability above 9.5–11 kbar and above 800 °C, muscovite to K-feldspar breakdown between 650–850 °C for the investigated pressure range, and ilmenite stability below 11 kbar and ~ 700 °C. The H_2O -saturated solidus lies at ~ 650 °C below 10 kbar while dry melting occurs at ~ 700 °C for higher pressures.

Garnet from sample EV340B hosts biotite and rutile inclusions in the core, whereas similar neighbouring samples show kyanite included in garnet and K-feldspar (Fig. 80b, d). It suggests that kyanite was developed before abundant garnet and K-feldspar blastesis. Additionally, the onset of garnet growth at subsolidus conditions could be indicated by significant Ca values (grs_{07}), and probably occurred in the rutile stability field. In the pseudosection, these conditions are met at 9–10.5 kbar and 600–650 °C where the modelled $z(g)=0.7$ –0.8 values are similar to the garnet core composition, but $x(g)=0.80$ is significantly

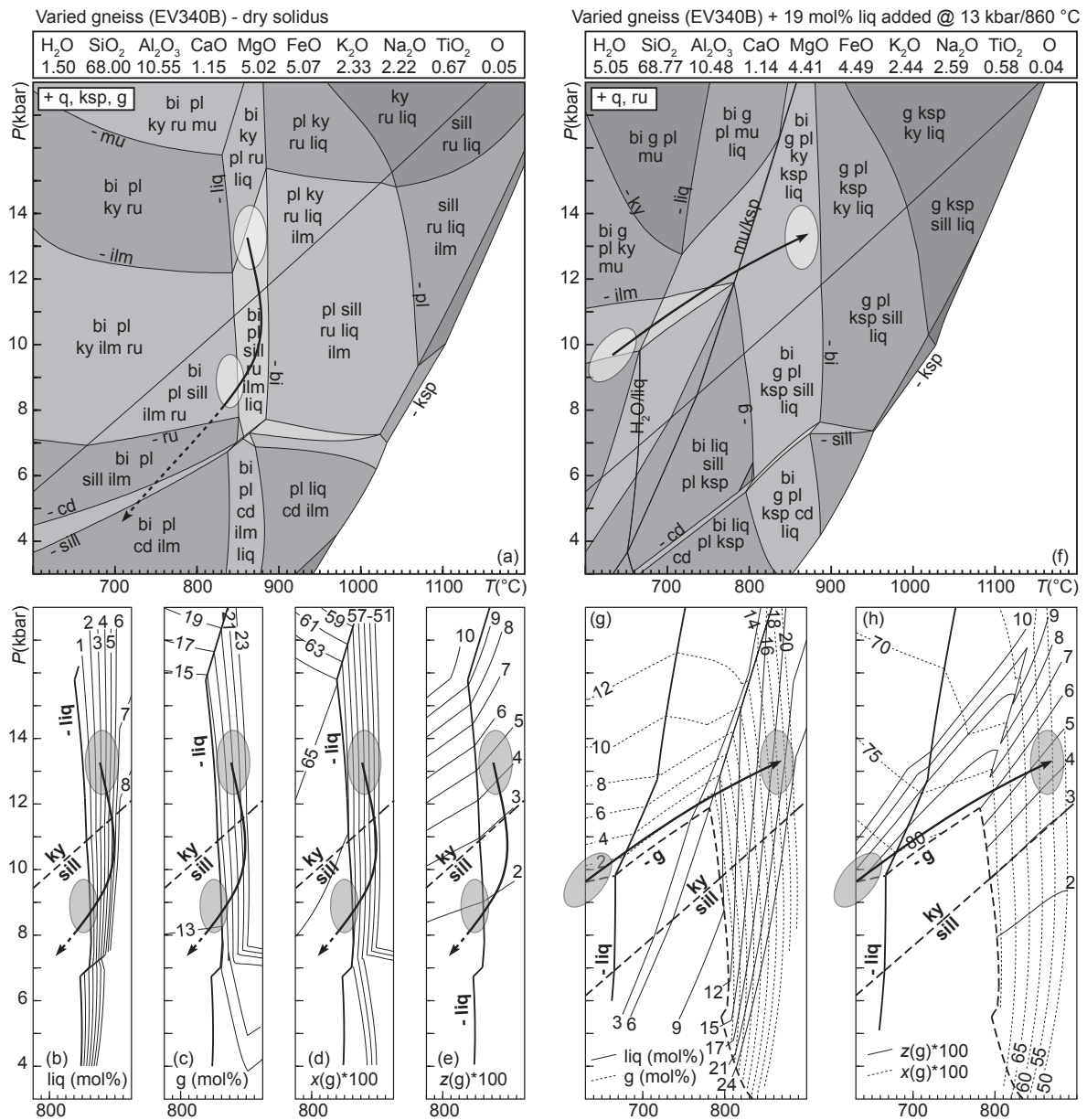


Figure 82. Pseudosections for varied gneiss sample EV340B. (a–e) Pseudosection calculated with the original whole-rock composition and contoured with modal isopleths of granitic melt and garnet, and compositional $z(g)$ and $x(g)$ isopleths. (f–h) Pseudosection calculated with 19% of re-integrated melt and contoured with modal isopleths of granitic melt and garnet, and compositional $z(g)$ and $x(g)$ isopleths.

higher (Fig. 82f, h). The discrepancy between the modelled $x(g)$ and the observed X_{Fe} in garnet core could be explained by important Fe and Mg diffusion which is commonly reported at high temperature (e.g. Yardley, 1977). A subsequent increase in pressure and temperature would produce, as a result of incongruent melting, additional garnet with nearly constant $z(g)$ and decreasing $x(g)$ (Fig. 82g, h). Moreover, a crossing of the $\mu+q=ky+ksp$ discontinuous reaction is likely to explain kyanite inclusions in K-feldspar, and the presence of K-feldspar in the inferred peak $P-T$ assemblage (Fig. 82f).

Felsic granulite - Pseudosection with dry solidus

The pseudosection for felsic granulite sample EV390M was calculated using the whole-rock composition reported in Tab. 18, and with H_2O adjusted to 0.23 mol%. In the pseudosection calculated up to K-feldspar breakdown, rutile is always present, the dry solidus lies at ~ 800 °C from 3 to 13 kbar, and biotite is stable below 840–850 °C (Fig. 83a).

Garnet from felsic granulite sample EV390M commonly hosts perthitic K-feldspar and rutile inclusions, and kyanite is frequent in the matrix (Fig. 80e, g). The same minerals display a clear textural equilibrium in a neighbouring felsic granulite sample (Fig. 80f), but kyanite is commonly surrounded by sillimanite needles. In addition, garnet is generally replaced by biotite and chlorite. Garnet shows no zoning with nearly constant $X_{Fe}=0.76-0.78$ and grossular (grs_{02}) values (Fig. 81b) that are indicative of HT resetting (e.g. Bohlen, 1987).

The observations indicate an evolution from the $g-ksp-pl-ky-ru-q-liq$ to the $g-ksp-pl-sill-ru-q-liq$ field, followed by biotite and chlorite crystallisation without melt. The decompression from the kyanite to the sillimanite stability field was nearly isothermal, and may have occurred while a minor amount of biotite and melt was stable (Fig. 83a, b). It is supported by the steep shape of the $x(g)$ isopleths which show values compatible with the garnet X_{Fe} in the $bi-g-ksp-pl-ky/sill-ru-q-liq$ fields (Fig. 83c,d). However, the Ca content in garnet (grs_{02}) only accounts for $P-T$ conditions in the sillimanite stability field (Fig. 83d), and peak pressure above 10 kbar can only be derived from kyanite occurrence. The inferred $P-T$ path therefore stretches from 10–13 kbar and 810–830 °C to garnet rim equilibration close the melt-out line at 6.5–8.5 kbar and 800–820 °C (Fig. 83d). Assuming that the felsic granulite and the varied gneiss units shared the end of the $P-T$ path, it is speculated that further decompression and cooling towards ~ 4.5 kbar and ~ 700 °C occurred.

Felsic granulite - Pseudosection with re-integrated melt

Several authors have postulated that the protolith of felsic granulite may correspond to a rock of granitic composition (Fiala *et al.*, 1987; Vellmer, 1992; Janoušek *et al.*, 2004). Therefore, melt was re-integrated in order to allow the existence, at MP/MT conditions, of a $ksp-pl-\mu-bi-ru$ field corresponding to a typical granitic mineralogy. The addition of 6 mol% of melt

at 11 kbar and 800 °C produced a pseudosection with the ksp–pl–mu–bi–ru field stretching from 6–10 kbar at 600 °C to 12 kbar and 500 °C (Fig. 83f). The lower pressure boundary of this field corresponds to the dry melting curve while the upper pressure one is represented by garnet appearance. The major features of the pseudosection involve rutile stability in the whole P – T range, garnet stability above 10–12 kbar and above ~780 °C, partial melting above ~650 to ~750 °C for 3–18 kbar, biotite stability below ~850 °C, and muscovite to Al_2SiO_5 breakdown from ~650 to ~850 °C with increasing pressure.

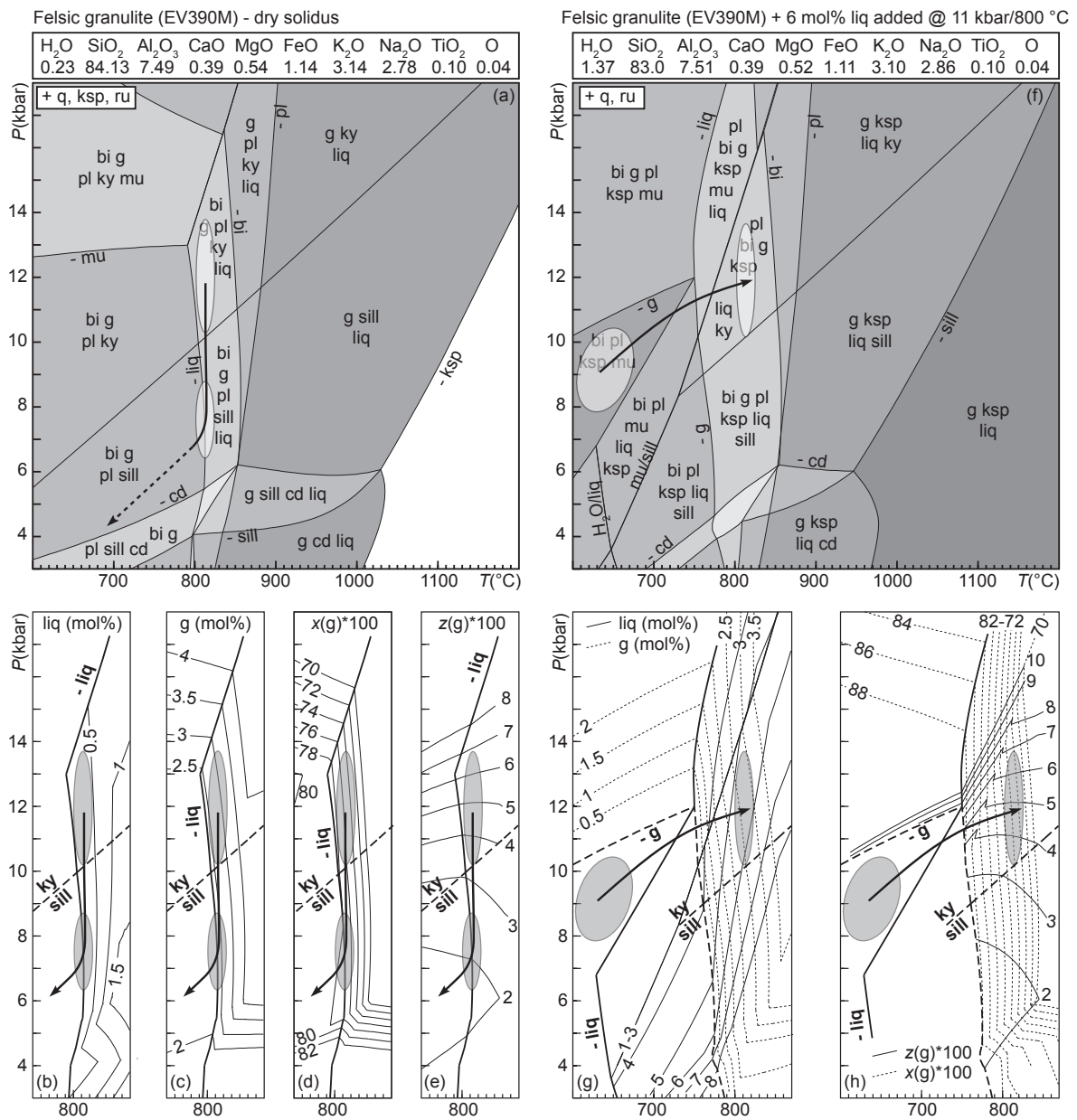


Figure 83. Pseudosections for felsic granulite sample EV390M. (a–e) Pseudosection calculated with the original whole-rock composition and contoured with modal isopleths of granitic melt and garnet, and compositional $z(g)$ and $x(g)$ isopleths. (f–h) Pseudosection calculated with 6% of re-integrated melt and contoured with modal isopleths of granitic melt and garnet, and compositional $z(g)$ and $x(g)$ isopleths.

The evolution from a granitic assemblage towards P – T conditions of 10–13 kbar and 810–830 °C would (1) generate partial melting, (2) trigger garnet growth and thus embayment of pre-existing K-feldspar, quartz and rutile, and (3) lead to kyanite crystallisation (Fig. 83f). However, any P – T path starting from 7–11 kbar and 600–700 °C, and showing increasing pressure and temperature is likely to produce such features. Moreover, the proposed evolution can not be confirmed by garnet isopleths, because no garnet zoning is preserved (Fig. 81b & 83h). Nevertheless, the pseudosection predicts that a P – T increase towards peak conditions is associated with a small amount of partial melting (< 8 mol%) and only minor garnet (< 3.5 mol%) growth (Fig. 83g).

Assessing zircon behaviour through the P – T evolution

Following the same approach as for the NCKFMASHTO system, pseudosections using both the original whole-rock composition and re-integrated melt have been calculated in the NCKFMASHTZr system. In addition, ZrO_2 partition between garnet, rutile, zircon and silicate melt has been investigated along the P – T evolutions inferred from pseudosections in the NCKFMASHTO system. This was performed in order to (1) examine zircon dissolution and crystallisation along the inferred P – T paths, (2) confront the modelled zircon behaviour to the obtained U–Pb age results, and (3) question the P – T estimates in the light of dissolved and recrystallised zircon proportions.

Preliminary calculations as well as zircon modal isopleths (Figs 84 & 85) indicate that pressure has a little effect on zircon dissolution or growth. Zircon preservation has therefore been evaluated along a prograde path reaching varying peak temperature conditions at a constant pressure. In addition, the retrograde path for both the varied gneiss and the felsic granulite involves isothermal decompression followed by P – T decrease (Figs 82 & 83). After adjusting the peak temperature with respect to the inferred amount of preserved zircon, the zircon behaviour was therefore investigated at different steps of a hypothetical P – T path along different retrograde gradients.

Varied gneiss - Pseudosections with Zr-bearing models

The pseudosection topologies are nearly similar to those presented in Fig. 82 except for rutile and ilmenite. Indeed, in the absence of modelled ferric iron and because Zr is present in the rutile model, ilmenite is never stable, whereas rutile is always present in the investigated P – T range. In the pseudosection with 19% of re-integrated melt, zircon stability is bounded by a steep line stretching from 4 kbar and ~ 900 °C to 18 kbar and ~1000 °C, while it is extended towards higher temperatures of 930–1080 °C with the original whole-rock composition (Fig. 84a, b).

For the varied gneiss, the early P – T evolution is believed to proceed from ~ 9 kbar/600 °C to ~ 13 kbar/860 °C (Fig. 82). In addition, CL-controlled U–Pb dating reveals that zircon grains preserving Proterozoic to Early Palaeozoic ages roughly represent 50–60% of the total zircon volume, whereas Variscan ages are recorded in 40–50% of the total zircon volume. At the onset of the P – T evolution nearly all ZrO_2 is trapped in zircon, and with increasing P – T conditions zircon progressively dissolves while the amount of ZrO_2 in melt, rutile and garnet increases (Fig. 84c). The zircon modal isopleths show that zircon dissolution is non-linear (Kelsey & Powell, 2011) and increases after crossing of the muscovite–K-feldspar transition (Fig. 84a, c). Along the modelled P – T path, the preservation of $\sim 60\%$ of the zircon volume is achieved between 850 and 950 °C. Assuming that all Variscan ages are derived from newly formed grains ($\sim 40\%$), the zircon dissolution model could be in agreement with the peak temperature estimates of 840–880 °C.

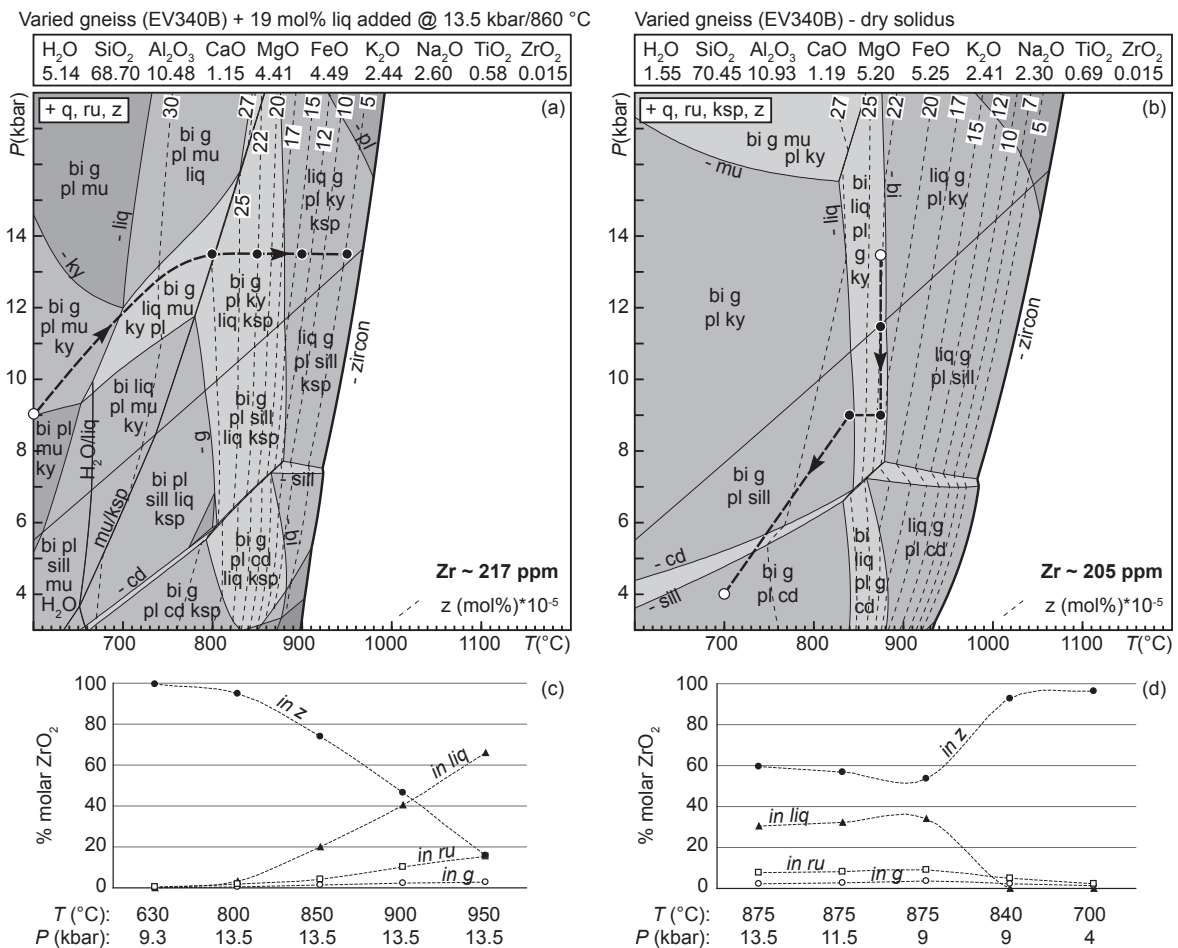


Figure 84. Pseudosections with Zr-bearing models for varied gneiss sample EV340B, and modelled ZrO_2 partition along hypothetical P – T paths. Pseudosection calculated (a) with 19% of re-integrated melt, and (b) with the original whole-rock composition. (c, d) Evolution of ZrO_2 partition between zircon, rutile, garnet and granitic melt along the indicated prograde and retrograde paths.

The hypothetical retrograde path starts at 13.5 kbar/875 °C where the proportion of remaining zircon lies close to 60% (Fig. 84b-d). According to previous estimates, the varied gneiss subsequently follows a nearly isothermal decompression path to ~9 kbar/840 °C and later P - T decrease. The modelled zircon behaviour indicates that isothermal decompression is not associated with zircon growth, and that even a slight dissolution occurs (Fig. 84b, d). By contrast, cooling, i.e. melt crystallisation is responsible for significant zircon growth while only a little amount of zircon forms at subsolidus conditions when the retrograde P - T path reaches ~4 kbar/700 °C.

Felsic granulite - Pseudosections with Zr-bearing models

Pseudosections for the felsic granulite calculated in the NCKFMASHTZr system display nearly similar topologies to those obtained without Zr-bearing models (Fig. 83a, f). In the pseudosection with 6 mol% of re-integrated melt zircon is stable below a steep line stretching from ~900 °C at 3 kbar to ~1000 at 18 kbar, whereas in the pseudosection using the original composition the zircon-out line extends from ~1000 °C at 3 kbar to ~1200 °C at 18 kbar (Fig. 85a, b).

A possible prograde path for the felsic granulite starts at ~9 kbar/600 °C and ends up at ~11 kbar/820 °C (Fig. 83f). The CL images of zircon extracted from the felsic granulite together with U-Pb dating results show that hardly more than 20% of the total zircon volume preserves inherited ages, while 70–80% corresponds to Variscan ages. In the field with a granitic mineralogy all available ZrO_2 is in zircon, but zircon gradually dissolves, mostly in melt, as long as the rock is heated (Fig. 85a, c). When reaching 850 °C at 11 kbar, ~80% of the zircon volume is preserved and a higher temperature of ~950 °C is needed to leave about 30% of the original zircon volume (Fig. 85c). If all Variscan zircon grains are assumed to be newly grown, peak temperature estimates should consequently be closer to ~950 °C.

Assuming that peak temperature conditions could have been higher, the beginning of the hypothetical retrograde path is set at 11kbar/950 °C with ~30% of preserved zircon (Fig. 85b, d). As suggested by the pseudosection without Zr (Fig. 83a), the retrograde path involves isothermal decompression followed by cooling towards melt-free assemblages. Like for the varied gneiss, isothermal decompression is associated with a renewed zircon dissolution hardly exceeding 10%, while zircon crystallises only when the rock is cooled (Fig. 85b, d). As mentioned above, the cooling path associated with melt crystallisation is responsible for a major zircon growth during retrograde evolution.

Table 18. Major element and Zr composition of samples EV340B and EV390M used for mineral equilibria modelling.

	Oxides (wt.%)	SiO ₂	Al ₂ O ₃	Fe ₂ O ₃	FeO	MgO	CaO	Na ₂ O	K ₂ O	TiO ₂	P ₂ O ₅	MnO	LOI	Total	Zr (ppm)
EV 340 B	varied gneiss	63.76	16.78	7.01*	<i>n.a.</i>	3.16	1.09	2.15	3.43	0.84	0.07	0.08	1.30	99.69	213.3
EV 390 M	felsic granulite	77.82	11.77	0.20	1.27	0.33	0.52	2.66	4.55	0.13	0.15	0.02	0.40	99.82	83.1

*: total Fe expressed as Fe₂O₃; LOI = loss on ignition; *n.a.* = not analysed

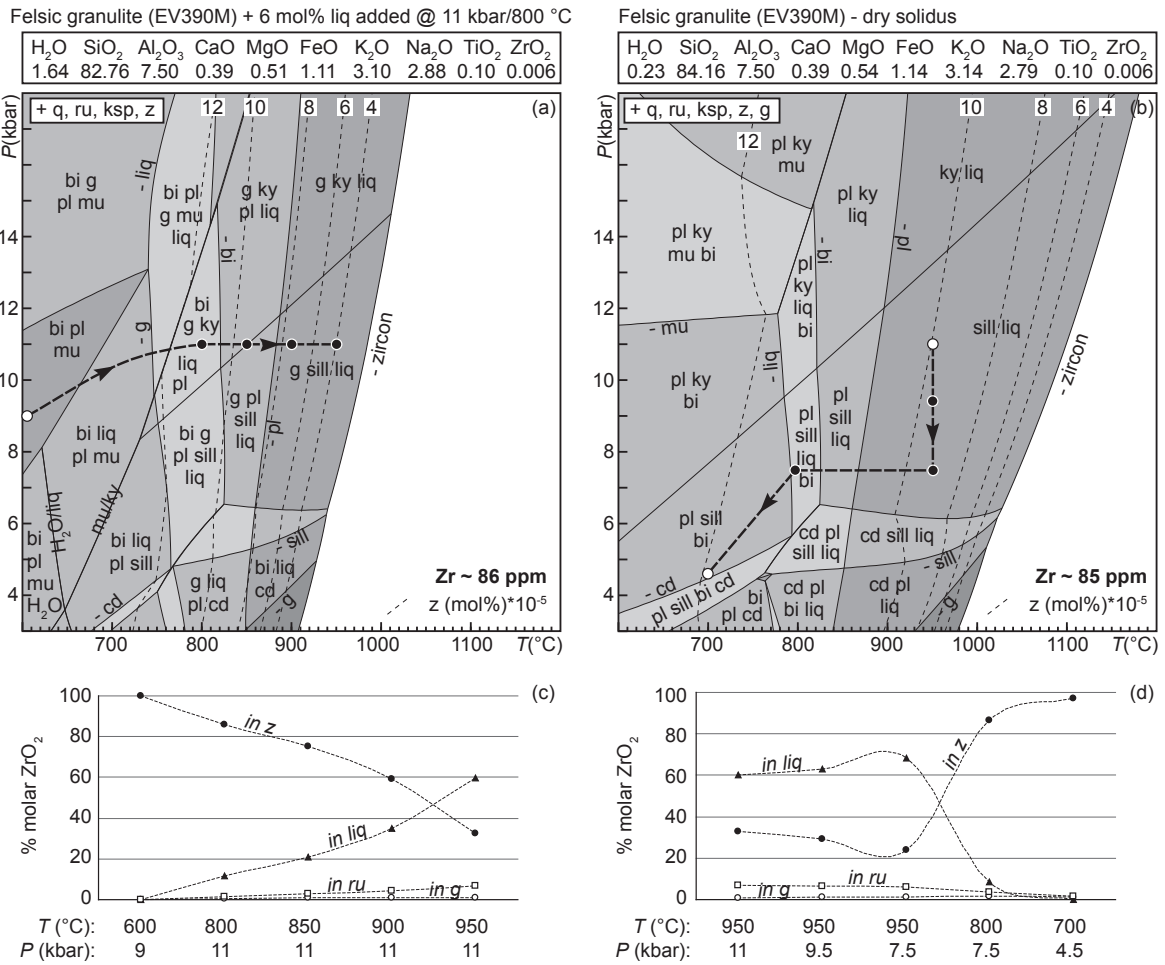


Figure 85. Pseudosections with Zr-bearing models for felsic granulite sample EV390M, and modelled ZrO₂ partition along hypothetical *P-T* paths. Pseudosection calculated (a) with 6% of re-integrated melt, and (b) with the original whole-rock composition. (c, d) Evolution of ZrO₂ partition between zircon, rutile, garnet and granitic melt along the indicated prograde and retrograde paths.

5) Metamorphic evolution of the orogenic root

Monotonous gneiss unit

The P – T evolution of the monotonous gneiss unit can be described using previous studies combined with unpublished observations. Some samples containing a garnet–staurolite assemblage indicate that the metapelitic–metapsammitic monotonous unit underwent metamorphism in the amphibolite facies. It is confirmed by rare garnet relicts that show decreasing Mn content from core (sps₁₃) to rim (sps₀₅), which is a feature commonly related to prograde metamorphism in metasedimentary rocks (e.g. Hollister, 1966). According to Rey *et al.* (1989) and Latouche *et al.* (1992), the rocks further reached peak conditions of 5–7 kbar and 600–660 °C, possibly in the kyanite stability field (Fig. 86). Additionally, the noticeable absence of muscovite and the widespread occurrence of sillimanite suggest muscovite breakdown probably associated with limited partial melting. All these observations therefore support the idea that temperature hardly exceeded ~700 °C and that the monotonous gneiss only straddled the limit of anatexis (Fig. 86).

Later growth of cordierite led Rey *et al.* (1989) and Latouche *et al.* (1992) to propose retrograde metamorphism below 5 kbar and 550 °C (Fig. 86). In addition, rare spinel rims around staurolite can be indicative of relatively high temperature and low pressure conditions, as already reported by Latouche *et al.* (1992).

Varied gneiss unit

In the varied gneiss unit, a possible prograde stage of garnet growth under H₂O-saturated conditions has been erased by subsequent anatexis. Conversely, the observed garnet porphyroblasts commonly show a texture with cores rich in tiny rutile inclusions (Fig. 80a, b). Montel & Vielzeuf (1997) have demonstrated that garnet produced via incongruent melting of metasedimentary rocks preserves a significant amount of Ti, especially in the core region. Following the idea of Tropper *et al.* (2005), it is therefore proposed that the rutile needles found in garnet cores actually represent exsolutions from an originally Ti-rich garnet which was formed through partial melting. The present interpretation together with the occurrence of kyanite inclusions in garnet and K-feldspar (Fig. 80b, d) indicate that the varied gneiss unit underwent prograde metamorphism associated with up to 20% of granitic melt production, and reached granulite-facies conditions of 12–14 kbar and 840–880 °C (Fig. 82).

The peak P – T conditions for the varied gneiss were mostly constrained using garnet chemistry. However, considering that intracrystalline diffusion may have contributed to a partial resetting of the garnet profile (Fig. 81a), they could only represent minimum estimates.

In the absence of an additional barometer, kyanite occurrence is therefore the only indicator of relatively high pressure above 11 kbar, and contradicts to the idea of Latouche *et al.* (1992) who believed that HP metamorphism was only restricted to the felsic granulite unit.

The end of the subsequent isothermal decompression path is documented by garnet rim equilibration with the last liquid phase. It occurs in the sillimanite stability field at 8–10 kbar and 820–860 °C (Fig. 82a-e). Widespread matrix sillimanite and cordierite growth indicate a subsequent pressure decrease below 4–5 kbar (Fig. 86). It is in line with previous estimates of final equilibration at P – T conditions below 5 kbar and 600–650 °C (Rey *et al.*, 1989; Latouche *et al.*, 1992).

Felsic granulite unit

The protolith of the felsic granulite is believed to be a meta-igneous rock of granitic composition (e.g. Fiala *et al.*, 1987; Vellmer, 1992; Janoušek *et al.*, 2004). Modelling its metamorphic evolution was possible with a small amount (6 mol%) of melt re-integration, which is concordant with results suggesting that the felsic granulite lost only a minor amount of melt (Janoušek *et al.*, 2004). In order to reach the assemblage perthitic K-feldspar–garnet–kyanite–rutile, the rock has to undergo prograde metamorphism associated with partial melting, and garnet and kyanite growth (Fig. 83f). The end of this path lies at peak conditions of 10–13 kbar and 810–830 °C (Fig. 83f).

Like for the varied gneiss, peak P – T conditions are probably underestimated due to strong garnet resetting (Fig. 81b). Considering that Gayk & Kleinschrodt (2000) reported garnet with higher grossular content (up to 11 mol%) in rocks with nearly the same bulk composition, it can be confidently envisaged that peak pressure may have reached at least ~13 kbar, suggesting a coupled evolution with the varied gneiss unit. Peak temperatures of 810–830 °C may also be undervalued as indicated by zircon dissolution modelling. Gayk & Kleinschrodt, (2000) found them to be abnormally high and attributed them to heating by the neighbouring peridotite bodies. Nevertheless, the investigated samples being located relatively far from mantle slices, it is proposed that the HT conditions merely correspond to regional metamorphism and not to an additional heating. Importantly, the occurrence of kyanite places the Vosges felsic granulite in the HP granulite field defined by O'Brien & Rötzler (2003), thus making it a member of this rock type which is characteristic for the Variscan orogenic root. With respect to other Variscan HP granulite massifs where peak P – T conditions above 15 kbar and 800 °C are generally proposed (e.g. Pin & Vielzeuf, 1988; Carswell & O'Brien, 1993; Kryza *et al.*, 1996; Willner *et al.*, 1997), the felsic granulite unit of the Vosges Mountains therefore indicates slightly lower pressures but similar temperatures.

Following the peak of metamorphism, sillimanite growing around kyanite is the best witness of decompression (Fig. 80f, g) and is in agreement with garnet rim equilibration at 6.5–8.5 kbar and 800–820 °C (Fig. 83a). Later growth of biotite and chlorite after garnet points to a drop in pressure and temperature, probably towards retrograde conditions below 4 kbar and 500 °C (Fig. 86).

6) Origin of Variscan metamorphic zircons

Monotonous gneiss unit

In the monotonous gneiss unit, no Variscan ages were obtained from the analysed zircon grains (Fig. 87a). Previous petrological works coupled with several own observations further suggest that P – T conditions for this unit never exceeded ~10 kbar and 700 °C, and hardly reached abundant partial melting (Fig. 86). Upper amphibolite-facies conditions therefore seem insufficient to allow the formation of Variscan zircon, either through crystallisation from an anatectic melt or via recrystallisation of older grains. It does not mean, however, that Variscan ages should be entirely absent from the monotonous gneiss unit, and later finding of zircon rim overgrowths yielding Variscan ages is not excluded. Nonetheless, the present work shows that such an age population should be statistically insignificant.

Varied gneiss unit

The varied gneiss unit records Variscan ages which are in the range of 340–320 Ma (Fig. 77). Such ages seem to correspond to ~40% of the total zircon volume and are represented by two zircon populations showing distinct morphologies, CL patterns and U–Th chemical signatures.

The zircon dissolution model suggests about 40% of zircon resorption during prograde metamorphism (Fig. 84). However, the older zircon grains, and especially the large and nicely prismatic Neoproterozoic–Ordovician grains do not show low-angle truncations or embayments (Fig. 75b) which are typical for resorption in melt (e.g. Hanchar & Miller, 1993). It suggests that a major amount of Variscan zircon probably did not originate from the crystallisation of an anatectic melt. Indeed, the blurred zoning which is observed in some zircon (Fig. 75b) is commonly taken as an indicator of solid-state recrystallisation during metamorphism (Hoskin & Schaltegger, 2003). Additionally, the blurred zircon grains show U–Th concentrations which are in the same range than those of Neoproterozoic–Ordovician zircon analyses (Fig. 79b). It is concordant with the observation that, in some cases, recrystallisation can be associated with rehomogenisation of the initial oscillatory zoning

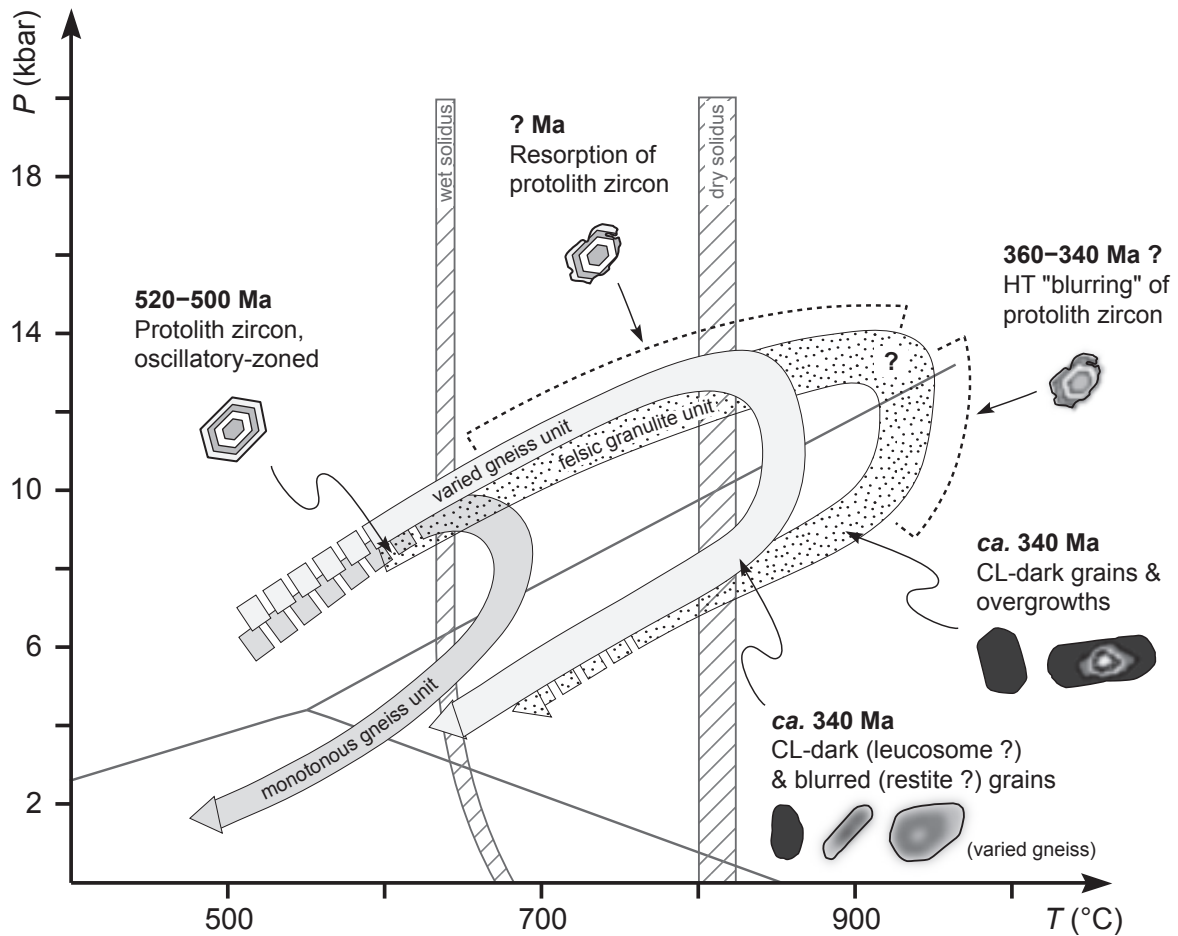


Figure 86. P - T evolution, zircon behaviour and age constraints for the Central Vosges metamorphic units.

without strong chemical changes (Black *et al.*, 1986). Therefore, Variscan ages which are derived from blurred zircon are thought to reflect recrystallisation of older and most likely Neoproterozoic–Ordovician zircon grains (Fig. 86).

By contrast, a second less abundant zircon population shows anhedral to prismatic grains with a homogeneous dark CL pattern (Fig. 75b) and high U–Th concentrations (Fig. 79b). Although featureless zircon can result from recrystallisation (Hoskin & Black, 2000), the strong difference in U and Th concentrations between these grains and the older zircon analyses suggests that the CL-dark grains are derived from a different source. The source could correspond to an anatectic melt which would have crystallised along an isobaric cooling path, as predicted by the modelled zircon isopleths (Fig. 84b). Even if no distinction was made between zircon grains from leucosomes and restites, it could be further postulated that the CL-dark crystals belong to the leucosomes where Schaltegger *et al.* (1999) already found zircon grains yielding similar ages of *ca.* 330 Ma. It is therefore proposed that solid-state recrystallisation was dominant in the restitic part, although small zircon overgrowths related to partial melting can occur (Schaltegger *et al.*, 1999). On the other hand, crystallisation of

new grains from melt mostly took place in the leucosomes. Both events are associated with a short period of 340–330 Ma (Fig. 86).

Felsic granulite unit

Apart from rare inheritance, U–Pb zircon ages in the felsic granulite unit define a nearly continuous array from 520 to 325 Ma (Fig. 78). Only few euhedral and partially resorbed zircon cores preserve a well-defined oscillatory zoning and ages around 520–500 Ma (Fig. 75c). Because fine concentric zoning in euhedral crystals is generally considered as an indicator of igneous crystallisation (Hanchar & Miller, 1993), these zircon cores are attributed to the igneous protolith of the felsic granulite (Fig. 86).

The zircon cores showing a blurred CL pattern bear similarities to the undisturbed oscillatory-zoned cores. They are anhedral, partially resorbed crystals of variable size (Fig. 75c) that have similar U and slightly lower Th concentrations than the 520–500 Ma zircon group (Fig. 79c). There is therefore little doubt that they represent partly reset protolith zircon grains. The progressive thickening and fading of bands has been interpreted as a late magmatic process by Pidgeon *et al.* (1998). However, given that several blurred cores yield *ca.* 340 Ma ages, a metamorphic origin is presently favoured, as proposed by Hoskin & Black (2000). The metamorphic event is reflected by a mixing in age results between protolith ages of 520–500 Ma and a 340 Ma end member, with additional peaks at *ca.* 430 and 370 Ma (Fig. 78). Although such ages are commonly regarded as meaningless (e.g. Bröcker *et al.*, 2010), they carry an indirect information. Diffusion of Dy which is the major CL contributor in zircon (e.g. Hanchar & Rudnick, 1995 and references therein) can result from HT metamorphism. At conditions of 850–950 °C probably close to those reached by the felsic granulite, blurring to complete loss of 1–10 µm thick bands occurs on the order of tens of million years (Cherniak *et al.*, 1997; Cherniak & Watson, 2003). Considering that variable blurring is observed, it is therefore proposed that the HT event may have lasted about 10 Ma (Fig. 86).

The major amount (~80%) of zircon from the felsic granulite corresponds to uniform CL-dark overgrowths or single grains (Fig. 75c). They have higher U and much lower Th concentrations than the previously described zircon types (Fig. 79c). Such featureless zircon domains have been ascribed by several authors to a transgressive recrystallisation process (see Hoskin & Schaltegger, 2003 for a review). The replacement process is thought to progress from the crystal rim towards the centre along irregular or curved fronts. It may leave a faint trace of the former zoning (Pidgeon, 1992), or even result in complete recrystallisation (Hoskin & Black, 2000). Whereas several works document a decrease in Th and U between the original and the secondary domains (Pidgeon, 1992; Bowring & Williams, 1999), others observe a

U increase (Nemchin & Pidgeon, 1997; Hoskin & Black, 2000). The zircon grains analysed in this study differ on several points. The CL-dark overgrowths are large, isometric and developed into new crystals with prismatic faces and rounded tips. The dark CL pattern is also commonly observed in single euhedral to subhedral grains (Fig. 75c). These morphological features are closer to the prismatic to isometric types of overgrowths described by Vavra *et al.* (1999). According to these authors, U enrichment in the overgrowths is explained by preferential incorporation in the zircon lattice during crystallisation from melt. It is explained by U having a smaller ionic radius than Th (Speer, 1982). Accordingly, the dark CL domains are interpreted as the result of crystallisation from an anatectic melt at *ca.* 340 Ma (Fig. 86).

7) Zircon dissolution/crystallisation model

The inferred mechanisms of zircon growth can be confronted to the modelling of zircon behaviour during metamorphism. For the varied gneiss, it is proposed that only a small amount (< 10%) of Variscan zircon actually crystallised from melt. It implies limited dissolution during prograde metamorphism, which would be achieved for peak temperature conditions of 800–825 °C (Fig. 84a, c). Conversely, strong dissolution has to occur in the felsic granulite in order to produce a large zircon proportion (~80%) after partial melting. This view is also supported by frequent resorption features observed in zircon cores. Following the model, the required zircon dissolution is associated with a peak temperature of ~950 °C (Fig. 85b, d).

In both lithological units, the constraints inferred from zircon dissolution modelling differ significantly. Peak temperature estimates are either slightly lower or markedly higher than those predicted by garnet chemistry (Figs 82 & 83). It can be explained by the fact that the proposed approach ignores some important factors. Harrison & Watson (1983) demonstrated that zircon dissolution depends on the original crystal size, and more importantly on the water content of the melt. Because re-integrated compositions are presently used, it can be argued that the original amount of H₂O remains speculative, and that any higher H₂O content associated with an initial small zircon size may enhance dissolution. Nevertheless, it is demonstrated the controlling factor for zircon dissolution is not only the degree of partial melting, but also the Zr concentration in the protolith.

The modelling of zircon crystallisation carries additional information. As proposed by Roberts & Finger (1997), a nearly isobaric cooling path at middle pressure conditions would result in zircon crystallisation, chiefly because Zr saturation in melt is attained (Watson & Harrison, 1983). It is in agreement with the *P–T* evolution of both units which shows cooling after isothermal decompression. Accordingly, it is suggested that zircon crystallised from the anatectic melt during cooling below ~800 °C at pressures between 6 and 8 kbar.

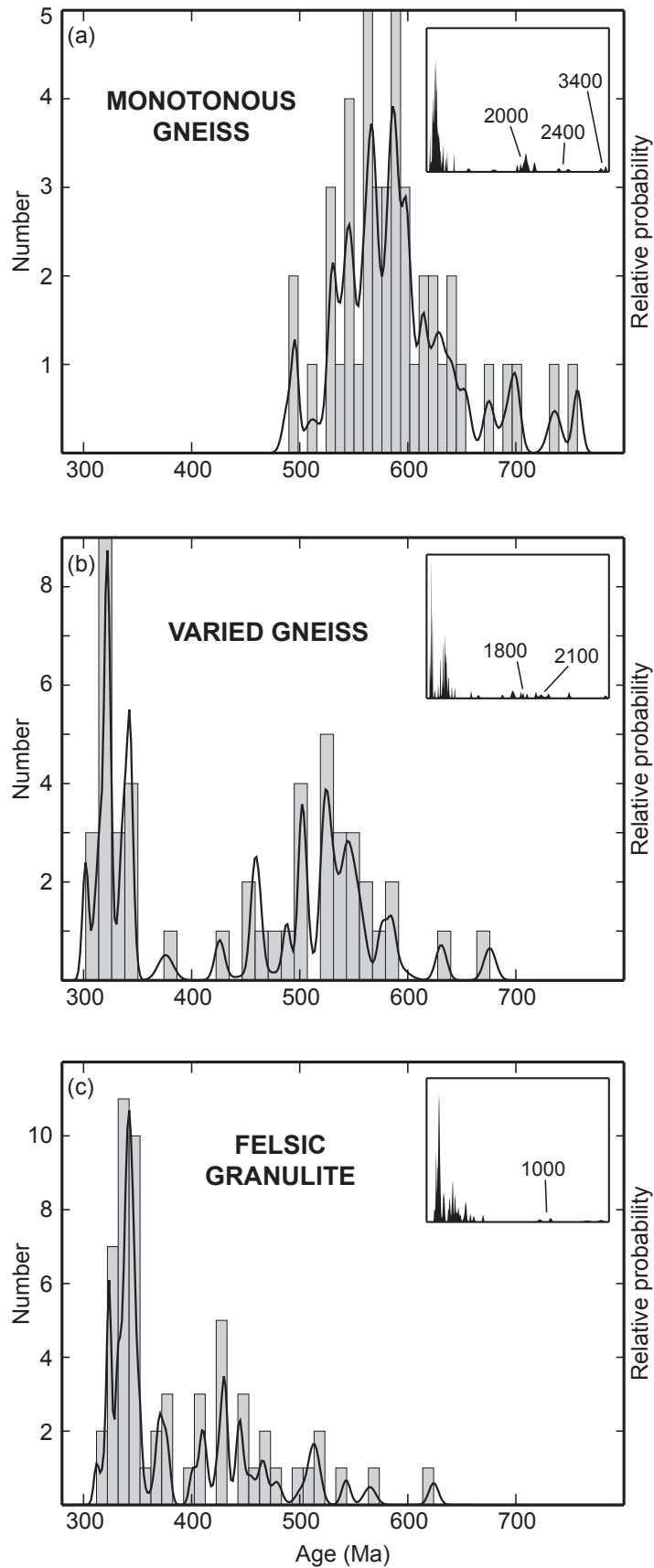


Figure 87. Summary of U–Pb zircon ages for the Central Vosges metamorphic units. Histograms and relative probability curves are calculated with $^{206}\text{Pb}/^{238}\text{U}$ ages and focus on the Neoproterozoic–Palaeozoic period. Insets show older inheritance. (a) Monotonous gneiss unit. (b) Varied gneiss unit. (c) Felsic granulite unit.

8) Geological implications

Protolith ages

The oldest protolith ages are found in the felsic granulite unit where few zircon cores indicate an igneous crystallisation at *ca.* 500 Ma (Fig. 87). In addition, rare inheritance points to a probable I-type magmatic origin. Given that several cores are partly blurred and reset, these results can be considered as minimum estimates. Nevertheless, they are relatively close to Cambro-Ordovician ages from the Saxonian Granulite Massif (Kröner & Willner, 1998), Southeast Bohemia (Kröner *et al.*, 2000a; Friedl *et al.*, 2003) or the West Sudetes (Bröcker *et al.*, 2009). It is therefore proposed that the felsic granulite unit represents metamorphosed acid rocks which were emplaced during the Early Cambrian.

U–Pb zircon ages provide a maximum deposition age for the metasedimentary monotonous and varied gneiss units. The youngest $^{206}\text{Pb}/^{238}\text{U}$ ages in the monotonous gneiss are about 490 Ma old, suggesting a deposition during the Lower Ordovician. By contrast, slightly younger ages of *ca.* 460 Ma obtained in varied gneiss samples point to a later sedimentation during the Upper Ordovician (Fig. 87). Both units can correspond to a continuous deposition episode in the same basin, with the varied unit representing a later, more proximal part than the distal monotonous sedimentation. Alternatively, they can be separated successions, both spatially and temporally, which have been juxtaposed during later orogeny. Despite that unclear origin, the Ordovician sedimentation ages are strongly compatible with the age of similar “monotonous/varied” associations found in the Variscan Belt of Europe, especially in the West Sudetes (Jastrzębski *et al.*, 2010) or in the neighbouring Black Forest (Kober *et al.*, 2004).

High-pressure metamorphism ?

Petrological data indicate the monotonous gneiss unit probably reached peak *P–T* conditions in the upper amphibolite facies, whereas the varied gneiss and felsic granulite units document equilibration in the HP granulite facies. However, considering that the younger varied unit is presently thrust over the less metamorphosed monotonous unit, both lithologies can not correspond to an originally homogenous sedimentary succession. In addition, the generation of felsic granulite has commonly been interpreted as a result of continental subduction (e.g. O’Brien & Rötzler, 2003). In this view, the varied unit would represent deposits which were originally separated from the monotonous unit, and which were later brought in contact after subduction to 40–50 km depth and exhumation together with its basement substratum, i.e. the protolith of the felsic granulite unit. The timing of the associated HP metamorphic event is

unknown, probably because it is not recorded in zircon. However, blurring of protolith zircon in felsic granulite suggests that HT conditions affected the rocks for a period of about 10 Ma and until *ca.* 340 Ma (Fig. 86). This would point to an age of *ca.* 350 Ma for peak pressure metamorphism.

High-temperature metamorphism

Following the peak of pressure, the varied gneiss and felsic granulite units further experienced higher temperature conditions, which is a classical feature documented by P – T loops (England & Thompson, 1984). Higher temperature conditions indicated by zircon dissolution modelling in the felsic granulite (Fig. 86) can be attributed to its lowermost position at the bottom of the crust, and probably not to localised heating due to the emplacement of peridotite slices (Gayk & Kleinschrodt, 2000). In the felsic granulite, zircon grains yielding 340 Ma ages are thought to reflect crystallisation from an anatectic melt. Similarly, the different zircon types recognised in the varied gneiss reflect HT metamorphism. It is therefore proposed that the repeated age of 340 Ma represents the end of an HT event, i.e. the onset of cooling at a mid-crustal level (Fig. 86). Accordingly, previous interpretations proposing very rapid exhumation of the orogenic root (Schulmann *et al.*, 2002) may be critically challenged.

Tectonic evolution

The inferred P – T – t paths indicate that only the varied gneiss and the felsic granulite units shared the prograde evolution towards the HP granulite facies, probably as a result of continental subduction, whereas the monotonous gneiss unit occupied a higher position in the crust. There is therefore a clear distinction between the middle (autochthonous ?) and the lower (allochthonous ?) orogenic crust on the basis of petrological and geochronological records. Conversely, the retrograde evolution from vanishing MP/HT to lower grade metamorphic conditions was nearly similar in all three units. It could be interpreted in terms of mixing of different lithologies at a mid-crustal level (Štípská *et al.*, 2008) through an exhumation process which affected a large part of the crustal column.

CHAPTER III

GEODYNAMIC EVOLUTION OF THE VARISCAN VOSGES MOUNTAINS

1) The Vosges Mountains in the Variscan Belt of Europe

The Variscan orogenic cycle started with a significant rifting episode at the northern margin of the Gondwana supercontinent during the Cambrian–Ordovician. It pulled apart several Cadomian microcontinental blocks which were subsequently affected by extensional events during the Early Palaeozoic (e.g. Tait *et al.*, 2000; Stampfli & Borel, 2002; von Raumer *et al.*, 2003). The Early Ordovician opening of the Rheic Ocean was responsible for a major separation between the Avalonia microplate to the North and a group of blocks called the Armorican Terrane Assemblage (ATA) to the South (e.g. Crowley *et al.*, 2000; Nance *et al.*, 2010). According to faunal distributions, Avalonia rapidly moved towards the North and was probably docked to the Laurentia–Baltica craton in the Late Ordovician (Cocks & Fortey, 1982). Conversely, the ATA remained close to Gondwana and underwent extension–compression cycles during a slower northward drift. Successive divergent and convergent events from the Ordovician to the Devonian led to the opening and closure of oceanic basins between rifted basement blocks (e.g. Matte, 1986; Franke, 2000). The resulting mosaic of terranes was finally accreted between Laurentia–Baltica–Avalonia and Gondwana during the Devonian–Carboniferous closure of the system (e.g. Ziegler, 1984; Winchester *et al.*, 2002).

The Variscan orogen is traditionally seen as a simple juxtaposition of different terranes formed by continental belts with their surrounding basinal sequences (e.g. Behr *et al.*, 1984; Ziegler, 1986; Matte *et al.*, 1990; Franke, 2000). It is based on the assumption that the terranes represent coherent units with no or only minor allochthonous material. Following this view, the Variscan Belt of Europe was initially subdivided into a succession of lithotectonic zones by Kossmat (1927). However, this framework was mostly defined in Central and Eastern Europe and failed to be fully recognised in the West. It is therefore more suitable to presently consider the European Variscides as a non-cylindrical belt where some correlations between nearly similar but discontinuous lithotectonic domains can be drawn.

From North to South, the Variscan Belt of Europe comprises three major domains: the Rhenohercynian, Saxothuringian and Moldanubian zones (Fig. 88). The Rhenohercynian zone is represented by the Cadomian basement of Avalonia overlain by an Early to Middle Devonian passive margin sequence and Late Devonian to Carboniferous flysch sediments (e.g. Franke, 1995). The occurrence of MOR-type basalts in the Rhenish Massif additionally

indicates the presence of an Early Devonian Rheohercynian Ocean towards the South. This succession has clear equivalents in Cornwall (Floyd, 1984; Holder & Leveridge, 1986; Leveridge & Hartley, 2006) and possibly also in Moravia (Hladil *et al.*, 1999; Hartley & Otava, 2001; Kalvoda *et al.*, 2008) where similar Early Devonian oceanic remnants and Devonian–Carboniferous sediments are recognised. Carboniferous inversion and closure of the Rheohercynian basin subsequently produced a N-verging fold and thrust belt emplaced over the northerly Avalonia basement (Oncken *et al.*, 1999; Shail & Leveridge, 2009).

Towards the South, the boundary between the Rheohercynian and the Saxothuringian zones corresponds to the Mid-German Crystalline Rise (MGCR). It is a heterogeneous assemblage of Lower Palaeozoic basement, Carboniferous magmatic arc and sediments of Rheohercynian affinity which was interpreted as a result of frontal and basal accretion of contrasted units (Oncken, 1997). Such an interpretation slightly challenges the basic idea of homogeneous lithotectonic zones across the Varican Belt of Europe. Nevertheless, lateral equivalents of the MGCR have been proposed in the Northern Armorican Massif (Faure *et al.*, 2010) and suggest a relative along-strike continuity of this domain (Ballèvre *et al.*, 2009).

The Saxothuringian zone is exclusively present across Central and Eastern Europe (Fig. 88). It is bounded to the North by the MGCR and to the South by several Cadomian continental blocks, the largest being the Teplá-Barrandian basement in the Bohemian Massif. Rifting of the Cadomian Saxothuringian basement and opening of a Saxothuringian oceanic basin during the Cambro-Ordovician are indicated by magmatic rocks and ophiolites found at the northern margin of the Bohemian Massif (Bowes & Aftalion, 1991; Kemnitz *et al.*, 2002). The autochthonous Thuringian facies documents proximal passive margin sedimentation from the Ordovician to the Devonian, whereas the allochthonous Bavarian facies preserves Early Palaeozoic distal deposits overlain by Devonian–Carboniferous syn-orogenic flysch sediments (Falk *et al.*, 1995). From the Devonian to the Carboniferous, the Saxothuringian basin underwent oceanic to continental subduction towards the Southeast and experienced intense deformation in both the basement and the sedimentary cover. It resulted in exhumation of the basement in a large anticline and folding of the overlying sediments (Franke, 1984; Schäfer *et al.*, 2000). Similar features are partly found in the Sudetes (Franke & Żelaźniewicz, 2000), suggesting a prolongation of the Saxothuringian zone towards the East (Fig. 88), but are never recognised to the West of the Vosges.

Farther to the South, the Moldanubian zone is generally regarded as the metamorphic root of the Variscan orogen (e.g. Schulmann *et al.*, 2009b). In contrast to the other lithotectonic zones, the Moldanubian can be quite consistently followed from East to West (Fig. 88). Along its northern part, it is bounded by a discontinuous belt of Cadomian blocks which correspond

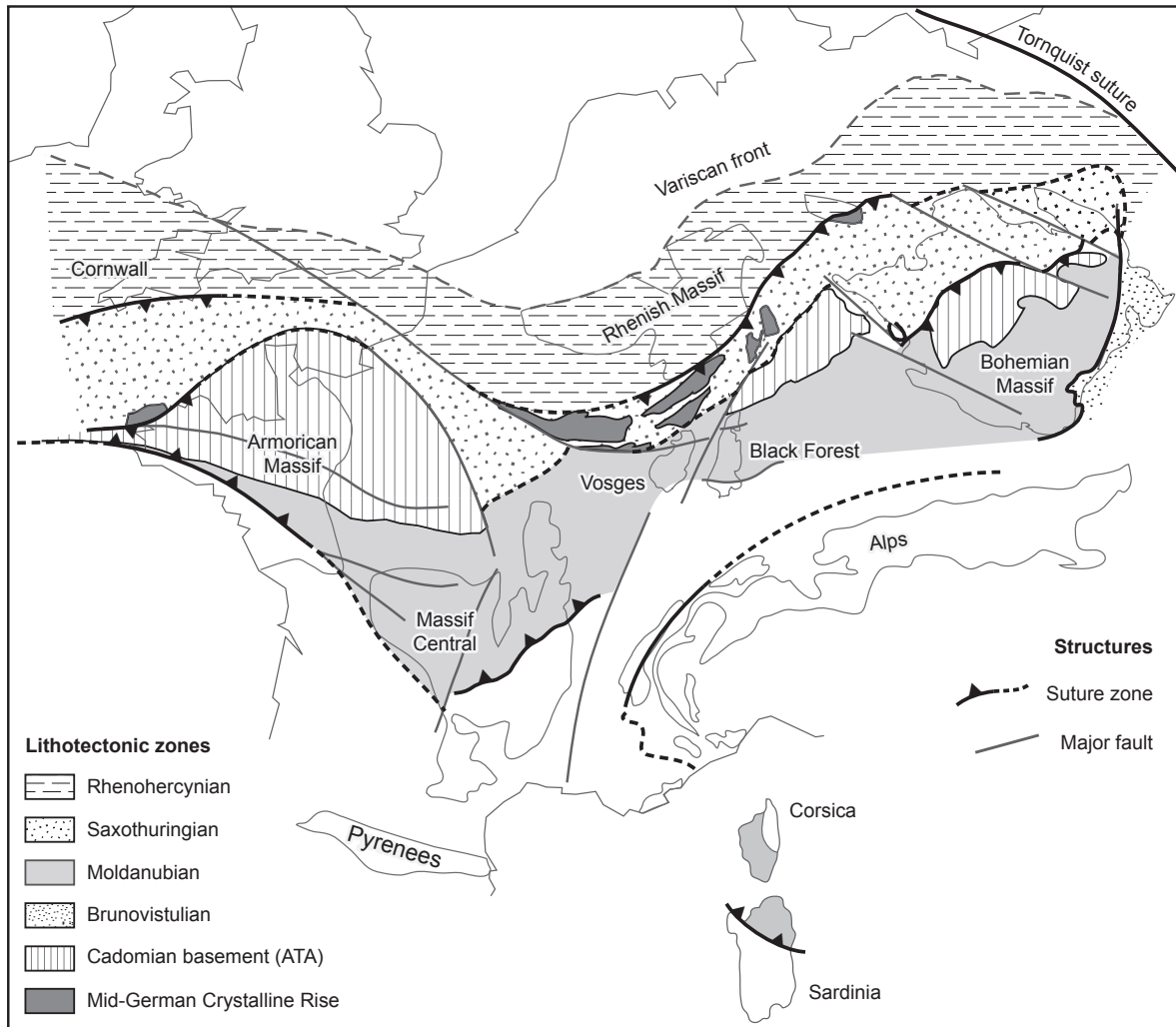


Figure 88. Lithotectonic zones in the Variscan Belt of Europe. The names of the major Variscan massifs are indicated. Modified after Edel & Schulmann (2009) and Ballèvre *et al.* (2009).

to relicts of the ATA (from West to East: Iberia, Armorica, Kraichgau and Teplá-Barrandian), whereas Cadomian blocks forming its southern margin could already belong to the northern margin of Gondwana (e.g. Linnemann *et al.*, 2004). Kossmat (1927) emphasised that the Saxothuringian–Moldanubian boundary is characterised by a major NW- to W-directed thrusting of high-grade Moldanubian units over the Saxothuringian succession. Contrastingly, the southern margin of the Moldanubian zone shows a clear S-verging structure where granulite-facies metasedimentary and meta-igneous rocks are emplaced onto less metamorphosed Early Palaeozoic metasediments and Neoproterozoic metagranitoids (e.g. Schulmann *et al.*, 2005). Importantly, the south vergence can be observed from the Armorican Massif through the Massif Central, Vosges, Black Forest and up to the Bohemian Massif (e.g. Burg & Matte, 1978; Maass *et al.*, 1990; Schulmann *et al.*, 2008; Ballèvre *et al.*, 2009). It further supports the existence of an oceanic domain between the Moldanubian zone and Gondwana (Finger & Steyrer, 1990; Finger *et al.*, 1997; Loeschke *et al.*, 1998; Lardeaux *et al.*, 2001; von Raumer *et*

al., 2003; Guillot & Ménot, 2009; Rossi & Oggiano, 2009). Notwithstanding this debate, the oppositely dipping structures on both sides of the root have been used to describe the Variscan Belt of Europe as a bivergent orogenic system.

For about a century, the Palaeozoic basement of the Vosges Mountains has been subdivided according to the work of Kossmat (1927). The Northern Vosges Mountains are seen as a prolongation of the Saxothuringian zone while the Central and Southern Vosges Mountains are correlated with the Moldanubian zone. Accordingly, the suture is commonly traced along the Lalaye-Lubine and Baden-Baden Fault Zones located in the Vosges and Black Forest, respectively (Krohe & Eisbacher, 1988; Fluck *et al.*, 1991). However, the Vosges clearly illustrate the lack of continuity between the eastern and western Variscan zones, and the non-cylindricity of the orogenic belt (Fig. 88). Indeed, Kossmat (1927) recognised that the characteristic thrust of the Moldanubian over the Saxothuringian was much less developed in the Vosges. By comparison with the Bohemian Massif, Franke (2000) additionally pointed out that the Teplá-Barrandian basement was missing between the Saxothuringian and Moldanubian Vosges. Any correlation between the western Armorica block and the Vosges basement is also hampered by the presence of the Bristol Channel-Bray discontinuity (Fig. 88).

Notwithstanding, such peculiarities do not preclude tentative correlations with the neighbouring Variscan massifs. The northern Black Forest is thought to be a lateral equivalent to the Northern Vosges (e.g. Montenari & Servais, 2000) while the Central Schwarzwald Gneiss Complex shows geochemical similarities with the Central Vosges metamorphic basement (Müller, 1989). By contrast, the suture zone of a S-dipping oceanic domain recognised in the southern Black Forest (Badenweiler-Lenzkirch zone) can not be directly followed in the Southern Vosges, but is probably located farther to the South (Maass *et al.*, 1990). In this view, the Southern Vosges could correspond to a back-arc basin possibly connected with the Brévenne unit in the NE French Massif Central (Part 2-Chapter I). In addition, the Moldanubian affinity of the Central and Southern Vosges may be supported by the bivergent structure of the root (Wickert & Eisbacher, 1988; Eisbacher *et al.*, 1989). However, the Variscan lithotectonic zonation was recently questioned by Edel & Schulmann (2009) who proposed that both the Rhenohercynian and Saxothuringian sutures could lie to the North of the presently exposed Vosges basement (Fig. 88).

2) Lithostratigraphy

The exposed Palaeozoic basement of the Vosges is formed by a wide central zone of granitoids and metamorphic rocks surrounded by Early Palaeozoic to Carboniferous sediments to the North and by Late Devonian to Carboniferous sediments to the South (Fig. 89). The later

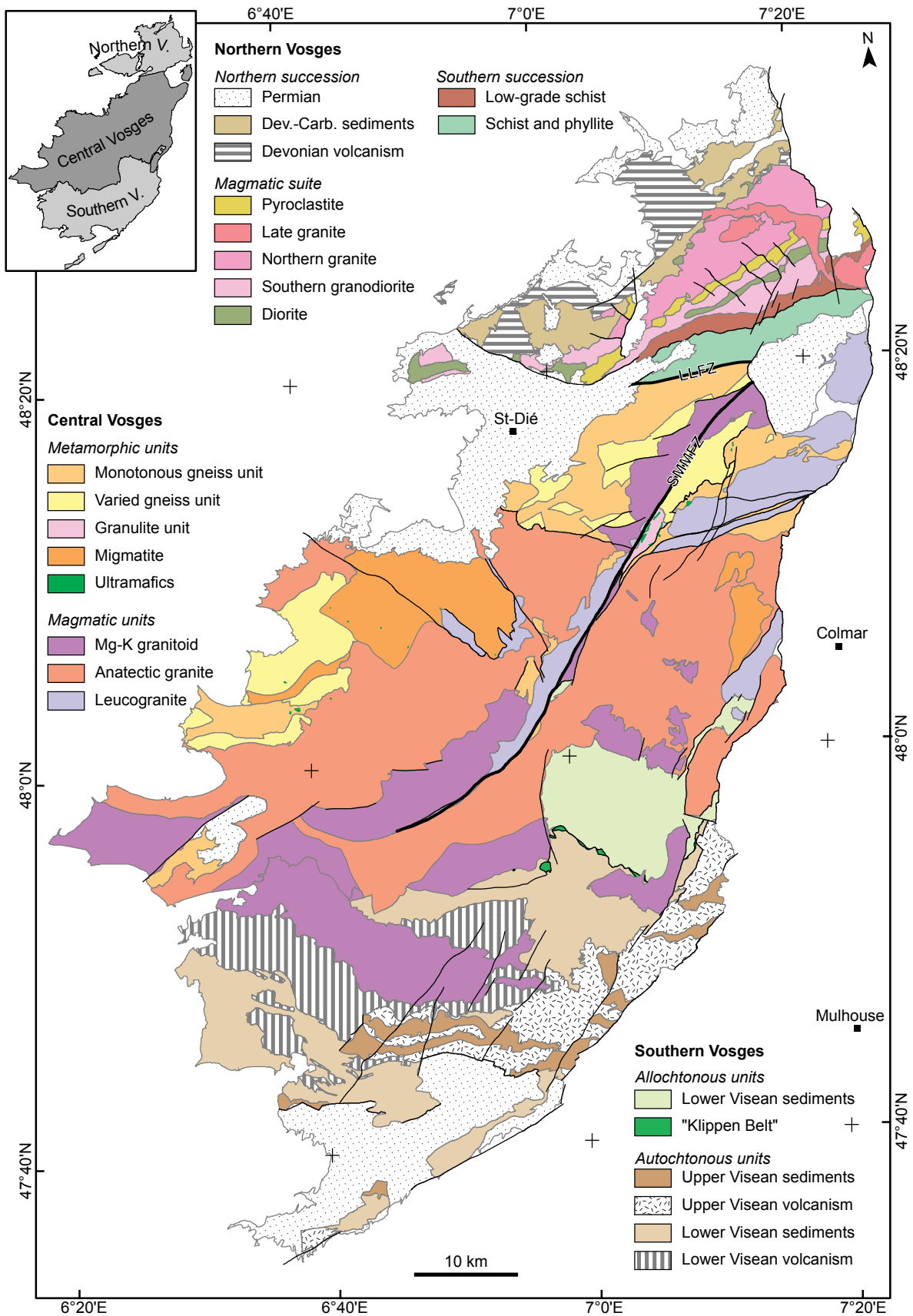


Figure 89. Synthetic geological map of the Palaeozoic Vosges Mountains. Post-Permian cover has been omitted. Inset shows the subdivision of the Vosges into a Northern, Central and Southern part. LLFZ=Lalaye-Lubine Fault Zone; SMMFZ=Sainte-Marie-aux-Mines Fault Zone.

Permian clastic sediments can be found around the different parts of this Variscan basement. Following the lithological variations, the Vosges have been subdivided into three parts (Fig. 89 inset). The Northern Vosges are separated from the Central Vosges by the Lalaye-Lubine Fault Zone, while the Southern Vosges are defined by the dominant volcano-sedimentary rocks occurring to the South of the Central Vosges granitic basement.

Northern Vosges

In detail, the Northern Vosges correspond to a succession of NE–SW striking sedimentary belts intruded by a central magmatic suite. This igneous complex separates the older and weakly-metamorphosed sediments of the Southern succession from the younger sediments and volcanics of the Northern succession (Fig. 89).

Northern succession (“Bruche” unit)

The base of the Northern succession is represented by basaltic lava flows, acid volcanic rocks and coarse-grained sediments that could possibly be Early Devonian in age (e.g. Juteau, 1971; Fig. 90). They are overlain by early Middle Devonian (Eifelian, former Couvinian) conglomerates and sandstones which correspond to the oldest dated sediments of the Bruche unit (Benecke & Bücking, 1898), and by Givetian greywacke and pelite alternating with bimodal volcanism (Firtion, 1945; 1957). The volcanic association is composed of mostly submarine altered basalt and rhyolite (“spilite-keratophyre”) and pyroclastic breccias which show a probable tholeiitic affinity (Ikenne & Baroz, 1985; Rizki & Baroz, 1988). The Givetian age has also been recognised in scarce carbonate lenses which preserve evidences for a reef environment influenced by the neighbouring continent (Jaeckel, 1888; Bücking, 1918; Blanalt, 1969), as well as in the surrounding polymictic conglomerate containing Late Cambrian granitic pebbles (Dörr *et al.*, 1992). Various observations indicate that the Middle Devonian is associated with the erosion of a Cambrian basement, conglomeratic sedimentation along a possibly N–S trending shoreline, and development of reef limestone in a relatively shallow-marine siliciclastic basin located to the East.

The sedimentary succession continuously passes to thick Frasnian and Famennian sandy-pelitic deposits with radiolarite (phtanite) intercalations and numerous plant debris (Figge, 1968; Blanalt & Lillié, 1973; Braun *et al.*, 1992; Aghai Soltani *et al.*, 1996; Fig. 90). This record is still interpreted as quiet sedimentation in a coastal environment receiving continental flora (Blanalt & Doubinger, 1973). However, late Upper Devonian sedimentary breccias with clasts of the underlying greywacke, pelite and radiolarite seem to indicate subsequent sedimentary instabilities in the Bruche basin. It is further supported by the Lower

Visean greywacke and pelite alternations documenting syn-sedimentary tectonic activity and preserving characters of flysch-type turbiditic deposits (Corsin & Dubois, 1932; Dubois, 1946; Corsin *et al.*, 1960). The Lower Carboniferous tectonic activity probably culminates during the Middle Visean as indicated by the sedimentary hiatus, contact metamorphism in the Bruche unit (Bonhomme & Prévôt, 1968), and associated magmatism to the South. Few Upper Visean deposits are found in the axial part of the magmatic suite (Fig. 89) and have been juxtaposed with granitic rocks as a result of late normal faulting. They chiefly correspond to pyroclastic rocks and ignimbrite, but rare pelite and greywacke are also observed (Elsass *et al.*, 2008). According to Rizki *et al.* (1992), the calc-alkaline to shoshonitic volcanism is related to the upper part of the magmatic suite and is indicative of an active margin setting during the late Lower Carboniferous.

Upper Carboniferous to Permian sediments and volcanics are present on both sides of the central magmatic suite (Fig. 89). They are represented by Stephanian to Autunian coal-bearing coarse-grained sediments (Doubinger, 1956; 1965), Saxonian rhyolitic volcanism (Mihara, 1935; Lippolt & Hess, 1983; Boutin *et al.*, 1995) and Thuringian arkosic sandstones and conglomerates (Hollinger, 1969; Fig. 90). In the Stephanian–Autunian deposits, numerous pebbles of Mg-K granite, gneiss and schist from the Central Vosges magmatic and metamorphic units indicate that deep crustal levels were already close to the surface in the Late Carboniferous. It was followed by a widespread Middle Permian subaerial acid volcanism which is also documented in the neighbouring Black Forest or Saar regions (Lippolt *et al.*, 1983; Schleicher *et al.*, 1983), and by Upper Permian continental sedimentation.

Magmatic suite (“Champ du Feu” magmatic suite)

The Northern Vosges magmatic suite corresponds to NE–SW trending or circular-shaped magmatic bodies intruding the surrounding sedimentary successions (Fig. 89). According to several geochronological studies, they were emplaced during a short Middle Visean event at 335–330 Ma (Fig. 90). The oldest magmatic rocks are found in narrow belts of diorite and are probably derived from an enriched lithospheric mantle source (Altherr *et al.*, 2000). The I-type magmatism was nearly coeval with the intrusion of the southern granodiorite which documents melting of a meta-igneous protolith (Altherr *et al.*, 2000). Al-in-hornblende barometry points to an intrusion depth of ~10 km for the diorite (Altherr *et al.*, 2000), whereas the southern granodiorite body was probably emplaced at a slightly shallower level as indicated by intrusive contacts with the low-grade Steige metasediments, and by the presence of numerous metasedimentary xenoliths.

The calc-alkaline magmatic activity was followed by the intrusion of the S-type northern granite (Fig. 89). This heterogeneous body shows geochemical features indicating melting of a metagreywacke protolith (Altherr *et al.*, 2000) and hosts abundant xenoliths of sedimentary and volcanic rocks (Elsass *et al.*, 2008). All these arguments suggest that the northern granite was emplaced at a shallow depth and was associated with magmatic stoping of the overlying Bruche unit. The last magmatic episode is reflected by the intrusion of circular-shaped granites which cross-cut the NE–SW trending bodies. The high-K to shoshonitic granites are still related to the melting of a metasedimentary protolith (Altherr *et al.*, 2000) and are characterised by a granophyric texture towards their margins. Accordingly, they represent the youngest and shallowest intrusions of the Northern Vosges magmatic suite.

Southern succession (“Villé” and “Steige” units)

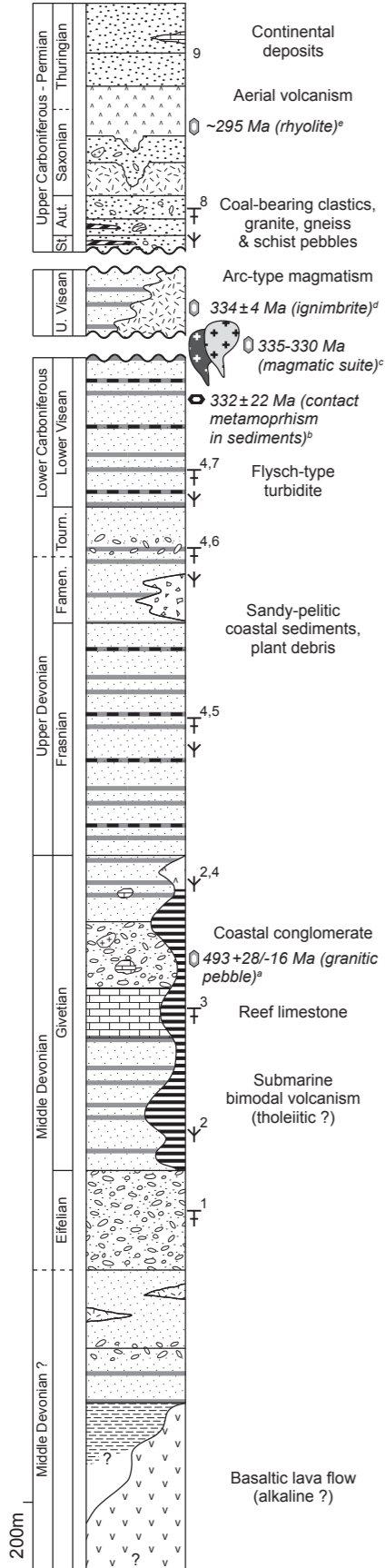
The Southern succession is represented by the two NE–SW trending belts of the Villé and Steige units (Fig. 89). The structurally deeper Villé unit corresponds to the oldest known deposits in the Vosges Mountains. It is formed by Cambrian to Ordovician pelite followed by quartzo-pelitic sediments with quartzite and acid tuff intercalations that have all been metamorphosed at greenschist-facies conditions (Doubinger & von Eller, 1963b; Ross, 1964; Reitz & Wickert, 1989; Figs 90 & 91). Although a Precambrian age has been proposed (Doubinger & von Eller, 1963b), the Villé unit seems to be well correlated with similar Late Cambrian to Early Ordovician low-grade sediments in the northern Black Forest (Montenari & Servais, 2000). The Villé unit is overlain by Ordovician to Silurian sandy and chiefly pelitic metasediments of

Figure 90. Synthetic lithostratigraphic columns for the Palaeozoic Vosges Mountains.

References for lithology and paleontology: **Northern Vosges, northern succession. Bruche unit:** 1–Benecke & Bücking (1898), 2–Firtion (1945; 1957), 3–Jaekel (1888); Bücking (1918); Blanalt (1969), 4–Blanalt & Doubinger (1973); Blanalt & Lillie (1973), 5–Figge (1968), 6–Braun *et al.* (1992); Aghai Soltani *et al.* (1996), 7–Corsin & Dubois (1932); Dubois (1946); Corsin *et al.* (1960). *Upper Carboniferous-Permian stratigraphy*, 8–Doubinger (1956; 1965), 9–Velain (1885); Benecke & von Verweke (1890); Choubert & Gardet (1935); Laubacher & von Eller (1966); Hollinger (1969). **Northern Vosges, southern succession. Villé unit:** 10–Doubinger & von Eller (1963b); Ross, (1964); Reitz & Wickert (1989). *Steige unit:* 11–Doubinger (1963); Doubinger & von Eller (1963a); Ross (1964); Tobschall (1974). **Southern Vosges. Allocthonous units:** 12–Doubinger & Ruhland (1963); Maas & Stoppel (1982), 13–Corsin & Mattauer (1957); Corsin & Ruhland (1959), 14–Markstein sedimentology after Krecher *et al.* (2007). *Autocthonous units:* 15–Chevillard (1866); Asselberghs (1926); Bain (1964), 16–Fournet (1847); Mathieu (1968); Corsin *et al.* (1956); Mattauer & Théobald (1957); Corsin & Mattauer (1957); Mattauer (1959); Coulon *et al.* (1978), 17–Hahn *et al.* (1981); Vogt (1981); Hammel (1996); Montenari *et al.* (2002), 18–Tornquist (1895; 1896; 1897; 1898); Delépine in Mattauer (1959); Doubinger & Rauscher (1966); Coulon & Lemoigne (1969); Corsin *et al.* (1973); Coulon *et al.* (1975a; 1975b); Coulon *et al.* (1978); Hahn *et al.* (1981); Hammel (1996), 19–Mathieu (1968); Creuzot (1983).

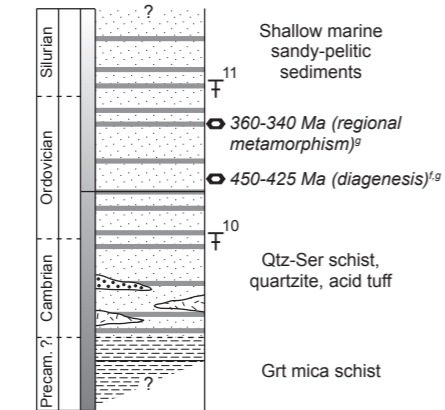
References for radiometric ages: **Northern Vosges:** a–Dörr *et al.* (1992), b–Bonhomme & Prévôt (1968), c–Boutin *et al.* (1995); Hess *et al.* (1995); Reischmann & Anthes (1996); Altherr *et al.* (2000); Edel *et al.* (2011), d–Edel *et al.* (2011), e–Lippolt & Hess (1983); Boutin *et al.* (1995), f–Bonhomme & Dunoyer de Ségonzac (1962), g–Clauer & Bonhomme (1970). **Central Vosges:** h–Part 2–Chapter II, i–Boutin *et al.* (1995), j–Schaltegger *et al.* (1999), k–Schulmann *et al.* (2002), l–Kratinova *et al.* (2007). **Southern Vosges:** m–Part 2–Chapter I, n–Schaltegger *et al.* (1996).

Northern succession



Northern Vosges

Southern succession



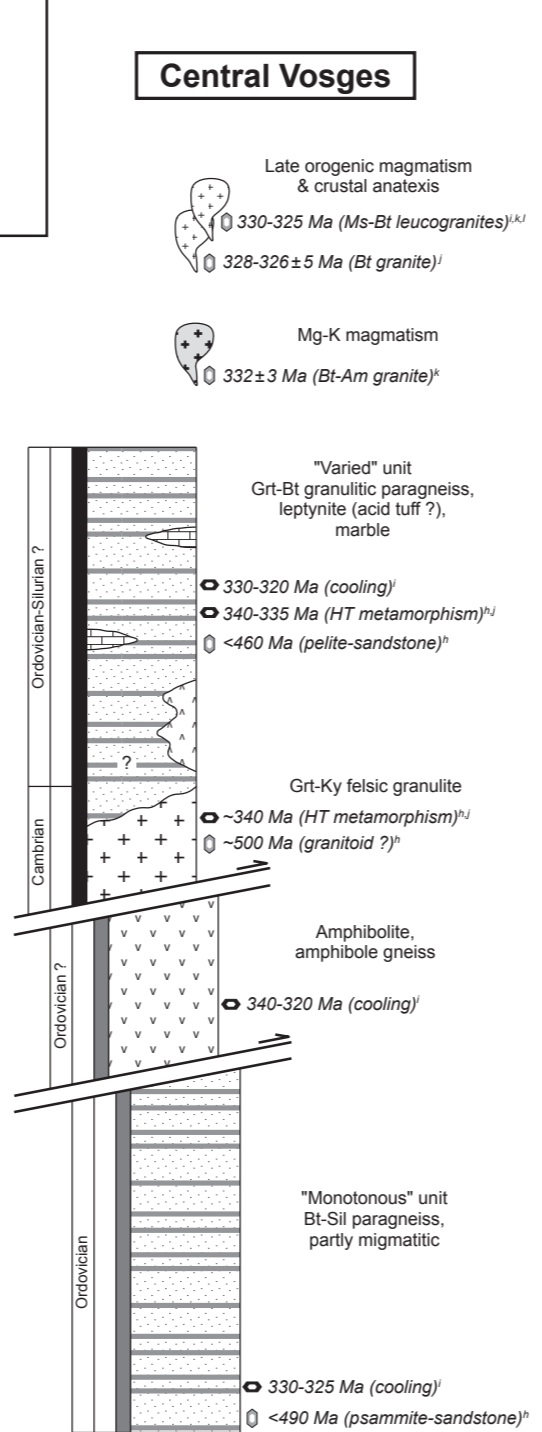
Sedimentation	Magmatism	Metamorphism	Paleontological ages
Sandstone	Tuff / pyroclastite	Non-metamorphic to anchizonal	Flora
Pelite	Acid	Greenschist-facies	Fauna
Sandstone-pelite	Intermediate	Amphibolite-facies	
Radiolarite	Basic	Granulite-facies	
Breccia	Bimodal		
Conglomerate	Mantle		
Quartzite			
Coal			
Limestone			

Metamorphism
 S-type plutonism
 I-type, acid plutonism
 I-type, intermediate plutonism

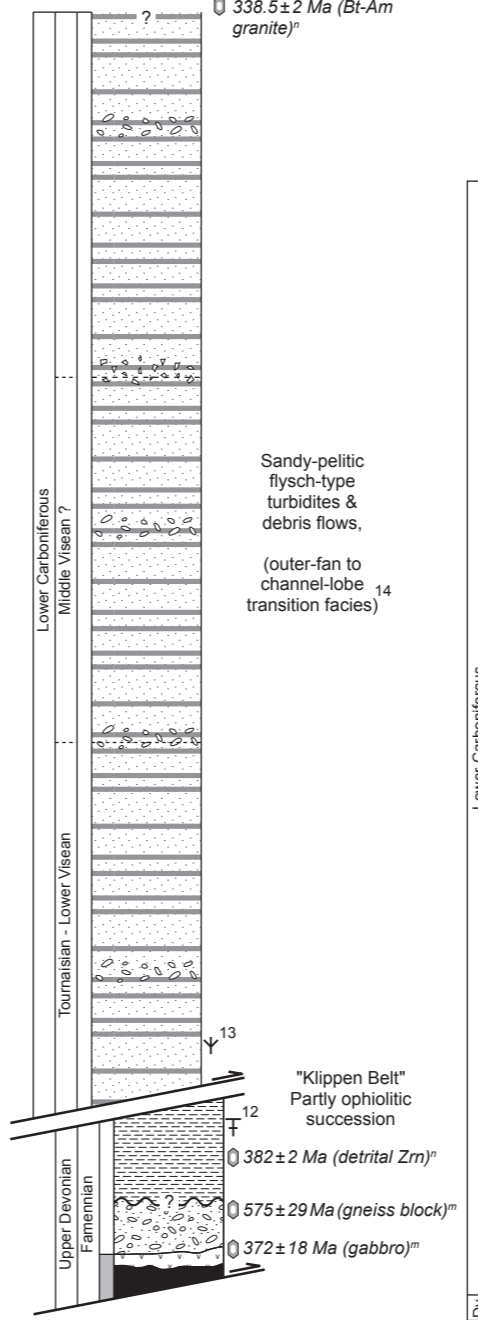
Radiometric ages
 Emplacement / deposition age (lithology)
 Metamorphic age (interpretation)

Stratigraphic unconformity
Tectonic unconformity

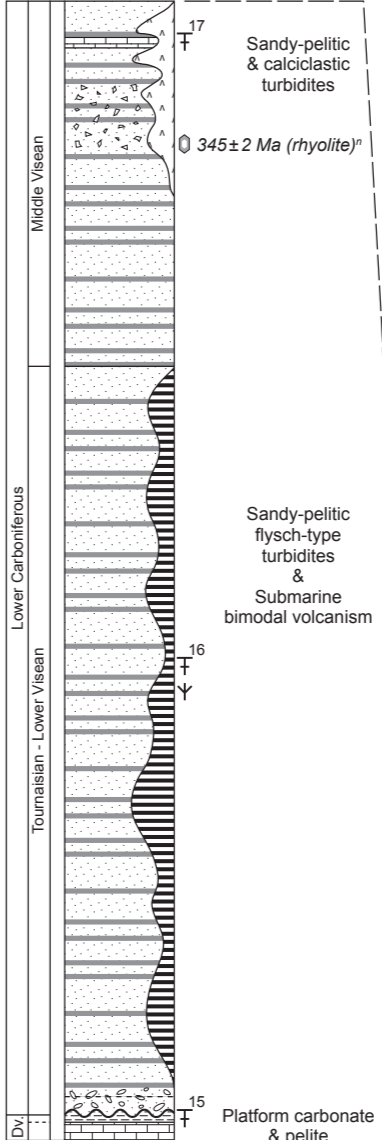
Central Vosges



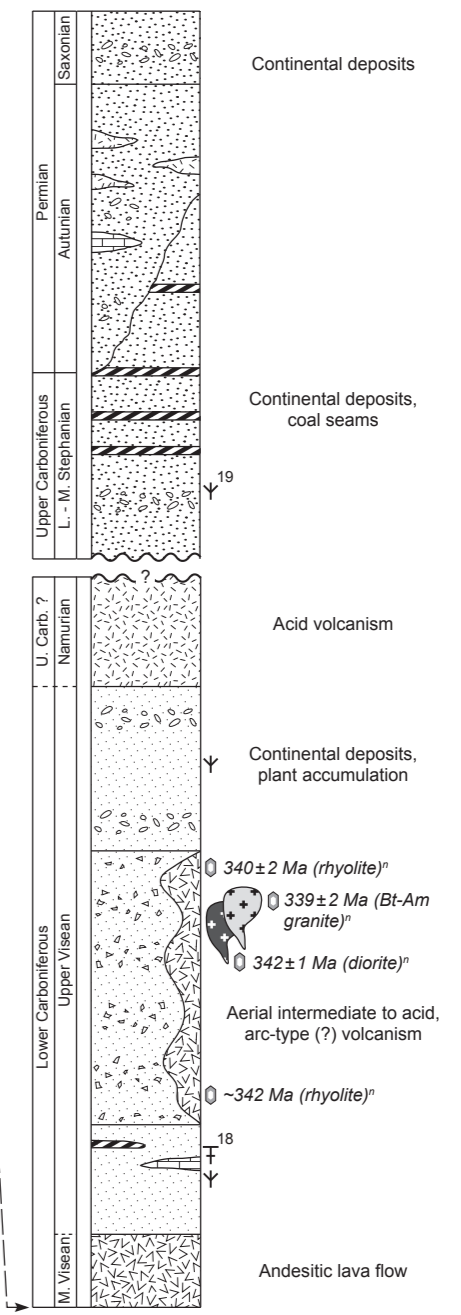
Allocthonous units



Southern Vosges



Autocthonous units



the Steige unit which underwent low-grade metamorphism (Doubinger, 1963; Doubinger & von Eller, 1963a; Ross, 1964). Based on geochemical arguments, Tobschall (1974) proposed that the Steige unit was deposited in a shallow-marine, probably platform environment.

Central Vosges

In the Central Vosges, it is possible to distinguish between a narrow zone of metamorphic units to the North and a larger zone of magmatic rocks to the South (Fig. 89). The latter frequently hosts metamorphic bodies which correspond to lithologies found in the northern metamorphic units.

Metamorphic units

The metamorphic units of the Central Vosges have been classically divided into a felsic granulite unit which is most likely of igneous origin, and into the varied and monotonous gneiss units which have sedimentary protoliths (Fig. 89). New U–Pb zircon ages reveal that the igneous activity associated with the emplacement of the felsic granulite protolith occurred at *ca.* 500 Ma (Part 2-Chapter II). A zircon provenance study indicates that this event was followed by the sedimentation of both the monotonous and varied units during the Ordovician (Part 2-Chapter II). The older quartzo-pelitic monotonous sediments were probably deposited during the Early Ordovician, whereas pelites with limestone and acid volcanic intercalations of the varied unit point to a Late Ordovician maximum sedimentation age (Fig. 90). Because the varied sediments gradually and laterally pass to the felsic granulite, it is further proposed that they were originally deposited on a Cambrian granitic basement. In addition, a thick layer of amphibolite occurs along the tectonic boundary between the monotonous and varied units. Since it is considered as the base of the varied unit (Fluck, 1980), it may reflect a significant Ordovician basic magmatic event.

Magmatic units

The numerous magmatic rocks of the Central Vosges can be divided into two distinct groups. The oldest I-type magmatic event is associated with elongated bodies of biotite–amphibole-bearing porphyritic granitoids (Mg-K granitoids) and occurred at 340–335 Ma across a large part of the Vosges (Figs 89 & 90). The Mg-K granitoids are intrusive in the Central Vosges metamorphic units as well as in the Southern Vosges sediments where microgranite sills are developed. The younger S-type granites represent a second event of widespread anatexis in the Central Vosges Mountains at 330–325 Ma (Fig. 90). Detailed mapping of the voluminous biotite-bearing anatectic granite reveals the presence of numerous xenoliths of Mg-K granitoid, gneiss or sedimentary rocks (von Eller, 1961) suggesting that the magma invaded a

heterogeneous crustal assemblage over a large area. On the other hand, the biotite–muscovite-bearing leucogranites correspond to narrow and elongated plutons that are associated with major tectonic discontinuities (Fig. 89).

Southern Vosges

The Southern Vosges are dominantly composed of (volcanic)-sedimentary successions that have long been divided into allochthonous and autochthonous units (Jung, 1928). The boundary between both units lies close to the Southern Vosges Klippen Belt which corresponds to discontinuous exposures of partly ophiolitic material. Towards the South, an E–W trending Mg-K magmatic unit is intrusive in the autochthonous sediments and volcanics (Fig. 89).

Autochthonous units (“Oderen” and “Thann” units)

The oldest autochthonous sediments are found in the southernmost part of the Vosges near Belfort (Fig. 89). They are represented by limestones of probable Frasnian age conformably overlain by a thin layer of Fammenian pelites (Chevillard, 1866; Asselberghs, 1926; Bain, 1964) which preserve a fauna indicating an Upper Devonian platform environment (Fig. 90). The pelites are in turn unconformably overlain by a Lower Carboniferous conglomeratic greywacke which is also observed farther to the North. There, the autochthonous succession corresponds to thick Tournaisian to Lower Visean pelites and greywackes with episodic conglomerate and carbonate deposits (Corsin *et al.*, 1956; Corsin & Mattauer, 1957; Mattauer & Théobald, 1957; Mattauer, 1959). The sediments are locally interlayered with mostly submarine altered basalt and rhyolite (“spilite-keratophyre” magmatism) showing a tholeiitic affinity (Lefevre *et al.*, 1994). Towards the top of the Oderen unit, acid volcanism is found together with more abundant carbonate intercalations which indicate an early Middle Visean age (Hammel, 1996; Montenari *et al.*, 2002), although Tournaisian fossils are reported (Hahn *et al.*, 1981; Vogt, 1981). Following Gagny (1962), the Oderen unit represents flysch-type turbiditic deposits that were later affected by Middle-Upper Visean sedimentary instabilities as indicated by the resedimented fauna occurring at its top (Schneider *et al.*, 1989).

The boundary with the younger Thann unit is marked by the emplacement of abundant andesitic lavas (Fig. 90). They are overlain by Upper Visean sandstones or conglomerates alternating with trachytic to rhyolitic volcanic rocks (Corsin *et al.*, 1973; Coulon *et al.*, 1975a; 1975b; 1978). Up to the Namurian, the coarsening of sediments and the increasing amount of plant debris indicate the progressive filling of small basins associated with an ultimate episode of high-K rhyolitic volcanism (Lefevre *et al.*, 1994). The continental sedimentation is later characterised by Stephanian to Saxonian sandstones, conglomerates, pelites and rhyolitic tuffs with some coal-bearing strata (Mathieu, 1968; Creuzot, 1983).

Allochthonous units (Klippen Belt and “Markstein” units)

The allochthonous units are represented by the dominant Markstein unit and the Southern Vosges Klippen Belt which is regarded as the base of the allochthonous succession (Jung, 1928; Schneider *et al.*, 1990; Part 2-Chapter I). The klippen preserve serpentinite, ophicalcite and Famennian gabbro overlain by a conglomeratic greywacke with Neoproterozoic gneiss blocks. The succession is capped by Famennian siliceous pelites (Maass & Stoppel, 1982; Fig. 90) and is in turn overlain by thick Lower Visean pelites and greywackes of the Markstein unit with only minor conglomerates and carbonate material (Corsin & Mattauer, 1957; Corsin & Ruhland, 1959). The sedimentation is thought to last up to the Upper Visean (e.g. Krecher, 2005), but Middle Visean granitic intrusions in the already folded allochthonous units makes this hypothesis rather unlikely. To summarize, the allochthonous lithologies testify for the presence a deep Upper Devonian basin subsequently filled by Lower Visean flysch turbidites which indicate a prograding system of sandy submarine fans (Krecher *et al.*, 2007).

Magmatic unit (“Ballons” magmatic unit)

The southeastern part of the allochthonous volcanic-sedimentary unit is intruded by the E–W trending Ballons magmatic unit (Fig. 89). The oldest intrusions correspond to a peripheral zone of gabbro, diorite and monzogranite which were probably emplaced at *ca.* 345 Ma. They were shortly followed by the intrusion, at *ca.* 340 Ma, of a large biotite–amphibole-bearing granite with a fine-grained to porphyritic texture (Fig. 90). The high amounts of U and Th (e.g. Rothé, 1962) indicate that the granite is strongly similar to the Mg-K granitoids found in the Central Vosges. In addition, previous studies showed that the magmatic unit has a high-K signature and was probably derived from a basaltic source, either of tholeiitic (André & Bébien, 1983) or shoshonitic affinity (Pagel & Leterrier, 1980).

3) Metamorphic record

Contrasted metamorphic conditions have been documented across the Vosges basement (Fig. 91). They can range from limited contact metamorphism around the granitoids to ultrahigh-pressure conditions in the peridotite slices of the Central Vosges. Nevertheless, geochronological studies have demonstrated that metamorphism in the Vosges was restricted to a relatively short Late Devonian to Lower Carboniferous period.

Contact metamorphism

The various granitoid intrusions are commonly associated with narrow metamorphic aureoles in the neighbouring sedimentary rocks. In the Northern Vosges, the polyphase intrusion of the magmatic suite is responsible for contact metamorphism in both the Northern and Southern successions (Fig. 91a). The sediments of the Bruche unit document a resetting of the Rb–Sr isotopic system (Bonhomme & Prévôt, 1968), whereas an aureole of hornfels and spotted slate in the Steige unit was generated by the southern granodiorite and the younger Andlau granite (Rosenbuch, 1877; von Eller, 1964).

In the Southern Vosges, the border of the allochthonous Markstein unit as well as part of the allochthonous Oderen unit are affected by contact metamorphism over a relatively large area (Fig. 91a). In the northern part, the Mg–K magmatism mostly produced hornfels, while both the Mg–K and anatectic granites probably transformed the southern sediments into spotted slates. Hornfels are additionally found in the autochthonous unit around the southern Mg–K magmatic unit.

Low- to medium-grade metamorphism (Northern Vosges)

In the Northern Vosges, the Northern succession shows only limited contact metamorphism while the Southern succession exhibits a low- to medium-grade overprint increasing towards the South (Fig. 91a). In volcanic rocks of the central magmatic suite, the presence of prehnite and actinolite (Reibel & Wurtz, 1984) indicates P – T conditions of 200–300 °C at pressures probably not exceeding 1–2 kbar. In the Steige unit, the assemblage paragonite–chlorite–illite together with the transition from kaolinite to dickite point to a temperature above 100 °C and most likely below 200 °C at ~1 kbar (Fig. 91b), except along the tectonic contact with the Villé unit where pyrophyllite may indicate a slightly higher temperature (Clauer, 1970). By contrast, pyrophyllite and illite with increasing crystallinity are common in the Villé unit (Clauer, 1970) suggesting P – T conditions of 1–2 kbar and 250–350 °C (Fig. 91b). Towards the South, mica schist with a garnet–biotite assemblage pervasively replaced by muscovite–chlorite is found in a narrow zone along the Lalaye-Lubine Fault Zone (Ighid, 1985). Chemical analyses further reveal a significant spessartine proportion in garnet core (0.1–0.2 mol%) and point to peak P – T conditions between 350–500 °C at pressures probably higher than 2 kbar (Fig. 91b). The review of metamorphic data therefore indicates that the Southern succession experienced metamorphism along a relatively standard geothermal gradient and that P – T conditions reached the upper greenschist facies towards the boundary with the Central Vosges metamorphic units.

Medium- to high-grade metamorphism (Central Vosges)

In the Central Vosges, petrological studies mostly focused on the northern metamorphic units where the high-grade varied and felsic granulite units are mantled by a large zone of medium-grade monotonous gneiss (Fig. 91a). Previous works have recognised relicts of a medium- to high-pressure/high-temperature stage which was pervasively overprinted by a low- to medium-pressure/high-temperature metamorphic event.

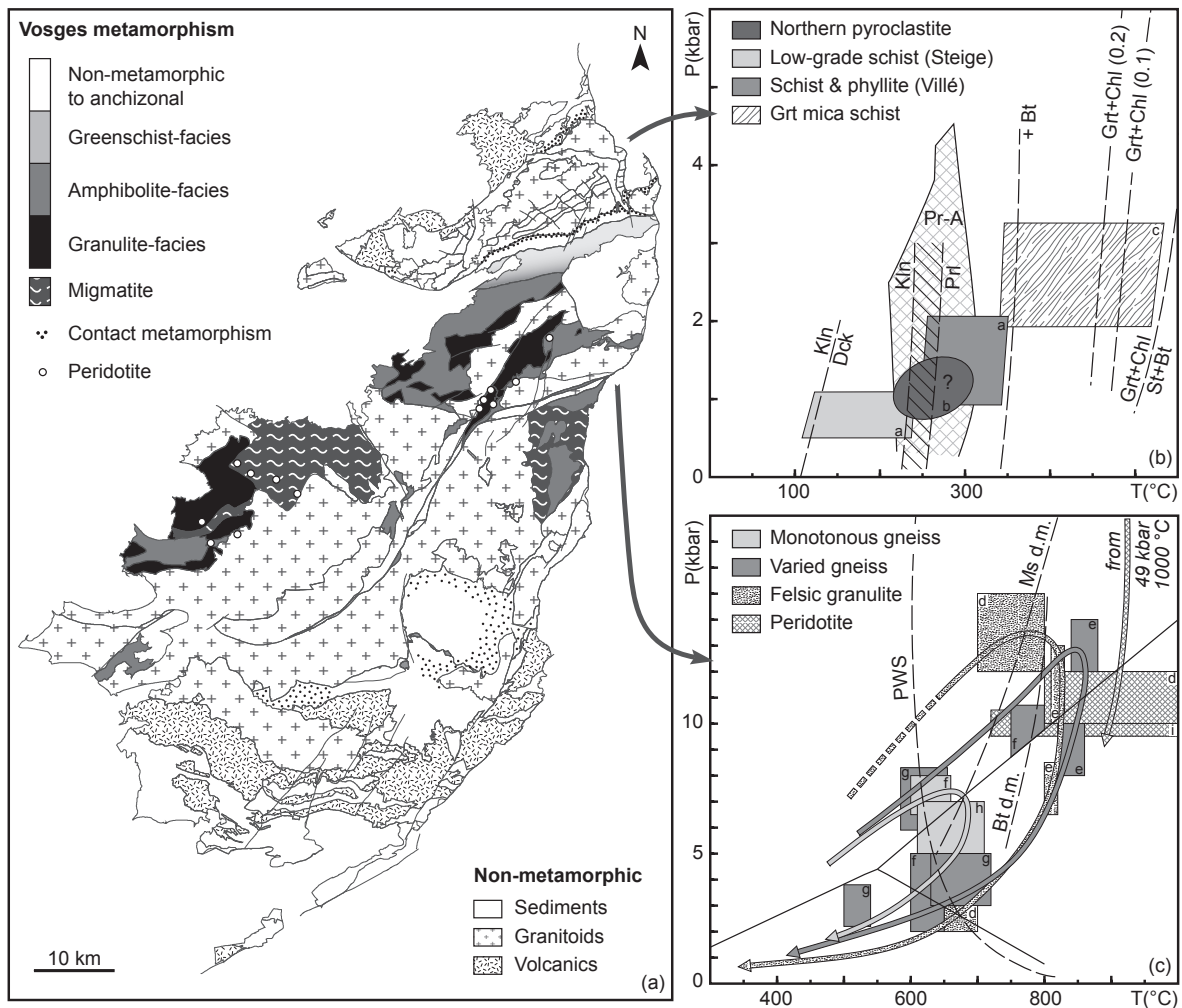


Figure 91. Summary of metamorphic results for the Vosges Mountains. (a) Spatial distribution of the different metamorphic grades. (b) P - T estimates for the Northern Vosges metamorphic rocks. (c) Peak and retrograde P - T evolutions for the Central Vosges metamorphic units and peridotite intercalations.

Reactions: Kaolinite–dickite (Ehrenberg *et al.*, 1993), kaolinite–pyrophyllite (Frey, 1987), Cld+Bt=Grt+Chl with $\text{Mn}/(\text{Mn+Fe+Mg})\%$ in garnet indicated and Grt+Chl=St+Bt (Spear & Cheney, 1989), prehnite–actinote (Pr-A) field (Schiffman & Day, 1999). Pelite wet solidus (PWS), muscovite and biotite dehydration melting (d.m.) curves compiled by Thompson & Connolly (1995). In the present chapter, mineral abbreviations follow IUGS recommendations after Kretz (1983).

References: a–Clauer & Bonhomme (1970); Clauer (1970), b–Reibel & Wurtz (1984), c–Ighid (1985) and own observations, d–Gayk & Kleinschrodt (2000), e–Part 2-Chapter II, f–Rey *et al.* (1989), g–Rey *et al.* (1992), h–Latouche *et al.* (1992), i–Altherr & Kalt (1996).

In the monotonous unit, a relict garnet–staurolite–kyanite assemblage points to prograde metamorphism up to 6–7 kbar and 600–700 °C (Rey *et al.*, 1989; Latouche *et al.*, 1992) suggesting that the gneissic rocks straddled the limit of partial melting (Fig. 91c). The subsequent development of abundant sillimanite, cordierite and biotite indicates a drop in pressure below 4–5 kbar at temperatures probably still above 550–600 °C. Conversely, the metamorphic evolution of the varied gneiss and felsic granulite units is markedly different (Fig. 91c). In both units, the occurrence of garnet–kyanite–K-felspar has been used to propose HP granulite-facies metamorphism with maximum P – T estimates of 9–14 kbar at 750–880 °C for the varied gneiss (Rey *et al.*, 1989; Part 2-Chapter II) and 10–15 kbar at 700–850 °C for the felsic granulite (Pin & Vielzeuf, 1988; Gayk & Kleinschrodt, 2000; Part 2-Chapter II). However, their retrograde evolution was nearly shared with that of the monotonous unit (Fig. 91c). In the varied gneiss, the assemblage biotite–sillimanite–cordierite with minor hercynite indicates a LP/HT stage at 2–5 kbar and 600–700 °C (Rey *et al.*, 1989; Rey *et al.*, 1992), whereas the felsic granulite was retrogressed at 2–3 kbar and 650–700 °C (Gayk & Kleinschrodt, 2000). According to Altherr & Kalt (1996), the garnet peridotites originally equilibrated at 49 kbar and 950 °C close to the graphite–diamond transition before being incorporated into the felsic granulite unit at 10 kbar/700–1000 °C (Fig. 91c).

Towards the South, partially molten gneiss bodies are entirely surrounded by anatectic granite (Fig. 91a). They correspond to orthogneiss with a relatively low melt fraction (10–30%), metasedimentary migmatite with a variable amount of former melt (10–80%, Schulmann *et al.*, 2009a) or nebulitic migmatite with scarcely oriented biotite. In the western migmatitic domain, the activity of the prism [c] gliding system additionally indicates that deformation acted at subsolidus conditions of about 650 °C (Blumenfeld *et al.*, 1986).

4) Geochronology

The geochronological data obtained on the Palaeozoic Vosges basement all emphasise the importance of Late Devonian to Lower Carboniferous thermal events. They not only reveal widespread magmatism across the entire Vosges, but also low- to high-grade metamorphism in the Northern and Central Vosges.

Age of magmatism

A synthesis of existing ages for igneous rocks indicates distinct pulses of magmatic activity between 350 and 290 Ma (Fig. 92a). The oldest igneous rocks correspond to the basic plutonism developed along the margin of the Southern Vosges magmatic unit. Although $^{40}\text{Ar}/^{39}\text{Ar}$ amphibole ages on a diorite yielded 360–355 Ma (Boutin *et al.*, 1995), this initial magmatic

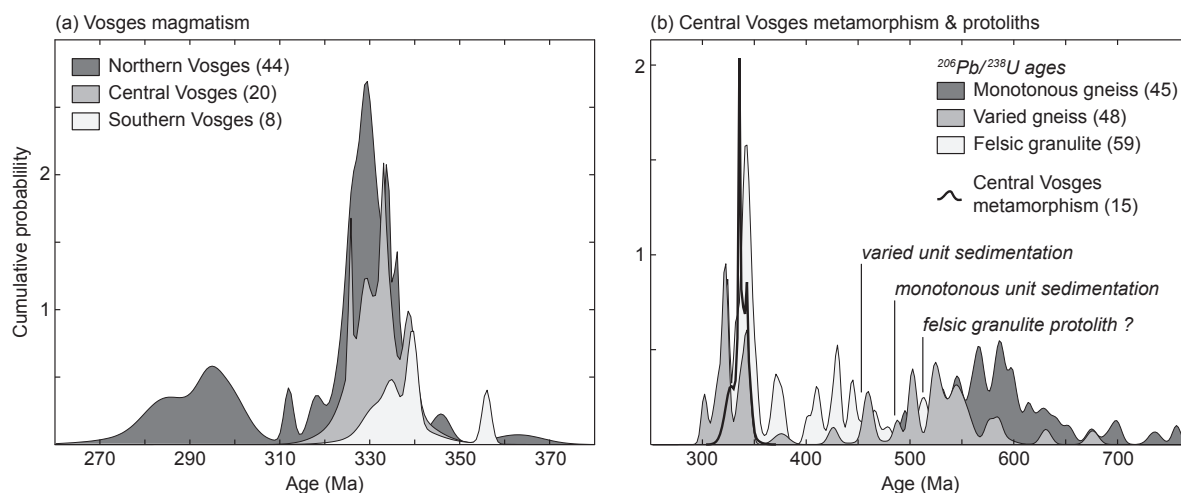


Figure 92. Summary of existing geochronological data for the Palaeozoic Vosges basement. Cumulative probability curves for (a) magmatic events and (b) metamorphic events and protolith ages. Ages used for probability curves are listed in Tab. 19 and $^{206}\text{Pb}/^{238}\text{U}$ ages are after the results of Part 2-Chapter II.

stage probably occurred around 345 Ma as indicated by U–Pb zircon data (Schaltegger *et al.*, 1996; Tabaud, personal communication). It was shortly followed by more abundant Mg–K magmatism with the intrusion of granite at 339 ± 2 Ma (Schaltegger *et al.*, 1996) and aerial rhyolitic volcanism in the autochthonous Thann unit at 340–335 Ma (Boutin *et al.*, 1995; Schaltegger *et al.*, 1996). This event is nearly coeval with Mg–K magmatism in the Central Vosges (Fig. 92a) where durbachitic to granitic intrusions preserve U–Pb zircon ages between 340 and 332 Ma (Schaltegger *et al.*, 1996; Schulmann *et al.*, 2002).

Shortly after, arc-type magmatism took place in the Northern Vosges (Fig. 92a). The successive intrusions of I- to S-type plutons have been dated by various methods and there is a general agreement to consider that this episode was relatively short and lasted from 335 to 330 Ma (Boutin *et al.*, 1995; Hess *et al.*, 1995; Reischmann & Anthes, 1996; Altherr *et al.*, 2000; Edel *et al.*, 2011). However, recent U–Pb zircon and monazite data show inheritance at 360–345 Ma (Elsass *et al.*, 2008; Edel *et al.*, 2011) indicating that the igneous activity in the Northern Vosges could have started earlier. Conversely, several $^{40}\text{Ar}/^{39}\text{Ar}$ ages of *ca.* 320 Ma reported for the magmatic suite could represent partial resetting due to the younger and widespread Middle Permian acid volcanism estimated at 299–293 Ma in the northernmost part of the Vosges (Lippolt & Hess, 1983; Boutin *et al.*, 1995).

The latest Carboniferous magmatism covers the largest part of the present-day Vosges basement (Fig. 89). It is associated with the emplacement of the Central Vosges anatectic granite at 328–326 Ma (Schaltegger *et al.*, 1999) and biotite–muscovite-bearing leucogranites between 330 and 323 Ma (Boutin *et al.*, 1995; Schulmann *et al.*, 2002; Kratinová *et al.*, 2007). In addition, the anatectic granite commonly preserves inherited zircon or monazite ages of

ca. 335 Ma. These observations have been used to propose that the granite digested host rocks emplaced or metamorphosed during the Lower Carboniferous, i.e. most likely rocks belonging to the Central Vosges metamorphic units (Schaltegger *et al.*, 1999).

Age of metamorphism

A glance at the previous geochronological studies shows that metamorphic ages cluster around 350–330 Ma. Few data document Late Devonian to Lower Carboniferous metamorphism in the Northern Vosges Mountains. Contact metamorphism due to the intrusion of the northern granite is estimated at 339 ± 22 Ma in the Bruche unit (recalculated age after Bonhomme & Prévôt, 1968) and Rb–Sr whole-rock data from the Steige and Villé units point to a probable metamorphic age of 339 ± 38 Ma (recalculated pooled age after Clauer & Bonhomme, 1970). In the Central Vosges metamorphic units, U–Pb and $^{40}\text{Ar}/^{39}\text{Ar}$ ages indicate a prominent event at *ca.* 335 Ma (Fig. 92b). The monotonous unit seems to lack Lower Carboniferous zircon record (Fig. 92b), but preserves an $^{40}\text{Ar}/^{39}\text{Ar}$ biotite cooling age of 330 ± 14 Ma (Boutin *et al.*, 1995). Conversely, U–Pb zircon ages in both the varied gneiss leucosomes and restites indicate that high-temperature metamorphism and partial melting occurred from 335 to 325 Ma (Schaltegger *et al.*, 1999; Part 2-Chapter II). In the felsic granulite unit, zircon grains similarly point to granulite-facies metamorphism at 335–330 Ma (Schaltegger *et al.*, 1999) although the peak pressure event may have a slightly older age of 360–340 Ma (Part 2-Chapter II). In the two high-grade units, $^{40}\text{Ar}/^{39}\text{Ar}$ ages between 340 and 325 Ma lie close to U–Pb zircon ages and indicate rapid cooling of this deep part of the crust. In the Central Vosges migmatite, inherited ages of *ca.* 335 Ma indicate that this domain was also affected by Lower Carboniferous metamorphism before being pervasively invaded by anatectic granite (Schaltegger *et al.*, 1999).

5) Structural geology

New and existing observations allow to constrain the structural succession for the different lithotectonic units of the Vosges. Observations include a detailed mapping of planar and linear structures as well as a study of the anisotropy of magnetic susceptibility (AMS) in magmatic rocks. The summary of superposed structural trends further gives an overview of the deformation events which have affected distinct parts of the orogenic crust.

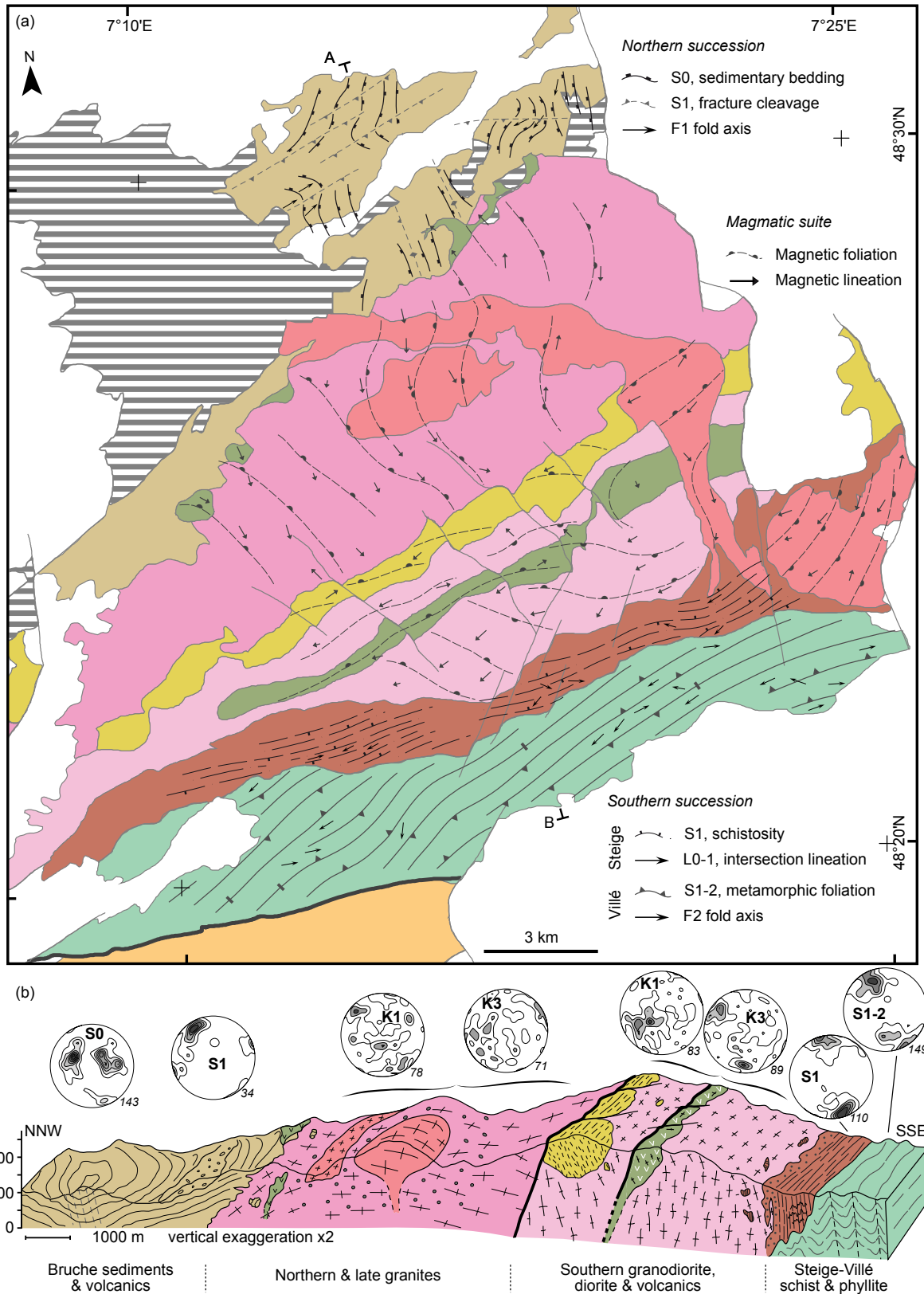


Figure 93. Structural record in the Northern Vosges. (a) Map showing the trend of the dominant planar and linear structures. Long arrow=shallow plunge, short arrow=steep plunge. (b) Schematic section across the Northern Vosges basement. Lower hemisphere, equal-area diagrams show the orientation of the main structures described in the text (number of measurements is given in italics). K1=magnetic lineation, K3=pole to magnetic foliation. Lithologies as in Fig. 89. Structures in the magmatic suite after Edel *et al.* (2011).

Northern Vosges

Northern succession

The dominant planar structure in the Bruche unit is represented by the S0 sedimentary bedding. It is defined by mm- to cm-scale alternations of sediments showing varying grain size or color, and is most clearly visible when light-coloured sandstone alternates with darker fine-grained pelite. Structural mapping of the primary bedding reveals that the S0 is affected by a first gentle km-scale folding with a general N–S trending axis (Fig. 93a). The folding produces S0 planes which dip moderately to the E in the western part, and to the W in the eastern part of the Bruche unit, suggesting that the sedimentary unit defines a large N–S trending syncline. Locally, the sediments are affected by a weak N–S striking fracture cleavage probably related to this first deformation event. The already weakly deformed S0 is subsequently affected by a moderate km-scale NE–SW folding which produces NE- and SE-dipping bedding planes and a spaced cleavage S1 in Lower Carboniferous sediments to the Northwest of the Bruche unit (Fig. 93). The NE–SW striking S1 cleavage steeply dips to the SE and generally cross cuts the S0 bedding at high angle (Fig. 94a). The second deformation is responsible for the main NE–SW trending synformal shape of the Bruche unit which has been recognised by several authors (Blanalt & Lillié, 1973; Wickert & Eisbacher, 1988). However, the structural succession shows that the final deformation pattern results from two quasi-orthogonal compression events.

Magmatic suite

Following the work of Edel *et al.* (2011), the AMS record in the Northern Vosges magmatic suite shows a clear distinction between the northern granitic domain and the southern dioritic to granodioritic domain (Fig. 93a). In the northern granite, the magnetic ellipsoid is of plane strain to oblate shape with a medium to high degree of anisotropy. The magnetic foliation strikes NW–SE and dips moderately to the NE while the lineation trends N–S to NW–SE with a variable plunge (Fig. 93). Similar orientations are observed in the late granites intruding the northern part. Conversely, the belts of volcanic rocks, diorite and granodiorite preserve magnetic structures which are nearly perpendicular to those observed in the northern domain. These are E–W to NE–SW striking foliations steeply dipping to the N or SE, and NE–SW trending lineations moderately plunging towards the SW (Fig. 93). The structures are nearly parallel to the record in the late Andlau granite which is entirely intrusive in the Steige unit. Across the southern granodioritic domain, the magnetic ellipsoid is moderately anisotropic and shows a variable shape from oblate to strongly prolate.

Southern succession

In the low-grade Steige unit, the original S0 sedimentary bedding is only rarely visible. It corresponds to thin (< 5 mm), grey quartz-rich layers alternating with thicker reddish pelitic beds, but is commonly folded by upright to slightly N-verging asymmetrical F1 folds with E–W trending axis. The folding is responsible for the almost complete obliteration of S0 by a pervasive mm-spaced S1 schistosity which is the dominant structural feature in the Steige unit (Fig. 94b, d). The E–W striking S1 is mostly subvertical and is parallel to the axial planar cleavage of F1 folds (Fig. 93). At the contact with the granodiorite, magmatic veins are additionally found parallel to the subvertical S1 in spotted slates. In samples showing a pervasive S1 fabric, the relicts of S0 are at high angle or parallel to the S1 schistosity,

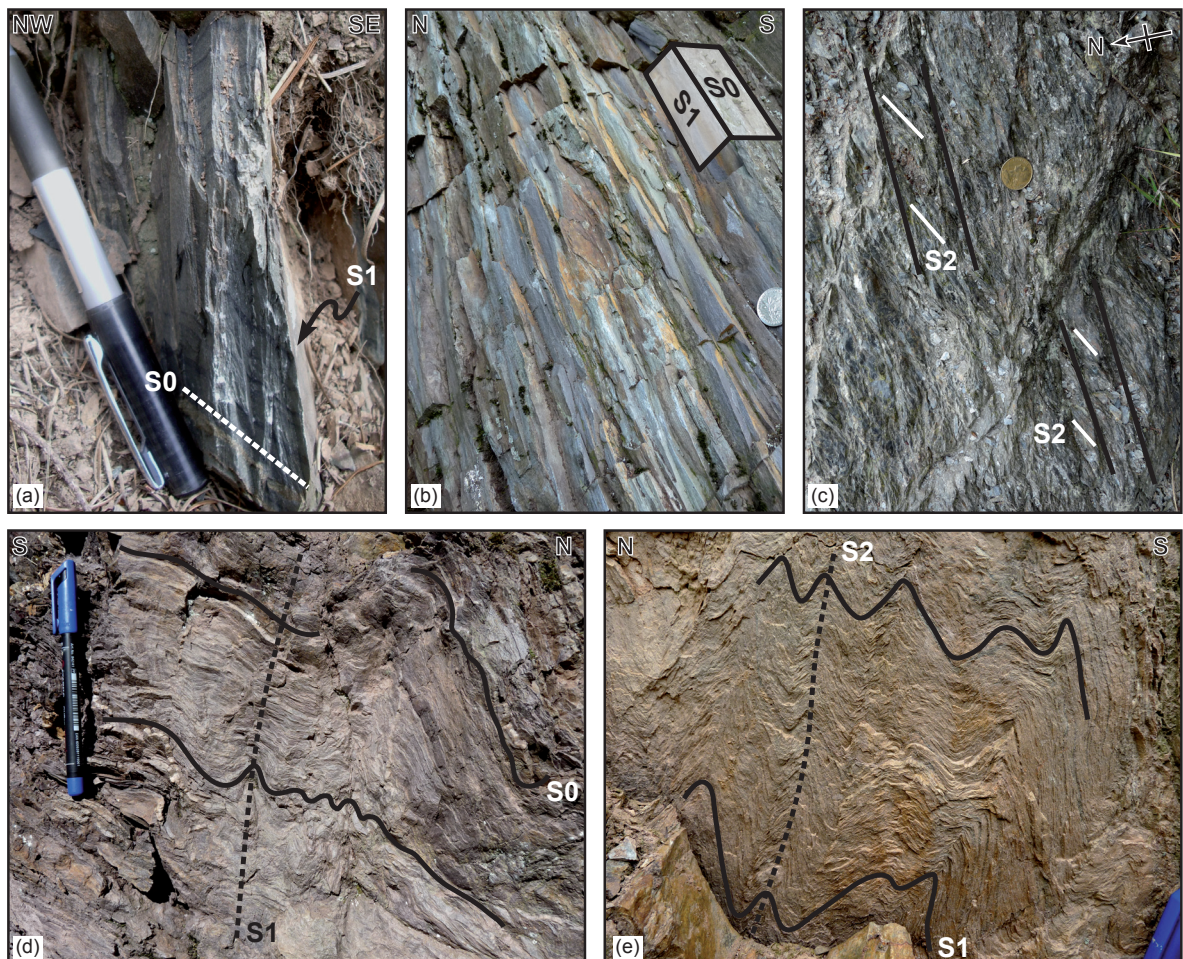


Figure 94. Field photographs illustrating the superposition of structures in the Northern Vosges. (a) Pervasive subvertical fracture cleavage S1 affecting the primary bedding in the Bruche sediments (EV202). (b) Typical pencil cleavage in the low-grade Steige metasediments. The pencil appearance results from the intersection of the primary bedding S0 (and a possibly superimposed fracturing) and the S1 cleavage (EV154). (c) Subvertical S2 schistosity crosscut by subvertical E–W striking shear planes in black schists located along the Lalaye-Lubine Fault Zone (plane view, EV62). (d) F1 folds affecting the primary bedding S0 and incipient subvertical S1 cleavage in the low-grade Steige unit (EV602). (e) Chevron-type F2 folds affecting the S1 foliation and producing the subvertical S2 cleavage in schists of the Villé unit (EV241).

and define a variably plunging intersection lineation which is well visible on S1 surfaces. A later deformation event generates cm- to m-spaced subhorizontal fracture planes, and the superposition of orthogonal fabrics with a high degree of mechanical anisotropy gives rise to a typical pencil cleavage appearance (Fig. 94b).

In the greenschist-facies Villé unit, the dominant S1 metamorphic foliation most likely developed parallel to the sedimentary bedding (Ruhland & Bronner, 1965). The foliation is marked by cm-scale alternations of quartz-rich and mica-rich layers or by a pervasive schistosity in more pelitic lithologies. The S1 was probably originally subhorizontal, but has been transposed by the subsequent D2 deformation. Indeed, S1 is commonly affected by mm- to m-scale, E–W to NE–SW trending chevron-type folds that range from open to isoclinal (Fig. 94e). In the limbs of the asymmetrical F2 folds, the S1 metamorphic foliation is variably rotated and transposed into an E–W to NE–SW striking S1–2 fabric that dips moderately to the SE or steeply to the NW (Fig. 93b). The F2 folding is associated with an S2 axial plane cleavage steeply dipping to the SE. A later vertical shortening probably operated close to the contact with the Steige unit, but occurrences of kink bands with subvertical N–S striking axial planes also point to a late-stage E–W horizontal compression event.

At the southern margin of the Villé unit, it is possible to observe a narrow zone of black schist with quartz augen surrounded by sigmoidal mica-rich bands. The black schist preserves a subvertical NE–SW striking schistosity crosscut by subvertical E–W striking shear planes that bear a subhorizontal lineation (Fig. 94c). This fabric superposition reflects a dextral sense of shear which is compatible with the latest kinematics of the neighbouring Lalaye-Lubine Fault Zone (e.g. Bouyalaoui, 1992).

Central Vosges

Metamorphic units

The structural analysis of the Central Vosges metamorphic units has revealed the superposition of three main structures. The oldest structure corresponds to the S1 metamorphic foliation which is dominant on both sides of the Mg-K granitoid (Fig. 95a). It is developed in the monotonous and varied gneisses as well as in the granulite, indicating that the deformation was shared between the different units (Fig. 96a). The S1 is defined by alternating mica-rich and quartz-rich layers in the gneissic lithologies and by highly stretched quartz and K-feldspar bands in the felsic granulite. In the varied gneiss, coarse-grained quartz–K-feldspar–garnet leucosomes are additionally found parallel to the S1 fabric. In all units, the S1 consistently strikes N–S to NE–SW and dips steeply to the NW in the eastern part, and to the SE in the

western part, thereby defining a fan-like structure (Fig. 95b). In rare places, the subvertical S1 fabric bears a subhorizontal N–S mineral lineation marked by biotite and K-feldspar ribbons.

The S1 foliation was subsequently affected by a heterogeneous D2 flattening event which produced the subhorizontal S2 fabric. The S2 foliation is nearly indistinguishable from the original S1, but can be recognised thanks to rare fabric superpositions. In general, the S1 foliation is folded by mm- to m-scale recumbent F2 folds that are open to tight (Fig. 96b, c), but in the eastern monotonous gneisses rootless isoclinal folds are commonly crosscut by a shallow-dipping S2 fabric (Fig. 96d). The orientation of S2 differs between the western and eastern side of the Mg-K granitoid. To the West of the granitoid, the S1 foliation is flattened

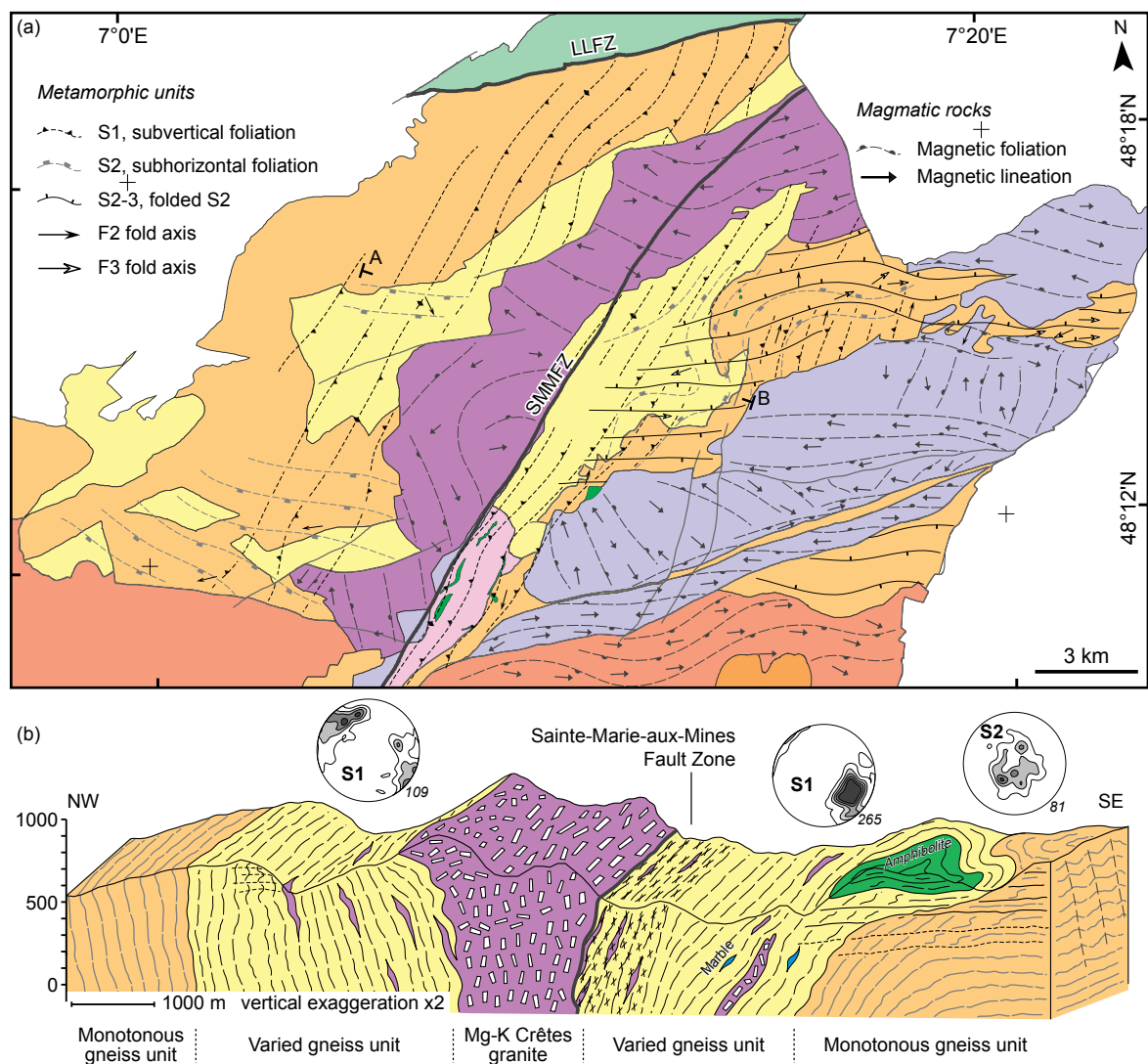


Figure 95. Structural record in the Central Vosges metamorphic units. (a) Map showing the trend of the dominant planar and linear structures. Long arrow=shallow plunge, short arrow=steep plunge. (b) Schematic section across the Central Vosges metamorphic basement. Lower hemisphere, equal-area diagrams show the orientation of the main structures described in the text (number of measurements is given in italics). K1=magnetic lineation, K3=pole to magnetic foliation. Lithologies as in Fig. 89. Structures in the leucogranites after Kratinová *et al.* (2007).

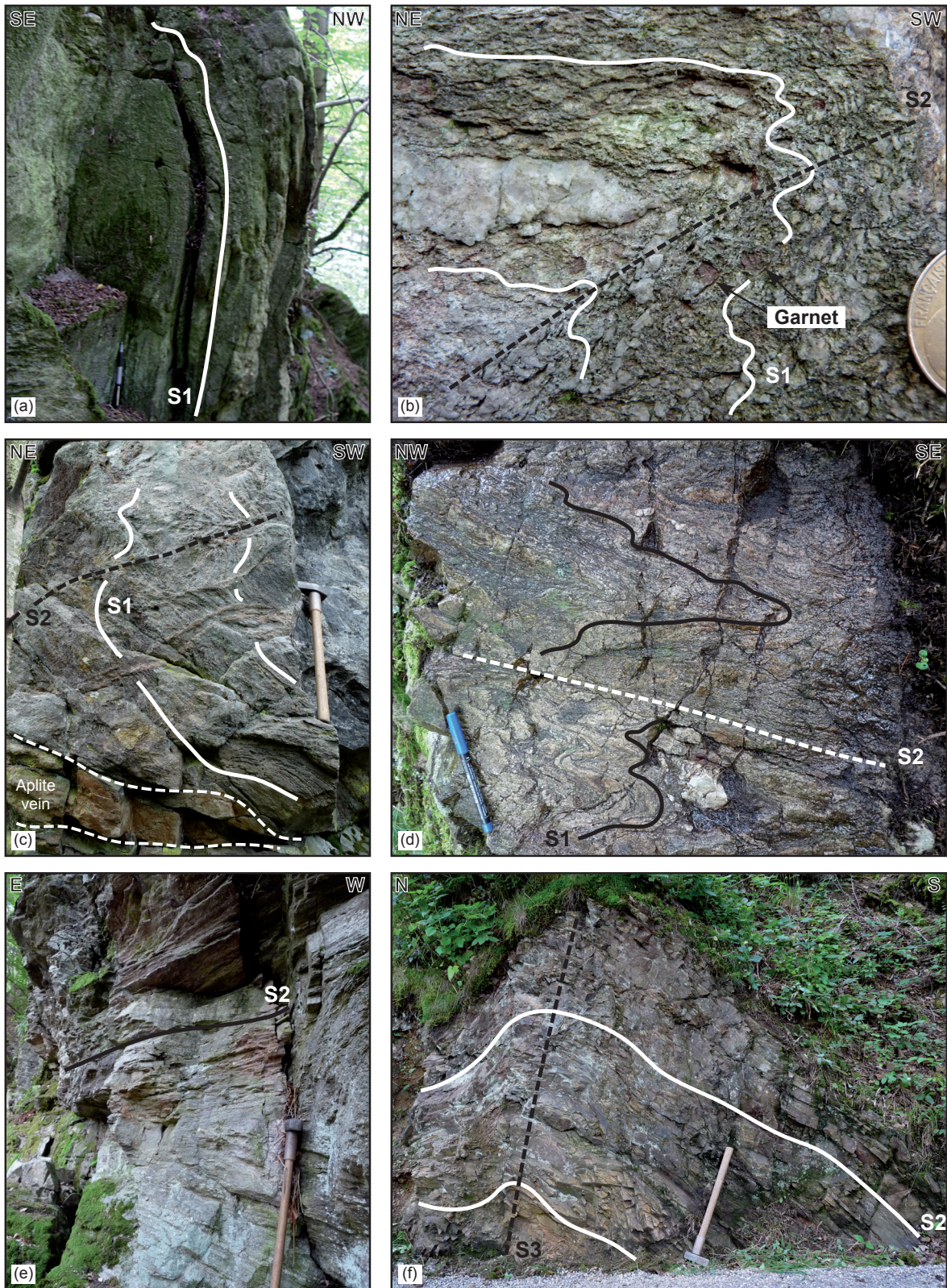


Figure 96. Field photographs illustrating the superposition of structures in the Central Vosges metamorphic units. (a) Subvertical S1 foliation in monotonous gneiss (EV333). (b) Tightly crenulated S1 foliation and incipient S2 cleavage in monotonous gneiss. Note that garnet porphyroblasts are associated with the S1 metamorphic fabric (EV709). (c) F2 fold affecting the subvertical S1 foliation in monotonous gneiss. The F2 axial plane is invaded by numerous aplitic veins or veinlets (EV708). (d) Tight F2 folds in monotonous gneiss showing biotite accumulated in the hinge zone (EV817). (e) Subhorizontal S2 foliation in varied gneiss (EV803). (f) Open asymmetrical F3 fold and incipient N-dipping S3 cleavage in varied gneiss (EV755).

into S2 planes shallowly dipping to the S or SW, and it is only visible in the southernmost part of the metamorphic basement (Fig. 95a). There, the E–W trending F2 folds show anatectic veins emplaced parallel to the subhorizontal axial plane cleavage or to the newly developed S2 foliation (Fig. 96c). To the East of the granitoid, the S2 corresponds to the axial planar cleavage of N–S trending F2 folds or more commonly to a continuous foliation shallowly dipping to the W (Fig. 96e). The S2 is dominantly present close to the contact between the varied and monotonous gneiss units and suggests a thrust of the varied unit over the less metamorphosed monotonous unit.

The later D3 deformation event chiefly affected the monotonous gneiss to the East of the granitoid and only locally the neighbouring varied unit (Fig. 95a). It resulted in a m- to km-scale asymmetrical folding of S2 and produced moderate to tight E–W trending F3 folds (Fig. 96f), but also close asymmetrical kink bands. Although an incipient S3 axial plane cleavage steeply dipping to the N can rarely be observed, the weak F3 folding is essentially associated with variably rotated S2–3 planes. The S2–3 planes consistently trend E–W and mostly dip to the N at a moderate to steep angle (Fig. 97a).

Leucogranites

The structural record in the leucogranites intruding the Central Vosges metamorphic units has been detailed by Kratinová *et al.* (2007). From North to South, the Thannenkirch and Brézouard bodies consistently preserve a northern isotropic zone and a southern anisotropic margin with a magmatic to solid-state fabric, whereas the Bilstein granite only exhibits a strong solid-state deformation. Similarly, the AMS record highlights domains of N–S to NW–SE trending lineations crosscut by narrow zones of E–W trending lineations and subvertical E–W magnetic foliations (Fig. 95a). The AMS data indicate that the domains with E–W trending structures are characterised by a high degree of anisotropy and a dominantly prolate shape of the magnetic ellipsoid, whereas the isotropic domains show more plane to oblate shapes. The observations document the development of pure shear and wrench dominated domains and are interpreted as a record of granite emplacement during sinistral transtension.

Western anatectic domain

The NE–SW trending Sainte-Marie-aux-Mines Fault Zone divides the Central Vosges into two distinct anatectic domains (Fig. 97a). The western domain exhibits a large zone of anatectic granite surrounding a migmatitic unit, the structural record of which was investigated by Blumenfeld (1986). In this unit, both a migmatitic foliation and lineation are visible. The foliation is marked by alternating biotite and quartz–K-feldspar bands in the layered migmatite while a mineral lineation is mostly defined by the alignment of biotite in the more nebulitic

varieties. In the western part of the migmatitic unit the foliation strikes NE–SW and dips moderately to steeply to the NW, whereas in the eastern part the NW–SE striking foliation is subhorizontal and shallowly dips to the N or NE (Fig. 97a). The lineation in the migmatite shows a very consistent NE–SW trend and is shallowly plunging either to the NE or SW (Fig. 97a).

To the North of the migmatitic unit, the anatectic granite preserves a magmatic to dominantly solid-state fabric that was also described by Rey (1992). The structures indicate a reactivation of the subhorizontal S2 fabric which is developed in the southwestern part of the metamorphic basement (Fig. 97a). In the anatectic granite, the reactivated S2 ranges from a weak mm-spaced gneissosity defined by stretched quartz and K-feldspar layers (Fig. 98a) to more intensely deformed muscovite–chlorite-bearing shear planes towards the South. The foliation dips shallowly to moderately towards the migmatitic unit, i.e. it corresponds to S- or SW-dipping planes to the North, and to E- or N-dipping planes along the eastern margin of the migmatite. The subsolidus foliation bears a mineral lineation and fault striations that are moderately plunging towards the S or SW (Fig. 97a). Close to the migmatite, the striations together with other shear indicators indicate a top to the SW normal shearing (Fig. 98b).

To the South of the migmatitic unit, the anatectic granite shows an isotropic magmatic texture. Nevertheless, AMS data reveal a dominant NE–SW striking magnetic foliation moderately dipping towards the SE, and rare NW–SE striking and NE-dipping foliations (Fig. 97a). In addition, two contrasted magnetic lineations are observed. Close to the migmatitic unit, few lineations moderately plunge towards the migmatite, i.e. to the NW, while most lineations plunge at variable angle to the E or NE in the rest of the area. The magnetic structures are moderately anisotropic and chiefly correspond to a plane magnetic ellipsoid.

Eastern anatectic domain

The eastern anatectic domain comprises relictual bodies of migmatitic orthogneiss, metagreywacke and Mg-K granitoid surrounded by more abundant anatectic granite (Fig. 97). The metamorphic and magmatic structures in the migmatitic units have been detailed by Schulmann *et al.* (2009a). Relicts of a metamorphic foliation are marked by planar biotite aggregates in the largest orthogneiss body. They define an E–W striking foliation steeply dipping to the S or SW in the centre of the body, but tend to have a NW–SE strike towards the margins. The orientation of the foliation is supported by AMS data which reveal a steeply dipping NW–SE foliation associated with a variably SW plunging lineation (Fig. 97). On the other hand, the smaller orthogneiss body as well as the surrounding metasedimentary migmatite indicate a dominant reworking of the original E–W subvertical fabric. In the smaller orthogneiss body, the metamorphic foliation is transposed into shallowly S- to SW-dipping

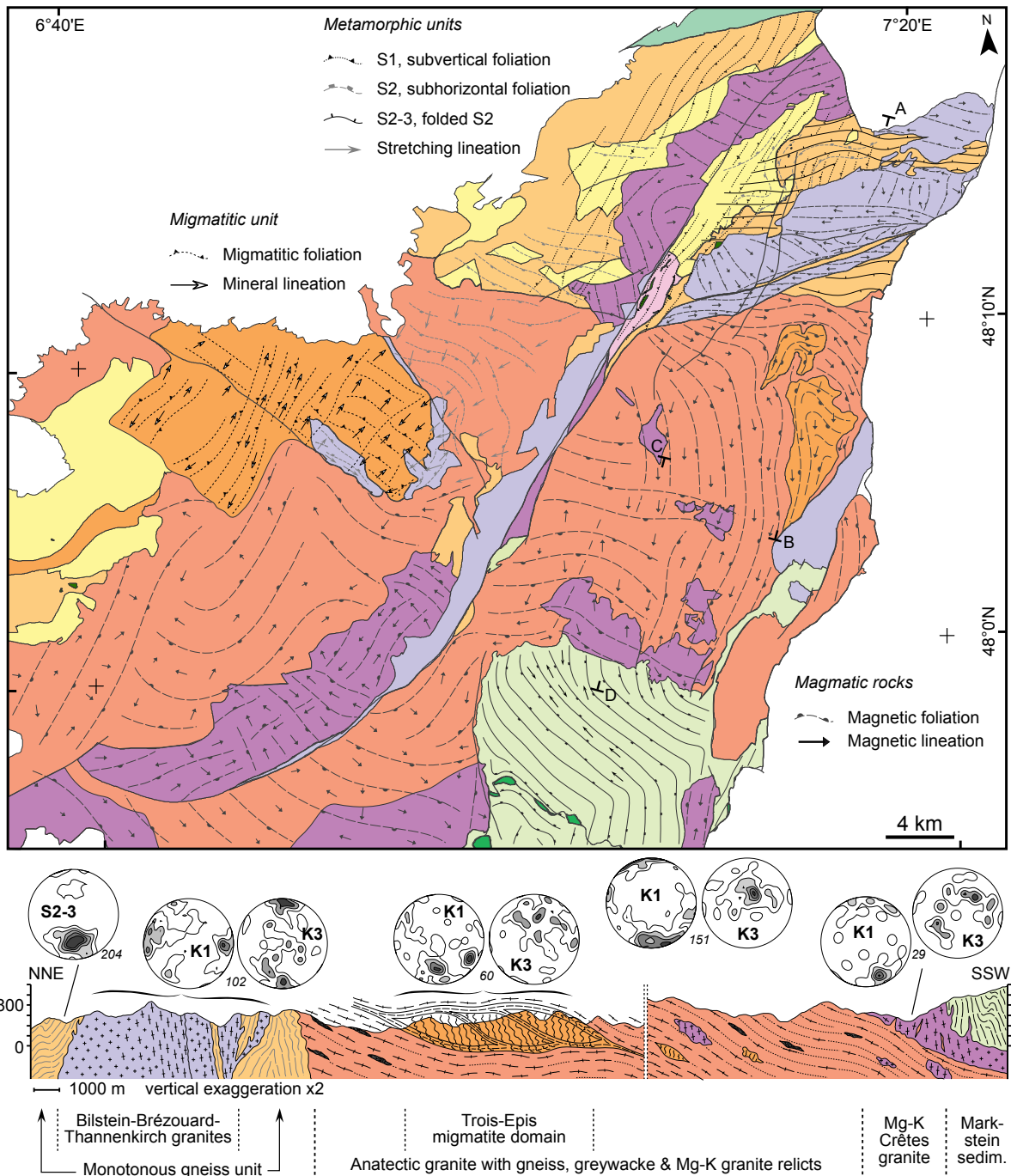


Figure 97. Structural record in the Central Vosges. (a) Map showing the trend of the dominant planar and linear structures. Long arrow=shallow plunge, short arrow=steep plunge. (b) Schematic section across the eastern anatectic domain. Lower hemisphere, equal-area diagrams show the orientation of the main structures described in the text (number of measurements is given in italics). K1=magnetic lineation, K3=pole to magnetic foliation. Lithologies as in Fig. 89. Structures in the leucogranites after Kratinová *et al.* (2007), in the western anatectic granite partly after Rey (1992), in the western migmatite after Blumenfeld (1986), in the eastern anatectic granite after Kratinová *et al.* (2011), and in the eastern migmatite after Schulmann *et al.* (2009a).

planes, while in the metasedimentary migmatite subhorizontal shear planes document top to the S normal displacement. The AMS record is in agreement with the observed solid-state structures. It shows a dominant E–W to NW–SE striking magnetic foliation dipping shallowly to moderately towards the S or SW, and subhorizontal lineations plunging to the SW or SE (Fig. 97). Importantly, the older structures found in the orthogneiss core are characterised by a low degree of anisotropy and an oblate shape of the magnetic ellipsoid, whereas the younger structures occurring at the margins show a higher anisotropy and a more pronounced prolate shape.

In addition, the surrounding anatectic granite exhibits a northern zone with magmatic to subsolidus structures and a larger zone of isotropic granite towards the South (Kratinová *et al.*, 2011). To the North of the orthogneiss bodies, a solid-state foliation defined by aligned biotite and K-feldspar phenocrysts strikes E–W and dips shallowly to the S. In this area, the magnetic foliation has a similar orientation and is associated with a subhorizontal E–W

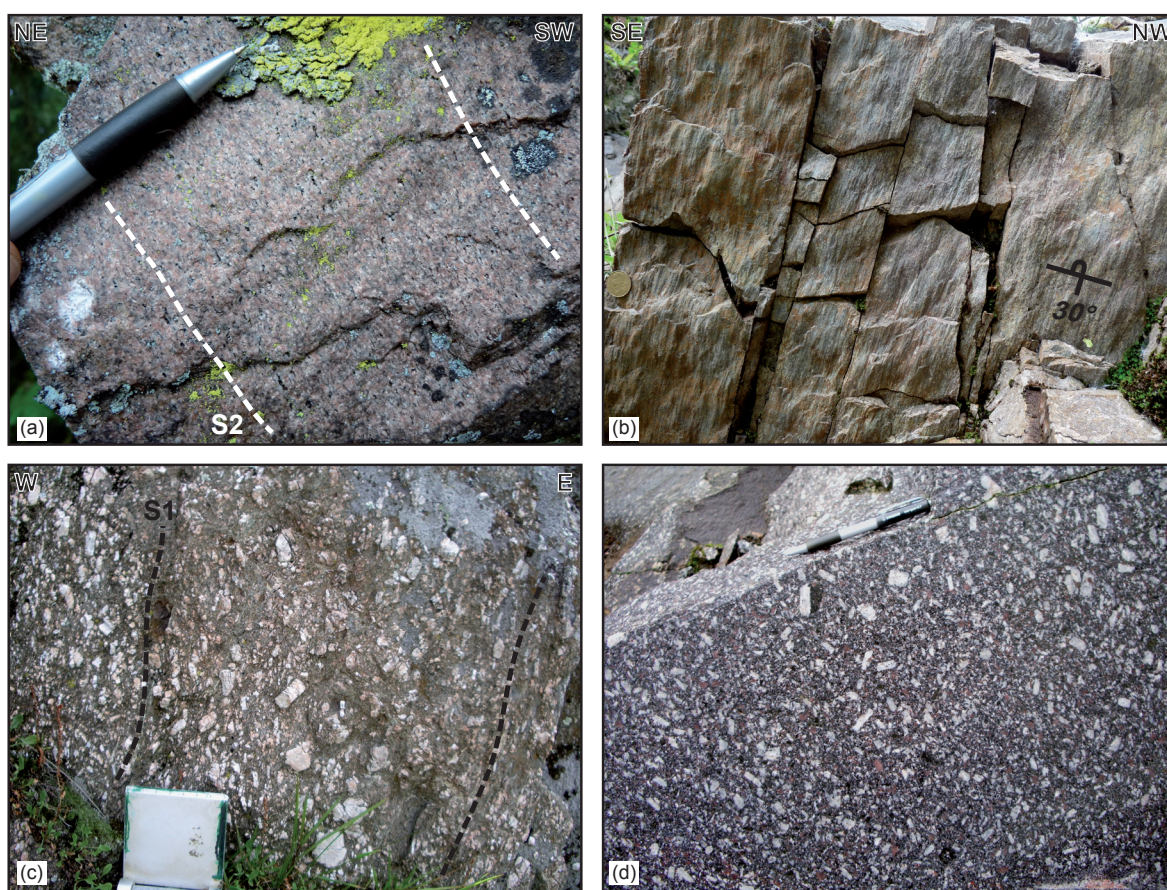


Figure 98. Field photographs illustrating the structural record in the Central Vosges magmatic rocks. (a) Weak gneissosity in granite of the western anatectic domain (EV718). (b) SW-dipping fault striations developed on a chlorite-bearing shear surface in granite of the western anatectic domain. The striations indicate normal shearing (view of the lower surface of a shear plane dipping 30° to the SW, EV729). (c) Subvertical K-feldspar fabric in durbachite intruding the felsic granulite unit. The fabric is parallel to the S1 foliation in the surrounding felsic granulite (EV381). (d) Weak alignment of K-feldspar phenocrysts in the southern Mg-K granite body (CS1).

lineation shallowly plunging to the E (Fig. 97). Across the wider isotropic domain to the West, the northern part corresponds to N–S striking foliations moderately dipping to the E, whereas the southern part shows E–W planes shallowly to moderately dipping to the S. Despite this contrast between the magnetic foliations, the magnetic lineation is consistently oriented across the entire isotropic granite. It consists of N–S trending lines that are mostly gently plunging to the S or SE (Fig. 97). While the entire area has a relatively low degree of anisotropy, the AMS data reveal that the magnetic ellipsoid is plane to prolate in the domain with N–S foliations and more oblate in the part with E–W foliations.

Farther to the South, a large body of anatectic granite is found around the Southern Vosges sedimentary units (Fig. 97a). Like in the isotropic anatectic granite, the magnetic foliation strikes E–W and dips moderately to steeply to the S. The magnetic lineation has a consistent NW–SE trend and plunges moderately to the SE (Fig. 97a). In this area, the overall anisotropy is relatively low and the magnetic ellipsoid shows a prolate to oblate shape.

Mg-K magmatism

Three distinct Mg-K granitoid bodies occur within the Central Vosges (Fig. 97). The northernmost granitoid body is intrusive in the metamorphic units and locally shows a magmatic fabric highlighted by the alignment of K-feldspar phenocrysts (Fig. 98c). The K-feldspar fabric mostly strikes NE–SW and dips moderately to steeply to the NW, but is also locally subhorizontal. Two nearly orthogonal AMS records are documented in the granite. Towards the South a rare NE–SW subvertical foliation bears a magnetic lineation shallowly plunging to the SW, whereas to the North the magnetic foliation which strikes E–W and dips shallowly to the S is associated with a subhorizontal E–W lineation (Fig. 95a). The AMS data are characterised by a relatively low degree of anisotropy and a plane to oblate magnetic ellipsoid. Importantly, the NE–SW magnetic structures are nearly concordant with the S1 foliation in the surrounding metamorphic units. It is further indicated by the numerous durbachite intrusions emplaced parallel to the S1 fabric on both sides of the Mg–K granite (Fig. 95b).

The largest Mg-K granitoid is represented by an elongated body entirely surrounded by anatectic granite in the southern part of the Central Vosges. The K-feldspar fabric (Fig. 98d) as well as the magnetic foliation in this Mg-K granitoid are homogeneously subhorizontal and dip gently to the NW. Conversely, the magnetic lineations define an axial domain with variably plunging NE–SW trending lines crosscut by zones with subhorizontal NW–SE trending lineations (Fig. 97a). The shape of the magnetic ellipsoid is dominantly of plane strain type and the degree of anisotropy remains consistently low.

The last Mg-K granitoid crops out at the northern margin of the allochthonous sedimentary unit. Along the boundary, numerous biotite-rich xenoliths are found in the granite and suggest a clear intrusive contact with the sedimentary unit. There, the Mg-K granite commonly shows a subvertical N–S solid-state fabric defined by the alignment of biotite aggregates. Within the allochthonous unit, granitic and microgranitic intrusions are also found parallel to the subvertical N–S to NW–SE striking sedimentary bedding. In the main granite body, Kratinová *et al.* (2011) showed that the magnetic foliation is gently to moderately dipping to the SW and that the N–S trending lineation gently plunges to the S or SE (Fig. 97). In this area, the magnetic anisotropy is low and the ellipsoid has a clear prolate shape.



Figure 99. Photographs illustrating the structural record in the Southern Vosges. (a) Primary bedding defined by alternating pelite and greywacke beds in the allochthonous Markstein unit (EV499). (b) Upright asymmetrical F1 fold affecting the sedimentary bedding in the allochthonous Markstein unit (EV433). (c) Section of a hand specimen showing the typical S0 sedimentary layering observed in autochthonous Oderen sediments. The S0 is defined by dark pelite layers alternating with coarser sandstone layers (EV428). (d) Nearly orthogonal K-feldspar phenocrysts in the Mg-K “Ballons” granite (BL29).

Southern Vosges

Autochthonous units

The dominant structure of the autochthonous units corresponds to the S0 sedimentary bedding. It is mostly visible in sediments of the Oderen unit and only rarely in the dominantly volcanic Thann unit. The S0 is defined by mm- to cm-scale alternations of dark pelite and yellowish siltstone or fine-grained sandstone, and by a graded bedding in greywacke beds. The primary bedding is finely laminated but can also be more chaotic when sandstone lenses are discontinuous (Fig. 99c). Locally, cm-scale plant debris are found in coarse-grained layers. According to new data and observations summarized by Krecher (2005), two distinct S0 trends can be recognised within the autochthonous units. In the largest central part, the bedding strikes NW–SE and dips at moderate to steep angle mostly to the NE (Fig. 100a). By contrast, narrower zones to the North and to the South show a N–S striking S0. In the northern part, the primary bedding is subhorizontal and only gently dipping to the E, whereas in the southern part the sediments exhibit a moderately E-dipping to subvertical S0 (Fig. 100). The orientation of S0 in the northern part is concordant with the subhorizontal fabric in the underlying granite while the S0 in the southern part probably reflects the influence of the large Mg-K “Ballons” granitoid.

Allochthonous units

Like in the autochthonous units, the allochthonous Markstein and Klippen units mostly preserve the S0 sedimentary bedding. The S0 is visible thanks to graded-bedding or alternating pelite and siltstone, but the sediments are more fine-grained. At a larger scale, the bedding is also defined by the succession of m-scale greywacke and pelite beds (Fig. 99a). New structural observations complement the works carried out by Ruhland (1958) and Petrini & Burg (1998). They indicate that the S0 is deformed by km-scale asymmetrical folds (Fig. 99b) that produce NW–SE striking bedding planes variably dipping to the NE or SW (Fig. 100). Due to the large wavelength of this folding, only few subhorizontal NW–SE trending hinge zones are exposed. On both sides of the Klippen Belt, the bedding has a monoclinical character and consistently dips to the NE. This orientation is nearly perpendicular to the S0 observed in the neighbouring autochthonous sediments and suggests the presence of a thrust of the allochthonous units over the autochthonous units (Fig. 100b). Conversely, the S0 is consistently curved towards the margins of the allochthonous units and corresponds to N–S striking subvertical bedding planes. The change in orientation of S0 coincides with the zone affected by contact metamorphism and points to an influence of the surrounding Mg-K granitoid (Figs 91 & 100). It is also reflected

by the numerous microgranite intrusions parallel to the subvertical bedding or locally oblique to the moderately dipping S0.

The sedimentary bedding is weakly affected by a mm- to m-spaced S1 cleavage which is rarely observed in the northeastern part of the allochthonous sediments. More commonly, the subvertical S0 planes bear NW–SE trending subhorizontal striations mostly indicating a dextral displacement. It is interpreted as a reactivation of the subvertical bedding planes by later transcurrent movements.

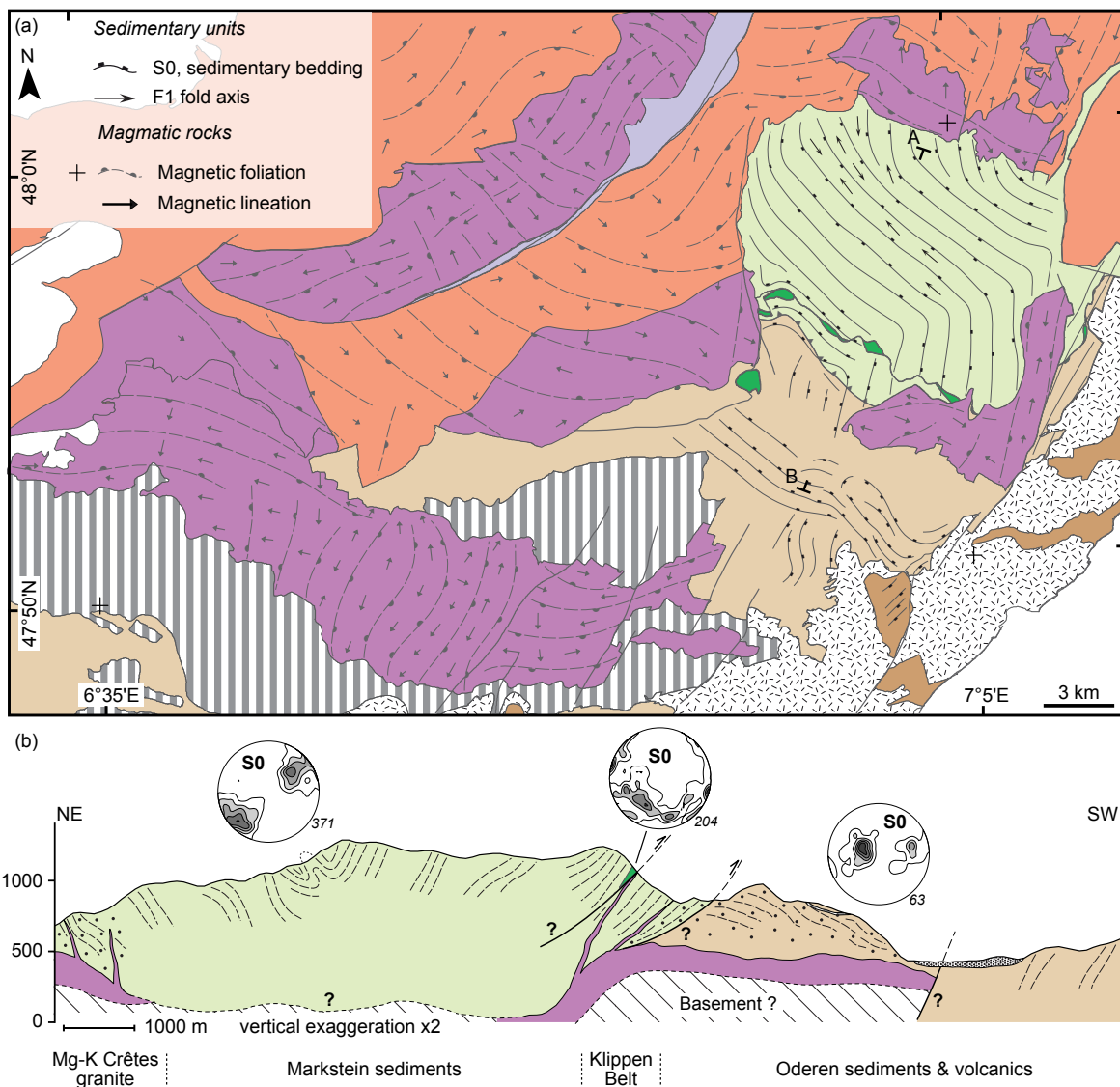


Figure 100. Structural record in the Southern Vosges. (a) Map showing the trend of the dominant planar and linear structures. Long arrow=shallow plunge, short arrow=steep plunge. (b) Schematic section across the Southern Vosges sedimentary units. Lower hemisphere, equal-area diagrams show the orientation of the main structures described in the text (number of measurements is given in italics). K1=magnetic lineation, K3=pole to magnetic foliation. Lithologies as in Fig. 89. Structures in the autochthonous units partly after Krecher (2005).

Mg-K magmatism

The E–W trending Mg–K granitoid located in the Southern Vosges is characterised by a juxtaposition of orthogonal structures (Fig. 99d). An earlier study of K-feldspar phenocrysts proposed that a dominant E–W to NW–SE subvertical foliation is crosscut by narrow corridors exhibiting a N–S to NE–SW subvertical fabric (Blanchard, 1978). Similarly, new AMS data reveal the occurrence of E–W and N–S oriented structures (Fig. 100a). In the centre of the magmatic body, the magnetic foliation strikes N–S and dips steeply to the E or W. It is associated with a N–S trending lineation which is moderately to steeply plunging either to the N or to the S. By contrast, the eastern and western parts of the granite exhibit E–W foliations steeply dipping to the S, and subhorizontal E–W trending lineations. The structural contrast could correspond to various exposed levels of the magmatic body. Indeed, the central part which shows N–S trending structures corresponds to porphyritic granite surrounded by basic plutonic rocks while the western part with E–W oriented structures exhibits fine-grained granite indicative of a shallower emplacement level. Across the whole magmatic body, both the degree of anisotropy and the shape of the magnetic ellipsoid show significant variations.

6) Interpretations and discussion

Early Palaeozoic: the pre-collisional history

The record of the Neoproterozoic to Early Palaeozoic evolution in the Vosges is cryptic (Fig. 101). Only the metagranite found in the Klippen Belt directly testifies for the presence of Cadomian basement (Part 2-Chapter I). In addition, the Northern Vosges Villé unit preserves Cambrian–Ordovician siliciclastic sediments with acid tuffs and quartzite indicative of a shallow marine basin (Fig. 90). Together with contemporaneous pelite and carbonate lenses present in the Northern Black Forest (Traisbach Serie - Sittig, 1965; Montenari & Servais, 2000), they define a succession which is typical for the margin of the Gondwana macrocontinent. Similar deposits are documented on other Cadomian blocks which are commonly regarded as peri-Gondwana terranes (e.g. Chlupač, 1993; Doré, 1994; Linnemann *et al.*, 2000). In addition, Cambro-Ordovician protolith ages for granitic pebbles in Northern Vosges sediments (Dörr *et al.*, 1992) and for the felsic granulite (Part 2-Chapter II) point to abundant acid magmatism around 500 Ma (Fig. 101). This magmatic activity announces the break-up of the northern Gondwana margin and the associated opening of sedimentary (oceanic ?) basins bounded by microcontinental blocks (e.g. Pin & Marini, 1993; Crowley *et al.*, 2000; Schätz *et al.*, 2002; Figs 102 & 103).

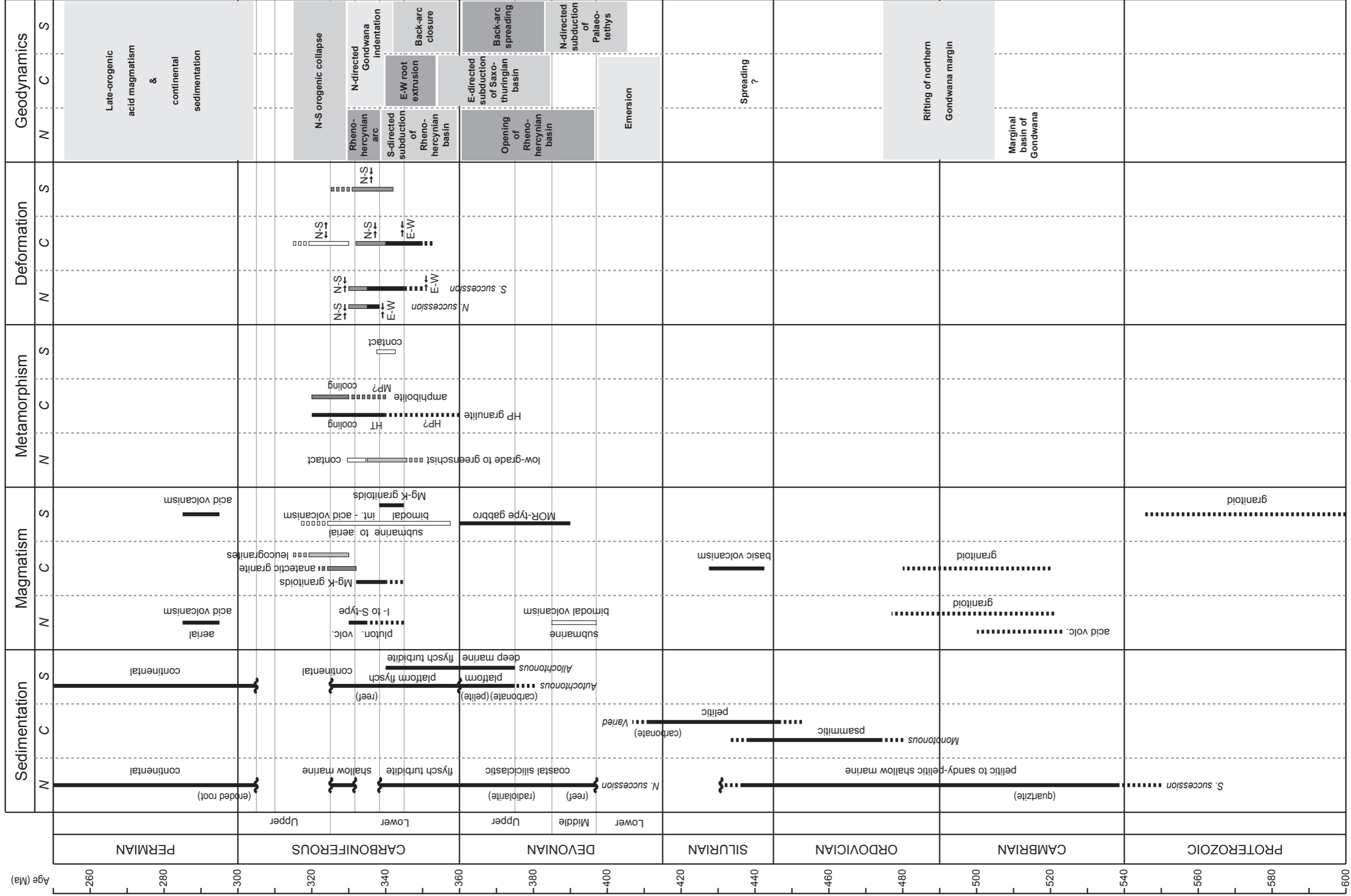
The Saxothuringian basin

The opening of an Early Palaeozoic basin is indicated by thick deposits corresponding to the sedimentary precursors of the monotonous and varied gneiss units. The monotonous unit comprises psammitic sediments derived from a dominant Cadomian source and probably started to be deposited in the Middle Ordovician (Fig. 92b). By contrast, the varied unit has a more pelitic composition and originated from the Late Ordovician to Silurian sedimentation of chiefly Cambro-Ordovician detritus (Fig. 92b). It additionally involves a basal layer of basic magmatic rocks and scarce carbonate lenses. Moreover, Ordovician to Silurian shallow-marine pelites of the Steige unit with possible carbonates (von Eller, 1963) are found in the Northern Vosges (Fig. 101).

The Early Palaeozoic sedimentary record bears strong similarities to the lithostratigraphy of the Saxothuringian zone and especially to the Thuringian facies. The Thuringian succession is characterised by Ordovician sandy-pelitic sediments overlain by Silurian shales with intercalations of carbonates and basic lavas (Falk *et al.*, 1995). Accordingly, the monotonous unit can be seen as the base of the Thuringian facies while the varied unit resembles the overlying Silurian succession. The monotonous and varied units are therefore interpreted as proximal deposits of the Saxothuringian passive margin sequence (Fig. 103b, c). A continuity of the Saxothuringian sediments from the Vosges up to Eastern Germany (Fig. 102b) is even envisaged since similar sedimentation ages are proposed for some high-grade metasediments of the central Black Forest (Kober *et al.*, 2004).

However, structural and petrological data demonstrate that the varied unit was not originally located above the monotonous sediments. Indeed, the younger and more metamorphosed varied unit is thrust over the monotonous unit (Figs 91c & 95). It is incompatible with the idea of a homogeneous Thuringian succession. Alternatively, both units should represent different sedimentation areas. The monotonous unit had to be deposited close to a Neoproterozoic and mostly Cadomian basement. Because such a basement is known to underlie the monotonous unit in the Bohemian Massif (e.g. Fritz, 1996; Friedl *et al.*, 2004; Schulmann *et al.*, 2005), the Vosges monotonous unit is considered to rest on a similar Moldanubian basement (Fig. 103b). Conversely, the varied unit is related to the erosion of a predominantly Cambro-Ordovician basement. Considering that Cambro-Ordovician magmatism is more abundant in the northern part of the ATA (e.g. Kröner *et al.*, 2000b; Kemnitz *et al.*, 2002), the varied unit could have been deposited on a Saxothuringian substratum (Fig. 103c).

Figure 101. Synoptic view of Palaeozoic sedimentation, magmatic, metamorphic and deformation events in the Variscan Vosges. N=Northern Vosges, C=Central Vosges, S=Southern Vosges.



If this view is compared to the succession of terranes in the Bohemian Massif, the varied and monotonous units should be separated by the Teplá-Barrandian block. However, such a large piece of Cadomian basement is not found in the Vosges, suggesting that the Teplá-Barrandian basement does not extend towards the West (Fig. 102). Oppositely, it is proposed that an oceanic domain originally separated the monotonous and varied sedimentary basins. By analogy with the Thuringian facies, an episode of Silurian spreading can be indicated by basic magmatism found at the base of the varied unit. The rare eclogite occurrences reported in the Central Vosges metamorphic units (Hameurt, 1967; Fluck, 1971) could additionally represent possible relicts of oceanic crust. To sum up, both the monotonous and varied units are interpreted as relatively proximal sediments which were deposited on conjugate margins of the Saxothuringian basin (Fig. 103c).

The Palaeotethys Ocean

The Early Palaeozoic break-up of Gondwana produced the large Rheic oceanic realm between Avalonia and the ATA, and the Saxothuringian basin between Cadomian blocks of the ATA (Fig. 102a, b). Several paleogeographic reconstructions have also proposed the existence of an Ordovician–Silurian oceanic domain between the ATA and northern Gondwana (e.g. Matte, 2001; Stampfli & Borel, 2002; Winchester *et al.*, 2002; von Raumer *et al.*, 2003). Due to the variety of names encountered in the literature, the single term Palaeotethys Ocean *sensu* Stampfli & Borel (2002) will be further used. Based on Cambrian to Silurian ophiolitic remnants, Matte (1986) initially traced this ocean from Galicia to the northern French Massif Central, while other eclogite and ophiolite occurrences have later been used to infer a continuation in the NE Massif Central (Lardeaux *et al.*, 2001), Corsica-Sardinia (Rossi & Oggiano, 2009) or in various parts of the Alps (e.g. Ménot *et al.*, 1988; von Raumer, 1998). The Palaeotethys Ocean could even extend up to the southern Black Forest where the suture zone of an ocean originally located to the South has been proposed (Loeschke *et al.*, 1998). However, the existence of a wide Palaeotethys Ocean is seriously questioned by paleontological data. Indeed, faunal distributions suggest that the ATA remained close to Gondwana until at least *ca.* 420 Ma (Cocks & Fortey, 1982). According to Paris *et al.* (1990), paleoclimatic and paleontologic records rule out the presence of a large oceanic domain between the ATA and Gondwana. It could be supported by zircon provenance showing that the Saxothuringian block may have remained attached to Gondwana during the whole Variscan orogeny (Linnemann *et al.*, 2004).

Consequently, the best way to reconcile the divergent interpretations is to propose the existence of a narrow seaway between the northern margin of Gondwana and the ATA (Fig. 102b). Considering that the Saxothuringian basement hardly left Gondwana (Linnemann *et*

al., 2004) and that ophiolitic remnants are more abundant to the West, this oceanic domain should have been non-cylindrical and possibly wider towards the West. In this view, the narrow oceanic domain would resemble the Theic Ocean as drawn by Rey *et al.* (1997) and could correspond to a ramification of the larger Rheic Ocean (Fig. 102b). Relicts of the Palaeotethys Ocean are not observed in the Vosges Mountains but a southerly oceanic domain is inferred from Ordovician to Silurian sediments found in the southern Black Forest (Hann *et al.*, 1995; Sawatzki *et al.*, 1997). According to Maass *et al.* (1990), equivalents for these deposits are expected to lie to the South of the presently exposed Vosges basement. Consequently, the possible presence of the Palaeotethys Ocean should not be neglected for further reconstructions of the evolution of the Vosges Mountains (Fig. 103c, d).

The Rhenohercynian basin

No trace of Lower Devonian sediments can be found across the Vosges Mountains. In the northern succession (Bruche unit) of the Northern Vosges, the oldest sediments correspond to Middle Devonian coastal conglomerates and sandstones with few reef limestones (Fig. 90). In addition, pebbles in the conglomerate point to the erosion of a Cambro-Ordovician granitic basement (Dörr *et al.*, 1992) which is also found farther to the North in the Saar basin (Sommermann, 1993). However, the basement in the Saar basin is overlain by thick Middle to Upper Devonian platform limestones (Hering & Zimmerle, 1976). These scarce data indicate the presence of a Devonian sedimentary basin in the northern part of the Vosges. Importantly, the coarse-grained character of the first sediments suggests that a probable episode of Lower Devonian emersion was followed by a marine transgression (Fig. 101). The correlation with the Middle Devonian deposits in the Saar basin additionally points to a relatively shallow marine platform environment which may be slightly deepening towards the North (Fig. 103d).

Nearly similar Devonian siliciclastic and/or carbonated sediments are document in the Rhenish Massif (Franke, 1995), SW England (Leveridge & Hartley, 2006) or Moravia (Hladil *et al.*, 1999). These successions are interpreted as the infill of the Rhenohercynian basin which started to open in the Early Devonian (e.g. Clark *et al.*, 1998). By contrast, Devonian black shales or cherts in both the Thuringian and Bavarian facies of the Saxothuringian basin indicate a deeper sedimentary environment (Falk *et al.*, 1995). Therefore, the Middle Devonian record of the Northern Vosges is tentatively correlated with that of the Rhenohercynian basin (Fig. 102c). In this view, the Northern Vosges could represent a proximal part of the southern margin of this basin (Fig. 103d).

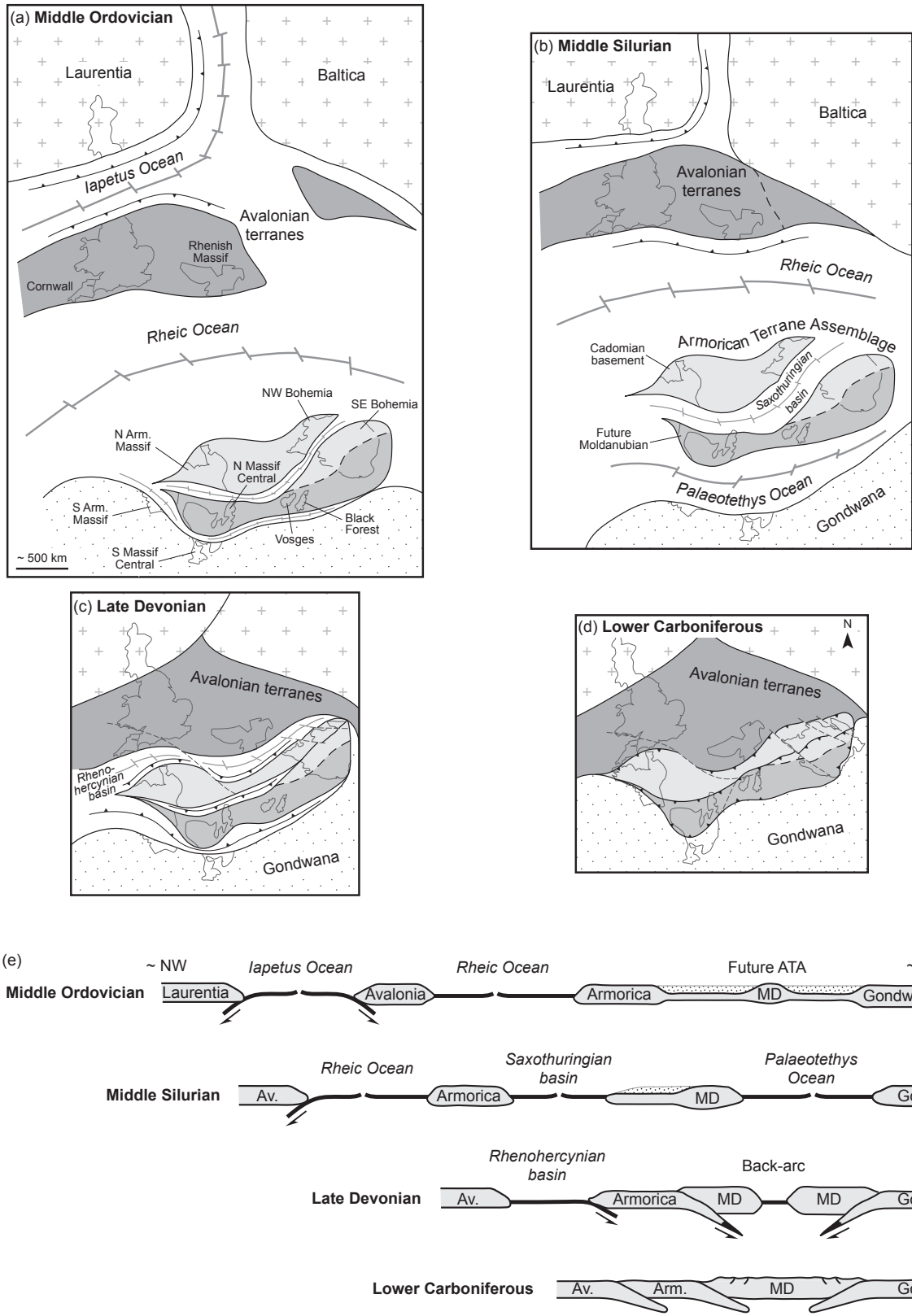


Figure 102. Tentative paleogeographic reconstructions and schematic sections for the Palaeozoic evolution of the Variscan Belt of Europe. Reconstructions for (a) Middle Ordovician, (b) Middle Silurian, (c) Late Devonian and (d) Early Carboniferous times are largely inspired by the works of Tait *et al.* (2000), Winchester *et al.* (2002) and Cocks & Torsvik (2002). For scale and paleolatitudes, see these references. (e) Schematic sections showing a simplistic plate tectonic framework during the Palaeozoic. The sections are nearly NW–SE and partly run across the Variscan Vosges basement. The Moldanubian zone is treated here as (Ordovician) passive margin deposits of the southern ATA which subsequently formed the internal part of the orogen.

Late Devonian: onset of collision

Across the Variscan Belt of Europe, multiple arguments testify for a general subduction setting during the Late Devonian (e.g. Matte, 1998). It is best reflected by the consistent 390–360 Ma ages obtained on HP metamorphic rocks in the Armorican Massif (Bosse *et al.*, 2000; Bosse *et al.*, 2005; Cocherie *et al.*, 2005), in the Sudetes (Maluski & Patočka, 1997) or in the NE Bohemian Massif (Schmädicke *et al.*, 1995). The timing and polarity of subduction between the Saxothuringian and Moldanubian zones is particularly well constrained thanks to numerous ages reflecting HP metamorphism at ~380 Ma (Gebauer & Grünenfelder, 1979; Stosch & Lugmair, 1990; Beard *et al.*, 1995), and to the Upper Devonian flysch sedimentation in the Saxothuringian basin followed by the northwestward emplacement of high-grade nappes (e.g. Franke, 1984). Similarly, evidences for subduction can be found in the Vosges Mountains. They are represented by HP granulite-facies rocks which were probably metamorphosed in the Late Devonian–Early Carboniferous (Part 2-Chapter II) and by ophiolitic remnants of a Late Devonian back-arc basin (Part 2-Chapter I). The subduction-related lithologies are the key for understanding the early collisional history of the Vosges basement. Their significance will therefore be discussed in the framework of the large-scale Variscan evolution.

Subduction of the Saxothuringian passive margin - thickening of the orogenic root

HP granulite-facies metamorphism is a peculiar feature of the European Variscides (e.g. Pin & Vielzeuf, 1988) and its significance has been extensively explored by petrological, geochemical and geochronological studies (Kröner *et al.*, 2000a; e.g. O'Brien & Rötzler, 2003; Janoušek *et al.*, 2004; see also Kotoková, 2007 for a review). The HP felsic granulite type is commonly thought to derive from acid volcanic or granitic rocks, and this view is supported by petrological experiments (Tropper *et al.*, 2005). Based on geochronological and geochemical arguments, Janoušek *et al.* (2004) further proposed that the felsic granulites which are now found within the Moldanubian zone represent metamorphosed and partially molten equivalents of Ordovician granites located in the Saxothuringian zone (Fichtelgebirge). It has been integrated in a tectonic model where HP granulite-facies rocks are interpreted as a part of a subducted continental crust which was subcreted to the Moldanubian basement (Guy *et al.*, 2011; Chopin *et al.*, 2011a) through a relamination process (Hacker *et al.*, 2011). Such a model additionally suggests that Mg-K granitoids which are frequently occurring with HP granulite-facies rocks are the products of mixing between the melt lost from the felsic granulite and the overlying lithospheric mantle (Janoušek & Holub, 2007; Lexa *et al.*, 2011).

In the Central Vosges metamorphic units, a clear distinction between the monotonous and varied gneiss units can be made on the basis of geochronological data (Fig. 92b). The

contrasted inherited zircon ages have been used to propose that the two units were deposited in different sedimentary basins (Fig. 103). In addition, petrological investigations reveal that the felsic granulite and varied gneiss underwent HP granulite-facies metamorphism probably at *ca.* 360 Ma (Part 2-Chapter II), whereas the monotonous gneiss only reached peak amphibolite-facies conditions (Fig. 91c). Similarities between these data and those reported for the Bohemian Massif suggest that an identical tectonic scenario has occurred in both regions. Accordingly, the Central Vosges root zone is interpreted as a juxtaposition of the allochthonous varied and felsic granulite units with the autochthonous monotonous unit. It is most likely the result of a SE-directed continental subduction of a Saxothuringian-type passive margin and its subsequent relamination at the base of the Moldanubian basement (Fig. 103e).

This interpretation requires locating the continuation of the Saxothuringian–Moldanubian suture, which has been classically defined along the E–W Lalaye-Lubine Fault Zone in the Vosges Mountains (Fluck *et al.*, 1991). However, this zone is devoid of any ophiolitic remnants in the Vosges as well as in the neighbouring Black Forest. More importantly, its E–W strike is in total contradiction with the N–S to NE–SW orientation of the earliest compressive structures observed in the Central Vosges (Figs 93 & 95). The structural data therefore indicate that the suture zone could correspond to the NE–SW lineament traced by Edel & Schulmann (2009) to the North of the presently exposed Vosges basement (Figs 88 & 102c). Alternatively, the suture could lie within the Northern Vosges basement and could be presently obliterated by the magmatic suite. The subduction polarity would be further supported by the quasi-systematic occurrence of eclogitic rocks in the western part of the Vosges (Hameurt, 1967).

The significance of the Early Palaeozoic Steige and Villé units in this subduction scenario remains obscure. These units could either correspond to sediments of the lower Saxothuringian plate which did not suffer subduction but were accreted in a prism, or to sediments deposited on the Moldanubian upper plate. Sediments involved in an oceanic accretionary prism are commonly expected to record pressure-dominated metamorphism coeval with HP metamorphism in the subducted material (e.g. Maruyama & Liou, 1988). Ongoing accretion can further result in thrusting of high-grade units over less metamorphosed rocks producing inverted metamorphic sequences which have been repeatedly described along the major Variscan suture zones (e.g. Pitra *et al.*, 2010). However, such features are incompatible with the *P–T–D–t* record in the Steige and Villé units. These units preserve a continuous Barrovian metamorphic gradient reaching garnet grade towards the South (Fig. 91b), and possibly kyanite grade if mica schists occurring in the northern Black Forest are

considered (Wickert *et al.*, 1990). Importantly, the peak metamorphic assemblages were developed in the originally subhorizontal foliation which was transposed much later into a subvertical cleavage during Lower Carboniferous N–S compression. It indicates that the metasedimentary units represent a normal metamorphic succession. In addition, metamorphic ages of 345–340 Ma (Clauer & Bonhomme, 1970; unpublished EMP monazite ages) are in agreement with those obtained in the deep orogenic root (Fig. 92b). Consequently the Steige and Villé units are regarded as autochthonous sediments of the upper Moldanubian crust which were weakly metamorphosed during the Early Carboniferous, probably as a result of moderate crustal thickening (Fig. 103e).

Subduction of the Palaeotethys Ocean

In the Southern Vosges Klippen Belt, ophiolitic remnants testify for the opening of a Late Devonian basin (Fig. 103e). It has been further proposed that the basin represents a back-arc environment related to the subduction of an Early Palaeozoic oceanic domain (Part 2-Chapter I). However, it is difficult to infer along which direction the basin was opened. The sedimentary record indicates a clear N–S zonality: a deep marine environment is present towards the North, whereas platform deposits are observed to the South. In addition, the subsequent Carboniferous inversion of the basin is characterised by NW–SE striking structures (Fig. 100). Considering that the shape of the basin strongly controls its future inversion (e.g. Oncken *et al.*, 1999), it can be postulated that the Southern Vosges basin opened parallel to a nearly E–W trending axis (Fig. 102e). The E–W trend is well correlated with the orientation of structures in the Badenweiler-Lenzkirch zone located in the southern Black Forest (e.g. Sawatzki & Hann, 2003). Based on Silurian to Carboniferous arc magmatism (Hann *et al.*, 2003), this zone is thought to record the N-directed subduction of a southern oceanic domain (Loeschke *et al.*, 1998). Consequently, Late Devonian back-arc spreading in the Southern Vosges is tentatively correlated with the closure of the Palaeotethys Ocean (Fig. 103e).

The role of the Rhenohercynian basin

In the Northern Vosges, Late Devonian sediments chiefly indicate an undisturbed coastal environment (Fig. 90). Only breccias and resedimented Middle Devonian carbonates could point to incipient instabilities in the basin during the Famennian (Blanalt & Lillié, 1973). Conversely, contemporaneous flysch-type sedimentation is clearly documented in typical Rhenohercynian successions. Syn-orogenic clastics first appeared in the Middle Devonian and became more widespread during the Late Devonian in Cornwall or NW Germany (Franke, 1995; Leveridge & Hartley, 2006). They are thought to reflect S-directed subduction

of the Rhenohercynian basin below a southern active margin which could correspond to the Mid-German Crystalline Rise (e.g. Holder & Leveridge, 1986; Oncken, 1997). Although the Northern Vosges magmatic suite bears similarities to the MGCR and points to later Carboniferous collision (e.g. Altherr *et al.*, 2000), no evidence for Late Devonian convergence is recorded in the sedimentary basin. Consequently, the Northern Vosges are still interpreted as a relatively quiet passive margin environment during the Late Devonian (Fig. 103e). Because the stable setting is coeval with subduction and exhumation of HP rocks along the southern Saxothuringian–Moldanubian suture (e.g. Stosch & Lugmair, 1990), the continuous opening of the Rhenohercynian basin (Fig. 102c) can be further considered as the main factor controlling the rate of the Saxothuringian subduction (Schulmann *et al.*, 2011).

Early Lower Carboniferous: polyphase collisional tectonics

A range of arguments indicates that the early Carboniferous was a period of generalised collision in the vicinity of the Variscan Vosges (Fig. 101). In the Northern Vosges basin, Lower Carboniferous flysch-type sedimentation is thought to reflect S-directed subduction of the Rhenohercynian basin. This process culminated with the development of a nearly E–W trending magmatic arc at 335–330 Ma (Altherr *et al.*, 2000) in the Northern Vosges. In the southern Black Forest, similar Lower Carboniferous flysch sediments subsequently deformed in a S-verging accretionary prism indicate the prolonged subduction of the Palaeotethys Ocean towards the North (Maass *et al.*, 1990; Hann & Sawatzki, 1998). All these features testify for a bulk N–S compressional regime (Fig. 104). However, in the same time the Central Vosges orogenic root experienced polyphase deformation and metamorphism in a quasi-orthogonal E–W to NW–SE oriented stress field. This evolution will be discussed in terms of intracontinental tectonic processes.

Burial and exhumation in the orogenic crust (D1)

The earliest fabric observed in the Vosges metamorphic units is the NE–SW subvertical S1 foliation (Fig. 95). In a few felsic granulite samples, kyanite relicts oriented perpendicular to S1 suggest that peak metamorphic conditions were achieved in an earlier, probably subhorizontal fabric. It is in line with studies proposing that HP metamorphism in the Variscan lower crust could be associated with a subhorizontal subduction-related fabric (e.g. Štípská *et al.*, 2004; 2011). The S1 foliation can be connected with sillimanite growth after kyanite in both the felsic granulite and varied gneiss (Fig. 91c). By contrast, the metamorphic conditions of S1 are not known for the monotonous unit, but garnet-staurolite relicts could point to a prograde evolution. The observations therefore indicate a lower crust exhumation and possibly

a contemporaneous burial of the middle crust. Importantly, the material transfer occurred during complete coupling between the already welded autochthonous and allochthonous crustal portions since S1 is equally developed in all lithologies.

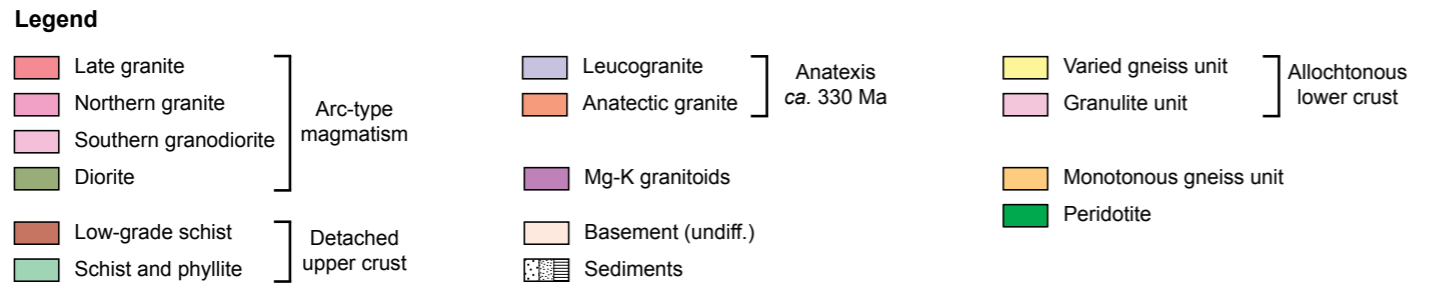
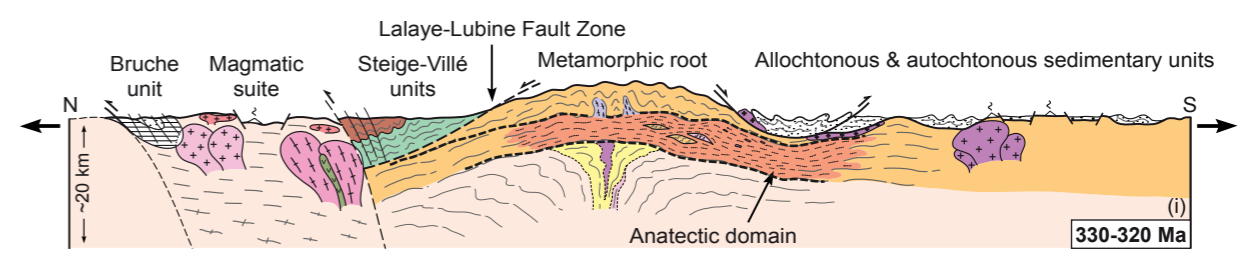
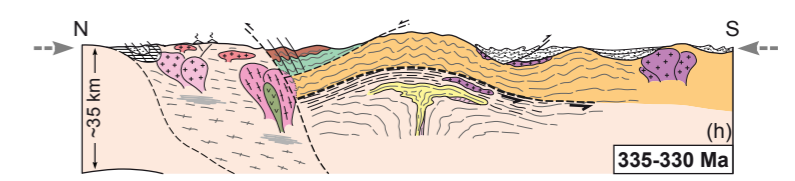
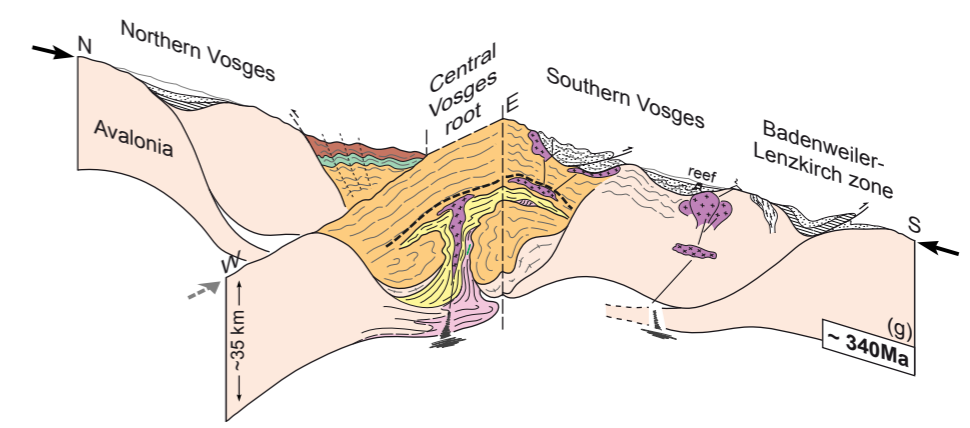
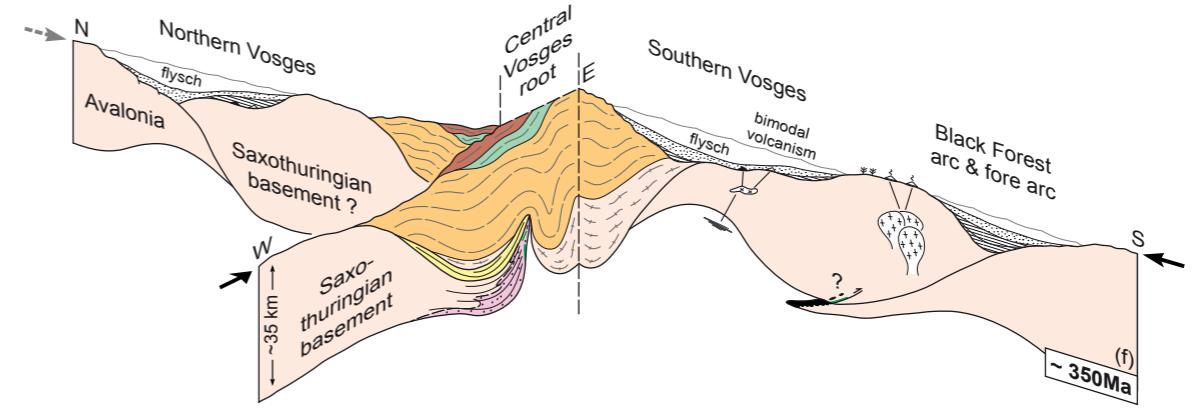
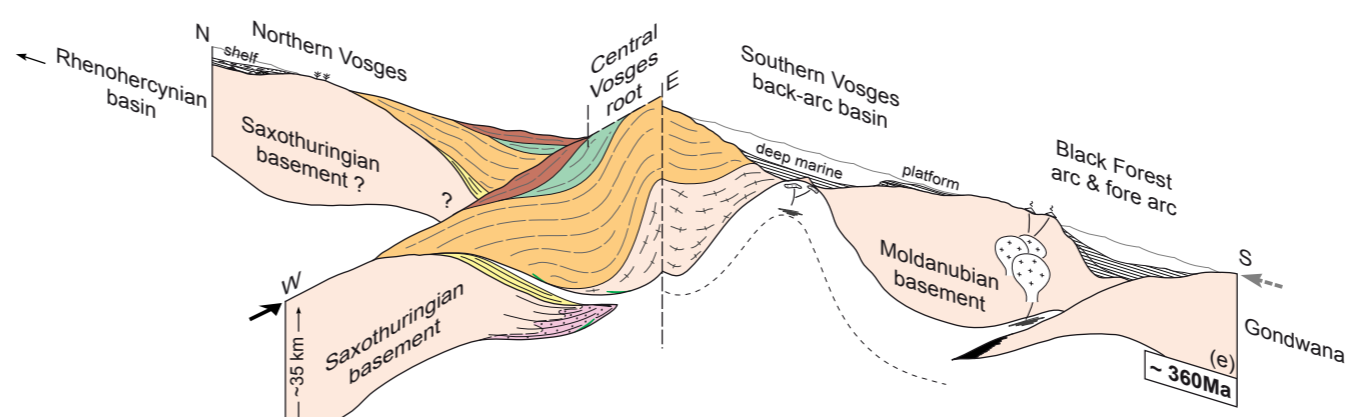
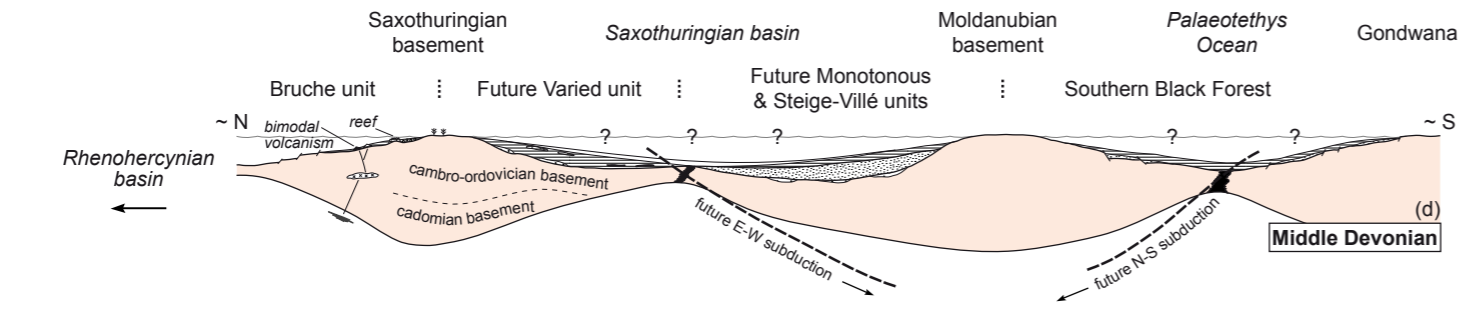
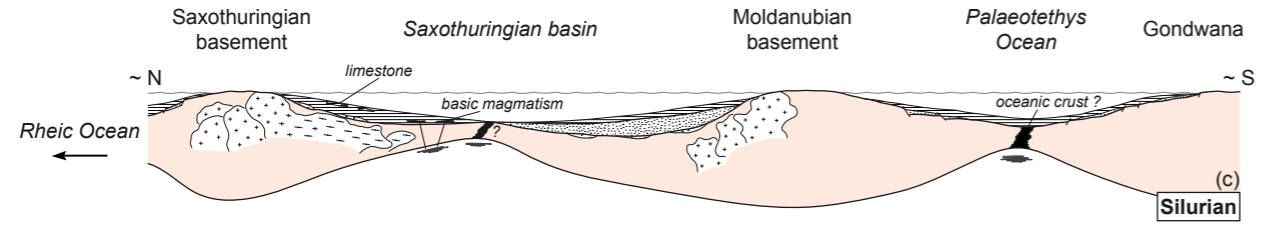
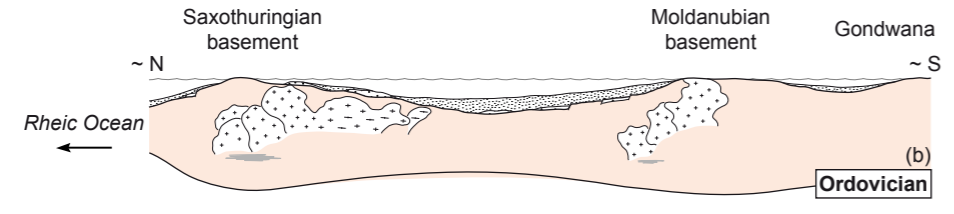
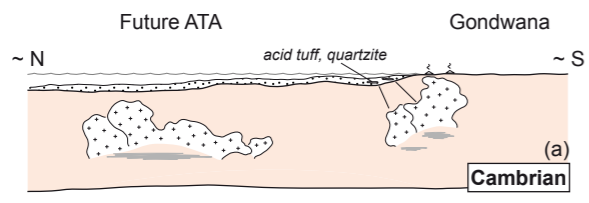
Exhumation of the lower crust in a vertical structure can essentially be achieved by buoyancy-driven ascent in a diapiric structure (Calvert *et al.*, 1999; Norlander *et al.*, 2002) or by crustal-scale folding (Burg *et al.*, 1997; Štípská *et al.*, 2004). Both mechanisms can account for isothermal decompression P – T paths and for a possible exchange between the autochthonous and allochthonous units (Warren & Ellis, 1996; Racek *et al.*, 2006). Nevertheless, the presently exposed orogenic root clearly shows an asymmetrical architecture. Amphibolite which forms the base of the varied unit, together with the felsic granulite which is thought to represent the former granitic basement, are only present to the West of the Sainte-Marie-aux-Mines Fault Zone (Fig. 95). It is incompatible with the simple diapiric or folding models which ideally produce a symmetrical architecture. Consequently, an additional parameter has to be considered in order to explain the asymmetrical structure of the exhumed root.

The role of lateral tectonic forces has generally been underestimated in the discussion of exhumation mechanisms (e.g. Ring *et al.*, 1999). Yet, exhumation in orogens is commonly a syn-convergent process (e.g. Platt, 1986). It is therefore proposed that horizontal compression could explain the asymmetrical structure of the exhumed root. In orogenic wedge systems, horizontal compression has been ascribed to the presence of a rigid crustal portion acting as a buttress (e.g. Chopin *et al.*, 2011a). In the case of the Vosges, exhumation of the root requires a stronger crustal layer towards the East. The rigid indentation can be explained by two different processes. Following the idea already proposed by Schulmann *et al.* (2002), the rheological structure of the crust which is inherited from rifting can be invoked, and a possible piece of thinned Moldanubian basement could act as an indenter (Fig. 103f). Alternatively, it should be noted that vertical extrusion is coeval with the closure of the Southern Vosges back-arc basin. Although the closure occurs parallel to a N–S direction, the underthrust continental crust could still trigger a minor buttressing effect on the orogenic root (Fig. 103f).

Genesis of an intra-orogenic boundary zone (D2)

In the Central Vosges metamorphic units, the subvertical S1 foliation is subsequently transposed into a subhorizontal S2 fabric (Fig. 95). Metamorphism associated with S2 is characterised by sillimanite-bearing assemblages similar to those observed in the S1 fabric,

Figure 103. Schematic cross-sections illustrating the Palaeozoic evolution of the different parts forming the present-day Vosges basement. This view tries to integrate all lithological, structural, petrological and geochronological data available for the Vosges. (a) Cambrian, (b) Ordovician, (c) Silurian, (d) Middle Devonian, (e) Late Devonian, (f–h) early Lower Carboniferous and (i) late Lower Carboniferous.



but also by spinel occurrences, suggesting that the LP/HT metamorphic overprint which is commonly documented in the Vosges (Rey *et al.*, 1989; Latouche *et al.*, 1992) is related to the development of the subhorizontal S2 foliation. Due to its high temperature character, the metamorphic event is correlated with the zircon ages of 340–335 Ma that are repeatedly obtained in metamorphic rocks (Fig. 92b), and especially in leucosomes parallel to S2 in varied gneiss (Schaltegger *et al.*, 1999). The combined observations are interpreted as widespread flattening and limited exhumation of the metamorphic units which have been previously juxtaposed at a mid-crustal depth. This event is responsible for the fan-like structure of the root as well as the apparent thrust of the allochthonous units over the autochthonous rocks (Fig. 95b) which has been previously interpreted as a result of nappe tectonics (Fluck *et al.*, 1991).

Pervasive flattening of the orogenic middle crust has been recognised in various tectonic settings. In the Himalayas, the development of a horizontal channel has been proposed to explain exhumation of deep-seated rocks (Beaumont *et al.*, 2004; Jamieson *et al.*, 2004). A variant of this channel flow model has also been used to account for horizontal spreading of lithologies previously exhumed in a vertical fabric (Schulmann *et al.*, 2008; Štípská *et al.*, 2008). Horizontal foliations can also be found in the apical part of a dome structure (Dixon, 1975; Burg *et al.*, 2004). It is further illustrated by analogue experiments where vertical fabrics are progressively replaced by horizontal foliations at some critical level of a rising diapir (Kratinová *et al.*, 2006). Alternatively, subhorizontal overprinting of vertical fabrics during ductile thinning is considered as a major exhumation process in accretionary wedge systems (Ring & Brandon, 1999).

Considering that no kinematic indicators are observed in the S2 foliation, the hypothesis of a significant lateral transport in a channel flow appears unlikely. Only the fan-like structure of the root can point to limited lateral spreading of the extruded material (Fig. 95b). Conversely, the observed transposition of vertical fabrics at a localised crustal level is better in agreement with the mechanical behaviour of a diapiric body. Consequently, the S2 foliation is interpreted as a result of a localised flattening due to continuous accumulation of allochthonous felsic material at the base of the crust (Fig. 103g). Moderate exhumation could have been accommodated by ductile thinning, but petrological data indicate that the flattening zone mostly remained at mid-crustal depth.

The localised flattening zone separates two crustal domains with different structural records. In the underlying part of the crust, the Central Vosges metamorphic units and the associated Mg-K granitoid intrusions mostly preserve the subvertical N–S striking S1 fabric (Fig. 97). By contrast, the overlying Lower Carboniferous sediments of the Southern Vosges were affected by NW–SE upright folds during basin inversion (Fig. 100) and syntectonic

migmatism at *ca.* 340 Ma (Schaltegger *et al.*, 1996). Therefore, the structural contrast indicates that at that moment, a major boundary zone developed in the orogenic middle crust (Fig. 103g).

N-S Gondwana indentation (D3)

At *ca.* 340 Ma, the Vosges basement experienced a tectonic switch from E–W (D2) to N–S (D3) oriented compression (Fig. 104). The change in stress reorientation is probably best reflected by the structural record in Mg-K granitoids. These bodies which were emplaced between 340 and 335 Ma (Schaltegger *et al.*, 1996; Schulmann *et al.*, 2002) systematically preserve two orthogonal fabric sets (Figs 97 & 100) and show some prolate AMS ellipsoids that could reflect fabric superposition (e.g. Schulmann & Ježek, 2011). Bulk N–S compression is indicated by E–W to NE–SW subvertical cleavage planes developed in the Northern Vosges and by NW–SE trending upright folds in the Southern Vosges sedimentary units (Figs 93 & 100). In addition, E–W upright folding of the previously subhorizontal S2 foliation is observed in the eastern part of the metamorphic units and kink bands indicate that this deformation probably occurred at relatively low-grade conditions (Fig. 95).

N–S compression is only visible in upper crustal lithologies, whereas deeper parts of the orogen still preserve the original E–W compressional fabrics. It is therefore proposed that the upper crust experienced N–S thin-skinned tectonics while the orogenic lower crust behaved as a rigid basement and was underthrust towards the S or SE without experiencing significant shortening. It was achieved thanks to the presence of a major decoupling horizon which is represented by the intra-orogenic boundary zone. The mechanical weakness of the mid-crustal boundary zone was most likely facilitated by the presence of Mg-K magmas which were chiefly invading the sub-horizontal mechanical anisotropy (Fig. 103h).

It is assumed that the tectonic switch resulted from a change in far-field forces. However, it can equally be explained by rigid block rotation. Indeed, paleomagnetic data document a ~80° anticlockwise rotation of the Vosges basement during the Lower Carboniferous (Edel *et al.*, 2011). Notwithstanding, on the basis of structural data alone, the indentation of the upper crust is characterised by N–S compression in present-day coordinates. In addition, deformation-age relationships reveal that the N–S compression is progressively younger towards the N (Fig. 104). The data are in good agreement with the idea of a northward indentation of Gondwana (Fig. 102d) which has already been invoked to explain N–S Carboniferous compression in the southern part of the Variscan Belt of Europe (Vollbrecht *et al.*, 1989). It additionally accounts for the general S-verging structures observed in the southern part of the Variscan orogen, and especially in the Southern Vosges Mountains (Wickert & Eisbacher, 1988; Eisbacher *et al.*, 1989).

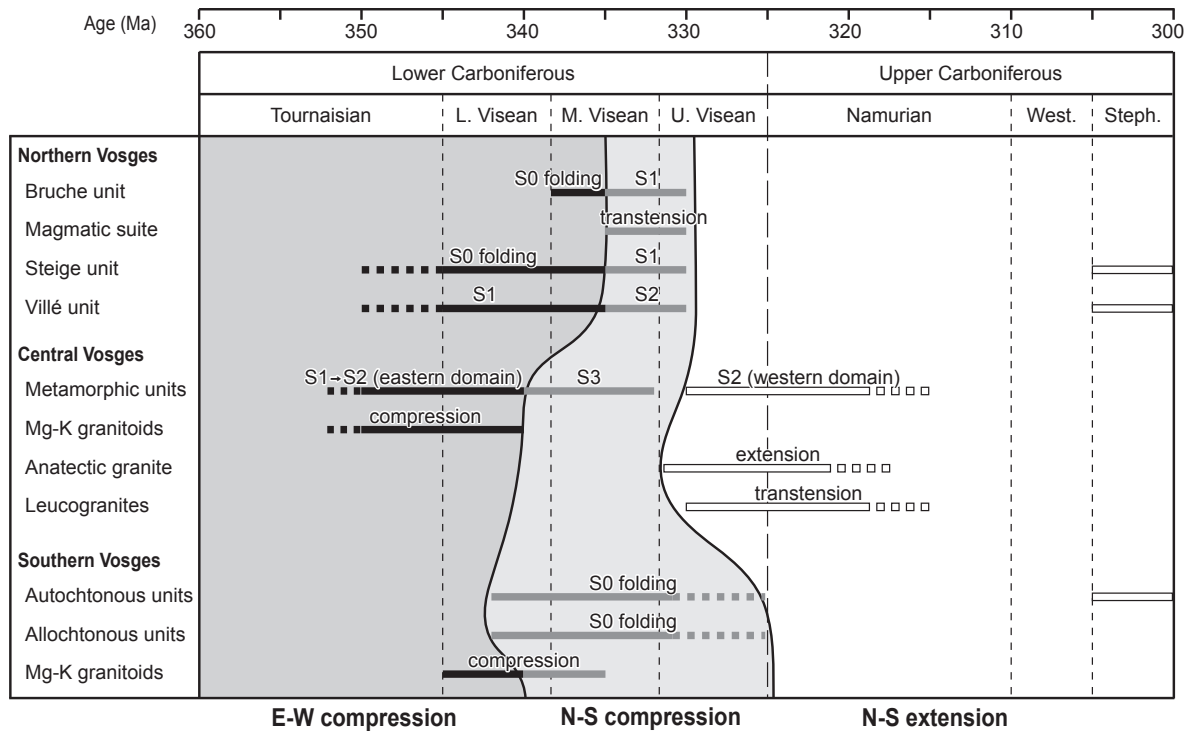


Figure 104. Table summarizing the orientation and timing of the successive deformation events developed across the Vosges.

Late Lower Carboniferous: orogenic collapse

The N–S compressional regime is followed by global N–S extension at *ca.* 330–320 Ma (Fig. 104), which is revealed by normal faulting in the uppermost crust, but is mostly visible in the Central Vosges basement. There, extension is reflected by detachment systems with contrasted thermal regimes which point to the contribution of competing parameters during orogenic collapse.

Kinematics and thermal conditions of extensional tectonics (D4)

To the West of the Sainte-Marie-aux-Mines Fault Zone, the subvertical S1 foliation is transposed into a subhorizontal fabric (S2) in the southern part of the metamorphic units (Fig. 97a). The structures related to the later N–S compression are not developed because this part of the root probably remained below the intra-orogenic boundary zone. A subhorizontal foliation is also dominant in the adjacent western anatectic domain where it is associated with kinematic indicators compatible with W- to SW-directed extension (Rey *et al.*, 1992). From N to S, the shallow-dipping fabric is represented by a magmatic foliation in the anatectic granite emplaced at *ca.* 330 Ma (Schaltegger *et al.*, 1999) and by greenschist-facies S–C structures at the base of the overlying migmatitic unit (Blumenfeld & Bouchez, 1988; Rey *et al.*, 1991). It suggests that shearing developed while migmatites were already at a relatively shallow crustal level. It is in agreement with $^{40}\text{Ar}/^{39}\text{Ar}$ cooling ages on micas showing that high-grade rocks

reached the upper crust after *ca.* 335 Ma (Boutin *et al.*, 1995). Therefore, the structural record in the western anatectic domain is interpreted as a late Lower Carboniferous low- to high-temperature extensional reactivation of the subhorizontal S2 foliation. The reactivation was associated with a major W- to SW-directed detachment (D4) parallel to the D2 intra-orogenic boundary zone.

The eastern anatectic domain is dominantly composed of isotropic granite and relictual migmatite bodies where an E–W subvertical foliation is commonly preserved. However, Schulmann *et al.* (2009a) showed that the older fabric in migmatite is progressively overprinted towards the margin and becomes parallel to the structure of the surrounding granite (Fig. 97a). The anatectic granite is characterised by a subhorizontal foliation and a consistently oriented lineation which suggests homogeneous S- to SE-directed magmatic flow (Kratinová *et al.*, 2011). In the same time, leucogranites were emplaced in the metamorphic units under a transtensional regime (Kratinová *et al.*, 2007) and their intrusion was probably controlled by the opening of the E–W subvertical anisotropy which was acquired during D3. All these structural features related to late Lower Carboniferous magma emplacement indicate bulk N–S extension and southward flow across the eastern anatectic domain. It is interpreted as a high temperature S- to SE-directed detachment which reactivated the mid-crustal boundary zone (Fig. 103i).

In the Vosges, the Lalaye-Lubine Fault Zone separates Early Palaeozoic metasediments to the North from partly migmatitic gneissic rocks to the South (Fig. 89). The apparent metamorphic gap between these rocks has been an argument to trace a suture zone along the fault (e.g. Fluck *et al.*, 1991). However, petrological data together with kyanite occurrence in lateral equivalents of the Black Forest (Wickert *et al.*, 1990) only reveals a minor P – T difference between the metasediments and the neighbouring monotonous gneiss unit. In addition, the normal metamorphic gradient increasing towards the South has been used to propose that the Steige and Villé units correspond to the supracrustal continuity of the autochthonous crust. A similar setting is observed at the margin of the Orlica-Śnieżnik Dome in the West Sudetes. In this region, greenschist- to amphibolite-facies rocks have been juxtaposed with migmatitic orthogneiss as a result of a late-orogenic transtension (Mazur *et al.*, 2005). In the case of the Vosges, the lack of detachment structures along the Lalaye-Lubine Fault Zone is ascribed to a later pervasive strike-slip reactivation (e.g. Bouyalaoui, 1992). Nevertheless, considering the inferred structure of the root, this area is also thought to represent a former low temperature N-directed detachment system which developed along an originally subhorizontal discontinuity, i.e. most likely the prominent intra-orogenic boundary zone (Fig. 103i).

Origin of orogenic collapse

In the Variscan Vosges, the late Lower Carboniferous tectonic evolution was dominated by detachment systems. They mostly developed in the upper to middle crust, but left the orogenic lower crust unaffected due to major decoupling along the mid-crustal boundary zone. Therefore, lower crustal flow can not be a driving mechanism of orogenic collapse as proposed in the model of orogenic core complexes (e.g. Vanderhaeghe *et al.*, 1999). Alternatively, it is proposed that late orogenic extension is the result of an interplay between three major factors, namely gravitational forces, thermal structure of the crust and far-field forces.

The detachment systems which have been identified across the Vosges basement show different directions of transport. Early Palaeozoic metasediments of the Villé and Steige units are thought to be located above a N-directed detachment, whereas the western and eastern anatectic domains to the South show SW and SE directions of normal shearing, respectively (Fig. 97a). Thus, linear elements are arranged in a nearly radial pattern and diverge away from a core zone which corresponds to the Central Vosges metamorphic units. In addition, the subhorizontal foliation along which detachments occurred defines a quasi-concentric pattern around the metamorphic units (Fig. 97a). These features are similar to the typical geometry observed around gneiss domes or metamorphic core complexes (e.g. Coney, 1980; Kruckenberg *et al.*, 2011). Because extensional processes occurring at the top of these structures are commonly ascribed, at least partly, to gravity redistribution (e.g. Rey *et al.*, 2001), a similar view is adopted to explain the orogenic collapse in the Vosges.

Yet, gravitational forces can not be the only parameter responsible for late-orogenic extension. The different thermal conditions of the detachment systems argue for a role of the specific thermal regime at mid-crustal level. The eastern anatectic domain exhibits a high temperature detachment zone which is interpreted as a result of intense melting of the intra-orogenic boundary during N–S extension. Nevertheless, low-grade D3 deformation in the eastern part of the root demonstrates that the intra-orogenic boundary zone was at relatively low thermal conditions prior to extensional reactivation. During the subsequent detachment, the zone of anatexis developed above the deep crustal rocks which show no signs of melting and older $^{40}\text{Ar}/^{39}\text{Ar}$ cooling ages than in the anatectic domain (Boutin *et al.*, 1995). It may suggest that the heat source was not located deep in the crust but at mid-crustal level. Large sill-like bodies of Mg-K granitoids have been emplaced in the mid-crustal boundary zone at *ca.* 340 Ma (Schaltegger *et al.*, 1996). Because they are known to be highly radiogenic (Rothé, 1960; 1961; 1962), the associated heat production may lead to a significant temperature increase in the time scale of ~10 Ma. Conversely, the Mg-K granitoids intruding the sedimentary units of

the Southern Vosges are not surrounded by a molten zone (Fig. 100). Since radiogenic heat production is strongly dependent on the volume of radioactive rocks and their position in the vertical column (e.g. McLaren *et al.*, 1999), these shallow Mg-K granitoids are not expected to generate a significantly high perturbation of the geotherm. Such a contrast emphasises the influence of radioactive heat production on the late-orogenic tectonic evolution. Accordingly, detachment in the eastern anatectic domain is thought to be not only gravity-induced, but also thermally-induced.

So far, only parameters acting in the internal part of the orogen have been considered. Nevertheless, N–S extension can also be correlated with the larger-scale Variscan evolution. Arc-type magmatism at 330 Ma in the Northern Vosges is thought to reflect the climax of Rhenohercynian subduction (Edel & Schulman, 2009). S-directed subduction is therefore likely to drive extension in the back-arc region, i.e. precisely in the Central Vosges basement (Fig. 103i). Consequently, although different directions of post-thickening extension have been documented in the Variscan Belt of Europe (Burg *et al.*, 1990; Burg *et al.*, 1994), the case of the Vosges illustrates that the orientation of extension is chiefly controlled by far-field forces. Any other feature of the observed orogenic collapse is gravity- and/or thermally-driven.

Table 19. List of radiometric ages used for Fig. 92.

Locality/Unit	Lithology	Age	Method	Mineral	Reference
<i>Northern Vosges magmatism</i>					
Neuntelstein	diorite	331 ± 11	K–Ar	Am	Edel et al., 1986
Neuntelstein	diorite	326 ± 5	K–Ar	Am	Altherr et al., 2000
Neuntelstein	diorite	331 ± 3	Ar–Ar	Am	Altherr et al., 2000
Neuntelstein	Am-bearing enclave	327 ± 10	K–Ar	Am	Edel et al., 1986
Muckenbach	diorite	326 ± 11	K–Ar	Bt + Am	Edel et al., 1986
Muckenbach	diorite	284 ± 18	K–Ar	Am, altered	Edel et al., 1986
Muckenbach	diorite	282 ± 23	K–Ar	Am	Edel et al., 1986
Hohwald	granodiorite	336 ± 11	K–Ar	Bt, chloritized	Edel et al., 1986
Hohwald	granodiorite	297 ± 10	K–Ar	Bt, chloritized	Edel et al., 1986
Hohwald	granodiorite	284 ± 9	K–Ar	Pl	Edel et al., 1986
Hohwald	granodiorite	331 ± 12	Ar–Ar	Am	Boutin et al., 1995
Hohwald	granodiorite	346 ± 4	U–Pb	Zrc	Edel et al., 2011
Hohwald	granodiorite	326 ± 2	U–Pb	Zrc	Edel et al., 2011
Champ du Feu	granite	318 ± 3	U–Pb	Zrc	Cocherie, 2007
Champ du Feu	granite	363 ± 11	U–Th–Pb	Mnz	Edel et al., 2011
Champ du Feu	granite	328 ± 6	K–Ar	Am	Altherr et al., 2000
Champ du Feu	granite	330 ± 3	Ar–Ar	Am	Altherr et al., 2000
Serva granite	enclave	327 ± 10	K–Ar	Am	Boutin et al., 1995
Waldersbach	granite	335 ± 4	K–Ar	Bt	Altherr et al., 2000
Waldersbach	enclave	329 ± 4	K–Ar	Am + Bt	Altherr et al., 2000
Waldersbach	enclave	329 ± 4	Ar–Ar	Am + Bt	Altherr et al., 2000
Natzwiller	granite	336 ± 1	Ar–Ar	Bt	Boutin et al., 1995
Natzwiller	granite	338 ± 2	Ar–Ar	Bt	Montigny & Thuizat, 1989
Natzwiller	granite	330 ± 4	K–Ar	Bt, chloritized	Altherr et al., 2000
Natzwiller	granite	312 ± 2	U–Pb	Zrc	Cocherie, 2007
Andlau	granite	328 ± 4	K–Ar	Bt, chloritized	Altherr et al., 2000
Senones	granite	325 ± 4	K–Ar	Am	Altherr et al., 2000
Senones	granite	328 ± 4	Ar–Ar	Am	Altherr et al., 2000
Windstein	granodiorite	334 ± 1	Ar–Ar	Bt	Boutin et al., 1995
Windstein	granodiorite	334 ± 2	U–Pb	Zrc	Reischmann & Anthes, 1996
Weiler	ignimbrite	325 ± 4	Rb–Sr	whole-rock	Reischmann & Anthes, 1996
Weiler	ignimbrite	327 ± 21	Sm–Nd	whole-rock	Reischmann & Anthes, 1996
Kagenfels	granite	284 ± 9	K–Ar	Bt	Edel et al., 1986
Kagenfels	granite	286 ± 10	K–Ar	Bt	Montigny & Thuizat, 1989
Kagenfels	granite	329 ± 2	Ar–Ar	Bt	Boutin et al., 1995
Kagenfels	granite	331 ± 5	K–Ar, Ar–Ar	Bt	Hess et al., 1995
Kagenfels	granite	330 ± 6	U–Pb	Zrc	Hess et al., 1995
Kagenfels	lamprophyre	329 ± 5	K–Ar, Ar–Ar	Bt	Hess et al., 1995
Saint-Nabor	ignimbrite	334 ± 4	U–Pb	Zrc	Edel et al., 2011
Nideck	rhyolite	297 ± 9	K–Ar	Bt	Boutin et al., 1995
Nideck	rhyolite	299 ± 9	K–Ar	Bt	Boutin et al., 1995
Nideck	rhyolite	293 ± 8	K–Ar	Bt, chloritized	Boutin et al., 1995
Nideck	rhyolite	299 ± 7	K–Ar	Bt	Lippolt & Hess, 1983
Nideck	rhyolite	294 ± 5	Ar–Ar	Bt	Lippolt & Hess, 1983
<i>Central Vosges magmatism</i>					
Trois-Epis	migmatite	328 ± 10	K–Ar	Bt	Boutin et al., 1995
Trois-Epis	granitoid gneiss	328 ± 4	U–Pb	Zrc	Schaltegger et al., 1999
Kaysersberg	migmatite	333 ± 10	K–Ar	Bt	Boutin et al., 1995
Kaysersberg	migmatitic granite	326 ± 5	U–Pb	Zrc	Schaltegger et al., 1999
Bramont	granite	336 ± 11	K–Ar	Bt	Boutin et al., 1995
Bramont	granite	342 ± 11	K–Ar	Bt	Boutin et al., 1995
Vic	granite	331 ± 5	Ar–Ar	Bt	Boutin et al., 1995
Tholy	granite	334 ± 11	K–Ar	Bt	Boutin et al., 1995
Tholy	granite	334 ± 4	Ar–Ar	Bt, chloritized	Boutin et al., 1995
Thanekirch	granite	326 ± 1	U–Pb	Zrc	Kratinová et al., 2007
Châtenois	granite	335 ± 10	K–Ar	Bt	Boutin et al., 1995
Châtenois	granite	330 ± 10	K–Ar	Bt	Boutin et al., 1995
Bilstein	granite	334 ± 2	Ar–Ar	Ms	Boutin et al., 1995

Table 19. *continued*

Central Vosges magmatism (continued)

Brézouard	granite	332 ± 8	Ar–Ar	Ms	Boutin et al., 1995
Brézouard	granite	329 ± 2	U–Pb	Zrc	Schulmann et al., 2002
Dambach	granite	323 ± 10	K–Ar	Ms	Boutin et al., 1995
Crêtes	durbachite	332 ± 3	U–Pb	Zrc	Schulmann et al., 2002
Crêtes	granite	333 ± 1	Ar–Ar	Bt	Boutin et al., 1995
Crêtes	microgranite	339 ± 2	U–Pb	Zrc	Schaltegger et al., 1996
Crêtes	granite	338 ± 2	U–Pb	Ttn	Schaltegger et al., 1996

Southern Vosges magmatism

Ballons Nord	diorite	356 ± 2	Ar–Ar	Am	Boutin et al., 1995
Sewen	monzonite	337 ± 19	K–Ar	Am + Chl	Boutin et al., 1995
Ballons	monzogranite	335 ± 13	K–Ar	Am	Boutin et al., 1995
Ballons	monzogranite	339 ± 2	U–Pb	Ttn	Schaltegger et al., 1996
Corravillers	granite	331 ± 5	Ar–Ar	Bt	Boutin et al., 1995
Molkenrain	rhyolite	337 ± 11	K–Ar	Am	Boutin et al., 1995
Molkenrain	rhyolite	335 ± 3	Ar–Ar	Am	Boutin et al., 1995
Molkenrain	rhyolite	340 ± 2	U–Pb	Zrc	Schaltegger et al., 1996

Central Vosges metamorphism

Monotonous unit	gneiss	330 ± 14	Ar–Ar	Bt	Boutin et al., 1995
Varied unit	leptynite	335 ± 4	U–Pb	Zrc	Schaltegger et al., 1999
Varied unit	leptynite	327 ± 8	U–Pb	Zrc	Schaltegger et al., 1999
Varied unit	kinzigite	335 ± 4	U–Pb	Zrc	Schaltegger et al., 1999
Varied unit	leucosome	337 ± 3	U–Pb	Zrc	Schaltegger et al., 1999
Varied unit	Bt–Sil gneiss	326 ± 11	U–Pb	Zrc	Schaltegger et al., 1999
Varied unit	Bt–Sil gneiss	335 ± 1	U–Pb	Zrc, Mnz	Schaltegger et al., 1999
Varied unit	kinzigite	327 ± 12	Ar–Ar	Bt	Boutin et al., 1995
Varied unit	amphibolite	339 ± 20	Ar–Ar	Am	Boutin et al., 1995
Varied unit	amphibolite	340 ± 4	Ar–Ar	Chl	Boutin et al., 1995
Varied unit	gneiss	339 ± 4	U–Pb	Zrc	Chapter II
Varied unit	gneiss	342 ± 11	U–Pb	Zrc	Chapter II
Granulite unit	felsic granulite	342 ± 4	U–Pb	Zrc	Chapter II
Granulite unit	felsic granulite	343 ± 2	U–Pb	Zrc	Chapter II
Granulite unit	felsic granulite	346 ± 4	U–Pb	Zrc	Chapter II

SUMMARY AND CONCLUSIONS TO PART TWO

Summary

Structural analysis across the entire Vosges basement reveals that a succession of four major deformation phases is variably recorded in the different crustal levels. The earliest D1 event corresponds to E–W compression. It generates subvertical N–S striking structures in upper crustal sediments of the Northern Vosges as well as in the Central Vosges metamorphic root. It is followed by a vertical compression D2 which produces subhorizontal fabrics only in the metamorphic units and in the syntectonic Mg-K granitoids. Accordingly, the subhorizontal fabrics are interpreted as a localised flattening zone which is developed at mid-crustal depth. The subsequent N–S compression D3 affects only the lithologies located above the subhorizontal flattening zone, i.e. in the orogenic upper crust. It creates an E–W striking cleavage in sedimentary units of the Northern and Southern Vosges, and in some gneissic rocks. The later D4 deformation corresponds to N–S extension during reactivation of the D2-related shallow-dipping fabrics. It is characterised by the activity of N- or S-directed detachment systems operating under contrasted thermal conditions. Crystallisation-deformation relationships in metamorphic rocks suggest that peak P – T conditions in the orogenic crust were probably achieved in a subhorizontal fabric before D1 deformation. During this pre-D1 event, upper crustal sediments underwent low- to medium-grade Barrovian-type metamorphism while deeper parts of the root reached upper amphibolite- or HP granulite-facies conditions up to 12–15 kbar and 800–900 °C. The subsequent D1 deformation is associated with retrogression of the high-grade varied and felsic granulite units, whereas the adjacent medium-grade monotonous unit probably undergoes contemporaneous prograde metamorphism. In the metamorphic root, the D2 deformation is related to a LP-HT overprint, and further retrograde metamorphism leads to greenschist-facies conditions during the activity of D3. Finally, the D4 detachment systems develop at low- to high-grade conditions and are mostly associated with the intrusion of large anatectic granite bodies. New geochronological data indicate Ordovician–Silurian protolith ages for the Central Vosges metamorphic units. In addition, it is believed that the age of HP metamorphism is not constrained by U–Pb zircon dating, but could lie at 360–350 Ma. Alternatively, the ages of 340–330 Ma obtained for the high-grade units are interpreted as the end of the HT metamorphic overprint.

Zircon petrogenesis

The present work discusses the petrological and geological significance of U–Pb zircon ages in high-grade rocks. The internal structure and chemistry of zircon together with modelling of zircon dissolution and growth are used to propose that:

- New zircon grains or zircon overgrowths in HP granulite-facies rocks do not reflect a HP metamorphic reaction, but more likely originate from crystallisation of an anatectic melt during cooling.
- Consequently, U–Pb zircon ages in high-grade rocks probably do not constrain the age of high-pressure metamorphism.
- Alternatively, zircon is thought to date the end of high temperature metamorphism.
- The lack of Variscan ages in the medium-grade monotonous unit suggests that a significant amount of partial melting is required to produce new zircon grains or relatively large overgrowths by a dissolution/recrystallisation process.

Regional and Variscan geology

The lithostratigraphic records and the synthesis of geochronological and petrological data are combined to propose a scenario for the evolution of the Vosges basement in the Variscan framework. The main features of the Palaeozoic history are:

- Ordovician to Silurian deposition of the protoliths of the monotonous and varied units in different parts of the Saxothuringian basin, probably on conjugate margins.
- Late Devonian E-directed subduction of the Saxothuringian basin and building of the orogenic root with allochthonous HP granulite-facies units (varied and felsic granulite) and autochthonous low- to medium-grade units (monotonous, Villé and Steige). In this view, the autochthonous units are considered as the cover of a Moldanubian basement block.
- Late Devonian back-arc opening in the Southern Vosges due to the N-directed closure of the southern Palaeotethys Ocean.

- Early Lower Carboniferous collision and syntectonic Mg-K magmatism in the Central Vosges. At *ca.* 340 Ma, a tectonic switch from E–W to N–S compression is evidenced.
- Late Lower Carboniferous extension triggered by the S-directed closure of the northern Rhenohercynian basin. This subduction event is reflected by arc-type magmatism in the Northern Vosges. At this time, the Lalaye-Lubine Fault Zone is thought to accommodate N-directed detachment of the upper crustal Steige-Villé units.

Intracontinental tectonic processes

The orientation, timing and P – T conditions of the different deformation phases are discussed in terms of tectonic processes operating in the orogenic crust during Lower Carboniferous collision. The following mechanisms are considered to be of importance:

- Vertical extrusion of the allochthonous lower crust and possible limited vertical exchange with the overlying middle crust (D1). At this time, the orogenic crust is characterised by complete mechanical coupling between the different levels.
- Development of a subhorizontal intra-orogenic boundary zone at mid-crustal depth (D2). This localised flattening zone is thought to result from continuous accumulation of felsic material at the base of the crust.
- Mechanical decoupling between the upper and lower orogenic crust along the intra-orogenic boundary zone during subsequent compression (D3). As a result, compression is accommodated in the upper crust while the lower crust behaves as a rigid basement. This deformation event therefore resembles thin-skinned tectonics.
- Extensional reactivation of the subhorizontal intra-orogenic boundary zone (D4). Extension is chiefly ascribed to gravitational collapse, but is also controlled by thermal weakening of the middle crust and far-field forces.

CONCLUSIONS

CONCLUSIONS

Analyse microstructurale et chronologie des processus métamorphiques

La compréhension des systèmes orogéniques repose sur l'intégration de différents types de données. Cependant, certains enregistrements s'avèrent parfois difficiles d'accès alors que d'autres peuvent souffrir des interprétations divergentes. Il convient alors de développer des nouvelles techniques d'analyse et de nuancer certains concepts. Dans le but d'accéder à l'enregistrement microstructural préservé dans les porphyroblastes, une nouvelle technique a été proposée. A l'inverse des approches précédemment utilisées, elle permet une mesure *in situ* des structures planaires et linéaires contenues dans les grenats. Les résultats obtenus permettent ainsi de déterminer l'orientation des structures antérieures qui sont parfois entièrement effacées à l'échelle macroscopique, mais aussi de caractériser le régime de déformation opérant pendant et après la cristallisation des minéraux porphyroblastiques. En perspective, il est envisagé de tester cette technique sur d'autres inclusions fortement anisotropes ainsi que dans d'autres types de porphyroblastes.

Par ailleurs, plusieurs parties de ce travail ont été orientées vers la discussion des processus métamorphiques gouvernant la croissance des minéraux à potentiel géochronologique. Bien que sommaire, l'exploration des âges obtenus par datation sur monazites à la microsonde électronique est éloquent. Dans les monazites, un contraste temporel est clairement associé à un contraste chimique, particulièrement en yttrium. En conjonction avec des arguments texturaux, il est démontré que la monazite, dans le cas des micaschistes étudiés, possède bien le potentiel de contraindre différentes réactions métamorphiques et ainsi des épisodes distincts de l'évolution orogénique. La poursuite de cette étude nécessitera assurément des datations isotopiques afin d'évaluer la très probable contribution de plomb initial, mais aussi une investigation détaillée de la distribution de l'yttrium, notamment dans le grenat.

A l'inverse, les estimations obtenues par analyse isotopique U–Pb sur zircons sont considérées comme le reflet d'un unique événement : l'évanouissement des conditions de haute température. En effet, la structure interne et la chimie des zircons, couplées à une modélisation des processus de croissance et résorption suggèrent que, dans les lithologies de haut degré métamorphique étudiées, la formation de zircon reflète la cristallisation à partir d'un liquide anatectique à la fin du métamorphisme de haute température et non un épisode de haute pression. De plus, l'absence d'âges hercyniens dans la série des gneiss monotones indique que la génération de nouveaux grains ou surcroissances de zircons nécessite une

fusion partielle non négligeable, probablement associée à des conditions supérieures à celles du faciès amphibolite. La perturbation apparente de l'enregistrement géochronologique dans les zircons des granulites de haute pression propose de nouvelles pistes de travail. Il pourrait être intéressant d'estimer la durée de la perturbation du système isotopique U–Pb en combinant datations isotopiques et modélisation de l'estompage de la zonation oscillatoire des zircons. Le but avoué d'une telle étude serait d'accéder à l'âge du métamorphisme de haute pression, ou encore d'estimer le début du processus de subduction continentale.

Evolution tectonique du dôme d'Orlica-Śnieżnik (Sudètes)

Les données discutées dans ce travail de thèse permettent de préciser trois phases majeures de l'évolution orogénique du dôme d'Orlica-Śnieżnik. Le premier épisode tectono-métamorphique témoigne de la subduction continentale tardi-dévonienne d'une marge passive, probablement d'affinité saxothuringienne, vers le SE et sous une croûte amincie. De manière importante, ceci s'observe depuis l'échelle macroscopique jusqu'à l'échelle microscopique dans la mesure où les porphyroblastes de grenat enregistrent des microstructures compatibles avec cette direction de convergence. Cette phase est suivie d'un phénomène de plissement d'échelle crustale affectant l'ensemble de la croûte orogénique vers 340 Ma. Interprétée comme un flux de matériel continental dans un prisme, cette évolution se traduit par des échanges verticaux de matière dans la croûte. Ils résultent de l'ascension de dômes gneissiques renfermant en leur cœur des témoins de haut degré métamorphique et de l'enfouissement contemporain de la croûte moyenne dans des synclinaux périphériques. La sensibilité de la croûte moyenne aux variations de pression et température est telle qu'il est possible d'évaluer l'influence spatiale et temporelle de dômes extrudés sur les parties moins profondes de l'orogène. L'alimentation continue du prisme orogénique par du matériel continental conduit à la formation, à environ 330 Ma, d'une zone d'intense remaniement horizontal par un mécanisme d'amincissement ductile au niveau de la croûte moyenne. Ce processus, attestant d'une déformation majoritairement coaxiale, est responsable de l'exhumation de l'ensemble de la croûte orogénique, et notamment des niveaux crustaux moyens et inférieurs préalablement juxtaposés.

Evolution tectonique du massif vosgien (NE France)

L'histoire pré-collision des Vosges correspond à un dépôt, de l'Ordovicien au Silurien, des séries variées et monotones à différents endroits du bassin saxothuringien. La collision dévono-carbonifère est ensuite caractérisée par quatre épisodes tectono-métamorphiques distincts. A la fin du Dévonien, la subduction continentale vers l'Est d'une marge passive

saxothuringienne sous un socle probablement de type moldanubien conduit à un épaississement de la croûte, puis à une extrusion verticale des lithologies de haut degré métamorphique dans les Vosges centrales. Dans le même temps, la subduction vers le Nord de l'Océan Paléotéthys est considérée comme responsable de l'ouverture d'un étroit bassin d'arrière-arc au niveau des Vosges du Sud. Le second épisode est caractérisé par la formation, à 340 Ma, d'une discontinuité intra-orogénique majeure au niveau de la croûte moyenne et reflète l'accumulation continue de matériel felsique à la base de l'orogène. Cet événement est accompagné d'une intrusion massive de granitoïdes magnésio-potassiques (Mg-K) à divers étages crustaux pendant une réorientation générale du régime de contrainte. Ainsi, au début du Carbonifère inférieur, la compression initialement E-O laisse place à un raccourcissement N-S qui s'exprime par une tectonique de couverture dans la croûte supérieure. En effet, ce troisième épisode voit s'effectuer un découplage total de la déformation le long de la discontinuité intra-orogénique, laissant ainsi la croûte profonde indemne de toute empreinte tectonique. Un ultime épisode d'extension N-S se manifeste à la fin du Carbonifère inférieur par l'activité de détachements ductiles réutilisant la discontinuité intra-orogénique. Cette tectonique extensive est guidée par un effondrement gravitaire et un affaiblissement thermique de la croûte moyenne dû à la production de chaleur par désintégration radioactive dans les granitoïdes Mg-K très fertiles. Dans les Vosges du Nord, la présence d'un magmatisme de type d'arc contemporain de l'extension témoigne d'une subduction vers le Sud du bassin rhénohercynien situé au Nord. Il n'est donc pas exclu que celle-ci puisse également contrôler l'orientation des systèmes de détachement développés dans les Vosges centrales.

Eléments de comparaison

La tectonique intracontinentale du dôme d'Orlica-Śnieżnik et du massif vosgien présente plusieurs traits communs. Dans les deux cas, l'épaississement de la croûte orogénique résulte d'un épisode de subduction continentale. Ainsi, l'amalgamation de portions crustales autochtones et allochtones, identifiées sur la base de critères pétrologiques et géochronologiques, peut-elle être considérée comme un processus important dans la genèse de la croûte orogénique hercynienne. Le comportement de la croûte, assimilable à un flux de matériel dans un prisme, est ensuite caractérisé par le développement de structures verticales associées à l'exhumation des lithologies de haut degré métamorphique et l'enfouissement variable de la croûte moyenne sus-jacente. La mise en évidence de ces transferts verticaux de matière suggère le développement de plis d'échelle crustale qui affectent probablement la croûte orogénique dans les deux massifs étudiés. Dans les Sudètes et les Vosges, les structures verticales sont intensément transposées en une zone à structuration horizontale et au

caractère métamorphique rétrograde. Cet enregistrement commun témoigne de la formation d'une discontinuité intra-orogénique, dont le rôle dans l'évolution future de l'orogène est déterminant. Cependant, cette zone intra-orogénique montre deux caractéristiques nettement différentes. Dans le dôme d'Orlica-Śnieżnik, elle se développe en régime principalement coaxial, tandis que dans les Vosges, les détachements ductiles indiquent un forte non-coaxialité. Cette différence peut toutefois refléter l'observation de deux parties distinctes de la zone intra-orogénique. A ce titre, les Sudètes correspondraient à la partie apicale de la croûte orogénique exhumée dans une structure en dôme, alors que les Vosges exposeraient les flancs de la zone intra-orogénique.

Un orogène « hercynotype » ?

Le caractère des processus tectoniques précisés par ce travail n'est que peu singulier au vu de ceux reconnus dans les orogènes plus récents ou anciens. En effet, les témoins ophiolitiques étudiés dans les Vosges montrent de très fortes similarités avec les successions téthysiennes ou même atlantiques. Ceci suggère que les mécanismes d'extension paléozoïques ont pu générer des environnements comparables à ceux plus récents voire actuels. Par ailleurs, l'étude du métamorphisme polyphasé dans les deux massifs hercyniens révèle clairement la présence d'assemblages de haute pression, indiquant ainsi que de telles conditions sont fréquentes et non pas restreintes aux orogènes de type alpin. Finalement, la thermicité élevée de l'orogénèse hercynienne a souvent été utilisée comme un paramètre discriminant. Cependant, la présence à des niveaux crustaux moyens de larges zones de fusion partielle a également été mise en évidence dans les Andes ou l'Himalaya. De même, des processus d'exhumation ou d'effondrement de l'orogène similaires à ceux invoqués ont été reconnus dans les systèmes mésozoïques et cénozoïques. En conséquence, les mécanismes discutés dans cette thèse ne doivent pas être considérés comme restreints à la seule orogénèse hercynienne, mais sont ou seront reconnus dans les systèmes orogéniques d'âge différent, suggérant ainsi une invariabilité de la tectonique intracontinentale au cours du Phanérozoïque.

CONCLUDING REMARKS

Microstructural analysis and chronology of metamorphic processes

Understanding of orogenic systems relies on integrating different types of data. Nevertheless, some geological records may be hardly accessible while others are commonly the purpose of dualistic views. Consequently, one needs to develop new techniques and to address existing concepts. With the aim of unravelling the microstructural record in porphyroblasts, a new technique has been proposed in this work. In contrast to previous methods, the present approach allows to measure *in situ* the planar and linear structures entrapped in garnet porphyroblasts. The technique yields results which are critical for reconstructing the orientation of past structures that may be completely obliterated on the macroscopic scale, and additionally provides information on the deformational regime during and after porphyroblast growth. As a perspective, it is envisaged to test the method on other strongly anisotropic inclusions as well as in different types of porphyroblastic minerals.

Several sections of this work also deal with the metamorphic processes governing the growth of minerals which can potentially be used for geochronology. Although briefly discussed, the electron microprobe monazite ages appear to be significant. They reveal a marked age contrast which is strongly correlated with monazite chemistry, and especially with the yttrium concentration. Together with textural arguments, the results indicate that the investigated monazites have the potential to date different metamorphic reactions and thus distinct episodes of the orogenic evolution. Further work should involve an analysis of yttrium distribution in garnet, and isotopic U–Pb dating of monazite in order to explore the contribution of initial lead.

Conversely, estimates obtained using isotopic U–Pb zircon dating are considered to reflect a single event: vanishing high temperature conditions. Indeed, the chemistry and internal structure of zircons together with dissolution/growth modelling suggest that zircon ages in the analysed high-grade lithologies reflect crystallization from an anatectic melt at the end of high temperature metamorphism, and not a high-pressure event. Moreover, the apparent lack of Variscan ages in the monotonous gneiss unit indicates that the crystallization of new zircon grains or overgrowths requires a significant amount of partial melting, at conditions probably higher than the upper amphibolite facies. The observed disturbance of the geochronological record in zircons from high-pressure granulites fosters performing additional work. The duration of the disturbance of the U–Pb isotopic system could be assessed by combining

precise isotopic dating with modelling of blurring of oscillatory zoning in zircon. The goal of such a study would be to gain access to the age of high-pressure metamorphism or to the initiation of the subduction process.

Tectonic evolution of the Orlica-Śnieżnik Dome (Sudetes)

Data presented in this thesis allow to recognise three major tectono-metamorphic events during the orogenic evolution of the Orlica-Śnieżnik Dome. The first tectono-metamorphic episode is associated with the late Devonian continental subduction of a Saxothuringian-type passive margin towards the SE and below an attenuated crust. It can be observed at both the macroscopic and microscopic scales since porphyroblast records are compatible with a SE direction of convergence. It is followed by crustal-scale folding affecting the entire orogenic crust at *ca.* 340 Ma. The orogenic evolution is approximated to a flux of continental material in a wedge which leads to vertical exchanges of material in the crust. The exchange mechanism results from the nearly diapiric ascent of gneissic domes cored by high-grade rocks, and the coeval burial of the overlying middle crust in marginal synclines. Thanks to the high sensitivity of the middle crust to pressure and temperatures variations, the influence of the rising gneiss domes can be precisely determined in space and time. Continuous accumulation of continental material in the orogenic wedge triggered widespread flattening and ductile thinning in a narrow mid-crustal zone at *ca.* 330 Ma. This process operated under a dominantly coaxial regime and was responsible for the exhumation of the previously juxtaposed lower and mid-crustal portions.

Tectonic evolution of the Vosges Mountains (NE France)

The pre-collisional history of the Vosges basement corresponds to the Ordovician–Silurian deposition of the varied and monotonous sediments in different parts of the Saxothuringian basin. The subsequent Devonian–Carboniferous collision is characterised by four tectono-metamorphic events. During the late Devonian, E-directed continental subduction of a Saxothuringian passive margin sequence below a Moldanubian-type basement produced crustal thickening and later vertical extrusion of high-grade lithologies in the Central Vosges. At the same time, the N-directed subduction of the southern Palaeotethys Ocean is thought to generate the opening of a narrow back-arc basin in the Southern Vosges. The second deformation event is associated with the formation, at 340 Ma, of a major intra-orogenic boundary zone in the middle orogenic crust, most likely as a result of continuous underplating of felsic material at the base of the orogenic system. Deformation was coeval

with the widespread intrusion of magnesio-potassic granitoids (Mg-K) at different crustal levels during a switch in stress orientation. In the early Lower Carboniferous, the originally E–W compressive stress field was replaced by N–S compression associated with thin-skinned tectonics in the upper orogenic crust. During this third tectonic event, a major decoupling occurred along the intra-orogenic boundary zone and left the deep part of the orogen devoid of any tectonic overprint. A later N–S extension event is reflected by the development of detachment systems which reactivated the intra-orogenic boundary zone during the late Lower Carboniferous. Extensional tectonics is explained in terms of gravitational collapse and thermal weakening of the middle crust due to high radiogenic heat production by the Mg-K granitoids. In the Northern Vosges, contemporaneous arc-type magmatism testifies for the S-directed subduction of the Rhenohercynian basin located to the North. It is therefore possible that this process could have additionally controlled the orientation of the detachment systems which developed in the Central Vosges.

Comparisons

Intracontinental tectonic processes in the Orlica-Śnieżnik Dome and in the Vosges Mountains have several features in common. In both cases, crustal thickening arose from continental subduction of a former passive margin sequence. Welding of autochthonous and allochthonous crustal portions can be considered as an important process in the genesis of the Variscan orogenic crust. The behaviour of the crust, which is paralleled to a flux of material in a wedge, was later characterised by the development of vertical structures connected with exhumation of high-grade lithologies and variable burial of the overlying middle crust. The associated vertical transfers of material point to the contribution of a crustal-scale folding mechanism which probably affected the orogenic crust of both massifs. In the Sudetes as well as in the Vosges Mountains, vertical structures are pervasively overprinted by subhorizontal fabrics associated with retrograde metamorphic assemblages. The similar records indicate the formation of an intra-orogenic boundary zone, which had a major role in the tectonic evolution. However, the deformation style in the intra-orogenic boundary zone differs between the two investigated areas. In the Orlica-Śnieżnik Dome, subhorizontal fabrics developed in a dominantly coaxial regime, whereas in the Vosges detachment zones testify for a highly non-coaxial deformation. The contrast can be considered as resulting from the observation of distinct parts of the intra-orogenic boundary zone. Accordingly, the Sudetes would correspond to the apical part of the orogenic crust which was exhumed in a domal structure, while the Vosges Mountains would exhibit the lateral termination of the boundary zone.

“Hercynotype” orogen ?

The tectonic processes recognised in this work are not markedly different from those reported in older or younger orogenic systems. Indeed, ophiolitic remnants located in the Vosges Mountains bear similarities to Tethysian or Atlantic-type successions. It means that extensional processes during the Palaeozoic produced similar settings to those generated much later. In addition, the study of polyphase metamorphism in both Variscan massifs has revealed that high-grade metamorphism is a common process and is probably not restricted to Alpine-type orogens. Finally, the high thermal regime of the Variscan Belt of Europe has classically been invoked as a characteristic feature of this orogen. Nevertheless, wide zones of partial melting occurring at mid-crustal depth have also been evidenced in the Andes or in the Himalayas. Similarly, hot exhumation mechanisms or orogen collapse have been recognised in Mesozoic and Cenozoic orogens. Therefore, the processes discussed in this work should not be seen as restricted to the Variscan orogeny, but are or could be documented in other orogens, suggesting that the character of intracontinental tectonics has not significantly changed throughout the entire Phanerozoic.

BIBLIOGRAPHIE

BIBLIOGRAPHIE

- Aerden, D. G. A. M., 1995. Porphyroblast non-rotation during crustal extension in the Variscan Lys-Caillaouas Massif, Pyrenees. *Journal of Structural Geology*, **17**(5), 709-725.
- Aerden, D. G. A. M., 2003. Preferred orientation of planar microstructures determined via statistical best-fit of measured intersection-lines: the 'FitPitch' computer program. *Journal of Structural Geology*, **25**, 923-934.
- Aerden, D. G. A. M., 2004. Correlating deformation in Variscan NW-Iberia using porphyroblasts; implications for the Ibero-Armorican Arc. *Journal of Structural Geology*, **26**, 177-196.
- Aghai Soltani, L., Bender, P., Braun, A. & Schmidt-Effing, R., 1996. Oberdevonische Radiolarien aus Kieselgesteinen des Breuschtales (Vallée de la Bruche, Nord-Vogesen, Frankreich). *Jahresbericht und Mitteilungen des oberrheinischen geologischen Vereins*, **78**, 183-208.
- Aleksandrowski, P., Kryza, R., Mazur, S. & Żaba, J., 1997. Kinematic data on major Variscan strike-slip faults and shear zones in the Polish Sudetes, northeast Bohemian Massif. *Geological Magazine*, **134**(5), 727-739.
- Allemand, P. & Lardeaux, J. M., 1997. Strain partitioning and metamorphism in a deformable orogenic wedge: Application to the Alpine belt. *Tectonophysics*, **280**(1-2), 157-169.
- Altherr, R. & Kalt, A., 1996. Metamorphic evolution of ultrahigh-pressure garnet peridotites from the Variscan Vosges Mts. (France). *Chemical Geology*, **134**, 27-47.
- Altherr, R., Holl, A., Hegner, E., Langer, C. & Kreuzer, H., 2000. High-potassium, calc-alkaline I-type plutonism in the European Variscides: northern Vosges (France) and northern Schwarzwald (Germany). *Lithos*, **50**, 51-73.
- Anczkiewicz, R., Szczepański, J., Mazur, S., Storey, C., Crowley, Q., Villa, I. M., Thirlwall, M. F. & Jeffries, T. E., 2007. Lu–Hf geochronology and trace element distribution in garnet: Implications for uplift and exhumation of ultra-high pressure granulites in the Sudetes, SW Poland. *Lithos*, **95**, 363-380.
- André, F. & Bébien, J., 1983. Minéralogie et pétrologie des cumulats gabbro-dioritiques situés en bordure septentrionale du massif des Ballons (Vosges méridionales, France) : cristallisation d'un magma basique en domaine "orogénique" intracontinental. *Bulletin de Minéralogie*, **106**, 341-351.
- Ansilewski, J., 1966. Petrografia metamorfiku Gór Bialskich. *Geologia Sudetica*, **2**, 121-259.
- Arevalo, R. J. & McDonough, W. F., 2010. Chemical variations and regional diversity observed in MORB. *Chemical Geology*, **271**, 70-85.
- Argand, E., 1916. Sur l'arc des Alpes Occidentales. *Eclogae Geologicae Helveticae*, **14**, 145-192.
- Asselberghs, E., 1926. Sur l'existence du Famennien (Néodévonien) à Chagey (Belfort). *Bulletin de la Société Géologique de France*, **26**(4), 67-74.
- Auzende, J.-M., Boespflug, X., Bougault, H., Dosso, L., Foucher, J.-P., Joron, J.-L., Ruellan, E. & Sibuet, J.-C., 1990. From intracratonic extension to mature spreading in back arc basins: examples from the Okinawa, Lau and Noth Fiji basins. *Oceanologica Acta*, **10**, 153-163.
- Azor, A., Rubatto, D., Simancas, J. F., González Lodeiro, F., Martínez Poyatos, D., Martín Parra, L. M. & Matas, J., 2008. Rheic Ocean ophiolitic remnants in southern Iberia questioned by SHRIMP U-Pb zircon ages on the Beja-Acebuches amphibolites. *Tectonics*, TC5006.

- Bain, A., 1964. *Etude d'un microplancton (Acritarches) du Dévonien supérieur*. Mémoire de DEA, Université Louis Pasteur, Strasbourg, 35 p.
- Bakun-Czubarow, N., 1968. Geochemical characteristics of eclogites from the environs of Nowa Wieś in the region of Śnieżnik Kłodzki. *Archiwum Mineralogiczne*, **28**, 244-371.
- Bakun-Czubarow, N., 1991. On the possibility of occurrence of quartz pseudomorphs after coesite in the eclogite-granulite rock series of the Złote Mountains in the Sudetes (SW Poland). *Archiwum Mineralogiczne*, **47**(1), 5-16.
- Bakun-Czubarow, N., 1992. Quartz pseudomorphs after coesite and quartz exsolutions in eclogitic omphacites of the Złote Mountains in the Sudetes (SW Poland). *Archiwum Mineralogiczne*, **48**(1-2), 3-25.
- Bakun-Czubarow, N., 1998. Ilmenite-bearing eclogites of the West Sudetes – their geochemistry and mineral chemistry. *Archiwum Mineralogiczne*, **51**, 29-110.
- Ballèvre, M., Bosse, V., Ducassou, C. & Pitra, P., 2009. Palaeozoic history of the Armorican Massif: Models for the tectonic evolution of the suture zones. *Comptes Rendus Géoscience*, **341**, 174-201.
- Baranowski, Z., Haydukiewicz, A., Solecki, A. & Urbanek, Z., 1990. Outline of the geology of the Góry Kaczawskie (Sudetes, Poland). *Neues Jahrbuch für Geologie und Paläontologie, Abhandlungen*, **179**, 223-257.
- Baratoux, L., Schulmann, K., Ulrich, S. & Lexa, O., 2005. Contrasting microstructures and deformation mechanisms in metagabbro mylonites contemporaneously deformed under different temperatures (c. 650°C and c. 750°C). In: *Deformation Mechanisms, Rheology and Tectonics: from Minerals to Lithosphere* (eds Gapais, D., Brun, J. P. & Cobbold, P. R.), **243**, 97-125, Geological Society Special Publication, London.
- Batt, G. E. & Braun, J., 1997. On the thermomechanical evolution of compressional orogens. *Geophysical Journal International*, **128**(2), 364-382.
- Bea, F. & Montero, P., 1999. Behavior of accessory phases and redistribution of Zr, REE, Y, Th, and U during metamorphism and partial melting of metapelites in the lower crust: an example from the Kinzigite Formation of Ivrea-Verbanò NW Italy. *Geochimica et Cosmochimica Acta*, **63**, 1133-1153.
- Beard, B. L., Medaris, L. G., Johnson, C. M., Jelínek, E., Tonika, J. & Riciputi, L. R., 1995. Geochronology and geochemistry of eclogites from the Mariánské Lázně Complex, Czech Republic: Implications for Variscan orogenesis. *Geologische Rundschau*, **84**, 552-567.
- Beaumont, C., Jamieson, R. A., Nguyen, M. H. & Medvedev, S., 2004. Crustal channel flows: 1. Numerical models with applications to the tectonics of the Himalayan-Tibetan Orogen. *Journal of Geophysical Research*, **109**, B06406.
- Bederke, E., 1944. Ein Profil durch das Grundgebirge des Grafschaft Glatz. *Geologische Rundschau*, **34**(1), 6-9.
- Behr, H.-J., Engel, W., Franke, W., Giese, P. & Weber, K., 1984. The Variscan belt in Central Europe: main structures, geodynamic implications, open questions. *Tectonophysics*, **109**, 15-40.
- Bell, T. H., 1981. Foliation development - the contribution, geometry and significance of progressive, bulk, inhomogeneous shortening. *Tectonophysics*, **75**, 273-296.
- Bell, T. H. & Rubenach, M. J., 1983. Sequential porphyroblast growth and crenulation cleavage development during progressive deformation. *Tectonophysics*, **92**, 171-194.
- Bell, T. H. & Johnson, S. E., 1989. Porphyroblast inclusion trails; the key to orogenesis. *Journal of Metamorphic Geology*, **7**, 279-310.

- Bell, T. H., Johnson, S. E., Davis, B., Forde, A., Hayward, N. & Witkins, C., 1992. Porphyroblast inclusion-trail orientation data: eppure non son girate! *Journal of Metamorphic Geology*, **10**(3), 295-307.
- Bell, T. H., Forde, A. & Wang, J., 1995. A new indicator of movement direction during orogenesis - measurement technique and application to the Alps. *Terra Nova*, **7**(5), 500-508.
- Bell, T. H., Hickey, K. A. & Upton, G. J. G., 1998. Distinguishing and correlating multiple phases of metamorphism across a multiply deformed region using the axes of spiral, staircase and sigmoidal inclusion trails in garnet. *Journal of Metamorphic Geology*, **16**(6), 767-794.
- Bell, T. H. & Welch, P. W., 2002. Prolonged Acadian Orogenesis: revelations from foliation intersection axis (FIA) controlled monazite dating of foliations in porphyroblasts and matrix. *American Journal of Science*, **302**, 549-581.
- Beltrando, M., Rubatto, D. & Manatschal, G., 2010. From passive margins to orogens: The link between ocean-continent transition zones and (ultra)high-pressure metamorphism. *Geology*, **38**(6), 559-562.
- Benecke, E. W. & Verveke, L. v., 1890. Über das Rotliegende der Vogesen. *Mitteilungen der geologischen Landesanstalt von Elsass-Lothringen*, **3**, 45-103.
- Benecke, E. W. & Bücking, H., 1898. Calceola sandalina im oberen Breuschtal. *Mitteilungen der geologischen Landesanstalt von Elsass-Lothringen*, **4**, 105-111.
- Białek, D. & Werner, T., 2004. Petrogenesis, Age and Tectono-Metamorphic Evolution of the Acid Metavolcanites of the Stronie Formation (Orlica-Śnieżnik Dome, Sudetes, SW Poland). *Geolines*, **17**, 22-23.
- Bingen, B., Austrheim, H. & Whitehouse, M., 2001. Ilmenite as a source for zirconium during high-grade metamorphism ? Textural evidence from the Caledonides of western Norway and implications for zircon geochronology. *Journal of Petrology*, **42**(2), 355-375.
- Bingen, B., Austrheim, H., Whitehouse, M. J. & Davis, W. J., 2004. Trace element signature and U-Pb geochronology of eclogite-facies zircon, Bergen Arcs, Caledonides of W Norway. *Contributions to Mineralogy and Petrology*, **147**, 671-683.
- Black, L. P., Williams, I. S. & Compston, W., 1986. Four zircon ages from one rock: the history of a 3930 Ma-old granulite from Mount Sones, Enderby Land, Antarctica. *Contributions to Mineralogy and Petrology*, **94**, 427-437.
- Blanalt, J.-G. & Doubinger, J., 1973. Contenu paléontologique du gisement frasien de la carrière Wenger et Petit à Hersbach (vallée de la Bruche, Vosges). *Sciences Géologiques*, **26**(1), 75-90.
- Blanalt, J. G., 1969. *Contribution à l'étude du conglomérat givétien de Russ (Vallée de la Bruche, Vosges). Essai de paléogéographie*. Thèse de 3^{ème} cycle, Université Louis Pasteur, Strasbourg, 72 p.
- Blanalt, J. G. & Lillié, F., 1973. Données nouvelles sur la stratigraphie des terrains sédimentaires dévono-dinantiens de la vallée de la Bruche (Vosges septentrionales). *Sciences Géologiques*, **26**(1), 69-74.
- Blanchard, J.-P., 1978. Dynamique magmatique du Granite porphyroïde des Ballons (Vosges méridionales). «Fluidalités planaires imbriquées» et «couloirs magmatiques». Phénomènes de percolation. *Bulletin de la Société Géologique de France*, **20**(2), 157-162.
- Blumenfeld, P., 1986. *Déformation et fusion partielle dans la croûte continentale : migmatites et granites de l'unité occidentale des Vosges moyennes (France)*. Thèse, Université de Nancy, 173 p.
- Blumenfeld, P., Mainprice, D. & Bouchez, J. L., 1986. C-slip in quartz from subsolidus deformed granite. *Tectonophysics*, **127**, 97-115.

- Blumenfeld, P. & Bouchez, J.-L., 1988. Shear criteria in granite and migmatite deformed in the magmatic and solid states. *Journal of Structural Geology*, **10**(4), 361-372.
- Bohlen, S. R., 1987. Pressure-Temperature-Time Paths and a Tectonic Model for the Evolution of Granulites. *Journal of Geology*, **95**(5), 617-632.
- Bonhomme, M. & Dunoyer de Segonzac, G., 1962. Mesures d'âge par la méthode Rubidium-Strontium dans les schistes de Steige (Vosges septentrionales). *Bulletin du Service de la Carte Géologique d'Alsace-Lorraine*, **15**(4), 129-137.
- Bonhomme, M. & Prévôt, L., 1968. Application de la méthode Rubidium-Strontium à l'étude de l'âge radiométrique de quelques dépôts dévono-dinantiens du massif de la Bruche (Vosges du Nord). *Bulletin du Service de la Carte Géologique d'Alsace-Lorraine*, **21**(4), 219-248.
- Bonhomme, M. & Fluck, P., 1981. Nouvelles données isotopiques Rb-Sr obtenues sur les granulites des Vosges. Age protérozoïque terminal de la série volcanique calco-alkaline et âge acadien du métamorphisme régional. *Comptes Rendus de l'Académie des Sciences*, **293**, 771-774.
- Bons, P. D., Jessell, M. W. & Griera, A., 2009. Porphyroblast rotation versus nonrotation: Conflict resolution! : COMMENT. *Geology*, **37**, e182-e188.
- Borkowska, M., Hameurt, J. & Vidal, P., 1980. Origin and age of Izera gneisses and Rumburk granites in the Western Sudetes. *Acta Geologica Polonica*, **30**, 121-146.
- Bosse, V., Féraud, G., Ruffet, G., Ballèvre, M., Peucat, J.-J. & de Jong, K., 2000. Late Devonian subduction and early orogenic exhumation of eclogite-facies rocks from the Champtoceaux complex (Variscan belt, France). *Geological Journal*, **35**, 297-325.
- Bosse, V., Féraud, G., Ballèvre, M., Peucat, J.-J. & Corsini, M., 2005. Rb-Sr and $^{40}\text{Ar}/^{39}\text{Ar}$ ages in blueschists from the Île-de-Groix (Armorican Massif, France): Implications for closure mechanisms in isotopic systems. *Chemical Geology*, **220**, 21-45.
- Boutin, R., Montigny, R. & Thuizat, R., 1995. Chronologie K-Ar et $^{39}\text{Ar}/^{40}\text{Ar}$ du métamorphisme et du magmatisme des Vosges. Comparaison avec les massifs varisques avoisinants. *Géologie de la France*, **1**, 3-25.
- Bouyalaoui, J., 1992. *Schistes de Steige, Phyllades de Villé et mylonites du Climont (Vosges du Nord). Le développement de la zone cisailée de Lalaye-Lubine*. Thèse, Université de Brest, 210 p.
- Bowes, D. R. & Aftalion, M., 1991. U-Pb isotopic evidence for Early Ordovician and Late Proterozoic units in the Mariánské Lázně Complex, Central European Hercynides. *Neues Jahrbuch für Mineralogie, Abhandlungen*, **7**, 315-326.
- Bowring, S. A. & Williams, I. S., 1999. Priscoan (4.00-4.03 Ga) orthogneisses from northwestern Canada. *Contributions to Mineralogy and Petrology*, **134**, 3-16.
- Boynton, W. V., 1984. Cosmochemistry of the rare earth elements: meteorite studies. In: *Rare Earth Element Geochemistry* (ed Henderson, P.), 63-114, Elsevier, Amsterdam.
- Braun, A., Maass, R. & Schmidt-Effing, R., 1992. Oberdevonische Radiolarien aus dem Breuschtal (Nord-Vogesen, Elsaß) und ihr regionaler und stratigraphischer Zusammenhang. *Neues Jahrbuch für Geologie und Paläontologie, Abhandlungen*, **185**(2), 161-178.
- Bröcker, M. & Klemd, R., 1996. Ultrahigh-pressure metamorphism in the Śnieżnik Mountains (Sudetes, Poland): P-T constraints and geological implications. *Journal of Geology*, **104**(4), 417-433.
- Bröcker, M., Żelaźniewicz, A. & Enders, M., 1998. Rb-Sr and U-Pb geochronology of migmatitic gneisses from the Góry Sowie (West Sudetes, Poland): the importance of Mid-Late Devonian metamorphism. *Journal of the Geological Society, London*, **155**, 1025-1036.

- Bröcker, M., Klemd, R., Cosca, M., Brock, W., Larionov, A. N. & Rodionov, N., 2009. The timing of eclogite facies metamorphism and migmatization in the Orlica–Śnieżnik complex, Bohemian Massif: constraints from a multimethod geochronological study. *Journal of Metamorphic Geology*, **27**, 385-403.
- Bröcker, M., Klemd, R., Kooijman, E., Berndt, J. & Larionov, A., 2010. Zircon geochronology and trace element characteristics of eclogites and granulites from the Orlica–Śnieżnik complex, Bohemian Massif. *Geological Magazine*, **147**(3), 339-362.
- Brown, M. & Dallmeyer, R. D., 1996. Rapid Variscan exhumation and the role of magma in core complex formation; southern Brittany metamorphic belt, France. *Journal of Metamorphic Geology*, **14**(3), 361-379.
- Brueckner, H. K., Medaris, L. G. & Bakun-Czubarow, N., 1991. Nd and Sr age and isotope patterns from Variscan eclogites of the eastern Bohemian Massif. *Neues Jahrbuch für Mineralogie, Abhandlungen*, **163**, 169-196.
- Bücking, H., 1918. Beiträge zur Geologie des oberen Breuschtals in den Vogesen. *Mitteilungen der geologischen Landesanstalt von Elsass-Lothringen*, **12**(1).
- Burg, J.-P. & Matte, P., 1978. A cross-section through the French Massif Central and the scope of its Variscan geodynamic evolution. *Zeitschrift der Deutschen Geologischen Gesellschaft*, **129**, 429-460.
- Burg, J.-P., Davy, P., Nievergelt, P., Oberli, F., Seward, D., Diao, Z. & Meier, M., 1997. Exhumation during crustal folding in the Namche-Barwa syntaxis. *Terra Nova*, **9**, 53-56.
- Burg, J.-P., Kaus, B. J. P. & Podlachikov, Y. Y., 2004. Dome structures in collision orogens: Mechanical investigation of the gravity/compression interplay. In: *Gneiss domes in orogeny* (eds Whitney, D. L., Teyssier, C. & Siddoway, C. S.), **380**, 47-66, Geological Society of America Special Paper, Boulder, Colorado.
- Burg, J. P., Brun, J. P. & Van Den Driessche, J., 1990. Le Sillon Houiller du Massif Central français : Faille de transfert pendant l'amincissement crustal de la chaîne varisque ? *Comptes Rendus de l'Academie des Sciences*, **311**(série II), 147-152.
- Burg, J. P., Van Den Driessche, J. & Brun, J. P., 1994. Syn- to post-thickening extension in the Variscan Belt of Western Europe: Modes and structural consequences. *Géologie de la France*, **3**, 33-51.
- Butkiewicz, T., 1968. Crystalline schists in the Krowiarki Range of the Kłodzko Mts. *Geologia Sudetica*, **4**, 47-113.
- Caddick, M. & Thompson, A. B., 2008. Quantifying the tectono-metamorphic evolution of pelitic rocks from a wide range of tectonic settings: mineral compositions in equilibrium. *Contributions to Mineralogy and Petrology*, **156**, 177-195.
- Calvert, A. T., Gans, P. B. & Amato, J. M., 1999. Diapiric ascent and cooling of a sillimanite gneiss dome revealed by ⁴⁰Ar/³⁹Ar thermochronology: the Kigluaik Mountains, Seward Peninsula, Alaska. In: *Exhumation Processes: Normal Faulting, Ductile Flow and Erosion* (eds Ring, U., Brandon, M. T., Lister, G. S. & Willett, S. D.), **154**, 181-204, Geological Society Special Publication, London.
- Cannat, M., Chatin, F., Whitechurch, H. & Ceuleneer, G., 1997. Gabbroic rocks trapped in the upper mantle at Mid Atlantic ridge. *Proceedings of the Ocean Drilling Program, Scientific Results*, **153**, 243-264.
- Carswell, D. A. & O'Brien, P. J., 1993. Thermobarometry and geotectonic significance of high-pressure granulites: Examples from the Moldanubian Zone of the Bohemian Massif in Lower Austria. *Journal of Petrology*, **34**(3), 427-459.

- Carswell, D. A., Brueckner, H. K., Cuthbert, S. J., Mehta, K. & O'Brien, P. J., 2003. The timing of stabilisation and the exhumation rate for ultra-high pressure rocks in the Western Gneiss Region of Norway. *Journal of Metamorphic Geology*, **21**, 601-612.
- Ceriani, S., Mancktelow, N. S. & Pennacchioni, G., 2003. Analogue modelling of the influence of shape and particle/matrix interface lubrication on the rotational behaviour of rigid particles in simple shear. *Journal of Structural Geology*, **25**, 2005-2021.
- Chaloupský, J., Chlupač, I., Mašek, J., Waldhausrová, J. & Cháb, J., 1995. Moldanubian Region: Teplá-Barrandian Zone - Stratigraphy. In: *Pre-Permian Geology of Central and Eastern Europe* (eds Dallmeyer, R. D., Franke, W. & Weber, K.), 379-391, Springer, Berlin.
- Chamberlain, C. P., 1986. Evidence for the repeated folding of isotherms during regional metamorphism. *Journal of Petrology*, **27**(1), 63-89.
- Chan, Y. C. & Crespi, J. M., 1999. Albite porphyroblasts with sigmoidal inclusion trails and their kinematic implications: an example from the Taconic Allochthon, west-central Vermont. *Journal of Structural Geology*, **21**(10), 1407-1417.
- Chemenda, A. I., Mattauer, M., Malavielle, J. & Bokun, A. N., 1995. A mechanism for syn-collisional rock exhumation and associated normal faulting: Results from physical modelling. *Earth and Planetary Science Letters*, **132**, 225-232.
- Cherniak, D. J., Hanchar, J. M. & Watson, E. B., 1997. Rare-earth diffusion in zircon. *Chemical Geology*, **134**, 289-301.
- Cherniak, D. J. & Watson, E. B., 2003. Diffusion in Zircon. In: *Zircon* (eds Hanchar, J. M. & Hoskin, P. W. O.) *Reviews in Mineralogy and Geochemistry*, **53**, 113-143, Mineralogical Society of America, Washington D.C.
- Cherniak, D. J., Watson, E. B., Grove, M. & Harrison, T. M., 2004. Pb diffusion in monazite: A combined RBS/SIMS study. *Geochimica et Cosmochimica Acta*, **68**, 829-840.
- Chevillard, M. J. L., 1866. Trilobites du Dévonien du Mont de la Revenue, commune de Chagey, près Héricourt (Haute-Saône). *Bulletin de la Société Géologique de France*, **24**(2), 124-129.
- Chèvremont, P., 2008. Carte géologique harmonisée du département des Vosges (88)-Notice géologique. *Rapport BRGM/RP-56439- FR*, 232 p.
- Chlupač, I., 1993. *Geology of the Barrandian. A field trip guide*. Waldemar Kramer Verlag, Frankfurt am Main, 154 p.
- Chopin, F., 2010. *Evolution du flux de matière, de l'architecture et de la rhéologie d'un prisme d'accrétion crustal (Dôme d'Orlica-Śnieżnik, Sudètes)*. Thèse, Université de Strasbourg, 191 p.
- Chopin, F., Schulmann, K., Skrzypek, E., Lehmann, J., Dujardin, J.-R., Martelat, J.-E., Lexa, O., Corsini, M., Edel, J.-B., Štípská, P. & Pitra, P., 2011a. Crustal influx, indentation, ductile thinning and gravity redistribution in a continental wedge: building a Moldanubian mantled gneiss dome with Saxothuringian material (European Variscan belt). *Tectonics*, in press.
- Chopin, F., Schulmann, K., Štípská, P., Martelat, J.-E., Pitra, P., Lexa, O. & Pétri, B., 2011b. Microstructural and metamorphic evolution of a high pressure granitic orthogneiss during continental subduction (Orlica-Śnieżnik dome, Bohemian Massif). *Journal of Metamorphic Geology*, in press.
- Choubert, G. & Gardet, G., 1935. Contribution à l'étude du Permien des Vosges. *Revue de Géographie physique et de Géologie dynamique*, **3**(4), 325-362.
- Clark, A. H., Scott, D. J., Sandeman, H. A., Bromley, A. V. & Farrar, E., 1998. Siegenian generation of the Lizard ophiolite: U-Pb zircon age data for plagiogranite, Porthkerris, Cornwall. *Journal of the Geological Society, London*, **155**, 595-598.

- Clauer, N., 1970. *Etude sédimentologique, géochimique et géochronologique des schistes de Steige et de la Série de Villé - Vosges*. Thèse de 3^{ème} cycle, Université Louis Pasteur, Strasbourg, 88 p.
- Clauer, N. & Bonhomme, M., 1970. Datations Rubidium-Strontium dans les schistes de Steige et la série de Villé (Vosges). *Bulletin du Service de la Carte Géologique d'Alsace-Lorraine*, **23**(3-4), 191-208.
- Cocherie, A., Bé Mezème, E., Legendre, O., Fanning, C. M., Faure, M. & Rossi, P., 2005. Electron-microprobe dating as a tool for determining the closure of Th-U-Pb systems in migmatitic monazites. *American Mineralogist*, **90**, 607-618.
- Cocherie, A. & Robert, M., 2008. Laser ablation coupled with ICP-MS applied to U-Pb zircon geochronology: A review of recent advances. *Gondwana Research*, **14**, 597-608.
- Cocherie, A., Fanning, C. M., Jezequel, P. & Robert, M., 2009. LA-MC-ICPMS and multi-ion counting system, and SHRIMP U-Pb dating of complex zircons from quaternary tephra from the French Massif Central: magma residence time and geochemical implications. *Geochimica et Cosmochimica Acta*, **73**, 1095-1108.
- Cocks, L. R. M. & Fortey, R. A., 1982. Faunal evidence for oceanic separations in the Palaeozoic of Britain. *Journal of the Geological Society, London*, **139**, 465-478.
- Cocks, L. R. M. & Torsvik, T. H., 2002. Earth geography from 500 to 400 million years ago: a faunal and palaeomagnetic review. *Journal of the Geological Society, London*, **159**, 631-644.
- Coggon, R. & Holland, T. J. B., 2002. Mixing properties of phengitic micas and revised garnet-phengite thermobarometers. *Journal of Metamorphic Geology*, **20**(7), 683-696.
- Coleman, R. G., 1977. *Ophiolites: ancient oceanic lithosphere ?* Springer, Berlin, 229 p.
- Collins, A. S., Kryza, R. & Zalasiewicz, J., 2000. Macrofabric fingerprints of Late Devonian-Early Carboniferous subduction in the Polish Variscides, the Kaczawa complex, Sudetes. *Journal of the Geological Society, London*, **157**, 283-288.
- Coney, P. J., 1980. Cordilleran metamorphic core complexes. In: *Cordilleran Metamorphic Core Complexes* (eds Crittenden, M. D., Coney, P. J. & Davis, G. H.), **153**, 7-34, Geological Society of America Memoir, Boulder, Colorado.
- Cook, C. A., Holdworth, R. E. & Styles, M. T., 2002. The emplacement of peridotites and associated oceanic rocks from the Lizard Complex, southwest England. *Geological Magazine*, **139**(1), 27-45.
- Corsin, P. & Dubois, G., 1932. Description de la flore dinantienne de Champenay. *Bulletin du Service de la Carte Géologique d'Alsace-Lorraine*, **2**, 1-33.
- Corsin, P., Gagny, C. & Mattauer, M., 1956. Découverte d'une florure d'âge viséen dans les schistes et grauwackes des environs de Felling (Haut-Rhin). *Comptes Rendus de l'Académie des Sciences*, **242**, 1908-1909.
- Corsin, P. & Mattauer, M., 1957. Quelques nouveaux gisements fossilifères du Massif des Ballons (Vosges méridionales). *Comptes rendus sommaires de la Société Géologique de France*, **5**, 92-94.
- Corsin, P. & Ruhland, M., 1959. Les gisements à plantes du Viséen dans les Vosges méridionales. *Comptes Rendus de l'Académie des Sciences*, **248**, 2145-2149.
- Corsin, P., Danze-Corsin, Millot, G. & Ruhland, M., 1960. Sur l'âge viséen inférieur des schistes de Schwarzbach (vallée de la Bruche) dans les Vosges du Nord. *Bulletin du Service de la Carte Géologique d'Alsace-Lorraine*, **13**, 163-164.
- Corsin, P., Coulon, M., Fourquin, C., Paicheler, J. C. & Point, R., 1973. Etude de la flore de la série de Giromagny (Viséen supérieur des Vosges méridionales). Comparaison avec les autres flores du Culm des Vosges. *Sciences Géologiques*, **26**(1), 43-68.

- Coulon, M. & Lemoigne, Y., 1969. Paleoxylon Bourbachensis : nouvelle structure ligneuse du Viséen des Vosges. *Comptes Rendus de l'Academie des Sciences*, **269**, 1498-1501.
- Coulon, M., Fourquin, C., Heddebaut, C. & Paicheler, J. C., 1975a. Mise au point sur l'âge des faunes de Bourbach-le-Haut et sur la chronologie des différentes séries du Culm des Vosges du Sud. *Sciences Géologiques*, **28**(2), 141-148.
- Coulon, M., Fourquin, C., Paicheler, J. C. & Point, R., 1975b. Contribution a la connaissance du tectorogène varisque dans les Vosges méridionales. II - Le Culm de la région comprise entre Giromagny et Bourbach-le Bas. *Sciences Géologiques*, **28**(2), 109-139.
- Coulon, M., Fourquin, C., Paicheler, J. C., Conil, R. & Lys, M., 1978. Stratigraphie du Viséen des Vosges méridionales et datations obtenues par l'étude de plusieurs niveaux à microfaunes et algues. *Sciences Géologiques*, **31**(2), 77-93.
- Creuzot, G., 1983. *Etude géologique du bassin permien de Ronchamp-Giromagny*. Thèse de 3^{ème} cycle, Université de Besançon, 187 p.
- Crowley, Q. G., Floyd, P. A., Winchester, J. A., Franke, W. & Holland, J. G., 2000. Early Palaeozoic rift-related magmatism in Variscan Europe: fragmentation of the Armorica Terrane Assemblage. *Terra Nova*, **12**, 171-180.
- Cruz Mermey, D., Skrzypek, E., Ménillet, F. & Chèvremont, P., 2007. Carte géologique harmonisée du département du Bas-Rhin (67)-Notice géologique. *Rapport BRGM/RP-56028-FR*, 322 p.
- Currie, C. A., Beaumont, C. & Huismans, R. S., 2007. The fate of subducted sediments: a case for backarc intrusion and underplating. *Geology*, **35**, 1111-1114.
- Currie, C. A., Huismans, R. S. & Beaumont, C., 2008. Thinning of continental backarc lithosphere by flow-induced gravitational instability. *Earth and Planetary Science Letters*, **269**, 436-447.
- Dallmeyer, R. D., Franke, W. & Weber, K., 1995. *Pre-Permian Geology of Central and Eastern Europe*. Springer, Berlin, 604 p.
- Davies, G. R., 1984. Isotopic evolution of the Lizard Complex. *Journal of the Geological Society, London*, **141**, 3-14.
- Davis, G. H. & Hardy, J. J., 1981. The Eagle Pass detachment, southeastern Arizona: product of mid-Miocene listric (?) normal faulting in the southern Basin and Range. *Geological Society of America Bulletin*, **92**, 749-762.
- Degeling, H., Eggins, S. & Ellis, D. J., 2001. Zr budgets for metamorphic reactions, and the formation of zircon from garnet breakdown. *Mineralogical Magazine*, **65**, 749-758.
- Delbos, J. & Kœchlin-Schlumberger, J., 1866. *Description géologique et minéralogique du département du Haut-Rhin, tome I*, E. Perrin, Mulhouse, 484 p.
- Delesse, A., 1849. *Mémoire sur la constitution minéralogique et chimique des roches des Vosges*, pagination multiple.
- Dewey, J. F. & Bird, J. M., 1970. Mountain Belts and the new global tectonics. *Journal of Geophysical Research*, **75**, 2625-2647.
- Dewey, J. F. & Burke, K., 1973. Tibetan, Variscan and Precambrian basement reactivation: Products of continental collision. *Journal of Geology*, **81**, 683-692.
- Dewey, J. F., Ryan, P. D. & Andersen, T. B., 1993. Orogenic uplift and collapse, crustal thickness, fabrics and metamorphic phase changes; the role of eclogites. In: *Magmatic processes and plate tectonics* (eds Prichard, H. M., Alabaster, T., Harris, N. B. W. & Neary, C. R.), **76**, 325-343, Geological Society Special Publication, London.

- Dixon, J. M., 1975. Finite strain and progressive deformation in models of diapiric structures. *Tectonophysics*, **28**(1-2), 89-124.
- Don, J., 1964. The Złote and Krowiarki Mountains as structural elements of the Śnieżnik metamorphic massif. *Geologia Sudetica*, **1**, 79-117.
- Don, J., 1982. The Sienna synform and the relationship of gneisses to the deformational stages distinguished in the Śnieżnik metamorphic massif (Sudetes). *Geologia Sudetica*, **17**, 103-124.
- Don, J. & Dowidar, H., 1988. Goszów Quartzites and the problem of the Młynowiec Series (Śnieżnik Metamorphic Massif, Sudetes). *Bulletin de l'Académie Polonaise des Sciences, série Sciences de la Terre*, **36**(3-4), 239-252.
- Don, J., Dumicz, M., Wojciechowska, I. & Żelaźniewicz, A., 1990. Lithology and tectonics of the Orlica-Śnieżnik Dome, Sudetes: recent state of knowledge. *Neues Jahrbuch für Geologie und Paläontologie, Abhandlungen*, **179**(2/3), 159-188.
- Don, J., Skácel, J. & Gotowała, R., 2003. The boundary zone of the East and West Sudetes on the 1:50 000 scale geological map of the Velké Vrbno, Staré Město and Śnieżnik Metamorphic Units. *Geologia Sudetica*, **35**, 25-59.
- Doré, F., 1994. Cambrian in the Armorican Massif. In: *Pre-Mesozoic Geology in France and Related Areas* (ed Keppie, J. D.), 136-141, Springer, Berlin.
- Dörr, W., Pique, A., Franke, W. & Kramm, U., 1992. Les galets granitiques du conglomérat de Russ (Dévono-Dinantien des Vosges du Nord) sont les témoins d'un magmatisme acide ordovicien. La distension crustale et le rifting saxothuringien au Paléozoïque inférieur. *Comptes Rendus de l'Académie des Sciences*, **315**(5), 587-594.
- Doubinger, J., 1956. Contribution à l'étude des flores autuno-stéphaniennes. *Mémoires de la Société Géologique de France*, **75**, 1-180.
- Doubinger, J., 1963. Chitinozoaires ordoviciens et siluriens des schistes de Steige dans les Vosges. *Bulletin du Service de la Carte Géologique d'Alsace-Lorraine*, **16**(3), 125-136.
- Doubinger, J. & Ruhland, M., 1963. Découverte d'une faune de Chitinozoaires d'âge Dévonien au Treh (région du Markstein, Vosges méridionales). *Comptes Rendus de l'Académie des Sciences*, **256**, 2894-2896.
- Doubinger, J. & von Eller, J.-P., 1963a. Présence de Spongiaires dans les schistes précambriens métamorphiques des Vosges. *Bulletin du Service de la Carte Géologique d'Alsace-Lorraine*, **16**(3), 111-123.
- Doubinger, J. & von Eller, J.-P., 1963b. Découverte de Chitinozoaires d'âge silurien dans les schistes de Steige (vallée de l'Andlau, Vosges). *Comptes Rendus de l'Académie des Sciences*, **256**, 469-471.
- Doubinger, J., 1965. Sur l'âge des gisements houillers des Vosges. *Bulletin du Service de la Carte Géologique d'Alsace-Lorraine*, **18**(2), 49-64.
- Doubinger, J. & Rauscher, R., 1966. Spores du Viséen marin de Bourbach-le-Haut dans les Vosges du Sud. *Pollen et Spores*, **8**(2), 361-405.
- Dubińska, E., Bylina, P., Kozłowski, A., Dörr, W., Nejbort, K., Schastok, J. & Kulicki, C., 2004. U-Pb dating of serpentinitization: hydrothermal zircon from a metasomatic rodingite shell (Sudetic ophiolite, SW Poland). *Chemical Geology*, **203**, 183-203.
- Dubois, G., 1946. Répartition des gisements certainement et vraisemblablement dinantiens dans la région de la Bruche (Vosges moyennes). *Comptes rendus sommaires de la Société Géologique de France*, **12**, 222-223.
- Duchêne, S., Lardeaux, J. M. & Albarede, F., 1997. Exhumation of eclogites: insights from depth-time path analysis. *Tectonophysics*, **280**(1-2), 125-140.

- Duchêne, S., Aïssa, R. & Vanderhaeghe, O., 2006. Pressure-temperature-time evolution of metamorphic rocks from Naxos (Cyclades, Greece): Constraints from thermobarometry and Rb/Sr dating. *Geodinamica Acta*, **19**(5), 301-321.
- Dudek, A., 1980. The crystalline basement block of the Outer Carpathians in Moravia-Brunovistulicum. *Rozprawy Československé Akademie Věd*, **90**(8), 1-85.
- Dumicz, M., 1979. Tectogenesis of the metamorphosed series of the Kłodzko district: a tentative explanation. *Geologia Sudetica*, **14**, 29-44.
- Duthou, J.-L., Couturie, J.-P., Mierzejewski, M. P. & Pin, C., 1991. Age determination of the Karkonosze granite using isochrone Rb-Sr whole rock method. *Przegląd Geologiczny*, **39**(2), 75-79.
- Dvořák, J., 1995. Moravo-Silesian Zone: Autochton - Stratigraphy. In: *Pre-Permian Geology of Central and Eastern Europe* (eds Dallmeyer, D., Franke, W. & Weber, K.), 477-489, Springer, Berlin.
- Dziedzic, K. & Teisseyre, A. K., 1990. The Hercynian molasse and younger deposits in the Intra-Sudetic Depression, SW Poland. *Neues Jahrbuch für Geologie und Paläontologie, Abhandlungen*, **179**, 285-305.
- Edel, J.-B. & Schulman, K., 2009. Geophysical constraints and model of the “Saxothuringian and Rhenohercynian subductions – magmatic arc system” in NE France and SW Germany. *Bulletin de la Société Géologique de France*, **180**(6), 545-558.
- Edel, J.-B., Schulmann, K., Skrzypek, E. & Cocherie, A., 2011. Tectonic evolution of the European Variscan belt constrained by palaeomagnetic, structural and anisotropy of magnetic susceptibility data from the Rhenohercynian magmatic arc (Northern Vosges, Eastern France). *Journal of the Geological Society, London*, submitted.
- Ehrenberg, S. N., Aagaard, P., Wilson, M. J., Fraser, A. R. & Duthie, D. M. L., 1993. Depth-dependent transformation of kaolinite to dickite in sandstones of the Norwegian continental shelf. *Clay Minerals*, **28**, 325-352.
- Eisbacher, G. H., Lüschen, E. & Wickert, F., 1989. Crustal-scale thrusting and extension in the Hercynian Schwarzwald and Vosges, Central Europe. *Tectonics*, **8**, 1-21.
- Elsass, P., von Eller, J.-P. & Stussi, J.-M., 2008. Géologie du massif du Champ du Feu et de ses abords. Éléments de notice pour la feuille géologique 307 Sélestat. *Rapport BRGM/RP-56088-FR*, 184 p.
- England, P. C. & Thompson, A. B., 1984. Pressure-Temperature-Time Paths of Regional Metamorphism I. Heat-Transfer during the Evolution of Regions of Thickened Continental-Crust. *Journal of Petrology*, **25**(4), 894-928.
- Eskola, P. E., 1949. The problem of mantled gneiss domes. *Geological Society of London Quarterly*, **104**, 461-476.
- Evans, J. A., Zalasiewicz, J. A., Fletcher, I., Rasmussen, B. & Pearce, N. J. G., 2002. Dating diagenetic monazite in mudrocks: constraining the oil window? *Journal of the Geological Society, London*, **159**, 619-622.
- Fajst, M., 1976. New discordance in the pre-Cambrian of the Bohemian massif (in Czech). *Časopis pro Mineralogii a Geologii*, **21**(3), 257-275.
- Falk, F., Franke, W. & Kurze, M., 1995. Saxothuringian Basin: Autochton and Nonmetamorphic Nappe Units - Stratigraphy, Structure, and Igneous Activity. In: *Pre-Permian Geology of Central and Eastern Europe* (eds Dallmeyer, D., Franke, W. & Weber, K.), 221-234, Springer, Berlin.

- Faure, M., Sommers, C., Melleton, J., Cocherie, A. & Lautout, O., 2010. The Léon Domain (French Massif Armoricain): a westward extension of the Mid-German Crystalline Rise? Structural and geochronological insights. *International Journal of Earth Sciences*, **99**, 65-81.
- Fay, C., Bell, T. H. & Hobbs, B. E., 2008. Porphyroblast rotation versus non-rotation: Conflict resolution! *Geology*, **36**, 307-310.
- Feehan, J. G. & Brandon, M. T., 1999. Contribution of ductile flow to exhumation of low-temperature, high-pressure metamorphic rocks: San Juan Cascade nappes, NW Washington State. *Journal of Geophysical Research*, **104**(B5), 10,883-10,902.
- Fiala, J., Matějovská, O. & Vaňková, V., 1987. Moldanubian granulites: source material and petrogenetic considerations. *Neues Jahrbuch für Mineralogie, Abhandlungen*, **157**, 133-165.
- Figge, K., 1968. Ober-Devon im Breuschtal der Vogesen. *Neues Jahrbuch für Geologie und Paläontologie, Monatshefte*, **4**, 195-199.
- Finger, F. & Steyrer, H. P., 1990. I-type granitoids as indicators of a late Paleozoic convergent ocean-continent margin along the southern flank of the central European Variscan orogen. *Geology*, **18**, 1207-1210.
- Finger, F., Roberts, M. P., Haunschmid, B., Schermaier, A. & Steyrer, H. P., 1997. Variscan granitoids of central Europe: their typology, potential sources and tectonothermal relations. *Mineralogy and Petrology*, **61**(1-4), 67-96.
- Finger, F. & Krenn, E., 2007. Three metamorphic monazite generations in a high-pressure rock from the Bohemian Massif and the potentially important role of apatite in stimulating polyphase monazite growth along a PT loop. *Lithos*, **95**, 103-115.
- Firtion, F., 1945. Apports à la connaissance paléontologique du Dévono-Dinantien de la région de Schirmeck. *Comptes rendus sommaires de la Société Géologique de France*, **4**, 39-41.
- Firtion, F., 1957. Les éléments paléontologiques dévoniens du Val de Bruche. *Annales Universitatis Saraviensis, Scientia*, **5-6**(2-3), 97-184.
- Fischer, G., 1935. Der Bau des Glatzer Scheegebirges. *Jahrbuch der Preussischen Geologischen Landesanstalt*, **56**, 712-732.
- Floyd, P. A., 1984. Geochemical characteristics and comparison of the basic rocks of the Lizard Complex and the basaltic lavas within the Hercynian troughs of SW England. *Journal of the Geological Society, London*, **141**, 61-70.
- Floyd, P. A., S., E. C. & Styles, M. T., 1993. *Igneous Rocks of South-West England*. Chapman and Hall, London, 256p.
- Floyd, P. A., 1995. Rhenohercynian Foldbelt: Autochton and Nonmetamorphic Nappe Units - Igneous Activity. In: *Pre-Permian Geology of Central and Eastern Europe* (eds Dallmeyer, D., Franke, W. & Weber, K.), 59-81.
- Floyd, P. A., Winchester, J. A., Ciesielczuk, J., Lewandowska, A., Szczepański, J. & Turniak, K., 1996. Geochemistry of early Palaeozoic amphibolites from the Orlica-Śnieżnik dome, Bohemian Massif: petrogenesis and palaeotectonic aspects. *Geologische Rundschau*, **85**, 225-238.
- Fluck, P., 1971. *Pétrographie et histoire métamorphique des gneiss de Sainte-Marie-aux-Mines (Vosges)*. Thèse de 3^{ème} cycle, Université Louis Pasteur, Strasbourg, 110 p.
- Fluck, P., 1980. Métamorphisme et magmatisme dans les Vosges moyennes d'Alsace. Contribution à l'histoire de la chaîne Varisque. *Mémoires des Sciences Géologiques*, **62**, 248 p.
- Fluck, P., 1987. Apports de la "microcartographie" à divers points-clés de la géologie du socle vosgien. *Colloque des Géologues et Géophysiciens du Socle Vosgien*, 11-14.
- Fluck, P., Edel, J.-B., Gagny, C., Montigny, R., Piqué, A., Schneider, J.-L. & Whitechurch, H., 1987. Géologie du socle vosgien. *Document du BRGM*, **146**, 97 p.

- Fluck, P., Piqué, A., Schneider, J.-L. & Whitechurch, H., 1991. Le socle vosgien. *Sciences Géologiques Bulletin*, **44**, 207-235.
- Foster, G., Kinny, P., Vance, D., Prince, C. & Harris, N., 2000. The significance of monazite U-Th-Pb age data in metamorphic assemblages; a combined study of monazite and garnet chronometry. *Earth and Planetary Science Letters*, **181**(3), 327-340.
- Foster, G., Gibson, H. D., Parrish, R., Horstwood, M., Fraser, J. & Tindle, A., 2002. Textural, chemical and isotopic insights into the nature and behaviour of metamorphic monazite. *Chemical Geology*, **191**, 183-207.
- Fournet, J., 1847. Résultats sommaires d'une exploration des Vosges. *Bulletin de la Société Géologique de France*, **4**, 220-254.
- Franěk, J., Schulmann, K. & Lexa, O., 2006. Kinematic and rheological model of exhumation of high pressure granulites in the Variscan orogenic root: example of the Blanský les granulite, Bohemian Massif, Czech Republic. *Mineralogy and Petrology*, **86**(3-4), 253-276.
- Franke, W., 1984. Variszischer Deckenbau im Raume der Münchberger Gneismasse, abgeleitet aus der Fazies, Deformation und Metamorphose im umgebenden Paläozoikum. *Geotektonische Forschungen*, **68**, 1-253.
- Franke, W., 1995. Rhenohercynian Foldbelt: Autochton and Nonmetamorphic Nappe Units - Stratigraphy. In: *Pre-Permian Geology of Central and Eastern Europe* (eds Dallmeyer, D., Franke, W. & Weber, K.), 33-49.
- Franke, W., 2000. The mid-European segment of the Variscides: tectonostratigraphic units, terrane boundaries and kinematic evolution. In: *Orogenic Processes: Quantification and Modelling in the Variscan Belt* (eds Franke, W., Haak, V., Oncken, O. & Tanner, D.), **179**, 35-63, Geological Society Special Publication, London.
- Franke, W., Haak, V., Oncken, O. & Tanner, D., 2000. *Orogenic Processes: Quantification and Modelling in the Variscan Belt*. The Geological Society of London, London, 459 p.
- Franke, W. & Żelaźniewicz, A., 2000. The eastern termination of the Variscides: terrane correlation and kinematic evolution. In: *Orogenic processes: Quantification and Modelling in the Variscan belt* (eds Franke, W., Haak, V., Oncken, O. & Tanner, D.), **179**, 63-86, Geological Society Special Publication, London.
- Fraser, G., Ellis, D. & Eggins, S., 1997. Zirconium abundance in granulite-facies minerals, with implications for zircon geochronology in high-grade rocks. *Geology*, **25**, 607-610.
- Frey, M., 1987. The reaction-isograd kaolinite + quartz = pyrophyllite + H₂O, Helvetic Alps, Switzerland. *Schweizerische Mineralogische und Petrographische Mitteilungen*, **67**, 1-11.
- Friedl, G., Cooke, R., Finger, F., McNaughton, N. J. & Fletcher, I., 2003. U-Pb shrimp dating and trace element investigations on multiple zircons from a South-Bohemian granulite. *Journal of the Czech Geological Society*, **48**, 51.
- Friedl, G., Finger, F., Paquette, J., Quadt, A., McNaughton, N. & Fletcher, I., 2004. Pre-Variscan geological events in the Austrian part of the Bohemian Massif deduced from U-Pb zircon ages. *International Journal of Earth Sciences*, **93**, 802-823.
- Fritz, H., 1996. Geodynamic and tectonic evolution of the southeastern Bohemian Massif: the Thaya section (Austria). *Mineralogy and Petrology*, **58**, 253-258.
- Froitzheim, N. & Manatschal, G., 1996. Kinematics of Jurassic rifting, mantle exhumation, and passive-margin formation in the Austroalpine and Penninic nappes (eastern Switzerland). *Geological Society of America Bulletin*, **108**(9), 1120-1133.
- Furnes, H., Kryza, R., Muszynski, A., Pin, C. & Garmann, L. B., 1994. Geochemical Evidence For Progressive, Rift-Related Early Paleozoic Volcanism in the Western Sudetes. *Journal of the Geological Society, London*, **151**, 91-109.

- Fyson, W. K., 1980. Fold fabrics and emplacement of an Archean granitoid pluton, Cleft Lake, Northwest Territories. *Canadian Journal of Earth Sciences*, **17**, 325-332.
- Gagny, C., 1962. Caractères sédimentologiques et pétrographiques des schistes et grauwackes du Culm dans les Vosges méridionales. *Bulletin du Service de la Carte Géologique d'Alsace-Lorraine*, **15**(4), 139-160.
- Ganssloser, M., Theye, T. & Wachendorf, H., 1996. Detrital glaucophane in graywackes of the Rhenohercynian Harz mountains and the geodynamic implications. *Geologische Rundschau*, **85**, 755-760.
- Gayk, T. & Kleinschrodt, R., 2000. Hot contacts of garnet peridotites in middle/upper crustal levels: new constraints on the nature of the late Variscan high-T/low-P event in the Moldanubian (Central Vosges/NE France). *Journal of Metamorphic Geology*, **18**, 293-305.
- Gebauer, D. & Grünenfelder, M., 1979. U–Pb zircon and Rb–Sr mineral dating of eclogites and their country rocks. Example: Münchberg Gneiss Massif, Northeast Bavaria. *Earth and Planetary Science Letters*, **42**, 35-44.
- Gebauer, D., Schertl, H.-P., Brix, M. & Schreyer, W., 1997. 35 Ma old ultrahigh-pressure metamorphism and evidence for very rapid exhumation in the Dora Maira massif, Western Alps. *Lithos*, **41**, 5-24.
- Gerya, T. V., Perchuk, L. L., Maresch, W. V. & Willner, A. P., 2004. Inherent gravitational instability of hot continental crust: Implications for doming and diapirism in granulite facies terrains. In: *Gneiss domes in orogeny* (eds Whitney, D. L., Teyssier, C. & Siddoway, C. S.), **380**, 97-115, Geological Society of America Special Paper, Boulder, Colorado.
- Gibson, H. D., Carr, S. D., Brown, R. L. & Hamilton, M. A., 2004. Correlations between chemical and age domains in monazite, and metamorphic reactions involving major pelitic phases: an integration of ID-TIMS and SHRIMP geochronology with Y–Th–U X-ray mapping. *Chemical Geology*, **211**, 237-260.
- Gordon, S. M., Schneider, D. A., Manecki, M. & Holm, D. K., 2005. Exhumation and metamorphism of an ultrahigh-grade terrane: geochronometric investigations of the Sudete Mountains (Bohemia), Poland and Czech Republic. *Journal of the Geological Society, London*, **162**, 841-855.
- Gotowała, R., 2003. The tectonic involvement of the Javorník granitoids–Skrzynka–Złoty Stok Shear Zone (Sudetes). *Mineralogical Society of Poland - Special Papers*, **23**, 61-63.
- Gradstein, F., Ogg, J. & Smith, A., 2004. *A geologic time scale*. Cambridge University Press, Cambridge.
- Groth, P., 1877. Das Gneissgebiet von Markkirch im Oberelsass. *Abhandlungen zur geologischen Spezialkarte Elsass-Lothringen*, **1**, 395-488.
- Grzeškowiak, A. & Żelaźniewicz, A., 2002. On the Significance of Gneissic Enclaves in the 500 Ma Metagranite, the Łądek–Śnieżnik Metamorphic Unit, the West Sudetes. *Geolines*, **14**, 28-29.
- Grzeškowiak, A. & Żelaźniewicz, A., 2005. Early Palaeozoic Syntectonic Migmatization Preceded Variscan Metamorphism in the Orlica–Śnieżnik Dome, Sudetes: U-Pb SHRIMP Evidence. *Geolines*, **19**, 46-48.
- Guillot, S. & Ménot, R.-P., 2009. Paleozoic evolution of the External Crystalline Massifs of the Western Alps. *Comptes Rendus Géoscience*, **341**, 253-265.
- Guiraud, M., Powell, R. & Rebay, G., 2001. H₂O in metamorphism and unexpected behaviour in the preservation of metamorphic mineral assemblages. *Journal of Metamorphic Geology*, **19**(4), 445-454.
- Gunia, T., 1984a. Microfossils from the quartzitic schists in vicinity of Goszów, Śnieżnik Kłodzki Massif, Central Sudetes. *Geologia Sudetica*, **18**(2), 47-57.

- Gunia, T., 1984b. Microflora of the crystalline limestones from the vicinity of Nowy Waliszów (Krowiarki Mts., Central Sudetes). *Geologia Sudetica*, **19**(2), 75-86.
- Gunia, T., 1990. Acritarcha and microproblematica of the crystalline limestones from the vicinity of Romanowo Górne (Central Sudetes Mts, Krowiarki). *Geologia Sudetica*, **24**, 101-137.
- Guy, A., Edel, J.-B., Schulmann, K., Tomek, Č. & Lexa, O., 2011. A geophysical model of lower crustal structure of the Palaeozoic crustal root (Bohemian Massif): implications for modern collisional orogens. *Lithos*, **124**(1-2), 144-157.
- Hacker, B. R., Kelemen, P. B. & Behn, M. D., 2011. Differentiation of the continental crust by reamination. *Earth and Planetary Science Letters*, **307**, 501-516.
- Hahn, G., Hahn, R. & Maass, R., 1981. Trilobiten aus dem Unterkarbon der S-Vogesen. *Oberrheinische geologische Abhandlungen*, **30**, 1-26.
- Hajdukiewicz, J., 1990. Stratigraphy of Paleozoic rocks of the Góry Bardzkie and some remarks on their sedimentation. *Neues Jahrbuch für Geologie und Paläontologie, Abhandlungen*, **179**, 275-284.
- Hameurt, J., 1967. Les terrains cristallins et cristophylliens du versant occidental des Vosges moyennes. *Mémoires du Service de la Carte géologique d'Alsace-Lorraine*, **26**, 402 p.
- Hammel, C., 1996. Une faune nouvelle de trilobites (Brachymetopus, Namuropyge) dans le Viséen des Vosges du Sud. Conséquences stratigraphiques et paléoécologiques. *Géobios*, **29**(6), 745-755.
- Hanchar, J. M. & Miller, C. F., 1993. Zircon zonation patterns as revealed by cathodoluminescence and backscattered electron images: implications for interpretation of complex crustal histories. *Chemical Geology*, **110**, 1-13.
- Hanchar, J. M. & Rudnick, R. L., 1995. Revealing hidden structures: The application of cathodoluminescence and back-scattered electron imaging to dating zircons from lower crustal xenoliths. *Lithos*, **36**(3-4), 289-303.
- Hann, H. P., Sawatzki, G. & Vaida, M., 1995. Acritarchen und Chitinozoen des Ordoviziums aus metamorphen Grauwacken der Zone von Badenweiler-Lenzkirch, Schwarzwald, SW-Deutschland. *Neues Jahrbuch für Geologie und Paläontologie, Monatshefte*, **1995**(6), 375-383.
- Hann, H. P. & Sawatzki, G., 1998. Deckenbau und Sedimentationsalter im Grundgebirge des Südschwarzwalds/SW-Deutschland. *Zeitschrift der deutschen geologischen Gesellschaft*, **149**(2), 183-195.
- Hann, H. P., Chen, F., Zedler, H., Frisch, W. & Loeschke, J., 2003. The Rand Granite in the southern Schwarzwald and its geodynamic significance in the Variscan belt of SW Germany. *International Journal of Earth Sciences*, **92**, 821-842.
- Harrison, T. M. & Watson, E. B., 1983. Kinetics of zircon dissolution and zirconium diffusion in granitic melts of variable water content. *Contributions to Mineralogy and Petrology*, **84**, 66-72.
- Hartley, A. J. & Otava, J., 2001. Sediment provenance and dispersal in a deep marine foreland basin: the Lower Carboniferous Culm Basin, Czech Republic. *Journal of the Geological Society*, **158**, 137-150.
- Hasalová, P., Štípská, P., Powell, R., Schulmann, K., Janoušek, V. & Lexa, O., 2008. Transforming mylonitic metagranite by open-system interactions during melt flow. *Journal of Metamorphic Geology*, **26**, 55-80.
- Hegner, E., Chen, F. & Hann, H.-P., 2001. Chronology of basin closure and thrusting in the internal zone of the Variscan belt in the Schwarzwald, Germany: evidence from zircon ages, trace element geochemistry, and Nd isotopic data. *Tectonophysics*, **332**, 169-184.

- Hering, O. & Zimmerle, W., 1976. Petrographische Beschreibung und Deutung der erbohrten Schichten (Saar 1). *Geologisches Jahrbuch*, **A-27**, 91-306.
- Hermann, J. & Rubatto, D., 2003. Relating zircon and monazite domains to garnet growth zones: age and duration of granulite facies metamorphism in the Val Malenco lower crust. *Journal of Metamorphic Geology*, **21**, 833-852.
- Hess, H. H., 1962. The history of ocean basins. In: *Petrologic studies: a volume in honor of A. F. Buddington* (eds Engel, A. E. J., James, H. L. & Leonard, B. F.), 599-620, Geological Society of America, Boulder, Colorado.
- Hess, J. C., Lippolt, H. J. & Kober, B., 1995. The age of the Kagenfels granite (northern Vosges) and its bearing on the intrusion scheme of late Variscan granitoids. *Geologische Rundschau*, **84**, 568-577.
- Hinchey, A., Carr, S. D. & Rayner, N., 2007. Bulk compositional controls on the preservation of age domains within metamorphic monazite: A case study from quartzite and garnet–cordierite–gedrite gneiss of Thor-Odin dome, Monashee complex, Canadian Cordillera. *Chemical Geology*, **240**, 85-102.
- Hladil, J., Melichar, R., Otava, J., Galle, A., Krs, M., Man, O., Pruner, P., Cejchan, P. & Orel, P., 1999. The Devonian in the Easternmost Variscides, Moravia: a Holistic Analysis Directed Towards Comprehension of the Original Context. *Abhandlungen der geologischen Bundesanstalt*, **54**, 27-47.
- Holder, M. T. & Leveridge, B. E., 1986. A model for the tectonic evolution of South Cornwall. *Journal of the Geological Society, London*, **143**, 125-134.
- Holland, T. & Powell, R., 2003. Activity-composition relations for phases in petrological calculations: an asymmetric multicomponent formulation. *Contributions to Mineralogy and Petrology*, **145**, 492-501.
- Holland, T. J. B., Baker, J. & Powell, R., 1998. Mixing properties and activity-composition relationships of chlorites in the system MgO-FeO-Al₂O₃-SiO₂-H₂O. *European Journal of Mineralogy*, **10**(3), 395-406.
- Holland, T. J. B. & Powell, R., 1998. An internally consistent thermodynamic data set for phases of petrological interest. *Journal of Metamorphic Geology*, **16**(3), 309-343.
- Hollinger, J., 1969. Beitrag zur Gliederung des Deckgebirges der Nordvogesen. *Zeitschrift der deutschen geologischen Gesellschaft*, **121**, 79-91.
- Hollister, L. H., 1993. The role of melt in the uplift and exhumation of orogenic belts. *Chemical Geology*, **108**(1-4), 31-48.
- Hollister, L. S., 1966. Garnet zoning: an interpretation based on the Rayleigh fractionation model. *Science*, **154**, 1647-1651.
- Hoskin, P. W. O. & Black, L. P., 2000. Metamorphic zircon formation by solid-state recrystallization of protolith igneous zircon. *Journal of Metamorphic Geology*, **18**, 423-439.
- Hoskin, P. W. O. & Schaltegger, U., 2003. The composition of zircon and igneous and metamorphic petrogenesis. In: *Zircon* (eds Hanchar, J. M. & Hoskin, P. W. O.) *Reviews in Mineralogy and Geochemistry*, **53**, 27-62, Mineralogical Society of America, Washington, D. C.
- Huddleston-Holmes, C. R. & Ketcham, R. A., 2005. Getting the inside story: using computed X-ray tomography to study inclusion trails in garnet porphyroblasts. *American Mineralogist*, **90**, ea1–ea17.

- Ighid, L., 1985. *Contribution à l'étude microstructurale des schistes de Steige et de la série de Villé - Vosges* - Mémoire de DEA, Université Louis Pasteur, Strasbourg, 33 p.
- Ikeda, T., Shimobayashi, N., Wallis, S. R. & Tsuchiyama, A., 2002. Crystallographic orientation, chemical composition and three-dimensional geometry of sigmoidal garnet: evidence for rotation. *Journal of Structural Geology*, **24**, 1633-1646.
- Ikenne, M. & Baroz, F., 1985. Mise en évidence des caractères orogénique, tholéïtique et calco-alkalin du volcanisme dévono-dinantien dans le massif du Rabodeau (Vosges septentrionales) : apport à la reconstitution géotectonique des Vosges. *Comptes Rendus de l'Académie des Sciences*, **301**(8), 529-532.
- Ilg, B. R. & Karlstrom, K. E., 2000. Porphyroblast inclusion trail geometries in the Grand Canyon; evidence for non-rotation and rotation? *Journal of Structural Geology*, **22**(2), 231-243.
- Jaekel, O., 1888. Über mitteldevonische Schichten im Breuschtal. *Mitteilungen der geologischen Landesanstalt von Elsass-Lothringen*, **1**, 229-239.
- Jamieson, R. A., Beaumont, C., Nguyen, M. H. & Lee, B., 2002. Interaction of metamorphism, deformation and exhumation in large convergent orogens. *Journal of Metamorphic Geology*, **20**(1), 9-24.
- Jamieson, R. A., Beaumont, C., Medvedev, S. & Nguyen, M. H., 2004. Crustal channel flows: 2. Numerical models with implications for metamorphism in the Himalayan-Tibetan orogen. *Journal of Geophysical Research*, **109**, B06407.
- Janoušek, V., Finger, F., Roberts, M. P., Frýda, J., Pin, C. & Dolejš, D., 2004. Deciphering the petrogenesis of deeply buried granites: whole-rock geochemical constraints on the origin of largely undepleted felsic granulites from the Moldanubian Zone of the Bohemian Massif. *Transactions of the Royal Society of Edinburgh, Earth Sciences*, **95**, 141-160.
- Janoušek, V., Hanzl, P., Aichler, J., Pecina, V., Erban, V., Wilimský, D., Žáček, V., Mixa, P., Buriánková, K., Pudilová, M. & Chlupáčová, M., 2006. Contrasting Petrogenesis of two Volcanic Suites in the Devonian Vrbno Group (Hrubý Jeseník Mts., Czech Republic). *Geolines*, **20**, 57-59.
- Janoušek, V. & Holub, F. V., 2007. The causal link between HP/HT metamorphism and ultrapotassic magmatism in collisional orogens: case study from the Moldanubian Zone of the Bohemian Massif. *Proceedings of the Geologists' Association*, **118**, 75-86.
- Jastrzębski, M., 2002. Tectonometamorphic Evolution of the Krzyżnik Mt. Region, the Łądek-Śnieżnik Metamorphic Unit, West Sudetes. *Geolines*, **14**, 40-41.
- Jastrzębski, M., 2005. The tectonometamorphic evolution of the marbles in the Łądek-Śnieżnik Metamorphic Unit, West Sudetes. *Geologia Sudetica*, **37**, 1-26.
- Jastrzębski, M., 2008. A Variscan continental collision of the West Sudetes and the Brunovistulian terrane: a contribution from structural and metamorphic record of the Stronie Formation, the Orlica-Śnieżnik Dome, SW Poland. *International Journal of Earth Sciences*, **8**, 1901-1923
- Jastrzębski, M., Żelaźniewicz, A., Nowak, I., Murtezi, M. & Larionov, A., 2010. Protolith age and provenance of metasedimentary rocks in Variscan allochthon units: U-Pb SHRIMP zircon data from the Orlica-Śnieżnik Dome, West Sudetes. *Geological Magazine*, **147**(3), 416-433.
- Jeffery, G. B., 1922. The motion of ellipsoidal particles immersed in a viscous fluid. *Proceedings of the Royal Society, London*, **102**(715), 161-179.
- Jessup, M. J., Law, R. D., Searle, M. P. & Hubbard, M. S., 2006. Structural evolution and vorticity of flow during extrusion and exhumation of the Greater Himalayan Slab, Mount Everest Massif, Tibet/Nepal: implications for orogen-scale flow partitioning. In: *Channel flow, Extrusion, and Exhumation in Continental Collision Zones* (eds Law, R. D., Searle, M. P. & Godin, L.), **268**, 379-413, Geological Society Special Publication, London.

- Ježek, J., Schulmann, K. & Segeth, K., 1996. Fabric evolution of rigid inclusions during mixed coaxial and simple shear flows. *Tectonophysics*, **257**, 203–221.
- Jiang, D., 2001. Reading history of folding from porphyroblasts. *Journal of Structural Geology*, **23**(9), 1327-1335.
- Johnson, S. E., 1990. Lack of porphyroblast rotation in the Otago schists, New Zealand; implications for crenulation cleavage development, folding and deformation partitioning. *Journal of Metamorphic Geology*, **8**(1), 13-30.
- Johnson, S. E. & Vernon, R. H., 1995. Stepping stones and pitfalls in the determination of an anticlockwise P-T-t-deformation path: the low-P, high-T Cooma Complex, Australia. *Journal of Metamorphic Geology*, **13**, 165-183.
- Johnson, S. E., Dupee, M. E. & Guidotti, C. V., 2006. Porphyroblast rotation during crenulation cleavage development: an example from the aureole of the Mooselookmeguntic pluton, Maine, USA. *Journal of Metamorphic Geology*, **24**, 55-73.
- Johnston, S. T. & Canil, D., 2007. Crustal architecture of SW Yukon, northern Cordillera: Implications for crustal growth in a convergent margin orogen. *Tectonics*, **26**(1), TC1006.
- Józefiak, D., 1999. Preliminary Data on P-T Conditions of Metamorphism of Metapelites from the Stronie Group (Orlica-Śnieżnik Dome, Sudetes, SW Poland). *Geolines*, **8**, 33.
- Jung, J., 1928. Contribution à la géologie des Vosges hercyniennes d'Alsace. *Mémoires du Service de la Carte géologique d'Alsace-Lorraine*, **2**, 463 p.
- Jung, W. S., Ree, J. H. & Park, Y., 1999. Non-rotation of garnet porphyroblasts and 3-D inclusion trail data; an example from the Imjingang Belt, South Korea. *Tectonophysics*, **307**(3-4), 381-395.
- Juteau, T., 1971. Nouvelles données cartographiques, pétrographiques et chimiques sur le massif dévono-dinantien du Rabodeau (Vosges septentrionales). Pétrogénèse d'une série spilite-kératophyre « hercynotype » complexe. *Sciences de la Terre*, **16**(1), 45-106.
- Kalt, A., Hanel, M., Schleicher, H. & Kramm, U., 1994. Petrology and geochronology of eclogites from the Variscan Schwarzwald (F.R.G.). *Contributions to Mineralogy and Petrology*, **115**, 287-302.
- Kalvoda, J., Bábek, O., Fatka, O., Leichmann, J., Melichar, R., Nehiba, S. & Spacek, P., 2008. Brunovistulian terrane (Bohemian Massif, Central Europe) from late Proterozoic to late Paleozoic: a review. *International Journal of Earth Sciences*, **97**, 497-518.
- Kam, M., 1983. *Etude pétrologique et géochimique de la « ligne des klippen » (Vosges méridionales)*. Mémoire de DEA, Université Louis Pasteur, Strasbourg, 72 p.
- Kasza, L., 1964. Budowa geologiczna górnego dorzecza Białej Łądeckiej. *Geologia Sudetica*, **1**, 119-167.
- Kelsey, D. E. & Powell, R., 2011. Progress in linking accessory mineral growth and breakdown to major mineral evolution in metamorphic rocks: a thermodynamic approach in the Na₂O-CaO-K₂O-FeO-MgO-Al₂O₃-SiO₂-H₂O-TiO₂-ZrO₂ system. *Journal of Metamorphic Geology*, **29**, 151-166.
- Kemnitz, H., Romer, R. L. & Oncken, O., 2002. Gondwana breakup and the northern margin of the Saxothuringian belt (Variscides of Central Europe). *Geologische Rundschau*, **91**, 246-259.
- Kim, H. S. & Bell, T. H., 2005. Combining compositional zoning and foliation intersection axes (FIAs) in garnet to quantitatively determine early P-T-t paths in multiply deformed and metamorphosed schists: north central Massachusetts, USA. *Contributions to Mineralogy and Petrology*, **149**, 141-163.

- Kingsbury, J. A., Miller, C. F., Wooden, J. L. & Harrison, T. M., 1993. Monazite paragenesis and U–Pb systematics in rocks of the eastern Mojave Desert, California, U.S.A.: implications for thermochronometry. *Chemical Geology*, **110**, 147-168.
- Klápová, H., Konopásek, J. & Schulmann, K., 1998. Eclogites from the Czech part of the Erzgebirge: multi-stage metamorphic and structural evolution. *Journal of the Geological Society*, **155**, 567-583.
- Klemd, R. & Brocker, M., 1999. Fluid influence on mineral reactions in ultrahigh-pressure granulites: a case study in the Śnieżnik Mts. (West Sudetes, Poland). *Contributions to Mineralogy and Petrology*, **136**(4), 358-373.
- Kober, B., Kalt, A., Hanel, M. & Pidgeon, R. T., 2004. SHRIMP dating of zircons from high-grade metasediments of the Schwarzwald/SW-Germany and implications for the evolution of the Moldanubian basement. *Contributions to Mineralogy and Petrology*, **147**, 330-345.
- Kohn, M. J. & Malloy, M. A., 2004. Formation of monazite via prograde metamorphic reactions among common silicates: implications for age determinations. *Geochimica et Cosmochimica Acta*, **68**, 101-113.
- Kossmat, F., 1927. Gliederung der varistischen Gebirgsbaues. *Abhandlungen des Sächsischen Geologischen Landesamts*, **1**, 1-39.
- Kotoková, J., 2007. High-pressure granulites of the Bohemian Massif: recent advances and open questions. *Journal of Geosciences*, **52**, 45-71.
- Koyi, H. A., Milnes, A. G., Schmeling, H., Talbot, C. J., Juhlin, C. & Zeyen, H., 1999. Numerical models of ductile rebound of crustal roots beneath mountain belts. *Geophysical Journal International*, **139**(2), 556-562.
- Kozłowska-Koch, M., 1973. Polimetamorfity strefy tektonicznej Złoty Stok-Skrzynka w Sudetach. *Geologia Sudetica*, **8**, 121-160.
- Kozłowski, K., 1965. The granulitic complex of Stary Gieraltów - East Sudetes. *Archiwum Mineralogiczne*, **25**, 5-112.
- Kratinová, Z., Zavada, P., Hrouda, F. & Schulmann, K., 2006. Non-scaled analogue modelling of AMS development during viscous flow: A simulation on diapir-like structures. *Tectonophysics*, **418**(1-2), 51-61.
- Kratinová, Z., Schulmann, K., Edel, J.-B. & Ježek, J., 2007. Model of successive granite sheet emplacement in transtensional setting: Integrated microstructural and anisotropy of magnetic susceptibility study. *Tectonics*, **26**, TC6003.
- Kratinová, Z., Schulmann, K., Edel, J.-B. & Tabaud, A.-S., 2011. AMS record of brittle dilation, viscous stretching and gravity driven magma ascent in area of magma rich crustal extension (Vosges Mts., NE France). *International Journal of Earth Sciences*, in press.
- Krecher, M., 2005. *Die Turbiditsandstein-Komplexe der devono-karbonischen Markstein Gruppe im Oberelsass (NE-Frankreich) und ihre Beziehungen zu den moldanubischen Gesteinseinheiten von Schwarzwald und Vogesen*. Dissertation, Albert-Ludwigs-Universität, Freiburg im Breisgau, 386 p.
- Krecher, M. & Behrmann, J. H., 2007. Tectonics of the Vosges (NE France) and the Schwarzwald (SW Germany): evidence from Devonian-Carboniferous active margin basins and their deformation. *Geotectonic Research*, **95**, 61-86.
- Krecher, M., Behrmann, J. H. & Müller-Sigmund, H., 2007. Sedimentology and tectonic setting of Devonian-Carboniferous turbidites and debris flow deposits in the Variscan Vosges Mountains (Markstein Group, NE-France). *Zeitschrift der Deutschen Gesellschaft für Geowissenschaften*, **158**(4), 1063-1087.

- Krenn, E. & Finger, F., 2007. Formation of monazite and rhabdophane at the expense of allanite during Alpine low temperature retrogression of metapelitic basement rocks from Crete, Greece: Microprobe data and geochronological implications. *Lithos*, **95**, 130-147.
- Kretz, R., 1983. Symbols for rock forming minerals. *American Mineralogist*, **68**, 277-279.
- Kriegsman, L. M., 2001. Quantitative field methods for estimating melt production and melt loss. *Physics and Chemistry of the Earth, Part a-Solid Earth and Geodesy*, **26**(4-5), 247-253.
- Krohe, A. & Eisbacher, G. H., 1988. Oblique crustal detachment in the Variscan Schwarzwald, southwestern Germany. *Geologische Rundschau*, **77**(1), 25-43.
- Kröner, A. & Hegner, E., 1998. Geochemistry, single zircon ages and Sm-Nd systematics of granitoid rocks from the Góry Sowie (Owl Mts, polish West Sudetes): evidence for early Palaeozoic arc-related plutonism. *Journal of the Geological Society, London*, **155**, 711-724.
- Kröner, A. & Willner, A. P., 1998. Time of formation and peak of Variscan HP-HT metamorphism of quartz-feldspar rocks in the central Erzgebirge, Saxony, Germany. *Contributions to Mineralogy and Petrology*, **132**(1), 1-20.
- Kröner, A., O'Brien, P. J., Nemchin, A. A. & Pidgeon, R. T., 2000a. Zircon ages for high pressure granulites from South Bohemia, Czech Republic, and their connection to Carboniferous high temperature processes. *Contributions to Mineralogy and Petrology*, **138**(2), 127-142.
- Kröner, A., Štípská, P., Schulmann, K. & Jaeckel, P., 2000b. Chronological constraints on the pre-Variscan evolution of the northeastern margin of the Bohemian Massif, Czech Republic. In: *Orogenic processes; quantification and modelling in the Variscan Belt* (eds Franke, W., Haak, V., Oncken, O. & Tanner, D.), **179**, 175-197, Geological Society Special Publication, London.
- Kröner, A., Jaeckel, P., Hegner, E. & Opletal, M., 2001. Single zircon ages and whole rock Nd isotopic systematics of early Palaeozoic granitoid gneisses from the Czech and Polish Sudetes (Jizerské hory, Krkonoše Mountains and Orlica-Sněžník Complex). *International Journal of Earth Sciences*, **90**(2), 304-324.
- Kruckenbergh, S. C., Vanderhaeghe, O., Ferré, E. C., Teyssier, C. & Whitney, D. L., 2011. Flow of partially molten crust and the internal dynamics of a migmatite dome, Naxos, Greece. *Tectonics*, **30**, TC3001.
- Kryza, R., Muszinski, A. & Vielzeuf, D., 1990. Glaucofane-bearing assemblage overprinted by greenschist-facies metamorphism in the Variscan Kaczawa complex, Sudetes, Poland. *Journal of Metamorphic Geology*, **8**, 345-355.
- Kryza, R., 1995. Western Sudetes (Lugicum): Igneous Activity. In: *Pre-Permian Geology of Central and Eastern Europe* (eds Dallmeyer, R. D., Franke, W. & Weber, K.), 341-350, Springer, Berlin.
- Kryza, R. & Mazur, S., 1995. Contrasting metamorphic paths in the SE part of the Karkonosze-Izera block (Western Sudetes, SW Poland). *Neues Jahrbuch für Mineralogie, Abhandlungen*, **169**, 157-192.
- Kryza, R., Pin, C. & Vielzeuf, D., 1996. High-pressure granulites from the Sudetes (south-west Poland): evidence of crustal subduction and collisional thickening in the Variscan Belt. *Journal of Metamorphic Geology*, **14**, 531-546.
- Kryza, R., Mazur, S., Aleksandrowski, P., Zalasiewicz, J., Sergeev, S. & Presnyakov, S., 2007. Early Palaeozoic initial-rift volcanism in the Central European Variscides (the Kaczawa Mountains, Sudetes, SW Poland): evidence from SIMS dating of zircons. *Journal of the Geological Society, London*, **164**, 1207-1215.
- Kryza, R. & Zalasiewicz, J., 2008. Records of Precambrian–Early Palaeozoic volcanic and sedimentary processes in the Central European Variscides: A review of SHRIMP zircon data from the Kaczawa succession (Sudetes, SW Poland). *Tectonophysics*, **461**, 60-71.

- Kusiak, M., Suzuki, K., Dunkley, D. J., Lekki, J., Bakun-Czubarow, N., Paszkowski, M. & Budzyń, B., 2008. EPMA and PIXE dating of monazite in granulites from Stary Gierałtów, NE Bohemian Massif, Poland. *Gondwana Research*, **14**, 675-685.
- Lange, U., Bröcker, M., Mezger, K. & Don, J., 2002. Geochemistry and Rb-Sr geochronology of a ductile shear zone in the Orlica-Śnieżnik dome (West Sudetes, Poland). *International Journal of Earth Sciences*, **91**(6), 1005-1016.
- Lange, U., Brocker, M., Armstrong, R., Trapp, E. & Mezger, K., 2005a. Sm-Nd and U-Pb dating of high-pressure granulites from the Złote and Rychleby Mts (Bohemian Massif, Poland and Czech Republic). *Journal of Metamorphic Geology*, **23**(3), 133-145.
- Lange, U., Brocker, M., Armstrong, R., Żelaźniewicz, A., Trapp, E. & Mezger, K., 2005b. The orthogneisses of the Orlica-Śnieżnik complex (West Sudetes, Poland): geochemical characteristics, the importance of pre-Variscan migmatization and constraints on the cooling history. *Journal of the Geological Society, London*, **162**, 973-984.
- Lardeaux, J. M., Ledru, P., Daniel, I. & Duchene, S., 2001. The Variscan French Massif Central - a new addition to the ultrahigh pressure metamorphic 'club': exhumation processes and geodynamic consequences. *Tectonophysics*, **332**(1-2), 143-167.
- Latouche, L., Fabries, J. & Guiraud, M., 1992. Retrograde evolution in the Central Vosges mountains (north-eastern France): implications for the metamorphic history of high-grade rocks during the Variscan orogeny. *Tectonophysics*, **205**, 387-407.
- Laubacher, G. & von Eller, J.-P., 1966. Contribution à l'étude géologique des dépôts permien du bassin de Villé. *Bulletin du Service de la Carte Géologique d'Alsace-Lorraine*, **19**(2), 163-186.
- Le Pichon, X., 1968. Sea-floor spreading and continental drift. *Journal of Geophysical Research*, **73**, 3661-3697.
- Lefevre, C., Lakhri, M. & Schneider, J.-L., 1994. Les affinités magmatiques du volcanisme dinantien des Vosges méridionales (France) ; approche géochimique et interprétation. *Comptes Rendus de l'Académie des Sciences*, **319**, 79-86.
- Lehmann, J., Schulmann, K., Lexa, O., Corsini, M., Kröner, A., Štípská, P., Tomurhuu, D. & Otgonbator, D., 2010. Structural constraints on the evolution of the Central Asian Orogenic Belt in Southern Mongolia. *American Journal of Science*, **310**, 575-628.
- Leloix, C., Faure, M. & Feybesse, J.-L., 1999. Hercynian polyphase tectonics in the northeast French Massif Central: the closure of the Brévenne Devonian-Dinantian rift. *International Journal of Earth Sciences*, **88**, 409-421.
- Lemoine, M., Tricart, P. & Boillot, G., 1987. Ultramafic and gabbroic ocean floor of the Ligurian Tethys (Alps, Corsica, Apennines): In search of a genetic model. *Geology*, **15**, 622-625.
- Leveridge, B. E. & Hartley, A. J., 2006. The Variscan Orogeny: the development and deformation of Devonian/Carboniferous basins in SW England and South Wales. In: *The Geology of England and Wales* (eds Brenchley, P. J. & Rawson, P. F.), 225-255, Geological Society, London.
- Lexa, O., Štípská, P., Schulmann, K., Baratoux, L. & Kroner, A., 2005. Contrasting textural record of two distinct metamorphic events of similar P-T conditions and different durations. *Journal of Metamorphic Geology*, **23**(8), 649-666.
- Lexa, O., Schulmann, K., Janoušek, V., Štípská, P., Guy, A. & Racek, M., 2011. Heat sources and trigger mechanisms of exhumation of HP granulites in Variscan orogenic root. *Journal of Metamorphic Geology*, **29**, 79-102.
- Linck, G., 1892. Geognostische Beschreibung des Thalhorns im oberen Amariner Thal. *Mitteilungen der geologischen Landesanstalt von Elsass-Lothringen*, **4**, 1-72.

- Linnemann, U., Gehmlich, M., Tichomirowa, M., Buschmann, B., Nasdala, L., Jonas, P., Lützner, H. & Bombach, K., 2000. From Cadomian subduction to Early Palaeozoic rifting: the evolution of Saxo-Thuringia at the margin of Gondwana in the light of single zircon geochronology and basin development (Central European Variscides, Germany). In: *Orogenic Processes: Quantification and Modelling in the Variscan Belt* (eds Franke, W., Haak, V., Oncken, O. & Tanner, D.), **179**, 131-153, Geological Society Special Publication, London.
- Linnemann, U., McNaughton, N. J., Romer, R. L., Gehmlich, M., Drost, K. & Tonk, C., 2004. West African provenance for Saxo-Thuringia (Bohemian Massif): did Armorica ever leave pre-Pangean Gondwana?—U–Pb–SHRIMP zircon evidence and the Nd isotopic record. *International Journal of Earth Sciences*, **93**, 683-705.
- Lippolt, H. J. & Hess, J. C., 1983. Isotopic evidence for the stratigraphic position of the Saar-Nahe Rotliegend volcanism I. $^{40}\text{Ar}/^{40}\text{K}$ and $^{40}\text{Ar}/^{39}\text{Ar}$ investigations. *Neues Jahrbuch für Geologie und Paläontologie, Monatshefte*, **12**, 713-730.
- Lippolt, H. J., Schleicher, H. & Raczek, I., 1983. Rb-Sr systematics of Permian volcanites un the Schwarzwald (SW-Germany) Part I: space of time between plutonism and late orogenic volcanism. *Contributions to Mineralogy and Petrology*, **84**, 272-280.
- Lister, G. S. & Williams, P. F., 1983. The partitioning of deformation in flowing rock masses. *Tectonophysics*, **92**, 1-33.
- Loeschke, J., Güldenpfennig, M., Hann, H. P. & Sawatzki, G., 1998. Die Zone von Badenweiler-Lenzkirch (Schwarzwald): Eine variskische Suturzzone. *Zeitschrift der deutschen geologischen Gesellschaft*, **149**(2), 197-212.
- Ludwig, K. R., 2004. Users manual for ISOPLOT/EX, version 3.1. A geochronological toolkit for Microsoft Excel. *Berkeley Geochronology Center, Special Publication*, **4**.
- Maass, R. & Stoppel, D., 1982. Nachweis von Oberdevon bei Markstein (Bl. Munster, Südvogesen). *Zeitschrift der Deutschen Geologischen Gesellschaft*, **133**, 403-408.
- Maass, R., Prosch, T. & Schuler, D., 1990. The zone of Badenweiler-Lenzkirch – a Carboniferous accretionary wedge? *Neues Jahrbuch für Geologie und Paläontologie, Monatshefte*, **12**, 717-734.
- Mahar, E. M., Baker, J. M., Powell, R., Holland, T. J. B. & Howell, N., 1997. The effect of Mn on mineral stability in metapelites. *Journal of Metamorphic Geology*, **15**(2), 223-238.
- Mainprice, D., 2005. PFch5 [Computer software], ftp://www.gm.univmontp2.fr/mainprice//CareWare_Unicef_Programs/.
- Maluski, H., Rajlich, P. & Souček, J., 1995. Pre-Variscan, Variscan and early Alpine thermo-tectonic history of the northeastern Bohemian Massif: an $^{40}\text{Ar}/^{39}\text{Ar}$ study. *Geologische Rundschau*, **84**, 345-358.
- Maluski, H. & Patočka, F., 1997. Geochemistry and $^{40}\text{Ar}/^{39}\text{Ar}$ geochronology of the mafic metavolcanic rocks from the Rýchory Mountains complex (west Sudetes, Bohemian Massif): Paleotectonic significance. *Geological Magazine*, **134**, 703-716.
- Manatschal, G. & Müntener, O., 2009. A type sequence across an ancient magma-poor ocean–continent transition: the example of the western Alpine Tethys ophiolites. *Tectonophysics*, **473**, 4-19.
- Maruyama, S. & Liou, J. G., 1988. Petrology of Franciscan metabasites along the jadeite-glaucophane type facies series, Cazadero, California. *Journal of Petrology*, **29**, 1-37.
- Massonne, H.-J. & Schreyer, W., 1983. A new experimental phengite barometer and its application to a variscan subduction zone at the southern margin of the Rhenohercynicum. *Terra Cognita*, **3**, 187.

- Mathieu, G., 1968. Observations stratigraphiques, sédimentologiques et structurales sur le bassin houiller de Ronchamp-St-Germain-Momont. *Travaux de l'Institut de Géologie et d'Anthropologie préhistorique de la Faculté des Sciences de Poitiers*, **9**, 184-213.
- Mattauer, M. & Théobald, N., 1957. Présence de *Lepidostrobus browni* (Unger) Schimper dans le Dinantien de la Haute-Vallée de la Thur. *Bulletin du Service de la Carte Géologique d'Alsace-Lorraine*, **10**(2), 133-142.
- Mattauer, M., 1959. Découverte d'une faune viséenne près de Rimbach (Vosges méridionales). *Comptes Rendus de l'Académie des Sciences*, **248**(3), 433.
- Matte, P., 1986. Tectonics and plate tectonics model for the Variscan Belt of Europe. *Tectonophysics*, **126**, 329-374.
- Matte, P., Maluski, H., Rajlich, P. & Franke, W., 1990. Terrane boundaries in the Bohemian Massif: Result of large-scale Variscan shearing. *Tectonophysics*, **177**, 151-170.
- Matte, P., 1998. Continental subduction and exhumation of HP rocks in Paleozoic orogenic belts: Uralides and Variscides. *Geological Society of Sweden (G.F.F.)*, **120**, 209-222.
- Matte, P., 2001. The Variscan collage and orogeny (480-290 Ma) and the tectonic definition of the Armorica microplate: a review. *Terra Nova*, **13**, 122-128.
- Mazur, S. & Aleksandrowski, P., 2001. The Tepla(?)/Saxothuringian suture in the Karkonosze-Izera massif, western Sudetes, central European Variscides. *International Journal of Earth Sciences*, **90**(2), 341-360.
- Mazur, S., Aleksandrowski, P. & Szczepański, J., 2005. The presumed Teplá-Barrandian/Moldanubian terrane boundary in the Orlica Mountains (Sudetes, Bohemian Massif): structural and petrological characteristics. *Lithos*, **82**, 85-112.
- Mazur, S., Aleksandrowski, P., Kryza, R. & Oberc-Dziedzic, T., 2006. The Variscan Orogen in Poland. *Geological Quarterly*, **50**(1), 89-118.
- Mazur, S., Kröner, A., Szczepański, J., Turniak, K., Hanzl, P., Melichar, R., Rodionov, N. V., Paderin, I. & Sergeev, S. S., 2010. Single zircon U–Pb ages and geochemistry of granitoid gneisses from SW Poland: evidence for an Avalonian affinity of the Brunian microcontinent. *Geological Magazine*, **147**(4), 508-526.
- McFarlane, C. R. M., Connelly, J. N. & Carlson, W. D., 2006. Contrasting response of monazite and zircon to a high-T thermal overprint. *Lithos*, **88**, 135-149.
- McKenzie, D. & Parker, R. L., 1967. The North Pacific: an example of tectonics on a sphere. *Nature*, **216**, 1276-1280.
- McLaren, S., Sandiford, M. & Hand, M., 1999. High radiogenic heat-producing granites and metamorphism - An example from the western Mount Isa inlier, Australia. *Geology*, **27**(8), 679-682.
- Ménot, R. P., Peucat, J.-J., Scarenzi, D. & Piboule, M., 1988. 496 Ma age of plagiogranites in the Chamrousse ophiolite complex (External Crystalline massifs in the French Alps): evidence of a Lower Paleozoic oceanization. *Earth and Planetary Science Letters*, **88**, 82-92.
- Mihara, S., 1935. Etude géologique et pétrographique de la région du Nideck. *Mémoires du Service de la Carte géologique d'Alsace-Lorraine*, **4**, 134 p.
- Milnes, A. G., Wennberg, O. P., Skar, O. & Koestler, A. G., 1997. Contraction, extension and timing in the South Norwegian Caledonides: the Sognefjord transect. In: *Orogeny through time* (eds Burg, J.-P. & Ford, M.), **121**, 123-148, Geological Society Special Publication, London.
- Milnes, A. G. & Koyi, H. A., 2000. Ductile rebound of an orogenic root; case study and numerical model of gravity tectonics in the Western gneiss complex, Caledonides, southern Norway. *Terra Nova*, **12**(1), 1-7.

- Mísař, Z. & Urban, M., 1995. Moravo-Silesian Zone - Introduction. In: *Pre-Permian Geology of Central and Eastern Europe* (eds Dallmeyer, D., Franke, W. & Weber, K.), 469-473, Springer, Berlin.
- Miyashiro, A., 1961. Evolution of metamorphic belt. *Journal of Petrology*, **2**(3), 277-311.
- Mohn, G., Manatschal, G., Masini, E., Müntener, O., 2011. Rift-related inheritance in orogens: A case study from the Austroalpine nappes in Central Alps (SE-Switzerland and N-Italy). *International Journal of Earth Sciences*, **100**(5), 937-961.
- Möller, A., O'Brien, P. J., Kennedy, A. & Kröner, A., 2002. Polyphase zircon in ultrahigh-temperature granulites (Rogaland, SW Norway): constraints for Pb diffusion in zircon. *Journal of Metamorphic Geology*, **20**(8), 727-740.
- Montel, J.-M., Foret, S., Veschambre, M., Nicollet, C. & Provost, A., 1996. A fast, reliable, inexpensive in-situ dating technique: electron microprobe ages on monazite. *Chemical Geology*, **131**, 37-53.
- Montel, J.-M., Kornprobst, J. & Vielzeuf, D., 2000. Preservation of old U-Th-Pb ages in shielded monazite; example from the Benmi Bousera Hercynian kinzigites (Morocco). *Journal of Metamorphic Geology*, **18**, 335-342.
- Montel, J. M. & Vielzeuf, D., 1997. Partial melting of metagreywackes 2. Compositions of minerals and melts. *Contributions to Mineralogy and Petrology*, **128**(2-3), 176-196.
- Montenari, M. & Servais, T., 2000. Early Paleozoic (Late Cambrian-Early Ordovician) acritarchs from the metasedimentary Baden-Baden-Gaggenau zone (Schwarzwald, SW Germany). *Review of Palaeobotany and Palynology*, **113**, 73-85.
- Montenari, M., Leppig, U. & Weyer, D., 2002. Heterocorallia from the Early Carboniferous of the Moldanubian Southern Vosges Mountains (Alsace, France). *Neues Jahrbuch für Geologie und Paläontologie, Abhandlungen*, **224**(2), 223-254.
- Moseley, D., 1981. Ilmenite exsolution in olivine. *American Mineralogist*, **66**, 976-979.
- Müller, H., 1989. Geochemistry of metasediments in the Hercynian and pre-Hercynian crust of the Schwarzwald, the Vosges and Northern Switzerland. *Tectonophysics*, **157**, 97-108.
- Murtezi, M. & Fanning, C. M., 2005. Petrogenesis, Age and Tectono-Metamorphic Evolution of the Acid Metavolcanites of the Stronie Formation (Orlica-Śnieżnik Dome, Sudetes, SW Poland). *Geolines*, **19**, 85.
- Murtezi, M., 2006. The acid meta-volcanic rocks of the Orlica-Śnieżnik Dome (Sudetes): their origin and tectono-metamorphic evolution. *Geologia Sudetica*, **38**, 1-38.
- Nance, R. D., Gutiérrez-Alonso, G., Keppie, J. D., Linnemann, U., Murphy, J. B., Quesada, C., Strachan, R. A. & Woodcock, N. H., 2010. Evolution of the Rheic Ocean. *Gondwana Research*, **17**, 194-222.
- Nemchin, A. A. & Pidgeon, R. T., 1997. Evolution of the Darling range batholith, Yilgarn craton, western Australia: A SHRIMP zircon study. *Journal of Petrology*, **38**(5), 625-649.
- Niu, Y., Gilmore, T., Mackie, S., Greig, A. & Bach, W., 2002. Mineral chemistry, whole-rock compositions, and petrogenesis of Leg 176 gabbros: data and discussion. *Proceedings of the Ocean Drilling Program, Scientific Results*, **176**, 1-56.
- Norlander, B. H., Whitney, D. L., Teyssier, C. & Vanderhaeghe, O., 2002. Partial melting and decompression of the Thor-Odin dome, Shuswap metamorphic core complex, Canadian Cordillera. *Lithos*, **61**(3-4), 103-125.
- Nowak, I. & Żelaźniewicz, A., 2002. Metabasites from the Stronie Schists in the Łądek-Śnieżnik Metamorphic Unit, West Sudetes: Geochemistry and P-T-d Path. *Geolines*, **14**, 72-73.

- O'Brien, P. J., Kröner, A., Jaeckel, P., Hegner, E., Żelaźniewicz, A. & Kryza, R., 1997. Petrological and isotopic studies on palaeozoic high-pressure granulites, Gory Sowie Mts, Polish Sudetes. *Journal of Petrology*, **38**(4), 433-456.
- O'Brien, P. J. & Rötzler, J., 2003. High-pressure granulites: formation, recovery of peak conditions and implications for tectonics. *Journal of Metamorphic Geology*, **21**(1), 3-20.
- Olesen, N. Ø., 1978. Distinguishing between inter-kinematic and syn-kinematic porphyroblastesis. *Geologische Rundschau*, **67**, 278-287.
- Oliver, G. J. H., Corfu, F. & Krogh, T. E., 1993. U-Pb ages from SW Poland: evidence for a Caledonian suture zone between Baltica and Gondwana. *Journal of the Geological Society, London*, **150**, 355-369.
- Oncken, O., 1997. Transformation of a magmatic arc and an orogenic root during oblique collision and its consequences for the evolution of the European Variscide (Mid-German Crystalline Rise). *Geologische Rundschau*, **86**, 2-20.
- Oncken, O., von Winterfeld, C. & Dittmar, U., 1999. Accretion of a rifted passive margin: The Late Paleozoic Rhenohercynian fold and thrust belt (Middle European Variscides). *Tectonics*, **18**(1), 75-91.
- Opletal, M. *et al.*, 1980. *Geologie Orlických hor. Oblastní regionální geologie ČSR*, Ústřední ústav geologický, Praha, , 208 p.
- Overstreet, W. C., 1967. The geologic occurrence of Monazite. *U.S. Geological Survey Professional Paper*, **530**.
- Pagel, M. & Leterrier, J., 1980. The subalkaline potassic magmatism of the Ballons massif (Southern Vosges, France): shoshonitic affinity. *Lithos*, **13**, 1-10.
- Pan, Y., 1997. Zircon- and monazite-forming metamorphic reactions at Manitouwadge, Ontario. *Canadian Mineralogist*, **35**, 105-118.
- Paquette, J.-L., Ménot, R.-P. & Peucat, J.-J., 1989. REE, Sm-Nd and U-Pb zircon study of eclogites from the Alpine External Massifs (Western Alps): evidence for crustal contamination. *Earth and Planetary Science Letters*, **96**, 181-198.
- Paris, F. & Robardet, M., 1990. Early Paleozoic paleogeography of the Variscan regions. *Tectonophysics*, **177**, 193-213.
- Parrish, R. R., 1990. U-Pb dating of monazite and its application to geological problems. *Canadian Journal of Earth Sciences*, **27**, 1431-1450.
- Parry, M., Stipska, P., Schulmann, K., Hrouda, F., Jezek, J. & Kroener, A., 1997. Tonalite sill emplacement at an oblique plate boundary; northeastern margin of the Bohemian Massif. In: *Thermal and mechanical interactions in deep-seated rocks*. (ed Schulmann, K.) *Tectonophysics*, **280**, 61-81, Elsevier, Amsterdam, Netherlands.
- Passchier, C. W., Trouw, R. A. J., Zwart, H. J. & Vissers, R. L. M., 1992. Porphyroblast rotation; eppur si muove? *Journal of Metamorphic Geology*, **10**(3), 283-294.
- Patočka, F. & Valenta, J., 1996. Geochemistry of the Late Devonian intermediate to acid metavolcanic rocks from the southern part of the Vrbno Group in the Jeseníky Mts. (Moravo-Silesian Belt, Bohemian Massif, Czech Republic): paleotectonic implications. *Geolines*, **4**, 42-54.
- Pattison, D. R. M. & Bégin, N. J., 1994. Zoning patterns in orthopyroxene and garnet in granulites - Implications for geothermometry. *Journal of Metamorphic Geology*, **12**(4), 387-410.
- Petrini, K. & Burg, J. P., 1998. Relationships between deformation, plutonism and regional metamorphism in the Markstein area (southern Vosges). *Géologie de la France*, **2**, 13-23.

- Pidgeon, R. T., 1992. Recrystallisation of oscillatory zoned zircon: some geochronological and petrological implications. *Contributions to Mineralogy and Petrology*, **110**, 463-472.
- Pidgeon, R. T., Nemchin, A. A. & Hitchen, G. J., 1998. Internal structures of zircons from Archaean granites from the Darling Range batholith: implications for zircon stability and the interpretation of zircon U-Pb ages. *Contributions to Mineralogy and Petrology*, **132**, 288-299.
- Pin, C. & Carme, F., 1988. Ecailles de matériaux d'origine océanique dans le charriage hercynien de la « Ligne des Klippes », Vosges méridionales (NE France). *Comptes Rendus de l'Académie des Sciences*, **306**, 217-222.
- Pin, C., Majerowicz, A. & Wojciechowska, I., 1988. Upper Palaeozoic oceanic crust in the Polish Sudetes: Nd-Sr isotope and trace element evidence. *Lithos*, **21**, 195-209.
- Pin, C. & Vielzeuf, D., 1988. Les granulites de haute-pression d'Europe moyenne témoins d'une subduction éo-hercynienne. Implications sur l'origine des groupes leptyno-amphiboliques. *Bulletin de la Société Géologique de France*, **4**(1), 13-20.
- Pin, C., 1990. Variscan oceans: Ages, origins and geodynamic implications inferred from geochemical and radiometric data. *Tectonophysics*, **177**, 215-227.
- Pin, C. & Marini, F., 1993. Early Ordovician continental break-up in Variscan Europe: Nd-Sr isotope and trace element evidence from bimodal igneous associations of Southern Massif Central, France. *Lithos*, **29**, 177-196.
- Pin, C. & Paquette, J.-L., 1997. A mantle-derived bimodal suite in the Hercynian Belt: Nd isotope and trace element evidence for a subduction-related rift origin of the Late Devonian Brévenne metavolcanics, Massif Central (France). *Contributions to Mineralogy and Petrology*, **129**, 222-238.
- Pin, C., Fonseca, P. E., Paquette, J.-L., Castro, P. & Matte, P., 2008. The ca. 350 Ma Beja Igneous Complex: A record of transcurrent slab break-off in the Southern Iberia Variscan Belt ? *Tectonophysics*, **461**, 356-377.
- Pitra, P., Ballèvre, M. & Ruffet, G., 2010. Inverted metamorphic field gradient towards a Variscan suture zone (Champtoceaux Complex, Armorican Massif, France). *Journal of Metamorphic Geology*, **28**, 183-208.
- Plank, T. & Langmuir, C. H., 1998. The chemical composition of subducting sediment and its consequences for the crust and mantle. *Chemical Geology*, **145**, 325-394.
- Platt, J. P., 1986. Dynamics of orogenic wedges and the uplift of high-pressure metamorphic rocks. *Bulletin of the Geological Society of America*, **86**, 133-147.
- Platt, J. P., 1993. Exhumation of high-pressure rocks; a review of concepts and processes. *Terra Nova*, **5**(2), 119-133.
- Pommier, A., Cocherie A., and Legendre, O. (2002) EPMA Dating User, 2002. EPMA Dating User's manual: Age calculation from electron probe microanalyser measurements of U-Th-Pb. *BRGM*, 9p.
- Porebski, S. J., 1990. Onset of coarse clastic sedimentation in the Variscan realm of the Sudetes (SW Poland): an example from the Upper Devonian-Lower Carboniferous Świebodzice succession. *Neues Jahrbuch für Geologie und Paläontologie, Abhandlungen*, **179**, 259-274.
- Powell, R., Holland, T. & Worley, B., 1998. Calculating phase diagrams involving solid solutions via non-linear equations, with examples using THERMOCALC. *Journal of Metamorphic Geology*, **16**(4), 577-588.
- Powell, R. & Holland, T. J. B., 1999. Relating formulations of the thermodynamics of mineral solid solutions; activity modeling of pyroxenes, amphiboles, and micas. *American Mineralogist*, **84**, 1-14.

- Prior, D. J., 1987. Syntectonic porphyroblast growth in phyllites: textures and processes. *Journal of Metamorphic Geology*, **5**, 27-39.
- Pyle, J. M. & Spear, F. S., 1999. Yttrium zoning in garnet: coupling of major and accessory phases during metamorphic reactions. *Geological Materials Research*, **1**, 1-49.
- Pyle, J. M., Spear, F. S., Rudnick, R. L. & McDonough, W. F., 2001. Monazite-xenotime-garnet equilibrium in metapelites and a new monazite-garnet thermometer. *Journal of Petrology*, **42**(11), 2083-2107.
- Racek, M., Štípská, P., Pitra, P., Schulmann, K. & Lexa, O., 2006. Metamorphic record of burial and exhumation of orogenic lower and middle crust: a new tectonothermal model for the Drosendorf window (Bohemian Massif, Austria). *Mineralogy and Petrology*, **86**(3-4), 221-251.
- Ramsay, J. G., 1962. The geometry and mechanics of formation of “similar” type folds. *Journal of Geology*, **70**, 309-327.
- Rasmussen, B., Fletcher, I. R. & Muhling, J. R., 2007. In situ U–Pb dating and element mapping of three generations of monazite: unravelling cryptic tectonothermal events in low-grade terranes. *Geochimica et Cosmochimica Acta*, **71**, 670-690.
- Reibel, G. & Wurtz, C. R., 1984. Etude pétrographique et géochimique de la bande médiane volcanique du Champ-du-Feu (Vosges du Nord). *Fortschritte der Mineralogie*, **62**(2), 48-52.
- Reischmann, T. & Anthes, G., 1996. Geochronology of the Mid-German crystalline rise west of the River Rhine. *Geologische Rundschau*, **85**, 761-774.
- Reitz, E. & Wickert, F., 1989. Late Cambrian to early Ordovician acritarchs from the Villé unit, northern Vosges Mountains (France). *Neues Jahrbuch für Geologie und Paläontologie, Monatshefte*, **6**, 375-384.
- Rey, P., Burg, J.-P., Lardeaux, J. M. & Fluck, P., 1989. Evolutions métamorphiques contrastées dans les Vosges orientales: témoins d’un charriage dans la chaîne varisque *Comptes Rendus de l’Académie des Sciences*, **309**, 815–821.
- Rey, P., Burg, J.-P. & Caron, J.-M., 1991. Tectonique extensive ductile et plutonisme viséo-namurien dans les Vosges. *Comptes Rendus de l’Académie des Sciences*, **312**, 1609-1616.
- Rey, P., 1992. *Effondrement de la chaîne varisque dans les Vosges et fabrication sismique de la croûte continentale*. Thèse de doctorat, Université de Grenoble, 284 p.
- Rey, P., Burg, J. P. & Caron, J. M., 1992. Middle and Late Carboniferous extension in the Variscan Belt: structural evidences from the Vosges massif (Eastern France). *Geodinamica Acta*, **5**(1-2), 17-36.
- Rey, P., Burg, J. P. & Casey, M., 1997. The Scandinavian Caledonides and their relationship to the Variscan Belt. In: *Orogeny through time* (eds Burg, J.-P. & Ford, M.), **121**, 179-200, Geological Society Special Publication, London.
- Rey, P., Vanderhaeghe, O. & Teyssier, C., 2001. Gravitational collapse of the continental crust: definition, regimes and modes. *Tectonophysics*, **342**(3-4), 435-449.
- Ribeiro, A., Munhá, J., Fonseca, P. E., Araújo, A., Pedro, J. C., Mateus, A., Tassinari, C., Machado, G. & Jesus, A., 2010. Variscan ophiolite belts in the Ossa-Morena Zone (Southwest Iberia): Geological characterization and geodynamic significance. *Gondwana Research*, **17**, 408-421.
- Richard, P., Shimizu, N. & Allegre, C. J., 1976. $^{143}\text{Nd}/^{146}\text{Nd}$, a natural tracer: An application to oceanic basalts. *Earth and Planetary Science Letters*, **31**, 269-278.

- Ring, U. & Brandon, M. T., 1999. Ductile deformation and mass loss in the Franciscan Subduction Complex: implications for exhumation processes in accretionary wedges. In: *Exhumation processes; normal faulting, ductile flow and erosion* (eds Ring, U., Brandon, M. T., Willett, S. D. & Lister, G. S.), **154**, 55-86, Geological Society Special Publication, London.
- Ring, U., Brandon, M. T., Willett, S. D. & Lister, G. S., 1999. Exhumation processes. In: *Exhumation processes; normal faulting, ductile flow and erosion* (eds Ring, U., Brandon, M. T., Lister, G. S. & Willett, S. D.), **154**, 1-27, Geological Society Special Publication, London.
- Rizki, A. & Baroz, F., 1988. Le volcanisme tholéïtique du massif de Schirmeck (Vosges septentrionales, France), témoin d'une zone de convergence de plaques au Paléozoïque supérieur. *Comptes Rendus de l'Académie des Sciences*, **307**, 511-516.
- Rizki, A., Deschamps, M., Baroz, F. & Bebien, J., 1992. Le volcanisme de la bande médiane du Champ du Feu : sa place et sa signification dans le magmatisme dévono-dinantien des Vosges septentrionales. *Comptes Rendus de l'Académie des Sciences*, **315**, 995-1001.
- Roberts, M. P. & Finger, F., 1997. Do U-Pb zircon ages from granulites reflect peak metamorphic conditions? *Geology*, **25**(4), 319-322.
- Roberts, S., Andrews, J. R., Bull, J. M. & Sanderson, D. J., 1993. Slow-spreading ridge-axis tectonics: evidence from the Lizard Complex, U.K. *Earth and Planetary Science Letters*, **116**, 101-112.
- Roby, M., Vonlanthen, P., Baumgartner, L. P. & Grobety, B., 2007. Growth mechanism of snowball garnets from the Lukmanier Pass area (Central Alps, Switzerland): a combined ICT/EPMA/EBSD study. *Terra Nova*, **19**, 240-244.
- Romanová, M. & Štípská, P., 2001. Structural and metamorphic evolution of the Stronie formation near Javorník. *Mineralogical Society of Poland, Special Papers*, **19**, 147-149.
- Rosenbuch, H., 1877. Die Steiger Schiefer und ihre Kontaktzone an den Granititen von Barr-Andlau und Hohwald. *Abhandlungen zur geologischen Spezialkarte von Elsass-Lothringen*, **1**(2), 79-393.
- Ross, P. H., 1964. Fossilfunde in den Steiger und Weiler Schiefen (Vogesen). *Nachrichten der Akademie der Wissenschaften zu Göttingen, Math-Phys. Kl.*, **3**, 37-43.
- Rossi, P. & Oggiano, G., 2009. A restored section of the "southern Variscan realm" across the Corsica-Sardinia microcontinent. *Comptes Rendus Géoscience*, **341**, 224-238.
- Rothé, J.-P., 1960. Carte radiogéologique des Vosges hercyniennes – Feuille de Munster. *Bulletin du Service de la Carte Géologique d'Alsace-Lorraine*, **13**(2), 75-94.
- Rothé, J.-P., 1961. Carte radiogéologique des Vosges hercyniennes – Feuille de Gérardmer. *Bulletin du Service de la Carte Géologique d'Alsace-Lorraine*, **14**(3), 73-86.
- Rothé, J.-P., 1962. Carte radiogéologique des Vosges hercyniennes – Feuille de Thann. *Bulletin du Service de la Carte Géologique d'Alsace-Lorraine*, **15**(1), 1-14.
- Rubatto, D. & Hermann, J., 2001. Exhumation as fast as subduction? *Geology*, **29**(1), 3-6.
- Rubatto, D., 2002. Zircon trace element geochemistry: partitioning with garnet and the link between U-Pb ages and metamorphism. *Chemical Geology*, **184**, 123-138.
- Rubatto, D., Williams, I.S., Buick, I.S., 2001. Zircon and monazite response to prograde metamorphism in the Reynolds Range, central Australia. *Contributions to Mineralogy and Petrology*, **140**(4), 458-468.
- Ruhland, M., 1958. Allure des plis et plis à axes subverticaux dans les terrains primaires des Vosges méridionales. *Bulletin du Service de la Carte Géologique d'Alsace-Lorraine*, **11**(2), 45-50.
- Ruhland, M. & Bronner, G., 1965. Caractères structuraux des schistes de Steige et des schistes de Villé. *Bulletin du Service de la Carte Géologique d'Alsace-Lorraine*, **18**(2), 91-110.

- Ruppel, C. & Hodges, K. V., 1994. Pressure-temperature-time paths from two-dimensional thermal models: prograde, retrograde and inverted metamorphism. *Tectonics*, **13**, 17-44.
- Sawatzki, G., Vaida, M. & Hann, H. P., 1997. Altpaläozoische Chitinozoen und Acritarchen in Gneisen des Südschwarzwaldes, SW-Deutschland. *Neues Jahrbuch für Geologie und Paläontologie, Monatshefte*, **3**, 165-178.
- Sawatzki, G. & Hann, H. P., 2003. Geologische Karte von Baden-Württemberg 1:50000, Blatt Badenweiler-Lenzkirch Zone. Landesamt für Geologie, Rohstoffe und Bergbau Baden-Württemberg.
- Sawyer, E. W., 1994. Melt segregation in the continental crust. *Geology*, **22**, 1019–1022.
- Schäfer, F., Oncken, O., Kemnitz, H. & Romer, R. L., 2000. Upper-plate deformation during collisional orogeny: a case study from the German Variscides (Saxo-Thuringian Zone). In: *Orogenic Processes: Quantification and Modelling in the Variscan Belt* (eds Franke, W., Haak, V., Oncken, O. & Tanner, D.), **179**, 281-302, Geological Society Special Publication, London.
- Schaltegger, U., Schneider, J.-L., Maurin, J.-C. & Corfu, F., 1996. Precise U-Pb chronometry of 345–340 Ma old magmatism related to syn-convergence extension in the Southern Vosges (Central Variscan Belt). *Earth and Planetary Sciences Letters*, **144**, 403–419.
- Schaltegger, U., Fanning, C. M., Günther, D., Maurin, J. C., Schulmann, K. & Gebauer, D., 1999. Growth, annealing and recrystallization of zircon and preservation of monazite in high-grade metamorphism: conventional and in situ U-Pb isotope, cathodoluminescence and microchemical evidence. *Contributions to Mineralogy and Petrology*, **134**, 186–201.
- Schätz, M., Reischmann, T., Tait, J., Bachtadse, V., Bahlburg, H. & Martin, U., 2002. The Early Palaeozoic break-up of northern Gondwana, new palaeomagnetic and geochronological data from the Saxothuringian Basin, Germany. *International Journal of Earth Sciences*, **91**, 838-849.
- Scheidegger, A. E., 1965. On the statistics of the orientation of bedding planes, grain axes, and similar sedimentological data. *U.S. Geological Survey Professional Paper*, **525(C)**, 164-167.
- Schiffman, P. & Day, H. W., 1999. Petrological methods for the study of very low-grade metabasites. In: *Low-grade metamorphism* (eds Frey, M. & Robinson, D.), 108-142, Blackwell Science, Oxford.
- Schleicher, H., Lippolt, H. J. & Raczek, I., 1983. Rb-Sr systematics of Permian volcanites in the Schwarzwald (SW-Germany) Part II: age of eruption and the mechanism of Rb-Sr whole rock age distortions. *Contributions to Mineralogy and Petrology*, **84**, 281-291.
- Schlunegger, F. & Willett, S. D., 1999. Spatial and temporal variations in exhumation of the central Swiss Alps and implications for exhumation mechanisms. In: *Exhumation processes; normal faulting, ductile flow and erosion* (eds Ring, U., Brandon Mark, T., Lister Gordon, S. & Willett Sean, D.), **154**, 157-179, Geological Society Special Publication, London.
- Schmädicke, E., Mezger, K., Cosca, M. A. & Okrusch, M., 1995. Variscan Sm–Nd and Ar–Ar ages of eclogite facies rocks from the Erzgebirge, Bohemian Massif. *Journal of Metamorphic Geology*, **13**, 537-552.
- Schneider, D. A., Zahniser, S. J., Glascock, J. M., Gordon, S. M. & Manecki, M., 2006. Thermochronology of the West sudetes (Bohemian Massif): rapid and repeated exhumation in the eastern Variscides, Poland and Czech Republic. *American Journal of Science*, **306**, 846-873.
- Schneider, J.-L., 1990. *Enregistrement de la dynamique varisque dans les bassins volcano-sédimentaires dévono-dinantiens : exemple des Vosges du Sud (zone moldanubienne)*. Thèse de doctorat, Université de Strasbourg, 222 p.

- Schneider, J.-L., Hassenforder, B. & Paicheler, J.-C., 1990. Une ou plusieurs «Ligne des Klippes» dans les Vosges du Sud (France) ? Nouvelles données sur la nature des « klippes » et leur signification dans la dynamique varisque. *Comptes Rendus de l'Academie des Sciences*, **311**, 1221-1226.
- Schneider, J.-L., Maass, R., Gall, J. C. & Düringer, P., 1989. L'événement intraviséen dans la zone moldanubienne de la chaîne varisque d'Europe : les données des formations volcano-sédimentaires dévono-dinantiennes du Massif Central Français, des Vosges du Sud (France) et de la Forêt Noire (R.F.A.). *Geologische Rundschau*, **78**(2), 555-570.
- Schulmann, K. & Gayer, R., 2000. A model for a continental accretionary wedge developed by oblique collision: the NE Bohemian Massif. *Journal of the Geological Society, London*, **157**, 401-416.
- Schulmann, K., Schaltegger, U., Ježek, J., Thompson, A. B. & Edel, J. B., 2002. Rapid burial and exhumation during orogeny: Thickening and synconvergent exhumation of thermally weakened and thinned crust (Variscan orogen in Western Europe). *American Journal of Science*, **302**(10), 856-879.
- Schulmann, K., Kröner, A., Hegner, E., Wendt, I., Konopásek, J., Lexa, O. & Štípská, P., 2005. Chronological constraints on the pre-orogenic history, burial and exhumation of deep-seated rocks along the eastern margin of the Variscan orogen, Bohemian Massif, Czech Republic. *American Journal of Science*, **305**, 407-448.
- Schulmann, K., Lexa, O., Štípská, P., Racek, M., Tajčmanová, L., Konopásek, J., Edel, J. B., Peschler, A. & Lehmann, J., 2008. Vertical extrusion and horizontal channel flow of orogenic lower crust: key exhumation mechanisms in large hot orogens? *Journal of Metamorphic Geology*, **26**, 273–297.
- Schulmann, K., Edel, J.-B., Hasalová, P., Cosgrove, J., Ježek, J. & Lexa, O., 2009a. Influence of melt induced mechanical anisotropy on the magnetic fabrics and rheology of deforming migmatites, Central Vosges, France. *Journal of Structural Geology*, **31**(10), 1223-1237.
- Schulmann, K., Konopásek, J., Janoušek, V., Lexa, O., Lardeaux, J.-M., Edel, J.-B., Štípská, P. & Ulrich, S., 2009b. An Andean type Palaeozoic convergence in the Bohemian Massif. *Comptes Rendus Geoscience*, **341**, 266-286.
- Schulmann, K., Edel, J.-B., Lexa, O., Janoušek, V., Shail, R. K., Leveridge, B. E. & Scrivener, R., 2011. Linking Rheno-Hercynian ocean and Variscan root processes in the Bohemian Massif. *Travaux Géophysiques*, **40**, 72.
- Schulmann, K. & Ježek, J., 2011. Some remarks on fabric overprints and constrictional AMS fabrics in igneous rocks. *International Journal of Earth Sciences*, in press.
- Seston, R., Winchester, J. A., Piasecki, M. A. J., Crowley, Q. G. & Floyd, P. A., 2000. A structural model for the western-central Sudetes: a deformed stack of Variscan thrust sheets. *Journal of the Geological Society, London*, **157**, 1155-1167.
- Shail, R. K. & Leveridge, B. E., 2009. The Rhenohercynian passive margin of SW England: Development, inversion and extensional reactivation. *Comptes Rendus Géoscience*, **341**, 140-155.
- Sittig, E., 1965. Der geologische Bau des variszischen Sockels nordöstlich von Baden-Baden (Nordschwarzwald). *Oberrheinische geologische Abhandlungen*, **14**, 167-207.
- Sleep, N. H., 1979. A Thermal Constraint on the Duration of Folding with Reference to Acadian Geology, New England (USA). *Journal of Geology*, **87**(5), 583-589.
- Smith, H. A. & Barreiro, B., 1990. Monazite U–Pb dating of staurolite grade metamorphism in pelitic schists. *Contributions to Mineralogy and Petrology*, **105**, 602-615.
- Smulikowski, K., 1967. Eclogites of the Śnieżnik Mts in the Sudetes. *Geologia Sudetica*, **3**, 157-174.

- Smulikowski, K., 1979. Polymetamorphic evolution of the crystalline complex of Śnieżnik and Góry Złote Mts in the Sudetes. *Geologia Sudetica*, **14**, 7-76.
- Smulikowski, W., 1995. Evidence of glaucophane-schist facies metamorphism in the East Karkonosze complex, West Sudetes, Poland. *Geologische Rundschau*, **84**, 720-737.
- Sommermann, A. E., 1993. Zirkonalter aus dem Granit der Bohrung Saar 1. *Beihefte zum European Journal of Mineralogy*, **5**, 145.
- Souček, J., 1978. Metamorphic zones of the Vrbno and Rejvíz series, the Hrubý Jeseník Mountains, Czechoslovakia. *Tschermaks mineralogische und petrographische Mitteilungen*, **25**, 195-217.
- Spear, F. S. & Selverstone, J., 1983. Quantitative P-T Paths From Zoned Minerals - Theory and Tectonic Applications. *Contributions to Mineralogy and Petrology*, **83**(3-4), 348-357.
- Spear, F. S. & Cheney, J. T., 1989. A Petrogenetic Grid For Pelitic Schists in the System SiO₂-Al₂O₃-FeO-MgO-K₂O-H₂O. *Contributions to Mineralogy and Petrology*, **101**(2), 149-164.
- Spear, F. S., Kohn, M. J. & Cheney, J. T., 1999. P-T paths from anatectic pelites. *Contributions to Mineralogy and Petrology*, **134**(1), 17-32.
- Spear, F. S. & Pyle, J. M., 2002. Apatite, monazite, and xenotime in metamorphic rocks. In: *Phosphates: Geochemical, Geobiological, and Materials Importance* (eds Kohn, M. J., Rakovan, J. & Hughes, J. M.) *Reviews in Mineralogy and Geochemistry*, **48**, 293-335, Mineralogical Society of America, Washington, D. C.
- Spear, F. S., 2010. Monazite–allanite phase relations in metapelites. *Chemical Geology*, **279**, 55-62.
- Speer, J. A., 1982. Zircon. In: *Orthosilicates* (ed Ribbe, P. H.) *Reviews in Mineralogy*, **5**, 67-112.
- St Onge, M. R., 1987. Zoned Poikiloblastic Garnets: P-T Paths and Syn-Metamorphic Uplift through 30 km of Structural Depth, Wopmay Orogen, Canada. *Journal of Petrology*, **98**(28), 1-21.
- Stacey, J. S. & Kramers, J. D., 1975. Approximation of terrestrial lead isotope evolution by a two-stage model. *Earth and Planetary Science Letters*, **26**, 207-221.
- Stallard, A. & Hickey, K. A., 2001. Fold mechanisms in the Canton schist: constraints on the contribution of flexural flow. *Journal of Structural Geology*, **23**, 1865-1881.
- Stampfli, G. M. & Borel, G. D., 2002. A plate tectonic model for the Paleozoic and Mesozoic constrained by dynamic plate boundaries and restored synthetic oceanic isochrons. *Earth and Planetary Science Letters*, **196**, 17-33.
- Steltenpohl, M. G., Cymerman, Z., Krogh, E. J. & Kunk, M. J., 1993. Exhumation of eclogitized continental basement during Variscan lithospheric delamination and gravitational collapse, Sudety Mountains, Poland. *Geology*, **21**, 1111-1114.
- Štípská, P., 1999. *Thermomechanical evolution of collisional boundary during Variscan convergence - eastern margin of the Bohemian Massif (examples of the Staré Město belt and the Thaya dome)*. PhD. Thesis, Charles University, Prague, 175 p.
- Štípská, P., Schulmann, K., Thompson, A. B., Ježek, J. & Kröner, A., 2001. Thermo-mechanical role of a Cambro-Ordovician paleorift during the Variscan collision: the NE margin of the Bohemian Massif. *Tectonophysics*, **332**(1-2), 239-253.
- Štípská, P., Schulmann, K. & Kröner, A., 2004. Vertical extrusion and middle crustal spreading of omphacite granulite: a model of syn-convergent exhumation (Bohemian Massif, Czech Republic). *Journal of Metamorphic Geology*, **22**(3), 179-198.
- Štípská, P., Pitra, P. & Powell, R., 2006. Separate or shared metamorphic histories of eclogites and surrounding rocks? An example from the Bohemian Massif. *Journal of Metamorphic Geology*, **24**(3), 219-240.

- Štípská, P., Schulmann, K. & Powell, R., 2008. Contrasting metamorphic histories of lenses of high-pressure rocks and host migmatites with a flat orogenic fabric (Bohemian Massif, Czech Republic): a result of tectonic mixing within horizontal crustal flow? *Journal of Metamorphic Geology*, **26**(6), 623-646.
- Štípská, P., Chopin, F., Skrzypek, E., Schulmann, K., Pitra, P., Lexa, O., Martelat, J.-E., Bollinger, C. & Žáčková, E., 2011. The juxtaposition of eclogite and mid-crustal rocks in the Orlica–Śnieżnik Dome, Bohemian Massif. *Journal of Metamorphic Geology*, in press.
- Stosch, H. G. & Lugmair, G. W., 1990. Geochemistry and evolution of MORB-type eclogites from the Münchberg Massif, southern Germany. *Earth and Planetary Science Letters*, **99**, 230-249.
- Suess, F. E., 1912. Die Moravischen Fenster und ihre Beziehung zum Grundgebirge des Hohen Gesenkes. *Akademie der Wissenschaften, Denkschrift Mathematisch-Naturwissenschaftliche Klasse*, **88**, 541-631.
- Suess, F. E., 1926. *Intrusionstektonik und Wandertektonik im variszischen Grundgebirge*. Borntraeger Verlag, Berlin, 268 p.
- Sun, S. S. & McDonough, W. F., 1989. Chemical and isotopic systematics of oceanic basalts: implications for mantle composition and processes. In: *Magmatism in the Ocean Basins* (eds Saunders, A. D. & Norry, M.), **42**, 313-345, Geological Society Special Publication, London.
- Suzuki, K. & Adachi, M., 1991. The chemical Th-U-total lead isochron ages of zircon and monazite from the gray granite of the Hida Terrane, Japan. *Journal of Earth Sciences Nagoya University*, **38**, 11-37.
- Tait, J., Schätz, M., Bachtadse, V. & Soffel, H., 2000. Paleomagnetism and Palaeozoic palaeogeography of Gondwana and European terranes. In: *Orogenic Processes: Quantification and Modelling in the Variscan Belt* (eds Franke, W., Haak, V., Oncken, O. & Tanner, D.), **179**, 21-34, Geological Society Special Publication, London.
- Tajčmanová, L., Konopásek, J. & Schulmann, K., 2006. Thermal evolution of the orogenic lower crust during exhumation within a thickened Moldanubian root of the Variscan belt of Central Europe. *Journal of Metamorphic Geology*, **24**(2), 119-134.
- Teisseyre, A. K., 1968. Sedimentology of the lowermost continental Culm deposits in the northern part of the Intra-Sudetic Basin. *Geologia Sudetica*, **4**, 221-298.
- Teisseyre, A. K., 1971. Sedimentology of the Culm from Ciechanowice and palaeogeography of the lowermost Culm deposits of the Intra-Sudetic Basin. *Geologia Sudetica*, **5**, 237-280.
- Teisseyre, A. K., 1975. Sedimentology and paleogeography of the Culm alluvial fans in the western Intra-Sudetic Basin (central Sudetes, SW Poland). *Geologia Sudetica*, **9**(2), 5-135.
- Teisseyre, H., 1968. Serie metamorficzne sudetów. Uwagi o stratygrafii, następstwie i wieku deformacji oraz metodach badawczych. *Geologia Sudetica*, **4**, 7-45.
- Tera, F. & Wasserburg, G. J., 1972. U–Th–Pb systematics in three Apollo 14 basalts and the problem of initial Pb in lunar rocks. *Earth and Planetary Science Letters*, **14**, 281-304.
- Teysier, C. & Whitney, D. L., 2002. Gneiss domes and orogeny. *Geology*, **30**, 1139-1142.
- Thompson, A. B. & England, P. C., 1984. Pressure Temperature Time Paths of Regional Metamorphism .2. Their Inference and Interpretation Using Mineral Assemblages in Metamorphic Rocks. *Journal of Petrology*, **25**(4), 929-955.
- Thompson, A. B. & Connolly, J. A. D., 1995. Melting of the continental crust: Some thermal and petrological constraints on anatexis in continental collision zones and other tectonic settings. *Journal of Geophysical Research*, **100**(B8), 15,565-15,579.

- Thompson, A. B., Schulmann, K. & Ježek, J., 1997. Extrusion tectonics and elevation of lower crustal metamorphic rocks in convergent orogens. *Geology*, **25**(6), 491-494.
- Tikhomirova, M., 2002. Zircon inheritance in diatexite granodiorites and its consequence on geochronology—a case study in Lusatia and the Erzgebirge (Saxo-Thuringia, eastern Germany). *Chemical Geology*, **191**, 209-224.
- Timmermann, H., Parrish, R., Noble, S. & Kryza, R., 2000. New U-Pb monazite and zircon data from the Sudetes Mountains in SW Poland: evidence for a single-cycle Variscan orogeny. *Journal of the Geological Society, London*, **157**, 265-268.
- Timmermann, H., Štědrá, V., Gerdes, A., Noble, S. R., Parrish, R. R. & Dörr, W., 2004. The Problem of Dating High-pressure Metamorphism: a U–Pb Isotope and Geochemical Study on Eclogites and Related Rocks of the Mariánské Lázně Complex, Czech Republic. *Journal of Petrology*, **45**(7), 1311-1338.
- Timms, N. E., 2003. Garnet porphyroblast timing and behaviour during fold evolution: implications from a 3-D geometric analysis of a hand-sample scale fold in a schist. *Journal of Metamorphic Geology*, **21**, 853-873.
- Tinkham, D. K., Zuluaga, C. A. & Stowell Harold, H., 2001. Metapelite phase equilibria modeling in MnNCKFMASH: The effect of variable Al₂O₃ and MgO/(MgO+FeO) on mineral stability. *Geological Materials Research*, **3**(1), 1-42.
- Tobschall, H. J., 1974. *Geochemische Untersuchungen zum stofflichen Bestand und Sedimentationsmilieu paläozoischer mariner Tone: Die Gehalte der Hauptelemente und der Spurenelemente Ni, Cu, Zn, Rb, Sr, Y, Zr, Nb und Ba in den Steiger Schiefern (Vogesen)*. Habilitationsschrift, Mainz, 142 p.
- Tornquist, A., 1895. Das fossilführende Unterkarbon am östlichen Rossbergmassiv in den Südvogesen. 1. Einleitung, Beschreibung der Brachiopoden-Fauna. *Abhandlungen zur geologischen Spezialkarte von Elsass-Lothringen*, **5**(4), 379-528.
- Tornquist, A., 1896. Das fossilführende Unterkarbon am östlichen Rossbergmassiv in den Südvogesen. 2. Beschreibung der Lamellibranchiaten-Fauna. *Abhandlungen zur geologischen Spezialkarte Elsass-Lothringen*, **5**(5), 1-190.
- Tornquist, A., 1897. Das fossilführende Unterkarbon am östlichen Rossbergmassiv in den Südvogesen. 3. Beschreibung der Echiniden-Fauna. *Abhandlungen zur geologischen Spezialkarte Elsass-Lothringen*, **5**(6), 1-81.
- Tornquist, A., 1898. Vorläufige Mittheilungen über neue Fossilfunde im Unterkarbon des Ober-Elsass. *Mittheilungen der geologischen Landesanstalt von Elsass-Lothringen*, **4**, 97-104.
- Tricart, P. & Lemoine, M., 1983. Serpentinite oceanic bottom in South Queyras ophiolites (French western Alps): Record of the incipient oceanic opening of the Mesozoic Ligurian Tethys. *Eclogae Geologicae Helvetiae*, **76**, 611-629.
- Tropper, P., Konzett, J. & Finger, F., 2005. Experimental constraints on the formation of high-P/high-T granulites in the Southern Bohemian Massif. *European Journal of Mineralogy*, **17**, 343–356.
- Turniak, K., Mazur, S. & Wysoczanski, R., 2000. SHRIMP zircon geochronology and geochemistry of the Orlica-Śnieżnik gneisses (Variscan belt of Central Europe) and their tectonic implications. *Geodinamica Acta*, **13**, 1-20.
- Urbanek, Z., Żelaźniewicz, A., Kemnitz, H., Hermsdorf, N. & Linnemann, U., 1995. Western Sudetes (Lugicum): Stratigraphy. In: *Pre-Permian Geology of Central and Eastern Europe* (eds Dallmeyer, R. D., Franke, W. & Weber, K.), 315-327, Springer, Berlin.

- Vanderhaeghe, O., Burg, J. P. & Teyssier, C., 1999. Exhumation of migmatites in two collapsed orogens; Canadian Cordillera and French Variscides. In: *Exhumation processes; normal faulting, ductile flow and erosion* (eds Ring, U., Brandon Mark, T., Lister Gordon, S. & Willett Sean, D.), **154**, 181-204, Geological Society Special Publication, London.
- Vanderhaeghe, O. & Teyssier, C., 2001. Partial melting and flow of orogens. *Tectonophysics*, **342**(3-4), 451-472.
- Vangerow, E. F., 1943. Das Normalprofil des Algonkiums und Kambriums in den mittleren Sudeten. *Geologische Rundschau*, **34**, 10-12.
- Vavra, G., Gebauer, D., Schmid, R. & Compston, W., 1996. Multiple zircon growth and recrystallisation during polyphase Late Carboniferous to Triassic metamorphism in granulites of the Ivrea Zone (Southern Alps): an ion microprobe (SHRIMP) study. *Contributions to Mineralogy and Petrology*, **122**, 337-358.
- Vavra, G., Schmid, R. & Gebauer, D., 1999. Internal morphology, habit and U-Th-Pb microanalysis of amphibolite- to granulite-facies zircons: geochronology of the Ivrea zone (Southern Alps). *Contributions to Mineralogy and Petrology*, **134**, 380-404.
- Velain, C., 1885. Le Permien dans la région des Vosges. *Bulletin de la Société Géologique de France*, **12**, 536-564.
- Vellmer, C., 1992. *Stoffbestand und Petrogenese von Granuliten und granitischen Gesteinen der südlichen Böhmisches Masse in Niederösterreich*. PhD. thesis, Georg-August-Universität, Göttingen, 111 p.
- Verner, K., Buriánek, D., Vrána, S., Vondrovic, L., Pertoldová, J., Hanzl, P. & Nahodilová, R., 2009. Tectonometamorphic features of geological units along the northern periphery of the Moldanubian Zone (Bohemian Massif). *Journal of Geosciences*, **54**, 87-100.
- Vernon, R. H., 1978. Porphyroblast-matrix microstructural relationships in deformed metamorphic rocks. *Geologische Rundschau*, **67**(1), 288-305.
- Vernon, R. H., Paterson, S. R. & Foster, D., 1993. Growth and deformation of porphyroblasts in the Foothills terrane, central Sierra Nevada, California: negotiating a microstructural minefield. *Journal of Metamorphic Geology*, **11**, 203-222.
- Visser, P. & Mancktelow, N. S., 1992. The rotation of garnet porphyroblasts around a single fold, Lukmanier Pass, Central Alps. *Journal of Structural Geology*, **14**(10), 1193-1202.
- Vogt, C., 1981. Benthonische Klein-Foraminiferen aus dem Unter-Karbon der Südvogesen. *Neues Jahrbuch für Geologie und Paläontologie, Monatshefte*, **6**, 363-384.
- Vollbrecht, A., Weber, K. & Schmoll, J., 1989. Structural model for the Saxothuringian-Moldanubian suture in the Variscan basement of the Oberpfalz (NE Bavaria, FRG) interpreted from geophysical data. *Tectonophysics*, **157**, 123-133.
- von Eller, J.-P., 1961. Les gneiss de Sainte-Marie-aux-Mines et les séries voisines des Vosges moyennes. *Mémoires du Service de la Carte géologique d'Alsace-Lorraine*, **19**, 160 p.
- von Eller, J.-P., 1963. Présence d'une formation fossilifère d'âge silurien conservée au sein des diorites de la région du Hohwald (Vosges) ; origine métamorphique de ces diorites. *Comptes Rendus de l'Académie des Sciences*, **257**, 3960-3962.
- von Eller, J.-P., 1964. Dioritisation, granitisation et métamorphisme dans les Vosges cristallines du Nord. I Région comprise entre la plaine d'Alsace, d'Andlau à Saint-Nabor et le Champ du Feu. *Bulletin du Service de la Carte Géologique d'Alsace-Lorraine*, **17**(3), 171-210.
- von Raumer, J. F., 1998. The Palaeozoic evolution in the Alps - from Gondwana to Pangea. *Geologische Rundschau*, **87**, 407-435.

- von Raumer, J. F., Stampfli, G. M. & Bussy, F., 2003. Gondwana-derived microcontinents — the constituents of the Variscan and Alpine collisional orogens. *Tectonophysics*, **365**, 7-22.
- von Raumer, J. F. & Stampfli, G. M., 2008. The birth of the Rheic Ocean — Early Palaeozoic subsidence patterns and subsequent tectonic plate scenarios. *Tectonophysics*, **461**, 9-20.
- von Seidlitz, W., 1914. Leitlinien varistischer Tektonik im Schwarzwald und in den Vogesen. *Zeitschrift der Deutschen Geologischen Gesellschaft*, **66**, 100-124.
- Walsh, E. O. & Hacker, B. R., 2004. The fate of subducted continental margins: Two-stage exhumation of the high-pressure to ultrahigh-pressure Western Gneiss Region, Norway. *Journal of Metamorphic Geology*, **22**(7), 671-687.
- Warren, R. G. & Ellis, D. J., 1996. Mantle underplating, granite tectonics, and metamorphic P-T-t paths. *Geology*, **24**, 663-666.
- Watson, E. B. & Harrison, T. M., 1983. Zircon saturation revisited: temperature and composition effects in a variety of crustal magma types. *Earth and Planetary Science Letters*, **64**(295-304).
- Watson, E. B., 1996. Dissolution, growth and survival of zircons during crustal fusion: Kinetic principles, geological models and implications for isotopic inheritance. *Geological Society of America Special Paper*, **315**, 43-56.
- Wegener, A., 1912. Die Entstehung der Kontinente. *Geologische Rundschau*, **3**, 276-292.
- Weigand, B., 1875. Die Serpentine der Vogesen. *Mineralogische Mittheilungen*, **3**, 183-206.
- Wetherill, G. W., 1956. Discordant uranium-lead ages 1. *Transactions of the American Geophysical Union*, **37**, 320-326.
- White, R. W., Powell, R., Holland, T. J. B. & Worley, B. A., 2000. The effect of TiO₂ and Fe₂O₃ on metapelitic assemblages at greenschist and amphibolite facies conditions: mineral equilibria calculations in the system K₂O-FeO-MgO-Al₂O₃-SiO₂-H₂O-TiO₂-Fe₂O₃. *Journal of Metamorphic Geology*, **18**(5), 497-511.
- White, R. W., Pomroy, N. E. & Powell, R., 2005. An in situ metatexite-diatexite transition in upper amphibolite facies rocks from Broken Hill, Australia. *Journal of Metamorphic Geology*, **23**(7), 579-602.
- White, R. W., Powell, R. & Holland, T. J. B., 2007. Progress relating to calculation of partial melting equilibria for metapelites. *Journal of Metamorphic Geology*, **25**(5), 511-527.
- Whitehouse, M. J. & Platt, J. P., 2003. Dating high-grade metamorphism - constraints from rare-earth elements in zircon and garnet. *Contributions to Mineralogy and Petrology*, **145**(1), 61-74.
- Wickert, F. & Eisbacher, H., 1988. Two-sided Variscan thrust tectonics in the Vosges Mountains, north-eastern France. *Geodynamica Acta*, **2**, 101-120.
- Wickert, F., Altherr, R. & Deutsch, M., 1990. Polyphase Variscan tectonics and metamorphism along a segment of the Saxo-Thuringian boundary: the Baden-Baden zone, northern Schwarzwald (F.R.G.). *Geologische Rundschau*, **79**, 627-647.
- Wiedenbeck, M., Allé, P., Corfu, F., Griffin, W. L., Meier, M., Oberli, F., von Quadt, A., Roddick, J. C. & Spiegel, W., 1995. Three natural zircon standards for U-Th-Pb, Lu-Hf, trace element and REE analyses. *Geostandards Newsletter*, **19**, 1-23.
- Williams, P. F. & Jiang, D., 1999. Rotating garnets. *Journal of Metamorphic Geology*, **17**, 367-378.
- Willner, A. P., Rotzler, K. & Maresch, W. V., 1997. Pressure-temperature and fluid evolution of quartz-feldspathic metamorphic rocks with a relic high-pressure, granulite-facies history from the Central Erzgebirge (Saxony, Germany). *Journal of Petrology*, **38**(3), 307-336.

- Wilson, R. C. L., Manatschal, G. & Wise, S., 2001. Rifting along non-volcanic passive margins: stratigraphic and seismic evidence from the Mesozoic successions of the Alps and western Iberia. In: *Non-Volcanic Rifting of Continental Margins: a Comparison of Evidence from Land and Sea* (eds Wilson, R. C. L., Whitmarsh, R. B., Taylor, B. & Frotzheim, N.), **187**, 429-452, Geological Society Special Publication, London.
- Winchester, J. A., Pharaoh, T. C. & Verniers, J., 2002. Palaeozoic amalgamation of Central Europe: an introduction and synthesis of new results from recent geological and geophysical investigations. In: *Palaeozoic Amalgamation of Central Europe* (eds Winchester, J. A., Pharaoh, T. C. & Verniers, J.), **201**, 1-18, Geological Society Special Publication, London.
- Wing, B. A., Ferry, J. M. & Harrison, T. M., 2003. Prograde destruction and formation of monazite and allanite during contact and regional metamorphism of pelites: petrology and geochronology. *Contributions to Mineralogy and Petrology*, **145**, 228-250.
- Wojciechowska, I., Ziółkowska-Kozdrój, M. & Gunia, T., 2001. Petrography and geochemistry of leptytes from the Skrzyńka Dislocation Zone (Eastern Sudetes, SW Poland) – preliminary results. *Bulletin of the Polish Academy of Sciences, Earth Sciences*, **49**, 1-11.
- Yang, P. & Pattison, D., 2006. Genesis of monazite and Y zoning in garnet from the Black Hills, South Dakota. *Lithos*, **88**, 233-253.
- Yardley, B. W. D., 1977. Empirical-Study of Diffusion in Garnet. *American Mineralogist*, **62**(7-8), 793-800.
- Záčková, E., Konopásek, J., Jeřábek, P., Finger, F. & Košler, J., 2010. Early Carboniferous blueschist facies metamorphism in metapelites of the West Sudetes (Northern Saxothuringian Domain, Bohemian Massif). *Journal of Metamorphic Geology*, **28**, 361-379.
- Zeh, A., Brätz, H., Millar, I. L. & Williams, I. S., 2001. A combined zircon SHRIMP and SmNd isotope study of high-grade paragneisses from the Mid-German Crystalline Rise: evidence for northern Gondwanan and Grenvillian provenance. *Journal of the Geological Society, London*, **158**, 983-994.
- Żelaźniewicz, A., 1978. Makroskopowe struktury tektoniczne w metamorfiku w polskiej części Gór Orlickich. *Geologia Sudetica*, **13**, 67-86.
- Żelaźniewicz, A., 1987. Tectonic and metamorphic evolution of the Góry Sowie, Sudetes Mts, SW Poland. *Annales Societatis Geologorum Poloniae*, **57**, 203-348.
- Żelaźniewicz, A., 1990. Deformation and metamorphism in the Góry Sowie gneiss complex, Sudetes, SW Poland. *Neues Jahrbuch für Geologie und Paläontologie, Abhandlungen*, **179**, 129-157.
- Żelaźniewicz, A., 1995. Western Sudetes (Lugicum): Introduction. In: *Pre-Permian Geology of Central and Eastern Europe* (eds Dallmeyer, R. D., Franke, W. & Weber, K.), 311-314, Springer, Berlin.
- Żelaźniewicz, A., Kemnitz, H. & Hermsdorf, N., 1995. Western Sudetes (Lugicum): Structure. In: *Pre-Permian Geology of Central and Eastern Europe* (eds Dallmeyer, R. D., Franke, W. & Weber, K.), 328-359, Springer, Berlin.
- Żelaźniewicz, A. & Bakun-Czubarow, N., 2002. A Polyphase Exhumation of Ultra-High-P Eclogites from Nowa Wieś in the Łądek-Śnieżnik Metamorphic Unit, the Sudetes. *Geolines*, **14**, 107-108.
- Żelaźniewicz, A., Dörr, W., Bylina, P., Franke, W., Haack, U., Heinisch, H., Schastok, J., Grandmontagne, K. & Kulicki, C., 2004. The eastern continuation of the Cadomian orogen: U–Pb zircon evidence from Saxo-Thuringian granitoids in south-western Poland and the northern Czech Republic. *International Journal of Earth Sciences*, **93**, 773-781.

- Żelaźniewicz, A., Nowak, I., Larionov, A. & Presnyakov, S., 2006. Syntectonic Lower Ordovician migmatite and post-tectonic Upper Viséan syenite in the western limb of the Orlica- Śnieżnik Dome, West Sudetes: U-Pb SHRIMP data from zircons. *Geologia Sudetica*, **38**, 63-80.
- Ziegler, P. A., 1984. Caledonian and Hercynian crustal consolidation of Western and Central Europe - a working hypothesis. *Geologie en Mijnbouw*, **63**(1), 93-108.
- Ziegler, P. A., 1986. Geodynamic Model for the Palaeozoic Crustal Consolidation of Western and Central Europe. *Tectonophysics*, **126**, 303-328.
- Zoubek, V., 1946. Stratigrafie krystalinických sérií při rozhraní moravika a moldanubika v západní části svratecké klenby. *Sbor. Stát. geol. úst.*, **13**, 463-481.
- Zuluaga, C. A., Stowell, H. H. & Tinkham, D., 2005. The effect of zoned garnet on metapelite pseudosection topology and calculated metamorphic P-T paths. *American Mineralogist*, **90**, 1619-1628.
- Zwart, H. J., 1962. On the determination of polymetamorphic mineral associations, and its application to the Bosost area (central Pyrenees). *Geologische Rundschau*, **52**, 38-69.

Publications scientifiques associées au travail de thèse

- Chopin, F., Schulmann, K., Skrzypek, E., Lehmann, J., Dujardin, J.-R., Martelat, J.-E., Lexa, O., Corsini, M., Edel, J.-B., Štípská, P. & Pitra, P., 2011. Crustal influx, indentation, ductile thinning and gravity redistribution in a continental wedge: building a Moldanubian mantled gneiss dome with Saxothuringian material (European Variscan belt). *Tectonics*, in press.
- Cruz Mermy, D., Skrzypek, E., Ménillet, F. & Chèvremont, P., 2007. Carte géologique harmonisée du département du Bas-Rhin (67)-Notice géologique. *Rapport BRGM/RP-56028-FR*, 322 p.
- Edel, J.-B., Schulmann, K., Skrzypek, E. & Cocherie, A., 2011. Tectonic evolution of the European Variscan belt constrained by palaeomagnetic, structural and anisotropy of magnetic susceptibility data from the Rhenohercynian magmatic arc (Northern Vosges, Eastern France). *Journal of the Geological Society, London*, submitted.
- Skrzypek, E., Cruz Mermy, D., Ménillet, F. & Chèvremont, P., 2008. Carte géologique harmonisée du département du Haut-Rhin (68)-Notice géologique. *Rapport BRGM/RP-56029-FR*, 325 p.
- Skrzypek, E., Schulmann, K., Štípská, P., Chopin, F., Lehmann, J., Lexa, O. & Haloda, J., 2011a. Tectono-metamorphic history recorded in garnet porphyroblasts: insights from thermodynamic modelling and electron backscatter diffraction analysis of inclusion trails. *Journal of Metamorphic Geology*, **29**(4), 473-496.
- Skrzypek, E., Štípská, P., Schulmann, K., Lexa, O. & Lexová, M., 2011b. Prograde and retrograde metamorphic fabrics - a key for understanding burial and exhumation in orogens (Bohemian Massif). *Journal of Metamorphic Geology*, **29**(4), 451-472.
- Skrzypek, E., Tabaud, A.-S., Edel, J.-B., Schulmann, K., Cocherie, A., Guerrot, C. & Rossi, P., 2011c. The significance of Late Devonian oceanic domains during Variscan orogeny: a record from the Vosges Klippen Belt. *International Journal of Earth Sciences. International Journal of Earth Sciences*, in press.
- Štípská, P., Chopin, F., Skrzypek, E., Schulmann, K., Pitra, P., Lexa, O., Martelat, J.-E., Bollinger, C. & Žáčková, E., 2011. The juxtaposition of eclogite and mid-crustal rocks in the Orlica-Šniežnik Dome, Bohemian Massif. *Journal of Metamorphic Geology*, in press.

REMERCIEMENTS

Voici venue la fin de la thèse, et avec elle le moment de remercier les personnes ayant, de près ou de loin, facilité son déroulement. C'est tout d'abord à mes deux directeurs de thèse, K. Schulmann et P. Rossi, que je souhaite exprimer ma gratitude pour m'avoir guidé et soutenu scientifiquement, financièrement et humainement, mais aussi pour avoir su parfois me laisser quelques libertés. Je tiens également à ne pas oublier l'apport de P. Ledru qui fut à l'origine de ce projet de thèse.

En soutenant ce travail, j'ai aussi grandement bénéficié de la présence des différents membres du jury que furent S. Duchêne, J-P. Burg, M. Faure, G. Manatschal et A. Żelaźniewicz. A travers leur questions et désaccords, ils ont su attiser la curiosité qui m'anime.

Rien d'officiel ne dira plus tard que d'autres personnes ont contribué à encadrer ma thèse. C'est pourquoi je dois ici souligner que P. Štípská a agi pour moi comme un véritable soutien et une pédagogue de qualité tout au long de mon travail. Telles ont également été les qualités de J-E. Martelat pendant les missions de terrain successives dans les Sudètes. Je garde aussi en mémoire que ce travail de thèse a débuté par un court séjour au service géologique régional d'Alsace, où mes premiers pas de géologue vosgien ont pu être accompagnés, avec passion et professionnalisme, par D. Cruz-Mermy, P. Elsass et F. Ménillet.

On ne peut pas non plus juger, en lisant le manuscrit, de l'apport scientifique et humain qu'ont offert certaines personnes. J-B Edel a fait preuve d'une passion inaltérable à chaque fois que nous avons discuté du socle vosgien, et ses arguments géophysiques, toujours difficiles à intégrer, m'ont sans cesse tenu en alerte. A maintes reprises durant ma thèse, le soleil ne s'est pas levé seul à l'Est ; il a été accompagné par Z. Kratinová. Je dois à cette dernière un soutien conséquent dans l'étude des granites vosgiens, mais surtout un enthousiasme sans limite dans tous les travaux que nous avons entamés. Je suis aussi fortement redevable à J. Honnorez qui m'aura durement encadré depuis mon premiers cours de DEUG jusqu'au dernier signe de ponctuation de mon manuscrit de thèse. Sa relecture patiente, quoique pressée par les délais imposés, m'a permis d'améliorer mon travail final. A la faveur de brèves entrevues au cours de ma thèse, j'ai également pu profiter des conseils avisés prodigués par F. Hrouda. Enfin, je tiens à exprimer ma gratitude envers M. Doś pour trois années magnifiques d'apprentissage de la langue polonaise, ainsi que pour une ultime traduction, à distance, de mon résumé de thèse.

Nul n'ignore que le travail analytique nécessite bien souvent le soutien et les connaissances de personnes supplémentaires. A ce titre, je souhaiterais témoigner une vive reconnaissance à A. Aubert (Strasbourg), C. Guerrot (BRGM), J. Haloda (Prague), G. Morvan (Strasbourg), H. Müller-Sigmund (Freiburg i. Br.), M. Robert (BRGM), T. Theye (Stuttgart), P. Týcová (Prague) et G. Wille (BRGM). Une mention spéciale est à attribuer à D. Guinamant (BRGM) qui a su sauver mes plots de zircons d'une ruine que je pensais trop certaine.

Il me faut aussi mentionner les acteurs qui ont facilité mon travail de recherche. O. Lexa, par sa présence sur le terrain et ses conseils sur l'analyse microstructurale, a fréquemment agi comme un encadrant à part entière. Les études dans le dôme d'Orlica-Śnieżnik ont aussi pu s'appuyer sur les travaux précurseurs de M. Romanová. Pour les Vosges, et plus particulièrement pour la partie septentrionale, j'ai vivement apprécié les remarques pertinentes de J-P. von Eller, dont l'accueil chaleureux n'est plus à disputer. Mes interrogations en termes de géochronologie ont trouvé une oreille attentive auprès d'A. Cocherie ou R. Montigny, alors que mes besoins en bibliographie ont été fermement satisfaits par B. Kieffer et J. Hörth. Les rédactions scientifiques ont bénéficié de commentaires pointus, acerbes et encourageants de la part de D. Aerden, M. Caddick, G. Eisbacher, J-R. Martínez Catalán, J. Selverstone, N. Timms et M. Williams. Les étudiants de Master 1^{ère} année que sont P. Dietrich, A. Gicquel, A. Laurent, T. Mateeva, A. Weydmann et M. Wickert m'ont finalement aidé, par leur travail motivé, à faire progresser la connaissance des Vosges ou des Sudètes.

Quand j'ai débuté mes études à l'université, j'ai pu compter sur la franche amitié de T. Courjault, A. Gillmann, D. Machuca, J. Muhlhausen, C. Raepffel ou encore B. Thien. Ils m'ont accompagné pendant des durées variables, mais ont tous fait de mon parcours universitaire une période faste. Plus tard, depuis le DEA jusqu'à la thèse, j'ai subi les assauts et profité de la bonne humeur et des errements de F. Chopin, V. Kusbach, J. Lehmann et G. Mohn. Ces derniers m'ont sans conteste permis de tenir bon dans les moments difficiles, aussi bien à Strasbourg que sur le terrain. L. Jeannot a ensuite empli mon bureau de frénésie, puis a contribué à percer avec moi moult buttes vosgiennes. Cela a été mené de concert avec A-S. Tabaud qui m'a souvent épaulé pour la compréhension des Vosges, et nul doute que l'aventure vosgienne se poursuivra bientôt sous l'impulsion énergique d'E. Olliot. A toutes ces personnes, je tiens ici à exprimer ma très grande reconnaissance.

Une thèse n'est pas faite que de travail acharné. Aussi a-t-il été agréable, pendant trois ans et neuf mois, de partager confidences, soirées, journées de ski, marches dans les Vosges, jeux ou autres matches de football avec M-L. Bagard, F. Cobert, S. Fleury, F. Girard, F. Guéguen, A. Guy, F. Humbert, M. Jati, E. Le Garzic, E. Masini, A. Moussa, B. Petri, J. Place, M. Stanek, E. Sutra ou J. Tugend. J'adresse aussi une pensée amicale aux 12 loups-garous de Master 2^{ème} année, promotion 2011/2012, si volontaires avant et après ma soutenance de thèse.

Enfin, mon exercice s'achève ici avec les derniers remerciements qui vont à M^{lle} Breffi, mes parents et ma sœur Cécile.

APPENDIX



Annexe 1. Coordonnées géographiques des localités étudiées dans le dôme d'Orlica-Śnieżnik, Sudètes.

Localité	X_UTM_33N	Y_UTM_33N	Localité	X_UTM_33N	Y_UTM_33N
ES 1	640537.169761	5582832.90643	ES 59	635283.453424	5576255.69594
ES 2	639271.885968	5582276.18156	ES 60	635936.610607	5575384.81970
ES 3	638866.995155	5582107.47705	ES 61	633953.473944	5573811.08953
ES 4	637643.887489	5582099.04183	ES 62	630294.778145	5572251.63727
ES 5	636969.069466	5583204.05634	ES 63	629113.187293	5572177.22979
ES 6	637567.970461	5583372.76085	ES 64	628916.751534	5572385.57075
ES 7	638557.954846	5585803.18890	ES 65	628878.059642	5571421.24975
ES 8	638539.544946	5585692.72950	ES 66	629068.542802	5570736.10563
ES 9	638511.930098	5585608.04397	ES 67	628955.443426	5570453.35719
ES 10	638388.583775	5585523.35843	ES 68	633858.813482	5581716.18465
ES 11	638211.848744	5585416.58102	ES 69	634072.272823	5580264.56648
ES 12	638005.657875	5585173.57035	ES 70	633778.825393	5580070.51253
ES 13	636731.462739	5583956.21578	ES 71	635597.252853	5578326.86683
ES 14	637085.853295	5584163.32714	ES 72	636373.468635	5577706.84081
ES 15	643310.362405	5580163.48793	ES 73	636439.730958	5578800.16914
ES 16	642653.166010	5579688.84608	ES 74	640563.562684	5582456.67583
ES 17	642236.941626	5579272.62170	ES 75	640546.375529	5582338.51414
ES 18	635719.744040	5581927.69514	ES 76	640477.626910	5582372.88845
ES 19	635471.469846	5581460.35548	ES 77	639479.053228	5581840.08666
ES 20	634909.201819	5580671.71980	ES 78	639285.697738	5581889.49973
ES 21	636632.516811	5571160.62753	ES 79	639165.387656	5581223.06781
ES 22	636785.862636	5571036.49043	ES 80	637539.697669	5581146.15529
ES 23	636939.208462	5570802.82060	ES 81	639557.254781	5581956.52963
ES 24	634164.379237	5573380.49091	ES 82	640433.799666	5582894.51859
ES 25	639633.713683	5584720.04960	ES 83	628659.649076	5568099.83591
ES 26	638187.881613	5585238.50453	ES 84	629585.298683	5567314.14040
ES 27	637980.803267	5585342.15362	ES 85	629716.237829	5567301.36585
ES 28	637242.451670	5585422.61501	ES 86	629577.314589	5566898.32877
ES 29	636859.076802	5584646.39923	ES 87	629205.894526	5566904.71604
ES 30	636627.158672	5584163.63087	ES 88	632986.289693	5565927.95516
ES 31	636923.445915	5580339.82154	ES 89	631932.605282	5564464.87167
ES 32	637122.232884	5579738.72761	ES 90	632004.758666	5565057.80272
ES 33	637349.417991	5579525.74158	ES 91	631938.971757	5565263.65208
ES 34	637628.666351	5579331.68763	ES 92	632006.880825	5565327.31683
ES 35	638510.858106	5579469.10017	ES 93	631868.940531	5564975.03854
ES 36	638442.746318	5580449.15438	ES 94	630002.901029	5565249.15320
ES 37	638428.547249	5580524.88274	ES 95	630426.185240	5564714.29516
ES 38	639280.491400	5582072.58129	ES 96	630318.293665	5563396.02610
ES 39	638953.912809	5581509.35154	ES 97	629705.410299	5565957.78454
ES 40	638911.315601	5581348.42876	ES 98	631901.734251	5564845.97536
ES 41	638300.755626	5580695.27157	ES 99	631786.546813	5564208.43793
ES 42	638594.203056	5580974.51994	ES 100	629439.722917	5570272.59939
ES 43	638461.678410	5581977.92082	ES 101	629874.532108	5571159.12286
ES 44	639005.976063	5581992.11989	ES 102	629735.868496	5573293.92620
ES 45	640575.446510	5582582.32787	ES 103	629458.541272	5573518.86939
ES 46	635474.194254	5582175.28789	ES 104	629220.094361	5558092.91946
ES 47	631155.174899	5578698.17995	ES 105	629859.028714	5559098.08099
ES 48	629871.980526	5579421.24460	ES 106	629602.027187	5559487.15274
ES 49	629449.920164	5580571.60447	ES 107	630001.807341	5560418.78328
ES 50	632841.686826	5579166.97843	ES 108	630995.903527	5561059.14542
ES 51	632775.424504	5580061.51979	ES 109	628737.907708	5570681.25595
ES 52	633116.202164	5580705.21092	ES 110	628702.066225	5571135.53084
ES 53	632387.316612	5580686.27883	ES 111	628851.370391	5571076.71405
ES 54	632538.773350	5580743.07511	ES 112	630363.640618	5568446.24611
ES 55	631989.742675	5580965.52719	ES 113	630171.354949	5567701.53502
ES 56	632434.646843	5581192.71230	ES 114	630515.206968	5567561.27959
ES 57	633797.284183	5576940.56438	ES 115	630622.886942	5566378.60963
ES 58	635117.797617	5576945.29740	ES 116	631226.663941	5562848.24476

Localité	X_UTM_33N	Y_UTM_33N	Localité	X_UTM_33N	Y_UTM_33N
ES 117	636850.134456	5567455.15982	FC 7	640953.141750	5580841.52199
ES 118	637042.493452	5567599.42907	FC 8	639750.007288	5578926.54086
ES 119	636128.330223	5571640.49465	FC 9	641699.539487	5581456.81499
ES 120	636293.209362	5571523.70526	FC 10	640227.569315	5581873.32101
ES 121	636586.327833	5571475.61551	FC 11	641230.851194	5581340.21986
ES 122	636833.646542	5571317.60633	FC 12	641150.130878	5581255.80062
ES 123	637331.489944	5571290.12648	FC 13	640440.555353	5580372.95270
ES 124	637530.718905	5571122.95735	FC 14	640975.386959	5580235.69504
ES 125	638226.875272	5570490.92065	FC 15	641306.698573	5580959.84756
ES 126	638307.024854	5570188.64223	FC 16	641373.716764	5580884.99407
ES 127	638057.416156	5570550.46034	FC 17	643081.582221	5580888.85222
ES 128	636814.410643	5570637.47988	FC 223	621094.508969	5578685.31276
ES 129	636848.760463	5570742.81933	FC 286	638983.261456	5579607.56685
ES 130	637528.428917	5570715.33948	FC 287	642327.658074	5580304.75804
ES 131	627419.215413	5572127.29145	FC 288	642394.518340	5580505.33884
ES 132	627132.814241	5572939.47388	FC 295	634700.701987	5585979.93510
ES 133	626943.508562	5573110.45965	FC 296	635901.385866	5584366.49096
ES 134	626693.136535	5573650.89683	FC 490	597851.669176	5573922.16348
ES 135	624511.846584	5575076.79606	FC 491	597816.590162	5574415.96806
ES 136	621813.259886	5579305.13619	FC 492	597830.082090	5574788.34529
ES 137	621059.090488	5578899.04498	FC 493	598329.283445	5575284.84826
ES 138	620656.052591	5579231.85658	FC 494	599531.144438	5574742.47273
ES 139	620216.985549	5579619.62789	FC 495	599431.304167	5573582.16688
ES 140	620375.758053	5579097.51061	FC 496	599212.734925	5573617.24589
ES 141	620787.955902	5578352.50117	FC 497	598861.944783	5573711.68939
ES 142	630876.659406	5575095.96853	FC 503	601325.870752	5568376.98086
ES 143	630432.910610	5576272.51350	FC 504	601732.427531	5568952.63647
ES 144	630282.280285	5576301.01113	FC 505	602207.343415	5568567.66678
ES 145	630164.218679	5576590.05851	FC 506	601865.547892	5569463.53083
ES 146	629879.242388	5576590.05851	FC 507	602067.027358	5570129.13264
ES 147	630962.152293	5573935.70792	FC 508	600369.562858	5570107.54555
ES 148	631416.022271	5569163.59899	FC 509	600380.356401	5569963.63165
ES 149	632033.861047	5569761.28587	MS	630721.261629	5565302.68569
ES 150	632230.800019	5569882.65524	BM	632641.831031	5571793.15771
ES 151	632526.208477	5569942.19493	SP	630712.896745	5564710.95311
ES 152	632922.376410	5571192.52840			
ES 153	630284.246565	5569779.33013			
ES 154	627283.719043	5575258.81212			
ES 155	626502.069789	5574867.98750			
ES 156	626203.455347	5577600.70657			
ES 157	626356.121217	5577484.68051			
ES 158	630366.642314	5581709.00168			
ES 159	630053.168394	5583569.48974			
ES 160	629499.500173	5582262.66990			
ES 161	628226.063262	5581253.03961			
ES 162	627273.428233	5581362.95904			
ES 163	604499.269915	5568717.44457			
ES 164	604216.074086	5568604.16624			
ES 165	605062.121626	5566469.57768			
ES 166	605401.956621	5567124.46803			
ES 167	605571.874119	5567181.10720			
ES 168	643710.726145	5571476.40176			
ES 169	643431.070263	5569950.68423			
ES 170	643544.348595	5569826.78605			
ES 171	643303.632140	5569748.90720			
ES 172	642195.628458	5569752.44715			
ES 173	641951.372055	5569763.06699			
ES 174	641675.256121	5569894.04506			
ES 175	642892.998187	5571614.45973			

Annexe 2. Résultats des datations sur monazites à la microsonde électronique pour l'échantillon M81-2A (Javornik).

Spot	Zone	Age (Ma)	Err. (Ma)	U (ppm)	Err. U %	Th (ppm)	Err. Th %	Pb (ppm)	Err. Pb %	Th* (ppm)	Err. Th* %
1	zone2	502	141	3430	4.37	14520	2.00	580	25.86	25830	3.04
2	zone2	402	90	6480	2.31	18960	2.00	720	20.83	40161	2.17
3	zone2	347	99	5670	2.65	17780	2.00	560	26.79	36252	2.33
4	zone2	385	52	6160	2.44	54280	2.00	1280	11.72	74408	2.12
5	zone2	359	86	5600	2.68	24210	2.00	680	22.06	42471	2.29
6	zone2	408	99	4980	3.01	20490	2.00	670	22.39	36791	2.45
7	zone2	410	75	7390	2.03	24470	2.00	890	16.85	48663	2.01
8	zone2	425	82	6860	2.19	22330	2.00	850	17.65	44814	2.09
9	zone2	365	49	5820	2.58	60140	2.00	1290	11.63	79127	2.14
10	zone5	447	101	2220	6.76	30210	2.00	750	20.00	37498	2.92
12	zone5	392	109	1770	8.47	28430	2.00	600	25.00	34217	3.09
13	zone5	440	135	1770	8.47	21620	2.00	540	27.78	27428	3.37
16	zone5	364	82	3490	4.30	34150	2.00	740	20.27	45535	2.57
17	zone5	369	79	2120	7.08	40930	2.00	790	18.99	47849	2.73
18	zone5	382	71	3820	3.93	40800	2.00	910	16.48	53279	2.45
19	zone5	379	70	4570	3.28	38800	2.00	910	16.48	53726	2.36
20	zone5	374	73	3040	4.93	42100	2.00	870	17.24	52025	2.56
22	zone5	401	155	1960	7.65	17020	2.00	420	35.71	23432	3.55
23	zone5	350	149	1480	10.14	19500	2.00	380	39.47	24323	3.61
24	zone6	266	181	2260	6.64	12150	2.00	230	65.22	19468	3.74
25	zone6	225	158	3220	4.66	11670	2.00	220	68.18	22064	3.25
26	zone6	370	54	7530	2.00	45660	2.00	1160	12.93	70236	2.00
27	zone6	293	92	2130	7.04	32950	2.00	520	28.85	39861	2.87
28	zone6	385	104	2730	5.49	26520	2.00	610	24.59	35440	2.88
29	zone6	413	154	1220	12.30	19840	2.00	440	34.09	23835	3.73
30	zone6	361	146	1200	12.50	20910	2.00	400	37.50	24824	3.66
31	zone6	398	116	1450	10.34	27280	2.00	570	26.32	32022	3.24
32	zone6	418	135	1550	9.68	22190	2.00	510	29.41	27267	3.43
33	zone6	368	72	5050	2.97	35250	2.00	850	17.65	51729	2.31
34	zone9	420	80	5200	2.88	29340	2.00	870	17.24	46376	2.32
35	zone9	357	122	3200	4.69	19100	2.00	470	31.91	29533	2.95
36	zone9	279	99	7150	2.10	12300	2.00	440	34.09	35475	2.06
37	zone9	322	90	3600	4.17	28690	2.00	580	25.86	40396	2.63
38	zone9	348	92	1820	8.24	34610	2.00	630	23.81	40540	2.91
39	zone9	361	90	1710	8.77	35930	2.00	670	22.39	41507	2.91
40	zone9	370	80	3910	3.84	33820	2.00	770	19.48	46581	2.50
41	zone9	389	80	4400	3.41	32300	2.00	810	18.52	46681	2.43
42	zone9	372	76	5140	2.92	31970	2.00	810	18.52	48748	2.32
43	zone9	376	173	1470	10.20	16040	2.00	350	42.86	20840	3.89
44	zone9	334	108	3080	4.87	23510	2.00	500	30.00	33535	2.86
45	zone9	389	147	1710	8.77	19140	2.00	430	34.88	24729	3.53
46	zone9	408	131	1760	8.52	22190	2.00	510	29.41	27951	3.34
47	zone9	362	116	1760	8.52	25830	2.00	510	29.41	31570	3.19
48	zone9	333	110	2250	6.67	25670	2.00	490	30.61	32992	3.04
49	zone9	388	102	3780	3.97	23420	2.00	620	24.19	35774	2.68
50	zone9	421	107	2950	5.08	24900	2.00	650	23.08	34565	2.86
51	zone9	351	94	3250	4.62	28340	2.00	610	24.59	38932	2.71
52	zone8	375	138	1920	7.81	19990	2.00	440	34.09	26259	3.39
53	zone8	500	233	1030	14.56	12220	2.00	350	42.86	15616	4.73
54	zone8	585	241	1200	12.50	11240	2.00	400	37.50	15223	4.75
55	zone8	465	146	2490	6.02	16840	2.00	520	28.85	25026	3.32
56	zone8	455	253	1000	15.00	10960	2.00	290	51.72	14245	5.00
57	zone8	395	128	2600	5.77	19880	2.00	500	30.00	28381	3.13
58	zone8	345	119	2320	6.47	22960	2.00	470	31.91	30517	3.11
59	zone8	358	175	1250	12.00	16540	2.00	330	45.45	20616	3.98
60	zone7	329	73	4290	3.50	36540	2.00	740	20.27	50497	2.41
61	zone7	309	73	3660	4.10	38840	2.00	700	21.43	50730	2.49
62	zone7	374	45	7150	2.10	64720	2.00	1470	10.20	88062	2.03
63	zone7	337	69	4170	3.60	40320	2.00	810	18.52	53895	2.40
64	zone7	342	62	5380	2.79	43470	2.00	930	16.13	60991	2.23
65	zone10	393	114	4990	3.01	15060	2.00	550	27.27	31375	2.52

Spot	Zone	Age (Ma)	Err. (Ma)	U (ppm)	Err. U %	Th (ppm)	Err. Th %	Pb (ppm)	Err. Pb %	Th* (ppm)	Err. Th* %
66	zone10	329	109	5120	2.93	16090	2.00	480	31.25	32748	2.47
67	zone10	294	114	6110	2.45	10830	2.00	400	37.50	30656	2.29
68	zone10	394	99	5960	2.52	17010	2.00	640	23.44	36497	2.28
69	zone3	275	120	4310	3.48	15440	2.00	360	41.67	29406	2.70
70	zone3	341	72	5540	2.71	33340	2.00	780	19.23	51380	2.25
71	zone3	374	90	6160	2.44	20130	2.00	670	22.39	40240	2.22
72	zone3	357	85	6870	2.18	19800	2.00	670	22.39	42198	2.10
73	zone3	347	78	6310	2.38	26050	2.00	720	20.83	46607	2.17
74	zone3	377	85	5910	2.54	23530	2.00	720	20.83	42829	2.24
76	zone1	419	117	5150	2.91	13680	2.00	570	26.32	30551	2.50
78	zone1	352	39	6110	2.45	83940	2.00	1630	9.20	103853	2.09
79	zone1	392	76	6280	2.39	28140	2.00	850	17.65	48670	2.16
80	zone1	317	103	4740	3.16	19370	2.00	490	30.61	34777	2.52
83	zone1	293	125	3400	4.41	17340	2.00	370	40.54	28372	2.94
84	zone12	382	44	4780	3.14	76850	2.00	1580	9.49	92465	2.19
85	zone12	351	32	5540	2.71	116430	2.00	2110	7.11	134485	2.09
86	zone12	326	36	5220	2.87	98390	2.00	1680	8.93	115369	2.13
87	zone12	346	37	4990	3.01	96940	2.00	1750	8.57	113196	2.14
88	zone12	325	41	5180	2.90	80410	2.00	1410	10.64	97258	2.16
89	zone12	358	74	4090	3.67	37400	2.00	810	18.52	50736	2.44
90	zone12	356	65	6840	2.19	34460	2.00	900	16.67	56759	2.08
91	zone12	393	111	4180	3.59	18840	2.00	570	26.32	32506	2.67
92	zone12	323	112	3960	3.79	19150	2.00	460	32.61	32027	2.72
93	zone12	349	58	4650	3.23	50930	2.00	1030	14.56	66082	2.28
94	zone12	360	69	8920	2.00	23950	2.00	850	17.65	53040	2.00
95	zone12	368	73	8240	2.00	23150	2.00	820	18.29	50038	2.00
96	zone12	359	65	8970	2.00	27600	2.00	910	16.48	56851	2.00
97	zone12	386	72	6620	2.27	29550	2.00	880	17.05	51181	2.11
98	zone12	438	117	5280	2.84	13370	2.00	600	25.00	30693	2.47
99	zone12	289	142	3760	3.99	12670	2.00	320	46.88	24867	2.98
100	zone12	285	139	4770	3.14	9780	2.00	320	46.88	25248	2.70
102	zone12	360	114	5570	2.69	13080	2.00	500	30.00	31244	2.40
103	zone12	350	110	4310	3.48	18620	2.00	510	29.41	32665	2.64
104	zone13	471	147	2780	5.40	15570	2.00	520	28.85	24714	3.26
105	zone13	351	144	2920	5.14	15410	2.00	390	38.46	24926	3.20
106	zone13	353	120	3820	3.93	17470	2.00	470	31.91	29920	2.80
107	zone13	433	140	4610	3.25	10260	2.00	490	30.61	25379	2.75
108	zone13	575	136	4390	3.42	12270	2.00	690	21.74	26828	2.77
109	zone13	364	127	5850	2.56	8700	2.00	450	33.33	27784	2.39
110	zone13	425	160	4130	3.63	8650	2.00	420	35.71	22186	3.00
111	zone13	511	144	5260	2.85	7200	2.08	560	26.79	24556	2.63
112	zone13	342	111	4590	3.27	17220	2.00	490	30.61	32168	2.59
113	zone13	364	110	5130	2.92	15940	2.00	530	28.30	32675	2.47
114	zone13	377	132	4690	3.20	11490	2.00	450	33.33	26805	2.68
115	zone13	336	142	4970	3.02	8620	2.00	370	40.54	24798	2.66
116	zone14	358	155	2370	6.33	15440	2.00	370	40.54	23168	3.44
117	zone14	309	136	2860	5.24	16890	2.00	360	41.67	26181	3.15
118	zone14	401	111	3740	4.01	20690	2.00	590	25.42	32926	2.75
119	zone14	444	134	2970	5.05	17480	2.00	540	27.78	27228	3.09
120	zone14	524	128	3960	3.79	15520	2.00	670	22.39	28599	2.82
121	zone14	333	97	5390	2.78	19590	2.00	550	27.27	37131	2.37
122	zone14	371	132	3540	4.24	15690	2.00	450	33.33	27244	2.95
123	zone14	425	102	4560	3.29	20860	2.00	680	22.06	35806	2.54
124	zone14	431	137	3010	4.98	16600	2.00	510	29.41	26470	3.11

Annexe 3. Résultats des datations sur monazites à la microsonde électronique pour l'échantillon M35D (Bilá Voda).

Spot	Zone	Age (Ma)	Err. (Ma)	U (ppm)	Err. U %	Th (ppm)	Err. Th %	Pb (ppm)	Err. Pb %	Th* (ppm)	Err. Th* %
5	zone14	350	93	4820	3.11	23460	2.00	610	24.59	39166	2.45
6	zone14	438	143	3980	3.77	12040	2.00	490	30.61	25097	2.92
9	zone14	373	109	4140	3.62	19590	2.00	550	27.27	33104	2.66
11	zone14	374	165	2820	5.32	12370	2.00	360	41.67	21576	3.42
12	zone14	394	116	2180	6.88	24700	2.00	560	26.79	31828	3.09
16	zone14b	390	93	6500	2.31	17290	2.00	670	22.39	38537	2.17
17	zone14b	395	167	4380	3.42	6740	2.23	370	40.54	21062	3.04
18	zone14b	421	121	6020	2.49	9620	2.00	550	27.27	29344	2.33
19	zone14b	440	126	5860	2.56	8860	2.00	550	27.27	28088	2.38
20	zone14b	376	247	2010	7.46	7740	2.00	240	62.50	14303	4.51
21	zone14b	283	200	2460	6.10	9530	2.00	220	68.18	17506	3.87
23	zone14b	403	183	2700	5.56	10650	2.00	350	42.86	19484	3.61
24	zone14b	436	124	3640	4.12	17370	2.00	570	26.32	29310	2.86
25	zone14b	534	355	1660	9.04	4570	3.28	240	62.50	10057	6.42
26	zone14b	345	160	3140	4.78	11880	2.00	340	44.12	22109	3.28
27	zone14b	419	79	3780	3.97	35690	2.00	900	16.67	48073	2.51
29	zone14b	391	117	5160	2.91	13550	2.00	530	28.30	30418	2.50
30	zone14b	310	162	3510	4.27	10330	2.00	300	50.00	21734	3.19
31	zone12	393	61	3450	4.35	53100	2.00	1130	13.27	64379	2.41
34	zone12	435	64	2670	5.62	53320	2.00	1210	12.40	62078	2.51
35	zone12	377	55	2220	6.76	64430	2.00	1210	12.40	71679	2.48
36	zone12	362	53	6160	2.44	52350	2.00	1170	12.82	72442	2.12
37	zone12	393	64	3750	4.00	48650	2.00	1070	14.02	60910	2.40
38	zone12	414	59	3120	4.81	56810	2.00	1240	12.10	67027	2.43
40	zone12	360	67	6230	2.41	35720	2.00	900	16.67	56037	2.15
41	zone12	424	61	6850	2.19	39800	2.00	1180	12.71	62250	2.07
42	zone12	440	90	6170	2.43	20510	2.00	800	18.75	40755	2.21
43	zone12	358	53	7080	2.12	48940	2.00	1150	13.04	72025	2.04
44	zone12	400	59	7460	2.01	39420	2.00	1140	13.16	63823	2.00
45	zone12-p1	403	71	6190	2.42	31990	2.00	940	15.96	52243	2.16
46	zone12-p1	380	68	5740	2.61	36680	2.00	940	15.96	55428	2.21
47	zone12-p1	424	80	5710	2.63	27790	2.00	880	17.05	46503	2.25
48	zone12-p1	429	58	6910	2.17	43640	2.00	1270	11.81	66294	2.06
50	zone12-p2	395	70	6400	2.34	32400	2.00	940	15.96	53328	2.13
51	zone12-p2	456	87	3820	3.93	31090	2.00	890	16.85	43640	2.55
53	zone11-p1	417	59	5020	2.99	50120	2.00	1240	12.10	66562	2.24
54	zone11-p1	365	80	2770	5.42	38170	2.00	770	19.48	47207	2.65
55	zone11-p1	396	74	3010	4.98	42110	2.00	920	16.30	51953	2.57
56	zone11-p2	463	72	2630	5.70	46290	2.00	1140	13.16	54935	2.58
57	zone11-p2	453	120	1690	8.88	25500	2.00	630	23.81	31051	3.23
58	zone11-p2	412	109	2320	6.47	26610	2.00	630	23.81	34206	2.99
59	zone11-p3	455	71	2780	5.40	46330	2.00	1130	13.27	55463	2.56
60	zone11-p3	412	79	2540	5.91	40040	2.00	890	16.85	48356	2.67
61	zone11-p3	398	56	4220	3.55	55830	2.00	1240	12.10	69633	2.31
62	zone11-p3	363	61	4670	3.21	47080	2.00	1010	14.85	62313	2.30
66	zone10-p1	348	57	4670	3.21	52400	2.00	1050	14.29	67616	2.27
68	zone10-p2	395	59	3900	3.85	54040	2.00	1180	12.71	66793	2.35
69	zone10-p2	450	72	5110	2.94	35930	2.00	1060	14.15	52710	2.30
72	zone9-p1	416	115	3440	4.36	20520	2.00	590	25.42	31786	2.84
73	zone9-p1	406	79	4710	3.18	32000	2.00	860	17.44	47415	2.39
74	zone9-p1	481	93	3720	4.03	28190	2.00	870	17.24	40435	2.62
75	zone9-p1	455	95	3580	4.19	27580	2.00	800	18.75	39340	2.65
77	zone9-p2	420	120	1930	7.77	24540	2.00	580	25.86	30863	3.18
78	zone9-p2	385	91	3190	4.70	30320	2.00	700	21.43	40743	2.69
81	zone9-p3	482	126	2060	7.28	22890	2.00	640	23.44	29671	3.21
82	zone9-p3	454	115	2000	7.50	25900	2.00	660	22.73	32470	3.11
83	zone9-p3	363	110	2130	7.04	26350	2.00	540	27.78	33298	3.05
84	zone9-p4	393	94	2050	7.32	33180	2.00	700	21.43	39882	2.89
85	zone9-p4	474	121	1830	8.20	25050	2.00	660	22.73	31071	3.20
86	zone9-p4	479	131	2060	7.28	21660	2.00	610	24.59	28440	3.26
87	zone9-p4	564	139	2440	6.15	18800	2.00	680	22.06	26885	3.25

Spot	Zone	Age (Ma)	Err. (Ma)	U (ppm)	Err. U %	Th (ppm)	Err. Th %	Pb (ppm)	Err. Pb %	Th* (ppm)	Err. Th* %
88	zone9-p4	405	72	5550	2.70	33850	2.00	940	15.96	52012	2.25
90	zone9-p5	429	105	4340	3.46	20790	2.00	670	22.39	35018	2.59
91	zone9-p5	435	139	2660	5.64	17490	2.00	510	29.41	26215	3.21
92	zone9-p5	394	148	2320	6.47	16850	2.00	430	34.88	24436	3.39
94	zone9-p6	779	271	2210	6.79	5970	2.51	470	31.91	13422	4.89
96	zone9-p6	381	159	3280	4.57	11660	2.00	380	39.47	22374	3.23
97	zone9-p6	581	158	3380	4.44	11850	2.00	600	25.00	23065	3.19
99	zone7-p1	394	128	3070	4.89	18380	2.00	500	30.00	28418	3.02
100	zone7-p1	540	136	2970	5.05	17470	2.00	660	22.73	27292	3.10
101	zone7-p1	492	107	3620	4.14	23020	2.00	770	19.48	34947	2.73
102	zone7-p1	468	117	3420	4.39	20280	2.00	660	22.73	31527	2.85
103	zone7-p1	451	126	2510	5.98	21010	2.00	590	25.42	29253	3.12
104	zone7-p1	543	127	2410	6.22	21600	2.00	720	20.83	29572	3.14
105	zone7-p2	521	140	2340	6.41	18860	2.00	620	24.19	26587	3.28
106	zone7-p2	547	136	2500	6.00	19030	2.00	670	22.39	27303	3.21
107	zone7-p2	467	112	3070	4.89	22930	2.00	690	21.74	33025	2.88
108	zone7-p2	403	138	2780	5.40	17040	2.00	470	31.91	26136	3.18
109	zone7-p2	413	132	2680	5.60	18890	2.00	510	29.41	27665	3.14
110	zone7-p2	478	129	3030	4.95	18560	2.00	610	24.59	28532	3.03
111	zone8-p1	459	78	1550	9.68	45440	2.00	1040	14.42	50534	2.77
115	zone8-p2	437	92	1310	11.45	37580	2.00	820	18.29	41878	2.97
116	zone8-p2	423	85	1510	9.93	40480	2.00	860	17.44	45428	2.86
117	zone8-p2	422	85	1370	10.95	40980	2.00	860	17.44	45469	2.88
118	zone8-p2	416	96	1040	14.42	36320	2.00	740	20.27	39726	3.07
120	zone5_p1	384	70	6800	2.21	30930	2.00	910	16.48	53147	2.09
121	zone5_p1	439	102	5440	2.76	17850	2.00	700	21.43	35699	2.38
128	zone2-p1	398	75	7500	2.00	23960	2.00	860	17.44	48490	2.00
129	zone2-p1	378	75	6990	2.15	25820	2.00	820	18.29	48647	2.07
130	zone2-p1	414	69	7350	2.04	30030	2.00	1000	15.00	54100	2.02
131	zone2-p1	429	81	6960	2.16	22630	2.00	870	17.24	45449	2.08
132	zone2-p1	417	87	5620	2.67	24000	2.00	790	18.99	42409	2.29
133	zone3-p1	578	164	2440	6.15	14300	2.00	580	25.86	22394	3.50
134	zone3-p1	622	204	2080	7.21	11000	2.00	500	30.00	17924	4.01
135	zone3-p1	391	184	1960	7.65	13060	2.00	340	44.12	19467	3.86
136	zone3-p1	453	166	2370	6.33	13950	2.00	440	34.09	21734	3.55
140	zone4-p1	385	71	3170	4.73	43740	2.00	930	16.13	54097	2.52
141	zone1	475	96	6450	2.33	16500	2.00	800	18.75	37722	2.18
142	zone1	435	89	6770	2.22	18520	2.00	790	18.99	40726	2.12
143	zone1	415	71	8620	2.00	23690	2.00	960	15.63	51920	2.00
144	zone1	350	96	6280	2.39	16780	2.00	580	25.86	37244	2.21
145	zone1	401	86	6890	2.18	19480	2.00	750	20.00	42019	2.09
146	zone1	404	72	9370	2.00	20530	2.00	920	16.30	51189	2.00
147	zone1	407	80	8040	2.00	18880	2.00	820	18.29	45195	2.00
148	zone1	373	114	5210	2.88	14330	2.00	520	28.85	31337	2.48

Annexe 4. Résultats des datations sur monazites à la microsonde électronique pour l'échantillon ES95CIII (Międzygórze).

Spot	Zone	Age (Ma)	Err. (Ma)	U (ppm)	Err. U %	Th (ppm)	Err. Th %	Pb (ppm)	Err. Pb %	Th* (ppm)	Err. Th* %
5	-	587	154	1810	8.29	18280	2.00	640	23.44	24288	3.56
13	-	535	214	1410	10.64	12430	2.00	410	36.59	17091	4.36
23	-	425	72	1730	8.67	48950	2.00	1040	14.42	54620	2.69
33	-	310	59	1290	11.63	61570	2.00	910	16.48	65761	2.61
34	-	362	53	1580	9.49	69560	2.00	1210	12.40	74713	2.52
35	-	511	100	1430	10.49	34090	2.00	890	16.85	38808	3.03
38	-	408	72	1530	9.80	49150	2.00	990	15.15	54158	2.72
41	-	389	90	1510	9.93	37070	2.00	730	20.55	42005	2.93
43	-	359	63	3090	4.85	51080	2.00	980	15.31	61156	2.47
44	-	392	64	3000	5.00	51290	2.00	1070	14.02	61097	2.48
47	-	341	105	2330	6.44	27200	2.00	530	28.30	34788	2.97
48	-	396	74	4530	3.31	36060	2.00	900	16.67	50874	2.38
58	-	435	95	1120	13.39	36400	2.00	780	19.23	40074	3.04
59	-	340	82	1610	9.32	40840	2.00	700	21.43	46082	2.83
63	-	394	69	2630	5.70	47640	2.00	990	15.15	56239	2.57
64	-	380	44	2220	6.76	87580	2.00	1610	9.32	94831	2.36
66	-	393	49	1690	8.88	78050	2.00	1470	10.20	83575	2.45
72	-	407	74	5310	2.82	33220	2.00	920	16.30	50600	2.28
73	-	394	120	3360	4.46	19150	2.00	530	28.30	30136	2.90
74	-	422	130	2590	5.79	19590	2.00	530	28.30	28077	3.15
75	-	450	147	2200	6.82	17610	2.00	500	30.00	24835	3.40
80	-	505	142	1130	13.27	22770	2.00	600	25.00	26497	3.59
81	-	303	151	1290	11.63	19510	2.00	320	46.88	23699	3.70
83	-	402	91	2950	5.08	31510	2.00	740	20.27	41162	2.72
84	-	315	93	3430	4.37	28040	2.00	550	27.27	39187	2.68
85	-	415	106	2580	5.81	26560	2.00	650	23.08	35010	2.92
88	-	402	86	1370	10.95	40020	2.00	800	18.75	44502	2.90
91	-	399	71	1050	14.29	51980	2.00	990	15.15	55414	2.76
92	-	422	77	2390	6.28	42470	2.00	950	15.79	50301	2.67
94	-	564	124	1950	7.69	24340	2.00	780	19.23	30801	3.19
97	-	454	101	4100	3.66	23010	2.00	740	20.27	36478	2.61
98	-	481	102	4510	3.33	21440	2.00	780	19.23	36286	2.54
102	-	413	107	1640	9.15	29770	2.00	650	23.08	35140	3.09
103	-	416	106	1680	8.93	29960	2.00	660	22.73	35462	3.08
104	-	389	112	2080	7.21	26010	2.00	570	26.32	32808	3.08
106	-	517	98	2590	5.79	30750	2.00	910	16.48	39300	2.82
107	-	612	174	1640	9.15	16000	2.00	590	25.42	21455	3.82
108	-	323	137	1130	13.27	22690	2.00	380	39.47	26365	3.57
109	-	451	84	1800	8.33	40100	2.00	930	16.13	46012	2.81
111	-	466	140	1700	8.82	20800	2.00	550	27.27	26389	3.45
112	-	525	167	1680	8.93	16560	2.00	520	28.85	22109	3.74

Annexe 5. Analytical procedure for EBSD analysis (Part 1-Chapter IV).

Thin sections were polished and prepared for electron backscatter diffraction measurements using a CamScan CS 3200 electron microscope of the Czech Geological Survey, Prague. Operating conditions of 20 kV accelerating voltage, 5 nA beam current and 33 mm working distance were used for samples tilted at 70°.

Annexe 6. Mineral abbreviations used in Part 2-Chapter II.

and=andalusite; bi=biotite; chl=chlorite; cd=cordierite; g=garnet with end members alm=almandine [Fe/(Fe+Mg+Ca+Mn)], grs=grossular [Ca/(Fe+Mg+Ca+Mn)], prp=pyrope [Mg/(Fe+Mg+Ca+Mn)] and sps=spessartine [Mn/(Fe+Mg+Ca+Mn)]; ilm=ilmenite; ksp=K-feldspar; ky=kyanite; liq=granitic melt; mz=monazite; mu=muscovite; pa=paragonite; pl=plagioclase with end members ab=albite [Na/(Na+Ca+K)], an=anorthite [Ca/(Na+Ca+K)], or=orthoclase [K/(Na+Ca+K)]; q=quartz; ru=rutile; sill=sillimanite; z=zircon.

Annexe 7. Coordonnées géographiques des localités étudiées dans le massif vosgien.

Socle					
Localité	X_UTM_32N	Y_UTM_32N	Localité	X_UTM_32N	Y_UTM_32N
EV 1	373520.653561	5373259.24743	EV 58	361071.469203	5347646.56232
EV 2	371879.164223	5372011.47558	EV 59	360272.500359	5347160.38444
EV 3	371650.721157	5372095.28504	EV 60	360414.542633	5347793.90080
EV 4	371299.460785	5371745.14836	EV 61	366313.947604	5354839.87123
EV 5	370991.605637	5371645.65513	EV 62	366178.517261	5354854.75127
EV 6	370991.367174	5371142.31194	EV 63	373283.570965	5347304.95089
EV 7	372123.610453	5371513.96946	EV 64	373546.590129	5347048.58555
EV 8	368986.534369	5373026.14742	EV 65	373291.753798	5346418.14569
EV 9	368435.088376	5373308.96851	EV 66	371592.840199	5346373.98485
EV 10	368200.699102	5373604.81218	EV 67	371617.511164	5347009.28284
EV 11	368081.844610	5373655.14868	EV 68	372477.693942	5347222.32313
EV 12	370414.465746	5359091.32193	EV 69	368171.063299	5345787.23211
EV 13	370379.208397	5359363.70974	EV 70	368970.494879	5344221.13448
EV 14	369611.158803	5359558.24534	EV 71	369253.112896	5345805.61036
EV 15	369816.277635	5359263.51744	EV 72	366952.224881	5343980.07654
EV 16	369892.119111	5358644.10930	EV 73	367118.352324	5343977.40076
EV 17	369765.767811	5358034.18851	EV 74	366469.257505	5342807.18932
EV 18	369115.280274	5357722.86157	EV 75	366416.041826	5342903.97738
EV 19	368974.581019	5356500.26075	EV 76	366120.830279	5342687.64524
EV 20	369345.019863	5356184.19066	EV 77	366056.956964	5342813.89465
EV 21	371315.129318	5355648.57937	EV 78	365625.831866	5343191.16207
EV 22	371900.599336	5356646.71937	EV 79	364934.694157	5343008.68768
EV 23	370778.538706	5354379.80350	EV 80	364762.777779	5342667.61278
EV 24	370390.087352	5354562.35593	EV 81	364726.525143	5342352.81977
EV 25	369424.816824	5354539.50967	EV 82	364569.018856	5342687.47614
EV 26	369350.904861	5354531.19162	EV 83	364452.480419	5342807.79860
EV 27	369119.735424	5353848.23861	EV 84	366015.631910	5343445.24903
EV 28	369166.719509	5353507.49627	EV 85	366339.680031	5344769.25546
EV 29	369097.893343	5353387.47766	EV 86	363630.391465	5342564.32500
EV 30	368943.235085	5353270.40831	EV 87	363504.479961	5342196.25445
EV 31	368448.588104	5352142.96127	EV 88	363207.184732	5341775.85608
EV 32	369598.662477	5352135.36677	EV 89	363242.967836	5341475.21471
EV 33	369723.711887	5351817.22710	EV 90	363199.709373	5341303.22004
EV 34	369764.597637	5352124.10310	EV 91	363125.037348	5341226.15096
EV 35	370635.480664	5352857.75852	EV 92	363109.418028	5341146.22812
EV 36	370949.772335	5353999.15740	EV 93	362369.240418	5339881.92999
EV 37	367835.079669	5353179.26325	EV 94	362603.724917	5340415.31818
EV 38	367808.263997	5353125.92400	EV 95	362795.449332	5341090.72063
EV 39	367231.341523	5352924.55780	EV 96	362906.794336	5341570.94640
EV 40	366910.713883	5352939.90582	EV 97	363498.586256	5342712.85685
EV 41	366259.828716	5353186.64009	EV 98	362298.693466	5341925.29094
EV 42	365650.734450	5353085.02111	EV 99	362125.537539	5341852.25229
EV 43	364909.791077	5352884.87932	EV 100	361738.058997	5341661.37959
EV 44	365271.602249	5352442.16522	EV 101	361641.022071	5341225.22510
EV 45	365070.080096	5352191.48420	EV 102	361969.444623	5340674.17096
EV 46	364631.450741	5352167.51725	EV 103	362015.940219	5340620.78049
EV 47	364324.716633	5352329.91433	EV 104	361917.517861	5340548.48731
EV 48	364018.250553	5351242.71884	EV 105	361693.980325	5340727.37683
EV 49	363848.155064	5351154.05381	EV 106	361940.433000	5340431.22758
EV 50	368853.004369	5353817.00667	EV 107	361945.489686	5340374.79224
EV 51	363252.447520	5350185.61948	EV 108	361884.169082	5340505.21918
EV 52	363348.875628	5350157.60556	EV 109	361779.086440	5340566.91425
EV 53	363417.013633	5349824.55744	EV 110	362284.378683	5340658.76868
EV 54	363151.064614	5349488.24441	EV 111	362217.420831	5339529.06306
EV 55	362320.671625	5347907.18727	EV 112	362182.371160	5339581.47470
EV 56	362055.740736	5347856.64572	EV 113	362078.201087	5339750.15598
EV 57	361883.201732	5347345.79694	EV 114	361720.134632	5340050.90840

Socle

Localité	X_UTM_32N	Y_UTM_32N	Localité	X_UTM_32N	Y_UTM_32N
EV 115	361903.255746	5339900.18249	EV 174	375301.466524	5374452.92194
EV 116	361896.304219	5340088.55173	EV 175	375452.305348	5373968.19449
EV 117	361794.297712	5340186.22088	EV 176	374354.802504	5373944.15621
EV 118	361112.312176	5340216.26701	EV 177	373950.990464	5374019.74129
EV 119	360752.915037	5340071.30641	EV 178	373655.376626	5373471.92759
EV 120	360035.595765	5339223.42022	EV 179	371854.737009	5372204.13394
EV 121	360319.795230	5338001.07737	EV 180	372948.980309	5372261.78195
EV 122	360933.002365	5337698.27064	EV 181	372786.208581	5372247.50444
EV 123	359892.047861	5338392.34714	EV 182	372699.451029	5372162.61469
EV 124	359725.017088	5337877.34013	EV 183	372604.757926	5372134.81834
EV 125	359970.959372	5337825.56089	EV 184	369960.709541	5374822.93549
EV 126	359928.588890	5337843.73424	EV 185	368709.004283	5374753.14898
EV 127	359711.074108	5337231.46716	EV 186	368627.723366	5375121.67248
EV 128	359608.312148	5337358.85158	EV 187	368793.893696	5375325.41170
EV 129	359470.976474	5337255.29344	EV 188	369342.138052	5375720.81717
EV 130	359592.345362	5337538.11205	EV 189	369449.787056	5375660.31628
EV 131	359519.168740	5337606.96253	EV 190	369553.394566	5375312.96223
EV 132	359476.210963	5337720.99693	EV 191	369508.108132	5375083.48925
EV 133	359453.058561	5337854.75090	EV 192	369608.259315	5375085.17317
EV 134	359530.148403	5338082.05708	EV 193	370158.090290	5375253.50630
EV 135	359710.874713	5338365.56337	EV 194	370297.553772	5375564.66653
EV 136	359561.177316	5338406.36722	EV 195	370309.015152	5375189.30166
EV 137	359785.992420	5339128.36681	EV 196	370770.895825	5375498.50602
EV 138	359507.460139	5338837.57819	EV 197	370805.960278	5375428.83364
EV 139	361203.985361	5339695.15638	EV 198	371090.853314	5375383.93351
EV 140	361597.105430	5339720.83553	EV 199	371148.222792	5375514.92887
EV 141	366433.612058	5343702.87373	EV 200	371523.438947	5375848.21877
EV 142	374774.533305	5374245.78927	EV 201	371433.077719	5375481.57160
EV 143	374782.381081	5374155.62937	EV 202	371584.611601	5374885.23138
EV 144	375446.119694	5374141.62999	EV 203	368729.040438	5372297.35911
EV 145	375295.864351	5374181.72314	EV 204	369063.086646	5372425.18940
EV 146	375173.184702	5374316.72645	EV 205	368951.938438	5372534.71170
EV 147	370009.682458	5372575.24984	EV 206	368853.152040	5372668.81912
EV 148	370731.268747	5375056.35618	EV 207	367342.126691	5372026.30077
EV 149	370236.976210	5375077.26707	EV 208	368258.097202	5372283.82026
EV 150	371066.966059	5375132.67433	EV 209	371762.294056	5371568.47715
EV 151	373319.806009	5357308.76726	EV 210	371279.272417	5371617.50790
EV 152	373526.254451	5358899.10001	EV 211	371202.132743	5370566.33079
EV 153	372743.006730	5356429.09706	EV 212	371623.713946	5370937.97809
EV 154	369320.231133	5358264.02843	EV 213	371734.505207	5371333.65725
EV 155	362777.562793	5356182.46528	EV 214	371778.930998	5370893.92310
EV 156	365634.012223	5354633.19891	EV 215	372128.154640	5371169.18973
EV 157	372273.576537	5371856.34486	EV 216	370025.816748	5370059.25653
EV 158	372589.178624	5370880.93493	EV 217	369158.019212	5374181.30685
EV 159	371542.508267	5367418.49654	EV 218	370661.059904	5374473.19217
EV 160	375819.701585	5378354.25277	EV 219	370665.816369	5374229.17837
EV 161	375904.654385	5378036.07454	EV 220	369491.056092	5372332.14241
EV 162	375807.491436	5377874.51227	EV 221	369144.139272	5372802.89888
EV 163	375779.972890	5377665.32138	EV 222	367246.502889	5358051.01620
EV 164	375745.686474	5376740.33560	EV 223	367138.781009	5357954.54730
EV 165	375905.717276	5376550.35138	EV 224	366720.191183	5357570.72726
EV 166	376650.253271	5375429.86407	EV 225	366646.915283	5357640.71867
EV 167	376549.948181	5374497.37877	EV 226	366676.024632	5357544.97622
EV 168	376156.009791	5374718.27592	EV 227	366757.352907	5357569.10203
EV 169	376024.758475	5375042.34255	EV 228	367922.588185	5357824.07829
EV 170	375905.445413	5375296.15352	EV 229	368106.612455	5357940.44075
EV 171	376365.298388	5375426.04141	EV 230	368179.606690	5357976.15905
EV 172	375193.219453	5374626.29613	EV 231	381700.984916	5358855.07033
EV 173	375235.704164	5374553.42618	EV 232	381752.993794	5358910.49913

Socle

Localité	X_UTM_32N	Y_UTM_32N	Localité	X_UTM_32N	Y_UTM_32N
EV 233	382598.814570	5359441.34970	EV 292	366761.952681	5356289.74177
EV 234	381146.583810	5359261.40684	EV 293	366413.370978	5356088.08306
EV 235	380829.954960	5359105.70093	EV 294	366579.999593	5356213.25576
EV 236	380590.958572	5359037.89765	EV 295	367804.326801	5356210.46186
EV 237	379737.825089	5359425.97768	EV 296	367955.262526	5356082.10981
EV 238	380077.236915	5358972.78520	EV 297	367819.757406	5356706.28285
EV 239	380116.232331	5358857.57810	EV 298	367938.911161	5356679.59802
EV 240	380044.620338	5358720.31462	EV 299	367995.341372	5356357.83589
EV 241	380954.821923	5358362.02267	EV 300	368158.393947	5355962.78583
EV 242	378582.934404	5361465.62915	EV 301	368288.520701	5356661.98337
EV 243	378496.020042	5360957.09883	EV 302	368398.482398	5358280.31133
EV 244	378494.339753	5360461.36332	EV 303	368786.744765	5358297.46839
EV 245	378445.719673	5360099.10713	EV 304	369066.557110	5358548.78380
EV 246	378600.388987	5359289.26837	EV 305	368935.880317	5358580.95199
EV 247	377806.159261	5358907.71375	EV 306	366051.646464	5354595.98524
EV 248	377732.918590	5359051.04377	EV 307	365649.713248	5354594.38893
EV 249	377556.941690	5359199.08793	EV 308	365389.448232	5354507.51007
EV 250	377145.041275	5359316.28065	EV 309	366712.108830	5354780.56126
EV 251	376889.326209	5359376.14755	EV 310	373441.355271	5346876.92253
EV 252	376889.019323	5360166.00527	EV 311	373464.899172	5346748.97315
EV 253	377330.755890	5360755.95152	EV 312	373035.826629	5346715.79105
EV 254	377902.163962	5361268.58006	EV 313	372802.950217	5346783.67665
EV 255	373598.910717	5358976.30010	EV 314	372665.568263	5346527.05649
EV 256	374002.356999	5359174.34873	EV 315	372410.199780	5346519.50400
EV 257	374071.424092	5359397.95671	EV 316	372517.010590	5346057.29799
EV 258	374285.678274	5359505.13736	EV 317	372883.663152	5345477.82455
EV 259	374392.012283	5359491.69990	EV 318	373043.656106	5345402.67727
EV 260	374468.096954	5359530.79139	EV 319	373422.190181	5345400.60172
EV 261	375268.262743	5359852.11654	EV 320	374443.757480	5346310.56985
EV 262	375831.383963	5359650.00551	EV 321	374499.466118	5346488.71496
EV 263	373429.653298	5357884.66762	EV 322	374007.745210	5346489.07241
EV 264	376400.373206	5358249.84472	EV 323	374077.496620	5345866.91975
EV 265	376419.748309	5358672.75005	EV 324	369538.291742	5346150.62092
EV 266	376592.003878	5358709.59023	EV 325	369501.060632	5346000.12924
EV 267	377257.280186	5358688.67839	EV 326	369756.434724	5345729.78936
EV 268	377140.186236	5358553.57336	EV 327	370573.297858	5344918.18248
EV 269	376858.223333	5358374.03979	EV 328	370200.755883	5344988.64068
EV 270	376686.795916	5358243.10107	EV 329	370296.750884	5345409.97420
EV 271	376011.794085	5357972.20827	EV 330	371103.994432	5345288.10649
EV 272	375518.767069	5357763.47038	EV 331	370994.449511	5345891.93075
EV 273	374025.401644	5356428.47315	EV 332	370231.127517	5345598.12111
EV 274	372640.303785	5356998.18914	EV 333	370266.104698	5345897.60778
EV 275	372820.446912	5356895.82881	EV 334	366754.268043	5344458.81922
EV 276	372129.759140	5355684.48407	EV 335	366818.320967	5344462.71252
EV 277	371371.987905	5355222.17462	EV 336	367489.813096	5344033.09395
EV 278	371319.810772	5355116.07072	EV 337	367283.581029	5344426.67604
EV 279	371343.126644	5354928.54952	EV 338	367468.172333	5344897.78595
EV 280	370970.736008	5355202.14720	EV 339	367438.183279	5344941.58075
EV 281	370618.613169	5355625.05763	EV 340	366608.310222	5344286.18206
EV 282	370373.236822	5355735.99817	EV 341	366966.074569	5343977.09517
EV 283	369986.089326	5355968.50806	EV 342	367036.919907	5344038.50551
EV 284	369479.834321	5355781.30819	EV 343	366802.494943	5344058.55117
EV 285	369528.549491	5355934.55855	EV 344	366366.925867	5343755.83112
EV 286	370693.639137	5355684.98039	EV 345	366461.227478	5343434.03863
EV 287	371483.203686	5356134.67274	EV 346	366335.591292	5343564.72592
EV 288	372228.491046	5356391.00711	EV 347	366097.542212	5344747.78855
EV 289	368076.437198	5357155.07780	EV 348	366262.084970	5344151.61555
EV 290	367201.633447	5356816.73364	EV 349	360261.519457	5339506.32518
EV 291	366970.597051	5356341.75578	EV 350	360483.379778	5339523.33627

Socle					
Localité	X_UTM_32N	Y_UTM_32N	Localité	X_UTM_32N	Y_UTM_32N
EV 351	360565.187922	5339375.40057	EV 410	357323.772293	5315370.93566
EV 352	360871.319236	5339590.61691	EV 411	357758.302218	5315430.65800
EV 353	360991.415008	5339592.34138	EV 412	357782.960060	5315820.44808
EV 354	361349.419364	5339700.56579	EV 413	357816.413349	5316009.56018
EV 355	361505.313856	5339963.11448	EV 414	357886.244937	5316199.36858
EV 356	361326.348760	5339851.57415	EV 415	358067.990906	5315628.33595
EV 357	361132.017856	5339874.19032	EV 416	356601.748341	5314670.96805
EV 358	360500.277446	5339580.66596	EV 417	356273.745833	5314762.98494
EV 359	366703.632838	5342482.07500	EV 418	355978.808001	5314995.03223
EV 360	366604.424812	5342499.92851	EV 419	355834.188019	5315022.95501
EV 361	366081.712594	5342266.31477	EV 420	359719.830082	5315987.01462
EV 362	365462.107119	5342387.23391	EV 421	359470.339695	5315819.82051
EV 363	365157.808817	5342581.92749	EV 422	355615.391666	5313122.87993
EV 364	365323.692712	5342220.55769	EV 423	355736.284055	5313080.38215
EV 365	365171.596031	5341893.87468	EV 424	355577.976387	5312927.87680
EV 366	364849.190690	5341657.65708	EV 425	355496.252363	5312922.75295
EV 367	364692.922535	5341912.31650	EV 426	355432.474861	5312945.49715
EV 368	364616.937617	5342092.17293	EV 427	355277.388674	5313033.11634
EV 369	364020.281182	5341174.72497	EV 428	355276.736648	5313268.38336
EV 370	364018.900464	5341432.53985	EV 429	354730.570784	5312987.13721
EV 371	364284.117738	5341630.07387	EV 430	354692.080275	5312921.24601
EV 372	364163.149202	5341804.40671	EV 431	354652.753020	5312865.80327
EV 373	364510.773377	5342335.51993	EV 432	354297.249054	5312415.37702
EV 374	364690.938600	5342195.95115	EV 433	354402.951055	5313672.68646
EV 375	364796.775408	5341971.37381	EV 434	354520.300414	5314641.20757
EV 376	365092.242935	5342241.87182	EV 435	349410.223687	5318779.31037
EV 377	361995.972551	5340404.69387	EV 436	349792.154457	5318067.77317
EV 378	362097.969806	5340527.91354	EV 437	349835.415069	5317953.38678
EV 379	362068.678813	5340956.83099	EV 438	349015.868444	5318228.67734
EV 380	360095.971590	5338463.03468	EV 439	349145.220968	5318042.36277
EV 381	360696.784479	5338715.72584	EV 440	349165.937032	5317556.32812
EV 382	360995.453402	5338796.33962	EV 441	349908.821598	5314711.30314
EV 383	361117.871878	5338667.42181	EV 442	353983.539037	5314762.48084
EV 384	361178.008266	5338651.78381	EV 443	354188.665935	5315219.98631
EV 385	361462.001896	5338555.52951	EV 444	355224.587790	5316613.28430
EV 386	361530.284345	5338635.15380	EV 445	354543.625205	5316443.18564
EV 387	361266.859842	5337974.27237	EV 446	356046.154826	5310418.07662
EV 388	361056.835961	5337843.19526	EV 447	356254.874871	5310452.13068
EV 389	359881.325411	5337997.39508	EV 448	356722.963934	5310432.89619
EV 390	359903.346297	5339089.44880	EV 449	356373.751787	5310238.23978
EV 391	361893.006811	5341321.91835	EV 450	355687.750720	5309919.46642
EV 392	362042.748611	5341600.18377	EV 451	355307.651577	5309984.79918
EV 393	361222.590357	5340960.63688	EV 452	354726.423406	5308989.48094
EV 394	361357.534436	5340761.97807	EV 453	354960.020700	5310124.49492
EV 395	374067.555754	5339491.43772	EV 454	354940.974041	5310488.62768
EV 396	373587.698728	5339738.35158	EV 455	355720.185501	5310953.01513
EV 397	372216.702545	5339169.45778	EV 456	355408.209420	5311431.06897
EV 398	370851.856177	5339116.99779	EV 457	355404.195587	5311222.14202
EV 399	371172.321721	5339147.57818	EV 458	355127.455121	5311153.08412
EV 400	373137.340517	5338295.54607	EV 459	354954.247502	5311129.83320
EV 401	372811.735826	5338883.11070	EV 460	354771.144691	5311233.68185
EV 402	357626.192914	5316374.12765	EV 461	359260.460505	5313761.67015
EV 403	357811.925794	5316503.53215	EV 462	359103.925958	5314347.84206
EV 404	358210.827902	5316334.54970	EV 463	359161.410307	5314372.90825
EV 405	358683.281650	5316273.42783	EV 464	359253.024819	5314203.66467
EV 406	359119.676214	5316227.49396	EV 465	359295.439894	5314322.25635
EV 407	359118.963793	5315996.49973	EV 466	360260.527958	5314689.92599
EV 408	358965.234165	5315978.50435	EV 467	360230.582585	5314420.38339
EV 409	357220.317149	5315811.79684	EV 468	359708.593466	5314059.59281

Socle

Localité	X_UTM_32N	Y_UTM_32N	Localité	X_UTM_32N	Y_UTM_32N
EV 469	359670.077842	5313797.69914	EV 528	366832.517893	5320266.02191
EV 470	359553.429460	5313673.91939	EV 529	366479.613273	5320618.38330
EV 471	358582.797822	5305917.30886	EV 530	366363.376828	5320360.81633
EV 472	351149.522476	5310015.37374	EV 531	366413.326914	5319949.22318
EV 473	350581.487052	5309972.08763	EV 532	358523.164683	5310534.03999
EV 474	351278.092543	5309728.21034	EV 533	357922.418951	5310209.90660
EV 475	353806.347039	5318397.58671	EV 534	357464.448970	5309745.13151
EV 476	353675.158189	5318345.43334	EV 535	357398.483177	5309474.11683
EV 477	353594.012967	5318308.50002	EV 536	357372.095601	5308983.99973
EV 478	353347.805995	5318222.30832	EV 537	357532.474456	5308393.94523
EV 479	352953.118958	5317414.00478	EV 538	357783.382141	5308092.56933
EV 480	352876.276108	5317028.18953	EV 539	358205.885355	5309722.96422
EV 481	352781.792233	5316977.77273	EV 540	358894.890458	5309464.85680
EV 482	352691.217476	5316773.48046	EV 541	359046.346612	5309040.24078
EV 483	352944.023407	5316737.25159	EV 542	359184.343327	5308959.29158
EV 484	353217.549396	5316772.36699	EV 543	359221.125841	5309351.36142
EV 485	353403.058457	5317716.75182	EV 544	351896.364019	5307269.23231
EV 486	353587.682904	5317766.77581	EV 545	351809.355958	5307703.69367
EV 487	353732.086222	5317773.93153	EV 546	351902.157747	5307879.17410
EV 488	354705.603949	5318416.99809	EV 547	351825.993671	5307963.49091
EV 489	354928.689170	5318631.89692	EV 548	351809.523361	5307857.44642
EV 490	354242.866131	5318449.23457	EV 549	351742.908377	5308183.63989
EV 491	352531.839187	5318329.94109	EV 550	351779.499165	5308308.34402
EV 492	352330.169174	5318301.48144	EV 551	351730.433860	5308449.62930
EV 493	352142.830059	5318397.91993	EV 552	351734.073014	5308687.37897
EV 494	351770.892458	5318186.60371	EV 553	351831.242935	5308935.66345
EV 495	351565.406071	5318070.73251	EV 554	352131.443969	5308741.42769
EV 496	351004.912552	5317505.38649	EV 555	352319.504702	5308947.67319
EV 497	350963.252411	5316547.47983	EV 556	353158.477301	5308339.66734
EV 498	351677.802356	5316483.66660	EV 557	353090.675806	5308023.10674
EV 499	351867.670356	5316758.98616	EV 558	351104.915456	5309283.39690
EV 500	352024.269838	5317179.72296	EV 559	350786.465939	5308852.08352
EV 501	352097.009364	5317496.12596	EV 560	350777.558506	5308661.09865
EV 502	351681.922750	5316217.23372	EV 561	350766.029590	5308352.69631
EV 503	351423.787849	5315739.98557	EV 562	350470.618442	5308125.97953
EV 504	351614.127598	5315142.16839	EV 563	350639.377742	5307824.40436
EV 505	351827.126228	5314885.07924	EV 564	350487.985715	5308220.83207
EV 506	351765.524085	5314485.02055	EV 565	350519.170226	5308325.61975
EV 507	351948.387691	5314035.67753	EV 566	350382.428267	5308667.99603
EV 508	352441.576789	5313789.89093	EV 567	350159.315236	5308853.79528
EV 509	352865.925236	5313975.87079	EV 568	350289.577929	5309055.71659
EV 510	352533.164672	5314527.11393	EV 569	350521.467453	5309254.51211
EV 511	352516.934667	5314360.10611	EV 570	350618.217049	5309411.12832
EV 512	352469.690419	5315159.12287	EV 571	350399.289610	5309472.44459
EV 513	352346.123906	5315798.22466	EV 572	350235.215679	5309653.19946
EV 514	356023.483838	5312056.86117	EV 573	349964.621540	5309565.16359
EV 515	355615.687314	5312619.30790	EV 574	349960.830800	5310388.04967
EV 516	359088.487403	5315449.14890	EV 575	350280.029088	5310481.19433
EV 517	357676.461793	5314014.43620	EV 576	350465.035097	5310326.43996
EV 518	357623.624272	5313297.19428	EV 577	350733.771838	5310479.47505
EV 519	357468.081860	5311896.51112	EV 578	350549.614117	5305989.05274
EV 520	357643.672310	5312025.01802	EV 579	350900.634261	5305608.91752
EV 521	366531.825082	5321834.37579	EV 580	351286.232234	5306522.66936
EV 522	366895.724205	5321930.95430	EV 581	351219.444537	5306803.48991
EV 523	367269.584477	5321859.49738	EV 582	351115.373593	5306994.86445
EV 524	367404.636947	5321732.45008	EV 583	351078.398989	5307494.52630
EV 525	367767.289490	5321351.90045	EV 584	350943.835624	5306984.74067
EV 526	368357.847240	5320863.73066	EV 585	350986.096868	5306796.33073
EV 527	367700.360330	5320070.29446	EV 586	350606.938167	5306759.24998

Socle

Localité	X_UTM_32N	Y_UTM_32N	Localité	X_UTM_32N	Y_UTM_32N
EV 587	350425.550420	5306831.71506	EV 646	367526.652653	5351924.74859
EV 588	350450.006990	5307036.65696	EV 647	367110.236313	5352041.02997
EV 589	350430.381742	5307246.05961	EV 648	368380.108009	5352112.94475
EV 590	350381.171877	5307481.61080	EV 649	365745.048029	5353144.97393
EV 591	349849.664781	5307829.23206	EV 650	365659.218864	5352051.83599
EV 592	350020.841213	5306693.99663	EV 651	365041.119048	5351000.38207
EV 593	350234.989979	5306442.26909	EV 652	365580.274498	5350545.18055
EV 594	353712.818223	5306568.39793	EV 653	364967.039756	5352581.58631
EV 595	353072.744202	5306384.08910	EV 654	364748.445045	5353191.82006
EV 596	354183.896742	5307127.47395	EV 655	362409.498265	5350542.78217
EV 597	354485.549510	5307188.77778	EV 656	362944.305556	5350735.27256
EV 598	354827.043890	5307391.18075	EV 657	363446.178737	5350730.97220
EV 599	354899.697240	5307092.26443	EV 658	364084.531547	5350402.70766
EV 600	354969.872874	5307002.90309	EV 659	364450.474526	5349637.36084
EV 601	355021.962742	5306766.87900	EV 660	364467.841643	5349539.29050
EV 602	368999.269059	5358445.95384	EV 661	364242.766628	5349429.76336
EV 603	368784.941010	5358538.36768	EV 662	364175.244924	5349129.68664
EV 604	368280.954218	5358558.69149	EV 663	364274.891036	5349014.91955
EV 605	367586.892411	5358605.25053	EV 664	362932.388257	5348827.12328
EV 606	367218.745770	5358648.14481	EV 665	362414.116615	5350220.43627
EV 607	367455.912766	5358756.06593	EV 666	357301.167016	5347090.91652
EV 608	368063.084044	5359075.93402	EV 667	357185.181656	5346563.16419
EV 609	368256.075579	5359250.31586	EV 668	358611.594751	5344306.52215
EV 610	369419.790122	5359578.12762	EV 669	357776.913329	5344410.12207
EV 611	375037.885179	5360110.41211	EV 670	359412.624759	5347196.81432
EV 612	374347.247144	5360096.83096	EV 671	360064.143304	5347324.49226
EV 613	364160.086403	5341877.46520	EV 672	360113.248657	5347644.46200
EV 614	364370.683355	5342485.46352	EV 673	360011.951657	5347031.95124
EV 615	364314.422576	5343499.57312	EV 674	359624.171732	5347114.02285
EV 616	367987.087916	5355313.93729	EV 675	358760.984351	5345661.17533
EV 617	367501.421615	5355214.33407	EV 676	358312.882352	5342535.96163
EV 618	367775.320713	5355421.03804	EV 677	358263.202829	5341503.48067
EV 619	367628.457673	5355659.13324	EV 678	357401.654091	5341956.93597
EV 620	367642.722522	5355449.25770	EV 679	357461.154797	5341664.49048
EV 621	367393.031815	5355421.52232	EV 680	357531.509160	5339847.40027
EV 622	367047.097717	5355305.36378	EV 681	356681.832409	5340077.03706
EV 623	367152.298476	5355172.09115	EV 682	356138.879545	5340589.53236
EV 624	367214.902300	5355007.17518	EV 683	356416.550679	5341746.60299
EV 625	367334.471670	5354826.64644	EV 684	356257.677764	5341187.89338
EV 626	367410.091832	5354634.53499	EV 685	356092.254495	5341286.56112
EV 627	369172.607805	5354982.39342	EV 686	355998.317532	5341091.75580
EV 628	368667.906312	5355001.01718	EV 687	370398.157260	5349375.47345
EV 629	368055.472441	5355191.48603	EV 688	370320.863865	5349030.47448
EV 630	368250.790519	5355340.47469	EV 689	370003.943796	5348943.78597
EV 631	379377.613389	5361268.54034	EV 690	370033.594032	5349157.45030
EV 632	379047.689925	5360458.50798	EV 691	369808.053827	5349181.28891
EV 633	379266.652434	5360334.63315	EV 692	369784.463736	5349331.23244
EV 634	380595.857835	5360949.62470	EV 693	369071.221433	5349307.16937
EV 635	380779.036960	5360996.16333	EV 694	369007.290122	5349198.27804
EV 636	381442.011268	5361232.71131	EV 695	368897.998777	5349077.90413
EV 637	381050.229254	5361396.53721	EV 696	368972.309421	5349088.61766
EV 638	380938.097224	5361280.24134	EV 697	369063.753917	5349120.05496
EV 639	380134.072306	5361212.74065	EV 698	368968.642315	5349025.77792
EV 640	379806.508750	5361209.64980	EV 699	368806.906831	5348851.00249
EV 641	369766.576363	5352313.17144	EV 700	368413.958781	5348028.33499
EV 642	369889.826988	5352429.38538	EV 701	368468.534784	5348446.96805
EV 643	369848.873061	5352669.11313	EV 702	368813.178877	5348465.28676
EV 644	369712.879296	5353122.46567	EV 703	369166.226899	5348581.88448
EV 645	367755.319969	5351993.53511	EV 704	370273.539465	5348676.65376

Socle

Localité	X_UTM_32N	Y_UTM_32N	Localité	X_UTM_32N	Y_UTM_32N
EV 705	370364.047419	5349515.50614	EV 764	379219.233109	5345010.36515
EV 706	353101.640580	5340510.11956	EV 765	379486.998999	5345261.81398
EV 707	353548.140821	5340662.53905	EV 766	379375.794129	5345857.39199
EV 708	354567.147033	5339906.89775	EV 767	379274.140787	5346090.53349
EV 709	353435.960976	5340053.27962	EV 768	379589.281688	5346057.36486
EV 710	352097.236143	5340734.44511	EV 769	377729.802642	5345237.41990
EV 711	350725.839022	5341003.23279	EV 770	377512.344418	5344991.02379
EV 712	350852.055358	5340921.93013	EV 771	377569.612089	5345113.94417
EV 713	351953.928123	5340707.53780	EV 772	377905.334955	5345175.65565
EV 714	354499.392469	5341617.80347	EV 773	378152.366192	5344892.67768
EV 715	354447.943437	5341016.40902	EV 774	378312.001597	5344754.33669
EV 716	348558.682896	5336486.12645	EV 775	376135.557817	5347305.75081
EV 717	349003.118679	5336665.48426	EV 776	376093.227150	5346852.77844
EV 718	348429.469101	5337185.23954	EV 777	376069.916744	5346495.63373
EV 719	347828.667658	5338227.14416	EV 778	376092.532195	5346316.83878
EV 720	343393.641728	5336979.53089	EV 779	376035.198190	5346110.58823
EV 721	347864.356997	5333249.25298	EV 780	376174.667988	5345968.72702
EV 722	347962.124686	5333656.61211	EV 781	376010.034150	5345583.95741
EV 723	348195.426333	5333888.33450	EV 782	375951.246321	5345466.26163
EV 724	348963.358594	5334827.11104	EV 783	375729.800425	5345050.25255
EV 725	347521.053346	5333728.05145	EV 784	375496.873316	5345133.32811
EV 726	346688.892037	5332248.69880	EV 785	375390.187176	5345173.12787
EV 727	346619.834767	5332045.61936	EV 786	375254.868626	5345511.34997
EV 728	346467.012765	5331546.33644	EV 787	375221.800437	5346180.11879
EV 729	346137.620755	5330401.48341	EV 788	374949.529109	5346858.50634
EV 730	346223.239361	5329931.23851	EV 789	375086.247922	5347106.69761
EV 731	346881.151255	5330976.08236	EV 790	368243.626869	5346227.59854
EV 732	367555.862093	5346839.04908	EV 791	368280.011132	5345614.17882
EV 733	367508.061994	5346786.31776	EV 792	368185.722169	5345036.28411
EV 734	367140.528210	5346664.87785	EV 793	368249.283804	5344929.02241
EV 735	366705.585622	5346688.54523	EV 794	368317.614575	5344561.59079
EV 736	365651.645472	5346054.90798	EV 795	368335.927894	5344362.60551
EV 737	365245.980763	5346262.76616	EV 796	368768.064278	5344215.51684
EV 738	365376.563439	5346239.42259	EV 797	368632.388013	5343892.54358
EV 739	365595.714385	5346381.66884	EV 798	368680.289905	5343699.34063
EV 740	364918.353488	5346940.15357	EV 799	368639.428378	5343488.78975
EV 741	366049.759855	5346802.80438	EV 800	368287.686662	5343360.92819
EV 742	367890.071349	5347440.88790	EV 801	368027.193914	5343765.57287
EV 743	368077.740514	5347262.49957	EV 802	368066.608437	5344420.96162
EV 744	368147.525252	5347129.36594	EV 803	368105.491767	5344511.15136
EV 745	370580.814515	5347764.74872	EV 804	367964.617750	5344807.89678
EV 746	370628.657402	5347822.01010	EV 805	367917.408039	5345082.08637
EV 747	370615.337411	5348001.07064	EV 806	367940.497892	5345740.94601
EV 748	370706.041690	5348081.25290	EV 807	371507.476692	5347367.05737
EV 749	371091.340695	5348234.40849	EV 808	371467.217956	5346540.56860
EV 750	371276.603533	5347985.42940	EV 809	371440.307483	5345932.94001
EV 751	371592.179594	5348136.36706	EV 810	371565.688628	5345600.26290
EV 752	372202.514213	5348123.03769	EV 811	371911.424560	5345397.20481
EV 753	372287.504226	5348064.64434	EV 812	372097.092610	5345225.71866
EV 754	371067.987558	5347841.70656	EV 813	372212.135357	5346006.46603
EV 755	365319.881392	5344142.80676	EV 814	372427.436718	5345574.88168
EV 756	365250.563669	5343547.46131	EV 815	370444.999870	5345379.48750
EV 757	365335.297886	5343916.52242	EV 816	370934.029104	5346496.72424
EV 758	378572.024629	5344707.92872	EV 817	370742.785352	5346895.84727
EV 759	378577.907563	5344821.09700	EV 818	373776.892602	5346438.79533
EV 760	378660.837054	5345192.91251	EV 819	373970.088819	5345797.44954
EV 761	378722.235715	5345286.64784	EV 820	373923.853509	5345954.03234
EV 762	378909.565777	5345071.12231	EV 821	373059.674345	5345832.35275
EV 763	379023.967928	5345133.04572	EV 822	357126.450521	5317145.29925

Socle

Localité	X_UTM_32N	Y_UTM_32N
EV 823	357055.238364	5317479.35617
EV 824	357152.753701	5317501.08726
EV 825	357212.147920	5317300.59555
EV 826	357633.847317	5317645.82704
EV 827	358075.083625	5317388.10967
EV 828	358253.853415	5317065.36184
EV 829	358431.736028	5317020.09834
EV 830	358625.155586	5316996.73863
EV 831	358334.159862	5316645.80358
EV 832	358216.608570	5316613.48494
EV 833	358081.353747	5316981.71033
EV 834	357747.698406	5317155.07452
EV 835	357291.064961	5316704.86939
EV 836	357521.938359	5317231.76065
EV 837	357365.692770	5317242.37886

Complexe magmatique du Champ du Feu - ASM (Edel et al., 2011)

Localité	X_UTM_32N	Y_UTM_32N	Localité	X_UTM_32N	Y_UTM_32N
CF1	381707.536642	5363216.30832	CF24	380712.778801	5361461.15434
CF10	366300.538267	5365708.06446	CF25	374861.520770	5363020.25277
CF10	368994.453504	5365699.52127	CF26	375450.636464	5363829.56266
CF100	370956.027507	5361851.02750	CF27	373928.098152	5363123.73465
CF101	372456.380088	5359926.32378	CF28	372878.607947	5359856.31681
CF102	377035.658632	5361938.07951	CF29	369756.855038	5361335.26788
CF103	371470.889766	5367319.91955	CF3	375581.683996	5365197.12092
CF103	370787.273352	5362848.40338	CF30	370427.552425	5360051.25748
CF104	371070.431718	5361899.84466	CF31	369861.283900	5360157.68985
CF105	370869.054895	5362762.84174	CF32	369918.963940	5360206.28081
CF106	369468.739414	5362651.65070	CF33	369036.350102	5360785.82948
CF107	372534.598149	5371191.88599	CF36	375875.039056	5371421.51926
CF108	372451.001433	5371279.16649	CF37	373830.192952	5371793.02090
CF11	365907.767243	5364602.75798	CF38	373098.670835	5371438.48634
CF110	372549.735391	5371009.72369	CF4	372064.434153	5360443.06298
CF111	372625.347210	5371593.17991	CF44	375898.826602	5370528.31826
CF112	372616.780821	5371686.71038	CF5	369137.908523	5367731.74313
CF113	381374.738867	5361882.15617	CF5	372353.701807	5360245.95118
CF114	377715.086753	5361449.96798	CF51	370619.699806	5367661.93707
CF115	373087.708030	5359989.34793	CF53	369212.400844	5360289.03420
CF116	370265.640966	5368102.56466	CF54	371029.001187	5363015.05864
CF117	369877.377911	5366982.67736	CF6	373916.886444	5362122.62804
CF118	369306.335627	5362473.94448	CF62	371842.516658	5365474.80134
CF119	369346.164396	5362475.20976	CF63	372433.034820	5365126.77337
CF12	368886.963828	5362324.09223	CF64	370431.926288	5366683.26418
CF120	369392.951718	5362475.87965	CF65	370978.085797	5367470.22877
CF121	369380.634628	5362413.84497	CF66	372462.495614	5367274.95804
CF122	369356.589404	5362413.77071	CF67	372284.777129	5367068.40403
CF123	382202.270109	5361417.71522	CF68	371580.497731	5367465.70799
CF124	374200.073684	5362757.92720	CF69	371632.402428	5367422.78811
CF125	374073.978452	5362906.58791	CF7	365083.964481	5364896.91106
CF126	375053.836036	5363154.89117	CF7	375521.652215	5361453.15655
CF127	374891.101194	5363317.53527	CF70	371366.000300	5367407.10613
CF128	375079.618134	5363154.62456	CF71	370922.949807	5368074.92481
CF128	376756.037785	5365030.06318	CF72	365324.082518	5364702.41358
CF13	369634.034181	5362871.24980	CF73	372008.079481	5371679.97704
CF130	376621.412121	5364723.14086	CF74	377913.159844	5361411.25578
CF131	375322.200117	5367708.53367	CF75	366576.610441	5366116.70766
CF133	378935.388841	5367985.88837	CF76	366525.771121	5366106.27413
CF134	378737.801962	5367911.17059	CF77	377857.472511	5362219.47191
CF135	377023.059813	5366910.61454	CF78	377602.387992	5362093.41296
CF136	371433.904298	5368737.23831	CF79	378021.627073	5365522.17243
CF137	371309.743935	5369359.95770	CF8	366453.162174	5366164.20238
CF138	378921.640642	5366521.15280	CF8	376756.203353	5362342.36541
CF14	368728.629817	5362819.36946	CF80	382567.537737	5363840.31307
CF140	372103.982630	5369024.52056	CF81	382362.031957	5363743.71729
CF141	372248.835337	5369094.42311	CF82	366374.529925	5366216.18256
CF142	372320.768959	5369003.39762	CF83	372242.022054	5371815.28650
CF15	368597.785763	5363062.50906	CF84	372087.671577	5371680.62227
CF16	368073.199983	5364427.58842	CF85	366352.363566	5366714.86829
CF17	383813.019933	5363849.17177	CF86	371067.640972	5365329.09024
CF18	373831.586465	5370366.48941	CF87	370666.906647	5365640.99751
CF18	382795.202351	5363795.32021	CF87a	374715.541644	5365457.68311
CF19	383330.515901	5363592.40993	CF88	370931.753130	5365104.89350
CF2	381840.250591	5363142.24955	CF89	370955.567100	5365100.72217
CF20	380734.360719	5363646.43612	CF9	366179.295086	5365888.24420
CF21	381214.271917	5362563.22393	CF92	367326.777553	5364287.38391
CF22	378419.062252	5364012.91346	CF93	367179.270495	5364126.58042
CF23	376825.932134	5362631.15650	CF94	378868.351833	5365055.86443

Complexe magmatique du Champ du Feu - ASM(Edel *et al.* , 2011)

Localité	X_UTM_32N	Y_UTM_32N
CF95	382194.300240	5363850.08678
CF96	373561.934867	5370574.07493
CF97	373408.108193	5369639.01570
CF98	374892.786774	5367139.87598
CF99	374836.262277	5366822.59058
VN11	370444.954799	5366303.33041
VN13	382336.917990	5363752.32766
VN2	376625.266351	5364592.97498
VN20	372622.347672	5370914.67549
VN20	377878.196414	5362217.69949
VN21	378966.804601	5362738.91451
VN28	373690.932792	5360913.08874
VN3	375983.733923	5370223.99760
VN30	377327.545481	5361544.23674
VN31	377901.143304	5361561.65211
VN4	369957.135902	5367712.93734
VN40	371368.796560	5367380.47627
VN50	368810.818305	5367839.54448

Granite des Crêtes Nord (Col de Fouchy - Col du Bonhomme) et Sud (La Bresse - Thiéfosse)

Localité	X_UTM_32N	Y_UTM_32N	Localité	X_UTM_32N	Y_UTM_32N
DN 1	370450.653442	5351547.15751	CS 33	331609.814969	5315227.00942
DN 2	367649.070024	5351282.01336	CS 34	330590.988338	5313605.11112
DN 3	372178.400687	5349946.08199	CS 35	331760.173303	5312959.05714
DN 4	364814.030263	5348615.81773	CS 36	333382.288374	5312546.69302
DN 5	365947.837362	5347591.67371	CS 37	331075.637620	5313399.92404
DN 6	362978.508419	5345360.01703	CS 38	331005.014057	5314345.61337
DN 7	362572.393147	5346912.08719	CS 39	333783.714851	5314974.71742
DN 8	361081.066460	5345605.04413	CS 40	332675.539320	5316083.91412
DN 9	359670.675391	5343491.02116	CS 41	333041.310734	5317020.59860
DN 10	356522.921509	5333983.48647	CS 42	337645.225155	5316681.17075
DN 11	357143.279115	5334556.19601	CS 43	338226.580375	5317217.20855
DN 12	358101.368767	5337984.78229	CS 44	337996.645335	5314973.22221
DN 13	359637.919526	5340201.17592	CS 45	338429.018480	5316449.62569
DN 14	356460.256541	5339099.75733	CS 46	338680.561822	5315966.15361
DN 15	355878.338185	5339587.22275	CS 47	333943.325592	5314033.93261
DN 16	360399.232568	5341848.11177	CS 48	340462.778734	5315690.30271
DN 17	359900.204096	5340665.46125	CS 49	341190.671999	5316446.86695
DN 18	361650.533289	5342805.22532	CS 50	341096.915035	5317107.52287
34	370220.896934	5349830.63424	CS 51	342600.903845	5318180.22838
35	369104.428226	5349681.66220	CS 52	345301.950922	5321183.97344
36	370945.916999	5350079.75133	CS 53	346069.989744	5321771.33407
37	370570.093579	5350882.27287	CS 54	346006.172756	5322405.13865
38	367337.623331	5348684.57973	CS 55	345763.082323	5323583.17344
39	366824.787980	5349617.36049	CS 56	345374.638651	5323328.55246
40	367142.407411	5349953.16956	CS 57	345015.032818	5322531.90668
			CS 58	342310.033280	5321317.24298
			CS 59	341394.728401	5320458.22388
			CS 60	341459.724350	5319433.18046
CS 1	342482.298253	5320888.01811			
CS 2	343206.786209	5322189.87719			
CS 3	343192.224620	5321246.74653			
CS 4	344646.078650	5321898.65576			
CS 5	345485.967090	5322061.35919			
CS 6	344900.591426	5321424.65238			
CS 7	344157.491463	5320525.34658			
CS 8	340551.334233	5318703.84631			
CS 9	340679.326131	5319775.45690			
CS 10	339352.538365	5319478.72331			
CS 11	339002.959346	5318544.94838			
CS 12	342627.908354	5320029.47362			
CS 13	341666.378819	5318400.52924			
CS 14	339022.187973	5317187.46853			
CS 15	340798.134261	5315844.13924			
CS 16	342108.827099	5317205.70289			
CS 17	339638.361853	5316747.60274			
CS 18	337048.725482	5313943.33836			
CS 19	336963.162310	5314483.35282			
CS 20	335671.858058	5315741.72384			
CS 21	335782.028062	5316722.94223			
CS 22	337293.266851	5317262.07708			
CS 23	333904.965713	5317535.05542			
CS 24	334612.819219	5316574.76880			
CS 25	334479.602123	5315275.37066			
CS 26	333321.590007	5314837.92307			
CS 27	332450.033579	5313724.97203			
CS 28	334751.952876	5313530.52879			
CS 29	331687.150185	5313741.66290			
CS 30	328631.913617	5315023.85772			
CS 31	324737.547782	5315526.76860			
CS 32	330357.916131	5314781.77069			

Granites et migmatites des Vosges moyennes (Kratinová *et al.*, 2007; Schulmann *et al.*, 2009)

(Granite fondamental - Kaisersberg, Trois Epis - Bilstein, Brézouard, Thannenkirch)

Localité	X_UTM_32N	Y_UTM_32N	Localité	X_UTM_32N	Y_UTM_32N
bil10	361084.959247	5337849.66901	ho10	352676.511457	5321432.03793
bil11	372907.854362	5340148.60471	ho11	353029.908316	5321023.54834
bil3	373759.190451	5340156.39464	ho12A	352615.375130	5319742.52044
bil4	364873.420647	5338467.16032	ho12B	352615.375130	5319742.52044
bil41	364096.931443	5337962.91641	ho13A	352778.435893	5320171.08291
bil5	365601.392612	5338116.36171	ho13B	352778.435893	5320171.08291
bil6	366100.822366	5338672.88860	ho14	352814.553489	5320405.80165
bil7	363899.712499	5337551.69886	ho15A	349444.276591	5319586.13712
bil8	362248.032670	5337872.65299	ho15B	349444.276591	5319586.13712
bil9	361772.768524	5337165.72783	ho16	352138.229510	5322389.13771
brz1	371939.007644	5340735.16445	ho17	351737.400506	5324061.94941
brz10	374239.124479	5341661.43742	ho18	351099.954852	5324070.29261
brz11	369731.440587	5339892.18768	ho19	353852.281856	5325807.63953
brz12	372992.907348	5340863.94970	ho1A	351820.186693	5318821.13128
brz13	373056.018827	5340526.72169	ho1B	351820.186693	5318821.13128
brz14	363134.115531	5340799.46960	ho20	354600.521306	5326132.98015
brz15	362786.193155	5340272.91543	ho2A	351642.826299	5319164.40613
brz16	365006.350462	5341006.19286	ho2B	351642.826299	5319164.40613
brz17	364599.335974	5340487.60672	ho4	350437.023376	5319508.29664
brz18	364322.995631	5338869.43695	ho5	350777.154911	5319378.88038
brz19	372829.292291	5340492.85066	ho6A	353428.829920	5321640.65243
brz2	370385.919776	5340983.74424	ho6B	353428.829920	5321640.65243
brz28	374293.284679	5341421.16547	ho7	353767.219753	5321631.79480
brz3	371468.809861	5340353.19844	ho8	356253.019136	5322164.83528
brz35	369694.965166	5339401.50443	ho9	357410.514593	5320469.52674
brz36	366037.172308	5340333.56856	k10a	371032.873116	5335838.18213
brz37	366900.503326	5341395.38743	k10b	371032.873116	5335838.18213
brz38	367147.015577	5340203.08917	k11	370748.116779	5336614.97948
brz39	364541.499831	5339867.33394	k12	372301.704235	5337184.48986
brz4	371648.662532	5340351.37398	k13a	371675.588013	5337488.82053
brz40	363900.655941	5339245.36138	k14a	371006.907254	5337295.15445
brz5	369476.122453	5341405.92893	k15	372147.129735	5335219.40566
brz6	366552.680707	5339584.19960	k154	372300.105055	5339665.10676
brz7	364859.814273	5339400.50466	k156	372146.381663	5339838.68567
brz8	364657.565144	5339023.85748	k16b	371690.062118	5336484.30935
cf41	379963.107887	5346341.02020	k17a	372005.886843	5336657.97214
cf42	380804.626790	5348492.97967	k18	371378.066757	5338116.21303
cf43	381766.815415	5350867.74292	k19a	370679.178082	5333460.52543
cf44	382518.391877	5351897.48772	k1a	371006.593588	5332830.57074
cf45	381734.339133	5355593.14817	k1b	371006.593588	5332830.57074
cf46	381386.755059	5353345.24783	k1c	371006.593588	5332830.57074
cf47	380979.890555	5352292.02430	k2	366677.655920	5335357.64384
cf48	380688.437956	5352938.65436	k20	369030.186482	5336186.27610
cf49	380238.263935	5352917.35597	k21	369885.766305	5337089.99856
cf50	381239.691712	5355820.75065	k22a	369500.135006	5337273.45287
cf55	377000.505738	5344787.01703	k23a	369014.903430	5337465.42187
cf56	375377.993388	5345280.41491	k24	367893.754179	5337260.27389
cf56	375377.993388	5345280.41491	k25a	368144.041005	5337840.84969
cf57	377869.779743	5348540.13284	k26a	368303.645070	5336773.75664
cf57	377869.779743	5348540.13284	k27	366847.943600	5337349.67534
cf58	376472.909599	5347755.19510	k28	366657.334885	5337115.14720
cf59	374550.195105	5347351.33157	k29	366419.737081	5337035.12965
cf60	374309.492745	5344651.14778	k3	363181.382116	5336710.00871
cf60	374309.492745	5344651.14778	k30	368159.335304	5333324.72931
cf61	378479.970379	5347604.13366	k31a	368041.005160	5334287.97634
cf61	378479.970379	5347604.13366	k31b	368041.005160	5334287.97634
gsm1	374083.686930	5345894.90023	k32	368560.639619	5333089.77085
gsm1	374083.686930	5345894.90023	k33a	368710.129839	5332725.83980

Granites et migmatites des Vosges moyennes (Kratinová *et al.*, 2007; Schulmann *et al.*, 2009)

(Granite fondamental - Kaysersberg, Trois Epis - Bilstein, Brézouard, Thannenkirch)

Localité	X_UTM_32N	Y_UTM_32N	Localité	X_UTM_32N	Y_UTM_32N
k33b	368710.129839	5332725.83980	mz66	358219.063514	5330281.00741
k34	366697.132471	5332416.30106	te10b	368941.256582	5336016.95413
k35	366818.869978	5332666.75590	te11	369651.233047	5336106.76264
k36a	366475.885916	5334170.93054	te12	369878.952495	5335836.47792
k36b	366475.885916	5334170.93054	te13	368290.874271	5336624.35518
k38	370193.938170	5333652.48821	te14	368464.535073	5336308.52451
k39	371808.097903	5332230.33478	te15a	368582.859217	5335345.28552
k40	370575.768326	5331663.43465	te16	368052.078124	5335591.31265
k41a	367614.933515	5331063.65700	te17a	368543.701040	5332539.40357
k42	367095.634485	5330857.21072	te17b	368543.701040	5332539.40357
k43	366069.801131	5330593.72466	te18	368347.046917	5333760.17005
k44	366210.694389	5330481.35128	te19	367699.632428	5333815.50523
k45	366429.910169	5330111.45506	te1a	368067.824633	5335188.64957
k46	366604.854177	5330397.49834	te20a	367518.734188	5334633.60615
k47	366949.211750	5330317.90240	te21a	368758.224506	5333875.52153
k48	366390.337087	5334930.71952	te21c	368758.224506	5333875.52153
k48	366390.337087	5334930.71952	te22a	368981.691282	5333555.43366
k49a	367393.172980	5330229.79475	te22b	368981.691282	5333555.43366
k4a	370353.125532	5334341.18627	te23	366700.632328	5334452.71023
k50	367407.655720	5329225.24250	te24	366806.187385	5333340.05471
k51	366372.670710	5325802.05302	te25	367535.761362	5334832.81015
k52m	366618.971787	5325279.34107	te26	367875.854600	5334703.41088
k53m	366032.723673	5326403.00070	te27a	367154.380939	5335066.06898
k55	366858.418735	5337589.56944	te27b	367154.380939	5335066.06898
k56a	366930.021426	5338075.05958	te28a	369285.192075	5331823.88851
k57b	366862.023777	5338214.71596	te28b	369285.192075	5331823.88851
k58	364681.141378	5333673.17259	te29	370182.883940	5332349.15155
k5a	370610.208739	5336175.29053	te2a	367914.165339	5335151.61902
k6	370573.177705	5336328.94764	te30	368667.567599	5332227.82706
k7a	370641.281199	5337125.74987	te31	368115.496294	5332224.84439
k7b	370641.281199	5337125.74987	te32a	368139.760086	5331921.77948
k8a	370674.055265	5336922.29308	te32b	368139.760086	5331921.77948
k9a	371400.209364	5334853.67058	te33a	368852.732814	5331459.52565
k9b	371400.209364	5334853.67058	te33b	368852.732814	5331459.52565
mz42	355553.864019	5319255.31817	te34	369224.339637	5330524.79499
mz43	355109.930251	5321388.41763	te35	369755.133801	5330278.77541
mz44	354345.955718	5322443.13864	te36	370059.465284	5330904.91591
mz45	358928.645496	5322306.43349	te37a	368979.587544	5330595.87587
mz46	360622.757670	5324686.03233	te38a	368339.408078	5330148.92994
mz47	356995.684490	5324559.57790	te38b	368270.867428	5331107.93021
mz48	354335.544240	5324354.04430	te39	368270.867428	5331107.93021
mz49	355580.302163	5324813.01663	te3a	367424.670212	5335293.78916
mz49	355580.302163	5324813.01663	te40	367858.414149	5330390.69722
mz50	365357.024917	5324612.95916	te41a	370763.956220	5329169.20199
mz51	365360.400733	5324057.97258	te42a	370365.290467	5329082.86984
mz52	364126.202809	5325931.96803	te43b	368896.102663	5328797.05367
mz53	364603.660120	5325225.64119	te44m	368164.575236	5328337.84049
mz54	365026.381998	5324880.94958	te45a	367697.883485	5328277.38896
mz55	362543.693038	5326420.08316	te46a	369150.749610	5327902.41178
mz56	363150.875422	5325381.34624	te46b	369150.749610	5327902.41178
mz58	364055.370285	5324861.62963	te47a	367930.768378	5331237.32646
mz59	354150.632705	5324940.38966	te47b	367930.768378	5331237.32646
mz60	353615.896150	5325283.20699	te4a	370380.819426	5331730.25883
mz61	355757.714066	5328485.23776	te5	368811.890659	5329807.56052
mz62	355648.247811	5327718.40175	te6a	368838.694559	5330708.24679
mz63	356546.099841	5327805.95360	te6b	368838.694559	5330708.24679
mz64	357325.001206	5327965.55645	te7a	369649.955199	5335504.90051
mz65	356704.871819	5329565.80204	te7b	369649.955199	5335504.90051

Granites et migmatites des Vosges moyennes (Kratinová *et al.*, 2007; Schulmann *et al.*, 2009)

(Granite fondamental - Kaisersberg, Trois Epis - Bilstein, Brézouard, Thannenkirch)

Localité	X_UTM_32N	Y_UTM_32N	Localité	X_UTM_32N	Y_UTM_32N
te8	369484.805438	5335920.33061	v562	364447.289396	5337024.90290
te9	368803.345274	5335577.26224	v563	365568.611724	5336406.79171
te9	368803.345274	5335577.26224	vc1	371170.729631	5324449.38163
thk1	371813.635808	5341474.12940	vc10	363990.336916	5329501.55307
thk10	374950.803899	5342496.45763	vc100	358667.822173	5317037.10900
thk11	376063.037735	5341943.98217	vc101	358458.105138	5317130.12370
thk12	369168.958673	5341688.74922	vc102	358314.978076	5318289.11154
thk13	376638.352876	5342706.55352	vc103	358802.323610	5318075.82942
thk14	377586.978874	5344704.33196	vc104	358831.970646	5318340.88858
thk15	374227.749688	5343942.38613	vc105	354617.903394	5321518.74021
thk16	374537.411997	5344274.71858	vc106	355279.208408	5321830.10824
thk17	375044.546971	5343756.50842	vc107	353384.316407	5321294.31795
thk18	374970.507296	5344817.85913	vc108	353730.800724	5321307.72376
thk19	375221.729480	5343909.41680	vc109	354421.150110	5320642.92203
thk2	371079.995638	5342226.81808	vc11	361743.967313	5329875.62946
thk20	375988.839386	5343145.42135	vc110	357704.839283	5317278.83340
thk21	376271.369272	5343154.84963	vc111	361665.425346	5319846.65498
thk22	377369.096494	5344036.27354	vc112	361658.769071	5319632.18763
thk23	378581.615582	5343523.27063	vc113	361357.503307	5319794.02822
thk24	375576.393974	5342289.28622	vc114	359522.913994	5317906.92713
thk25	375100.554673	5342107.31615	vc115	358787.404065	5319048.15625
thk26	374726.927390	5342351.25375	vc116	358720.523569	5321365.16465
thk27	374996.521544	5341700.38507	vc117	360041.016728	5322260.29326
thk29	374406.030537	5341951.32462	vc118	363909.181676	5323223.71118
thk3	371287.940412	5341792.88340	vc12	361338.066549	5329415.03766
thk30	374239.591992	5341884.93732	vc13	358465.065742	5331886.35757
thk31	373976.949574	5342678.02717	vc14	359617.305812	5331325.27925
thk32	373042.776387	5344439.03732	vc15	359472.774762	5327375.33211
thk33	373353.652890	5344188.59135	vc16	361125.605776	5326271.88697
thk34	371527.927582	5342945.07800	vc17	359574.350373	5327050.33485
thk4	374836.912880	5345600.29964	vc18	359561.900839	5326907.17996
thk42	373477.152586	5342690.20833	vc19	359787.044387	5327124.08519
thk5	375200.558702	5344130.05405	vc2	370985.256948	5324256.72843
thk6	373854.034601	5344913.63705	vc20	359941.192875	5326509.77854
thk8	374467.734985	5343235.42746	vc21	360045.196002	5326496.11710
thk9	374641.083343	5342975.85474	vc22	360126.028763	5326479.68672
v524	371441.531572	5341221.18119	vc23	363084.484101	5323129.90289
v527	371874.940720	5341589.51291	vc24	365208.215215	5321863.04929
v529	372015.304049	5341220.51122	vc25	359803.562588	5316376.52792
v530	373009.709093	5341351.74324	vc26	360536.196872	5320692.44814
v532	373814.617356	5341318.31236	vc27	356478.176756	5321245.06659
v533	374659.954705	5341399.75177	vc28	354701.085289	5321975.94199
v535	370305.205233	5340571.90740	vc29	360046.745170	5326620.63310
v536	362030.118421	5337534.27886	vc3	370605.367012	5324864.65343
v537	369621.036772	5341112.37609	vc30	354907.373680	5318595.44047
v538	369889.778221	5341130.70491	vc31	353124.823758	5320657.02240
v539	370080.180326	5340972.90643	vc32	353958.455585	5320491.18648
v540	366113.954313	5339423.21759	vc33	359537.261141	5319623.62340
v541	365325.852001	5338794.53758	vc34	359493.244066	5318036.65383
v542	362476.283173	5336354.72213	vc35	360695.747539	5319857.85907
v543	361709.172389	5336720.20817	vc36	362236.391480	5332293.63439
v555	373386.908779	5340028.97976	vc37	359966.029099	5330269.14733
v556	371440.676516	5340358.28027	vc38	360338.825393	5331903.70460
v557	371198.115326	5340447.15137	vc39	361464.135842	5335081.36827
v558	369548.361672	5341249.70471	vc4	371000.086244	5325943.29120
v559	370610.516609	5341644.74468	vc40	363078.785939	5335977.71610
v560	361115.280201	5337291.77291	vc41	362367.723108	5334069.79171
v561	362737.047700	5335440.99749	vc5	369825.523570	5325448.31508

Granites et migmatites des Vosges moyennes (Kratinová *et al.*, 2007; Schulmann *et al.*, 2009)

(Granite fondamental - Kaysersberg, Trois Epis - Bilstein, Brézouard, Thannenkirch)

Localité	X_UTM_32N	Y_UTM_32N	Localité	X_UTM_32N	Y_UTM_32N
vc6	356908.655499	5319210.29669	FS 48	325760.464465	5321811.48521
vc6	356908.655499	5319210.29669	FS 49	328271.598724	5324046.54169
vc6	356908.655499	5319210.29669	FS 50	329256.897843	5322153.24750
vc6	356908.655499	5319210.29669	FS 51	325403.089444	5319899.72733
vc7	358592.748509	5325985.72698	FS 52	325665.481360	5318785.08913
vc8a	364137.163780	5332956.55986	FS 53	328458.111960	5319671.05695
vc8b	364137.163780	5332956.55986	FS 54	332627.878577	5319925.55905
vc9	364174.654349	5330049.86787	FS 55	329752.473944	5317470.17791
vm2	366378.296035	5335623.82205	FS 56	330874.452877	5315465.39843
			FS 57	341310.119341	5321816.64694
			FS 58	346117.576334	5328062.94332
FS 1	351087.334063	5323699.66603	FS 59	343598.979259	5326769.21877
FS 2	348348.693849	5320912.11833	FS 60	336549.197228	5322826.85379
FS 3	346797.917146	5318858.14399	FS 61	327384.539705	5321744.23960
FS 4	346941.936254	5319747.55965	FS 62	323722.791727	5316796.18352
FS 5	347439.813377	5318011.83707	FS 63	327735.934728	5310938.75129
FS 6	347448.775817	5314376.69797	FS 64	335242.077287	5309946.26060
FS 7	346984.040430	5313033.61825	FS 65	337816.182330	5313203.48960
FS 8	347626.842639	5316336.87579	FS 66	360433.348208	5308393.35010
FS 9	347522.703919	5309967.48050	FS 67	360427.728630	5309027.91631
FS 10	339114.954792	5312836.95558	FS 68	360009.342270	5309311.90388
FS 11	341031.306064	5314477.93785	FS 69	360142.284412	5307296.59212
FS 12	341890.731825	5315626.45510	FS 70	359427.609856	5306352.65733
FS 13	343862.441530	5315562.42187	FS 71	358658.320273	5304243.89018
FS 14	342859.656369	5310203.00264	FS 72	356748.088474	5305235.55643
FS 15	342603.477621	5309255.67886	FS 73	356113.008056	5303892.97790
FS 16	340507.124203	5307608.54881	FS 74	357727.009400	5303333.01944
FS 17	342336.488835	5307740.33989	FS 75	355271.152879	5306320.46703
FS 18	347051.261273	5309595.47575	FS 76	353850.003247	5305654.09337
FS 19	344876.612860	5309967.25815	FS 77	352474.457506	5305591.76042
FS 20	341124.240159	5311641.04845	FS 78	340612.918138	5310053.10449
FS 21	333959.995147	5312050.03062	FS 79	344791.351274	5312994.28194
FS 22	333013.279690	5309976.48451	FS 80	356029.814491	5305642.15465
FS 23	331181.427288	5307560.10226	FS 81	352318.541554	5304720.00216
FS 24	330251.390296	5310082.71651			
FS 25	327721.592329	5308818.80949			
FS 26	324903.891211	5312239.00476			
FS 27	323388.542207	5313887.36881			
FS 28	325558.033545	5311032.86634			
FS 29	336805.956500	5307341.93692			
FS 30	332991.777649	5307274.50705			
FS 31	336200.020070	5309383.71638			
FS 32	342548.922016	5323895.69922			
FS 33	340681.845565	5325730.81039			
FS 34	337181.451753	5327200.29184			
FS 35	334907.252280	5325517.27296			
FS 36	331955.829998	5327998.72556			
FS 37	330877.900305	5325531.01450			
FS 38	330663.926004	5319219.00721			
FS 39	336476.455044	5319244.90183			
FS 40	334283.497858	5321482.05512			
FS 41	337181.005392	5323118.13222			
FS 42	336220.683047	5321485.02317			
FS 43	339508.222732	5321787.57270			
FS 44	318391.379240	5320435.81069			
FS 45	321560.853047	5319756.30144			
FS 46	323270.730868	5317739.45444			
FS 47	322920.366750	5320802.94321			

Complexe magmatique des Ballons(Bité-Essomé, 2007 et données personnelles)

Localité	X_UTM_32N	Y_UTM_32N	Localité	X_UTM_32N	Y_UTM_32N
BL 1	343495.764890	5299801.07394	mb1	331603.155016	5302960.32254
BL 2	341730.168642	5298764.76357	m2	332023.713101	5302949.46387
BL 3	340295.956939	5298062.82249	mb3a	332426.856641	5302676.16414
BL 4	337697.067255	5296377.87378	mb3b	332426.856641	5302676.16414
BL 5	338468.823034	5296920.52431	mb4a	334239.095188	5299398.27982
BL 6	338811.257708	5296905.99874	mb4b	334239.095188	5299398.27982
BL 7	338019.395875	5299194.51016	mb5	334113.566055	5299960.95182
BL 8	340600.418256	5297350.11876	mb6a	334112.072091	5300237.05178
BL 9	339320.626648	5297942.69470	mb6b	334112.072091	5300237.05178
BL 10	337446.747987	5300354.91518	mb7a	333856.621701	5300183.61660
BL 11	336771.002981	5299541.88720	mb7b	333856.621701	5300183.61660
BL 12	336490.709163	5300393.00910	mb8	333037.430137	5301307.33910
BL 13	335917.187797	5300065.45036	mb9a	330151.698959	5301453.62465
BL 14	335625.173154	5301370.87121	mb9b	330151.698959	5301453.62465
BL 15	333043.388226	5301272.19848	mb9c	330151.698959	5301453.62465
BL 16	334137.389205	5301580.28469	mb10a	334063.709656	5300692.77539
BL 17	334119.448593	5300699.60215	mb10b	334063.709656	5300692.77539
BL 18	334304.321368	5299386.06580	mb11a	331916.165954	5301691.18567
BL 19	334757.243849	5298161.34411	mb11b	331916.165954	5301691.18567
BL 20	336992.941892	5298408.57985	mb12	332735.953605	5301596.03176
BL 21	336211.242775	5297624.62893	mb15a	334494.479709	5296491.28113
BL 22	335468.664924	5297046.28580	mb15b	334494.479709	5296491.28113
BL 23	334300.117455	5296509.31064	mb16a	334748.616043	5296670.27614
BL 24	335386.012962	5298136.26782	mb16b	334748.616043	5296670.27614
BL 25	339654.822267	5299979.26865	mb17a	335324.619989	5298126.36843
BL 26	331816.411482	5302959.65679	mb17b	335324.619989	5298126.36843
BL 27	330582.776753	5302795.93471	mb18	332073.326118	5298692.20859
BL 28	329334.431021	5301315.49558	mb19a	332069.769875	5297476.21029
BL 29	328501.488335	5300050.75133	mb19b	332069.769875	5297476.21029
BL 30	330018.581518	5299143.39258	vs63	331054.951155	5303508.95164
BL 31	329673.228054	5299840.78756	vs64	333809.697123	5301830.41290
BL 32	331046.861267	5301176.47765	vs70	332247.871329	5302930.30421
BL 33	333244.233703	5299102.54377	vs73	330745.781346	5303848.48441
BL 34	333715.994083	5298450.20722	vs74	332425.834816	5302664.20904
BL 35	333202.248077	5297706.98278	vs75-76	334114.322972	5301578.58383
BL 36	332210.767467	5296681.05238	vs78	333584.552551	5301697.11767
BL 37	331571.399561	5297356.05522	vs84	333488.116757	5302623.59235
BL 38	330147.881381	5297689.96369			
BL 39	329092.535623	5304853.20890			
BL 40	329016.593650	5304427.17815			
BL 41	332683.886900	5298534.99986			
BL 42	327665.975366	5306191.84050			
BL 43	326367.264967	5304600.90533			
BL 44	325602.152188	5304439.85520			
BL 45	326445.019323	5303338.27209			
BL 46	325103.202963	5302082.04054			
BL 47	326776.174810	5302196.04185			
BL 48	327319.792213	5302747.68949			
BL 49	328182.280896	5304094.41763			
BL 50	324473.247922	5304671.30735			
BL 51	324042.424472	5306429.66210			
BL 52	325283.175533	5307142.12142			
BL 53	323089.649646	5308962.12479			
BL 54	319673.288606	5306205.12758			
BL 55	316059.287945	5306594.43047			
BL 56	318830.885049	5305636.51599			
BL 57	322393.367339	5306988.58434			

Ligne des Klippes

Localité	X_UTM_32N	Y_UTM_32N	Localité	X_UTM_32N	Y_UTM_32N
K1-1	362281.162867	5309336.38789	K3-2	347847.917904	5307533.22147
K1-2	362209.870667	5309138.15242	K3-3	347806.611174	5307705.47040
K1-3	362168.085409	5309032.99805	K3-4	347856.863545	5307731.75396
K1-4	362245.269050	5309003.91164	K3-5	347857.476901	5307882.07444
K1-5	362261.183740	5308861.02492	K3-6	347771.321085	5307872.58462
K1-6	362185.314782	5308850.63372	K3-7	347706.692487	5308025.96571
K1-7	362318.847449	5308767.99689	K3-8	347758.212913	5308056.35371
K1-8	362137.988146	5308351.36193	K3-9	347849.179500	5308064.88880
K1-9	362236.513906	5308253.90679	K3-10	347838.533328	5308092.97839
K1-10	362281.197366	5308184.48176	K3-11	347837.338017	5308123.52201
K1-11	362275.513613	5307909.40963	K3-12	347832.291609	5308140.80475
K1-12	362170.501899	5307832.14892	K3-13	347934.183169	5308232.66394
K1-13	362189.499933	5308208.24662	K3-14	347969.520270	5308181.80789
K1-14	362029.760424	5308271.56433	K3-15	347865.024860	5308199.43432
K1-15	362010.636560	5308475.64805	K3-16	347596.168880	5307886.10126
K1-16	361993.152510	5308534.31476	K3-17	347550.079602	5307957.44573
K1-17	362099.382466	5308713.63339	K3-18	347552.630236	5308029.70762
K1-18	362153.186803	5309157.05262	K3-19	347495.533570	5308057.05517
K1-19	362925.927791	5310945.70415	K3-20	347420.365859	5308086.67169
K1-20	363194.390103	5310831.39188	K3-21	347495.059125	5307985.34066
K1-21	363057.948316	5310583.65840	K3-22	347551.843569	5307894.96233
K1-22	362963.425098	5310242.36718	K3-23	347127.522582	5308145.76047
K1-23	362611.559347	5310162.05680	K3-24	347108.743594	5308182.15549
K1-24	362382.903979	5309909.54497	K3-25	347032.156556	5307901.67915
K1-25	362573.265118	5310270.06670	K3-26	347128.999049	5307769.46327
K1-26	362925.652811	5310535.91018	K3-27	347257.451743	5307667.88726
K1-27	362601.559416	5310395.58656	K3-28	347351.115710	5307661.33352
K1-28	363144.870248	5310809.61238	K3-29	347416.863373	5307726.74591
K1-29	362798.652132	5310714.76145	K3-30	347693.630925	5307666.13228
K1-30	361227.264297	5307530.89081	K3-31	347556.703115	5307632.89473
K2-1	348576.669567	5310699.93459	K3-32	347322.766071	5307429.64555
K2-2	348622.470803	5310672.68496	K3-33	347546.443805	5307791.05272
K2-3	348721.393107	5310627.04035	K3-34	347996.728373	5308241.09074
K2-4	348660.241426	5310585.59466	K3-35	347147.824264	5308525.81727
K2-5	348618.252116	5310589.18284	K3-36	347133.622372	5308642.30777
K2-6	348604.739195	5310533.45683	K4-1	350984.825282	5309930.21250
K2-7	348441.470512	5310653.87806	K4-2	350563.830967	5309990.82721
K2-8	348956.804336	5311239.90265	K4-3	350608.052813	5310058.80237
K2-9	348888.064696	5311348.59944	K4-4	351082.401631	5310045.81321
K2-10	348924.466291	5311356.42725	K4-5	351122.693219	5310127.17020
K2-11	348933.307796	5311400.15519	K4-6	351532.869732	5309168.02413
K2-12	349082.880060	5311452.27540	K4-7	351602.770921	5309299.03596
K2-13	349095.669079	5311508.06299	K4-8	351642.130641	5309479.76808
K2-14	348999.940493	5311522.80678	K4-9	351813.059677	5309656.50646
K2-15	349047.608297	5311636.86963	K4-10	351664.552468	5309579.32200
K2-16	348872.287636	5311249.31284	K4-11	351512.929676	5309543.71637
K2-17	349410.322593	5311384.18554	K4-12	351400.601080	5309399.65968
K2-18	349483.706115	5311474.90295	K4-13	351148.211092	5309740.85435
K2-19	349535.181516	5311420.18684	K4-14	351280.138045	5309764.37172
K2-20	349463.553965	5311418.28617	K4-15	351285.794108	5309716.05271
K2-21	349462.078404	5311204.74602	K4-16	351340.076567	5309734.24536
K2-22	349336.587574	5311212.55282	K4-17	351093.401109	5309964.60354
K2-23	349543.052811	5311375.76004	K5-1	353095.347219	5309334.57978
K2-24	349741.503071	5311337.65379	K5-2	352909.401041	5308829.34909
K2-25	349257.704711	5311352.74411	K5-3	352881.656818	5308725.17656
K2-26	349105.102652	5311420.47762	K5-4	353167.026628	5309053.76434
K2-27	348796.748279	5311418.38829	K5-5	353140.323447	5308902.39233
K2-28	348824.586013	5311348.19021	K5-6	353200.347657	5308841.45615
K3-1	347759.059958	5307615.10582	K5-7	353240.507244	5308802.51095

Ligne des Klippes

Localité	X_UTM_32N	Y_UTM_32N
K5-8	353339.987182	5308646.88171
K5-9	353328.864154	5308431.84741
K5-10	353091.056320	5308795.71001
K5-11	353103.996770	5308760.53977
K5-12	353102.893360	5308662.78863
K5-13	352989.938337	5308706.50349
K5-14	353072.598478	5308859.61806
K5-15	352837.212684	5308573.14557
K5-16	352796.124916	5308770.89735
K5-17	352707.016204	5308890.12670
K5-18	352673.738798	5309094.45900
K5-19	352814.084997	5308870.83232
K6-1	357364.223096	5306982.75958
K6-2	357433.443832	5306709.74310
K6-3	357135.180394	5305764.72925
K6-4	357067.758635	5305681.75940
K6-5	356993.996454	5305704.62209
K6-6	356945.746891	5305804.56978
K6-7	356978.803601	5305789.91593
K6-8	356824.356640	5306654.89937
K6-9	356614.735121	5306541.48626
K6-10	356350.659715	5306178.36927
K6-10	355616.331094	5306390.15651
K6-13	355723.033111	5306863.72599
K6-14	355435.355109	5307110.71225
K6-15	355646.520778	5306882.09205
K6-16	355775.265468	5306796.56287
K6-17	356161.059513	5306327.06518
K6-18	356103.020760	5306284.70068
K6-12	355379.311004	5306329.95475
K7-1	344265.926031	5307712.56839
K7-2	344477.260789	5307716.36983
K7-3	344848.230814	5307897.57878
K7-4	344573.580456	5307742.35652
K7-5	344426.565136	5307657.01894
K7-6	344338.844037	5307531.44590
K8-1	354548.470411	5300526.49219
K8-2	354461.798698	5300676.77381
K8-3	354262.344222	5300701.46151
K8-4	353845.885397	5300634.97020
K8-5	353753.637713	5300331.57318
K8-6	353098.276278	5300305.89587
K8-7	352879.874863	5300048.99176
K8-8	353465.660865	5299708.10063
K8-9	353839.395955	5299632.80978
K8-10	354040.183890	5299743.23491
K8-11	354197.136835	5299788.51458
K8-12	354436.546178	5300201.81319

Annexe 8. Analyses U–Pb sur zircons pour les échantillons de gneiss monotone.

<i>Monotonous gneiss EV67M (Farupå, 7°16'14"E, 48°15'48"N)</i>																				
Grain. spot	U (ppm)	Th (ppm)	Th/U	²⁰⁶ Pb* (ppm)	²⁰⁶ Pb/ ²⁰⁴ Pb	f ₂₀₆ %	Radiogenic ratios						Age (Ma)							
							²⁰⁶ Pb/ ²³⁸ U	±	²⁰⁷ Pb/ ²³⁵ U	±	²⁰⁷ Pb/ ²⁰⁶ Pb	±	p	²⁰⁶ Pb/ ²³⁸ U	±	²⁰⁷ Pb/ ²³⁵ U	±	²⁰⁷ Pb/ ²⁰⁶ Pb	±	Conc. %
1.1	247	54	0.22	20	304.3	0.585	0.0954	0.0006	0.7355	0.0354	0.05592	0.00267	0.137	587	4	560	21	449	103	131
2.1	67	18	0.27	9	787	2.197	0.1430	0.0008	1.0139	0.1591	0.05141	0.00806	0.035	862	4	711	77	259	325	332
2.2	1200	28	0.02	101	17903	0.099	0.0975	0.0010	0.8181	0.0125	0.06082	0.00067	0.695	600	6	607	7	633	24	95
3.1	108	9	0.08	8	1071	1.668	0.0889	0.0006	0.5563	0.0742	0.04537	0.00604	0.051	549	4	449	47	-	-	-
4.1	113	23	0.20	9	1564	1.141	0.0925	0.0010	0.6316	0.0649	0.04953	0.00507	0.103	570	6	497	40	173	223	330
5.1	127	49	0.38	11	4875	0.365	0.0979	0.0008	0.7639	0.0262	0.05659	0.00189	0.232	602	5	576	15	476	72	127
6.1	250	17	0.07	20	3980	0.448	0.0929	0.0007	0.7040	0.0252	0.05495	0.00193	0.198	573	4	541	15	410	77	140
6.2	668	22	0.03	53	19249	0.093	0.0912	0.0011	0.7221	0.0124	0.05744	0.00069	0.718	562	7	552	7	508	26	111
7.1	193	183	0.95	16	36705	0.049	0.0946	0.0009	0.7766	0.0097	0.05956	0.00050	0.736	583	5	584	6	587	18	99
8.1	312	179	0.58	26	-	-	0.0948	0.0007	0.7882	0.0070	0.06030	0.00027	0.862	584	4	590	4	614	10	95
9.1	222	39	0.17	94	103258	0.013	0.4998	0.0068	13.1757	0.1896	0.19121	0.00092	0.942	2613	29	2692	13	2753	8	95
9.2	145	24	0.16	58	14368	0.096	0.4669	0.0051	12.2124	0.1620	0.18970	0.00142	0.826	2470	22	2621	12	2740	12	90
10.1	212	78	0.37	17	2918	0.611	0.0944	0.0007	0.7060	0.0326	0.05424	0.00247	0.169	581	4	542	19	381	99	153
11.1	105	47	0.44	33	-	-	0.3642	0.0029	6.1729	0.0578	0.12292	0.00061	0.849	2002	14	2001	8	1999	9	100
11.2	275	88	0.32	84	11061	0.137	0.3529	0.0035	6.0354	0.0798	0.12405	0.00110	0.744	1948	17	1981	11	2015	16	97
12.1	589	64	0.11	46	16070	0.111	0.0907	0.0007	0.7121	0.0100	0.05696	0.00065	0.577	559	4	546	6	490	25	114
13.1	128	25	0.19	36.4	30176	0.051	0.3284	0.0025	5.2356	0.0503	0.11562	0.00069	0.787	1831	12	1858	8	1889	11	97
14.1	736	59	0.08	61.3	-	-	0.0962	0.0008	0.7839	0.0071	0.05910	0.00027	0.867	592	4	588	4	571	10	104
15.1	132	26	0.20	39.7	2208	0.685	0.3474	0.0031	5.9236	0.1152	0.12366	0.00214	0.458	1922	15	1965	17	2010	30	96
16.1	286	93	0.33	23.6	2375	0.750	0.0952	0.0011	0.7532	0.0352	0.05740	0.00261	0.242	586	6	570	20	507	97	116

Monotonous gneiss EV69 M (Gouitte St-Blaise, 7°13'28"E; 48°15'6"N)

Grain. spot	U (ppm)	Th (ppm)	Th/U	²⁰⁶ Pb* (ppm)	²⁰⁶ Pb/ ²⁰⁴ Pb	f ₂₀₆ %	Radiogenic ratios					Age (Ma)								
							²⁰⁶ Pb/ ²³⁸ U	²⁰⁷ Pb/ ²³⁵ U	²⁰⁷ Pb/ ²⁰⁶ Pb	±	ρ	²⁰⁶ Pb/ ²³⁸ U	²⁰⁷ Pb/ ²³⁵ U	²⁰⁷ Pb/ ²⁰⁶ Pb	±	% Conc.				
1.1	91	10	0.11	10	-	-	0.1209	0.0010	1.0492	0.0127	0.06296	0.00055	0.692	736	6	729	6	707	18	104
2.1	241	36	0.15	19	4947	0.361	0.0917	0.0008	0.7122	0.0185	0.05635	0.00138	0.335	565	5	546	11	466	53	121
3.1	339	18	0.05	34	25919	0.068	0.1147	0.0008	1.0140	0.0119	0.06412	0.00061	0.576	700	4	711	6	746	20	94
4.1	158	17	0.11	12	2601	0.687	0.0915	0.0008	0.7506	0.0414	0.05946	0.00324	0.160	565	5	569	24	584	114	97
5.1	272	32	0.12	20	4685	0.382	0.0857	0.0008	0.6670	0.0233	0.05648	0.00190	0.265	530	5	519	14	471	73	112
6.1	315	69	0.22	26	4514	0.395	0.0951	0.0008	0.7458	0.0225	0.05686	0.00164	0.281	586	5	566	13	486	63	121
7.1	117	18	0.15	10	7787	0.228	0.1016	0.0011	0.8612	0.0209	0.06149	0.00133	0.456	624	7	631	11	657	46	95
7.2	81	11	0.14	7	-	-	0.1046	0.0007	0.8927	0.0085	0.06191	0.00039	0.743	641	4	648	5	671	14	96
8.1	55	11	0.20	5	-	-	0.1066	0.0009	0.9769	0.0111	0.06645	0.00052	0.721	653	5	692	6	820	16	80
9.1	591	16	0.03	52	-	-	0.1018	0.0015	0.8532	0.0131	0.06076	0.00029	0.952	625	9	626	7	631	10	99
10.1	1325	82	0.06	105	12459	0.143	0.0919	0.0006	0.7494	0.0115	0.05915	0.00082	0.435	567	4	568	7	573	30	99
11.1	761	191	0.25	68	4862	0.365	0.1028	0.0009	0.8587	0.0276	0.06058	0.00187	0.268	631	5	629	15	624	65	101
12.1	450	73	0.16	34	3207	0.558	0.0880	0.0005	0.7082	0.0176	0.05837	0.00141	0.239	544	3	544	10	544	52	100
13.1	286	56	0.19	22	2432	0.735	0.0887	0.0006	0.7084	0.0287	0.05795	0.00232	0.153	548	3	544	17	528	85	104
14.1	160	47	0.30	13	7506	0.238	0.0921	0.0008	0.7341	0.0175	0.05779	0.00129	0.344	568	4	559	10	522	48	109
15.1	347	104	0.30	29	-	-	0.0976	0.0010	0.8223	0.0089	0.06109	0.00029	0.896	600	6	609	5	642	10	93

Monotonous gneiss EV372R (Hohltann, 7°10'19"E; 48°12'54"N)

Grain. spot	U (ppm)	Th (ppm)	Th/U	²⁰⁶ Pb* (ppm)	²⁰⁶ Pb/ ²⁰⁴ Pb	f ₂₀₆ %	Radiogenic ratios				Age (Ma)				%					
							²⁰⁶ Pb/ ²³⁸ U	±	²⁰⁷ Pb/ ²³⁵ U	±	²⁰⁶ Pb/ ²⁰⁷ Pb	±	ρ	²⁰⁶ Pb/ ²³⁸ U		±	²⁰⁷ Pb/ ²³⁵ U	±	²⁰⁷ Pb/ ²⁰⁶ Pb	±
1.1	183	104	0.57	14	-	-	0.0878	0.0007	0.6928	0.0063	0.05724	0.00028	0.847	542	4	534	4	501	11	108
2.1	342	119	0.35	25	-	-	0.0859	0.0006	0.6815	0.0056	0.05757	0.00028	0.803	531	3	528	3	513	11	103
3.1	122	67	0.54	12	9844	0.179	0.1134	0.0011	0.9864	0.0200	0.06306	0.00113	0.475	693	6	697	10	710	38	98
4.1	327	194	0.59	108	-	-	0.3838	0.0033	8.0748	0.0788	0.15260	0.00067	0.892	2094	16	2239	9	2375	7	88
4.2	333	173	0.52	111	20405	0.070	0.3852	0.0040	8.0669	0.1021	0.15187	0.00110	0.819	2101	19	2239	11	2367	12	89
5.1	68	25	0.37	21	2100	0.720	0.3583	0.0029	5.8839	0.1939	0.11909	0.00380	0.248	1974	14	1959	28	1943	56	102
5.2	137	37	0.27	42	9379	0.161	0.3548	0.0038	6.1039	0.0922	0.12477	0.00134	0.701	1957	18	1991	13	2026	19	97
6.1	287	68	0.24	84	1990741	0.001	0.3390	0.0021	8.2652	0.0633	0.17685	0.00076	0.828	1882	10	2261	7	2624	7	72
7.1	175	112	0.64	54	44414	0.034	0.3566	0.0028	6.1533	0.0615	0.12514	0.00079	0.776	1966	13	1998	9	2031	11	97
8.1	2757	324	0.12	197	14562	0.123	0.0826	0.0013	0.6542	0.0121	0.05745	0.00059	0.829	512	8	511	7	509	23	101
9.1	257	27	0.11	20	2091	0.856	0.0870	0.0006	0.6276	0.0224	0.05231	0.00182	0.204	538	4	495	14	299	78	180
10.1	14	7	0.54	1	745	2.375	0.1042	0.0024	0.5952	0.1528	0.04142	0.01059	0.090	639	14	474	93	-	-	-
11.1	115	118	1.02	10	6290	0.282	0.0998	0.0012	0.7552	0.0229	0.05489	0.00152	0.412	613	7	571	13	408	61	150
12.1	311	35	0.11	30	-	-	0.1103	0.0008	0.9223	0.0085	0.06062	0.00031	0.828	675	5	664	4	626	11	108
13.1	134	96	0.72	11	-	-	0.0972	0.0005	0.7907	0.0058	0.05899	0.00032	0.672	598	5	592	3	567	12	106
14.1	412	65	0.16	31	822	2.179	0.0856	0.0007	0.6378	0.0349	0.05406	0.00292	0.153	529	4	501	21	374	117	142
15.1	89	75	0.84	7	1661	1.075	0.0902	0.0008	0.6214	0.0597	0.04996	0.00478	0.092	557	5	491	37	193	208	288
16.1	109	29	0.26	24	13308	0.107	0.2574	0.0070	5.2718	0.1592	0.14852	0.00196	0.899	1477	36	1864	25	2329	22	63
17.1	262	123	0.47	28	-	-	0.1246	0.0007	1.1367	0.0091	0.06618	0.00038	0.707	757	4	771	4	812	12	93
18.1	157	120	0.76	13	-	-	0.0960	0.0007	0.7790	0.0071	0.05887	0.00032	0.811	591	4	585	4	562	12	105
19.1	160	88	0.55	25	-	-	0.1835	0.0043	2.6115	0.0670	0.10320	0.00109	0.911	1086	23	1304	19	1682	19	65
20.1	143	76	0.53	10	3118	0.576	0.0800	0.0005	0.5998	0.0278	0.05438	0.00250	0.146	496	3	477	18	387	100	128
21.1	119	59	0.49	11	919	1.932	0.1000	0.0006	0.5977	0.1147	0.04337	0.00832	0.030	614	3	476	70	-	-	-
22.1	279	173	0.62	155	27985	0.043	0.6398	0.0037	25.1516	0.1865	0.28510	0.00133	0.778	3188	14	3314	7	3391	7	94
22.2	289	191	0.66	155	26467	0.046	0.6212	0.0057	24.9157	0.2690	0.29091	0.00166	0.848	3115	23	3305	10	3422	9	91
23.1	624	246	0.39	43	5226	0.344	0.0789	0.0008	0.5950	0.0140	0.05466	0.00116	0.431	490	5	474	9	398	47	123

Notes :

1. Uncertainties given at 1σ level
2. f₂₀₆ % denotes the percentage of ²⁰⁶Pb that is initial Pb
3. The correction for initial lead is based on the ²⁰⁴Pb/²⁰⁶Pb ratio
4. % Conc. = percentage of concordancy. 100% expresses a concordant analysis

Annexe 9. Analyses U–Pb sur zircons pour les échantillons de gneiss varié.

Varied gneiss EV83M (St-Pierre sur l'Hâte, 7°10'32"E ; 48°13'26"N)																				
Grain. spot	U (ppm)	Th (ppm)	Th/U	²⁰⁶ Pb* (ppm)	²⁰⁶ Pb/ ²⁰⁴ Pb	f ₂₀₆ %	Radiogenic ratios				Age (Ma)				%					
							²⁰⁶ Pb/ ²³⁸ U	²⁰⁷ Pb/ ²³⁵ U	²⁰⁷ Pb/ ²⁰⁶ Pb	±	²⁰⁶ Pb/ ²³⁸ U	²⁰⁷ Pb/ ²³⁵ U	²⁰⁷ Pb/ ²⁰⁶ Pb	±						
1.1	106	13	0.12	10	1024	1.722	0.1106	0.0009	0.761	0.114	0.04992	0.00744	0.055	676	5	575	63	191	314	353
1.2	635	17	0.03	41	8263	0.218	0.0744	0.0005	0.619	0.013	0.06032	0.00121	0.344	463	3	489	8	615	43	75
2.1	44	5	0.11	6	-	-	0.1538	0.0015	2.182	0.030	0.10290	0.00100	0.714	922	8	1175	10	1677	18	55
3.1	371	45	0.12	186	118050	0.010	0.5777	0.0050	22.968	0.234	0.28834	0.00156	0.848	2939	20	3226	10	3409	8	86
4.1	554	7	0.01	41	8836	0.203	0.0848	0.0008	0.664	0.015	0.05680	0.00118	0.411	525	5	517	9	484	45	109
5.1	73	9	0.13	17	15126	0.099	0.2752	0.0034	4.857	0.077	0.12802	0.00128	0.773	1567	17	1795	13	2071	18	76
6.1	303	23	0.08	89	14455	0.103	0.3410	0.0024	6.210	0.068	0.13207	0.00111	0.634	1892	11	2006	9	2126	15	89
7.1	198	24	0.12	46	-	-	0.2703	0.0037	4.833	0.071	0.12967	0.00070	0.928	1542	19	1791	12	2094	10	74
8.1	267	64	0.24	22	-	-	0.0935	0.0007	0.778	0.007	0.06040	0.00035	0.791	576	4	585	4	618	12	93
9.1	83	15	0.18	6	-	-	0.0900	0.0012	0.727	0.012	0.05854	0.00049	0.851	556	7	555	7	550	18	101
10.1	255	17	0.06	67	53286	0.028	0.3017	0.0022	5.176	0.046	0.12442	0.00065	0.813	1700	11	1849	8	2021	9	84
11.1	129	12	0.09	8	-	-	0.0736	0.0006	0.568	0.006	0.05596	0.00031	0.818	458	4	457	4	451	12	102
12.1	315	36	0.12	80	19378	0.078	0.2950	0.0019	5.003	0.047	0.12302	0.00082	0.697	1666	10	1820	8	2000	12	83
13.1	103	14	0.13	28	24062	0.062	0.3137	0.0026	5.640	0.058	0.13038	0.00080	0.800	1759	13	1922	9	2103	11	84
14.1	485	6	0.01	23	-	-	0.0546	0.0006	0.405	0.005	0.05380	0.00032	0.885	343	4	345	4	363	13	94
15.1	18	13	0.71	6	-	-	0.3725	0.0084	6.049	0.143	0.11779	0.00079	0.959	2041	40	1983	20	1923	12	106
16.1	84	11	0.13	7	-	-	0.0901	0.0009	0.744	0.010	0.05986	0.00049	0.785	556	6	565	6	599	18	93
17.1	200	21	0.10	15	4402	0.406	0.0886	0.0009	0.680	0.025	0.05566	0.00200	0.274	547	5	527	15	439	78	125
18.1	987	179	0.18	69	3742	0.480	0.0808	0.0005	0.634	0.017	0.05685	0.00152	0.232	501	3	498	11	486	58	103
19.1	776	17	0.02	256	108501	0.013	0.3816	0.0033	8.776	0.089	0.16680	0.00087	0.856	2084	15	2315	9	2526	9	82
20.1	19	22	1.18	6	3880	0.398	0.3475	0.0075	5.400	0.164	0.11272	0.00241	0.711	1922	36	1885	26	1844	38	104
21.1	228	286	1.25	48	7221	0.214	0.2408	0.0031	3.681	0.066	0.11089	0.00138	0.722	1391	16	1567	14	1814	22	77
22.1	51	128	2.52	12	-	-	0.2688	0.0033	4.174	0.056	0.11262	0.00063	0.909	1535	17	1669	11	1842	10	83
23.1	428	196	0.46	27	-	-	0.0736	0.0007	0.576	0.006	0.05674	0.00029	0.881	458	4	462	4	482	11	95

Varied gneiss EV90M (Raurenthai, 7°9'33"E ; 48°12'37"N)

Grain. spot	U (ppm)	Th (ppm)	Th/U	²⁰⁶ Pb* (ppm)	²⁰⁶ Pb/ ²⁰⁴ Pb	f ₂₀₆ %	Radiogenic ratios				Age (Ma)				Conc. %					
							²⁰⁶ Pb/ ²³⁸ U	±	²⁰⁷ Pb/ ²³⁵ U	±	²⁰⁷ Pb/ ²⁰⁶ Pb	±	ρ	²⁰⁶ Pb/ ²³⁸ U		±	²⁰⁷ Pb/ ²³⁵ U	±	²⁰⁷ Pb/ ²⁰⁶ Pb	±
1.1	2786	226	0.08	123	44273	0.041	0.0512	0.0003	0.3599	0.0036	0.05103	0.00041	0.615	322	2	312	3	242	18	133
1.2	765	236	0.31	34	3142	0.582	0.0506	0.0006	0.3414	0.0136	0.04890	0.00185	0.300	318	4	298	10	143	87	223
2.1	296	152	0.51	24	438	4.069	0.0950	0.0007	0.7416	0.0481	0.05661	0.00364	0.117	585	4	563	28	476	136	123
2.2	400	131	0.33	29	184	9.736	0.0841	0.0008	0.5967	0.0793	0.05146	0.00683	0.071	521	5	475	49	262	279	199
3.1	243	99	0.41	11	6283	0.291	0.0512	0.0004	0.3517	0.0108	0.04984	0.00148	0.249	322	2	306	8	187	68	172
4.1	201	102	0.51	9	2598	0.703	0.0517	0.0003	0.3449	0.0235	0.04835	0.00324	0.179	325	4	301	18	116	151	280
5.1	548	246	0.45	24	1953	0.936	0.0508	0.0006	0.3561	0.0162	0.05081	0.00228	0.150	320	2	309	12	232	100	138
6.1	286	123	0.43	13	-	-	0.0538	0.0006	0.3923	0.0050	0.05292	0.00032	0.878	338	4	336	4	325	14	104
7.1	3198	404	0.13	143	2400	0.761	0.0514	0.0004	0.3595	0.0124	0.05073	0.00172	0.197	323	2	312	9	228	77	141
8.1	1037	95	0.09	43	14208	0.129	0.0479	0.0005	0.3387	0.0061	0.05126	0.00076	0.579	302	3	296	5	253	34	119
9.1	2391	420	0.18	104	30488	0.060	0.0501	0.0003	0.3561	0.0041	0.05154	0.00049	0.568	315	2	309	3	265	22	119
10.1	2783	305	0.11	123	-	-	0.0509	0.0004	0.3631	0.0032	0.05176	0.00025	0.839	320	2	315	2	275	11	116
10.2	2170	257	0.12	97	25407	0.072	0.0518	0.0003	0.3694	0.0042	0.05173	0.00051	0.508	325	2	319	3	274	22	119
10.3	2707	344	0.13	126	70305	0.026	0.0536	0.0005	0.3874	0.0046	0.05241	0.00033	0.848	337	3	332	3	303	14	111
11.1	398	103	0.26	33	977	1.822	0.0954	0.0018	0.6441	0.0628	0.04898	0.00468	0.197	587	11	505	38	147	210	399
12.1	2336	436	0.19	110	2694	0.680	0.0544	0.0005	0.3832	0.0134	0.05112	0.00172	0.276	341	3	329	10	246	76	138

Varied gneiss EV343M (Bourgonde, Fischthal, 7°12'24"E ; 48°14'19"N)

Grain. spot	U (ppm)	Th (ppm)	Th/U	²⁰⁶ Pb* (ppm)	²⁰⁶ Pb/ ²⁰⁴ Pb	f ₂₀₆ %	Radiogenic ratios				Age (Ma)									
							²⁰⁶ Pb/ ²³⁸ U	²⁰⁷ Pb/ ²³⁵ U	²⁰⁷ Pb/ ²⁰⁶ Pb	±	²⁰⁶ Pb/ ²³⁸ U	²⁰⁷ Pb/ ²³⁵ U	²⁰⁷ Pb/ ²⁰⁶ Pb	±	% Conc.					
1.1	162	13	0.08	11	-	-	0.0787	0.0006	0.6213	0.0057	0.05726	0.00034	0.764	488	3	491	4	502	13	97
2.1	748	69	0.09	291	100999	0.014	0.4489	0.0025	11.0860	0.0789	0.17911	0.00077	0.797	2390	11	2530	7	2645	7	90
3.1	327	21	0.07	25	-	-	0.0877	0.0007	0.7024	0.0069	0.05812	0.00037	0.764	542	4	540	4	534	14	101
3.2	625	18	0.03	37	-	-	0.0683	0.0008	0.5353	0.0066	0.05685	0.00028	0.913	426	5	435	4	486	11	88
4.1	69	36	0.53	21	-	-	0.3580	0.0043	6.2312	0.0785	0.12622	0.00052	0.944	1973	20	2009	11	2046	7	96
5.1	151	15	0.10	11	-	-	0.0854	0.0007	0.6822	0.0071	0.05796	0.00033	0.832	528	4	528	4	528	13	100
6.1	417	15	0.04	27	-	-	0.0759	0.0038	0.5860	0.0299	0.05598	0.00044	0.988	472	23	468	19	452	17	104
7.1	22	3	0.13	3	838	1.854	0.1733	0.0032	2.2887	0.1930	0.09581	0.00788	0.221	1030	18	1209	58	1544	147	67
8.1	249	2	0.01	11	-	-	0.0494	0.0004	0.3576	0.0034	0.05252	0.00029	0.803	311	2	310	3	308	13	101
9.1	186	7	0.04	13	-	-	0.0811	0.0009	0.6493	0.0082	0.05805	0.00038	0.853	503	5	508	5	532	14	95
10.1	203	14	0.07	14	9870	0.182	0.0811	0.0006	0.6178	0.0127	0.05524	0.00106	0.354	503	4	488	8	422	42	119
11.1	240	5	0.02	17	-	-	0.0815	0.0007	0.6887	0.0086	0.06126	0.00056	0.674	505	4	532	5	648	20	78
12.1	52	7	0.13	4	1982	0.902	0.0882	0.0009	0.6259	0.0523	0.05150	0.00427	0.128	545	6	494	32	263	180	207
12.2	179	17	0.10	13	9596	0.187	0.0845	0.0007	0.6664	0.0140	0.05722	0.00111	0.378	523	4	519	8	500	42	105
13.1	245	1	0.00	10	-	-	0.0479	0.0005	0.3503	0.0047	0.05304	0.00042	0.799	302	3	305	4	330	18	91
13.2	454	3	0.01	24	-	-	0.0601	0.0011	0.4552	0.0091	0.05495	0.00041	0.928	376	7	381	6	410	17	92
14.1	110	10	0.09	8	-	-	0.0887	0.0009	0.6963	0.0088	0.05695	0.00043	0.796	548	5	537	5	489	17	112
15.1	128	9	0.07	9	-	-	0.0847	0.0008	0.6598	0.0082	0.05650	0.00046	0.760	524	5	515	5	472	18	111
16.1	205	7	0.04	10	-	-	0.0550	0.0005	0.4015	0.0047	0.05298	0.00037	0.794	345	3	343	3	328	16	105
16.2	277	2	0.01	13	-	-	0.0533	0.0005	0.3870	0.0046	0.05262	0.00031	0.863	335	3	332	3	313	14	107
17.1	240	34	0.14	18	-	-	0.0866	0.0007	0.6934	0.0072	0.05806	0.00033	0.833	535	4	535	4	532	12	101
18.1	134	31	0.23	12	-	-	0.1029	0.0008	0.8595	0.0085	0.06059	0.00034	0.826	631	5	630	5	625	12	101
19.1	19	11	0.57	8	-	-	0.4506	0.0099	8.2281	0.1862	0.13243	0.00072	0.970	2398	44	2256	20	2130	10	113
20.1	481	110	0.23	23	-	-	0.0547	0.0004	0.4019	0.0036	0.05329	0.00032	0.748	343	2	343	3	341	13	101
21.1	103	36	0.35	8	-	-	0.0861	0.0008	0.6926	0.0077	0.05835	0.00035	0.843	532	5	534	5	543	13	98

Notes :

1. Uncertainties given at 1σ level
2. f₂₀₆ % denotes the percentage of ²⁰⁶Pb that is initial Pb
3. The correction for initial lead is based on the ²⁰⁴Pb/²⁰⁶Pb ratio
4. % Conc. = percentage of concordancy, 100% expresses a concordant analysis

Annexe 10. Analyses U–Pb sur zircons pour les échantillons de granulite felsique.

Felsic granulite EV136N (La Roche, Col des Bagennes, 7°6'40"E; 48°11'0"N)

Grain. spot	U (ppm)	Th (ppm)	Th/U	²⁰⁶ Pb* (ppm)	²⁰⁶ Pb/ ²⁰⁴ Pb	f ₂₀₆ %	Radiogenic ratios				Age (Ma)									
							²⁰⁶ Pb/ ²³⁸ U	±	²⁰⁷ Pb/ ²³⁵ U	±	²⁰⁶ Pb/ ²⁰⁶ Pb	±	ρ	²⁰⁶ Pb/ ²³⁸ U	±	²⁰⁷ Pb/ ²³⁵ U	±	²⁰⁷ Pb/ ²⁰⁶ Pb	±	% Conc.
1.1	696	10	0.01	31	-	-	0.0507	0.0005	0.372	0.004	0.05318	0.00033	0.836	319	3	321	3	336	14	95
2.1	202	20	0.10	14	-	-	0.0811	0.0010	0.646	0.009	0.05779	0.00037	0.892	503	6	506	6	522	14	96
3.1	150	32	0.21	10	-	-	0.0750	0.0006	0.591	0.006	0.05710	0.00034	0.805	466	4	471	4	496	13	94
4.1	270	28	0.10	17	-	-	0.0715	0.0005	0.553	0.005	0.05610	0.00031	0.792	445	3	447	3	456	12	98
5.1	127	36	0.29	7	4150	0.437	0.0657	0.0005	0.468	0.019	0.05161	0.00202	0.187	410	3	389	13	268	87	153
6.1	400	34	0.09	19	-	-	0.0554	0.0008	0.407	0.006	0.05326	0.00026	0.945	347	5	346	4	340	11	102
7.1	832	14	0.02	36	27127	0.067	0.0495	0.0004	0.356	0.005	0.05220	0.00051	0.640	312	2	310	3	294	22	106
8.1	312	79	0.25	22	7192	0.250	0.0825	0.0007	0.638	0.016	0.05605	0.00129	0.341	511	4	501	10	454	50	113
9.1	202	108	0.54	39	6599	0.235	0.2219	0.0039	3.206	0.070	0.10478	0.00130	0.819	1292	21	1459	17	1710	23	76
10.1	240	24	0.10	11	5074	0.360	0.0541	0.0004	0.386	0.016	0.05168	0.000210	0.189	340	3	331	12	271	91	125
11.1	490	11	0.02	23	-	-	0.0544	0.0004	0.394	0.004	0.05250	0.00027	0.814	342	2	337	3	307	12	111
12.1	986	116	0.12	75	-	-	0.0879	0.0007	0.701	0.006	0.05789	0.00027	0.851	543	4	540	4	526	10	103
13.1	513	16	0.03	26	4972	0.366	0.0590	0.0004	0.409	0.014	0.05031	0.00174	0.202	370	3	348	10	209	78	177
14.1	431	36	0.08	26	5122	0.353	0.0688	0.0006	0.499	0.017	0.05288	0.00172	0.241	429	3	411	11	315	73	136
15.1	489	29	0.06	23	-	-	0.0555	0.0005	0.396	0.004	0.05178	0.00030	0.819	348	3	339	3	276	13	126
16.1	308	5	0.02	19	-	-	0.0730	0.0006	0.553	0.006	0.05497	0.00033	0.817	454	4	447	4	411	14	110
17.1	643	51	0.08	99	23082	0.067	0.1782	0.0014	2.473	0.028	0.10066	0.00082	0.707	1057	8	1264	8	1636	15	65
18.1	370	13	0.03	17	-	-	0.0537	0.0004	0.386	0.004	0.05207	0.00032	0.779	337	3	331	3	289	14	117
19.1	1639	21	0.01	77	7816	0.233	0.0543	0.0004	0.402	0.017	0.05376	0.00219	0.178	341	2	343	12	361	89	94
20.1	62	12	0.20	9	2987	0.520	0.1657	0.0022	2.142	0.077	0.09378	0.00313	0.374	988	12	1162	25	1504	62	66
21.1	801	31	0.04	37.3	-	-	0.0537	0.0005	0.392	0.004	0.05290	0.00026	0.865	337	3	336	3	324	11	104
22.1	380	190	0.50	30.2	-	-	0.0917	0.0009	0.750	0.008	0.05932	0.00027	0.905	565	5	568	5	579	10	98
23.1	79	28	0.35	16.3	16260	0.093	0.2389	0.0031	3.991	0.062	0.12117	0.00108	0.821	1381	16	1632	13	1974	16	70
24.1	357	186	0.52	20.3	9077	0.200	0.0658	0.0007	0.492	0.011	0.05428	0.00111	0.477	411	4	406	8	383	45	107

Felsic granulite EV357N (Le Haïcot West, 7°7'54"E; 48°11'49"N)

Grain. spot	U (ppm)	Th (ppm)	Th/U	²⁰⁸ Pb* (ppm)	²⁰⁶ Pb/ ²⁰⁴ Pb	f ₂₀₆ %	Radiogenic ratios						Age (Ma)							
							²⁰⁶ Pb/ ²³⁸ U	±	²⁰⁷ Pb/ ²³⁵ U	±	ρ	²⁰⁶ Pb/ ²³⁸ U	±	²⁰⁷ Pb/ ²³⁵ U	±	²⁰⁶ Pb/ ²⁰⁶ Pb	±	²⁰⁷ Pb/ ²⁰⁶ Pb	±	% Conc.
1.1	196	23	0.12	9	-	-	0.0545	0.0004	0.400	0.004	0.05324	0.00033	0.746	342	2	342	3	339	14	101
2.1	1639	14	0.01	73	31650	0.058	0.0516	0.0003	0.370	0.004	0.05199	0.00053	0.517	324	2	320	3	285	23	114
3.1	92	11	0.12	5	4080	0.444	0.0681	0.0005	0.489	0.017	0.05209	0.00181	0.213	424	3	404	12	290	78	147
4.1	157	12	0.08	8	1088	1.672	0.0586	0.0006	0.370	0.039	0.04582	0.00477	0.091	367	3	320	28	-	-	-
5.1	131	19	0.14	6	-	-	0.0549	0.0005	0.398	0.005	0.05255	0.00040	0.762	345	3	340	3	309	17	111
6.1	1724	15	0.01	79	-	-	0.0528	0.0004	0.388	0.004	0.05330	0.00028	0.826	331	2	333	3	342	12	97
7.1	445	25	0.06	20	33971	0.054	0.0516	0.0005	0.369	0.005	0.05184	0.00048	0.733	324	3	319	4	278	21	116
8.1	291	40	0.14	17	787	2.304	0.0658	0.0007	0.505	0.051	0.05570	0.00562	0.112	411	5	415	34	441	210	93
9.1	232	16	0.07	14	-	-	0.0711	0.0009	0.540	0.007	0.05514	0.00023	0.948	443	5	439	5	418	9	106
10.1	342	45	0.13	18	-	-	0.0600	0.0006	0.447	0.005	0.05404	0.00024	0.904	375	3	375	3	373	10	101
11.1	383	30	0.08	24	3042	0.594	0.0712	0.0005	0.498	0.022	0.05068	0.00216	0.172	444	3	410	15	226	96	196
12.1	1223	18	0.01	55	35432	0.052	0.0515	0.0004	0.371	0.004	0.05224	0.00043	0.659	324	2	320	3	296	19	109
13.1	421	62	0.15	22	8771	0.207	0.0596	0.0006	0.427	0.010	0.05201	0.00113	0.418	373	4	361	7	286	49	131
14.1	385	25	0.07	25	-	-	0.0748	0.0010	0.585	0.009	0.05672	0.00033	0.919	465	6	467	6	481	13	97
15.1	378	27	0.07	23	10445	0.173	0.0692	0.0004	0.500	0.011	0.05236	0.00110	0.278	431	3	411	7	301	47	143
16.1	1029	59	0.06	87	194240	0.009	0.1017	0.0008	1.262	0.013	0.09001	0.00058	0.768	624	5	829	6	1426	12	44
17.1	264	23	0.09	12	1761	1.036	0.0539	0.0005	0.343	0.033	0.04609	0.00443	0.088	339	3	299	25	2	216	13993
18.1	115	15	0.13	5	2727	0.669	0.0551	0.0005	0.374	0.024	0.04923	0.00315	0.135	346	3	322	18	159	143	218
19.1	275	135	0.49	12.6	3496	0.522	0.0527	0.0003	0.351	0.018	0.04830	0.00240	0.121	331	2	305	13	114	113	290
20.1	505	81	0.16	23.9	1277	1.429	0.0547	0.0004	0.399	0.029	0.05294	0.00386	0.106	343	3	341	21	326	158	105
21.1	5345	86	0.02	249.6	59524	0.031	0.0539	0.0004	0.390	0.004	0.05241	0.00041	0.702	339	3	334	3	303	18	112

Falsic granulite EV389N (Les Belles Fourrières, 7°6'56"E; 48°10'47"N)

Grain. spot	U (ppm)	Th (ppm)	Th/U	²⁰⁶ Pb* (ppm)	²⁰⁶ Pb/ ²⁰⁴ Pb	f ₂₀₆ %	Radiogenic ratios					Age (Ma)					Conc. %			
							²⁰⁶ Pb/ ²³⁸ U	±	²⁰⁷ Pb/ ²³⁵ U	±	²⁰⁷ Pb/ ²⁰⁶ Pb	±	p	²⁰⁶ Pb/ ²³⁸ U	±	²⁰⁷ Pb/ ²³⁵ U		±	²⁰⁷ Pb/ ²⁰⁶ Pb	±
1.1	506	79	0.16	22	-	-	0.0513	0.0004	0.3696	0.0037	0.05222	0.00038	0.704	323	2	319	3	295	16	109
2.1	271	36	0.13	20	6180	0.290	0.0831	0.0009	0.6307	0.0185	0.05505	0.00151	0.359	515	5	497	11	414	60	124
4.1	218	11	0.05	10	19699	0.093	0.0516	0.0004	0.3707	0.0059	0.05211	0.00074	0.446	324	2	320	4	290	32	112
6.1	1237	13	0.01	57	-	-	0.0529	0.0003	0.3799	0.0034	0.05204	0.00031	0.737	333	2	327	2	287	14	116
7.1	239	10	0.04	14	-	-	0.0690	0.0005	0.5257	0.0042	0.05526	0.00024	0.839	430	3	429	3	423	10	102
8.1	596	114	0.19	43	3950	0.454	0.0834	0.0008	0.6560	0.0288	0.05706	0.00245	0.214	516	5	512	18	494	92	105
9.1	1488	115	0.08	89	1105	1.636	0.0690	0.0006	0.4863	0.0715	0.05215	0.00750	0.058	430	3	409	47	292	299	147
10.1	187	7	0.03	9	1503	1.214	0.0533	0.0005	0.3083	0.0382	0.04197	0.00518	0.079	335	3	273	29	-	-	-
11.1	313	23	0.07	15	5462	0.334	0.0548	0.0004	0.3731	0.0127	0.04936	0.00164	0.212	344	2	322	9	165	76	209
12.1	233	42	0.18	13	-	-	0.0643	0.0005	0.4818	0.0045	0.05438	0.00030	0.801	401	3	399	3	387	12	104
13.1	147	5	0.04	7	4327	0.421	0.0553	0.0004	0.3788	0.0155	0.04965	0.00200	0.185	347	3	326	11	179	91	194
14.1	870	122	0.14	42	1223	1.490	0.0562	0.0008	0.3987	0.0227	0.05144	0.00283	0.260	353	5	341	16	261	122	135
15.1	347	51	0.15	17	-	-	0.0551	0.0004	0.4029	0.0036	0.05301	0.00026	0.837	346	3	344	3	329	11	105
16.1	271	11	0.04	18	-	-	0.0771	0.0008	0.5993	0.0066	0.05639	0.00028	0.890	479	5	477	4	468	11	102
17.1	590	11	0.02	31	-	-	0.0603	0.0005	0.4550	0.0044	0.05470	0.00025	0.877	378	3	381	3	400	10	94
18.1	2617	26	0.01	127	32820	0.056	0.0561	0.0003	0.4035	0.0043	0.05216	0.00045	0.582	352	2	344	3	292	20	120
19.1	202	11	0.05	9.6	9966	0.183	0.0547	0.0004	0.3878	0.0084	0.05143	0.00103	0.375	343	3	333	6	260	45	132
20.1	298	38	0.13	14.0	-	-	0.0542	0.0004	0.4008	0.0036	0.05365	0.00026	0.833	340	2	342	3	356	11	95

Notes :

1. Uncertainties given at 1σ level
2. f₂₀₆ % denotes the percentage of ²⁰⁶Pb that is initial Pb
3. The correction for initial lead is based on the ²⁰⁴Pb/²⁰⁶Pb ratio
4. % Conc. = percentage of concordancy. 100% expresses a concordant analysis

Annexe 11. Analyses roches totales (Vosges).

		unit	SiO ₂	Al ₂ O ₃	Fe ₂ O ₃	MgO	CaO	Na ₂ O	K ₂ O	TiO ₂	P ₂ O ₅	MnO	Cr ₂ O ₃	LOI	Sum
		detection limit	wt.%	wt.%	wt.%	wt.%	wt.%	wt.%	wt.%	wt.%	wt.%	wt.%	wt.%	wt.%	wt.%
EV 308 A	micaschist		71.24	14.57	5.20	1.35	0.10	0.81	2.76	0.61	0.13	0.03	0.009	3	99.809
EV 67 M	gneiss		71.90	13.46	3.66	1.35	1.02	3.50	1.65	0.43	0.09	0.09	0.013	1.50	98.670
EV 69 M	gneiss		58.09	21.00	7.66	3.04	0.53	1.45	3.97	1.01	0.16	0.07	0.016	2.7	99.696
EV 315 A	gneiss		51.11	20.40	11.78	4.54	1.34	5.52	1.40	0.76	0.15	0.14	0.014	2.5	99.654
EV 315 P	gneiss		54.26	20.93	9.98	3.27	1.00	5.44	1.50	0.85	0.19	0.13	0.015	2.2	99.765
EV 83 M	gneiss		64.83	15.45	6.51	2.90	1.33	2.63	3.13	0.85	0.08	0.08	0.014	1.9	99.704
EV 90 M	gneiss		61.30	15.47	5.28	3.43	3.53	3.21	3.98	0.70	0.35	0.09	0.026	1.68	99.050
EV 141 C	gneiss		61.25	16.55	8.40	3.73	2.60	2.52	2.96	1.04	0.17	0.18	0.018	0.3	99.718
EV 342 A	gneiss		62.17	15.33	8.07	4.94	1.29	2.23	1.68	0.95	0.08	0.10	0.039	2.8	99.679
EV 340 B	gneiss		63.76	16.78	7.01	3.16	1.09	2.15	3.43	0.84	0.07	0.08	0.016	1.3	99.686
EV 341 B	gneiss		53.60	12.73	10.40	9.09	3.44	0.50	2.20	1.75	1.96	0.10	0.167	4.89	100.825
EV 343 M	gneiss		63.40	15.46	6.23	3.03	1.72	2.85	2.98	0.96	0.16	0.07	0.026	1.72	98.609
EV 136 M	granulite		75.90	13.06	1.27	0.62	0.34	3.24	4.74	0.12	0.15	0.02	d.l.	0.4	99.860
EV 136 N	granulite		78.80	12.18	0.96	0.31	0.29	3.00	4.45	0.11	0.30	0.02	d.l.	0.47	100.881
EV 350 M	granulite		68.32	15.43	4.30	1.48	0.90	2.50	5.15	0.68	0.19	0.05	0.006	0.7	99.706
EV 357 M	granulite		75.83	12.76	2.20	0.40	0.58	2.81	4.64	0.18	0.04	0.05	d.l.	0.4	99.890
EV 389 M	granulite		77.23	12.22	1.13	0.40	0.28	3.41	4.44	0.13	0.14	0.02	d.l.	0.5	99.900
EV 390 M	granulite		77.82	11.77	1.61	0.33	0.52	2.66	4.55	0.13	0.15	0.02	d.l.	0.4	99.960
EV 390 R	granulite		78.02	11.91	0.90	0.33	0.52	3.33	3.75	0.13	0.20	0.01	d.l.	0.8	99.900
EV 394 B	granulite		70.74	13.73	5.22	2.59	0.58	1.92	3.17	0.52	0.06	0.07	0.009	1.1	99.709
EV 380 M	durbachite		61.48	15.63	5.27	3.59	2.10	2.85	4.73	0.89	0.59	0.06	0.023	2.3	99.513
EV 380 N	durbachite		63.19	15.07	4.74	3.07	1.55	2.74	5.47	0.81	0.53	0.05	0.021	2.3	99.541
EV 381 M	durbachite		49.40	15.45	7.77	7.47	5.42	1.97	6.65	1.38	1.26	0.11	0.059	2.3	99.239
EV 381 N	durbachite		47.45	14.42	8.89	8.59	6.33	1.72	5.01	1.39	1.46	0.14	0.081	3.9	99.381
EV 382 M	durbachite		48.84	13.64	8.97	9.27	5.46	1.62	6.50	1.52	1.50	0.13	0.085	1.7	99.235
EV 382 N	durbachite		48.81	13.25	8.84	9.84	5.44	1.67	6.19	1.45	1.50	0.14	0.091	2.1	99.321
EV 382 O	durbachite		48.08	13.90	8.84	9.16	6.38	1.54	6.39	1.46	1.53	0.13	0.078	1.8	99.288
K1-30 A	gabbro		52.00	17.63	5.76	8.98	9.92	2.94	0.99	0.29	0.10	0.13	0.065	2.15	100.963
K1-17 D	gabbro		52.20	20.17	5.25	6.71	7.67	2.98	1.98	0.30	d.l.	0.12	0.112	1.99	99.474
K2-21 A	gabbro		48.40	16.58	7.01	10.80	7.67	3.24	0.96	0.31	d.l.	0.12	0.115	3.03	98.240
K3-14 A	gabbro		50.80	10.93	8.10	11.00	13.44	1.50	1.07	0.86	d.l.	0.18	0.492	1.29	99.664
K3-30 A	gabbro		52.60	13.79	7.73	9.93	9.32	2.85	0.90	0.60	d.l.	0.15	0.146	1.41	99.421
K3-30 B	gabbro		53.90	15.42	7.30	8.10	8.88	3.17	1.46	0.68	d.l.	0.16	0.139	1.53	100.727

n.a. = not analysed ; d.l. = below detection limit

	unit detection limit	La ppm	Ce ppm	Pr ppm	Nd ppm	Sm ppm	Eu ppm	Gd ppm	Tb ppm	Dy ppm	Ho ppm	Er ppm	Tm ppm	Yb ppm
EV 308 A		42.9	98.4	10.06	38.8	6.70	1.22	6.04	0.92	5.28	1.04	3.15	0.46	2.96
EV 67 M		26.2	52.8	6.09	22.90	4.47	0.84	3.80	0.60	3.72	0.77	2.10	0.33	2.05
EV 69 M		43.4	93.5	10.69	41.2	7.69	1.38	6.37	1.05	5.84	1.05	3.22	0.47	3.19
EV 315 A		42.2	89.4	10.42	39.1	7.49	1.44	7.31	1.32	7.57	1.69	5.12	0.78	4.96
EV 315 P		40.0	86.9	10.21	36.8	7.43	1.40	6.59	1.03	5.57	1.17	3.52	0.53	3.40
EV 83 M		44.2	91.8	10.24	38.1	6.76	1.51	5.79	0.94	5.63	1.13	3.65	0.54	3.68
EV 90 M		34.8	73.0	9.20	35.59	6.98	1.12	5.10	0.70	4.20	0.79	2.03	0.31	1.84
EV 141 C		43.8	93.9	10.49	38.5	7.32	1.57	6.83	1.10	6.10	1.33	3.82	0.59	3.69
EV 342 A		45.9	99.5	10.83	40.5	6.99	1.33	5.92	0.82	4.38	1.01	2.98	0.47	3.27
EV 340 B		44.0	94.4	10.05	36.2	6.93	1.44	6.56	1.03	5.72	1.19	3.51	0.53	3.50
EV 341 B		53.1	141.0	21.85	106.00	28.79	3.25	17.30	2.10	9.62	1.72	3.95	0.62	3.33
EV 343 M		57.3	117.0	14.11	53.15	10.41	1.44	8.40	1.30	7.21	1.54	3.94	0.69	3.88
EV 136 M		10.0	23.9	2.9	11.5	2.71	0.39	2.62	0.57	3.41	0.83	2.62	0.42	2.65
EV 136 N		7.4	15.6	1.74	6.05	1.37	0.21	1.50	0.40	2.99	0.70	1.96	0.41	2.43
EV 350 M		32.0	72.2	8.42	33.2	6.93	1.06	7.25	1.36	7.56	1.66	4.72	0.65	3.86
EV 357 M		15.4	33.6	3.82	15.3	3.82	0.31	5.00	1.13	7.36	1.80	5.29	0.83	5.27
EV 389 M		11.3	26.6	2.89	9.8	1.56	0.20	1.91	0.50	3.50	0.87	2.75	0.42	2.65
EV 390 M		9.6	20.3	2.17	7.4	1.64	0.36	2.01	0.53	4.15	1.02	3.45	0.53	3.20
EV 390 R		8.1	19.0	2.35	9.2	2.43	0.21	2.58	0.63	4.18	1.00	3.06	0.47	2.85
EV 394 B		33.1	70.5	7.74	29.4	5.29	1.23	5.47	0.99	5.60	1.16	3.54	0.53	3.25
EV 380 M		90.0	198.4	22.45	86.6	16.45	2.10	11.23	1.69	8.63	1.55	3.85	0.49	2.67
EV 380 N		58.9	144.0	15.34	58.1	10.91	1.85	8.35	1.33	6.68	1.24	3.35	0.41	2.29
EV 381 M		46.6	118.3	15.64	70.8	15.03	3.06	9.51	1.25	5.79	1.09	2.71	0.40	2.35
EV 381 N		51.1	132.0	17.42	78.6	17.21	3.16	10.57	1.37	6.64	1.14	3.08	0.42	2.41
EV 382 M		48.0	124.3	17.24	78.3	16.99	2.78	11.56	1.49	7.08	1.23	3.30	0.45	2.57
EV 382 N		56.6	140.7	18.66	86.2	18.89	2.85	11.54	1.50	6.82	1.19	3.18	0.44	2.71
EV 382 O		51.3	136.4	18.16	79.9	18.44	2.80	12.11	1.52	7.30	1.21	3.16	0.44	2.66
K1-30 A		0.8	1.8	0.26	1.70	0.72	0.40	1.00	d.l.	1.37	0.27	0.75	0.09	0.69
K1-17 D		1.1	1.5	0.32	1.90	0.68	0.43	0.90	d.l.	1.21	0.24	0.66	0.07	0.60
K2-21 A		0.9	2.0	0.35	2.18	0.88	0.41	1.10	0.20	1.56	0.31	0.88	0.11	0.82
K3-14 A		0.6	2.5	0.54	3.85	1.85	0.61	2.70	0.50	3.74	0.76	2.07	0.29	1.96
K3-30 A		1.0	2.8	0.52	3.33	1.38	0.81	1.90	0.40	2.67	0.56	1.50	0.22	1.40
K3-30 B		0.6	2.1	0.39	2.75	1.21	0.80	1.70	0.30	2.44	0.51	1.40	0.20	1.31

n.a. = not analysed ; 'd.l.' = below detection limit

		Lu	Mo	Cu	Pb	Zn	Ni	As	Cd	Sb	Bi	Ag	Au	Hg	Tl	Se	FeO
	<i>unit</i>	<i>ppm</i>	<i>ppm</i>	<i>ppm</i>	<i>ppm</i>	<i>ppm</i>	<i>ppm</i>	<i>ppm</i>	<i>ppm</i>	<i>ppm</i>	<i>ppm</i>	<i>ppm</i>	<i>ppb</i>	<i>ppm</i>	<i>ppm</i>	<i>ppm</i>	<i>wt%</i>
	<i>detection limit</i>	0.01	0.1	0.1	0.1	1	0.1	0.5	0.1	0.1	0.1	0.1	0.5	0.01	0.1	0.5	0.01
EY 308 A	metaschist	0.44	0.1	21.1	3.3	52	29.9	3.1	d.l.	d.l.	d.l.	d.l.	0.7	d.l.	d.l.	d.l.	n.a.
EY 67 M	gneiss	0.30	d.l.	d.l.	11.8	60	n.a.	9.1	n.a.	0.3	n.a.	n.a.	0.8	n.a.	n.a.	n.a.	n.a.
EY 69 M	gneiss	0.49	d.l.	26.3	3.8	94	28.5	0.6	d.l.	0.2	d.l.	d.l.	0.8	d.l.	0.3	d.l.	n.a.
EY 315 A	gneiss	0.74	0.7	2.1	6.6	108	70.2	10.4	d.l.	1.0	0.5	d.l.	2.9	d.l.	0.2	d.l.	n.a.
EY 315 P	gneiss	0.54	0.3	6.4	1.3	51	43.5	2.6	d.l.	0.7	d.l.	d.l.	d.l.	d.l.	d.l.	d.l.	n.a.
EY 83 M	gneiss	0.55	0.3	33.8	6.9	73	37.2	3.5	0.1	d.l.	d.l.	d.l.	d.l.	d.l.	d.l.	d.l.	n.a.
EY 90 M	gneiss	0.27	d.l.	d.l.	28.1	140	n.a.	29.2	n.a.	0.3	n.a.	n.a.	n.a.	n.a.	n.a.	n.a.	n.a.
EY 141 C	gneiss	0.59	1.1	17.1	1.7	79	39.6	d.l.	d.l.	d.l.	d.l.	d.l.	d.l.	d.l.	0.3	d.l.	7.25
EY 342 A	gneiss	0.48	0.7	40.0	6.3	121	71.7	2.0	0.2	d.l.	d.l.	d.l.	d.l.	d.l.	d.l.	d.l.	5.91
EY 340 B	gneiss	0.54	0.9	32.8	2.9	68	16.1	0.9	d.l.	d.l.	d.l.	d.l.	d.l.	d.l.	0.2	0.6	5.25
EY 341 B	gneiss	0.49	0.3	80.0	15.8	180	n.a.	52.8	n.a.	0.5	n.a.	n.a.	n.a.	n.a.	n.a.	n.a.	n.a.
EY 343 M	gneiss	0.62	0.7	d.l.	19.9	90	n.a.	4.8	n.a.	0.3	n.a.	n.a.	n.a.	n.a.	n.a.	n.a.	n.a.
EY 136 M	granulite	0.39	d.l.	0.9	0.7	5	8.1	d.l.	d.l.	d.l.	d.l.	d.l.	d.l.	d.l.	d.l.	d.l.	n.a.
EY 136 N	granulite	0.38	d.l.	d.l.	7.0	20	n.a.	0.5	n.a.	0.1	n.a.	n.a.	0.8	n.a.	n.a.	n.a.	n.a.
EY 350 M	granulite	0.57	0.3	17.5	1.4	16	10.5	2.8	d.l.	0.2	d.l.	d.l.	1.0	d.l.	d.l.	d.l.	n.a.
EY 357 M	granulite	0.78	d.l.	0.7	1.3	7	2.2	0.7	d.l.	d.l.	d.l.	d.l.	d.l.	d.l.	d.l.	d.l.	n.a.
EY 389 M	granulite	0.39	d.l.	1.0	2.1	10	2.0	1.4	d.l.	0.1	d.l.	d.l.	d.l.	d.l.	d.l.	d.l.	n.a.
EY 390 M	granulite	0.46	d.l.	0.3	1.0	8	2.9	0.6	d.l.	2.5	d.l.	d.l.	d.l.	d.l.	d.l.	d.l.	1.27
EY 390 R	granulite	0.39	d.l.	1.0	0.6	8	3.1	0.5	d.l.	d.l.	d.l.	d.l.	0.8	d.l.	d.l.	d.l.	n.a.
EY 394 B	granulite	0.53	0.2	12.9	1.4	27	24.1	0.8	0.1	d.l.	d.l.	d.l.	d.l.	d.l.	d.l.	d.l.	4.56
EY 380 M	durbachite	0.39	d.l.	27.0	5.6	63	38.5	8.4	d.l.	d.l.	d.l.	d.l.	1.2	d.l.	d.l.	d.l.	n.a.
EY 380 N	durbachite	0.34	d.l.	24.6	5.4	53	39.0	8.4	d.l.	d.l.	d.l.	d.l.	d.l.	d.l.	d.l.	0.5	n.a.
EY 381 M	durbachite	0.34	d.l.	28.7	4.8	75	66.7	1.2	d.l.	d.l.	d.l.	d.l.	d.l.	d.l.	1.4	d.l.	n.a.
EY 382 M	durbachite	0.35	d.l.	5.6	2.8	74	73.8	1.8	d.l.	d.l.	d.l.	d.l.	d.l.	d.l.	0.3	d.l.	n.a.
EY 382 N	durbachite	0.38	0.2	38.2	8.5	87	93.8	0.9	d.l.	d.l.	d.l.	d.l.	d.l.	d.l.	1.3	d.l.	n.a.
EY 382 O	durbachite	0.39	0.6	37.0	71.8	88	110.1	9.3	d.l.	d.l.	d.l.	d.l.	d.l.	d.l.	2.3	d.l.	n.a.
EY 382 O	durbachite	0.38	0.1	27.6	6.3	80	61.1	1.4	d.l.	d.l.	d.l.	d.l.	d.l.	d.l.	1.9	d.l.	n.a.
K1-30 A	gabbro	0.07	d.l.	d.l.	4.8	60	n.a.	1.5	n.a.	1.1	n.a.	n.a.	n.a.	n.a.	n.a.	n.a.	n.a.
K1-17 D	gabbro	0.06	d.l.	d.l.	6.8	120	n.a.	3.1	n.a.	2.1	n.a.	n.a.	n.a.	n.a.	n.a.	n.a.	n.a.
K2-21 A	gabbro	0.09	d.l.	30.0	8.8	70	n.a.	13.2	n.a.	0.8	n.a.	n.a.	n.a.	n.a.	n.a.	n.a.	n.a.
K3-14 A	gabbro	0.25	d.l.	d.l.	6.8	90	n.a.	4.8	n.a.	4.6	n.a.	n.a.	n.a.	n.a.	n.a.	n.a.	n.a.
K3-30 A	gabbro	0.19	d.l.	d.l.	6.2	60	n.a.	1.4	n.a.	0.6	n.a.	n.a.	n.a.	n.a.	n.a.	n.a.	n.a.
K3-30 B	gabbro	0.17	d.l.	d.l.	8.7	60	n.a.	2.7	n.a.	0.4	n.a.	n.a.	n.a.	n.a.	n.a.	n.a.	n.a.

n.a. = not analysed ; 'd.l.' = below detection limit

LISTE DES FIGURES

PART ONE - ORLICA-ŚNIEŻNIK DOME (SUDETES)

Chapter I : Geological background

- Figure 1.** Map of the Variscan Belt in Central Europe. 50
- Figure 2.** Geological map of the Sudetes. 53
- Figure 3.** Geological map of the Orlica-Śnieżnik Dome and the surrounding units. 57
- Figure 4.** Bederke's (1944) section across the central part of the OSD. 60

Chapter II : Structural evolution

- Figure 5.** Structural map of the northern domain. 64
- Figure 6.** Structural record in the Łądek Zdrój-Javorník valley (northern domain). 65
- Figure 7.** Photographs showing the succession of structures in the northern domain. 66
- Figure 8.** Photographs showing the structures in the Łądek Zdrój-Javorník valley. 67
- Figure 9.** Photographs showing structural details in the Łądek Zdrój-Javorník valley. 68
- Figure 10.** Structural map of the Młynowiec formation. 70
- Figure 11.** Photographs showing the structures in the Młynowiec formation. 71
- Figure 12.** Photographs showing the structures in the Stronie formation, central domain. 72
- Figure 13.** Structural map of the central domain. 73
- Figure 14.** Structural maps of the southern domain. 75
- Figure 15.** Photographs showing the structures in orthogneiss and eclogite, southern domain. 76
- Figure 16.** Photographs showing the structures in metasediments, southern domain. 77

Chapter III : Tectono-metamorphic evolution

- Figure 17.** Photomicrographs of S2 metamorphic minerals near the granulite belt. 85
- Figure 18.** Photomicrographs of S2 and S3 metamorphic minerals near the granulite belt. 86
- Figure 19.** Summary of crystallisation-deformation relationships near the granulite belt. 88
- Figure 20.** Photomicrographs and BSE image of sample M1B. 89
- Figure 21.** Measured and modelled garnet profiles for sample M1B. 89
- Figure 22.** *P-T* pseudosection for sample M1B. 91
- Figure 23.** Photomicrographs of S1 metamorphic minerals near the Javorník granitoid. 94
- Figure 24.** Photomicrographs of S2 and S3 metamorphic minerals near the Javorník granitoid. 96
- Figure 25.** Summary of crystallisation-deformation relationships near the Javorník granitoid. 97
- Figure 26.** Compositional X-ray maps for garnet porphyroblasts of samples M35D and M35H. 98
- Figure 27.** Compositional profiles for garnet porphyroblasts of samples M35D, M35H and M35i. 99

Figure 28. <i>P–T</i> pseudosection for sample M35i.	102
Figure 29. Illustrations of S1, S2 and S3 metamorphic minerals near the eclogite belt.	104
Figure 30. Summary of crystallisation-deformation relationships near the eclogite belt.	105
Figure 31. Garnet profile for sample ES95D.	106
Figure 32. <i>P–T</i> pseudosection for sample ES95D.	108
Figure 33. Photomicrographs of S2 and S3 metamorphic minerals in the central domain.	110
Figure 34. Summary of crystallisation-deformation relationships in the central domain.	111
Figure 35. Qualitative <i>P–T–D</i> evolutions for the different parts of the central domain.	113
Figure 36. Photomicrographs of metamorphic minerals in the Młynowiec formation.	115
Figure 37. Synthesis of <i>P–T–D</i> data for the Stronie-Młynowiec formation.	117
 Chapter IV : Constraints from garnet porphyroblasts	
Figure 38. Schematic view of the structural domains sampled for EBSD analysis.	120
Figure 39. Photomicrographs of the different structural domains.	121
Figure 40. Photomicrographs of the different garnet types.	123
Figure 41. SEM images of ilmenite inclusions in garnet porphyroblasts.	125
Figure 42. Representative microstructural results obtained using EBSD analysis.	127
Figure 43. S_i – S_e relationships in garnet porphyroblasts and microstructural results (1).	129
Figure 44. S_i – S_e relationships in garnet porphyroblasts and microstructural results (2).	130
Figure 45. Summary of planar and linear structures measured in garnet porphyroblasts.	131
Figure 46. Ilmenite axial ratio and histogram of [c] axis plunge vs. [c] axis plunge.	131
Figure 47. Idealised sketches illustrating garnet internal records.	132
Figure 48. Qualitative and quantitative garnet chemistry for samples ES2C and ES36L.	135
Figure 49. <i>P–T</i> pseudosections for samples ES2C and ES36L.	138
Figure 50. Summary of internal records in garnet porphyroblasts.	140
 Chapter V : Chronological constraints	
Figure 51. BSE images of monazite grains near the granulite belt (M81-2A).	145
Figure 52. PbO, ThO ₂ , UO ₂ and Y ₂ O ₃ concentrations in analysed monazite grains.	146
Figure 53. Monazite chemistry for the different metapelite samples.	147
Figure 54. Compositional X-ray maps for monazites of samples M81-2A and M35D.	147
Figure 55. U–Th–Pb monazite age results for the investigated samples.	148
Figure 56. BSE images of monazite grains near the Javorník granitoid (M35D).	150
Figure 57. BSE images of monazite grains near the eclogite belt (ES95CIII).	152
Figure 58. Summary of monazite growth along the different <i>P–T–D</i> evolutions.	155

Chapter VI : Burial and exhumation processes

Figure 59. Compilation of P – T paths for various burial and exhumation mechanisms.	160
Figure 60. Tectono-metamorphic evolution of the orogenic crust in the OSD.	165
Figure 61. Schematic evolution of the orogenic crust from thickening to exhumation.	168

PART TWO - VOSGES MOUNTAINS (NE FRANCE)

Chapter I : Late Devonian ophiolites (Southern Vosges Klippen Belt)

Figure 62. Devonian ophiolites in the Variscan Belt of Europe.	183
Figure 63. Lithology of the Southern Vosges and detailed maps of the Klippen Belt.	184
Figure 64. Lithostratigraphic columns for the Southern Vosges units.	185
Figure 65. Photographs of lithologies and structures within and around the Klippen Belt.	187
Figure 66. Structural and gravity anomaly maps for the Southern Vosges.	191
Figure 67. Mineral chemistry for pyroxene and plagioclase in gabbro of the Klippen belt.	192
Figure 68. Trace element compositions of gabbro.	194
Figure 69. Images of samples and zircon crystals used for geochronology.	196
Figure 70. U–Pb Concordia diagrams for gneiss sample K2-16B of the Klippen Belt.	197
Figure 71. Sm–Nd isochron for gabbro sample K2-21A of the Klippen Belt.	198
Figure 72. A possible geodynamic scenario for the Southern Vosges.	203
Figure 73. Chronological relationships between Palaeozoic basin sequences.	205

Chapter II : Significance of zircon records in high-grade rocks (Central Vosges root)

Figure 74. Geology of the Vosges orogenic root and position in the Variscan framework.	212
Figure 75. Cathodoluminescence images of analysed zircon grains.	214
Figure 76. Concordia diagrams with U–Pb zircon data for the monotonous gneiss unit.	217
Figure 77. Concordia diagrams with U–Pb zircon data for the varied gneiss unit.	219
Figure 78. Concordia diagrams with U–Pb zircon data for the felsic granulite unit.	222
Figure 79. U and Th zircon chemistry for the different lithological units.	223
Figure 80. Metamorphic assemblages in the varied gneiss and felsic granulite units.	225
Figure 81. Chemical profiles of garnet for the varied gneiss and felsic granulite samples.	226
Figure 82. Pseudosections for varied gneiss sample EV340B.	231
Figure 83. Pseudosections for felsic granulite sample EV390M.	233
Figure 84. Pseudosections with Zr-bearing models for varied gneiss sample EV340B.	235
Figure 85. Pseudosections with Zr-bearing models for felsic granulite sample EV390M.	237
Figure 86. Zircon behaviour during high-grade metamorphism in the Central Vosges.	241
Figure 87. Summary of U–Pb zircon ages for the Central Vosges metamorphic units.	244

Chapter III : Geodynamic evolution of the Variscan Vosges Mountains	
Figure 88. Lithotectonic zones in the Variscan Belt of Europe.	251
Figure 90. Synthetic lithostratigraphic columns for the Palaeozoic Vosges Mountains.	255
Figure 91. Summary of metamorphic results for the Vosges Mountains.	261
Figure 92. Summary of geochronological data for the Vosges Mountains.	263
Figure 93. Structural record in the Northern Vosges.	265
Figure 94. Photographs of structures in the Northern Vosges.	267
Figure 95. Structural record in the Central Vosges metamorphic units.	269
Figure 96. Photographs of structures in the Central Vosges metamorphic units.	270
Figure 97. Structural record in the Central Vosges.	273
Figure 98. Photographs of structures in the Central Vosges magmatic rocks.	274
Figure 99. Photographs of structures in the Southern Vosges.	276
Figure 100. Structural record in the Southern Vosges.	278
Figure 101. Synoptic view of Palaeozoic events in the Variscan Vosges.	281
Figure 102. Paleogeographic reconstructions for the evolution of the Variscan Belt.	285
Figure 103. Palaeozoic evolution of the Vosges basement.	291
Figure 104. Orientation and timing of Variscan deformation in the Vosges basement.	295

LISTE DES TABLES

PART ONE - ORLICA-ŚNIEŻNIK DOME (SUDETES)

Chapter III : Tectono-metamorphic evolution

Table 1. Major and minor element analyses for mica schist samples of the OSD.	81
Table 2. Major oxide compositions of samples used for mineral equilibria modelling.	83
Table 3. Representative chemical analyses for minerals of sample M1B.	90
Table 4. Representative chemical analyses for minerals of sample M35i.	100
Table 5. Representative chemical analyses for minerals of samples M35D, M35E and M35H.	101
Table 6. Representative chemical analyses for minerals of sample ES95D.	107

Chapter IV : Constraints from garnet porphyroblasts

Table 7. Orientation data of internal structures measured using EBSD analysis.	133
Table 8. Representative chemical analyses of garnet porphyroblasts.	136

Chapter V : Chronological constraints

Table 9. Analytical conditions and standards used for EMP monazite analysis.	144
Table 10. Representative monazite analyses for the investigated samples.	151

PART TWO - VOSGES MOUNTAINS (NE FRANCE)

Chapter I : Late Devonian ophiolites (Southern Vosges Klippen Belt)

Table 11. Summary of lithologies from the different klippen.	189
Table 12. Representative mineral analyses for gabbro of the Vosges Klippen Belt.	193
Table 13. Major and trace element compositions for gabbro of the Vosges Klippen Belt.	195
Table 14. LA-MC-ICP-MS U–Pb zircon data for gneiss sample K2-16B.	197
Table 15. Sm and Nd concentrations, and isotopic ratios for gabbro sample K2-21A.	199

Chapter II : Significance of zircon records in high-grade rocks (Central Vosges root)

Table 16. Representative chemical analyses for varied gneiss sample EV340B.	227
Table 17. Representative chemical analyses for felsic granulite sample EV390M.	228
Table 18. Major element and Zr composition of samples EV340B and EV390M.	237

Chapter III : Geodynamic evolution of the Variscan Vosges Mountains

Table 19. List of radiometric ages used for Fig. 92.	299
---	-----

LISTE DES ANNEXES

Annexe 1. Coordonnées géographiques des localités, dôme d'Orlica-Śnieżnik, Sudètes.	361
Annexe 2. Résultats des datations sur monazites, échantillon M81-2A (Javorník).	363
Annexe 3. Résultats des datations sur monazites, échantillon M35D (Bílá Voda).	365
Annexe 4. Résultats des datations sur monazites, échantillon ES95CIII (Międzygórze).	367
Annexe 5. Analytical procedure for EBSD analysis (Part 1-Chapter IV).	367
Annexe 6. Mineral abbreviations used in Part 2-Chapter II.	367
Annexe 7. Coordonnées géographiques des localités étudiées dans le massif vosgien.	368
Annexe 8. Analyses U–Pb sur zircons pour les échantillons de gneiss monotone.	386
Annexe 9. Analyses U–Pb sur zircons pour les échantillons de gneiss varié.	389
Annexe 10. Analyses U–Pb sur zircons pour les échantillons de granulite felsique.	392
Annexe 11. Analyses roches totales (Vosges).	395

TABLE DES MATIÈRES

SOMMAIRE	3
RÉSUMÉ	5
ABSTRACT	6
ZUSAMENFASSUNG	7
STRESZCZENIE	8
AVANT PROPOS	9
RÉSUMÉ ÉTENDU	10
INTRODUCTION	39
PART ONE : CONTRIBUTION OF MID-CRUSTAL STRUCTURAL, PETROLOGICAL AND GEOCHRONOLOGICAL RECORDS TO THE UNDERSTANDING OF INTRACONTINENTAL BURIAL AND EXHUMATION PROCESSES (SUDETES)	45
INTRODUCTION TO PART ONE	47
CHAPTER I – GEOLOGICAL BACKGROUND	49
1) Sudetes	49
<i>Western units (Lusatian zone, Görlitz Belt, Kaczawa unit)</i>	51
<i>Izera-Karkonosze Block</i>	51
<i>Intra-Sudetic Basin</i>	52
<i>Góry Sowie Block</i>	53
<i>Western and southern OSD mantle (Nové Město and Zabřeh units)</i>	54
<i>Eastern OSD mantle (Staré Město unit)</i>	55
<i>Moravo-Silesian zone</i>	56
2) Orlica-Śnieżnik Dome	56
<i>Lithology</i>	58
<i>Structure</i>	59
<i>Metamorphism</i>	60
<i>Protolith ages</i>	61
<i>Metamorphic ages</i>	62
CHAPTER II – STRUCTURAL EVOLUTION OF THE OROGENIC MIDDLE CRUST	63
1) Northern domain	63
<i>D1 structures</i>	63
<i>D2 structures</i>	64
<i>D3 structures</i>	68
2) Central domain	69
<i>S0 sedimentary bedding</i>	69
<i>D1 structures</i>	70
<i>D2 structures</i>	71
<i>D3 structures</i>	73

3) Southern domain	74
<i>D1 structures</i>	74
<i>D2 structures</i>	76
<i>D3 structures</i>	78
CHAPTER III – TECTONO-METAMORPHIC EVOLUTION OF THE OROGENIC MIDDLE CRUST	79
1) Methodology	79
<i>Petrography</i>	79
<i>Chemistry</i>	80
<i>Mineral equilibria modelling</i>	80
2) Tectono-metamorphic evolution near the granulite belt (northern domain)	83
<i>Petrography</i>	83
<i>Chemistry</i>	88
<i>Mineral equilibria modelling</i>	90
3) Tectono-metamorphic evolution near the Javornik granitoid (northern domain)	93
<i>Petrography</i>	93
<i>Chemistry</i>	98
<i>Mineral equilibria modelling</i>	101
4) Tectono-metamorphic evolution near the eclogite belt (southern domain)	105
<i>Petrography</i>	105
<i>Chemistry</i>	106
<i>Mineral equilibria modelling</i>	108
5) Tectono-metamorphic evolution across the central domain	109
<i>Petrography</i>	109
<i>Qualitative P–T–D evolutions</i>	112
6) Tectono-metamorphic evolution of the Mlynowiec formation (central domain)	114
<i>Petrography</i>	114
<i>Qualitative P–T–D evolution</i>	116
7) Summary of P–T–D relationships	116
<i>D1 parageneses</i>	116
<i>D2 parageneses</i>	116
<i>D3 parageneses</i>	118
CHAPTER IV – MICROSTRUCTURAL AND PETROLOGICAL CONSTRAINTS FROM GARNET PORPHYROBLASTS	119
1) Review of concepts and techniques	119
2) Sampled structural domains	119
<i>Domain of preserved S2 foliation – stages 1 to 2 of crenulation cleavage development</i>	120
<i>Domain of F3 fold hinge – stages 2 to 4 of crenulation cleavage development</i>	121
<i>Domain of F3 fold limb – stage 4 of crenulation cleavage development</i>	122
<i>Domain of continuous S3 foliation – stages 5 to 6 of crenulation cleavage development</i>	122

2) Garnet types	122
<i>Type I garnet</i>	122
<i>Type II garnet</i>	124
<i>Type III garnet</i>	124
<i>Type IV garnet</i>	124
3) Measurement technique	125
<i>Data processing</i>	125
<i>Matrix ilmenite data</i>	126
<i>Included ilmenite data</i>	126
4) Microstructural analysis of porphyroblast inclusion trails	128
<i>Internal foliations</i>	128
<i>Internal lineation</i>	130
<i>Foliation intersection axis</i>	132
5) Garnet chemistry and modelling	134
Garnet chemistry	134
<i>Sample ES2C, F3 fold hinge domain, Type I and III garnet porphyroblasts</i>	134
<i>Sample ES36L, S3 domain, Type II garnet porphyroblasts</i>	134
Garnet growth modelling	137
<i>Sample ES2C</i>	137
<i>Sample ES36L</i>	137
6) Microstructural evolution: garnet rotation and non-rotation	139
7) Metamorphic evolution: polyphase garnet growth and resorption	141
CHAPTER V – CHRONOLOGICAL CONSTRAINTS	115
1) Analytical procedure and data processing	143
<i>Electron microprobe analyses</i>	143
<i>Age calculation</i>	143
2) Monazite record near the granulite belt (northern domain)	144
<i>Sample description and monazite petrography</i>	144
<i>Monazite chemistry</i>	145
<i>Age results</i>	146
3) Monazite record near the Javorník granitoid (northern domain)	149
<i>Sample description and monazite petrography</i>	149
<i>Monazite chemistry</i>	149
<i>Age results</i>	149
4) Monazite record near the eclogite belt (southern domain)	151
<i>Sample description and monazite petrography</i>	151
<i>Monazite chemistry</i>	152
<i>Age results</i>	153

4) Interpretations	153
<i>Age significance near the granulite belt</i>	153
<i>Age significance near the Javorník granitoid</i>	154
<i>Age significance near the eclogite belt</i>	157
CHAPTER VI – BURIAL AND EXHUMATION PROCESSES	159
1) Burial–exhumation mechanisms and associated <i>P–T</i> paths	159
2) <i>P–T–D–t</i> relationships between metasediments and neighbouring rocks	160
<i>P–T–D–t relationships between metasediments and the granulite belt</i>	160
<i>P–T–D–t relationships between metasediments and the Javorník granitoid</i>	161
<i>P–T–D–t relationships between metasediments and the eclogite belt</i>	163
3) Tectonic significance of the <i>P–T–D–t</i> evolutions	164
<i>Tectonic significance of <i>P–T–D–t</i> evolutions in the subhorizontal S1 fabric</i>	164
<i>Tectonic significance of <i>P–T–D–t</i> evolutions in the subvertical S2 fabric</i>	166
<i>Tectonic significance of <i>P–T–D–t</i> evolutions in the shallow-dipping S3 fabric</i>	168
4) Diagnostic paired <i>P–T–D</i> paths?	170
SUMMARY AND CONCLUSIONS TO PART ONE	171
Summary	171
Porphyroblast microstructures	171
Monazite petrogenesis	172
Regional geology	172
Intracontinental tectonic processes	173
PART TWO : STRUCTURAL, PETROLOGICAL AND GEOCHRONOLOGICAL CHARACTERISATION OF INTRACONTINENTAL TECTONIC PROCESSES IN THE OROGENIC CRUST (VOSGES MOUNTAINS)	177
INTRODUCTION TO PART TWO	179
CHAPTER I – THE SIGNIFICANCE OF LATE DEVONIAN OPHIOLITES IN THE VARISCAN OROGEN: A RECORD FROM THE VOSGES KLIPPEN BELT	181
1) Introduction	181
2) Geological background	182
<i>Devonian ophiolites in the Variscan belt of Europe</i>	182
<i>Southern Vosges Mountains</i>	183
3) The Vosges Klippen Belt	185
<i>Lithology</i>	186
<i>Structural setting</i>	189
<i>Geophysical constraints</i>	190

4) Petrology and geochemistry of gabbroic rocks	192
<i>Analytical techniques</i>	192
<i>Mineral chemistry</i>	192
<i>Whole-rock geochemistry</i>	194
5) Geochronology	194
<i>U–Pb zircon dating</i>	194
<i>Sm–Nd dating</i>	198
6) Significance of the Southern Vosges Klippen Belt	199
<i>Lithological significance</i>	199
<i>Tectonic significance</i>	200
<i>Geochemical significance</i>	201
<i>Age significance</i>	202
<i>Geodynamic evolution of the Southern Vosges</i>	203
6) Significance in the Variscan Belt of Europe	205
<i>Origin of the Southern Vosges basin</i>	205
<i>A tentative link</i>	206

CHAPTER II – THE ORIGIN OF ZIRCON AND THE SIGNIFICANCE OF U–Pb AGES DURING HIGH-GRADE METAMORPHISM: A CASE STUDY FROM THE VARISCAN OROGENIC ROOT (VOSGES MOUNTAINS, NE FRANCE)

1) Geological background	211
2) Geochronology	213
<i>Monotonous gneiss unit</i>	215
<i>Sample description</i>	215
<i>Zircon morphology and internal structures</i>	215
<i>U–Pb age results</i>	215
<i>Zircon chemistry</i>	216
<i>Varied gneiss unit</i>	217
<i>Sample description</i>	217
<i>Zircon morphology and internal structures</i>	218
<i>U–Pb age results</i>	218
<i>Zircon chemistry</i>	220
<i>Felsic granulite unit</i>	220
<i>Sample description</i>	220
<i>Zircon morphology</i>	221
<i>U–Pb age results</i>	221
<i>Zircon chemistry</i>	224
3) Petrography and mineral chemistry	224
<i>Varied gneiss unit</i>	224
<i>Felsic granulite unit</i>	226

4) Mineral equilibria modelling	229
<i>Calculation method</i>	229
<i>Assessing the P–T evolution in the NCKFMASHTO system</i>	229
<i>Varied gneiss - Pseudosection with dry solidus</i>	229
<i>Varied gneiss - Pseudosection with re-integrated melt</i>	230
<i>Felsic granulite - Pseudosection with dry solidus</i>	232
<i>Felsic granulite - Pseudosection with re-integrated melt</i>	232
<i>Assessing zircon behaviour through the P–T evolution</i>	234
<i>Varied gneiss - Pseudosections with Zr-bearing models</i>	234
<i>Felsic granulite - Pseudosections with Zr-bearing models</i>	236
5) Metamorphic evolution of the orogenic root	238
<i>Monotonous gneiss unit</i>	238
<i>Varied gneiss unit</i>	238
<i>Felsic granulite unit</i>	239
6) Origin of Variscan metamorphic zircons	240
<i>Monotonous gneiss unit</i>	240
<i>Varied gneiss unit</i>	240
<i>Felsic granulite unit</i>	242
7) Zircon dissolution/crystallisation model	243
8) Geological implications	245
<i>Protolith ages</i>	245
<i>High-pressure metamorphism ?</i>	245
<i>High-temperature metamorphism</i>	246
<i>Tectonic evolution</i>	246
CHAPTER III – GEODYNAMIC EVOLUTION OF THE VARISCAN VOSGES MOUNTAINS	247
1) The Vosges Mountains in the Variscan Belt of Europe	247
2) Lithostratigraphy	250
<i>Northern Vosges</i>	252
<i>Northern succession (“Bruche” unit)</i>	252
<i>Magmatic suite (“Champ du Feu” magmatic suite)</i>	253
<i>Southern succession (“Villé” and “Steige” units)</i>	254
<i>Central Vosges</i>	257
<i>Metamorphic units</i>	257
<i>Magmatic units</i>	257
<i>Southern Vosges</i>	258
<i>Autochthonous units (“Oderen” and “Thann” units)</i>	258
<i>Allochthonous units (Klippen Belt and “Markstein” units)</i>	259
<i>Magmatic unit (“Ballons” magmatic unit)</i>	259

3) Metamorphic record	259
<i>Contact metamorphism</i>	260
<i>Low- to medium-grade metamorphism (Northern Vosges)</i>	260
<i>Medium- to high-grade metamorphism (Central Vosges)</i>	261
4) Geochronology	262
<i>Age of magmatism</i>	262
<i>Age of metamorphism</i>	264
5) Structural geology	264
<i>Northern Vosges</i>	266
<i>Northern succession</i>	266
<i>Magmatic suite</i>	266
<i>Southern succession</i>	267
<i>Central Vosges</i>	268
<i>Metamorphic units</i>	268
<i>Leucogranites</i>	271
<i>Western anatectic domain</i>	271
<i>Eastern anatectic domain</i>	272
<i>Mg-K magmatism</i>	275
<i>Southern Vosges</i>	277
<i>Autochthonous units</i>	277
<i>Allochthonous units</i>	277
<i>Mg-K magmatism</i>	279
6) Interpretations and discussion	279
<i>Early Palaeozoic: the pre-collisional history</i>	279
<i>The Saxothuringian basin</i>	280
<i>The Palaeotethys Ocean</i>	283
<i>The Rhenohercynian basin</i>	284
<i>Late Devonian: onset of collision</i>	286
<i>Subduction of the Saxothuringian passive margin - thickening of the orogenic root</i>	286
<i>Subduction of the Palaeotethys Ocean</i>	288
<i>The role of the Rhenohercynian basin</i>	288
<i>Early Lower Carboniferous: polyphase collisional tectonics</i>	289
<i>Burial and exhumation in the orogenic crust (D1)</i>	289
<i>Genesis of an intra-orogenic boundary zone (D2)</i>	290
<i>N-S Gondwana indentation (D3)</i>	294
<i>Late Lower Carboniferous: orogenic collapse</i>	295
<i>Kinematics and thermal conditions of extensional tectonics (D4)</i>	295
<i>Origin of orogenic collapse</i>	297

SUMMARY AND CONCLUSIONS TO PART TWO	301
Summary	301
Zircon petrogenesis	302
Regional and Variscan geology	302
Intracontinental tectonic processes	303
CONCLUSIONS	305
Analyse microstructurale et chronologie des processus métamorphiques	307
Evolution tectonique du dôme d’Orlica-Śnieżnik (Sudètes)	308
Evolution tectonique du massif vosgien (NE France)	308
Eléments de comparaison	309
Un orogène « hercynotype » ?	310
CONCLUDING REMARKS	311
Microstructural analysis and chronology of metamorphic processes	311
Tectonic evolution of the Orlica-Śnieżnik Dome (Sudetes)	312
Tectonic evolution of the Vosges Mountains (NE France)	312
Comparisons	313
“Hercynotype” orogen ?	314
BIBLIOGRAPHIE	315
Publications scientifiques associées au travail de thèse	353
REMERCIEMENTS	355
APPENDIX	359
LISTE DES FIGURES	399
LISTE DES TABLES	403
LISTE DES ANNEXES	404
TABLE DES MATIÈRES	405

CARTE HORS TEXTE – CARTE GÉOLOGIQUE ET STRUCTURALE DES VOSGES HERCYNiennes

ORGANISMES HÔTES / FINANCEURS



UNIVERSITÉ LOUIS PASTEUR,
STRASBOURG



UNIVERSITÉ DE STRASBOURG



RÉGION ALSACE



BUREAU DE RECHERCHES
GÉOLOGIQUES ET MINIÈRES

CARTE GÉOLOGIQUE ET STRUCTURALE DES VOSGES HERCYNIENNES

E. SKRZYPEK - 2011

Documents consultés pour l'établissement de la carte

Lithologie

- Carte géologique de la France au 1/50 000, feuilles : (270) Cirey-sur-Vézouze, (271) Molsheim, (305) Rambervillers, (306) Saint-Dié, (307) Sélestat, (340) Bruyères, (341) Gérardmer, (342) Colmar–Artolsheim, (375) Plombières-les-Bains, (376) Remiremont, (377) Munster, (378) Neuf-Brisach–Obersaasheim, (411) Giromagny, (412) Thann, (443) Lure et (444) Belfort.
- Carte géologique simplifiée du socle vosgien (Fluck *et al.*, 1987).
- Carte géologique harmonisée du département du Bas-Rhin (67) (Cruz-Mermy *et al.*, 2007).
- Carte géologique harmonisée du département du Haut-Rhin (67) (Skrzypek *et al.*, 2008).
- Carte géologique harmonisée du département du Vosges (88) (Chèvremont, 2008).
- Levés inédits de F. Ménillet pour l'établissement des cartes harmonisées des départements du Bas-Rhin, Haut-Rhin et Vosges.

Structure

- Complexe magmatique du Champ du Feu (Edel *et al.*, 2011).
- Granites de Thannenkirch–Bilstein–Brézouard (Kratinová *et al.*, 2007).
- Granito-gneiss (Rey, 1992).
- Migmatites de Gerbépal (Blumenfeld, 1986).
- Granite fondamental et migmatites de Kaysersberg–Trois-Epis (Schulmann *et al.*, 2009a; Kratinová *et al.*, 2011).
- Séries sédimentaires d'Oderen et Thann (Krecher, 2005).

CARTE GEOLOGIQUE ET STRUCTURALE

DES

VOSGES HERCYNiennes

E. SKRZYPEK

2011

Lithologie

- | | |
|--|--|
| Sédiments de la série de la Bruche (Dévonien moyen-Carbonifère) | Migmatites de Trois-Epis, Gerbépal (Cambrien-Ordovicien ?) |
| Volcanisme de Schirmeck-Rabodeau (Dévonien moyen) | Péridotites |
| Granites d'Andlau, Natzwiller, Kagenfels (Carbonifère inférieur) | Leucogranites (Carbonifère) |
| Granites du Champ du Feu Nord (Carbonifère inférieur) | Granite fondamental (Carbonifère) |
| Volcanisme de la Bande Médiane (Carbonifère inférieur) | Granites des Crêtes et Ballons (Carbonifère inférieur) |
| Granodiorite du Champ du Feu Sud (Carbonifère inférieur) | Sédiments de la série du Markstein (Viséen) |
| Diorites (Carbonifère inférieur) | Ligne des Klippes (Dévonien supérieur) |
| Schistes de Steige (Ordovicien-Silurien) | Sédiments de la série de Thann (Viséen supérieur) |
| Schistes de Villé (Cambrien-Ordovicien) | Volcanisme de la série de Thann (Viséen supérieur) |
| Unité des gneiss monotones (Ordovicien ?) | Sédiments de la série d'Oderen (Viséen inférieur) |
| Unité des gneiss variés (Ordovicien-Silurien ?) | Volcanisme de la série d'Oderen (Viséen inférieur) |
| Unité granulitique (Cambrien-Ordovicien) | Sédiments continentaux (Permien) |

Structure

Sédiments de la Bruche

- S0, stratigraphie
- S1, schistosité
- Axe de pli F1

Schistes de Steige

- S1, schistosité
- L0-1, linéation d'intersection

Schistes de Villé

- S1-2, foliation métamorphique
- Axe de pli F2

Roches magmatiques

- Foliation magnétique
- Linéation magnétique

Unités métamorphiques

- S1, foliation subverticale
- S2, foliation subhorizontale
- S2-3, S2 plissée
- Axe de pli F2
- Axe de pli F3
- Linéation d'étirement

Migmatites de Gerbépal

- Foliation migmatitique
- Linéation minérale

Sédiments des Vosges du Sud

- S0, stratigraphie
- Axe de pli F1

